

Београд, 21. априла 2017.

Научном већу Института за физику у Београду

**МОЛБА ЗА РЕИЗБОР У ЗВАЊЕ
НАУЧНИ САРАДНИК**

Молим Научно веће Института за физику, Прегревица 118, 11080 Земун-Београд, да одобри покретање поступка за реизбор др. Анђелије Илић, научног сарадника, у звање научни сарадник.

У прилогу су дати биографија кандидата, мишљење руководиоца пројекта ИИИ 45003, спискови и фотокопије научних радова и саопштења на научним скуповима, списак цитата, попуњена табела са квантитативним критеријумима, копија дипломе о стеченом научном степену доктора наука, као и одлука о претходном реизбору у звање научни сарадник.

С поштовањем,

Кандидат,

др. Анђелија Илић, научни сарадник

Београд, 21. априла 2017.

Научном већу Института за физику у Београду

Предмет: Мишљење руководиоца пројекта за реизбор др Анђелије Илић у звање научни сарадник

Др Анђелија Илић је запослена у Институту за физику од 1. новембра 2014. године. На пројекту интегралних и интердисциплинарних истраживања ИИИ 45003, „Оптоелектронски нанодимензиони системи - пут ка примени“, ангажована је од 1. јануара 2013. године. Бави се примењеном физиком и примењеном електромагнетиком, укључујући прорачуне електромагнетских поља различитих структура, анализу динамике честица и јонских снопова у сложеним пољима, развој нумеричких метода, примене нових материјала у електротехници, акцелераторске технологије и интеракцију електромагнетских поља са биолошким системима. Са обзиром на то да др Илић испуњава све услове за реизбор у звање предвиђене Правилником о поступку и начину вредновања и квантитативном исказивању научноистраживачких резултата Министарства просвете, науке и технолошког развоја, сагласан сам са покретањем поступка и предлажем реизбор др Анђелије Илић у звање научни сарадник.

С поштовањем,

Руководилац пројекта ИИИ 45003,

др. Небојша Ромчевић, научни саветник

др Анђелија Илић,
научни сарадник

Биографија

Др Анђелија Илић је рођена 18. јуна 1973. године у Београду. Основну школу „Браћа Рибар“ (сада „Краљ Петар Први“) завршила је 1988. године, као ђак генерације и носилац диплома „Вук Караџић“, „Михаило Петровић Алас“ и „Никола Тесла“. Средњу школу „Математичка гимназија“ завршила је 1992. године, као изузетна ученица и носилац дипломе „Вук Караџић“. Тада уписује Електротехнички факултет (ЕТФ) Универзитета у Београду, где се одлучује за Одсек за Електронику, Телекомуникације и Аутоматику, а као смер студија бира Електронику. Дипломирала је 1998. године, са просечном оценом 9,05 и оценом 10 на дипломском раду из области рачунарских телекомуникација. Ментор тезе под насловом „Комбиновани поступак синхронизације рама и заштитног кодовања за DS3 формат дигиталног преноса“ је проф. др Душан Драјић.

По дипломирању, од 1999. до 2001. године, др Илић је била ангажована као асистент у настави на предметима Основи Електротехнике и Електромагнетика на Електротехничком факултету Универзитета у Београду. Тада је отпочела и постдипломске студије. Била је ангажована на микроталасним мерењима у оквиру пројекта карактеризације диелектричних и магнетских материјала. Наредне две и по године је провела у Сједињеним Америчким Државама, где је 2002. године уписала постдипломске студије на University of Massachusetts Dartmouth (North Dartmouth, MA). Магистрирала је у јануару 2004. године са просечном оценом 3,88 (од могућих 4,00). Магистарску тезу „Optimal Large-Domain Hexahedral Meshing for Higher Order Finite Element Modeling in Electromagnetics“ је урадила и одбранила под руководством проф. др Бранислава Нотароша. Током студија је радила као Research Assistant на пројекту финансираном од стране National Science Foundation (NSF), у оквиру кога је развила методу и софтвер за аутоматизацију генерисања прорачунских мрежа за метод коначних елемената вишег реда. Сечена диплома магистра техничких наука је нострификована на Електротехничком факултету у Београду 2004. године.

Почев од 2004. године, др Илић је била запослена у Лабораторији за физику 010 Института за нуклеарне науке „Винча“. Наредних осам година се највише бавила анализом динамике јонских снопова, помоћу софтвера за анализу транспорта и убрзавања честица који је сама развила, и различитим применама у области акцелераторске физике. Била је укључена на пројекте Министарства просвете, науке и технолошког развоја: АИ Тесла 122473/111247, ОИ 151005, ИИИ 45006. Докторску дисертацију насловљену „Оптимално убрзавање честица у вишенамениским изохроним циклотронима“ одбранила је 12. октобра 2010. године на Електротехничком факултету Универзитета у Београду. Израдом тезе је руководила др Јасна Ристић-Ђуровић из Института за нуклеарне науке „Винча“, а ментор тезе је био проф. др Владимир Петровић са Електротехничког факултета. Између осталог, предложена је метода оптимизације убрзавања честица у изохроном циклотрону, која се истовремено одликује

веома високом тачношћу и релативно кратким временом израчунавања по једном скупу почетних услова. У звање научни сарадник изабрана је 25. маја 2011. године.

Након доктората, др Илић наставља истраживања у области акцелераторске физике и технологије, али се окреће и проналажењу нових тема и праваца истраживања којима ће се такође бавити. У јануару 2013. године почела је да ради на пројекту ИИИ 45003, чији руководилац, др Небојша Ромчевић, је научни саветник Института за физику. У јануару 2013. године је прешла из Института „Винча“ у Иновациони центар Електротехничког факултета у Београду, а од 1. новембра 2014. године је запослена у Институту за физику у Београду. У периоду од 2010. године на даље, заједно са колегама са пројекта, др Илић је била изузетно активна и дала значајан допринос приликом формирања мултидисциплинарног тима чије језгро сада чине три сарадника Института за физику и три професора Медицинског факултета Универзитета у Београду.

У периоду од 16. септембра 2013. године до 16. јула 2014. године, др Илић је била ангажована као пост-докторски истраживач у Групи за истраживања бежичних телекомуникација на University of Westminster, London, UK. Како је у питању била универзитетска размена преко EUROWEB програма, тема истраживања није била ограничена програмом. У договору са проф. др Ђурађем Будимиром, др Илић је отпочела истраживање могућности употребе нових дводимензионих материјала у уређајима за примене у области милиметарских и субмилиметарских таласа. Добијени су одлични први резултати, чиме је отворен нов правац даљег истраживања и успостављена је сарадња која ће се и даље наставити.

Након избора у звање научни сарадник др Илић је као први аутор публиковала седам радова у часописима са SCI листе, једно предавање по позиву штампано у изводу, два рада са међународног научног скупа штампана у целини, рад у часопису националног значаја и једно техничко решење категорије M_{84} . Од тога, два рада категорије M_{21} , објављена у *IEEE Transactions on Nuclear Science*, се ослањају на истраживања везана за тему доктората. Преосталих пет радова, категорија M_{21} , M_{22} , и M_{23} , отварају истраживачке правце којима се др Илић није раније бавила. Др Илић је коаутор бројних других радова у часописима и саопштења на конференцијама.

др Анђелија Илић,
научни сарадник

Преглед научне активности

Научно-истраживачки рад кандидаткиње је у области примењене физике и примењене електромагнетике. Рад укључује прорачуне електромагнетских поља различитих структура, анализу динамике честица и јонских снопова у сложеним пољима, развој нумеричких метода у физици и електромагнетици, примене нових материјала у електротехници, акцелераторску физику, интеракцију електромагнетских поља са биолошким системима, као и развој и оптимизацију иновативних уређаја за различите намене.

У периоду после избора у звање научног сарадника, издвајамо пет тема и праваца истраживања који говоре о самосталности кандидаткиње у научном раду и оригиналности њеног приступа решавању проблема. Затим ћемо укратко изложити најважније резултате осталих публикација и доприносе кандидаткиње у тим радовима.

У публикацији број 6, категорије M_{21} , кандидаткиња је развила нову методу за прецизно израчунавање параметара статичке равнотежне орбите честице у задатом магнетском пољу изохроног циклотрона. Поређење нове методе са највише коришћеном методом у литератури сведочи о потпуном слагању резултата за бетатронске учестаности и о чак нешто мањим одступањима у прорачуну орбиталних учестаности. Корак интеграције у временском домену се одређује на основу максималног дозвољеног одступања позиције и импулса у једном кораку. Језгро нове методе чини оптимизациони критеријум који узима у обзир симетричност, затвореност и центрираност статичке равнотежне орбите, коришћењем параметара орбите у неколико контролних тачака дуж пута интеграције. Кандидаткиња је развила ову методу током рада на докторској дисертацији и она је уграђена као помоћна процедура у софтвер за налажење оптималних убрзавајућих равнотежних орбита циклотрона. У другом делу рада број 6 наводе се различити проблеми где је од значаја тачно израчунавање статичких равнотежних орбита и где је истраживачки тим чији члан је и кандидаткиња имплементирао нову методу.

У публикацији број 7, категорије M_{21} , кандидаткиња је анализирао интеракцију електромагнетских таласа са покретним срединама користећи се методом коначних елемената. Извела је потребне математичке изразе за Лоренцове трансформације између референтног система из кога долази талас и референтног система везаног за покретну средину. На основу развијених израза саставила је нов алгоритам и нов софтвер заснован на методи коначних елемената вишег реда, што је, према претраживању постојеће литературе, први пример употребе пуноталасне (full-wave) методе у фреквенцијском домену за решавање проблема овог типа. Тренутно развијена метода и софтвер намењени су решавању једнодимензионих (1-D) проблема. Поређење резултата добијених новом методом са аналитичким решењима (где је то било могуће) показало је изузетно добро слагање и брзу конвергенцију нумеричког решења са повећањем броја непознатих. У новој методи коначних

елемената вишег реда, конвергенција се може постићи повећањем редова полиномске апроксимације поља (p -рафинирање) и/или повећањем броја елемената на основу уситњавања меша (h -рафинирање). У оквиру истраживачког рада у овој области извршена је и студија фактора који ограничавају домен примене нове методе и разлога који до тога доводе.

У раду број 2, категорије M_{21} , кандидаткиња је предложила и детаљно анализира нове тип фреквенцијски подесивих таласоводних резонатора за примене на субмилиметарским учестаностима. Овај ново отворени правац истраживања, који се бави могућностима и ограничењима реализације нових типова уређаја за примене у опсегу милиметарских, субмилиметарских и терахерц таласа, започет је у периоду од септембра 2013. године до јула 2014. године, када је кандидаткиња била ангажована као пост-докторски истраживач на University of Westminster, London, UK. Прелиминарни резултати рада на овој теми приказани су у раду број 23, док је у раду број 2 осим нове идеје у вези са веома актуелном темом дата и аналитичка припрема са великим бројем новоизведених израза, извршен је велики број нумеричких симулација са поређењем резултата и указано је на детаље и инжењерске компромисе у дизајну и фабрикацији. Због сложености структура и губитака који се не могу занемарити, коришћени су комерцијални софтверски алати за пуноталасну електромагнетску (EM) анализу, Wipl-D и HFSS, засновани на методи момената и методи коначних елемената, респективно. Добијена је добра фреквенцијска подесивост, од око 5%, у односу на централну учестаност резонатора.

У склопу мултидисциплинарне сарадње са колегама са Медицинског факултета (УБ), кандидаткиња је иницирала да се уместо описа појединачног случаја магнетног низа, којим је произведено статичко магнетско поље за потребе биомедицинских експеримената, обради генерални случај дводимензионог (2-D) низа перманентних магнета. Овим се бави рад број 22, категорије M_{22} . У оквиру тог рада, кандидаткиња је извела комплетне аналитичке изразе у затвореној форми који у потпуности дефинишу магнетску индукцију у свакој тачки изнад низа магнета, за произвољан случај. На основу изведених израза написала је софтвер који аналитички израчунава магнетску индукцију тих низова и процењује средње параметре поља у експерименталној запремини. Софтвер се већ у датој форми, или евентуално уз додатак алгоритма оптимизације, може користити за дизајн експерименталних уређаја који обезбеђују жељену магнетску индукцију. Као прелиминарно истраживање у том смеру, кандидаткиња је испитала утицај варирања геометријских параметара низа и коришћеног магнетског материјала на магнетску индукцију и вертикални градијент индукције који је могуће остварити. Резултате је публиковала у радовима број 31 и 47, категорија M_{33} односно M_{52} . Из рада на овој теми проистекло је и техничко решење под редним бројем 62, категорије M_{84} . Дводимензиони низови магнета имају различите практичне примене, које укључују микросензоре и микроактуаторе, синхроне планарне моторе са сталним магнетима, и аутоматско склапање микро-компоненти.

У раду под редним бројем 1 (2017. година), кандидаткиња је показала како се додатном оптимизацијом параметара комбинованог магнета, са засебно подесивом скретном и фокусирајућом функцијом, могу ефикасније остварити жељене перформансе. Овај рад се

ослања на истраживање из 2013. године, када је др Ристић-Ђуровић предложила принцип засебног подешавања функција магнета употребом два закренута дипола. Оптимизација је сада проширена увођењем додатних параметара, чиме је омогућено приближавање од концептуалног дизајна уређаја ка магнету који би исплативије и ефикасније одговорио на постављене захтеве пројектовања. Приступ дизајну комбинованих магнета и оптимизацији њихових параметара који је кандидаткиња дефинисала је генералне природе и може се користити као општа процедура за дизајн ових магнета. Тиме се одређују опсеци параметара који могу дати жељене перформансе, и процењују вредности скретне и фокусирајуће функције које се могу истовремено остварити. На конкретном примеру који је анализиран у раду број 1 и у претходном истраживању под бројем 5, задати захтеви су остварени двоструко краћим магнетом уз пажљиво обликовање полова. Магнетомоторне силе потребне за остваривање жељених профила поља су значајно испод максимално дозвољених. Релативно мала густина струје по попречном пресеку оставља довољно толеранције за практично извођење намотаја, узимајући у обзир облик намотаја и канала за хлађење.

Седми рад у коме је кандидаткиња први аутор, рад број 13, категорије M_{21} , проистекао је из рада на докторској дисертацији и бави се испитивањем и побољшањем ефикасности акцелерације у вишенаменским изохроним циклотронима. Испитана је спрега координата фазног простора, зависност параметара фазних елипси од енергије јона и фазног одступања јона, утицај координата фазног простора, а посебно десинхронизације у односу на фазу радиофреквентног система и радијалне децентрираности убрзавајуће орбите, на ефикасност убрзавања.

Осим наведених тема, које углавном одсликавају области рада кандидаткиње, она се такође бави и математичким моделовањем у електромагнетици, што је у овом изборном периоду резултовало радом број 14, категорије M_{21} . У том раду је показано како се и до пет пута мања грешка нумеричког прорачуна радарског попречног пресека расејача може добити одговарајућим избором параметризације пресликавања из реалног у параметарски домен. Пресликавање које уједначава дужину лука у правцу посматране координате (arc-length parametrization) се показало супериорно у односу на пресликавање пројекцијом зрака из заједничког центра (ray casting parametrization), које је нешто једноставније за имплементацију.

У раду број 3, категорије M_{21} , који се бави ефектима излагања живих организама статичком магнетском пољу, осим описа магнетског поља добијеног коришћењем дводимензионих магнетских низова, кандидаткиња је написала део рада о механизмима деловања статичког магнетског поља на живе организме и указала на могући механизам уочене прерасподеле цинка и бакра у организму. Сличним темама се бави и рад под бројем 42, са скупа међународног значаја, штампан у изводу. У радовима број 4 и број 11, категорије M_{21} , кандидаткиња је учествовала у писању радова и ревизији радова.

У раду број 12, категорије M_{21} , кандидаткиња је израчунала и приказала параметре убрзавања протонског снопа у коначно подешеном магнетском пољу и написала одељак о постојећим системима за мерење магнетског поља циклотрона. У радовима који се баве линеарним структурама за фокусирање и убрзавање честица, под бројевима 8, 9 и 10, сви M_{21} ,

кандидаткиња је учествовала у писању радова. За потребе рада број 5, кандидаткиња је извршила претрагу и студију обимне постојеће литературе у датој области.

Први рад по позиву, број 27, категорије M_{31} , пореди апроксимативно и пуноталасно електромагнетско нумеричко моделовање са мереним подацима. Кандидаткиња је реализовала великодоменске нумеричке моделе погодне за примену у методи момената (Wipl-D), генерисала резултате везане с тим моделима и извршила потребна поређења. Други рад по позиву, број 28, категорије M_{32} , је на тему расејања таласа у интеракцији са покретним срединама. Овде је кандидаткиња, везано за истраживање под редним бројем 7, на неколико додатних примера поређења са аналитичким резултатима показала прецизност и ефикасност нове методе; такође, дала је примере слојевитих средина произвољних профила пермитивности, за које нема аналитичких решења.

За рад број 48, категорије M_{52} и рад број 52, категорије M_{63} , награђен као најбољи рад у секцији за Антене и простирање на Конференцији ЕТРАН-а 2013. године, написала је софтверску процедуру за аналитички прорачун модова сферне шупљине. Написала је рад број 32, категорије M_{33} , за који је израчунала део резултата. У раду број 33, категорије M_{33} , који се ослања на рад број 7, израчунала је све приказане резултате. Учествовала је у нумеричком моделовању и прорачунима приказаним у радовима број 34, 35, 36, категорије M_{33} , и број 51, категорије M_{53} . број 32, категорије M_{33} и број 43, категорије M_{53} . Учествовала је у припреми радова број 43 и 44, категорије M_{34} .

Квалитативна анализа рада кандидата

1. Показатељи успеха у научном раду

1.1 Награде и признања за научни рад

- На конференцији ЕТРАН, 2006. године, кандидаткиња је остварила „Награђени рад младог истраживача“. (Прилог Б.1.1.а)
- Добитница је награде ЕТРАН-а за најбољи рад у секцији за Антене и простирање, 2013/2014. године. (Прилог Б.1.1.б)

1.2 Уводна предавања на конференцијама и друга предавања по позиву

- Предавање по позиву, штампано у целини (M_{31}), на седамнаестој ICEAA конференцији (*International Conference on Electromagnetics in Advanced Applications*), Torino, Italy, 2015. (Прилог Б.1.2.а)
- Предавање по позиву, штампано у изводу (M_{32}), на тринаестој конференцији *International Workshop on Finite Elements for Microwave Engineering*, Firenze, Italy, 2016. (Прилог Б.1.2.б)

1.3 Чланства у одборима међународних научних конф. и одборима научних друштава

1.4 Чланства у уређивачким одборима часописа, уређивање монографија, рецензије научних радова и пројеката

- Рецензент је у међународним часописима *Progress in Electromagnetics Research* (ISSN: 1559-8985), *Journal of Electromagnetic Waves and Applications* (ISSN: 0920-5071), и *Computer Methods and Programs in Biomedicine* (ISSN: 0169-2607).

2. Развој услова за научни рад, образовање и формирање научних кадрова

2.1 Допринос развоју науке у земљи

- Кандидаткиња је била изузетно ангажована и својим радом и залагањем је дала значајан допринос формирању мултидисциплинарног тима састављеног од три сарадника Института за физику и три професора Медицинског факултета Универзитета у Београду, о чему сведоче четири заједничка рада објављена у водећим међународним часописима.

2.2 Менторство при изради магистарских и докторских радова, руковођење специјалистичким радовима

- Кандидаткиња је помогла Слободану В. Савићу са Електротехничког факултета у Београду, приликом израде заједничких научних радова, који су део његове докторске дисертације. (Прилог Б.2.2.а)
- Учествовала је у руковођењу израдом докторске дисертације Бранка М. Буквића са Електротехничког факултета Универзитета у Београду, са којим је објавила један рад M_{21} , а тренутно завршавају и ревизију другог рада. (Прилог Б.2.2.б)

2.3 Педагошки рад

- Две године радног искуства у држању наставе на Електротехничком факултету Универзитета у Београду 1999-2001. године. (Прилог Б.2.3)

2.4 Међународна сарадња

- Кандидаткиња је, у периоду од 16. септембра 2013. године до 16. јула 2014. године, била ангажована као пост-докторски истраживач на University of Westminster, у Лондону, Велика Британија. (Прилог Б.2.4)

2.5 Организација научних скупова

3. Организација научног рада

3.1 Руковођење научним пројектима, потпројектима и задацима

- Кандидаткиња је, почев од 2013. године, у интересу пројекта ИИИ 45003 уз постојеће области отворила и нову тему и област истраживања, везану за примене нових материјала у електротехници. Извршено је и повезивање са страном истраживачком институцијом, као неопходни чинилац даљег напретка у научном раду.
- Руководила је израдом радова везаних за дизајн и оптимизацију општег случаја дво-димензионог магнетног низа. Тренутно развија и софтвер за оптимизацију низа према задатим спецификацијама.

3.2 Примењеност у пракси кандидатових технолошких пројеката, патената, иновација и других резултата

- Први аутор и одговорно лице приликом израде техничког решења „Употреба МАДУ трака у биомедицинским експериментима“. (Прилог Б.3.2)

3.3 Руковођење научним и стручним друштвима

3.4 Значајне активности у комисијама и телима Министарства науке и телима других министарстава везаних за научну делатност

3.5 Руковођење научним институцијама

4. Квалитет научних резултата

4.1 Утицајност кандидатових научних радова

После избора у звање научни сарадник др Анђелија Илић је објавила:

- четрнаест радова категорије M_{21} у међународним часописима са SCI листе;
- један рад категорије M_{22} у међународном часопису са SCI листе;
- један рад категорије M_{23} у међународном часопису са SCI листе;
- једно предавање по позиву са међународног скупа штампано у целини;
- једно предавање по позиву са међународног скупа штампано у изводу;
- шест саопштења на међународним скуповима штампаних у целини;
- три саопштења на међународним скуповима штампаних у изводу;
- два рада у националним часописима категорије M_{52} ;
- један рад у националном часопису категорије M_{53} ;
- једно саопштење на скупу националног значаја M_{53} ;
- једно техничко решење категорије M_{84} .

Велики део наведених радова представља детаљне студије које укључују аналитичку припрему, имплементацију софтвера, нумеричке прорачуне, анализу конвергенције, анализу утицаја различитих параметара на појаву која се разматра. Део радова се бави развојем нових метода у физици и електромагнетици.

О утицајности научних радова кандидаткиње сведочи и позитивна цитираност радова. Од укупно 131 цитата у базама SCOPUS и Web of Science, хетероцитата има 64, односно око 50%. Према SCOPUS-у, h -фактор, односно h -индекс, износи 7.

4.2. Позитивна цитираност кандидатових радова

Преглед цитираних радова кандидаткиње, као и списак радова који их цитирају, дат је у посебној табели на крају овог документа (Прилог А2). Сви радови су цитирани у позитивном смислу. Правих, односно хетероцитата има 64, што је скоро 50% од укупног броја цитата, 131. Према SCOPUS-у, h -фактор, односно h -индекс, износи 7.

4.3 Углед и утицајност публикација у којима су кандидатови радови објављени

Од радова објављених у часописима са SCI листе:

- седам радова је објављено у часопису *IEEE Transactions on Nuclear Science*, водећем часопису за област акцелераторских технологија средњих и ниских енергија, а један у следећем из области – *Nuclear Instruments and Methods in Physics Research Section A*;
- на тему примене графена у таласоводним резонаторима намењеним високим учестаностима објављен је рад у водећем часопису из области примењене физике *Journal of Physics D: Applied Physics*. Почетни резултати су објављени у часопису *Microwave and Optical Technology Letters*.
- два рада објављена у часопису *IEEE Antennas and Wireless Propagation Letters* који постоји свега десетак година уназад, баве се изузетно занимљивим темама из области нумеричких метода у електромагнетици;
- од четири рада мултидисциплинарног карактера, урађена у сарадњи са Медицинским факултетом Универзитета у Београду, два су објављена у водећим часописима из области екологије и заштите животне средине, један у водећем часопису *International Journal of Radiation Biology* и један у часопису *IEEE Transactions on Magnetics*.

4.4 Ефективни број радова и број радова нормиран на основу броја коаутора, укупан број кандидатових радова, удео самосталних и коауторских радова у њему, кандидатов допринос у коауторским радовима

Од пет радова експерименталног карактера, три рада су мултидисциплинарног карактера и имају 10, 10 и 11 коаутора. Друга два рада имају 5, односно 7, коаутора, што одговара максимално дозвољеном броју до седам коаутора за експериментални рад. Остали радови се заснивају на нумеричким симулацијама и имају од два до пет коаутора. Ово се у потпуности уклапа у максимално дозвољени број од пет коаутора за истраживања која укључују нумеричке симулације. Према томе, за тринаест од шеснаест радова потпуно је задовољен критеријум за прихватање пуног ефективног броја поена. Евентуално нормирање броја поена два мултидисциплинарна рада не утиче на остваривање ни квантитативног нити квалитативних критеријума.

4.5 Степен самосталности у научноистраживачком раду и улога у реализацији радова у научним центрима у земљи и иностранству

Кандидаткиња је показала велики степен самосталности у научноистраживачком раду, тиме што је сама дала велики број предлога који се показао као изузетно добар, радила је са различитим коауторима и остварила је студијски боравак у иностранству. У публикацијама у којима није први аутор, показала се као веома користан члан тима који је својим радом значајно допринео укупном квалитету публикованих радова.

Квантитативна анализа рада кандидата

Табела 1. Збирне вредности коефицијената M_{ij} публикација кандидата
За природно-математичке и медицинске науке

Диференцијални услов- Од првог избора у претходно звање до избора у звање.....	потребно је да кандидат има најмање XX поена, који треба да припадају следећим категоријама:		
		Неопходно XX=	Остварено
Научни сарадник	Укупно	16	140,5
	$M_{10}+M_{20}+M_{31}+M_{32}+M_{33}$ $M_{41}+M_{42} \geq$	10	131
	$M_{11}+M_{12}+M_{21}+M_{22}+M_{23} \geq$	6	120
Виши научни сарадник	Укупно	50	
	$M_{10}+M_{20}+M_{31}+M_{32}+M_{33}$ $M_{41}+M_{42}+M_{90} \geq$	40	
	$M_{11}+M_{12}+M_{21}+M_{22}+M_{23} \geq$	30	
Научни саветник	Укупно	70	
	$M_{10}+M_{20}+M_{31}+M_{32}+M_{33}$ $M_{41}+M_{42}+M_{90} \geq$	50	
	$M_{11}+M_{12}+M_{21}+M_{22}+M_{23} \geq$	35	

Прилог A1: Укупни списак публикација кандидата

Радови објављени након претходног избора у звање обележени су звездицом (*).

КАТЕГОРИЈА M₂₁ *:

1. * **A. Ž. Ilić**, S. T. Ćirković, M. M. Ilić, and J. L. Ristić-Djurović, “Design of a combined function magnet with individually adjustable functions”, accepted for publication in *IEEE Transactions on Nuclear Science*. (DOI (identifier) 10.1109/TNS.2017.2684745)
2. * **A. Ž. Ilić**, B. Bukvić, M. M. Ilić, and Dj. Budimir, “Graphene-based waveguide resonators for submillimeter-wave applications”, *J. Phys. D: Appl. Phys.*, vol. 49, no.32, August 2016, p. 325105. (DOI (identifier) 10.1088/0022-3727/49/32/325105)
3. * S. R. De Luka, **A. Ž. Ilić**, S. Janković, D. M. Djordjevich, S. Ćirković, I. D. Milovanovich, S. Stefanović, S. Vesković-Moračanin, J. L. Ristić-Djurović, and A. M. Trbovich, “Subchronic exposure to static magnetic field differently affects zinc and copper content in murine organs”, *International Journal of Radiation Biology*, vol. 92, no. 3, Mar 2016, pp. 140-147. (DOI (identifier) 10.3109/09553002.2016.1135266)
4. * I. D. Milovanovich, S. Ćirković, S. R. De Luka, D. M. Djordjevich, **A. Ž. Ilić**, T. Popović, A. Arsić, D. D. Obradović, D. Oprić, J. L. Ristić-Djurović, and A. M. Trbovich, “Homogeneous static magnetic field of different orientation induces biological changes in subacutely exposed mice”, *Environ. Sci. Pollut. Research*, vol. 23, no. 2, Jan 2016, pp. 1584-1597. (DOI (identifier) 10.1007/s11356-015-5109-z)
5. * J. L. Ristić-Djurović, S. Ćirković, and **A. Ž. Ilić**, “Magnet with uncoupled combined functions”, *IEEE Transactions on Nuclear Science*, Vol. 60, No. 6, Part 2, December 2013, pp. 4618–4626. (DOI (identifier) 10.1109/TNS.2013.2290309)
6. * **A. Ž. Ilić**, J. L. Ristić-Djurović, and S. Ćirković, “Importance of Accurate Static Equilibrium Orbit Calculation in Cyclotron Design”, *IEEE Transactions on Nuclear Science*, Vol. 60, No. 6, Part 2, December 2013, pp. 4627–4633. (DOI (identifier) 10.1109/TNS.2013.2284194)
7. * **A. Ž. Ilić** and M. M. Ilić, “Higher-Order Frequency-Domain FEM Analysis of EM Scattering Off a Moving Dielectric Slab”, *IEEE Antennas and Wireless Propagation Letters*, Vol. 12, December 2013, pp. 890–893. (DOI (identifier) 10.1109/LAWP.2013.2272717)
8. * J. L. Ristić-Djurović, S. Ćirković, and **A. Ž. Ilić**, “Optimization of Equally Charged Quadrupole Parameters”, *IEEE Transactions on Nuclear Science*, Vol. 60, No. 3, Part 3, June 2013, pp. 2161–2169. (DOI (identifier) 10.1109/TNS.2013.2253618)
9. * J. L. Ristić-Djurović, S. Ćirković, and **A. Ž. Ilić**, “Ion Beam Acceleration with Radio Frequency Powered Rainbow Lens”, *IEEE Transactions on Nuclear Science*, Vol. 60, No. 2, Part 2, April 2013, pp. 1272–1279. (DOI (identifier) 10.1109/TNS.2012.2230452)
10. * J. L. Ristić-Djurović and **A. Ž. Ilić**, “Role and significance of uniform distribution in a study of ensemble of particles”, *IEEE Transactions on Nuclear Science*, Vol. 60, No. 1, Part 2, February 2013, pp. 236–245. (DOI (identifier) 10.1109/TNS.2012.2225153)
11. * D. M. Djordjevich, S. R. De Luka, I. D. Milovanovich, S. Janković, S. Stefanović, S. Vesković-Moračanin, S. Ćirković, **A. Ž. Ilić**, J. L. Ristić-Djurović, and A. M. Trbovich, “Hematological Parameters’ Changes in Mice Subchronically Exposed to Static Magnetic Fields of Different Orientations”, *Ecotoxicology and Environmental Safety*, Vol. 81, July 2012, pp. 98-105. (DOI (identifier) 10.1016/j.ecoenv.2012.04.025)

12. * S. Ćirković, A. Ž. Ilić, A. Dobrosavljević, R. Balvanović, and J. L. Ristić-Djurović, “Minimization of the Measurement Errors Induced by the Cyclotron Magnetic Field Measurement System”, *Nuclear Instruments and Methods in Physics Research Section A*, Vol. 679, July 2012, pp. 54-60. (DOI (identifier) 10.1016/j.nima.2012.03.018)
13. * A. Ž. Ilić, J. L. Ristić-Djurović, S. Ćirković, and N. Nešković, “Enhancement of Ion Beam Acceleration Efficiency in Isochronous Cyclotrons”, *IEEE Transactions on Nuclear Science*, Vol. 59, No. 2, April 2012, pp. 272-280. (DOI (identifier) 10.1109/TNS.2011.2180737)
14. * M. M. Ilić, S. V. Savić, A. Ž. Ilić, and B. M. Notaroš, “Constant speed parametrization mapping of curved boundary surfaces in higher order moment-method electromagnetic modeling”, *IEEE Antennas and Wireless Propagation Letters*, Vol. 10, December 2011, pp. 1457-1460. (DOI (identifier) 10.1109/LAWP.2011.2180354)
15. S. Ćirković, J. L. Ristić-Djurović, A. S. Vorozhtsov, A. Ž. Ilić, and N. Nešković, “Method for Fine Magnet Shaping in Cyclotrons”, *IEEE Transactions on Nuclear Science*, Vol. 56, No. 5, October 2009, pp. 2821-2827.
16. M. M. Ilić, A. Ž. Ilić, and B. M. Notaroš, “Continuously Inhomogeneous Higher Order Finite Elements for 3-D Electromagnetic Analysis”, *IEEE Transactions on Antennas and Propagation*, Vol. 57, No. 9, September 2009, pp. 2798-2803.
17. A. Ž. Ilić, J. L. Ristić-Djurović, S. Ćirković, A. Dobrosavljević, and N. Nešković, “Optimal Acceleration in Isochronous Straight Sector Cyclotrons”, *IEEE Transactions on Nuclear Science*, Vol. 56, No. 3, June 2009, pp. 1498-1506.
18. M. M. Ilić, M. Djordjević, A. Ž. Ilić, and B. M. Notaroš, “Higher Order Hybrid FEM-MoM Technique for Analysis of Antennas and Scatterers”, *IEEE Transactions on Antennas and Propagation*, Vol. 57, No. 5, May 2009, pp. 1452-1460.
19. S. Ćirković, J. L. Ristić-Djurović, A. Ž. Ilić, V. Vujović, and N. Nešković, “Comparative Analysis of Methods for Isochronous Magnetic-Field Calculation”, *IEEE Transactions on Nuclear Science*, Vol. 55, No. 6, December 2008, pp. 3531-3538.
20. M. M. Ilić, A. Ž. Ilić, and B. M. Notaroš, “Efficient Large-Domain 2-D FEM Solution of Arbitrary Waveguides Using p -Refinement on Generalized Quadrilaterals”, *IEEE Trans. on Microwave Theory and Techniques*, Vol. 53, No. 4, April 2005, pp. 1377-1383.
21. M. M. Ilić, A. Ž. Ilić, and B. M. Notaroš, “Higher Order Large-Domain FEM Modeling of 3-D Multiport Waveguide Structures with Arbitrary Discontinuities”, *IEEE Transactions on Microwave Theory and Techniques*, Vol. 52, No. 6, June 2004, pp. 1608-1614.

КАТЕГОРИЈА M₂₂ *:

22. * Andjelija Ž. Ilić, Saša Ćirković, D. M. Djordjevic, S. R. De Luka, I. D. Milovanovich, A. M. Trbovich, and J. L. Ristic-Djurović, “Analytical Description of Two-dimensional Magnetic Arrays Suitable for Biomedical Applications”, *IEEE Transactions on Magnetism*, Vol. 49, No. 12, December 2013, pp. 5656–5663. (DOI (identifier) 10.1109/TMAG.2013.2277831)

КАТЕГОРИЈА M₂₃ *:

23. * Andjelija Ž. Ilić and Djuradj Budimir, “Electromagnetic analysis of graphene based tunable waveguide resonators,” *Microwave and Optical Technology Letters*, Vol. 56, No. 10, October 2014, pp. 2385–2388. (DOI (identifier) 10.1002/mop.28603)

КАТЕГОРИЈА M₂₄:

24. Milan M. Ilić, **Andjelija Ž. Ilić**, and Branislav M. Notaroš, “Comparison of Higher Order FEM and MoM/SIE Approaches in Analyses of Closed- and Open-Region Electromagnetic Problems”, *Facta Universitatis Series: Elec. Energ.*, Vol. 21, No. 2, August 2008, pp. 209-220.
25. S. T. Ćirković, Jasna L. Ristić-Đurović, **A. Ilić**, N. Nešković, A. S. Vorozhtsov and S. B. Vorozhtsov, “Focusing limit of a cyclotron: axial betatron instability against beam dynamics approach”, *Nuclear Technology & Radiat. Protection*, Vol. XXI, No. 2, December 2006, pp. 1-7.
26. **Andjelija Ž. Ilić**, Jasna L. Ristić-Djurović, and Saša T. Ćirković, “Preliminary Results of Ion Trajectory Tracking in the Acceleration Region of the VINCY Cyclotron”, *Nuclear Technology & Radiation Protection*, Vol. XXI, No. 1, June 2006, pp. 29-33.

КАТЕГОРИЈА M₃₁ *:

27. * **B. Bukvić**, **A. Ilić**, and M.M. Ilić, “Comparison of approximate and full-wave electromagnetic numerical modeling of microstrip matching networks”, invited paper, Special Session on Numerical Methods in Electromagnetics, *Proc 2015 Int. Conf. on Electromagnetics in Advanced Applications (ICEAA)*, September 7–11, Torino, Italy, 2015, pp. 76–79.

КАТЕГОРИЈА M₃₂ *:

28. * **A. Ž. Ilić**, S. V. Savić, and M. M. Ilić, “Finite Element 1-D Solutions in the Presence of Moving Media”, invited paper, Special Session on Advanced FEM and Hybrid Techniques (part 1), *Proc. of the 13th International Workshop on Finite Elements for Microwave Engineering*, May 16–18, Firenze, Italy, 2016, p. 138.
29. J. L. Ristić-Djurović, S. Ćirković, **A. Ž. Ilić**, Đ. Košutić and N. Nešković, “Some Contributions of the TESLA Team to Accelerator Physics and Technologies,” invited paper, Session on ADS and Accelerators, *CONUSS 2008*, Sept. 22-25, 2008, Belgrade, Serbia, Book of Abstracts, p. 25.
30. B. M. Notaroš, M. M. Ilić, **A. Ž. Ilić**, and M. Djordjević, “Higher Order Hierarchical FEM Solutions with Enhanced Efficiency and Practicality”, invited paper, Special Session on Numerical Methods, *PIERS 2006*, March 26-29, 2006, Cambridge, MA, USA (Electromagnetic Academy, Cambridge, MA, USA, 2006), p. 253.

КАТЕГОРИЈА M₃₃ *:

31. * **A. Ž. Ilić**, S. Ćirković, and J. L. Ristić-Djurović, “Evaluation of SMF exposure field levels and gradients obtainable using the 2D magnetic arrays”, *Proc. of the 3rd Int. Conf. on Radiation and Applications in Various Fields of Research (RAD 2015)*, June 8-12, Slovenska Plaža, Budva, Montenegro, 2015, pp. 447–450.
32. * **A. Ž. Ilić**, J. L. Ristić-Djurović, S. Ćirković, M. M. Ilić, and A. M. Trbovich, “Experimental electromagnet for *in vivo* exposure of small animals to ELF electromagnetic fields”, *Proc. of the 2nd Int. Conf. on Radiation and Dosimetry in Various Fields of Research (RAD 2014)*, May 27-30, 2014, Niš, Serbia, pp. 1–4.
33. * M. M. Ilić and **A. Ž. Ilić**, “Convergence of the Higher Order Frequency-Domain FEM Solution to Scattering from a Moving Dielectric Slab”, *Proc. of the 21st Telecommunications Forum (TELFOR 2013)*, November 26-28, 2013, Belgrade, Serbia.

34. * S. V. Savić, A. Ž. Ilić, B. M. Notaroš, and M. M. Ilić, “Acceleration of Higher Order FEM Matrix Filling by OpenMP Parallelization of Volume Integrations”, *Proceedings of the 20th Telecommunications Forum (TELFOR 2012)*, November 20-22, 2012, Belgrade, Serbia.
35. * B. M. Notaroš, M. M. Ilić, S. V. Savić, N. J. Šekeljić, and A. Ž. Ilić, “Accurate and Efficient Curvilinear Geometrical Modeling Using Interpolation Parametric Elements in Higher Order CEM Techniques”, *Proceedings of the 28th Annual Review of Progress in Applied Computational Electromagnetics, ACES 2012*, April 10-14, 2012, Columbus, Ohio, USA.
36. * M. M. Ilić, S. V. Savić, A. Ž. Ilić, and B. M. Notaroš, “Hybrid Higher Order FEM-MoM Analysis of Continuously Inhomogeneous Electromagnetic Scatterers”, *Proceedings of the 18th Telecommunications Forum (TELFOR 2010)*, November 23-25, 2010, Belgrade, Serbia.
37. B. M. Notaroš, M. M. Ilić, A. Ž. Ilić, M. Djordjević, and S. V. Savić, “Efficient higher order finite element–moment method modeling of 3-D radiation and scattering problems”, *Proceedings of the 25th Annual Review of Progress in Applied Computational Electromagnetics, ACES 2009*, March 8-12, 2009, Monterey, California, USA, pp.627-632.
38. A. Ž. Ilić, S. V. Savić, M. M. Ilić, and B. M. Notaroš, “Analysis of Electromagnetic Scatterers using Hybrid Higher Order FEM-MoM Technique”, *Proceedings of the 16th Telecommunications Forum (TELFOR 2008)*, November 25-27, 2008, Belgrade, Serbia.
39. A. Ž. Ilić, M. M. Ilić and B. M. Notaroš, “Influence of the Accuracy of Geometrical Modeling with Large Curvilinear Elements on FEM Solutions to EM Problems”, *Proc. of the 14th Telecomm. Forum (TELFOR 2006)*, November 21-23, 2006, Belgrade, Serbia, pp. 422-424.
40. B. M. Notaroš, M. M. Ilić, A. Ž. Ilić, and M. Djordjević, “Very-High-Order CEM Modeling”, Special Session on Higher Order Computational Electromagnetics, *2005 IEEE APS International Symposium Digest*, July 3-8, 2005, Washington, D.C., U.S.A., pp.3A.48-51.
41. S. B. Vorozhtsov, A. S. Vorozhtsov, A. Dobrosavljević, P. Beličev, S. Ćirković, A. Ilić, Đ. Košutić, N. Nešković, M. Rajčević, J. Ristić-Đurović, V. Vujović, Lj. Vukosavljević, “Final Shaping of the Magnetic Structure of the VINCY Cyclotron”, *The 17th International Conference on Cyclotrons and Their Appl.*, October 18-22, 2004, Tokyo, Japan, pp.390-392.

КАТЕГОРИЈА M₃₄*:

42. * S. R. De Luka, A. Ž. Ilić, S. Ćirković, D.M. Djordjević, J.L. Ristić-Djurović, and A.M. Trbovich, “Static magnetic field effects on biochemical reactions involving reactive oxygen species”, *The Fourth Int. Conf. on Radiation and Applications in Various Fields of Research (RAD 2016)*, May 23-27, 2016, Niš, Serbia, Book of Abstracts, p. 52.
43. * S. Gajić, S. Ćirković, J. Ristić-Djurović, A. Ilić, D. Djordjević, and V. Spasić-Jokić, “Exposure system with homogeneous static and ELF magnetic fields in experimental volume”, *The Fourth Int. Conf. on Radiation and Applications in Various Fields of Research (RAD 2016)*, May 23-27, 2016, Niš, Serbia, Book of Abstracts, p. 27.
44. * S. V. Savić, A. Ž. Ilić, B. M. Notaroš, and M. M. Ilić, “Nonrigorous symmetric second-order absorbing boundary condition: Accuracy, convergence and possible improvements”, *Proc. of the 13th International Workshop on Finite Elements for Microwave Engineering*, May 16-18, 2016, Firenze, Italy, p. 139.
45. M. M. Ilić, D. Olčan, A. Ž. Ilić, and B. M. Notaroš, “Large-Domain High-Order Curvilinear Finite Element Solution of 2D and 3D Vector-Type Problems in Engineering”, *The First Int. Conf. on Computational Mechanics*, November 15-17, 2004, Belgrade, Serbia and Montenegro, Book of Abstracts, p. 15.

46. **A. Ž. Plić**, M. M. Ilić, and B. M. Notaroš, “On the Higher-Order Hexahedral Meshing for FEM in Electromagnetics”, *2004 IEEE AP-S Int. Symp. on Antennas and Prop. and USNC/URSI National Radio Science Meeting*, URSI Digest, June 20-26, 2004, Monterey, CA, U.S.A.

КАТЕГОРИЈА M₅₂*:

47. * **A. Ž. Plić**, S. Ćirković, and J. L. Ristić-Djurović, “Evaluation of SMF exposure field levels and gradients obtainable using the 2D magnetic arrays”, *Radiation and Applications*, vol. 1, no. 2, October 2016, pp. 147-150. (DOI: 10.21175/RadJ.2016.02.027)
48. * M. Davidović, **A. Plić**, M. Tasić, B. Notaroš, and M. Plić, “A comparison of modal electromagnetic field distributions in analytical and numerical solutions”, *Microwave Review*, vol. 19, no. 1, September 2013, pp. 26-30.
49. **A. Ž. Plić**, S. V. Savić, M. M. Ilić, and B. M. Notaroš, “Analysis of electromagnetic scatterers using hybrid higher order FEM-MoM technique”, *Telfor Journal*, Vol. 1(2), 2009, pp.53-56.
50. **A. Ž. Plić**, J. L. Ristić-Djurović, and S. T. Ćirković, “Preliminary Results of the Ion Trajectory Tracking in the Acceleration Region of the VINCY Cyclotron”, *Journal of Automatic Control, University of Belgrade*, Vol. 16, No. 1, 2006, pp. 5-8.

КАТЕГОРИЈА M₅₃*:

51. * M. M. Plić, S. V. Savić, **A. Ž. Plić**, and B. M. Notaroš, “Hybrid Higher Order FEM-MoM Analysis of Continuously Inhomogeneous Electromagnetic Scatterers”, *Telfor Journal*, Vol. 3, No. 2, 2011, pp. 121-124.

КАТЕГОРИЈА M₆₃*:

52. * M. Davidović, **A. Plić**, M. Tasić, B. Notaroš, and M. Plić, “Convergence of modal electromagnetic fields in a B-spline finite element method”, *Proceedings of 57th ETRAN Conference*, Zlatibor, Serbia, June 3-6, 2013, pp. AP1.5.1-4. (najbolji rad na sekciji za Antene i prostiranje)
53. **Анђелија Ж. Илић**, Јасна Љ. Ристић-Ђуровић, Саша Т. Ћирковић, Небојша Б. Нешковић, “Подешавање параметара РФ система Циклотрона Винси”, *LII Конференција ЕТРАН-а*, Палић, 8-12. јуна 2008, Зборник радова, NT1.4.
54. Саша Т. Ћирковић, Јасна Љ. Ристић-Ђуровић, **Анђелија Ж. Илић**, “Израчунавање изохроног магнетског поља помоћу динамике снопа”, *LII Конференција ЕТРАН-а*, Палић, 8-12. јуна 2008, Зборник радова, NT1.5.
55. Саша Ћирковић, Љубиша Вукосављевић, Јасна Ристић-Ђуровић, **Анђелија Илић**, Александар Добросављевић, Ђорђе Кошутић, “Минимизација утицаја мерног система на први хармоник магнетског поља циклотрона VINCY”, *LI Конференција ЕТРАН-а*, Херцег Нови – Игало, 4-8. јуна 2007, Зборник радова на CD-у, NT1.4.
56. **Анђелија Ж. Plić**, Jasna L. Ristić-Djurović, Saša T. Ćirković, “Initial Conditions Corresponding to Optimal Ion Acceleration in the VinCy Cyclotron”, *LI Конференција ЕТРАН-а*, Херцег Нови – Игало, 4-8. јуна 2007, Зборник радова на CD-у, NT1.5.
57. **Андјелија Ж. Plić**, Jasna L. Ristić-Djurović, Saša T. Ćirković, “Preliminary results of the trajectory tracking analysis in the acceleration region of the VINCY Cyclotron”, *L Конференција ЕТРАН-а*, Београд, 6-8. јуна 2006. Зборник радова, Свеска IV, стр. 25-28. (nagradajeni rad mladog istraživača)

58. M. M. Ilić, A. Ž. Ilić, and B. M. Notaroš, “Large Lagrange-Type Finite Elements in Electromagnetics – Benefits and Limitations”, *L Konferencija ETPAH-a*, Београд, 6-8. јуна 2006. Зборник радова, Свеска II, стр. 262-265.

КАТЕГОРИЈА М₆₄:

59. V. Likar-Smiljanić, T. Čajkovski, A. S. Nikolić, Č. Jovalekić, J. Puzović, A. Ilić, B. M. Andrić, M. B. Pavlović, “Concurrent Analysis of Absorption Coefficients of NiFe₂O₄ and Ni-ZnFe₂O₄ Ferrite Powder Samples Synthesized by Classic, Mechanochemical and Chemical Procedures”, *The Fourth Yugoslav Materials Research Society Conference YUCOMAT 2001*, September 10-14, 2001, Herceg Novi, Serbia and Montenegro, Book of Abstracts, p. 7.

КАТЕГОРИЈА М₇₁:

60. Анђелија Ж. Илић, “Оптимално убрзавање честица у вишенаменским изохроним циклотронима”, докторска дисертација, Електротехнички факултет Универзитета у Београду, октобар 2010.

КАТЕГОРИЈА М₇₂:

61. Andjelija Ž. Ilić, “Optimal Large-Domain Hexahedral Meshing for Higher Order Finite Element Modeling in Electromagnetics”, MSEE thesis, University of Massachusetts Dartmouth, MA, USA, January 2004. (Нострификација: Електротехнички факултет Универзитета у Београду, јула 2004).

КАТЕГОРИЈА М₈₄*:

62. * Анђелија Илић, Саша Ћирковић, Јасна Ристић-Ђуровић, Драго Ђорђевић, Александар Трбовић, “Употреба МАДУ трака у биомедицинским експериментима”, децембар 2013.

Прилог A2: Цитираност публикација Анђелије Илић

Списак радова обухвата само цитате који нису ауто-цитати ни ко-цитати.

Рад који цитира	Цитирани рад
1) Mangadlao, J.D., De Leon, A.C.C., Felipe, M.J.L., Cao, P., Advincula, P.A., Advincula, R.C., "Grafted carbazole-assisted electrodeposition of graphene oxide," <i>ACS Applied Materials and Interfaces</i> 7 (19), pp. 10266-10274, 2015.	A. Ž. Ilić and D. Budimir, "Electromagnetic analysis of graphene based tunable waveguide resonators," <i>Microwave and Optical Technology Letters</i> , Vol. 56, No. 10, October 2014, pp. 2385–2388.
2) Andriollo, M., Martinelli, G., Tortella, A., "Optimization of an electrodynamic linear actuator for biometric applications," <i>IEEE Transactions on Magnetics</i> 51 (8), art. no. 8002406, 2015.	A. Ž. Ilić , S. Ćirković, D. M. Djordjevic, S. R. De Luka, I. D. Milovanovich, A. M. Trbovich, and J. L. Ristić-Djurović, "Analytical description of two-dimensional magnetic arrays suitable for biomedical applications", <i>IEEE Transactions on Magnetics</i> , Vol. 49, No. 12, December 2013, pp. 5656–5663.
3) Kuang, L., Xu, F., Zhu, S., Gao, J., Zheng, Z., "Relativistic FDTD analysis of far-field scattering of a high-speed moving object," <i>IEEE Antennas and Wireless Propagation Letters</i> 14, pp. 879-882, 2015.	A. Ž. Ilić and M. M. Ilić, "Higher-order frequency-domain FEM analysis of EM scattering off a moving dielectric slab", <i>IEEE Antennas and Wireless Propagation Letters</i> , Vol. 12, December 2013, pp. 890–893.
4) Brignone, M., Ramakrishnan, P.K., Raffetto, M., "A first numerical assessment of the reliability of finite element simulators for time-harmonic electromagnetic problems involving rotating axisymmetric objects," in <i>Proc. of the 2016 URSI International Symposium on Electromagnetic Theory (EMTS)</i> , Espoo, Finland, August 14-18, 2016, pp. 787-790.	
5) Telečki I.N., Beličev P.D., Petrović S.M., and Nešković N.B., "Focusing properties of a square electrostatic rainbow lens doublet," <i>Nuclear Technology and Radiation Protection</i> 30(4), pp. 239-248, 2015.	J. L. Ristić-Djurović, S. Ćirković, and A. Ž. Ilić , "Optimization of equally charged quadrupole parameters", <i>IEEE Transactions on Nuclear Science</i> , Vol. 60, No. 3, Part 3, June 2013, pp. 2161–2169.
6) Telečki I.N., Beličev P.D., Petrović S.M., and Nešković N.B., "Focusing properties of a square electrostatic rainbow lens doublet," <i>Nuclear Technology and Radiation Protection</i> 30(4), pp. 239-248, 2015.	J. L. Ristić-Djurović, S. Ćirković, and A. Ž. Ilić , "Ion beam acceleration with radio frequency powered rainbow lens", <i>IEEE Transactions on Nuclear Science</i> , Vol. 60, No. 2, Part 2, April 2013, pp. 1272–1279.
7) Safari, M., Jadidi, M., Baghian, A., Hasanzadeh, H., "Proliferation and differentiation of rat bone marrow stem cells by 400 μ T electromagnetic field," <i>Neuroscience Letters</i> 612, pp. 1-6, 2016.	D. M. Djordjevich, S. R. De Luka, I. D. Milovanovich, S. Janković, S. Stefanović, S. Vesković-Moračanin, S. Ćirković, A. Ž. Ilić , J. L. Ristić-Djurović, and A. M. Trbovich, "Hematological Parameters' Changes in Mice Subchronically Exposed to Static Magnetic Fields of Different Orientations", <i>Ecotoxicology and Environmental Safety</i> , Vol. 81, July 2012, pp. 98-105.
8) Elferchichi, M., Mercier, J., Ammari, M., Belguith, H., Abdelmelek, H., Sakly, M., Lambert, K., "Subacute static magnetic field exposure in rat induces a pseudoanemia status with increase in MCT4 and Glut4 proteins in glycolytic muscle," <i>Environmental Science and Pollution Research</i> 23 (2), pp. 1265-1273, 2016.	
9) Chen, Z., Wang, Y., Zhuo, L., Chen, S., Zhao, L., Luan, X., Wang, H., Jia, G., "Effect of titanium dioxide nanoparticles on the cardiovascular system after oral administration," <i>Toxicology Letters</i> 239 (2), pp. 123-130, 2015.	

<p>10) Chen, Z., Wang, Y., Zhuo, L., Chen, S., Zhao, L., Chen, T., Li, Y., Zhang, W., Gao, X., Li, P., Wang, H., Jia, G., "Interaction of titanium dioxide nanoparticles with glucose on young rats after oral administration," <i>Nanomedicine : Nanotechnology, Biology and Medicine</i> 11 (7), pp. 1633-1642, 2015.</p> <p>11) Yu, S., Shang, P., "A review of bioeffects of static magnetic field on rodent models," <i>Progress in Biophysics and Molecular Biol.</i> 114 (1), pp. 14-24, 2014.</p> <p>12) Jadidi, M., Safari, M., Baghian, A., "Effects of extremely low frequency electromagnetic fields on cell proliferation," <i>Koomesh Journal</i> 15 (1), pp. 1-10, 2013.</p>	
<p>13) Peterson, A. F., Bibby, M. M., "Progress in Controlled Accuracy Numerical Solutions of Integral Equations," in <i>Proc. 2014 Int. Conf. on Electromagnetics in Advanced Applications (ICEAA)</i>, August 3–8, Palm Beach, Aruba, Netherlands, pp. 407-410, 2014.</p>	<p>M. M. Ilić, S. V. Savić, A. Ž. Ilić, and B. M. Notaroš, "Constant speed parametrization mapping of curved boundary surfaces in higher order moment-method electromagnetic modeling", <i>IEEE Antennas and Wireless Propagation Letters</i>, Vol. 10, Dec. 2011, pp. 1457-1460.</p>
<p>14) Chen, D. Z., Liu, K. F., Yang, J., Chen, Z. H., Li, D., Qin, B., Huang, J., Xiong, Y. Q., Fan, M. W., "Fast and accurate magnetic field shimming for a compact cyclotron," <i>IEEE Transactions on Nuclear Science</i> 60 (3), pp. 2175-2179, 2013.</p> <p>15) Chen, D.Z., Chen, Z.H., Liu, K.F., Yang, J., Li, D., Qin, B., Xiong, Y.Q., "Magnetic field calculation for a 10 MeV positron emission tomography cyclotron," <i>Review of Scientific Instruments</i> 84 (5), art. no. 053306, 2013.</p> <p>16) Qin, B., Yang, J., Liu, K. F., Chen, D. Z., Li, D., Xiong, Y. Q., Yu, T. Q., Fan, M. W., "Precise isochronous field shimming using correlation matrix for compact cyclotrons," <i>Nuclear Instruments & Methods in Physics Research Section A-Accelerators Spectrometers Detectors and Associated Equipment</i> vol. 691, pp. 129-134, 2012.</p> <p>17) Qin, B., Chen, D. Z., Zhao, L. C., Yang, J., Fan M. W., "An improved matrix method for magnet shimming in compact cyclotrons," <i>Nuclear Instruments & Methods in Physics Research Section A-Accelerators Spectrometers Detectors and Associated Equipment</i> vol. 620, no. 2-3, pp. 121-127, 2010.</p>	<p>S. Ćirković, J. L. Ristić-Djurović, A. S. Vorozhtsov, A. Ž. Ilić, and N. Nešković, "Method for Fine Magnet Shaping in Cyclotrons", <i>IEEE Transactions on Nuclear Science</i>, Vol. 56, No. 5, October 2009, pp. 2821-2827.</p>
<p>18) Ansari Oghol Beig, D., Wang, J., Peng, Z., Lee, J.-F., "A universal array approach for finite elements with continuously inhomogeneous material properties and curved boundaries," <i>IEEE Transactions on Antennas and Propagation</i> 60 (10) , art. no. 6232441 , pp. 4745-4756, 2012.</p>	<p>M. M. Ilić, A. Ž. Ilić, and B. M. Notaroš, "Continuously Inhomogeneous Higher Order Finite Elements for 3-D Electromagnetic Analysis," <i>IEEE Transactions on Antennas and Propagation</i>, vol. 57, no. 9, September 2009, pp. 2798-2803.</p>
<p>19) Cai, Q.M., Zhao, Y.W., Huang, W.F., Zheng, Y.T., Zhang, Z.P., Nie, Z.P., Liu, Q.H., "Volume surface integral equation method based on higher order hierarchical vector basis functions for EM scattering and radiation from composite metallic and dielectric structures," <i>IEEE Transactions on Antennas and Propagation</i> 64(12), pp. 5359-5372, 2016.</p>	<p>M. M. Ilić, M. Djordjević, A. Ž. Ilić, and B. M. Notaroš, "Higher Order Hybrid FEM-MoM Technique for Analysis of Antennas and Scatterers," <i>IEEE Transactions on Antennas and Propagation</i>, vol. 57, no. 5, May 2009, pp. 1452-1460.</p>

20) Ren, Y., Liu, Q.H., Chen, Y.P., "A hybrid FEM/MoM method for 3-D electromagnetic scattering in layered medium," *IEEE Transactions on Antennas and Propagation* 64(8), pp. 3487-3495, 2016.

21) Li, Z., Li, Y., Zhao, C., "A new preconditioned SQMR method for solving FEM linear system from electromagnetic problems," *Journal of Computational Information Systems* 11 (4), pp. 1379-1386, 2015.

22) Lambot, S., André, F., "Full-wave modeling of near-field radar data for planar layered media reconstruction," *IEEE Transactions on Geoscience and Remote Sensing* 52 (5), pp. 2295-2303, May 2014.

23) Lambot, S., Anh, P.T., André, F., "Near-field modeling of radar antennas: an intrinsic approach," *EuCAP 2014 – Proc. of the 8th European Conference on Antennas and Propagation*, pp. 3582-3583, 2014.

24) Ardekani, M.R.M., Lambot, S., "Full-wave calibration of time- and frequency-domain ground-penetrating radar in far-field conditions," *IEEE Transactions on Geoscience and Remote Sensing* 52 (1), pp. 664-678, Jan 2014.

25) Lambot, S., Tran, A.P., André, F., "Intrinsic modeling of radar antennas: From far-field to near-field conditions," *IWAGPR 2013 - Proceedings of the 2013 7th International Workshop on Advanced Ground Penetrating Radar*, art. no. 6601520, pp. 159-163, 2013.

26) Chew, W.C., Jiang, L.J., "Overview of large-scale computing: The past, the present, and the future," *Proceedings of the IEEE* 101 (2) , art. no. 6353109 , pp. 227-241, 2013.

27) Lysko, A.A., "On equivalent radius of curvature for PWL geometrical modeling of a loop antenna," *IEEE Antennas and Wireless Propagation Letters* 11 , art. no. 6362161 , pp. 1323-1325, 2012.

28) Lambot, S., André, F., Slob, E., Vereecken, H., "Effect of antenna-medium coupling in the analysis of ground-penetrating radar data," *Near Surface Geophysics* 10 (6) , pp. 631-639, 2012.

29) André, F., Tran, A.P., Mourmeaux, N., Lambot, S., "Integrated modeling of near-field ground-penetrating radar and electromagnetic induction data for reconstructing multilayered media," *14th International Conference on Ground Penetrating Radar, GPR 2012*, pp. 407-412, 2012.

30) Lambot, S., Tran, A.P., André, F., "Near-field modeling of radar antennas for wave propagation in layered media: When models represent reality," *14th International Conference on Ground Penetrating Radar, GPR 2012*, pp. 42-46, 2012.

<p>31) Qin, D.-C., Su, D.-L., Wu, N.-K., Wu, L.-G., "Electromagnetic susceptibility analysis method of electro-explosive devices based on resonance effect," <i>Xi Tong Gong Cheng Yu Dian Zi Ji Shu/Systems Engineering and Electronics</i> 34 (10) , pp. 2005-2009, 2012.</p> <p>32) Webb, J.P., "Gradient-singular, hierarchical finite elements for vector electromagnetics," <i>IEEE Transactions on Antennas and Propagation</i> 60 (6) , art. no. 6183485, pp. 2814-2820, 2012.</p> <p>33) Garcia-Doñoro, D., Martinez-Fernandez, I., Garcia-Castillo, L.E., Zhang, Y., Sarkar, T.K., "RCS computation using a parallel in-core and out-of-core direct solver," <i>Progress in Electromagnetics Research</i> 118 , pp. 505-525, 2011.</p> <p>34) Demaldent, E., Levadoux, D.P., Cohen, G., "Fast and accurate point-based method for time-harmonic maxwell problems involving thin layer materials," <i>Journal of Computational Physics</i> 230 (14) , pp. 5774-5786, 2011.</p> <p>35) Serres, A., Fontgalland, G., De Farias, J.E.P., Baudrand, H., "An efficient algorithm for planar circuits design," <i>IEEE Transactions on Magnetics</i> 46 (8) , art. no. 5512862 , pp. 3441-3444, 2010.</p>	
<p>36) Qin, B., Chen, D. Z., Zhao, L. C., Yang, J., Fan M. W., "An improved matrix method for magnet shimming in compact cyclotrons," <i>Nuclear Instruments & Methods In Physics Research Section A-Accelerators Spectrometers Detectors And Associated Equipment</i> vol. 620, no. 2-3, pp. 121-127, 2010.</p>	<p>S. Ćirković, J. L. Ristić-Djurović, A. Ž. Ilić, V. Vujović, and N. Nešković, "Comparative Analysis of Methods for Isochronous Magnetic-Field Calculation", <i>IEEE Transactions on Nuclear Science</i>, Vol. 55, No. 6, December 2008, pp. 3531-3538.</p>
<p>37) Khodapanah, E., "Efficient 2-D finite-element solution of vector wave equation in a class of curved polygons," <i>IEEE Transactions on Antennas and Propagation</i> 64(8), pp. 3687-3691, 2016.</p> <p>38) Wang, F., Nie, Y.F., Zhang, W.W., Guo, W., "NPBS-based adaptive finite element method for static electromagnetic problems," <i>Journal of Electromagnetic Waves and Applications</i> 30(15), pp. 2020-2038, 2016.</p> <p>39) Petrović, V.V., Mancić, Ž.J., "Calculation of capacitance of rectangular coaxial line with offset inner conductor by using weak FEM formulation," in <i>Proc. 12th Int. Conf. on Telecomm. in Modern Satellite, Cable and Broadcasting Services (TELSIKS)</i>, pp. 342-345, 2015.</p> <p>40) Khodapanah, E., "Numerical separation of vector wave equation in a 2-D doubly connected domain," <i>IEEE Transactions on Microwave Theory and Techniques</i> 62 (11), pp. 2551-2562, 2014.</p> <p>41) Zhao, Y., Ho, S.L., Fu, W.N., "An Adaptive Degrees-of-Freedom Finite-Element Method for Transient Magnetic Field Analysis," <i>IEEE Transactions on Magnetics</i> 49 (12), pp. 5724-5729, 2013.</p>	<p>M. M. Ilić, A. Ž. Ilić, and B. M. Notaroš, "Efficient Large-Domain 2-D FEM Solution of Arbitrary Waveguides Using p-Refinement on Generalized Quadrilaterals," <i>IEEE Transactions on Microwave Theory and Techniques</i>, vol. 53, no. 4, April 2005, pp. 1377-1383.</p>

42) Zhao, Y., Zhang, X., Ho, S.L., Fu, W.N., "An adaptive mesh method in transient finite element analysis of magnetic field using a novel error estimator," *IEEE Transactions on Magnetics* 48 (11), art. no. 6332699, pp. 4160-4163, 2012.

43) Gomez-Revuelto, I., Garcia-Castillo, L.E., Demkowicz, L.F., "A comparison between PML, infinite elements and an iterative BEM as mesh truncation methods for HP self-adaptive procedures in electromagnetics," *Progress in Electromagnetics Research* 126, pp. 499-519, 2012.

44) Mančić, Ž.J., Petrovic, V.V., "Strong FEM Formulation for quasi-static analysis of shielded striplines in anisotropic homogeneous dielectric," *Microwave and Optical Technology Letters* 54 (4), pp. 1001-1006, 2012.

45) Lin, G., Liu, J., Li, J., Fang, H., "Scaled boundary finite element approach for waveguide eigenvalue problem," *IET Microwaves Antennas & Propagation* 5 (12), pp. 1508-1515, 2011.

46) Tuchkin, Yu.A., Suvorova, O., "Analytical regularization method for TE-modes in hollow waveguides modeling," *Proceedings - 2010 12th Int. Conf. on Electromagnetics in Advanced Applications, ICEAA'10*, art. no. 5651066, pp. 720-723, 2010.

47) Suvorova, O., Tuchkin, Y., "Waveguides modeling by analytical regularization method," *European Microwave Week 2009, EuMW 2009: Science, Progress and Quality at Radiofrequencies*, Conference Proceedings - 39th European Microwave Conference, EuMC 2009, art. no. 5296073, pp. 1571-1574, 2009.

48) Tuchkin, Y.A., "Analytical regularization method for hollow waveguides modeling," *Proc. of the 2009 Int. Conf. Electromagn. in Advanced Applications, ICEAA '09*, art. no. 5297288, pp. 709-712, 2009.

49) Zheng, Q., Xie, F., Yao, B., Zhong, R., Cai, W., Li, M., Lin, W., "Analysis of a ridge waveguide family based on subregion solution of multipole theory," *2008 World Automation Congress, WAC 2008*, art. no. 4699103, 2008.

50) Garcia-Castillo, L.E., Pardo, D., Demkowicz, L.F., "Energy-norm-based and goal-oriented automatic hp adaptivity for electromagnetics: Application to waveguide Discontinuities," *IEEE Trans. on Microwave Theory and Tech.* 56 (12), art. no. 4682660, pp. 3039-3049, 2008.

51) Suvorova, O., Tuchkin, Yu., Dikmen, F., "Arbitrary shaped hollow resonators and waveguides modeling. Analytical regularization method," *Mathematical Methods in Electromagnetic Theory, MMET, Conf. Proc.*, art. no. 4581025, pp. 447-449, 2008.

<p>52) Chen, H.H., Yeh, S.F., Chou, Y.H., Hsieh, R.C., "Finite-element method-method of lines approach for the analysis of three-dimensional electromagnetic cavities," <i>IET Microw. Antennas & Propag.</i> 1 (3), pp. 751-756, 2007.</p> <p>53) E. Lezar, D. B. Davidson, [Book Group Author(s): IEEE], "Implementation of arbitrarily high order hierarchical vector basis functions for the finite element analysis of a rectangular waveguide," <i>2007 AFRICON, 8th IEEE Africon Conference</i>, September 26-28, 2007, Windhoek, NAMIBIA, Vols 1-3: 416-421.</p> <p>54) Marais, N, Davidson, DB, "Numerical evaluation of hierarchical vector finite elements on curvilinear domains in 2-D," <i>IEEE Trans. on Antennas and Propagation</i>, 54 (2): 734-738 Part 2 FEB 2006.</p>	
<p>55) Gentili, G.G., Accatino, L., Bertin, G., "The generalized 2.5-D finite-element method for analysis of waveguide components," <i>IEEE Trans. on Microwave Theory and Techniques</i> 64(8), pp. 2392-2400, Aug 2016.</p> <p>56) Petrović, V.V., Mancić, Ž.J., "Calculation of effective permittivity of transmission lines with multilayered medium by using weak FEM formulation of the third order," in <i>Proc. 12th Int. Conf. on Telecomm. in Modern Satellite, Cable and Broadcasting Services (TELSIKS)</i>, pp. 346-349, 2015.</p> <p>57) Mocker, M.S.L., Hipp, S., Spinnler, F., Tazi, H., Eibert, T.F., "Comparison of electromagnetic solvers for antennas mounted on vehicles," <i>Advances in Radio Science</i> 13, pp. 49-55, 2015.</p> <p>58) Lilonga-Boyenga, D., Mabika, C.N., Diezaba, A., "A new multimodal variational formulation analysis of cylindrical waveguide uniaxial discontinuities," <i>Research Journal of Applied Sciences, Engineering and Technology</i> 6 (5) , pp. 787-792, 2013.</p> <p>59) Zhang, Q., Yuan, C.-W., Liu, L., "Theoretical design and analysis for TE 20-TE 10 rectangular waveguide mode converters," <i>IEEE Trans. on Microwave Theory and Techniques</i> 60 (4), pp. 1018-1026, 2012.</p> <p>60) H. H. Chen, S. F. Yeh, Y. H. Chou, et al., "Finite-element method-method of lines approach for the analysis of three-dimensional electromagnetic cavities," <i>IET Microwaves Antennas & Propagation</i>, Vol. 1, No. 3, June 2007, pp. 751-756.</p> <p>61) Ban, Y.-L., Nie, Z.-P., "Higher order hexahedral vector finite element-boundary integral method and an efficient preconditioner for solving the FE-BI matrix equations," <i>Dianbo Kexue Xuebao/Chinese Journal of Radio Science</i> 22 (2) , pp. 196-203, 2007.</p>	<p>M. M. Ilić, A. Ž. Ilić, and B. M. Notaroš, "Higher Order Large-Domain FEM Modeling of 3-D Multiport Waveguide Structures with Arbitrary Discontinuities," <i>IEEE Transactions on Microwave Theory and Techniques</i>, Vol. 52, No. 6, June 2004, pp.1608-1614.</p>

62) J. H. Lee, T. Xiao, Q. H. Liu, "A 3-d spectral-element method using mixed-order curl conforming vector basis functions for electromagnetic fields," *IEEE Transactions on Microwave Theory and Techniques*, Vol. 54, No. 1, January 2006, pp. 437-444.

63) N. Marais, D. B. Davidson, "Numerical evaluation of hierarchical vector finite elements on curvilinear domains in 2-D," *IEEE Transactions on Antennas and Propagation*, Part 2, February 2006, 54 (2): 734-738.

64) Y. L. Ban, Z. P. Nie, (Editors: B. Q. Gao, X. W. Xu), "Condition numbers for higher order vector FEM matrices," *Proc. 2004 3rd International Conference on Computational Electromagnetics and its Applications*, November 01-04, 2004, Beijing, China, pp. 33-35.

РЕПУБЛИКА СРБИЈА



ЕЛЕКТРОТЕХНИЧКИ ФАКУЛТЕТ
УНИВЕРЗИТЕТА У БЕОГРАДУ

ДИПЛОМА

О СТЕЧЕНОМ НАУЧНОМ СТЕПЕНУ
ДОКТОРА НАУКА

ИЛИЋ (Живота) АНЂЕЛИЈА

РОЂЕНА 18. ЈУНА 1973. ГОДИНЕ У БЕОГРАДУ, САВСКИ ВЕНАЦ, РЕПУБЛИКА СРБИЈА, ДАНА 15. ЈУНА 2004. ГОДИНЕ СТЕКЛА ЈЕ АКАДЕМСКИ НАЗИВ МАГИСТРА ТЕХНИЧКИХ НАУКА, А 12. ОКТОБРА 2010. ГОДИНЕ ОДБРАНИЛА ЈЕ ДОКТОРСКУ ДИСЕРТАЦИЈУ НА ЕЛЕКТРОТЕХНИЧКОМ ФАКУЛТЕТУ ПОД НАЗИВОМ „ОПТИМАЛНО УБРЗАВАЊЕ ЧЕСТИЦА У ВИШЕНАМЕНСКИМ ИЗОХРОНИМ ЦИКЛОТРОНИМА”.

НА ОСНОВУ ТОГА ИЗДАЈЕ ЈОЈ СЕ ОВА ДИПЛОМА О СТЕЧЕНОМ НАУЧНОМ СТЕПЕНУ

ДОКТОРА ЕЛЕКТРОТЕХНИЧКИХ НАУКА

Редни број из евиденције о издатим дипломама 13575

У Београду, 2. децембра 2010. године

ДЕКАН


др Миодраг Поповић

(М. П.)

РЕКТОР


др Бранко Ковачевић

Република Србија
МИНИСТАРСТВО ПРОСВЕТЕ
И НАУКЕ
Комисија за стицање научних звања

Број:06-00-75/296
25.05.2011. године
Београд

На основу члана 22. става 2. члана 70. став 5. Закона о научноистраживачкој делатности ("Службени гласник Републике Србије", број 110/05 и 50/06 – исправка и 18/10), члана 2. става 1. и 2. тачке 1 – 4.(прилози) и члана 38. Правилника о поступку и начину вредновања и квантитативном исказивању научноистраживачких резултата истраживача ("Службени гласник Републике Србије", број 38/08) и захтева који је поднео

Института за нуклеарне науке "Винча" у Београду

Комисија за стицање научних звања на седници одржаној 25.05.2011. године, донела је

**ОДЛУКУ
О СТИЦАЊУ НАУЧНОГ ЗВАЊА**

Др Анђелија Илић

стиче научно звање
Научни сарадник

у области природно-математичких наука - физика

О Б Р А З Л О Ж Е Њ Е

Института за нуклеарне науке "Винча" у Београду

утврдио је предлог број 355/13 од 04.03.2011. године на седници научног већа Института и поднео захтев Комисији за стицање научних звања број 355/21 од 21.03.2011. године за доношење одлуке о испуњености услова за стицање научног звања *Научни сарадник*.

Комисија за стицање научних звања је по предходно прибављеном позитивном мишљењу Матичног научног одбора за физику на седници одржаној 25.05.2011. године разматрала захтев и утврдила да именована испуњава услове из члана 70. став 5. Закона о научноистраживачкој делатности ("Службени гласник Републике Србије", број 110/05 и 50/06 – исправка и 18/10), члана 2. става 1. и 2. тачке 1 – 4.(прилози) и члана 38. Правилника о поступку и начину вредновања и квантитативном исказивању научноистраживачких резултата истраживача ("Службени гласник Републике Србије", број 38/08) за стицање научног звања *Научни сарадник*, па је одлучила као у изреци ове одлуке.

Доношењем ове одлуке именована стиче сва права која јој на основу ње по закону припадају.

Одлуку доставити подносиоцу захтева, именованој и архиви Министарства просвете и науке у Београду.

ПРЕДСЕДНИК КОМИСИЈЕ
др Станислава Стошић-Грујичић,
научни саветник

С. С. Грујичић



Република Србија
МИНИСТАРСТВО ПРОСВЕТЕ,
НАУКЕ И ТЕХНОЛОШКОГ РАЗВОЈА
Комисија за стицање научних звања

Број:660-01-00001/85
28.09.2016. године
Београд

ИНСТИТУТ ЗА ФИЗИКУ			
ПРИМЉЕНО: 2-11-2016			
Рад.јед.	б р о ј	Арх.шифра	Прилог
0801	1839/1		

На основу члана 22. става 2. члана 70. став 5. и члана 86. став 1. и 2. Закона о научноистраживачкој делатности ("Службени гласник Републике Србије", број 110/05 и 50/06 – исправка и 18/10), члана 50. став 1. Закона о изменама и допунама Закона о научноистраживачкој делатности ("Службени гласник Републике Србије", број 112/15), члана 2. става 1. и 2. тачке 1 – 4.(прилози), члана 31. став 1., члана 37. и 38. Правилника о поступку и начину вредновања и квантитативном исказивању научноистраживачких резултата истраживача ("Службени гласник Републике Србије", број 38/08) и захтева који је поднео

Инстѿиѿуѿ за физику у Београду

Комисија за стицање научних звања на седници одржаној 28.09.2016. године, донела је

**ОДЛУКУ
О СТИЦАЊУ НАУЧНОГ ЗВАЊА**

Др Анђелија Илић

стиче научно звање
Научни сарадник
Реизбор

у области природно-математичких наука - физика

О Б Р А З Л О Ж Е Њ Е

Инстѿиѿуѿ за физику у Београду

утврдио је предлог број 201/1 од 09.02.2016. године на седници Научног већа Института и поднео захтев Комисији за стицање научних звања број 237/1 од 17.02.2016. године за доношење одлуке о испуњености услова за реизбор у научно звање **Научни сарадник**.

Комисија за стицање научних звања је по претходно прибављеном позитивном мишљењу Матичног научног одбора за физику на седници одржаној 28.09.2016. године разматрала захтев и утврдила да именована испуњава услове из члана 70. став 5. и члана 86. став 1. Закона о научноистраживачкој делатности ("Службени гласник Републике Србије", број 110/05 и 50/06 – исправка и 18/10), члана 2. става 1. и 2. тачке 1 – 4.(прилози), члана 31. став 1., 37. и 38. Правилника о поступку и начину вредновања и квантитативном исказивању научноистраживачких резултата истраживача ("Службени гласник Републике Србије", број 38/08) за реизбор у научно звање **Научни сарадник**, па је одлучила као у изреци ове одлуке.

Доношењем ове одлуке именована стиче сва права која јој на основу ње по закону припадају.

Одлуку доставити подносиоцу захтева, именованој и архиви Министарства просвете, науке и технолошког развоја у Београду.

ПРЕДСЕДНИК КОМИСИЈЕ

Др Станислава Стошић-Грујичић,
научни саветник

С. Стошић-Грујичић



PRELIMINARY RESULTS OF THE ION TRAJECTORY TRACKING IN THE ACCELERATION REGION OF THE VINCY CYCLOTRON

Andjelija Ž. Ilić, Jasna L. Ristić-Djurović, and Saša T. Ćirković,
 Vinča Institute of Nuclear Sciences, Laboratory of Physics (010), P.O. Box 522, 11001 Belgrade, Serbia and Montenegro

Nagrađeni rad mladog istraživača

Abstract – In an accelerating region of a cyclotron an ion makes a large number of turns; thus its tracking requires fast as well as highly accurate computation. Computer code, based on the adaptive time step fourth order Runge-Kutta method, has been developed. Accuracy requirement is set simultaneously on the position and momentum calculation. Magnetic fields, used as input, have been evaluated in terms of the radial fluctuations of the orbital frequency, i.e. their isochronism. Ion trajectory tracking has been performed for the four test beams: H^- , H_2^+ , $^4He^+$, and $^{40}Ar^{6+}$.

1. INTRODUCTION

In a cyclotron design and its beam dynamics analysis it is common to treat separately its central, acceleration, and extraction regions. This is because each of these regions imposes different requirements and challenges. In the acceleration region, ions travel through an isochronized magnetic field, tracing a spiral orbit. Very large number of turns is performed, resulting in a large trajectory length. As a consequence the crucial requirement is to improve computation speed, while preserving high accuracy over the long integration time. The software package VINDY tailored to accommodate primarily the extraction region beam dynamics and analysis, has been developed previously [1]. However, a beam trajectory in the extraction region is several hundreds times shorter than in the acceleration region. Also in the extraction region a beam trajectory is shaped by the magnetic field solely while in the acceleration region the fundamental i.e. accelerating effect comes from the electric field. Thus the particle tracking code of the VINDY package had to be changed substantially. A new software package for the acceleration region beam dynamics simulation and analysis is developed and added to the VINDY package. Note that it could be easily applied to the central region as well, if the numerically calculated electric field maps are used as input and if the procedures describing the obstacles in the central region (such as posts) are integrated with the rest of the code. Our goal is to describe the simulation and analysis method and assess its efficiency. The results of the simulation for the four test beams are given as an illustration of the trajectory tracking computational method.

2. THE VINCY CYCLOTRON

The VINCY Cyclotron [2] is a multipurpose machine whose function is to accelerate light ions as well as heavy ions with specific charges ranging from $\eta = 0.15$ to $\eta = 1$. The cyclotron magnet has four straight sectors per pole, a pole diameter of 2 m, a sector-to-sector gap of 36 mm, and a valley-to-valley gap of 190 mm. The maximum magnetic induction in the machine center is 1.97 T.

The isochronized magnetic fields in the median plane used as input are calculated according to Gordon's procedure [3] and they are based on the measured magnetic field maps as well as on the simulated magnetic field maps obtained using MERMAID – the finite element software package [4].

The test ion beams of the VINCY Cyclotron are 65 MeV H^- , 30 MeV per nucleon H_2^+ , 7 MeV per nucleon $^4He^+$, and 3 MeV per nucleon $^{40}Ar^{6+}$ beams. These four ion beams have been chosen to check the four acceleration regimes, employing acceleration with harmonic numbers 1, 2, 3, and 4, respectively. The corresponding RF frequencies and peak dee voltages are shown in Table 1.

3. METHOD DESCRIPTION

Charged particle motion inside the cyclotron may be described by the following equations:

$$\frac{d\mathbf{r}(t)}{dt} = \frac{1}{m_0} \sqrt{1 - \left(\frac{v(t)}{c}\right)^2} \mathbf{p}(t), \quad (1)$$

and

$$\frac{d\mathbf{p}(t)}{dt} = \frac{q}{m_0} \left(m_0 \mathbf{E}(t, \mathbf{r}) + \sqrt{1 - \left(\frac{v(t)}{c}\right)^2} \mathbf{p}(t) \times \mathbf{B}(\mathbf{r}) \right), \quad (2)$$

where \mathbf{r} represents the position of the particle, \mathbf{p} is the momentum, and v is the velocity intensity. The rest-mass of the particle is m_0 , q is the electric charge, and c is the speed of light. Electric field inside the cyclotron is \mathbf{E} and magnetic induction is \mathbf{B} .

An algorithm with the adaptive time step is proposed for tracking beam trajectories in the accelerating region. Previously developed computer code for the extraction region utilized the fourth order Runge-Kutta ODE integration scheme. It is often used in the problems of trajectory tracking for its simplicity, good accuracy as well as stability. Without the adaptive time step, however, it would result in intolerably long computation times and further to an insufficient accuracy. Thus, the above equations are solved using the adaptive time step Runge-Kutta method of the fourth order. The chosen time steps have to comply with the two accuracy requirements – the local position calculation error must not exceed the required maximal position error x_{err} , while the local error of the momentum calculation must not be greater than the maximal momentum error, p_{err} , given as a fraction of the initial momentum. In addition to the described main procedure, other changes have been made and a set of auxiliary procedures has been developed.



Društvo za elektroniku, telekomunikacije,
računarstvo, automatiku i nuklearnu tehniku

Na 57. konferenciji ETRAN dodeljena je

NAGRADA

koju dobijaju

**Miloš Davidović, Anđelija Ilić, Miodrag Tasić,
Branislav Notaroš, Milan Ilić**

autori rada

**CONVERGENCE OF MODAL
ELECTROMAGNETIC FIELDS IN A B-SPLINE
FINITE ELEMENT METHOD**

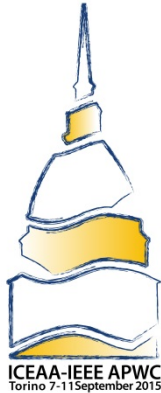
za najbolji rad na sekciji za

AP
Antene
i prostiranje

Predsednik Programskog odbora
Dr Zoran Jakšić, dipl. inž, naučni savetnik

Predsednik Predsedništva
Prof. dr Bratislav Milovanović, dipl. inž.

- Vrnjačka Banja, 2. juna 2014.



Torino, January 8, 2015

Dear Dr. Ilic

We are organizing a special session on “Numerical Methods in Electromagnetics” for the seventeenth edition of ICEAA (International Conference on Electromagnetics in Advanced Applications) to be held in Torino, Italy on September 7-11, 2015. This session will consist of 12/14 papers contributed and presented by experts in the field.

Because of your recognized expertise in the area, we are inviting you to submit a paper to this session. The session will concentrate on methods such as finite, boundary element (integral equation), and related methods (e.g., fast or hybrid numerical methods).

To provide some background on the conference, ICEAA is held in Torino every two years (on odd years), while it has an off-shore edition on even years. In our opinion, the Torino edition of this Conference has many desirable features. It is relatively small (no more than four parallel sessions and roughly 300 participants). Invited speakers completely comprise many of the sessions, and hence the technical level tends to be quite high. Additionally, the Conference is well organized, informal, and structured to promote interaction among participants. The city of Torino is also a very interesting and comfortable venue—and the Piedmontese cuisine is, of course, outstanding!

ICEAA 2015 is coupled to the fifth edition of the *IEEE-APS Topical Conference on Antennas and Propagation in Wireless Communications* (APWC 2015). The two conferences share a common organization, registration fee, submission site, workshops and short courses, and social events. The proceedings of the conferences will be published on IEEE Xplore.

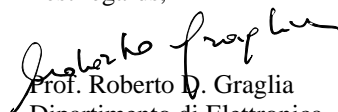
More details on ICEAA and Torino may be found on the conference web site at


<http://www.iceaa.net/>

We are hoping you will agree to present a paper and will let us know your intentions very soon. Since your paper is invited for a Special Session, an abstract is desirable but not essential. However, we would like to receive (via email) the title and list of authors for your submission by February 20, 2015 if possible. A four-page manuscript to appear in the Conference Proceedings will be due by June 5, 2015. You will also need to register your paper for this Special Session via the web (<http://www.iceaa.net/>), and execute an IEEE copyright form, since the ICEAA Proceedings will appear on IEEE Xplore. Please keep in mind that all participants are responsible for registration and all other expenses.

Please email or call us if you have any additional questions. Thank you very much for considering this request.

Best regards,


Prof. Roberto D. Graglia
Dipartimento di Elettronica,
Politecnico di Torino
Corso Duca degli Abruzzi 24,
10129 Torino, ITALY
ph.: (39) 011 090 4056
fax: (39) 011 090 4099
email: roberto.graglia@polito.it


Prof. Donald R. Wilton
Dept. of Electrical Engineering
University of Houston
N308 Engineering Building 1
Houston, Texas 77204-4005, USA
ph.: (1) 713 743 4442
fax: (1) 713 743 4444
email: wilton@uh.edu

December 10, 2015

Dear Dr. Ilic,

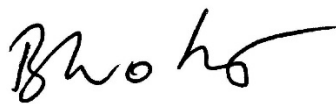
We are organizing the Special Session “Advanced FEM and Hybrid Techniques” for the 13th International Workshop on Finite Elements for Microwave Engineering – FEM2016, to be held from May 16-18, 2016, in Florence, Italy. This has been a great biannual Workshop, and the venue and program for its 2016 edition is extremely promising.

Given your expertise in the field, we would like to cordially invite you to contribute a paper on your work for the Special Session that we are organizing. With several invited contributions, we expect a considerable amount of high quality recent results to be discussed.

More information about the conference can be found at the Conference web page: <http://www.dinfo.unifi.it/cmpro-v-p-138.html> .

Please respond by Friday December 18, 2015 and let us know whether or not you will be able and willing to contribute an abstract to this session.

Thanks and best regards,



Prof. Branislav Notaros
Department of Electrical and
Computer Engineering,
Colorado State University,
1373 Campus Delivery,
Fort Collins, CO 80523-1373, USA
phone: (970) 491-3537
email: notaros@engr.colostate.edu



Prof. Juan Zapata
Departamento de Electromagnetismo
y Teoría de Circuitos,
Universidad Politécnica de Madrid,
Ciudad Universitaria s/n,
28040 Madrid, Spain
phone: +34 914533526
email: jzapata@etc.upm.es

Универзитет у Београду – Електротехнички факултет
Катедра за општу електротехнику
1. децембар 2015.

Научном већу Института за физику у Београду
Комисији МПНТР за стицање научних звања

Предмет: Учешће у изради заједничких научно-стручних радова
са студентима мастер / докторских студија

Поштовани,

Овим потврђујем да ми је др Анђелија Илић из Института за физику у Београду помогла приликом израде заједничких научних радова који се односе на генерисање и оптимизацију великодоменских прорачунских мрежа за метод коначних елемената, параметризацију пресликавања из реалног у прорачунски домен и оптимално подешавање редова елемената према задатом проблему. Др Анђелија Илић је експерт за поменуте теме јер их је обрађивала у оквиру истраживачког рада на својој магистарској тези.

Три рада у научним часописима, од којих један у часопису са SCI листе, објављени су као резултат заједничког рада и саветовања о поменутим темама и део су моје докторске дисертације. Ти радови су:

1. М. М. Илић, S. V. Savić, A. Ž. Илић, and B. M. Notaroš, “Constant speed parametrization mapping of curved boundary surfaces in higher order moment-method electromagnetic modeling”, *IEEE Antennas and Wireless Propagation Letters*, Vol. 10, December 2011, pp. 1457-1460. (DOI (identifier) 10.1109/LAWP.2011.2180354),
2. М. М. Илић, S. V. Savić, A. Ž. Илић, and B. M. Notaroš, “Hybrid higher order FEM-MoM analysis of continuously inhomogeneous electromagnetic scatterers”, *Telfor Journal*, Vol. 3, No. 2, 2011, pp. 121-124 и
3. A. Ž. Илић, S. V. Savić, M. M. Илић, and B. M. Notaroš, “Analysis of electromagnetic scatterers using hybrid higher order FEM-MoM technique”, *Telfor Journal*, Vol. 1(2), 2009, pp.53-56.

Заједно је публиковано и пет саопштења на међународним скуповима, где смо др Анђелија Илић и ја коаутори.

Веће научних области техничких наука Универзитета у Београду одобрило је усмену одбрану моје докторске дисертације под насловом „Закривљени континуално нехомогени и неизотропни коначни елементи вишег реда за великодоменско електромагнетско моделовање“ на седници одржаној 23.11.2015. године. Усмена одбрана је заказана за 17.12.2015. године.

Ову потврду састављам како би др Анђелија Илић могла да је приложи приликом конкурсана за наредно научно звање.

С поштовањем,

Слободан Савић, асистент у настави
Електротехнички факултет у Београду

Захвалница

Ова докторска дисертација је настала као резултат мог вишегодишњег настојања да разумем и савладам основне концепте у пројектовању микроталасних појачавача снаге, да усвојена знања искористим за развој новог појачавача побољшаних перформанси у односу на постојећа решења, као и да у свом раду на правилан начин користим напредне технике нумеричке анализе сложених микроталасних кола које значајно скраћују времена пројектовања уређаја. Успешно савладавање наведених концепата и висок квалитет постигнутих истраживачких резултата не би били могући без изузетног ангажовања ментора в. проф. др Милана Илића, на чему сам му веома захвалан.

У делу докторске дисертације који се бави пуноталасним нумеричким моделовањем и анализом сложених микроталасних кола, велику помоћ ми је пружила и др Анђелија Илић, научни сарадник Института за физику Универзитета у Београду. Др Илић је значајно допринела и мом разумевању могућности и ограничења примене нових дводимензионих материјала на високим учестаностима, чиме се бави један део дисертације. Заједнички рад и консултације резултовали су високим квалитетом публикованог истраживања из ове области. Стога се посебно захваљујем др Анђелији Илић.

Током докторских студија, добио сам и искористио прилику да две године проведем на University of Westminster, London, у Великој Британији. У том периоду су настављена моја истраживања у вези са микроталасним колима, али и отпочета истраживања могуће примене графена у микроталасној техници. На сарадњи и свему што сам научио током боравка у склопу међу-универзитетске размене, захваљујем се проф. др Ђурађу Будимиру, руководиоцу Групе за истраживање бежичних телекомуникација. Такође сам захвалан и академику Антонију Ђорђевићу на консултацијама и многим корисним саветима које ми је дао у току докторских студија, као и в. проф. др Наташи Нешковић, која је отпочела руковођење мојим студијским радом, а затим ме је несебично упутила на ментора који би могао да руководи темом истраживања из уже области коју сам изабрао.

Конечно, колегама из компаније ИМТЕЛ Комуникације се захваљујем на пруженој подршци и разумевању, а на изузетној подршци захваљујем се породици и пријатељима.

У Београду, 23. јула 2016.

Прилог Б.2.3

ПОДАЦИ О ЗАПОСЛЕЊУ

Број евиденције	Назив и седиште послодавца, основ осигурања	Почетак рада - осигурања
957	ЕЛЕКТРОТЕХНИЧКИ ФАКУЛТЕТ БЕОГРАД Булевар револуције 73, ПФ 816 11001 БЕОГРАД	01.10. 1999.
3645	ИНОВАЦИОНИ ЦЕНТАР ЕЛЕКТРОТЕХНИЧКИ ФАКУЛТЕТ	01.04. 2004.
	ИЦ Број: 659/11 Датум: 01.01. за 13 год БЕОГРАД Булевар револуције 73	01.01. 2013

И СТАЖУ ОСИГУРАЊА

Престанак рада - осигурања	Стаж		
	година	месеци	дана
01.09. 2001.	01	11	01
31.12. 2012.	=8=	=9=	=0=





EUROWEB Project - Erasmus Mundus Action 2

Scholarship Award Letter

May 1st, 2013

To: Andjelija ILIC

Date of birth: 1973-06-18

Address: Nehruova 146, 11070 Belgrade, Serbia

Host institution: University of Westminster, UK

Mobility type and period: Post-Doctorate starting on 2013-09-16 for 10 months

Dear applicant,

Congratulations! You have been selected by the EUROWEB Project for the award of a mobility scholarship, based on a multi-level selection process.

The EUROWEB project is coordinated by the Mälardalen University, Sweden, and is funded by the European Commission under the Erasmus Mundus Action 2 programme.

During the mobility period, you will receive* a monthly subsistence allowance from the Host Institution, depending on the mobility type:

- 1000€ for Undergraduates/Masters students
- 1500€ for Ph.D scholars
- 1800€ for Post-Docs
- 2500€ for Staff

The EUROWEB Scholarship also covers:

- Travel costs (one return ticket, up to a pre-defined maximum amount, based on the travel distance)
- Full Insurance costs (health, travel and accident)
- Tuition fees for the scholarship period are waived by the Host Institution.

The regulations and procedures concerning this scholarship as prescribed by the funding agency and the EUROWEB Project are described at the project web sites listed below:

- Erasmus Mundus: http://eacea.ec.europa.eu/erasmus_mundus/programme/action2_en.php
- EUROWEB Project: <http://www.mrtc.mdh.se/euroweb/>

* Please note that any violation to the regulations or requirements at the Home- or Host Institution may result in cancellation/revocation of the award.

Congratulations again, and best wishes for achieving excellence in your Education/ Research/ Work Assignment.

Best regards,

Prof. Sasikumar Punnekkat

Project Director

EUROWEB – European Research and Educational Collaboration with Western Balkans

ОЦЕНА ТЕХНИЧКОГ РЕШЕЊА

Прилог Б.3.2.

На основу сагласности Наставно-научног већа Електротехничког факултета у Београду датој на својој 758. седници одржаној 22.01.2013. године Комисија за студије трећег степена донела је одлуку да се прихвати техничко решење:

Назив техничког решења: Употреба МАДУ трака у биомедицинским експериментима

Аутори техничког решења: Анђелија Илић, Саша Ћирковић, Јасна Ристић – Ђуровић, Драго Ђорђевић, Александар Трбовић

Врста техничког решења: Битно побољшано решење на националном нивоу

М фактор техничког решења (М81-М86 фактор): М84

Београд, 15.01.2014.

Б.а. Председник Комисије за студије трећег степена

Бранко Колунџија
Проф. др Бранко Колунџија



Универзитет у Београду
Иновациони центар Електротехничког факултета

А. Илић, С. Ђирковић, Ј. Ристић-Ђуровић, Д. Ђорђевић и А. Трбовић

УПОТРЕБА МАДУ ТРАКА
У БИОМЕДИЦИНСКИМ ЕКСПЕРИМЕНТИМА
– Техничка документација –



Београд, 2013.

M84: Битно побољшано техничко решење на националном нивоу УПОТРЕБА МАДУ ТРАКА У БИОМЕДИЦИНСКИМ ЕКСПЕРИМЕНТИМА

Руководилац пројекта: Небојша Ромчевић
Одговорно лице: Анђелија Илић
Аутори: Анђелија Илић, Саша Ђирковић, Јасна Ристић-Ђуровић, Драго Ђорђевић, Александар Трбовић
Развијено: у оквиру пројекта Интегралних и интердисциплинарних истраживања (ИИИ), број ИИИ-45003
Година: 2013.
Примена: 01.03.2013.

Кратак опис

У склопу овог техничког решења, изведене су и дате егзактне формуле за рачунање магнетске индукције произвољног дводимензионог магнетског низа, на основу њих је предложен једноставан начин одређивања средњих параметара магнетског поља који су од интереса за кориснике оваквих низова, написана је процедура за MATLAB која рачуна расподелу поља и средње параметре за произвољан случај. За конфигурације које се уобичајено користе подаци су дати и табеларно, у оквиру “Упутства за употребу МАДУ трака у биомедицинским огледима“, припремљеног за студенте и сараднике Медицинског факултета у Београду.

Реализатори:

Иновациони центар Електротехничког факултета, Универзитет у Београду

Корисници:

Медицински факултет, Универзитет у Београду

Подтип решења:

Битно побољшано техничко решење на националном нивоу (M84)

Стање у свету

Стални магнети, као и њихове комбинације у виду површинских низова, користе се већ дуго времена у области физикалне терапије и рехабилитације. Иако сви механизми деловања нису у потпуности разјашњени, емпиријски је утврђен благотворан, односно позитиван, утицај на ублажавање тегоба проузрокованих артритисом, ублажавање запаљења и залечивање рана, ублажавање бола и стреса и побољшање микроциркулације [1]-[6]. Такође, различите комбинације сталних магнета су погодне као извор статичког магнетског поља у биомедицинским огледима *in vitro* или огледима на малим животињама, као у [7]. Овде је потребно нагласити, да током прегледа постојеће литературе нисмо наишли на пример коришћења дводимензионог магнетског

Design of a Combined Function Magnet With Individually Adjustable Functions

Andjelija Ž. Ilić, *Member, IEEE*, Saša T. Ćirković, Milan M. Ilić, *Member, IEEE*, and Jasna L. Ristić-Djurović

Abstract—Design of combined function magnets for accelerators is often limited to minor modifications of the existing components, maintaining the high quality of the main harmonic field component, but restricting the range of operation. We investigate the possibility to achieve a wide range of both steering magnetic flux density and focusing field gradients, by utilizing two individually powered magnet parts. A general design methodology is presented, enabling fully customized design and optimization of magnets for different applications. The design procedure is illustrated via a detailed design of a magnet proposed for application in the stripping extraction system of a multipurpose cyclotron.

Index Terms—Accelerator magnets, analytical modeling, combined function magnets (CFMs), design optimization, finite-element analysis, ion beam focusing, ion beam steering.

I. INTRODUCTION

SPACE and cost reduction in the design of system components is one of the current topics in accelerator physics and related technologies. Combined function magnets (CFMs) present an attractive solution to achieve the desired compact design. Most often, the CFMs are used in beam lines, storage rings, synchrotrons, and linear accelerators [1]–[7]. A reduction in an otherwise very large number of magnets, required in these structures, is facilitated by combining of dipole, quadrupole, and/or sextupole fields in a fewer number of components. In many cases, the CFM design relies on the standard quadrupole or sextupole design, with the addition of extra coils, resulting in the combined function. This seems to be the most straightforward solution from the standpoint of maintaining the high field quality, while avoiding a cumbersome custom CFM design, as well as possible fabrication errors. If independent powering of the additional coils is enabled, a combined function is established; however, additional field components remain supplemental and adjustable within a limited range. Without independent powering, the ratios of the harmonic field

components are fixed by design. When CFMs are incorporated into compact structures, such as medical gantries or medical accelerators [8], [9], it is reasonable to undertake a custom design and optimization of magnets. After fabrication and assembly, further analyses are usually conducted to assess the performance and to ensure fulfillment of the design goals [10], [11].

We investigate a general design methodology and parameter optimization for the customized CFM design with the individually adjustable bending and focusing functions. Namely, the ferromagnetic structure and the pole profile shapes are sought, that allow the CFM operation in various regimes, depending on the powering of the coils. The feasibility of the proposed concept has been confirmed in our previous study [12]. Two independently powered slanted dipoles comprised the CFM, whose design specifications were set having in mind its utilization in the extraction system of a multipurpose cyclotron. The increased design complexity for the extraction system comes as a price for the cost-efficient acceleration of a number of ion beams for various applications, obtained by changing the operating mode of the machine. Stripping extraction systems are a good solution for the extraction of more than one beam into a single transport line [13]–[15]. If both the negative and positive ion beams are accelerated, beam paths, as well as transverse emittances, will vary significantly after the stripping extraction, depending on the sign of ion charge during acceleration [16]–[19]. Directions of ion beams accelerated as positive will not differ very much among themselves; however, focusing of the beams in the horizontal direction will be required as soon as they leave the cyclotron. For the ion beams accelerated as negative, focusing after extraction is usually not required, due to the change of sign during stripping. However, directions after the extraction will be significantly different from those of ion beams accelerated as positive. Therefore, adjustable strong horizontal focusing, combined with weak horizontal bending, is needed for the ion beams accelerated as positive, whereas strong horizontal bending in the opposite direction is required for beams accelerated as negative. As explained in [12], a single device per cyclotron is required, ion beams will pass through the CFM only once, off-centered from the device axis, and the minimization of higher multipole harmonics is not critical to the extracted beam quality.

The design optimization that is the subject of this paper is quite general and applicable to diverse slanted dipole CFM designs. We employ it in the detailed development of the

Manuscript received December 7, 2016; revised February 5, 2017 and March 15, 2017; accepted March 15, 2017. This work was supported by the Serbian Ministry of Education, Science, and Technological Development under Grant III-45003.

A. Ž. Ilić, S. T. Ćirković, and J. L. Ristić-Djurović are with the Institute of Physics, University of Belgrade, 11080 Zemun-Belgrade, Serbia (e-mail: andjelija@iee.org; sasa.cirkovic@ipb.ac.rs; jasna@stanfordalumni.org).

M. M. Ilić is with the School of Electrical Engineering, University of Belgrade, 11120 Belgrade, Serbia, and also with the Department of Electrical and Computer Engineering, Colorado State University, Fort Collins, CO 80523-1373 USA (e-mail: milanilic@etf.rs).

Color versions of one or more of the figures in this paper are available online at <http://ieeexplore.ieee.org>.

Digital Object Identifier 10.1109/TNS.2017.2684745

CFM for the stripping extraction in a multipurpose cyclotron, building upon the results of our previous study, which was to check on the validity of the proposed concept rather than to achieve the final device configuration. While the superconducting CFM design relies mostly on optimizing the coil winding configuration [8], [20], modeling of the ferromagnetic core electromagnets, as well as ferromagnetic dominated superconducting magnets (superferric magnets), focuses on achieving the most suitable pole profile configuration [2], [21]. However, unless a large degree of angular (polar) symmetry is assumed, it is preferable to perform both the linear and the nonlinear analysis. Although extensive numerical calculations are indispensable in the accurate modeling of ferromagnetic cores, mapping of the complete design space in that way would be unpractical. On the other hand, analytical modeling of current sheets can provide a good first approximation of the field due to the coils, permanent magnets, or highly saturated ferromagnetic parts. Therefore, we suggest the following methodology. In the first step, an individual slanted dipole is modeled analytically, mapping the relevant magnetic field parameters for that case. The purpose of analytical modeling is to estimate the relative changes in magnetic field parameters of interest with variation of dipole geometrical parameters. With the use of obtained data, the ranges of input parameters for accurate but time consuming numerical calculations can be narrowed. A more realistic analytical model for the slanted dipole is assumed in this paper, in comparison to [12], and the optimization is extended to the six-parameter design space. Additionally, a pool of the best solutions is selected instead of a single set of parameters, to ensure that no good solutions are omitted. Some of the parameters are then fixed, and the rest of the analysis is performed using the finite-element software tools. Special attention is directed to the linearity of the magnetic flux density within the beam area. In particular, poor linearity in the single dipole case prevents obtaining the field of satisfactory quality for different combinations of coil currents. Excellent linearity of the single dipole magnetic flux density, obtained analytically, will be somewhat deteriorated in practice due to the nonlinear behavior of magnetic materials. Sum of the dipole fields additionally includes the coupling effects; even so, satisfactory field quality can be expected if the initial requirements were stringent enough. Pole profiling is performed last, followed by the analysis of operating modes that can be attained. Iterative pole profiling can be done if further improvements in any of the design criteria are required. An outline of the necessary steps in the optimization process is next illustrated through the design of the CFM for the stripping extraction system.

II. ANALYTICAL PROBLEM MODELING

Analytical modeling of a single slanted off-centered dipole, relying on the two-parameter ideal dipoles model, as well as the four-parameter current stripes model, has been performed in [12]. Despite the fact that the first model is point-based, whereas the second model is infinitely long in parallel to the CFM axis, general conclusions regarding the pole positioning and the slant angle optimization were similar. The positioning of the poles with respect to the CFM axis is defined using the

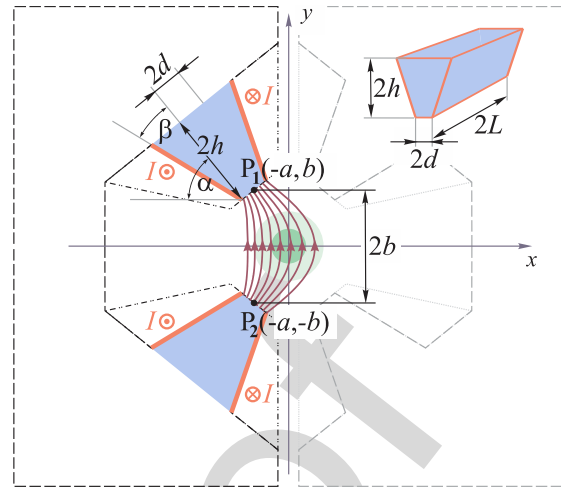


Fig. 1. Generalized slanted dipole CFM design. Only half of the CFM and its magnetic flux lines are shown. Independent powering of the two identical halves allows the CFM operation in various regimes. Linearity of the achieved fields within the beam area, depicted by the green circle about the origin, should be as good as possible. Geometrical parameters that can be varied in the design optimization are denoted in the figure. These are: the normalized half-distance between the poles of a dipole, b/a , slant angle, α , wedge angle, β , normalized half-width of the poles, d/a , normalized half-height of the poles, h/a , and normalized half-length of the poles, L/a . The small top right figure shows a side view of a pole tip, with denoted dimensions.

aspect ratio, b/a , of the rectangle whose sides equal the vertical and the horizontal distance of the pole midline from the CFM axis, as shown in Fig. 1. The slant angle is denoted by α . The four-parameter model additionally considered the pole width and height. However, in order to realistically model the actual pole geometry, we must also account for the finite length of the structure, as well as the widening of the poles toward the yoke. Widening of the poles toward the yoke improves the magnetic flux leading capabilities of the entire dipole, whereas the narrower pole tips result in the desired good field linearity in the beam area. With this proper positioning of the ferromagnetic–vacuum boundary surface, and assuming the uniform magnetization over the volume of a single pole, effect of the ferromagnetic material on the magnetic flux density can be modeled using the equivalent magnetization currents

$$\mathbf{J}_{mS} = \mathbf{M} \times \mathbf{n}. \quad (1)$$

In (1), \mathbf{M} denotes the magnetization vector, \mathbf{J}_{mS} the surface current density vector due to the equivalent magnetization currents, and \mathbf{n} the surface normal, i.e., the unit vector perpendicular to the boundary surface, directed from the ferromagnetic outwards. The assumption of uniform magnetization is appropriate for modeling of permanent magnets or highly saturated ferromagnetic cores, whereas for a smaller magnetomotive force this model gives a first approximation of the magnetic flux density due to the ferromagnetic material. Magnetic flux density components resulting from the current coils in a vacuum are typically several times smaller than the total magnetic flux density components due to the coils and magnetic cores. Therefore, to keep the analytical model simple, we assume close adherence of the current coils to the core boundary surfaces. Four current sheets per pole are

170 modeled—two rectangular current sheets perpendicular to the
 171 xOy plane as shown in Fig. 1, as well as two trapezoidal
 172 current sheets parallel to the xOy plane at a distance $z = \pm L$
 173 from the xOy plane.

174 Denoting the coil current per unit width of the current sheet
 175 by J_{ccS} , the total model current, I , results from integration
 176 over the current sheet width of the total surface current density
 177 $\mathbf{J}_0 = \mathbf{J}_{ccS} + \mathbf{J}_{ms}$. For the rectangular and trapezoidal sheets,
 178 $J_0^R = |\mathbf{J}_0^R| = I \cos \beta / (2h)$ and $J_0^T = |\mathbf{J}_0^T| = I / (2h)$,
 179 respectively. Each of the four current sheets can be
 180 regarded as a collection of finite straight thin wires carry-
 181 ing the current dI and producing the magnetic flux density
 182 component dB [22], [23]

$$dB = \frac{\mu_0 dI}{4\pi R} (\sin \theta_2 - \sin \theta_1). \quad (2)$$

184 The shortest (perpendicular) distance of the considered field
 185 point F to the thin finite wire axis is denoted by R . Angles
 186 θ_1 and θ_2 are measured between the direction of R and the
 187 lines connecting the field point F to the two wire ends, with
 188 θ_1 corresponding to the point of current entrance into the wire
 189 and θ_2 corresponding to the point of current exit from the
 190 wire. Free space permeability is denoted by μ_0 . Vector $d\mathbf{B}$ is
 191 perpendicular to the plane defined by the wire and the field
 192 point F , and related to dI by the right-hand rule. Closed-
 193 form analytical expressions for the magnetic flux density of the
 194 rectangular current sheets [23] are obtained by integrating (2)

$$\begin{aligned}
 & B_{x_S} \\
 &= \frac{\mu_0 J_0^R}{4\pi} \\
 & \times \begin{cases} \sum_{tq=0,1} (-1)^{tq} \ln \left(\frac{\sqrt{L^2 + u_S^2} - L}{\sqrt{L^2 + u_S^2} + L} \right) & x_S = 0 \\ \sum_{tq=0,1} 2(-1)^{tq} \ln \left(\frac{|x_S| \cdot (-1 + \sqrt{1 + (x_S^2 + u_S^2)/L^2})}{\sqrt{x_S^2 + u_S^2}} \right) & x_S \neq 0 \end{cases} \\
 & B_{y_S} \\
 &= \frac{\mu_0 J_0^R}{4\pi} \\
 & \times \begin{cases} 0, & x_S = 0 \\ \sum_{tq=0,1} 2(-1)^{(tq+1)} \arcsin \left(\frac{u_S \cdot \text{sgn}(x_S) \cdot L}{\sqrt{L^2 + x_S^2} \sqrt{x_S^2 + u_S^2}} \right) & x_S \neq 0 \end{cases} \\
 & u_S = y_S + 2h(1 - tq) / \cos \beta. \quad (3)
 \end{aligned}$$

202 Local coordinate axes, x_S and y_S , for the rectangular sheet of
 203 the upper pole closer to the global x -axis (shown in Fig. 1),
 204 are rotated by $(3\pi/2 + \beta - \alpha)$ with respect to the x - and y -axes.
 205 Local coordinates, x_S and y_S , of the upper pole sheet closer
 206 to the y -axis, are rotated by $(3\pi/2 - \beta - \alpha)$ with respect to the
 207 x - and y -axes. Local y_S -axis belongs to the plane of the sheet,
 208 whereas x_S -axis is perpendicular to y_S , as well as a sheet

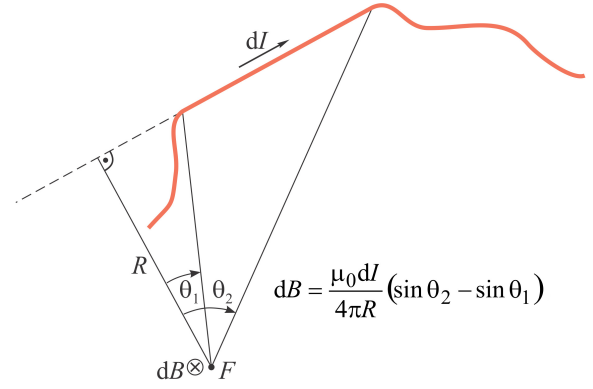


Fig. 2. Magnetic flux density for a finite straight thin wire. Current sheets corresponding to the vacuum–ferromagnetic material boundary surfaces can be regarded as collections of finite straight wires.

209 edge closest to the beam area. Sign of the B_{x_S} component for
 210 the rectangular sheet closer to the y -axis is opposite than that
 211 shown in (3).

212 Field points of interest for analytical modeling all belong to
 213 the x -axis. Therefore, local coordinates are calculated using

$$\begin{aligned}
 x_S &= (x + a + d \sin \alpha - (b - d \cos \alpha) / \tan(\alpha - \beta)) \cdot \sin(\alpha - \beta) \\
 y_S &= (x + a + d \sin \alpha - (b - d \cos \alpha) / \tan(\alpha - \beta)) \cdot \cos(\alpha - \beta) \\
 & \quad + (b - d \cos \alpha) / \sin(\alpha - \beta) \quad (4)
 \end{aligned}$$

217 for the rectangular sheet closer to the x -axis, and using

$$\begin{aligned}
 x_S &= (x + a - d \sin \alpha - (b + d \cos \alpha) / \tan(\alpha + \beta)) \cdot \sin(\alpha + \beta) \\
 y_S &= (x + a - d \sin \alpha - (b + d \cos \alpha) / \tan(\alpha + \beta)) \cdot \cos(\alpha + \beta) \\
 & \quad + (b + d \cos \alpha) / \sin(\alpha + \beta) \quad (5)
 \end{aligned}$$

221 for the rectangular sheet closer to the y -axis. Due to symmetry,
 222 the lower pole contributions are exactly the same as those of
 223 the upper pole. Vertical magnetic flux density component due
 224 to the rectangular sheets equals

$$B_y = \mp 2B_{x_S} \cos(\alpha \mp \beta) \mp 2B_{y_S} \sin(\alpha \mp \beta). \quad (6)$$

226 Upper signs correspond to the sheet closer to the x -axis and
 227 lower (plus) signs to the sheet closer to the y -axis.

228 Contributions to the magnetic flux density B_y , of all four
 229 trapezoidal current sheets located at a distance $z = \pm L$ from
 230 the xOy plane, are identical. These are obtained by numerical
 231 integration of (2), taking care of different distances R and
 232 angles θ_1 , θ_2 , in every integration step, as well as different
 233 $d\mathbf{B}$ directions. With B_y determined everywhere along the
 234 x -axis, relevant magnetic field parameters for analytical opti-
 235 mization can be calculated.

236 The horizontal distance of the pole midline from the
 237 CFM axis, a , is used as the scaling factor in the geometrical
 238 description of a slanted dipole. Six parameters are used for
 239 the description: normalized half-distance between the poles
 240 of a dipole, b/a , slant angle, α , wedge angle, β , normalized
 241 half-width of the poles, d/a , normalized half-height of the
 242 poles, h/a , and normalized half-length of the poles, L/a , as
 243 shown in Fig. 1. Size of the beam area, represented by the

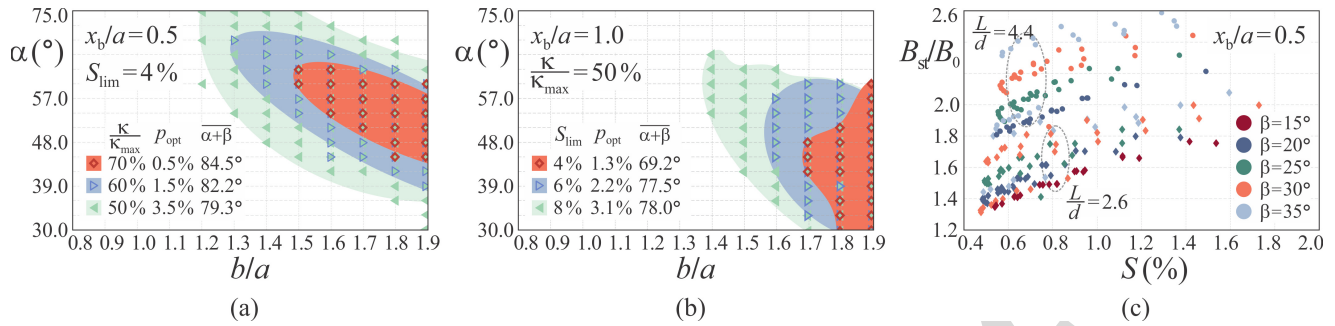


Fig. 3. Summary of the analytical optimization results. (a) Considered beam area, $2x_b$, is set equal to the horizontal distance between a pole and the CFM axis, a , whereas the linearity coefficient S is required to be smaller or equal to 0.040. Sets of model parameters are depicted as areas in the space defined by the pole positioning parameter, b/a , and the slant angle, α . Regions of the best field quality in terms of the bending and focusing coefficients embedded in the parameters κ/κ_{max} and p_{opt} , as well as the corresponding magnet geometry parameter combined of the slant and wedge angles, $\alpha + \beta$, are shown in different colors (shades of gray). (b) If the extended beam area ($x_b/a = 1$) is considered and the beam quality parameter, $\kappa = |B_{st}/B_0| \cdot |aG/B_0|$, is limited to the half of the maximum obtainable, the S_{lim} constraint is more stringent. The regions corresponding to $S \leq 0.040$, $S \leq 0.060$, and $S \leq 0.080$ in the extended beam area, which provide $S \leq 0.012$, $S \leq 0.018$, and $S \leq 0.025$ in the main beam area, respectively, are shown in different colors (shades of gray). (c) Best solutions conforming to the $\kappa/\kappa_{max} \geq 60\%$ requirement, under the restriction $S \leq 0.040$, are shown as data points indicating the achieved combinations of the linearity and bending coefficients for the two pole aspect ratios, L/d , depicted as circles and diamonds. The results are arranged with the wedge angle β as a parameter. Increased β results in improved steering capabilities of the device.

normalized beam area radius, x_b/a , and depicted by the green circle in Fig. 1, is taken as an additional parameter. Adopting variable ratio x_b/a broadens the possibilities to optimize the position of the poles, as a is not fixed by the given beam area size. Although L/a can be considered a design parameter for short magnets, the CFM in our example is intended to steer and focus the beam over a longer distance of about 40 cm. Pole aspect ratio, $L/d = (L/a)/(d/a)$, is therefore used as a parameter for the design space mapping. Its value is kept fixed in every optimization run, while b/a , α , β , d/a , h/a , and x_b/a are varied. Different pole aspect ratios are investigated to account for the corresponding different widths of the pole tips.

The most important parameters in assessing the quality of the magnetic field are the steering and focusing capabilities, as well as linearity of the magnetic flux density within the beam area, hence enabling wide range of operating currents for the two dipoles comprising the CFM. All parameters are calculated in the midplane between the upper and the lower part of the slanted dipole. Steering magnetic flux density is defined as

$$B_{st} \equiv B_y(x=0) \quad (7)$$

and the focusing gradient, G , is defined as the x -component of the magnetic flux density gradient along the x -axis, where both of the horizontal magnetic field components vanish

$$G \equiv \left. \frac{\partial B_y}{\partial x} \right|_{x=0}. \quad (8)$$

Both B_{st} and G are calculated at the origin. The linearity coefficient of B_y is defined as the averaged discrepancy between the actual magnetic flux density and its linear approximation as $Gx + B_{st}$ along the line segment $x \in [-x_b, x_b]$

$$S = \frac{2\pi}{x_b \mu_0 J_0} \int_{-x_b}^{x_b} |B_y - Gx - B_{st}| dx. \quad (9)$$

Please note the normalization of S by B_0 , $B_0 = \mu_0 J_0 / (4\pi)$. Due to the assumption of uniform magnetization, analytical

model serves only to estimate the impact of varying geometrical parameters to the overall field quality. Thus, it helps reduce the range of parameters for further investigation. Bending and focusing coefficients are scaled to B_0 as well, and expressed as B_{st}/B_0 and aG/B_0 , respectively.

The limiting linearity coefficient, S_{lim} , is defined and results exceeding this limit are rejected. The optimization criterion is taken to be $\kappa_{max} = \max(|B_{st}/B_0| \cdot |aG/B_0|)$, as in [12]. Instead of adopting a single set of parameters corresponding to κ_{max} , a pool of the solutions is selected, such that $\kappa = |B_{st}/B_0| \cdot |aG/B_0|$ does not fall below a certain percentage of κ_{max} . The best solutions pool usually does not exceed a few percent of the initial design parameter combinations; this percentage is denoted by p_{opt} . For example, if $S \leq 4\%$ for $x_b/a = 0.5$ is required, sets of parameters resulting in κ larger than $0.7 \cdot \kappa_{max}$ comprise 0.5% of the initial design parameter combinations. Using the described procedure, regions of good field quality to be further considered in the CFM design are obtained. Separate pool of results is determined for every x_b/a value, since S increases for a larger x_b/a and, consequently, κ as a function of S_{lim} decreases. Smaller x_b/a corresponds to the placement of poles farther away from the beam area. Large x_b/a leads to a smaller magnet size, which is desired, while it can present an obstacle to attaining the required values of the magnetic field parameters. Thus we adopt moderate $x_b/a = 0.5$ to represent the main beam area, with linearity coefficient also checked in the extended beam area defined by $x_b/a = 1.0$. We set $S_{lim} = 4\%$, as the linearity coefficient in the main beam area should not exceed 5% in the final design. Field linearity is even improved after the numerical design, as presented below. Therefore, a further tradeoff is possible between the field linearity and magnet size. The summary of the optimization results is shown in Fig. 3. Fig. 3(a) shows the regions of the best magnetic field in terms of the bending and focusing coefficients. Fig. 3(b) investigates the effects of setting more stringent requirement of $S \leq 4\%$, $S \leq 6\%$, and $S \leq 8\%$, for the extended beam area, resulting in $S \leq 1.2\%$, $S \leq 1.8\%$, and $S \leq 2.5\%$, in the main beam area,

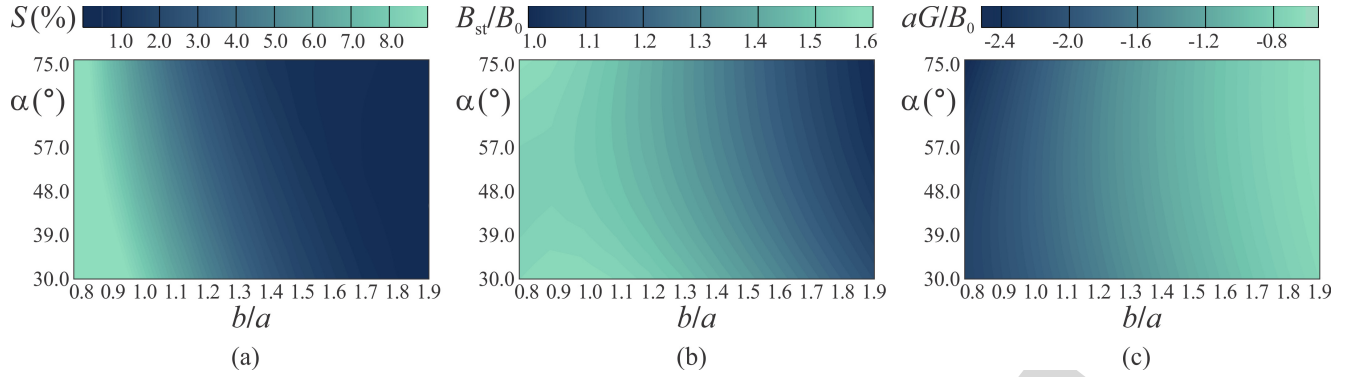


Fig. 4. Influence of pole distance, b/a , and slant angle, α , on slanted dipole properties. The remaining design parameters are fixed to: $\beta = 15^\circ$, $d/a = 0.45$, $h/a = 1.5$, $x_b/a = 0.5$, and $L/d = 4.4$. (a) Field linearity coefficient, S . (b) Normalized steering magnetic flux density, B_{st}/B_0 . (c) Focusing coefficient, aG/B_0 . Parameter optimization requires a tradeoff between linearity and bending / focusing capabilities of the device.

315 respectively. Ranges of the two parameters that describe the
 316 pole positioning, b/a and α , are narrower than the ones in [12],
 317 as $b/a > 2$ produces weaker bending and focusing, while the
 318 linearity coefficient worsens for too small b/a . Similarly, previ-
 319 ous results show a slant angle variation from 30° to 75° to be a
 320 good optimization range for most purposes. The six-parameter
 321 data is represented against b/a and α , where multiple solutions
 322 with same b/a and α may be overlapping. When checking
 323 on pole position and angle α selected in [12], $b/a = 1.65$
 324 and $\alpha = 51^\circ$, these values fall into the region of excellent κ
 325 product, $\kappa/\kappa_{\max} \approx 0.7$, with the linearity better than 4% within
 326 the main beam area. In the extended beam area, $S \leq 6\%$
 327 is achievable. Fig. 3(c) shows best solutions corresponding
 328 to the $\kappa = 0.6 \cdot \kappa_{\max}$ region in Fig. 3(a), rearranged with
 329 the wedge angle β as a parameter, indicating the achieved
 330 combinations of the linearity and bending coefficients. Wedge
 331 angle, β , is varied from zero up to the limiting value defined
 332 by either $\alpha - \beta = 0$ or $\alpha + \beta = 90^\circ$. Average sum of angles
 333 $\alpha + \beta$ is very close to the maximal allowed value of 90°
 334 for the regions of best solutions in Fig. 3. As can be seen
 335 from Fig. 3(c), increased β enables stronger steering, while
 336 not necessarily impairing linearity.

337 Fig. 4 shows the effect of varying pole position and slant
 338 angle on the linearity, bending and focusing coefficients, with
 339 other parameters fixed. There is a tradeoff between linearity
 340 on one side and bending and focusing capabilities on the
 341 other. In this model, as opposed to [12], the surface current
 342 density, J_0 , is kept constant rather than the total current, I .
 343 Thus, the material magnetization can be assumed to be almost
 344 uniform for different values of h/a . Increase of h/a produces
 345 only a slight increase of bending and focusing coefficients,
 346 along with a slight decrease in linearity. Effect of the pole half-
 347 width, d/a , is pronounced, with worse linearity and stronger
 348 bending and focusing in the case of wider poles. For $h/a =$
 349 1.5 , $d/a = 0.45$, $\beta = 15^\circ$, $x_b/a = 0.5$, and $L/d = 4.4$,
 350 the obtained values of the field linearity, bending and focusing
 351 coefficients are 0.73%, 1.19, and -0.89 , respectively.

352 III. NUMERICAL PARAMETER OPTIMIZATION

353 Unlike the analytical optimization utilizing the closed-form
 354 expressions or 1-D numerical integration, large number of

355 parameters for the numerical optimization would result in
 356 the unreasonably long design times. Based on the results of
 357 analytical modeling, positioning of the poles is defined by
 358 $b/a = 1.65$ and $\alpha = 51^\circ$, and relatively large pole half-
 359 height, $h/a = 1.45$. At this point, size of the CFM has to be
 360 determined, and we adopt the scaling parameter $a = 100$ mm,
 361 which is commensurate with twice the radius of the main beam
 362 area. This results in the total pole height of $2h = 290$ mm,
 363 whereas the planned CFM length is $2L = 400$ mm. Pole width
 364 has been shown to significantly impact the field quality, hence
 365 the comparison of the two values is performed: $2d = 90$ mm
 366 and $2d = 156$ mm. Parameter d corresponds to the width
 367 of the pole face that is initially flat and will be shaped
 368 subsequently. Wedge angle, β , has been varied between zero
 369 and 30° , as an increase of the bending and focusing coefficients
 370 is expected with the initial pole widening. Too large β could
 371 lead to deteriorated linearity, without much further gain in
 372 bending and focusing coefficients, due to the coupling with the
 373 other slanted dipole. By means of numerical calculations, field
 374 parameters and spatial distribution are accurately determined.
 375 Calculations were performed utilizing the first-order node-
 376 based elements for 3-D modeling in the Mermaid finite-
 377 element suite for magnetostatics [24]. Although a notably
 378 high magnetic flux saturation density material is considered
 379 in the analyzed model, i.e., a measured BH curve of the
 380 Steel 1010 [25], other standard magnetic materials, with lower
 381 saturation densities, can be utilized just as well, with no influ-
 382 ence on the proposed design and derived conclusions. First,
 383 normalized magnetic field parameters are used for analytical
 384 modeling. Second, maximal magnetomotive force assumed in
 385 the final design, NI, represents 78% of the one corresponding
 386 to the saturation of the Steel 1010. Please note that other high
 387 quality steels can produce slightly different results, e.g., Steel
 388 1008 yields less than only 1% difference in magnetic flux
 389 density in the beam area, from the results reported here, with
 390 up to 6% higher magnetic flux density inside the ferromagnetic
 391 material. Examples of other BH curves showing high B -field
 392 saturations, i.e., magnetic flux density over 2 T, can be found
 393 in [26]. Energy error in all computational simulations was kept
 394 below 0.035%. Effects of the pole width and wedge angle to
 395 the magnetic flux density, illustrated in Figs. 5 and 6, are taken

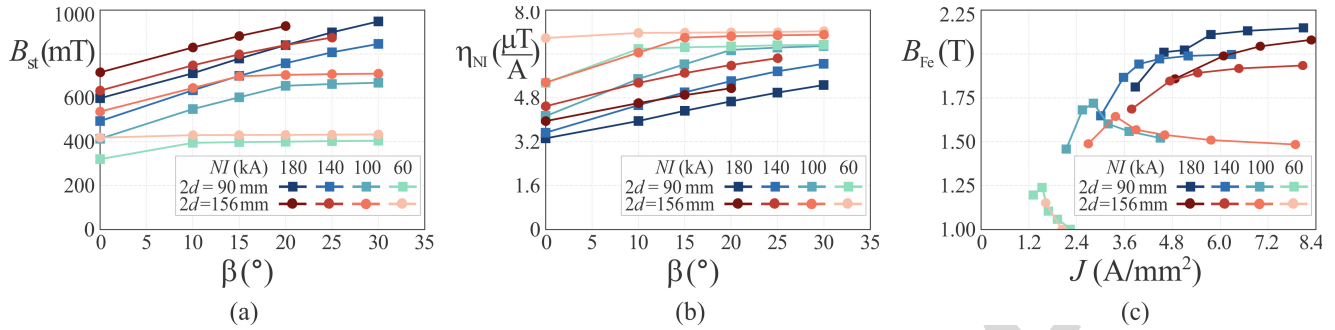


Fig. 5. Influence of the wedge angle, β , on the steering magnetic flux density and magnet efficiency, defined as $\eta_{NI} \equiv B_{st}/NI$, for two pole widths. To account for the coupling between the two slanted off-centered dipoles comprising the CFM, magnetomotive forces in the two dipoles were set as equal ($NI_1 = NI_2 = NI$). (a) Larger angles β result in the increased B_{st} , except where limited by the coupling. (b) Efficiency in utilization of magnetomotive force, calculated as the obtained B_{st} per unit current, is higher for smaller NI and larger β . (c) Current coil cross section is reduced with the widening of ferromagnetic wedge, as reflected in the increase of coil current density, J , with the increase in β . Magnetic flux density inside the ferromagnetic material, B_{Fe} , is checked. As we assumed, the CFM is less sensitive to the coupling of its dipoles for larger currents NI, where the material is in saturation.

396 into account when defining these parameters. Shaping of the
397 pole tips is explained with the aid of Fig. 7.

398 As the magnetic flux density is dominated by the ferro-
399 magnetic material contribution, and the limitations on current
400 density exclude the realization of a very thin coil current sheet
401 as supposed in the analytical model, the current coils in the
402 numerical model fill the entire cross section between the angle
403 $\alpha + \beta$ and the 90° . This is denoted in Fig. 1 by the outer wedges
404 outlined by the dashed lines, and also in Fig. 8 as the current
405 coils of the optimized CFM. Current coil cross section is thus
406 reduced with the increase in wedge angle, β . Consequently,
407 the coil current density, J , is increased as well as the magnetic
408 flux density in the beam area, due to the wider pole shape.
409 For the water-cooled coils, the commonly used rule of thumb
410 value for maximal coil current density of 10 A/mm^2 leads to
411 J_{max} in the range $7.4\text{--}8.4 \text{ A/mm}^2$ when taking into account
412 that water-cooling passages and insulation can comprise up
413 to 25% of the actual cross section of the coils. When the two
414 halves of the CFM are powered by magnetomotive forces of
415 similar intensities, coupling by the material magnetization may
416 hinder the effectiveness of further increase in angle β .

417 Obtainable steering magnetic flux density, B_{st} , for different
418 parameter settings is shown in Fig. 5(a). Comparison of
419 different models is facilitated if we look at the coil current
420 required to produce a desired B_{st} , as a measure of efficiency
421 in utilization of magnetomotive force

$$422 \quad \eta_{NI} \equiv \frac{B_{st}}{NI}. \quad (10)$$

423 Fig. 5(b) demonstrates that the utilization of weaker currents
424 is generally more efficient; however, for very low currents
425 we observe no gain in an increase of the wedge angle. (For
426 a larger pole half-width, d , the limiting occurs at smaller
427 angles β ; yet, the produced field is stronger for a large d and
428 the η_{NI} is therefore higher.) For moderate currents, the CFM
429 is less sensitive to the coupling of its dipoles. For example, for
430 the magnetomotive force of $NI = 140 \text{ kA}$ and $2d = 90 \text{ mm}$,
431 the increase of β from zero to 10° , 15° , and 20° , results in an
432 increase of B_{st} by a factor of 1.29, 1.42, and 1.54, respectively.
433 In this case, ferromagnetic material is in saturation, as shown
434 in Fig. 5(c) by the magnetic flux density, B_{Fe} , at the point

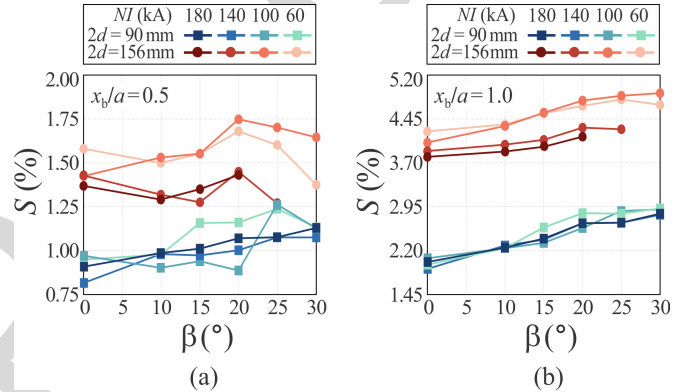


Fig. 6. Influence of wedge angle, β , on the linearity coefficient, S , for two pole widths. The effect, on the linearity coefficient, of varying pole width, d , is much more pronounced than an increase in S with the increase in β . (a) Field linearity in the main beam area is significantly better (S is lower) for the narrower poles. (b) Field linearity in the extended beam area.

(x_f, y_f) = $(-135 \text{ mm}, 165 \text{ mm})$. Data is represented as a function of coil current density, J , which remains below the critical value of $J_{max} = 8.4 \text{ A/mm}^2$ for all the analyzed cases. Additionally, only the four right-most data points in Fig. 5(c) correspond to $J > 7 \text{ A/mm}^2$. Some of the calculation results were left out due to large J , which is the reason, for example, why the dark red curve, corresponding to $2d = 156 \text{ mm}$ and $NI = 180 \text{ kA}$, shows only four data points instead of six.

Variation of the linearity coefficient, S , with the angle β and the pole width, d , is shown in Fig. 6. For the numerical model, linearity coefficient is normalized to B_{st} instead of B_0

$$442 \quad S = \frac{1}{2x_b B_{st}} \int_{-x_b}^{x_b} |B_y - Gx - B_{st}| dx. \quad (11) \quad 443$$

444 The effect of varying pole width, d , is much more pronounced
445 than an increase in S due to the increase in β . Therefore, the
446 pole width is adjusted first, based on the linearity requirements
447 and simulated data for various d and β . In our case, the
448 smaller d ($2d = 90 \text{ mm}$) is adequate, as it keeps the linearity
449 coefficient for the main beam area about 1% and produces
450 moderately high magnetic flux density. The latter can be
451 further improved through the pole tips shaping. The wedge
452 angle is chosen as $\beta = 20^\circ$, to avoid B_{st} limiting observed
453
454
455

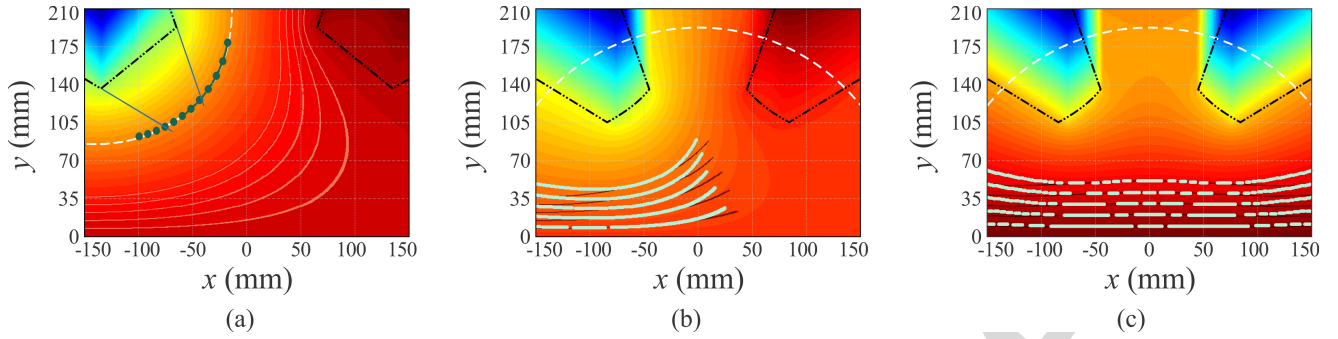


Fig. 7. Shaping of the pole tips aimed at preserving the obtained good linearity coefficient of the magnetic flux density in the beam area. (a) Magnetostatic equipotential lines corresponding to the magnetic flux density component due to the ferromagnetic cores, which are outlined by the black dashed-dotted-dotted lines. We extend the ferromagnetic cores so that the pole tip (green dots) conforms to the shape of an equipotential line (white dashed line). The resulting increase in bending and focusing capabilities is obtained with minimal disruption to the shape of equipotential lines close to the x -axis and thus to the linearity coefficient. (b) Equipotential lines after the pole tips correction for the magnetomotive force of the dipole on the right equal to zero. New (light green) equipotential lines do not deviate a lot from the initial ones (dark red). (c) Comparison of equipotential lines after the correction (solid light green) with the initial ones (dark red) for the magnetomotive forces of the two dipoles set equal. Actual pole tips after the correction are denoted by the black dashed-dotted-dotted lines. There are no free currents inside the circles denoted by the white dashed lines.

456 for $NI_1 = NI_2 = 100$ kA at larger β . The corresponding coil
 457 cross section area equals 312.2 cm². With the wedge shape
 458 completely defined, the next step is the design of pole tips.

459 Placement of the pole surfaces closer to the beam area
 460 increases the magnetic flux density and thus the steering and
 461 focusing capabilities of the CFM. Care should be taken at this
 462 point to avoid the unwanted increase of the linearity coeffi-
 463 cient. We use the simple approach of shaping pole surfaces to
 464 conform to the already attained magnetic equipotential lines
 465 due to the ferromagnetic material. Magnetic scalar potential
 466 is defined for the source-free domains, where $\nabla \times \mathbf{H} =$
 467 $\nabla \times (\mathbf{B}/\mu_0 - \mathbf{M}) = 0$ and $\nabla \cdot \mathbf{H} = -\nabla \cdot \mathbf{M}$. In the
 468 initial design, the region bounded by the white dashed lines
 469 in Fig. 7(b) and (c) is vacuum. We subtract the magnetic
 470 flux density for the current coils in vacuum from the one
 471 due to the coils and ferromagnetic cores, thus extracting the
 472 influence of the ferromagnetic. Component \mathbf{B}_m , due to the
 473 magnetization \mathbf{M} , can be represented as a scalar function
 474 gradient, $\mathbf{B}_m = -\mu_0 \nabla \phi_m$. Horizontal components of B_m
 475 vanish along the x -axis due to symmetry. For the reference
 476 point R at infinity and the field point F , the magnetic scalar
 477 potential, ϕ_m , is obtained by the numerical integration

$$478 \quad \phi_m = \int_F^R \mu_0^{-1} \mathbf{B}_m \cdot d\mathbf{l} = - \int_{y=0}^{y_F} \int_{x=x_F}^{x_F} \mu_0^{-1} B_y \cdot dy. \quad (12)$$

479 Analysis for several magnetomotive forces of the left
 480 dipole (NI_1), namely, 60, 80, 100, 120, and 140 kA, and
 481 $NI_2 = 0$, results in the same shapes of the equipotential lines
 482 which differ only in the associated values of the potential.
 483 An arbitrary line can be used to fit the pole surface profile.
 484 We extend the ferromagnetic wedge toward the beam area and
 485 adapt the pole surface to the part of the chosen equipotential
 486 line between the wedge surfaces, as shown in Fig. 7(a). Compar-
 487 ison of the newly obtained equipotential lines (light green)
 488 with the initial dark red ones reveals some deviation for a
 489 limiting case of $NI_2 = 0$, i.e., when a single coil is on,
 490 but taking into account both ferromagnetic cores. There is
 491 almost no change in the line shapes for similar magnetomotive

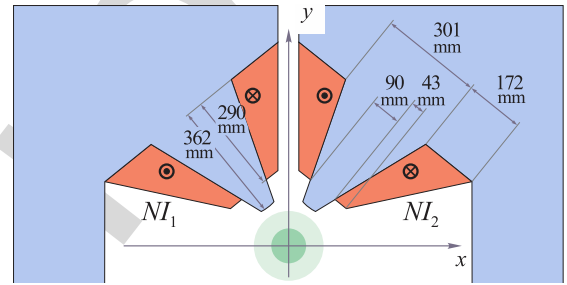


Fig. 8. Finally obtained CFM comprising the two slanted off-centered dipoles (upper half). Optimized values of geometrical parameters are: $a = 100$ mm, $b = 165$ mm, $d = 45$ mm, $h = 145$ mm, $L = 200$ mm, $\alpha = 51^\circ$, and $\beta = 20^\circ$. Width of the coil cross section increases from $w_1 = 43$ mm, close to the pole tips, to $w_2 = 172$ mm. The cross section area is 312.2 cm². Wide range of operating conditions is achieved using different magnetomotive forces NI_1 and NI_2 .

492 forces NI_1 and NI_2 . Relevant field quality parameters before
 493 and after the correction, for the two cases, are compared
 494 in Tables I and II. We notice a slight linearity improvement,
 495 as both the linearity coefficient and the maximal relative
 496 error inside the beam area, denoted as $M.R.E.$, are expressed
 497 as a percentage of the steering magnetic flux density. For
 498 $NI_2 = 0$, an increase of B_{st} in comparison to the initial wedge
 499 model ranges from 31% at 0.20 T (60 kA) to 8% at 0.30 T
 500 (140 kA), along with an increase of focusing gradient, G ,
 501 of about 50%. When a strong dipolar field component is
 502 desired, magnetomotive forces NI_1 and NI_2 are taken almost
 503 equal, resulting in a strong positive coupling between the two
 504 dipoles. Such coupling is beneficial as it helps attain the higher
 505 magnetic flux density. Compared to the initial model, B_{st} is
 506 increased by 50% at 0.40 T and by 25% at 0.75 T.

507 If necessary, the linearity can be further improved by the
 508 additional pole shaping. If acceptable from the standpoint of
 509 coil current density and the required magnetic field parameters,
 510 further reduction of the magnet size can be done in an iterative
 511 procedure aimed at preserving the attained linearity and the
 512 shape of the magnetic field lines. Finally, pole shaping with
 513 the intent to optimize the magnetic field quality by reducing

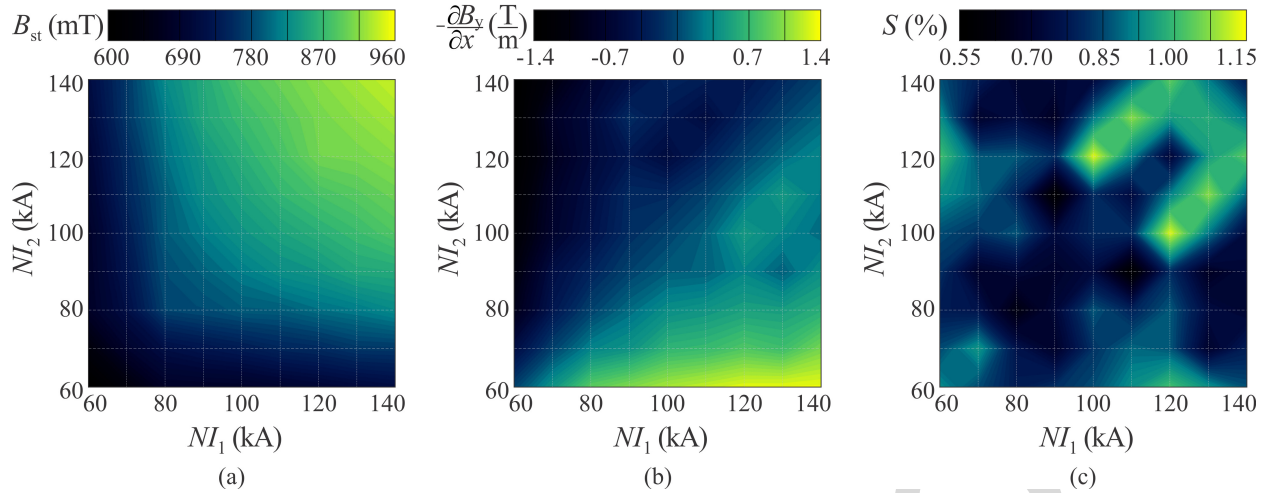


Fig. 9. Available combinations of steering magnetic flux density and focusing field gradient for the magnetomotive forces, NI_1 and NI_2 , of the same signs and moderate magnitudes between 60 kA and 140 kA. (a) Steering magnetic flux density from 0.6 T up to almost 1 T is achieved with the chosen wedge geometry and pole surface placement. (b) Focusing gradient, $G = \partial B_y / \partial x|_{x=0}$, of up to ± 1.4 T/m can be attained in combination with the strong steering ($B_{st} > 0.6$ T). (c) Linearity coefficient, S , for the above shown ranges of magnetomotive forces is excellent, below 1% for a large part of this region of CFM operation.

TABLE I
OBTAINED FIELD CHARACTERISTICS FOR
THE LEFT DIPOLE CURRENT ONLY

NI_1 (kA)	B_{st} (mT)	G (T/m)	S (%)	$M.R.E.$ (%)
Initial wedge model for magnetic poles				
60.0	198.26	-2.02	3.77	10.92
80.0	240.60	-1.97	1.47	6.49
100.0	267.28	-2.23	1.39	4.72
120.0	284.08	-2.31	1.69	6.91
140.0	299.96	-2.52	1.48	4.62
Magnetic poles with shaped pole tips				
60.0	259.99	-3.02	0.90	2.63
80.0	284.07	-3.32	1.44	3.14
100.0	298.08	-3.51	1.36	3.61
120.0	313.07	-3.74	0.89	4.00
140.0	324.92	-3.94	1.20	5.50

TABLE II
OBTAINED FIELD CHARACTERISTICS FOR EQUAL DIPOLE CURRENTS

NI (kA)	B_{st} (mT)	S (%)	$M.R.E.$ (%)
Initial wedge model for magnetic poles			
60.0	400.61	1.13	2.38
80.0	529.15	1.22	2.90
100.0	654.66	1.02	2.28
120.0	700.71	1.82	3.38
140.0	752.20	1.77	3.50
Magnetic poles with shaped pole tips			
60.0	600.66	0.93	1.76
80.0	780.48	0.63	1.54
100.0	837.55	0.81	1.73
120.0	905.76	0.72	1.75
140.0	942.68	0.79	1.81

514 the higher multipole harmonics could be performed. Such
515 additional pole shaping should utilize the methods similar to
516 those described in [7] and [26].

517 IV. SELECTION OF THE OPERATING CONDITIONS

518 The upper half of finally obtained CFM is shown in Fig. 8.
519 In order to define the available range of operating conditions
520 for the final design, we performed the mapping of the field
521 parameters of interest, B_{st} , G , and S , as well as of the
522 magnetic flux density vector throughout the beam area. Both
523 magnetomotive forces, NI_1 and NI_2 , are allowed to take values
524 from the $[-140$ kA, 140 kA] interval. Sets of operating
525 diagrams that correspond to different magnetomotive force
526 ranges are used to locate the pairs (NI_1, NI_2) that produce
527 the desired steering and focusing of the beam. For example,
528 the dependence of the magnetic flux density, focusing gradient
529 and linearity coefficient on the (NI_1, NI_2) pair is presented by
530 the diagrams in Fig. 9, for the strong steering ($B_{st} > 0.6$ T)

531 achieved using the coil currents in the $[60$ kA, 140 kA] range.
532 When using a single coil current, larger focusing gradients of
533 up to 4 T/m are available, compared to maximal 1.4 T/m for
534 the combinations illustrated in Fig. 9. Even stronger focusing
535 is available by the magnetomotive forces of the opposite signs,
536 albeit combined with very weak steering.

537 The two limiting field requirements from [18] are easily
538 achieved, with an excellent magnetic field quality in the main
539 beam area. For the beam of protons which are accelerated
540 as H^- ions, $B_{st} = 0.70$ T is required and no focusing is
541 needed. Magnetomotive forces should be set as $NI_1 = NI_2 =$
542 70.91 kA, resulting in the linearity coefficient $S = 0.95\%$
543 for the main beam area and $S = 0.99\%$ for the $[-100$ mm,
544 100 mm] interval. Maximal relative error of B_{st} is 1.88%
545 and 2% for the two beam areas, respectively. The reported
546 required coil current density, $J = 2.27$ A/mm², being rather
547 low, provides a vast space of tolerance for manufacturing of
548 the required ampere-turns. Namely, depending on the actual
549 size and shape of the conductor, as well as the actual space

taken up by the water-cooling passages, it might be necessary to use higher current density to compensate for fewer ampere-turns. Ion beam accelerated as H_2^+ requires $B_y = -1.00 \text{ T/m} \cdot x - 0.15 \text{ T}$ in the main beam area. It is achieved using $NI_1 = -8.55 \text{ kA}$ and $NI_2 = -9.75 \text{ kA}$, with $S = 0.59\%$ and maximal error of 1.66% in the main beam area. Maximal deviation from the requirements at the edges of the extended beam area equals 18.56%, increasing the overall linearity coefficient to 4.59%.

V. CONCLUSION

The design procedure for CFMs is outlined. It can serve: 1) to determine the limits to the regions of parameters resulting in the desired beam steering and focusing along with the acceptable magnetic field linearity; 2) to assess the ranges of the desired functions that can be jointly achieved; and 3) to optimize magnet parameters according to specifications. It is illustrated by performing the detailed design of the previously proposed CFM for the stripping extraction system of a multipurpose cyclotron. With the careful exploration of the design space, we fulfilled the field linearity requirement, simultaneously achieving somewhat stronger steering and focusing capability of the device than with the previously considered simple model of the proposed device. The limiting reference fields from [18] are achieved in the two cases with a very comparable quality. The gain of the newly proposed design strategy is best illustrated by the reduction of the device length, from $2L = 800 \text{ mm}$ to $2L = 400 \text{ mm}$, as well as by the significantly lower required magnetomotive forces and current densities. Magnetic flux density of 0.7 T is obtained for the equal coil currents of 70.91 kA, i.e., the current density of 2.27 A/mm^2 , in the two dipoles. The newly obtained results demonstrate that the stronger steering and focusing could be achieved if required, by increasing magnetomotive forces, device length, or by additional pole surface adjustments if necessary.

REFERENCES

- [1] H. Hahn and R. C. Fernow, "Superconducting combined function magnets," *IEEE Trans. Nucl. Sci.*, vol. 30, no. 4, pp. 3402–3404, Aug. 1983.
- [2] R. C. Gupta and G. H. Morgan, "A design for a high field combined function superferric magnet," *IEEE Trans. Nucl. Sci.*, vol. 32, no. 5, pp. 3687–3688, Oct. 1985.
- [3] G. H. Biallas, N. Belcher, D. Douglas, T. Hiatt, and K. Jordan, "Combined panofsky quadrupole & corrector dipole," in *Proc. 25th Particle Accel. Conf.*, Albuquerque, NM, USA, Jun. 2007, pp. 602–604.
- [4] A. Madur *et al.*, "Harmonic sextupoles for the advanced light source low emittance upgrade," *Nucl. Instrum. Methods Phys. Res. A, Accel. Spectrom. Detect. Assoc. Equip.*, vol. 649, no. 1, pp. 39–41, Sep. 2011.
- [5] M. Werner, V. Vrankovic, and D. C. George, "Design and measurement of the SLS booster combined function magnets," *IEEE Trans. Appl. Supercond.*, vol. 10, no. 1, pp. 248–251, Mar. 2000.
- [6] S. P. Møller *et al.*, "Status of the injection system for the Australian synchrotron project," in *Proc. 21st Particle Accel. Conf.*, Knoxville, TN, USA, May 2005, pp. 3271–3273.
- [7] G. Sinha and G. Singh, "Design and characterization of combined function multipole magnet for accelerators," *Rev. Sci. Instrum.*, vol. 79, no. 12, p. 123302, Dec. 2008.
- [8] D. S. Robin *et al.*, "Superconducting toroidal combined-function magnet for a compact ion beam cancer therapy gantry," *Nucl. Instrum. Methods Phys. Res. A, Accel. Spectrom. Detect. Assoc. Equip.*, vol. 659, no. 1, pp. 484–493, Dec. 2011.
- [9] A. Morita *et al.*, "Design and measurement of a combined function magnet intended for a cancer therapy accelerator," *Phys. Rev. ST-Accel. Beams*, vol. 4, no. 12, p. 122401, Dec. 2001.
- [10] M. Yoon, J. Corbett, M. Cornacchia, J. Tanabe, and A. Terebilo, "Analysis of a storage ring combined-function magnet: Trajectory calculation and alignment procedure," *Nucl. Instrum. Methods Phys. Res. A, Accel. Spectrom. Detect. Assoc. Equip.*, vol. 523, nos. 1–2, pp. 9–18, May 2004.
- [11] M. Seidl, "Identification and correction of antisymmetric field components in combined function magnets," *Phys. Rev. ST-Accel. Beams*, vol. 5, no. 6, p. 062402, Jun. 2002.
- [12] J. L. Ristić-Djurović, S. Ćirković, and A. Ž. Ilić, "Magnet with uncoupled combined functions," *IEEE Trans. Nucl. Sci.*, vol. 60, no. 6, pp. 4618–4626, Dec. 2013.
- [13] S.-Z. An *et al.*, "Stripping extraction calculation and simulation for CYCIAE-100," *Chin. Phys. C (HEP & NP)*, vol. 33, no. 2, pp. 42–46, Jun. 2009.
- [14] D. Vandeplassche *et al.*, "Extraction simulations for the IBA C70 cyclotron," in *Proc. 18th Int. Conf. Cyclotrons Appl.*, Giardini Naxos, Italy, 2007, pp. 63–65.
- [15] D. Solivajs *et al.*, "A study of charge-exchange beam extraction from the multi-purpose isochronous cyclotron DC-72," *J. Elect. Eng.*, vol. 55, nos. 7–8, pp. 201–206, 2004.
- [16] J. L. Ristić-Djurović and N. Nešković, "Analytical prediction of ion stripping extraction from isochronous cyclotrons," *IEEE Trans. Nucl. Sci.*, vol. 59, no. 2, pp. 268–271, Apr. 2012.
- [17] J. L. Ristić-Djurović and N. Nešković, "Influence of cyclotron magnet gap size on stripping extraction," *IEEE Trans. Nucl. Sci.*, vol. 58, no. 3, pp. 1188–1195, Jun. 2011.
- [18] J. L. Ristić-Djurović and S. Ćirković, "Unidirectional stripping extraction from a cyclotron which accelerates light as well as heavy ions," *Phys. Rev. ST-Accel. Beams*, vol. 6, no. 3, p. 033501, Mar. 2003.
- [19] J. L. Ristić-Djurović, "Stripping extraction of positive ions from a cyclotron," *Phys. Rev. ST-Accel. Beams*, vol. 4, no. 12, p. 123501, Dec. 2001.
- [20] P. R. Sarma, "Ideal coil shape for combined function superconducting magnets," *J. Phys. D, Appl. Phys.*, vol. 40, no. 10, pp. 3056–3059, 2007.
- [21] P. R. Sarma, S. K. Pattanayak, and R. K. Bhandari, "New method of designing pole profile in combined function magnets of high field quality," *Rev. Sci. Instrum.*, vol. 70, no. 6, pp. 2655–2660, Jun. 1999.
- [22] B. M. Notaroš, *Electromagnetics*. Upper Saddle River, NJ, USA: Prentice-Hall, 2010.
- [23] A. Z. Ilić *et al.*, "Analytical description of two-dimensional magnetic arrays suitable for biomedical applications," *IEEE Trans. Magn.*, vol. 49, no. 12, pp. 5656–5663, Dec. 2013.
- [24] *Mermaid 2-D and 3-D User's Guide*, SIM, Novosibirsk, Russia, 1994.
- [25] J. K. Cobb and R. A. Early, "The new SLAC permeameter," Tech. Rep. SLAC-TN-89-04, Dec. 1989; Available: [Online]. Available: <http://www.slac.stanford.edu/cgi-wrap/getdoc/slac-tn-89-004.pdf>
- [26] *Steel 1008 BH Curve*. [Online]. Available: <http://fieldp.com/Myblog/2010/saturation-curves-for-common-soft-magnetic-materials/>
- [27] S. Ćirković, J. L. Ristić-Djurović, A. S. Vorozhtsov, A. Ž. Ilić, and N. Nešković, "Method for fine magnet shaping in cyclotrons," *IEEE Trans. Nucl. Sci.*, vol. 56, no. 5, pp. 2821–2827, Oct. 2009.

Graphene-based waveguide resonators for submillimeter-wave applications

Andjelija Ž Ilić¹, Branko Bukvić², Milan M Ilić^{2,3} and Djuradj Budimir⁴

¹ Institute of Physics, University of Belgrade, Pregrevica 118, 11080 Zemun-Belgrade, Serbia

² School of Electrical Engineering, University of Belgrade, Bulevar Kralja Aleksandra 73, 11120 Belgrade, Serbia

³ ECE Department, Colorado State University, Fort Collins, CO, USA

⁴ Wireless Communications Research Group, University of Westminster, London W1W 6UW, UK

E-mail: andjelijailic@ieee.org

Received 12 March 2016, revised 22 May 2016

Accepted for publication 14 June 2016

Published 21 July 2016



Abstract

Utilization of graphene covered waveguide inserts to form tunable waveguide resonators is theoretically explained and rigorously investigated by means of full-wave numerical electromagnetic simulations. Instead of using graphene-based switching elements, the concept we propose incorporates graphene sheets as parts of a resonator. Electrostatic tuning of the graphene surface conductivity leads to changes in the electromagnetic field boundary conditions at the resonator edges and surfaces, thus producing an effect similar to varying the electrical length of a resonator. The presented outline of the theoretical background serves to give phenomenological insight into the resonator behavior, but it can also be used to develop customized software tools for design and optimization of graphene-based resonators and filters. Due to the linear dependence of the imaginary part of the graphene surface impedance on frequency, the proposed concept was expected to become effective for frequencies above 100 GHz, which is confirmed by the numerical simulations. A frequency range from 100 GHz up to 1100 GHz, where the rectangular waveguides are used, is considered. Simple, all-graphene-based resonators are analyzed first, to assess the achievable tunability and to check the performance throughout the considered frequency range. Graphene–metal combined waveguide resonators are proposed in order to preserve the excellent quality factors typical for the type of waveguide discontinuities used. Dependence of resonator properties on key design parameters is studied in detail. Dependence of resonator properties throughout the frequency range of interest is studied using eight different waveguide sections appropriate for different frequency intervals. Proposed resonators are aimed at applications in the submillimeter-wave spectral region, serving as the compact tunable components for the design of bandpass filters and other devices.

Keywords: tunable circuits and devices, submillimeter-wave devices, graphene, boundary conditions, graphene–metal combined waveguide resonators

(Some figures may appear in colour only in the online journal)

1. Introduction

Millimeter and submillimeter wave regions of the electromagnetic (EM) spectrum are traditionally utilized in astrophysics, remote sensing, defense and security, as well as in biomedical imaging applications [1–4]. Recently, there has

been an increased interest in utilization of these frequencies in a range of commercial applications, including broadband communications, motivated mainly by the availability of large bandwidths required for the multigigabit short-range wireless communications [5]. Consequently, there is a constant advance in the development of components and systems for millimeter

and submillimeter wave frequencies [6–8]. A major limiting factor hindering broader exploitation of this spectral region for some time is the shortage of efficient low-cost power sources. With the recent increased research efforts in this direction, more efficient power sources are to be devised [4]. Another difficulty to be resolved is the choice of appropriate materials for the design of devices and systems operating in this spectral region, i.e. at the boundary between microwaves and optics. Performance of PIN and varicap diodes, traditionally employed to obtain frequency reconfigurability and tunability, deteriorates with frequency. Micro electro-mechanical systems are used as an alternative; however, their switching speed is typically much lower and their power handling capability is low. Hence, there is a need to investigate alternative methods for attaining frequency tunability.

Graphene emerged, relatively recently, as a promising new material for photonics applications. In addition to its superior structural, mechanical and electrical properties, its electrically, magnetically and optically controllable conductivity makes it a good choice for the realization of tunable or reconfigurable components and devices. EM field interaction with graphene at terahertz frequencies has been successfully investigated for a variety of applications including plasmonic antennas, wave modulators, and terahertz lasers [9–15]. Possible utilization of this controllable conductivity in the millimeter and submillimeter wave range has yet to be addressed more thoroughly. The method for microwave and millimeter wave characterization of graphene surface impedance, presented in [16], has been illustrated by material characterization at X and K_a bands. The reactive component of surface impedance at these frequencies is not large enough to produce significant frequency tunability, regardless of the wave attenuation in graphene. Frequency independent surface inductivity, as well as the resistivity of graphene, leads to a linear increase of the reactive component—versus the resistive impedance component ratio in the considered frequency range [17, 18]. We show here that reasonable tunability can be achieved for frequencies above 100 GHz using the electrostatic tuning.

Rectangular waveguides and rectangular waveguide resonators are an attractive solution for millimeter and submillimeter applications requiring large power handling capability along with reasonably low losses. An additional good property of rectangular waveguides is the fact that they have a wide bandwidth of operation within the monomode regime. Dimensions and corresponding frequency ranges for the commercially available waveguide sections [19, 20] operating at frequencies from about 100 GHz up to 1100 GHz are listed in table 1. A good five percent tunability has been achieved in our preliminary study [18] using graphene-based resonators, where the focus was on the 300 GHz frequency, which is currently investigated as a good candidate for employment in the multigigabit short-range wireless communications. This work presents a significant extension of [18], where we have presented only a proof of concept that the chosen method of attaining frequency tunability could be successfully employed at higher frequencies. We here start with the development of theoretical expressions for EM fields in the vicinity of the proposed waveguide discontinuities, which for the first time

give some physical insight into functioning principles of the suggested devices. Physics of graphene-based resonators is further illustrated in section 3, where an appropriately chosen example shows the impact on the EM boundary conditions and thus the field distribution of four distinct choices of the graphene stripe widths. The developed theoretical expressions are also applicable to other 2D materials that could be developed in the future. In addition, they can be directly embedded in the specialized filter design software. Moreover, the necessity to perform certain trade-offs among the design parameters, indicated in [18], is now thoroughly investigated. In addition to the illustrative examples showing the resonance curves, detailed numerical EM analyses of the dependence of the tunability range, insertion loss, and loaded quality factor on the graphene stripe width are performed, systematically varying the width of the graphene stripe from nonexistent to completely covering the E -plane insert in steps of 2.5% of the insert length. Finally, the dependence of graphene-based waveguide resonator properties on the frequency is investigated.

We propose and investigate here applications of graphene in waveguide resonators in the spectral region from 100 to 1100 GHz. For the proposed applications we present the theoretical background and thorough numerical validations using rigorous full-wave computational simulations based on the method of moments (MoM), and the finite element method (FEM) algorithms. In analyses we consider standard rectangular waveguide sections as canonical examples for investigation of graphene efficiency in the considered frequency range, noting that graphene can be employed in the surface integrated waveguides and the hollow integrated waveguides as well. In particular, we study a single resonator, as a basic building block for millimeter and submillimeter wave filters.

An E -plane insert, considered in this study, is a waveguide discontinuity often employed in all-metal resonators and filters due to its simplicity and potential for accurate realization. Analytical expressions are initially derived to provide valuable insight into the underlying physical mechanisms of graphene-based resonator operation. However, equivalent analytical models of E -plane inserts exhibit nonlinear frequency dependence around the desired central frequency of operation. Hence, accurate analysis of E -plane inserts requires numerical simulations or optimization algorithms [21]. Moreover, losses in graphene are higher than in the purely metallic parts of the surrounding resonator structure, hence mandating full-wave numerical computations of wave propagation. Detailed investigation of the proposed structure is conducted using the full-wave computational EM analysis tools based on the MoM and FEM, namely utilizing, respectively, the state-of-the-art commercial software packages WIPL-D [22] and HFSS [23].

2. Theoretical background

Standard rectangular waveguide section containing the resonator, which consists of two equally sized and symmetrically placed E -plane inserts, is shown in figure 1. The length of an E -plane insert, l_T , is represented as $l_T = l_M + l_G$ to include the case where only a part of an insert (of length l_G) is covered

Table 1. Rectangular metallic waveguides: frequency bands and waveguide dimensions.

EIA designation/ extended MIL [17]	IEEE designation [16]	Frequency range (GHz)	Cut-off (TE ₁₀) frequency (GHz)	Aperture width a (μm)	Aperture height b (μm)
WR-10	WM-2540	75–110	59.01	2540.0	1270.0
WR-8	WM-2032	90–140	73.77	2032.0	1016.0
WR-6	WM-1651	110–170	90.79	1651.0	825.5
WR-5	WM-1295	140–220	115.75	1295.0	647.5
WR-4	WM-1092	170–260	137.27	1092.0	546.0
WR-3	WM-864	220–330	173.49	864.0	432.0
WR-2.8	WM-710	265–400	211.12	710.0	355.0
WR-2.2	WM-570	325–500	268.15	559.0	279.5
WR-1.9	WM-470	400–600	318.93	470.0	235.0
WR-1.5	WM-380	500–750	393.43	381.0	190.5
WR-1.2	WM-310	600–900	491.47	305.0	152.5
WR-1.0	WM-250	750–1100	590.15	254.0	127.0

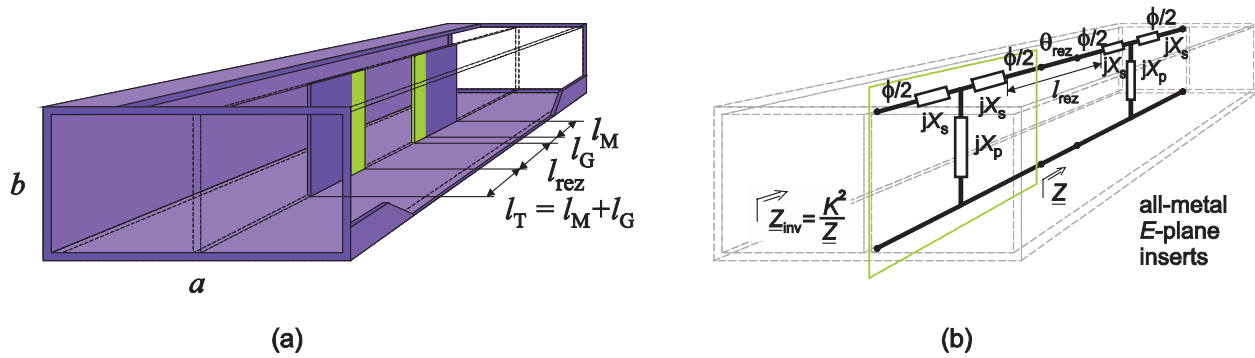


Figure 1. Waveguide resonator comprising two equal and symmetrically placed E -plane inserts: (a) the usual case of all-metal inductive inserts of the resonator, and (b) the normalized dominant mode equivalent circuit. When the resonator E -plane inserts consist of graphene layers, their surface impedance can be controlled via the bias voltage, influencing EM field distribution in the vicinity of waveguide discontinuities of total length l_T . The resulting effects are similar to the effects of varying the effective resonator length by changing the distance, l_{rez} , between the inserts. For the improved stop-band performance there should be the least difference in EM field distribution around the outer resonator edges, compared to the case of perfectly conducting inserts. This is addressed by applying graphene stripes, of length l_G , only along the inner edges of the resonator E -plane inserts, whereas the remaining part of each insert, of length l_M , is metallic.

by graphene. Propagation of the transverse electric (TE) and transverse magnetic (TM) modes is supported above the cutoff frequency, given by $f_{c,mn} = \sqrt{((m/a)^2 + (n/b)^2)/4\epsilon\mu}$, with integer m and n . These modes can be derived from a magnetic-type Hertzian potential and from an electric-type Hertzian potential, respectively [24]. Dominant mode of propagation is the TE₁₀ mode, since $a > b$ is usually considered. For standard waveguides $a = 2b$, so that $f_{c,20} = f_{c,01} = 2f_{c,10}$ and $f_{c,11} = \sqrt{5}f_{c,10}$, allowing for as large as possible single-mode bandwidth from $f_{c,10}$ to $2f_{c,10}$. Air filled waveguides are used in our analysis, with permittivity $\epsilon = \epsilon_0$ and permeability $\mu = \mu_0$.

Waveguide discontinuities lead to the excitation of higher order evanescent modes, which vanish at a distance from the discontinuity planes; however, changes are introduced in the reflection from and transmission through the considered section. Due to similarity of waveguide modal field solutions and wave propagation along a transmission line, formally identical systems of equations can be written for the modal field solutions and transmission line voltage and current relations. Namely, each mode can be represented as an equivalent transmission line, thus a circuit representation of waveguide

discontinuities is possible. This is often utilized to facilitate analytical description of waveguide discontinuities.

2.1. All-metal E -plane resonators

Waveguide resonators and bandpass filters consisting of all-metal E -plane inserts were introduced as an answer to the need for an efficient, low cost, device, which can easily be mass-produced with desired accuracy [25]. Ever since, all-metal inserts remain appealing due to their small size and low losses.

Variational expression for the normalized admittance of an inductive insert is obtained according to [24], leading to the normalized dominant mode equivalent circuit of the discontinuity shown in figure 1(b). The equivalent symmetrical T-circuit of an E -plane insert can be symmetrically embedded in a length of a waveguide, incorporating the electrical length of $\phi/2$ on each port. With the convenient choice of ϕ , equivalent T-circuit acts as an impedance inverter, or K -inverter, in a very narrow frequency range. In an idealized impedance inverter, impedance seen at one port, Z , appears at the other port as $Z_{inv} = K^2/Z$. In the case of an E -plane insert, however, parameter K has nonlinear frequency dependence and

can serve only as a first step approximation. Upon the calculation of equivalent circuit reactances X_s , X_p , normalized with respect to the waveguide characteristic impedance for the dominant mode, Z_C , the electrical length ϕ is chosen as

$$\phi = -\arctan(2X_p + X_s) - \arctan(X_s), \quad (1)$$

in order to approximate the equivalent circuit as a K -inverter defined by:

$$\tan(2 \arctan K) = \frac{2X_p}{1 + 2X_p X_s + X_s^2}. \quad (2)$$

The normalized reactances, X_s and X_p , are functions of the length, l_T , of an E -plane insert. Frequency dependent parameters ϕ and K are in the first approximation calculated at some predefined ‘center’ frequency, f_0 . The electrical length θ_{rez} , corresponding to the distance between the two inserts, l_{rez} , is then calculated taking into account the waveguide wavelength and subtracting the $\phi/2$ electrical lengths of the two impedance inverters, in this case equal. In accordance with the resonator and filter synthesis using the half-wave prototypes, the resulting electrical length must be equal to π at the frequency f_0 :

$$\theta_{\text{rez}} = l_{\text{rez}} \frac{\pi}{a} \sqrt{\varepsilon_0 \mu_0 (2af_0)^2 - 1} - \phi = \pi. \quad (3)$$

Given X_s and X_p , the dimensions of a resonator can be approximately determined using (1)–(3).

To determine X_s and X_p , EM field in the vicinity of the insert of width g has to be represented as a sum of modal field solutions including the higher order modes, for the rectangular waveguide of width a and height b , on one side of the discontinuity plane, and for the two waveguides of width $(a - g)/2$ and height b , on the other side of the discontinuity plane. (Due to symmetry, only odd modes are required for the main waveguide.) A sufficient finite number of modes in an expansion has to be matched over the discontinuity plane, whereas the sum of field components at the metallic insert tends to zero (exactly

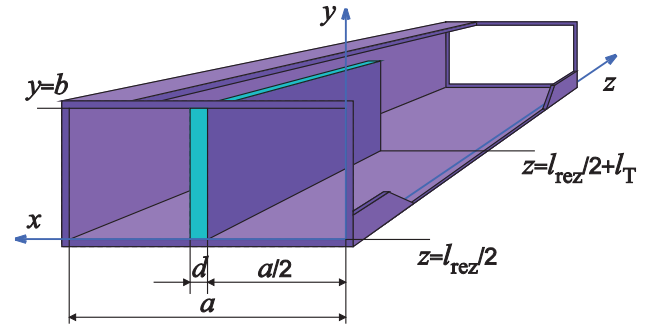


Figure 2. Waveguide discontinuity comprising a dielectric slab of finite length, l_T , and thickness, d , and a layer of metallization or graphene of negligible thickness covering the dielectric slab side along the midline of the waveguide. The coordinate system shown is used in analytical expressions throughout the paper.

2.2. Dielectric slab with and without conductive layer

If a metallic E -plane insert, or any part of it, is to be replaced by graphene, a dielectric holder is needed as a support. Phase shifts of the guided wave, introduced by the dielectric slab, should be accounted for in the resonator design. In our case, dielectric slab of finite length, l_T , is placed asymmetrically as shown in figure 2, so that a very thin layer of metallization or a graphene layer runs along the midline of the waveguide. An excellent example of analysis of asymmetrically placed dielectric slab, without the conductive layer, is given in [26] including the complete final expressions needed to numerically calculate the scattering matrix. A very limited outline of the major derivation steps pertinent to the special case in figure 2 will be given next.

Since the discontinuity is uniform along the y -axis, higher order modes excited at the junction are the TE_{m0} modes. The appropriate x -component of the Hertzian vector potential for the considered case is

$$Q_x = \begin{cases} \sum_{m=1}^{\infty} A_m^I \sin\left(\frac{m\pi}{a}x\right) e^{-jk_{zm}z}, & 0 \leq z \leq \frac{l_{\text{rez}}}{2} \text{ or } z \geq \frac{l_{\text{rez}}}{2} + l_T, 0 \leq x \leq a, \text{ (region I)} \\ \sum_{m=1}^{\infty} (A_m^{\text{II}} \cos(k_{xm}^D x) + B_m^{\text{II}} \sin(k_{xm}^D x)) e^{-jk_{zm}z}, & \frac{l_{\text{rez}}}{2} \leq z \leq \frac{l_{\text{rez}}}{2} + l_T, \frac{a}{2} \leq x \leq \frac{a}{2} + d, \text{ (region II)} \\ \sum_{m=1}^{\infty} A_m^{\text{III}} (-\tan(k_{xm}^A a) \cos(k_{xm}^A x) + \sin(k_{xm}^A x)) e^{-jk_{zm}z}, & \frac{l_{\text{rez}}}{2} \leq z \leq \frac{l_{\text{rez}}}{2} + l_T, \frac{a}{2} + d \leq x \leq a, \text{ (region III)} \\ \sum_{m=1}^{\infty} A_m^{\text{IV}} \sin(k_{xm}^A x) e^{-jk_{zm}z}, & \frac{l_{\text{rez}}}{2} \leq z \leq \frac{l_{\text{rez}}}{2} + l_T, 0 \leq x \leq \frac{a}{2}, \text{ (region IV)}. \end{cases} \quad (5)$$

equals zero for the perfect electric conductor (PEC)). For an accurate solution, computer aided calculations are required.

Alternatively, a commercial computer aided engineering (CAE) software tool can be used to determine the discontinuity scattering parameters, for different lengths of an insert in some predefined range of values. Equivalent T-circuit normalized reactances are obtained from S -parameters as:

$$jX_s = \frac{1 + S_{11} - S_{21}}{1 - S_{11} + S_{21}}, \quad jX_p = \frac{2S_{21}}{(1 - S_{11})^2 - S_{21}^2}. \quad (4)$$

Three components of the EM field vanish, namely: $E_x = 0$, $H_y = 0$, $E_z = 0$. The nonzero components of the EM field are calculated using:

$$E_y = -j\omega\mu_0 \frac{\partial Q_x}{\partial z}, \quad H_x = \omega^2 \mu_0 \varepsilon_0 \varepsilon_r Q_x + \frac{\partial^2 Q_x}{\partial x^2}, \quad H_z = \frac{\partial^2 Q_x}{\partial x \partial z}. \quad (6)$$

In the above, $\omega = 2\pi f$ is the angular frequency and ε_r is the relative permittivity, considered equal to unity everywhere

except in region II, which is defined by (5) for the coordinate system given in figure 2. Equality of the tangential field components, E_y and H_z , at the region's interfaces at $x = a/2$ and $x = a/2 + d$ yields a system of linear equations. For a non-trivial solution, the system's determinant has to vanish, leading to a transcendental equation for the transverse mode propagation constants in air, k_{xm}^A , and in dielectric, k_{xm}^D :

$$\tan(k_{xm}^D d) + \frac{k_{xm}^D}{k_{xm}^A} \left(\tan(k_{xm}^A \frac{a}{2}) + \tan(k_{xm}^A (\frac{a}{2} - d)) \right) - \left(\frac{k_{xm}^D}{k_{xm}^A} \right)^2 \tan(k_{xm}^D d) \tan(k_{xm}^A \frac{a}{2}) \tan(k_{xm}^A (\frac{a}{2} - d)) = 0. \quad (7)$$

Both k_{xm}^A and k_{xm}^D are expressed in terms of the longitudinal propagation factor k_{zm} , which is equal for regions II, III, and IV, defined by (5) and figure 2. Equation (7) is numerically solved for k_{zm} , further determining

$$k_{xm}^A{}^2 = k_0^2 - k_{zm}^2, \quad k_{xm}^D{}^2 = \epsilon_r k_0^2 - k_{zm}^2, \quad k_0^2 = \omega^2 \mu_0 \epsilon_0. \quad (8)$$

With respect to the longitudinal propagation factors of the main waveguide, k_{zm}^I , obtained from $k_{zm}^I{}^2 = k_0^2 - (m\pi/a)^2$, amplitudes of the modal propagation constants, k_{zm} , are larger, implying shorter modal wavelengths. Considering the TE₁₀ mode, the only one that can actually propagate in the main waveguide, the discontinuity section can be viewed as if it is filled with material of an equivalent dielectric constant ϵ_{re} , given by $\epsilon_{re} = k_0^{-2}(k_{z1}^2 + (\pi/a)^2)$, reducing the phase velocity by a factor of $\sqrt{\epsilon_{re}}$. The phase shift introduced by the dielectric slab is approximately equal to

$$\Delta\theta_D = l_T \left(|k_{z1}| - \sqrt{k_0^2 - \left(\frac{\pi}{a}\right)^2} \right). \quad (9)$$

If the dielectric slab side at $x = a/2$ were covered with a negligibly thick PEC sheet ($g \rightarrow 0$), the boundary conditions would dictate the vanishing of the tangential field components, E_y and H_z , at both sides of the PEC sheet. This simplifies the field equations derived from the following x -component of the Hertzian potential:

$$Q_x = \begin{cases} \sum_{m=1}^{\infty} A_m^I \sin(\frac{m\pi}{a}x) e^{-jk_{zm}^I z}, & 0 \leq z \leq \frac{l_{rez}}{2} \text{ or } z \geq \frac{l_{rez}}{2} + l_T, \quad 0 \leq x \leq a, \quad (\text{region I}) \\ \sum_{m=1}^{\infty} A_m^{II} \left(-\tan(k_{xm}^D \frac{a}{2}) \cos(k_{xm}^D x) + \sin(k_{xm}^D x) \right) e^{-jk_{zm}^D z}, & \frac{l_{rez}}{2} \leq z \leq \frac{l_{rez}}{2} + l_T, \quad \frac{a}{2} \leq x \leq \frac{a}{2} + d, \quad (\text{region II}) \\ \sum_{m=1}^{\infty} A_m^{III} \left(-\tan(k_{xm}^A a) \cos(k_{xm}^A x) + \sin(k_{xm}^A x) \right) e^{-jk_{zm}^A z}, & \frac{l_{rez}}{2} \leq z \leq \frac{l_{rez}}{2} + l_T, \quad \frac{a}{2} + d \leq x \leq a, \quad (\text{region III}) \\ \sum_{m=1}^{\infty} A_m^{IV} \sin(\frac{2m\pi}{a}x) e^{-jk_{zm}^{IV} z}, & \frac{l_{rez}}{2} \leq z \leq \frac{l_{rez}}{2} + l_T, \quad 0 \leq x \leq \frac{a}{2}, \quad (\text{region IV}). \end{cases} \quad (10)$$

In the above, $k_{zm}^I{}^2 = k_0^2 - (\frac{m\pi}{a})^2$ and $k_{zm}^{IV}{}^2 = k_0^2 - (2m\pi/a)^2$, whereas $k_{zm}^{II} = k_{zm}^{III} = k_{zm}$ is obtained from

$$\tan(k_{xm}^D d) + \frac{k_{xm}^D}{k_{xm}^A} \tan(k_{xm}^A (\frac{a}{2} - d)) = 0, \quad (11)$$

using dependencies given in (8). For a metal of finite conductivity σ_m , and permeability μ_0 , surface impedance of the thin metal sheet can be calculated as $Z_S = (1+j)\sqrt{\pi f \mu_0 / \sigma_m}$. It corresponds to the ratio of the total tangential electric field component and total tangential magnetic field component at any point on a surface, i.e. $Z_S = E_y/H_z$ for a thin metallic sheet located at $x = a/2$. The attenuation is small and EM field distribution is almost identical to the PEC case.

2.3. Influence of the graphene surface conductivity

Surface conductivity of graphene, in the considered range of frequencies, stems solely from the intraband contributions. It is given by [17, 27]

$$\sigma(\omega, \mu_c, \Gamma, T) = \frac{-jq_e^2 k_B T}{\pi \hbar^2 (\omega - j2\Gamma)} \left(\frac{\mu_c}{k_B T} + 2 \ln(e^{-\frac{\mu_c}{k_B T}} + 1) \right), \quad (12)$$

where ω is the angular frequency, μ_c is the chemical potential of graphene, Γ represents the carrier scattering rate, T is the temperature, and k_B the Boltzmann constant. The chemical potential, μ_c , $k_B T$ product, as well as the scattering rate, Γ , are expressed in electronvolts, although Γ in s^{-1} is used in (12). Elementary charge and the reduced Planck constant are denoted as q_e and \hbar , respectively. Room temperature, $T = 300$ K, is assumed throughout the paper. The above equation is accurate at room temperature, in the millimeter and submillimeter wave frequency range where spatial-dispersion effects are negligible, provided that there is no magnetic field bias. The chemical potential, μ_c , depends on the level of chemical doping; however, it is also tunable using the relation between the chemical potential and the electrostatic bias field, E_{bias} [27]:

$$\frac{\epsilon_0 \pi \hbar^2 v_F^2}{q_e} E_{bias} = \int_0^{+\infty} \vartheta \left[(1 + e^{(\vartheta - \mu_c)/k_B T})^{-1} - (1 + e^{(\vartheta + \mu_c)/k_B T})^{-1} \right] d\vartheta. \quad (13)$$

Electrostatic bias field, perpendicular to the graphene surface, is created by applying the bias voltage across the capacitor formed by the graphene layer and the gating electrode,

separated by a thin dielectric layer. A metallic gating electrode in proximity to the graphene layer would affect the EM wave propagation; a metallic layer parallel to the graphene surface would itself present an E -plane insert, masking the effects of the tunable conductivity of graphene. Therefore, another graphene layer has to play the role of the gate electrode. Utilization

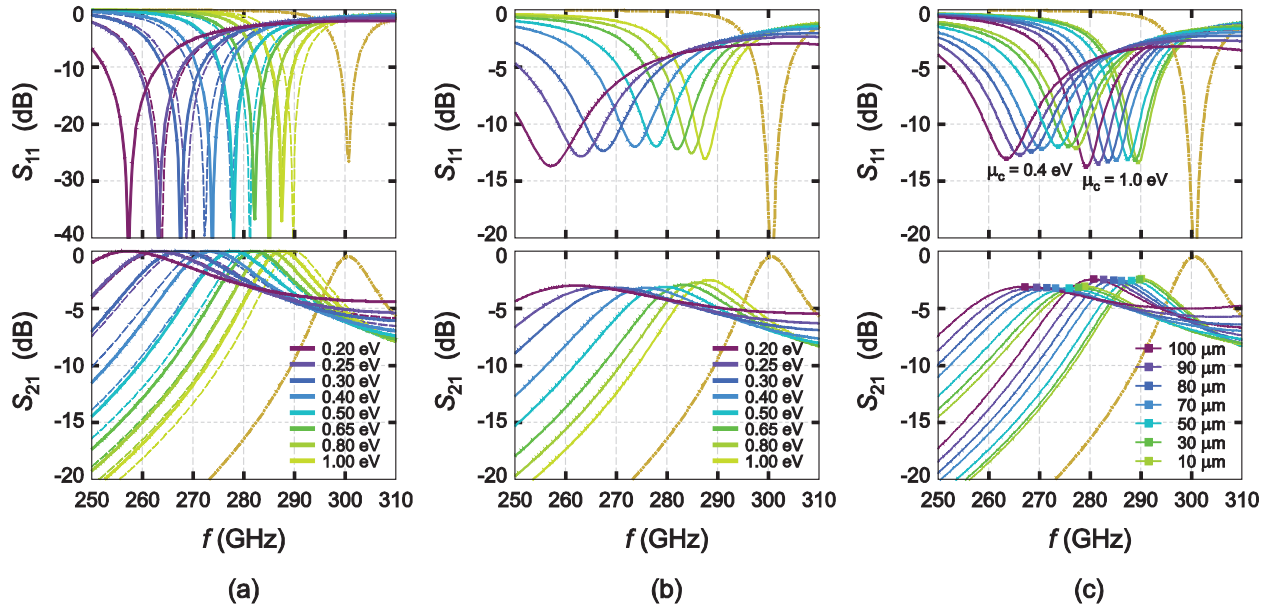


Figure 3. Effects on the resonator parameters of (a) the graphene surface inductance only, with R_g set to zero, (b) the realistic graphene surface impedance, and (c) the quartz support thickness. Standard WR-3 waveguide section with $l_{rez} = 360 \mu\text{m}$, and $l_T = 280 \mu\text{m}$ completely covered by the graphene layers, was analyzed. Scattering parameters for the all-metal case, with the $f_{rez}^M = 300.75 \text{ GHz}$, are presented by the dash-dot-dot line in all graphs. In part (a), the dashed lines correspond to the 2D graphene sheet without a dielectric support revealing the tunability effect due to the graphene only, whereas the solid lines show the combined resonant frequency shifts and tunability due to the graphene-on-quartz. Additional phase shifts introduced by the dielectric slab are functions of the graphene surface inductance, resulting in a broader tunability range when the dielectric support is used. Different line colors (shades) in parts (a) and (b) correspond to the graphene chemical potential values given in the legend. Scattering parameters accounting for the realistic loss in graphene-on-quartz resonators are shown in part (b). Results of an investigation into the effect of the quartz thickness on S -parameters are shown in part (c), through a comparison of S -parameters for two values of graphene chemical potential: 0.4 eV and 1.0 eV. Larger thickness yields a slightly broader tunability range, however at the expense of a larger shift between the reflected and the transmitted wave and somewhat worse quality factor (line colors/shades are explained in the legend). Therefore, the dielectric support should remain thin.

of such all-graphene gating and the graphene stacks, structures composed of two or more graphene layers separated by electrically thin dielectrics, has been theoretically investigated and experimentally verified [9, 12, 28–30]. Alumina, Al_2O_3 , is often employed as the dielectric layer in-between the graphene sheets. We will assume a 100 nm thick Al_2O_3 layer, which is thick enough to neglect the quantum capacitance of graphene, but still sufficiently thin to allow for the low bias voltages of the graphene-based top gate. From the point of view of EM wave propagation, the described graphene stack is electrically very thin and the boundary conditions can be assumed constant throughout the graphene stack. Likewise, very small slits needed to connect the outer voltage generator to the two graphene layers are not deemed influential on the EM field distribution along the resonator edges nor the further EM wave propagation. Without the loss of generality, we will perform numerical EM modeling of the proposed structures, replacing the graphene stacks with single layers of negligible thickness exhibiting tunable surface conductivity. All of the results will be given for several chemical potentials in the range of interest, rather than for the corresponding bias voltages, thus allowing for easier interpretation of results, once actual biasing conditions and the equivalent total stack conductivity are determined [29]. The Fermi velocity in graphene is $v_F \approx 10^6 \text{ m s}^{-1}$ and the chemical potential is easily tuned in the range $(-1 \text{ eV}, 1 \text{ eV})$. Graphene surface impedance,

$Z_g = R_g + j\omega L_g$, is obtained directly, with the surface resistance and surface inductance given by

$$R_g = 2\Gamma \frac{q_e}{\hbar} L_g, \quad L_g = \frac{\pi \hbar^2}{q_e^3 k_B T \left(\frac{\mu_c}{k_B T} + 2 \ln(e^{-\mu_c/(k_B T)} + 1) \right)}. \quad (14)$$

The Boltzmann constant $k_B = 8.6173325 \times 10^{-5} \text{ eV K}^{-1}$ and the reduced Planck constant $\hbar = 1.054571726 \times 10^{-34} \text{ Js}$ are used, whereas μ_c is varied in the range $(-1 \text{ eV}, 1 \text{ eV})$.

If in the dielectric slab configuration shown in figure 2, the slab side located at $x = a/2$ is covered with a graphene layer, the EM field at this boundary surface will be significantly reduced compared with the pure dielectric slab. This effect is brought by the graphene conductivity, leading to the resonating effect when there are two conducting surfaces as in figure 1. Still, the EM field at $x = a/2$ will be far from zero, due to the finite, much larger than in the metallic case, real part of the surface impedance, $R_g \gg \sqrt{\pi f \mu_0 / \sigma_m}$, in the frequency range of interest. The real part of the surface impedance induces attenuation of the guided wave, whereas the imaginary, reactive component of the surface impedance is responsible for the resonant frequency shift. This is illustrated in figure 3, for the standard WR-3 waveguide section. High quality, low resistivity graphene, should be used to minimize losses.

The appropriate x -component of the Hertzian vector potential is again given by (5). There is no need to introduce the new region at $x = a/2$, since the total tangential electric fields, E_y , can be considered constant at both sides and throughout the graphene layers belonging to the electrically thin conductive sheet. At the interface of regions II and III, where there are no free charges or currents, E_y , as well as H_z , have to be continuous over the interface. In order to satisfy the electric field boundary conditions at the graphene surface at $x = a/2$, and at $x = a/2 + d$ boundary, we have to enforce the equality of the longitudinal propagation factor, k_{xm} , for regions II, III, and IV. Resulting from the total E_y , the surface current density of the graphene sheet equals $\mathbf{J}_S = \sigma E_y \hat{t}_y = Z_g^{-1} E_y \hat{t}_y$. It is also related to the tangential magnetic fields at $x = a/2$, through $\mathbf{J}_S = \hat{n} \times (H_z^{\text{IV}} - H_z^{\text{II}}) \hat{t}_z$, where $\hat{n} \equiv -\hat{t}_x$ represents the region IV surface normal. We thus develop the field components, E_y and H_z , in regions II, III, and IV using (6). Appropriate boundary conditions lead to the following system of equations:

in magnitude with varying longitudinal propagation factors. As a result, elements of the equivalent T-circuit in figure 1(b) become tunable. Changes in the equivalent circuit elements are reflected in the varying appropriate electrical length ϕ needed to obtain the function of the K -inverter element, further affecting the total electrical length of a resonator, θ_{rez} . In short, the tunable graphene surface impedance can be considered as a tunable effective length of the E -plane inserts, changing the length of a resonator, and thus leading to the change in its resonant frequency. As the modifications of resonator length are desired, there is no benefit in changing the overall length of the section comprising the two E -plane inserts, i.e. the all-metal inserts exhibit the best stop band performance. This led us to the proposal of the graphene–metal combined waveguide resonators, where an inner side of each E -plane insert adjacent to the resonator, l_{rez} , is coated with graphene, whereas the rest of the inserts is purely metallic. With the aid of numerical simulations, different configurations will be analyzed and compared in the following sections.

$$\begin{bmatrix} \cos(k_{xm}^{\text{D}}(\frac{a}{2} + d)) & \sin(k_{xm}^{\text{D}}(\frac{a}{2} + d)) & \frac{\sin(k_{xm}^{\text{A}}(\frac{a}{2} - d))}{\cos(k_{xm}^{\text{A}}a)} & 0 \\ k_{xm}^{\text{D}} \sin(k_{xm}^{\text{D}}(\frac{a}{2} + d)) & -k_{xm}^{\text{D}} \cos(k_{xm}^{\text{D}}(\frac{a}{2} + d)) & \frac{k_{xm}^{\text{A}} \cos(k_{xm}^{\text{A}}(\frac{a}{2} - d))}{\cos(k_{xm}^{\text{A}}a)} & 0 \\ \cos(k_{xm}^{\text{D}}\frac{a}{2}) & \sin(k_{xm}^{\text{D}}\frac{a}{2}) & 0 & -\sin(k_{xm}^{\text{A}}\frac{a}{2}) \\ k_{xm}^{\text{D}} \sin(k_{xm}^{\text{D}}\frac{a}{2}) & -k_{xm}^{\text{D}} \cos(k_{xm}^{\text{D}}\frac{a}{2}) & 0 & \frac{j\omega\mu_0}{Z_g} \sin(k_{xm}^{\text{A}}\frac{a}{2}) + k_{xm}^{\text{A}} \cos(k_{xm}^{\text{A}}\frac{a}{2}) \end{bmatrix} \begin{bmatrix} A_m^{\text{II}} \\ B_m^{\text{II}} \\ A_m^{\text{III}} \\ A_m^{\text{IV}} \end{bmatrix} = \begin{bmatrix} 0 \\ 0 \\ 0 \\ 0 \end{bmatrix}. \quad (15)$$

For a non-trivial solution, the system's determinant has to vanish, yielding

2.4. Full-wave EM analysis

$$\xi_g \cdot \tan(k_{xm}^{\text{D}}d) + \frac{k_{xm}^{\text{D}}}{k_{xm}^{\text{A}}} \left(\tan(k_{xm}^{\text{A}}\frac{a}{2}) + \xi_g \cdot \tan(k_{xm}^{\text{A}}(\frac{a}{2} - d)) \right) - \left(\frac{k_{xm}^{\text{D}}}{k_{xm}^{\text{A}}} \right)^2 \tan(k_{xm}^{\text{D}}d) \tan(k_{xm}^{\text{A}}\frac{a}{2}) \tan(k_{xm}^{\text{A}}(\frac{a}{2} - d)) = 0, \quad (16a)$$

The numerical simulations assume quartz as a support for graphene layers and a thin film metallization. This choice has been motivated by two reasons. Firstly, fused silica quartz is an excellent substrate for the millimeter and submillimeter wave applications due to the relatively low dielectric constant and a small loss tangent. Secondly, quartz is a substrate material highly compatible with graphene. In addition to very usual wet-etching techniques for the transfer of graphene films grown on another substrate [31], there are also many recent techniques for direct generation of graphene on quartz, e.g. laser-based direct synthesis [32]. Reasonable adhesion of metallic thin films, copper (Cu) and gold (Au), on quartz, requires somewhat more complicated deposition techniques. Thin film metallization on quartz is usually comprised of two layers, the first one being a strongly oxidized metal such as chromium or titanium [33, 34]. The quartz dielectric constant and loss tangent equal $\epsilon_r = 3.78$ and $\tan \delta = 0.000228$, respectively. Quartz substrate thickness for the WR-3 waveguide is chosen as the commercially available $50 \mu\text{m}$. For consistency, the ratio of quartz support thickness and the waveguide broad wall is kept equal to $d/a = 1/16$ for all considered waveguide sections, given in table 1. Close to 1 THz, a different material might be a better choice. In that case, phase shift and loss could differ with the same qualitative behavior of resonators.

$$\xi_g = 1 + \frac{j\omega\mu_0}{Z_g k_{xm}^{\text{A}}} \tan(k_{xm}^{\text{A}}\frac{a}{2}), \quad (16b)$$

$$\xi_g = 1 + \frac{\omega^2 L_g \mu_0 a + j\omega R_g \mu_0 a \tan(k_{xm}^{\text{A}}\frac{a}{2})}{2(R_g^2 + \omega^2 L_g^2)} \frac{\tan(k_{xm}^{\text{A}}\frac{a}{2})}{k_{xm}^{\text{A}} a/2}.$$

In the limit $Z_g \rightarrow 0$, we have to multiply the equation (16a) with Z_g . The only remaining non-zero terms result in $(\sin k_{xm}^{\text{IV}}\frac{a}{2}) \left(\tan(k_{xm}^{\text{D}}d) + \frac{k_{xm}^{\text{D}}}{k_{xm}^{\text{A}}} \tan(k_{xm}^{\text{A}}(\frac{a}{2} - d)) \right) = 0$, leading to equations (10) and (11). In the limit $Z_g \rightarrow \infty$, we obtain $\xi_g \equiv 1$, and (16a) reduces to equation (7), describing the purely dielectric slab.

In between the two limits, Z_g modifies the EM fields significantly, depending on intrinsic material properties, frequency, and the applied bias field. With a change in Z_g , evanescent higher order modes of the coated surface at $x = a/2$ decrease

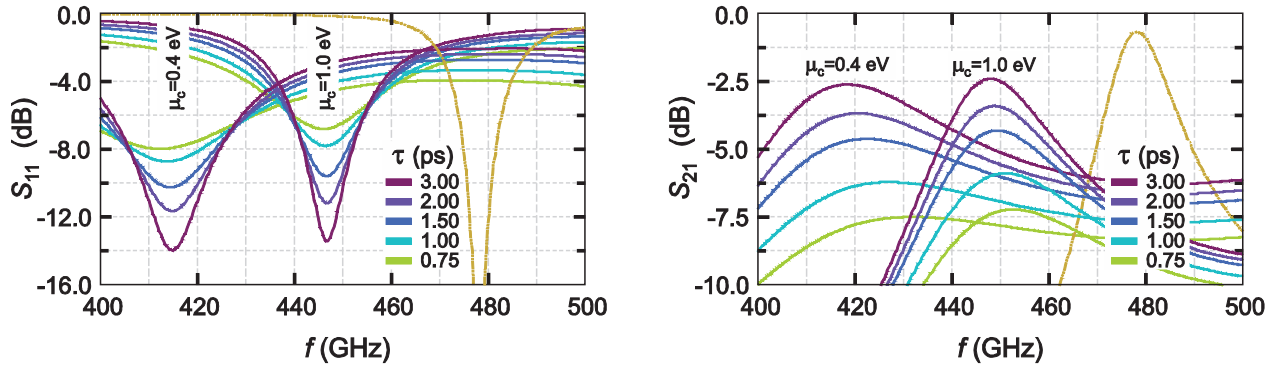


Figure 4. Dependence of the resonator S -parameters on the relaxation time of charge carriers, τ . Results are presented for the standard WR-2.2 waveguide section with $l_{\text{rez}} = l_T = 210 \mu\text{m}$, with l_T completely covered by the graphene layers (line colors/shades are explained in the legend). The S -parameters corresponding to the all-metal resonator are given for comparison by the dash-dot-dot line ($f_{\text{rez}}^M \cong 478 \text{ GHz}$). Results are shown for two values of the graphene chemical potential: 0.4 eV and 1.0 eV. There is no impact of the carrier relaxation time on the tunability range. However, the observed increase in the insertion loss makes the concept impractical for low quality graphene layers.

In the analyses of the graphene–metal combined waveguide resonators we assume a thin film metallization of Cu for the WR-6, WR-4 and WR-3 waveguide sections, and a thin film metallization of Au in all other cases. The skin effect has been modeled accordingly, taking the DC conductivities of Cu and Au, $\sigma_{\text{Cu}} = 58.0 \text{ MS m}^{-1}$ and $\sigma_{\text{Au}} = 41.0 \text{ MS m}^{-1}$, respectively. It has been shown previously, that the losses in graphene stripe were dominant in comparison with metallization as well as dielectric loss [18]; therefore, the effects of the metallization surface roughness were not considered here.

As mentioned above, the surface conductivity of graphene at room temperature, for a given frequency, depends on the chemical potential of graphene, μ_c , and the carrier scattering rate, Γ . The chemical potential, related to the level of chemical doping and the applied electrostatic bias field, is easily tuned in the range (-1 eV , 1 eV), with the $\pm(0.2 \text{ eV}$, 1.0 eV) interval of interest in this study. This choice of working interval corresponds to the concentration of charge carriers that is already somewhat increased, either by the chemical doping, or by the initially applied bias voltage. Further biasing allows for the precise control of the chemical potential, and thus the attained low resistivity, as the chemical potential variation with bias voltage in this interval is less steep than at zero chemical potential. Additionally, the relation between the chemical potential and the electrostatic bias field is more linear, as shown in figure 3 in [27]. The phenomenological scattering rate, Γ , is related to the relaxation time of charge carriers, $\tau = (2\Gamma)^{-1}$, which can differ significantly in the cases of intrinsic and doped graphene [35]. Carrier relaxation time at subterahertz frequencies can be identified with the DC relaxation time, $\tau \approx \tau_{\text{DC}} = \mu \hbar \sqrt{n_c \pi} / (q_e v_F)$, which arises mainly from impurities [36]. DC relaxation time is directly proportional to the charge carrier mobility, μ , and the square root of the carrier concentration, n_c . Experimental investigation of high-purity graphene, found in nature on the surface of bulk graphite, sets the low temperature scattering time limit at $\tau \approx 20 \text{ ps}$ [35]. High mobility of charge carriers has also been obtained in the case of the suspended graphene [37, 38], up to $\mu = 200\,000 \text{ cm}^2 \text{ V}^{-1} \text{ s}^{-1}$ at low temperatures and $\mu = 120\,000 \text{ cm}^2 \text{ V}^{-1} \text{ s}^{-1}$ near room temperature.

Influence of substrate type and quality on carrier mobility can be significant. In a study utilizing the Monte Carlo method to investigate the substrate influence on the carrier mobility for three different substrates [39], high charge carrier mobility was obtained only for the hexagonal boron nitride (h-BN) substrate ($\mu \approx 170\,000 \text{ cm}^2 \text{ V}^{-1} \text{ s}^{-1}$). That finding is in accordance with the experimental results [40]. High carrier mobility has been observed for the multiple-graphene-layer (MGL) structures grown epitaxially on SiC, as well [14, 41–44]. Growth on the Si-face of SiC results in a lower mobility few-layer graphene, whereas growth on the C-face results in a high mobility multilayer graphene ($\mu \approx 200\,000 \text{ cm}^2 \text{ V}^{-1} \text{ s}^{-1}$). The number and mobility of graphene layers can thus be controlled by controlling the crystal orientation of the SiC. Once fabricated, such MGL structures can be transferred to a different substrate [44]. The real part of the intraband graphene conductivity always contributes as a loss. Since introducing large losses is highly undesirable in the waveguiding applications, high-quality low-loss graphene should be used. Therefore, the moderately long relaxation time, $\tau = 3 \text{ ps}$, is considered in the numerical examples. The impact of the carrier relaxation time on tunability and insertion loss of the proposed waveguide resonators is illustrated in figure 4.

The tunability effect achieved by the utilization of the adjustable graphene surface impedance in resonators comprised of E -plane inserts stems from the adjustment of the boundary conditions, as described by equations (16a) and (16b). Numerical analysis of a resonator using the WR-3 waveguide section is performed first, to qualitatively illustrate the effects on the resonator parameters of the real and imaginary parts of the surface impedance as well as the dielectric support thickness. As listed in table 2, the resonator length and the E -plane insert length were chosen as $l_{\text{rez}} = 360 \mu\text{m}$ and $l_T = 280 \mu\text{m}$, respectively. The results are shown in figure 3. For this first resonator, all-graphene E -plane inserts were considered, i.e. the quartz support of the total length l_T was assumed to be covered completely by the graphene. Simulations confirm the dependence of the obtained tunability range on the graphene surface inductance, both with $R_g = 0$ and $R_g \neq 0$. The real part of the graphene surface impedance contributes as a loss, on

Table 2. Graphene-on-quartz waveguide resonators: considered dimensions and resonant frequencies.

EIA/Ext. MIL	$l_{\text{rez}} (\mu\text{m})$	$l_{\text{T}} (\mu\text{m})$	$f_{\text{rez}}^{\text{M}} (\text{GHz})$	$f_{\text{rez}}^{0.2\text{eV}} (\text{GHz})$	$f_{\text{rez}}^{0.4\text{eV}} (\text{GHz})$	$f_{\text{rez}}^{1.0\text{eV}} (\text{GHz})$
WR-6	720.0	535.3	155.00	143.00	147.50	151.25
WR-4	420.0	354.1	244.00	216.00	226.50	235.25
WR-3	360.0	280.0	300.75	262.00	276.00	288.50
WR-2.8	260.0	230.6	380.25	320.50	341.00	360.50
WR-2.2	210.0	181.2	479.50	393.75	421.25	449.50
WR-1.5	146.0	123.5	700.25	549.50	590.00	640.25
WR-1.2	132.0	98.8	840.50	656.00	700.00	762.00
WR-1.0	104.0	82.4	1029.50	786.50	835.00	915.50

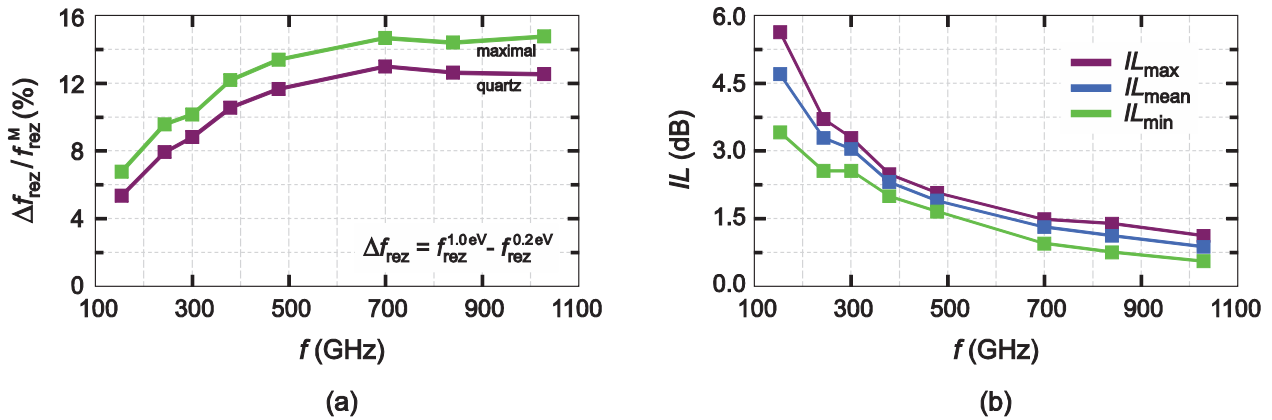


Figure 5. Tunability and loss analysis for the graphene-on-quartz waveguide resonators. (a) Realistic values for the tunability range ($R_g \neq 0$) are denoted as ‘quartz’. Theoretical maxima obtained assuming the lossless graphene are denoted as ‘maximal’ (for the chosen length of the E -plane inserts). (b) Insertion loss: mean value, maximum and minimum, for the graphene chemical potential varied in the range from 0.2 to 1.0 eV. Frequency points are determined by the $f_{\text{rez}}^{\text{M}}$ for the considered waveguide section.

the order of 3 dB for the considered case. Lower mobility graphene sheets have the same dependence of the graphene surface inductance on the chemical potential; therefore, the tunability range remains the same, regardless of the carrier relaxation time. Insertion loss, on the other hand, increases, which suggests that the low quality graphene is not appropriate for the considered resonator type. This has been illustrated by the results shown in figure 4, corresponding to several values of the carrier relaxation time, τ , and the WR-2.2 waveguide section with $l_{\text{rez}} = l_{\text{T}} = 210 \mu\text{m}$. A slightly broader tunability range with the increase in dielectric slab thickness, as seen from figure 3, does not compensate for the deteriorated quality factor and the larger frequency mismatch between the reflected and the transmitted wave; therefore, it should remain thin. With the above considerations in mind, we proceed with analyses of a total of eight waveguides chosen from table 1.

3. Results and discussion

We analyze the graphene-based waveguide resonators corresponding to the WR-6, WR-4, WR-3, WR-2.8, WR-2.2, WR-1.5, WR-1.2, and WR-1.0 waveguide sections listed in table 1. It is of interest to confirm the validity of the proposed concept throughout the frequency range from 100 to 1100 GHz, and to check for the expected frequency dependence of the obtained tunability and loss. For each of the eight considered waveguides, resonator length is chosen so that the all-metal

resonant frequency, $f_{\text{rez}}^{\text{M}}$, falls into the upper portion of the useful frequency range. Under the influence of the graphene surface impedance, the resonant frequency is shifted toward the lower end of the frequency range. To make different waveguide resonators comparable, the E -plane insert length is kept at a multiple of the waveguide broad wall a , in all analyzed cases. For the graphene-on-quartz resonators, where the complete length of an insert is covered by graphene, $l_{\text{T}} = 0.324a$ was considered. Similarly, in all simulations, the quartz thickness is a multiple of the waveguide broad wall, $d = a/16$. The results are summarized in table 2 and figure 5. The same eight values of the graphene chemical potential used in figure 3 were also utilized for the S -parameter calculation for each of the waveguide sections analyzed and presented in figure 5.

Results shown in figure 5 reveal the increase of the tunability range with frequency, with the obtained tunability percentage above 12% at higher frequencies, for the given insert length of $l_{\text{T}} = 0.324a$. Resonant frequencies for the all-metal resonators, for the two values of graphene chemical potential corresponding to the limits of the considered tunability range, as well as the resonant frequency for $\mu_c = 0.4 \text{ eV}$, located close to the center of the tunability range, are listed in table 2. As can be seen in figure 5, insertion loss decreases with frequency, which, along with the increase of tunability, makes the concept of graphene-based waveguide resonators appealing for the considered frequency range. However, as can be observed from figure 3(b), and this is similar for all

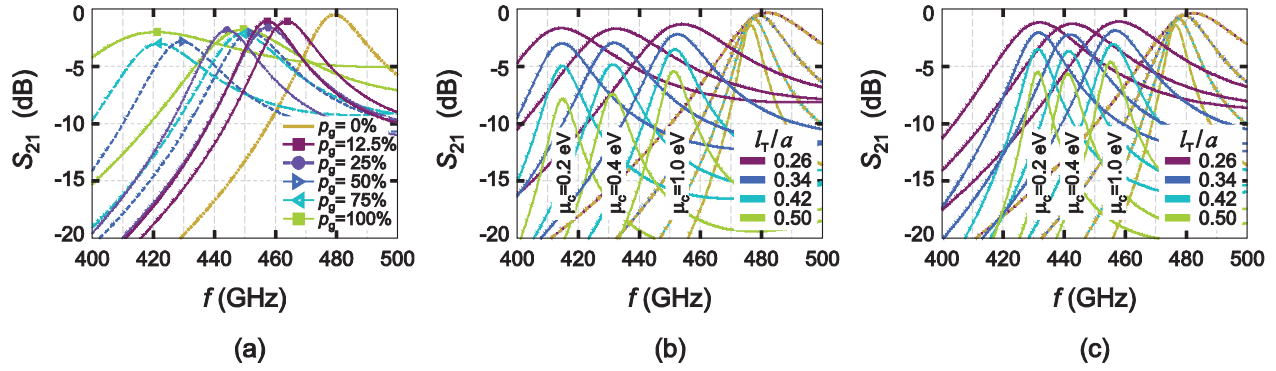


Figure 6. Graphene–metal combined waveguide resonators (WR-2.2 section). Graphene stripes are located along the inner edges of the *E*-plane inserts. (a) Effect of varying graphene stripe widths on tunability, insertion loss and quality factor of a resonator. A graphene percentage larger than 50% of an insert does not notably improve tunability; however, it worsens the quality factor. (b) Effect of the *E*-plane insert length on quality factor and losses in graphene for the fixed width of the graphene stripe, $l_G = 80 \mu\text{m}$. (c) Effect of the *E*-plane insert length on the quality factor and insertion loss for the fixed width $l_G = 50 \mu\text{m}$. Curves corresponding to the all-metal resonators are given by the golden dash–dot–dot lines ($f_{\text{rez}}^{\text{M}} \cong 480 \text{ GHz}$). (a) $l_T = 0.324a$, (b) $l_G = 80 \mu\text{m}$, (c) $l_G = 50 \mu\text{m}$.

Table 3. Dependence of resonator properties on the width of graphene stripes (fixed total inserts length)^a.

$p_g = \frac{l_G}{l_T} (\%)$	$\Delta f_{\text{rez}} (\text{GHz})^b$	$T_p = \frac{\Delta f_{\text{rez}}}{f_{\text{rez}}^{\text{M}}} (\%)$	IL ^{0.4eV} (dB)	IL ^{1.0eV} (dB)	$Q_L^{0.4\text{eV}}$	$Q_L^{1.0\text{eV}}$
100.0	28.25	5.89	2.03	1.82	4.92	11.75
75.0	27.50	5.74	3.03	2.18	13.50	17.12
50.0	22.50	4.69	2.84	2.09	17.71	19.44
25.0	13.50	2.82	1.87	1.62	22.21	22.06
12.5	6.25	1.30	1.05	1.08	24.73	23.48

^a Data is obtained for the standard WR-2.2 waveguide section, with $l_{\text{rez}} = 210.0 \mu\text{m}$ and $l_T = 181.2 \mu\text{m}$.

^b Chemical potential of graphene, μ_c , has been varied in the range (0.4–1.0) eV.

considered frequencies, the loaded quality factor declines significantly for the lower values of the graphene chemical potential. The loaded quality factor is calculated as $Q_L = f_{\text{rez}} / \text{BW}_{3\text{dB}}$, with $\text{BW}_{3\text{dB}}$ denoting the 3 dB bandwidth of the S_{21} parameter. The graphene-on-quartz resonators are, in any case, characterized by the notably lower loaded quality factors than their pure metallic counterparts, and this is particularly pronounced for the lower chemical potential and larger impedances. Increase in the graphene surface impedance produces effects similar to the effects of varying the effective resonator length by changing the distance, l_{rez} , between the *E*-plane inserts. The same holds for the total length of the *E*-plane insert which appears effectively shorter and leads to the decline in the resonator quality factor. We address this issue by introducing the graphene–metal combined waveguide resonators. The graphene stripes are now located along the inner edges of the *E*-plane inserts, at the l_{rez} side, whereas the remaining parts of the inserts are covered by the Cu or Au thin film. Such a configuration is expected to have less influence on the resonator quality factor; however, the decrease in tunability is also expected and has to be investigated.

The concept of the graphene–metal combined waveguide resonators is presented in figure 6, using the WR-2.2 waveguide section with the resonator length $l_{\text{rez}} = 210 \mu\text{m}$. The ratio l_T/a is varied as denoted in the figures. The S_{21} -parameter curves for the purely metallic resonators of the same sizes are denoted using the dash–dot–dot lines, with the resonant frequencies at about 480 GHz. In figure 6(a) we investigate the

effect on the resonator parameters of the width of the graphene stripe, expressed as the percentage graphene with respect to the *E*-plane insert length. To keep the graph less complicated, for each of the five compared graphene stripe widths, we only show the S_{21} -parameter for $\mu_c = 0.4 \text{ eV}$ and $\mu_c = 1.0 \text{ eV}$. Each pair of lines corresponding to the same percent of graphene, p_g , is presented in distinctive color (shade of gray) in different line style. For better legibility, the data shown in figure 6(a) is also summarized in table 3.

As can be concluded from figure 6(a) as well as table 3, a graphene percentage larger than 50% does not further improve the tunability; however, the quality factor decreases and the loss increases. Therefore, less than half of an insert could be covered by graphene. Please note, that the tunability range presented in table 3 differs from the one used throughout the paper due to the use of the (0.4–1.0) eV range for the chemical potential. There already is a significant quality factor deterioration for $\mu_c = 0.4 \text{ eV}$, in comparison with the one for $\mu_c = 1.0 \text{ eV}$, with the increase in the graphene stripe width. This is even more pronounced for $\mu_c \in (0.2–1.0) \text{ eV}$, whereas the tunability is approximately doubled.

As can be inferred from the above observations, the graphene–metal combined waveguide resonators can be carefully designed to meet the specific design requirements. Adjustment of the design parameters starts with the choice of the graphene stripe width, l_G , in accordance with the desired tunability range. This is illustrated by choosing $l_G = 80 \mu\text{m}$ for the figure 6(b) and $l_G = 50 \mu\text{m}$ for the figure 6(c). After

Table 4. Dependence of resonator properties on the total length of an *E*-plane insert^a.

<i>E</i> -plane insert length	Δf_{rez} (GHz) ^b	$T_p = \frac{\Delta f_{\text{rez}}}{f_{\text{rez}}^M}$ (%)	$IL^{0.2\text{eV}}$ (dB)	$IL^{1.0\text{eV}}$ (dB)	$Q_L^{0.2\text{eV}}$	$Q_L^{1.0\text{eV}}$	Q_L^M
Graphene stripe width $l_G = 80 \mu\text{m}$							
$l_T = 0.26a$	39.75	8.29	1.71	1.34	11.68	12.62	15.56
$l_T = 0.34a$	38.00	7.92	3.01	2.22	21.55	21.82	25.91
$l_T = 0.42a$	36.75	7.66	5.01	3.55	34.58	34.75	42.44
$l_T = 0.50a$	36.50	7.61	7.87	5.45	47.43	50.17	70.59
Graphene stripe width $l_G = 50 \mu\text{m}$							
$l_T = 0.26a$	26.00	5.42	1.19	1.12	14.40	13.77	15.56
$l_T = 0.34a$	25.00	5.21	2.09	1.91	26.17	24.04	25.91
$l_T = 0.42a$	24.75	5.16	3.54	3.07	42.10	38.02	42.44
$l_T = 0.50a$	23.75	4.95	5.55	4.64	63.93	55.18	70.59

^a Data is obtained for the standard WR-2.2 waveguide section, with $l_{\text{rez}} = 210.0 \mu\text{m}$ and $a = 2b = 559.0 \mu\text{m}$.

^b Chemical potential of graphene, μ_c , has been varied in the range (0.2–1.0) eV.

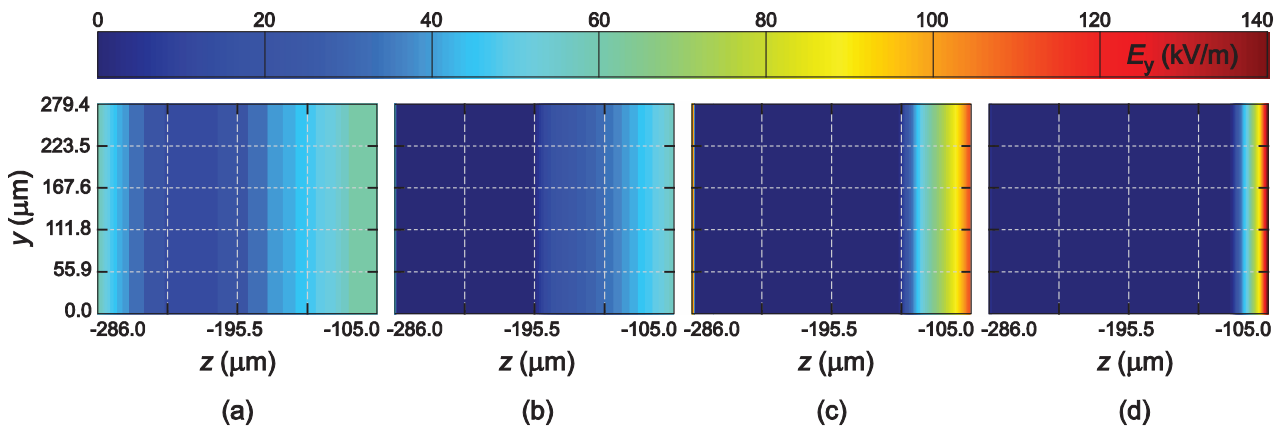


Figure 7. EM field distribution along the *E*-plane insert for various widths of the graphene stripe. Graphene–metal combined waveguide resonators comply with equations (16a) and (16b), along the given percentage of an *E*-plane insert covered by graphene. In the metallic part of an insert, E_y approaches zero. Due to the differences of the structures considered in (a)–(d), and thus the field distributions, the relative impact of the variations in graphene surface impedance is larger for the smaller graphene percentage. (a) $p_g = 100\%$, (b) $p_g = 50\%$, (c) $p_g = 25\%$, (d) $p_g = 12.5\%$.

that, the tunability remains almost the same for different total insert lengths, l_T . Optimizing a trade-off between the quality factor and the loss is the next step, in which the total *E*-plane insert length, l_T , is defined. With the increase of l_T , both the quality factor and the insertion loss increase. Relevant data for these two cases is summarized in table 4. We can conclude from table 4 that the obtained tunability percentages T_p (calculated very strictly, i.e. with respect to f_{rez}^M , which is always well above the device tunable bandwidth), in the considered examples range from around 5% to higher than 8%. Noting that a wide tunability range is hard to obtain in submillimeter applications, and that even better tunability can be achieved using stripe widths wider than $80 \mu\text{m}$, the reported tunability percentages are on the same order of magnitude as those in the state-of-the-art receivers [45], where several receivers are employed to cover a wider submillimeter bandwidth.

Reasons for the higher insertion loss of the graphene–metal combined waveguide resonators, in comparison with the initially analyzed graphene-on-quartz resonators, stem from the different boundary conditions at the *E*-plane inserts. Different boundary conditions mandate different EM field distribution in the vicinity of the inserts, as well as in the graphene stripe.

Along the part of an *E*-plane insert covered by graphene, EM field complies with equations (16a) and (16b), whereas in the metallic part of an insert the field vanishes. For a narrow graphene stripe and a longer metallic part of an insert, a stronger field is generated. Simulation results for different graphene percentages, p_g , are presented in figure 7.

Dependence of the tunability, quality factor, and insertion loss on the graphene percentage, illustrated in figure 6(a), has been studied in detail taking the values from zero to $p_g = 100\%$, with the step of 2.5%, as an input parameter. The results are presented in figure 8. For the relatively narrow graphene stripes, with $p_g \leq 20\%$, the loaded quality factor remains close to the one corresponding to purely metallic inserts, $Q_L^M = 42.44$. At the same time, insertion loss is low and varies only slightly for the considered graphene chemical potential interval from 0.2 to 1.0 eV. Tunability of up to 5% can be achieved. These results agree with the third row describing the $l_G = 50 \mu\text{m}$ case in table 4, where $p_g = 21.3\%$. At about 50% graphene coverage of an insert, 10% tunability can be expected with the still very good quality factor of about 70% of Q_L^M . In this case loss is the highest. According to figure 8,

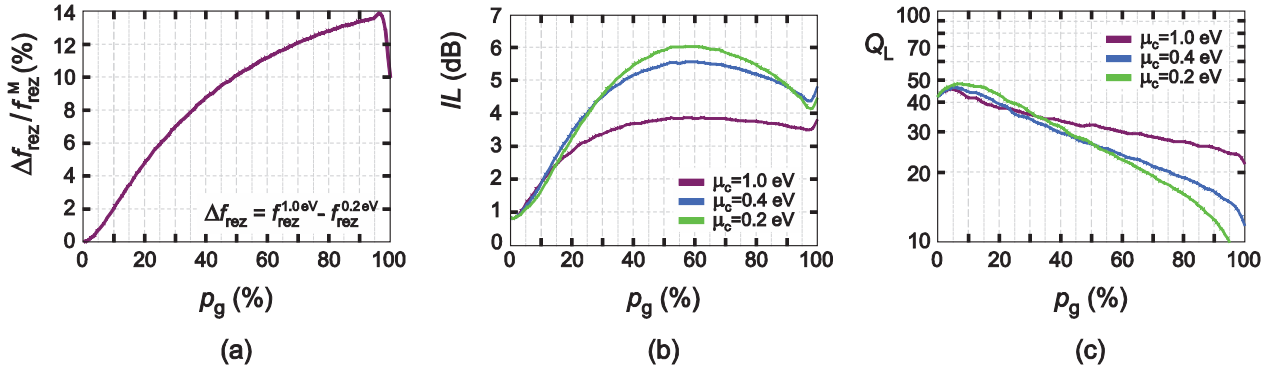


Figure 8. Detailed analysis of the dependence of (a) tunability range, (b) insertion loss, and (c) loaded quality factor, on the width of the graphene stripe expressed as the percentage of the E -plane insert length. WR-2.2 waveguide section with $l_{\text{rez}} = 210 \mu\text{m}$ and $l_T = 0.42a$ has been used for this analysis. Data is presented for the three values of graphene chemical potential, as denoted in the legend. The design of the graphene–metal combined waveguide resonators is subject to the trade-off between the tunability, quality factor, and loss. Optimal width of the graphene stripe is from 15% to about 40% of the E -plane insert length.

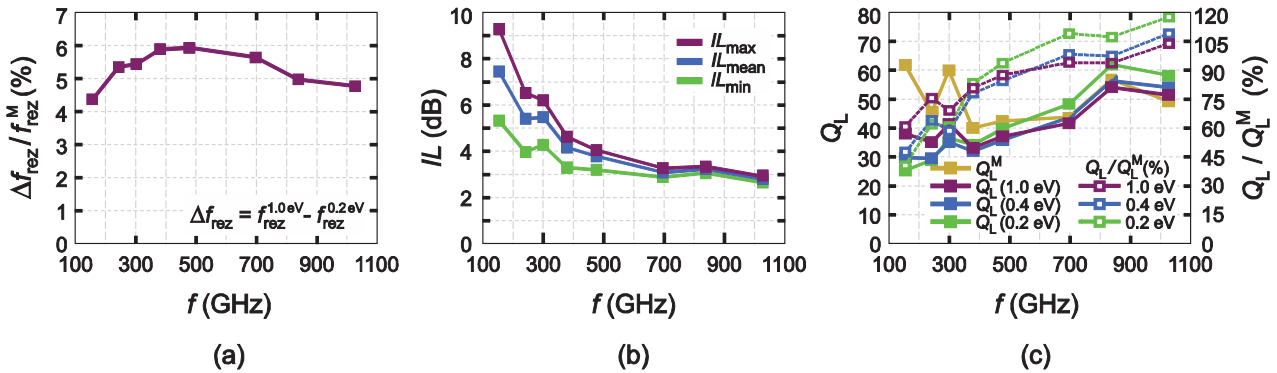


Figure 9. Comparative analysis of the (a) tunability range, (b) insertion loss, and (c) loaded quality factor, for the graphene–metal combined waveguide resonators covering the frequency range from 100 to 1100 GHz. Frequency points correspond to the f_{rez}^M of the considered waveguide section. Reasonable tunability of 5–6% was obtained in all frequency intervals (a). Loss, calculated using the interval from 0.2 to 1.0 eV for μ_c , is somewhat higher than in the graphene-on-quartz case and should be compensated in the design (b). Absolute values of the loaded quality factor, including the pure metallic resonators of the given sizes, are shown in (c) by the filled squares and the solid lines. Quality factors of the combined resonators are shown as the percentage of Q_L^M , using the empty squares and the dashed lines.

Table 5. Graphene–metal combined waveguide resonators: considered dimensions and resonant frequencies.

EIA/Ext. MIL	$l_{\text{rez}} (\mu\text{m})$	$l_T (\mu\text{m})$	$f_{\text{rez}}^M (\text{GHz})$	$f_{\text{rez}}^{0.2 \text{ eV}} (\text{GHz})$	$f_{\text{rez}}^{0.4 \text{ eV}} (\text{GHz})$	$f_{\text{rez}}^{1.0 \text{ eV}} (\text{GHz})$
WR-6	720.0	693.4	154.75	144.50	148.25	151.25
WR-4	420.0	458.7	243.25	222.50	228.75	235.50
WR-3	360.0	362.7	299.75	273.00	280.50	289.25
WR-2.8	260.0	298.7	378.75	340.00	350.00	362.25
WR-2.2	210.0	234.7	477.50	426.00	438.00	454.25
WR-1.5	146.0	160.0	697.50	614.50	629.50	653.75
WR-1.2	132.0	128.0	838.50	742.50	758.00	784.00
WR-1.0	104.0	106.7	1028.25	900.50	917.50	949.50

the optimal width of the graphene stripe is from about 15% to approximately 40%, where the quality factor is high and consistent throughout the achieved tunability range.

Frequency dependence of the key representative parameters of the graphene–metal combined waveguide resonators is given in figure 9. We again analyze the graphene-based waveguide resonators corresponding to the WR-6, WR-4, WR-3, WR-2.8, WR-2.2, WR-1.5, WR-1.2, and WR-1.0 waveguides. Resonator length has been kept the same as in the previous analyses; it is listed in table 5, along with

the chosen insert length, $l_T = 0.42a$. Quartz thickness is $d = a/16$, whereas the graphene stripe width is kept at 25% of an E -plane insert length in all the analyses. Resonant frequencies are listed in table 5, whereas the other results are shown in figure 9. There is a significant decrease of the insertion loss with frequency in the investigated frequency range. Quality factors at higher frequencies are excellent, represented in comparison with the Q_L^M . Tunability range in between 5% and 6% is obtained with the graphene–metal combined waveguide resonators, supporting the proposed concept as one of

the possible solutions for the millimeter and submillimeter wave applications.

4. Conclusion

A novel concept of tunable waveguide resonators for submillimeter wave applications has been studied in detail, following our promising preliminary investigation of WR-3 waveguide. Theoretical analysis has been presented, which could be used to develop customized software tools for the design of this type of waveguide resonator. Thorough full-wave numerical simulations covering several waveguide sections and frequencies ranging from 100 to 1100 GHz confirmed the possibility of obtaining 5% tunability with excellently preserved resonator loaded quality factors, as well as larger tunability ranges, where the trade-off with quality factor and insertion loss is carried out. Tunable waveguide resonators are important basic building blocks of tunable filter devices, and the proposed concept is of great significance for the development of the compact and flexible components in the submillimeter wave spectral region.

Acknowledgments

This work was supported by the Serbian Ministry of Education, Science, and Technological Development under grant III-45003 and in part by the EU—Erasmus Mundus Action 2 project EUROWEB.

References

- [1] Zmuidzinas J and Richards P L 2004 Superconducting detectors and mixers for millimeter and submillimeter astrophysics *Proc. IEEE* **92** 1597–616
- [2] Appleby R and Anderton R N 2007 Millimeter-wave and submillimeter-wave imaging for security and surveillance *Proc. IEEE* **95** 1683–90
- [3] Globus T R, Woolard D L, Samuels A C, Gelmont B L, Hesler J, Crowe T W and Bykhovskaia M 2002 Submillimeter-wave Fourier transform spectroscopy of biological macromolecules *J. Appl. Phys.* **91** 6105–13
- [4] García-García J, Marín F, Miles R E, Steenson D P, Chamberlain J M, Fletcher J R and Thorpe J R 2002 Parametric analysis of micromachined reflex klystrons for operation at millimeter and submillimeter wavelengths *J. Appl. Phys.* **92** 6900–4
- [5] Song H-J and Nagatsuma T 2011 Present and future of terahertz communications *IEEE Trans. Terahertz Sci. Technol.* **1** 256–63
- [6] Shang X, Ke M, Wang Y and Lancaster M J 2012 WR-3 band waveguides and filters fabricated using SU8 photoresist micromachining technology *IEEE Trans. Terahertz Sci. Technol.* **2** 629–37
- [7] Chen Z, Zheng Y, Kang X, Lu B and Cui B 2013 WR-2.8 band micromachined rectangular waveguide filter *J. Infrared Millim. Terahertz Waves* **34** 847–55
- [8] Samoska L A 2011 An overview of solid-state integrated circuit amplifiers in the submillimeter-wave and THz regime *IEEE Trans. Terahertz Sci. Technol.* **1** 9–24
- [9] Tamagnone M, Gomez-Diaz J S, Mosig J R and Perruisseau-Carrier J 2012 Reconfigurable terahertz plasmonic antenna concept using a graphene stack *Appl. Phys. Lett.* **101** 214102
- [10] Dragoman M, Muller A A, Dragoman D, Coccetti F and Plana R 2010 Terahertz antenna based on graphene *J. Appl. Phys.* **107** 104313
- [11] Mencarelli D, Bellucci S, Sindona A and Pierantoni L 2015 Spatial dispersion effects upon local excitation of extrinsic plasmons in a graphene micro-disk *J. Phys. D: Appl. Phys.* **48** 465104
- [12] Sensale-Rodriguez B, Yan R, Kelly M M, Fang T, Tahy K, Hwang W S, Jena D, Liu L and Xing H G 2012 Broadband graphene terahertz modulators enabled by intraband transitions *Nat. Commun.* **3** 780
- [13] Li H-J, Wang L-L, Sun B, Huang Z-R and Zhai X 2014 Tunable mid-infrared plasmonic band-pass filter based on a single graphene sheet with cavities *J. Appl. Phys.* **116** 224505
- [14] Otsuji T, Boubanga Tombet S A, Satou A, Fukidome H, Suemitsu M, Sano E, Popov V, Ryzhii M and Ryzhii V 2012 Graphene-based devices in terahertz science and technology *J. Phys. D: Appl. Phys.* **45** 303001
- [15] Carrasco E, Tamagnone M and Perruisseau-Carrier J 2013 Tunable graphene reflective cells for THz reflectarrays and generalized law of reflection *Appl. Phys. Lett.* **102** 104103
- [16] Gomez-Diaz J S, Perruisseau-Carrier J, Sharma P and Ionescu A 2012 Non-contact characterization of graphene surface impedance at micro and millimeter waves *J. Appl. Phys.* **111** 114908
- [17] Hanson G W 2008 Dyadic Green's functions and guided surface waves for a surface conductivity model of graphene *J. Appl. Phys.* **103** 064302
- [18] Ilić A Ž and Budimir D 2014 Electromagnetic analysis of graphene based tunable waveguide resonators *Microw. Opt. Technol. Lett.* **56** 2385–8
- [19] Ridler N M and Ginley R A 2011 IEEE P1785: a new standard for waveguide above 110 GHz *Microw. J.* **54** S20–4
- [20] Hesler J L, Kerr A R, Grammer W and Wollack E 2007 *Proc. 18th Int. Symp. on Space Terahertz Technology (Pasadena, CA, 21–23 March 2007)* ed A Karpov (Pasadena: Caltech) pp 100–3
- [21] Postoyalko V and Budimir D S 1994 Design of waveguide E-plane filters with all-metal inserts by equal ripple optimization *IEEE Trans. Microw. Theory Tech.* **42** 217–22
- [22] Kolundzija B and Djordjevic A 2002 *Electromagnetic Modeling of Composite Metallic and Dielectric Structures* (Norwood, MA: Artech House) (WIPL-D 2013 WIPL-D Pro v11.0 Available: <http://wipl-d.com/>)
- [23] ANSYS HFSS Available: <http://ansys.com>
- [24] Collin R E 1991 *Field Theory of Guided Waves* (Piscataway, NJ: IEEE)
- [25] Konishi Y and Uenakada K 1974 The design of a bandpass filter with inductive strip—planar circuit mounted in waveguide *IEEE Trans. Microw. Theory Tech.* **22** 869–73
- [26] Arndt F, Bornemann J, Grauerholz D and Vahldieck R 1982 Theory and design of low-insertion loss fin-line filters *IEEE Trans. Microw. Theory Tech.* **30** 155–63
- [27] Lovat G 2012 Equivalent circuit for electromagnetic interaction and transmission through graphene sheets *IEEE Trans. Electromagn. Compat.* **54** 101–9
- [28] Svintsov D, Vyurkov V, Orlikovsky A, Ryzhii V and Otsuji T 2014 All-graphene field-effect transistor based on lateral tunnelling *J. Phys. D: Appl. Phys.* **47** 094002
- [29] Gomez-Diaz J S, Moldovan C, Capdevila S, Romeu J, Bernard L S, Magrez A, Ionescu A M and Perruisseau-Carrier J 2015 Self-biased reconfigurable graphene stacks for terahertz plasmonics *Nat. Commun.* **6** 6334
- [30] Liu M, Yin X and Zhang X 2012 Double-layer graphene optical modulator *Nano Lett.* **12** 1482–5

- [31] Reina A, Jia X, Ho J, Nezich D, Son H, Bulovic V, Dresselhaus M S and Kong J 2009 Large area, few-layer graphene films on arbitrary substrates by chemical vapor deposition *Nano Lett.* **9** 30–5
- [32] Wei D, Mitchell J I, Tansarawiput C, Nam W, Qi M, Ye P D and Xu X 2013 Laser direct synthesis of graphene on quartz *Carbon* **53** 374–9
- [33] Vianco P T, Sifford C H and Romero J A 1997 Resistivity and adhesive strength of thin film metallizations on single crystal quartz *IEEE Trans. Ultrason. Ferroelectr. Freq. Control* **44** 237–49
- [34] Lee S M and Krim J 2005 Scanning tunneling microscopy characterization of the surface morphology of copper films grown on mica and quartz *Thin Solid Films* **489** 325–9
- [35] Neugebauer P, Orlita M, Faugeras C, Barra A-L and Potemski M 2009 How perfect can graphene be? *Phys. Rev. Lett.* **103** 136403
- [36] Jablan M, Buljan H and Soljačić M 2009 Plasmonics in graphene at infra-red frequencies *Phys. Rev. B* **80** 245435
- [37] Bolotin K I, Sikes K J, Jiang Z, Klima M, Fudenberg G, Hone J, Kim P and Stormer H L 2008 Ultrahigh electron mobility in suspended graphene *Solid State Commun.* **146** 351–5
- [38] Bolotin K I, Sikes K J, Hone J, Stormer H L and Kim P 2008 Temperature-dependent transport in suspended graphene *Phys. Rev. Lett.* **101** 096802
- [39] Hirai H, Tsuchiya H, Kamakura Y, Mori N and Ogawa M 2014 Electron mobility calculation for graphene on substrates *J. Appl. Phys.* **116** 083703
- [40] Mayorov A S *et al* 2011 Micrometer-scale ballistic transport in encapsulated graphene at room temperature *Nano Lett.* **11** 2396–9
- [41] Varchon F, Feng R, Hass J, Li X, Ngoc Nguyen B, Naud C, Mallet P, Veuillen J-Y, Berger C, Conrad E H and Magaud L 2007 Electronic structure of epitaxial graphene layers on SiC: effect of the substrate *Phys. Rev. Lett.* **99** 126805
- [42] Orlita M *et al* 2008 Approaching the dirac point in high-mobility multilayer epitaxial graphene *Phys. Rev. Lett.* **101** 267601
- [43] Forti S and Starke U 2014 Epitaxial graphene on SiC: from carrier density engineering to quasi-free standing graphene by atomic intercalation *J. Phys. D: Appl. Phys.* **47** 094013
- [44] Ryzhii V, Dubinov A A, Otsuji T, Mitin V and Shur M S 2010 Terahertz lasers based on optically pumped multiple graphene structures with slot-line and dielectric waveguides *J. Appl. Phys.* **107** 054505
- [45] de Graauw Th *et al* 2010 The Herschel-heterodyne instrument for the far-infrared (HIFI) *Astron. Astrophys.* **518** L6

RESEARCH ARTICLE

Subchronic exposure to static magnetic field differently affects zinc and copper content in murine organs

Silvio R. De Luka^{a*}, Andjelija Ž. Ilić^{b*}, Saša Janković^c, Drago M. Djordjević^a, Saša Ćirković^b, Ivan D. Milovanovich^a, Srdjan Stefanović^c, Slavica Vesković-Moračanin^c, Jasna L. Ristić-Djurović^b and Alexander M. Trbovich^a

^aDepartment of Pathological Physiology, School of Medicine, University of Belgrade, Belgrade, Serbia; ^bInstitute of Physics, University of Belgrade, Zemun-Belgrade, Serbia; ^cInstitute of Meat Hygiene and Technology, Belgrade, Serbia

ABSTRACT

Purpose Static magnetic fields (SMF) have been widely used in research, medicine and industry. Since zinc and copper play an important role in biological systems, we studied the effects of the subchronic continuous SMF exposure on their distribution in murine tissues.

Materials and methods For 30 days, mice were exposed to inhomogeneous, vertical, downward or upward oriented SMF of 1 mT averaged intensity with spatial gradient in vertical direction.

Results SMF decreased the amount of copper and zinc in liver. In brain, zinc levels were increased and copper levels were decreased. In spleen, zinc content was reduced, while copper amount remained unchanged.

Conclusions Subchronic exposure to SMF differently affected copper and zinc content in examined organs, and the changes were more pronounced for the downward oriented field. The outcome could be attributed to the protective, rather than the harmful effect of SMF.

ARTICLE HISTORY

Received 22 June 2015
Accepted 30 October 2015

KEYWORDS

Inhomogeneous SMF of different orientation; zinc; copper; brain; liver; spleen


Introduction

Elements, such as zinc (Zn) and copper (Cu), play important roles in biological processes. An essential micronutrient to nutritionists, zinc represents a constituent of enzymes and other proteins to biochemists, whereas to environmentalists and marine biologists, free zinc in water is regarded a toxic pollutant (Frederickson et al. 2005, Witeska and Kosciuk 2013). Zinc deficiency is associated with anorexia and alterations of the epidermal, gastrointestinal, central nervous, immune, skeletal and reproductive systems (Tapiero and Tew 2003). Zinc is crucial for normal development and function of cells mediating innate immunity, neutrophils and natural killer (NK) cells. It induces the production of metallothionein, an excellent scavenger of hydroxyl radical (OH[•]) (Prasad 2008), and may also play a relevant part in the control of both cell proliferation and mitosis (Wolford et al. 2010). It is a component of many transcription factors and proteins that control the cell cycle and can inhibit apoptosis (Chasapis et al. 2012).

Copper is a redox-active essential trace element that is predominantly used by organisms living in oxygen-rich environments and in such environments it fluctuates between the oxidized Cu²⁺ and reduced Cu¹⁺ states (Turski and Thiele 2009). Copper is required for functioning of over 30 proteins, including superoxide dismutase, ceruloplasmin, lysyl oxidase, cytochrome-c-oxidase, tyrosinase and dopamine-β-hydroxylase

(Rana 2008). Cu ions participate in DNA synthesis and cell proliferation. Central nervous system (CNS) development and function is particularly dependent on copper metabolism and homeostasis. In excess of cellular needs, it can lead to the generation of reactive oxygen species (ROS) or to the displacement of other metal cofactors from their natural ligands.

All living organisms are continually exposed to the Earth's magnetic field (geomagnetic field, GMF) ranging from 0.02–0.07 mT, although environmental fields from 0.01–0.1 mT can be recorded, depending on the geographic location and presence of magnetic materials in the vicinity (Repacholi and Greenebaum 1999). In recent years static magnetic fields (SMF) have been widely used in research, medicine and industry (Yamaguchi-Sekino et al. 2011, László et al. 2012, Mészáros et al. 2013, Lahbib et al. 2014). Moderate intensity SMF, between 1 mT and 1 T, can produce considerable effects on biological systems (Rosen 2003), yet for a large part of this intensity range research data is insufficient. We focus here on the average SMF intensity of about 1 mT for two reasons. Firstly, there is scarce data on the biological effects of moderate SMF at the lower end of the intensity range. It is known from previous in vitro experiments that the low-field effect (LFE) threshold falls into this intensity range, with its exact value dependent upon a number of factors (Brocklehurst

CONTACT Prof. Alexander M. Trbovich  aleksandar.trbovic@mfub.bg.ac.rs, alexander.m.trbovich@gmail.com  Department of Pathological Physiology, School of Medicine, University of Belgrade, Dr Subotića 9, 11000 Belgrade, Serbia

*These authors made equal contributions to the paper and, thus, share first authorship.

and McLauchlan 1996, Maeda et al. 2012). At field values below the LFE threshold, including the GMF, SMF affects biochemical reactions by increasing the proportion of free radicals surviving longer and diffusing into the surroundings, whereas exactly the opposite happens for SMF values above the threshold. Secondly, SMF of 1 mT has been shown to cause interference with cardiac pacemakers and implantable cardioverter-defibrillators at a distance of up to 24 cm (Ryf et al. 2008), raising a question about other possible effects on biological processes having lower interaction thresholds. Inhomogeneous SMF has been employed in this study, motivated by the recent investigations suggesting possible significance of local SMF gradients, in addition to the SMF intensity, in the effects produced on biological systems (László et al. 2007, Djordjevich et al. 2012, Vergallo et al. 2013). With our exposure set-up, lateral SMF gradients are almost negligible and the vertical SMF gradient is dominant. Field intensity decreases nearly as a linear function of height above the set-up. Also, gradient SMF can more truthfully than a homogeneous SMF mimic real life exposures of organisms to electromagnetic devices and SMF sources.

The effects of inhomogeneous, vertically decreasing, SMF on Zn and Cu distribution in different mouse tissues (brain, liver and spleen) have been investigated. The incentive for this particular choice of tissues has been the presence of trace elements in these tissues. Copper is most abundant in brain and liver, while zinc is most abundant in liver (Allen et al. 2006). Additionally, in respect to zinc, we decided to choose brain over kidney because of enormous importance of zinc for brain function. Spleen has been selected, since the SMF effect on spleen was obtained in previous studies (Hashish et al. 2008, Djordjevich et al. 2012).

Theoretical background

Direct mechanisms of action of SMF on the living systems include the magnetic forces and torques, motion-induced currents in tissues, presence of ferrimagnetic particles in an organism, SMF acting on a flux of ions across the cell membrane, diamagnetic anisotropy of organic molecules, magnetohydrodynamic forces and pressures, and SMF affecting the rates and yields of chemical reactions (Schenck 2000, Rosen 2003). Only three of the mechanisms remain plausible when considering the GMF, which also applies to other very weak SMF sources, as explained in detail by Johnsen and Lohmann (2008). These are the ferrimagnetism, electromagnetic induction and SMF effects on chemical reactions through the radical pair mechanism (RPM).

It has long been disputed that the weak SMF, being below the thermodynamic threshold of $k_B T$ associated with the random thermal energy, can exhibit significant effects on biological systems. In statistical mechanics, probability of a state with energy E is proportional to $\exp(-E/k_B T)$, implying that any weak SMF effect cannot be thermodynamic in origin and cannot affect the position of a system equilibrium. Biological systems, however, usually operate on the verge of equilibrium or oscillate about the equilibrium (Brocklehurst and McLauchlan 1996). The fact that the kinetic processes and

chemical reactions in an organism can be influenced by SMF is what matters in this case.

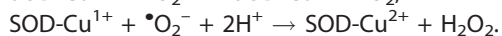
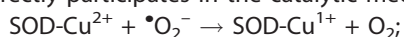
The RPM arises from the existence of spin angular momentum, an intrinsic property of elementary particles. Electrons, protons and neutrons belong to fermions, particles that have half-integer spin. Distribution of fermions over energy states is described by the Fermi-Dirac statistics and as such it obeys the Pauli exclusion principle, stating that no two identical fermions can simultaneously occupy the same quantum state. For an electron in an atom or a molecule, quantum state is determined by its energy, orbital angular momentum, magnetic moment and spin (spin up or spin down). General form of equations, describing the electron spin evolution, would have to take into account all of the degrees of freedom and all of the mutual interactions of the system constituents. Fortunately, the quantum chemists have succeeded in treating the time evolution of the electron spin and spatial coordinates separately, introducing a number of empirical parameters. Numerical models of different complexity are used in calculations, whereas the semi-classical vector model is excellent for the qualitative RPM illustration (Brocklehurst and McLauchlan 1996, Rodgers 2009). Excitation occurring in a complex molecule AB, where A and B are joined by an electron-pair bond, leads to the transfer of an electron into a different quantum state and from A to B, thus forming a spin-correlated radical pair A and B. In the bound state the two electrons have had the opposite spins ($\uparrow\downarrow$), forming a singlet state with total spin equal to zero. If the radical pair (RP) recombines before A and B separate due to diffusion, which is called the geminate cage recombination, the singlet product (SP) is formed. If the RP constituents separate definitely, an escape product (EP) is formed. If the re-encounter occurs at a later time, there is a possibility of the secondary geminate recombination. However, the electron spins that remain antiparallel for a short time after the RP formation, due to the short separation of electrons resulting in a strong exchange interaction between electron spins, soon begin to differ in their precession frequencies and phases of precession as well. Under the influence of molecular hyperfine interactions, the RP undergoes the singlet to triplet ($S \leftrightarrow T$) interconversion, with the secondary recombination possible only from the singlet spin state of the RP. The hyperfine interaction, made up of two contributions – magnetic moment coupling and spin coupling, couples the unpaired electron spin with the internal magnetic field from the spins of magnetic nuclei. A detailed account of kinetics of reactions involving RP, along with the explanations of hyperfine, exchange and Zeeman interactions, has been given by Rodgers (2009).

Spin evolution between singlet and triplet states ($S \leftrightarrow T$ interconversion) is affected by the externally applied magnetic fields, modifying the yields of reaction products SP and EP and consequently leading to the magnetic field effects (MFE). Three triplet spin states, of the total spin equal to one and differing in the total spin projections (+1, 0, or -1), were degenerate in energy at zero magnetic field. In the presence of an external magnetic field, energy levels change by the energy of the magnetic moment of an atom in the field, leading to the spectral line splitting into several components designated as the Zeeman effect. The Zeeman interaction occurs between

the unpaired electron spins on each radical and an external magnetic field; along with the hyperfine interactions it forms the hyperfine mechanism responsible for weak field MFE, up to about 50 mT (Rodgers 2009). In higher fields, the Δg -mechanism dominates, due to the different magnetic moments of the two radicals in RP and thus somewhat different g -tensors of the two radicals linking the field intensity with the produced Zeeman interaction. Due to a typical RP lifetime of 10 ns to 1 μ s, the RPM is expected to act similarly for the SMF and the low-frequency fields up to about 1 MHz (Rodgers 2009).

Much more than the thermal energy $k_B T$ is required for the generation of the RP. It has to be supplied prior to and independently of the RPM action, as a result of photochemical excitation, low-dose radiation exposure, thermolytic bond cleavage, etc. Additionally, RP are intrinsically widely present in biological systems, as reactants or products of usual biochemical reactions. Experimental confirmation of the biological MFE due to the RPM has been obtained for cryptochrome/photolyase protein family (Maeda et al. 2012, Evans et al. 2015). As pointed out by Brocklehurst and McLauchlan (1996), freely diffusing RP tend to be highly reactive and indiscriminating in their reactions and the MFE are expected to be small. Reactions involving single radicals become SMF dependent mostly through the effect of change of radical concentration, eventually leading to the change in the rate of reaction.

With regard to the trace elements, Zn and Cu, investigated here, possible target for the RPM action has to be a chemical reaction involving free radicals. Among their other roles, Zn and Cu are the constituents of Cu/Zn superoxide dismutase (CuZn-SOD), an enzyme that catalyses the metabolism of the superoxide radical ($\text{O}_2^{\cdot-}$) into hydrogen peroxide (H_2O_2) and oxygen (O_2), thus belonging to the ROS scavengers. CuZn-SOD is a metalloprotein, in which the Zn ion contributes to the structural stability (Roberts et al. 2007), whereas the Cu^{2+} ion directly participates in the catalytic mechanism of CuZn-SOD:



As the CuZn-SOD binds the superoxide byproducts of metabolism to produce H_2O_2 , that has to be further catalyzed into water and oxygen, both the diminished or highly increased activity of CuZn-SOD can be harmful to an organism. It is the balance of CuZn-SOD, as well as the balance between Cu and Zn, that is the prerequisite for the first step of antioxidant defense in nearly all living cells exposed to oxygen. In the excess of Cu^{2+} , copper-initiated reaction between H_2O_2 and CuZn-SOD results in the formation of OH^{\cdot} (Sato et al. 1992, Ramirez et al. 2009). The aforementioned $\text{O}_2^{\cdot-}$, H_2O_2 , and OH^{\cdot} are the biologically most relevant ROS, an unavoidable consequence of aerobic metabolism, also involved in cell signaling mechanisms and immune response (Dröge 2002, Sies 2014). Often the case with metalloprotein cofactors, both Cu and Zn belong to the transition metals, their atomic numbers being 29 and 30, and abbreviated electron configurations $[\text{Ar}]4s^13d^{10}$ and $[\text{Ar}]4s^23d^{10}$, respectively. Therefore, Cu, which due to its easy interconversion between Cu^{2+} and Cu^{1+} (Cu(II) and Cu(I)) plays a major catalytic role, has an unpaired electron spin both in its atomic state and as a Cu^{2+} ion. Moreover, Cu^{2+} ion is paramagnetic due to its $[\text{Ar}]3d^9$ electron configuration.

Taken all into account, cyclic redox reactions involving the superoxide dismutase could be sensitive to the externally applied SMF. This is suggested by the recent investigations of the SMF effect on ROS scavenger enzymes (Amara et al. 2006, 2009), albeit with the much stronger SMF of 128 mT. It is of interest to investigate possible MFE on these enzymes at different field strengths in the weak to moderate SMF range.

Materials and methods

Experimental animals

Male Swiss-Webster 6-month-old mice, obtained from the Military Medical Academy Animal Research Facility (Belgrade, Serbia), were maintained on a nutritionally and energetically adequate diet (21% protein, 62% carbohydrate, 5% fat, 0.25% vitamin premix, 2.25% mineral mixture; Veterinarski zavod, Subotica, Serbia) for 30 days. The animals were housed in cages with five animals per cage in a temperature-controlled room ($19 \pm 1^\circ\text{C}$) with a 12 h light-dark cycle. All animals were matched for initial body weight and were weighed at weekly intervals.

All experimental protocols involving animals were reviewed and approved by the University of Belgrade, Faculty of Medicine Experimental Animals Ethics Committee. Furthermore, all experiments were conducted in accordance with the procedures described in the National Institutes of Health Guide for Care and Use of Laboratory Animals (Washington, DC, USA), as well as the US-NIH guidelines for the conduction of magnetic field experiments on animals.

Static magnetic field

Experimental SMF was produced by the specialized medical device patented under the name MADU stripe (Mandić 1999). Primarily intended for use in physical therapy and rehabilitation, MADU stripes consist of small permanent magnets embedded into an elastic rubber stripe or sheet. We use the type L MADU stripe, which resembles a sheet due to the five rows of ferromagnetic rods ($\text{BaFe}_{12}\text{O}_{19}$), four rods per each row, with the magnetic axes of the rods all in the same direction perpendicular to the stripe. Accordingly with the dimensions of the cages, three MADU stripes type L were placed under each cage, as shown in Figure 1, to ensure optimal SMF coverage.

Detailed analysis of the general case of two-dimensional magnetic arrays is published (Ilić et al. 2013). That work describes in great detail the SMF produced by the type L MADU stripe, utilized here as an exposure setup. Analytical expressions and particularities of the finite element calculations, along with the SMF measurements, are presented. The SMF calibration procedure utilizes field values measured on a 9×9.75 mm grid, at eight heights above the MADU stripe, to determine the SMF scaling factor proportional to the remanent magnetization of ferromagnetic rods.

Were the magnetic axes of the neighboring rods oriented in the opposite directions, SMF would be predominantly parallel to the sheet's surface and confined to a thin layer above it. The same direction of all magnetic axes, on the contrary, produces SMF perpendicular to the MADU sheet's surface, much

stronger and extending several centimeters from the surface. As shown in Figure 1, using the two vertical cross sections of the cage, SMF decrease with height is dominant in comparison with its variation in the horizontal planes due to the discrete positions of individual magnets. Right on top of each individual magnet, at height $z = 0$ m, maximal magnetic flux density is 98 mT. Figure 2 shows the magnetic flux density in four planes parallel to the MADU surface at the heights 5, 10, 20 and 30 mm.

Given the relatively dense placement of the stripe's magnetic rods in respect to the size of the animals, as well as that the mice were freely moving, magnetic field and its vertical gradient were averaged in horizontal planes first. Further averaging is performed over the volume between the horizontal planes $z = 20$ mm and $z = 50$ mm, resulting in mean magnetic flux density and its mean gradient of 1.23 mT and 0.02 T/m, respectively. Field decrease is almost linear from $z = 20$ mm to $z = 50$ mm. The summary of the relevant SMF parameters, required for the complete SMF description (Colbert et al. 2009), is given in Table 1.

Experimental design

The effects of the subchronic continuous exposure to SMF were studied for both the upward oriented and the downward oriented SMF. The experiment was performed on the Earth's Northern hemisphere; therefore, the vertical GMF component was directed downwards and our SMF had the same or opposite direction in respect to the GMF. Mice were randomly divided into three groups (control and two experimental groups), each containing 10 animals. Since the magnets embedded in the MADU stripes cannot be removed or turned off, instead of sham exposure, the first experimental group, which served as a control, was exposed to the measured ambient magnetic field of 40 μ T intensity. The second experimental group was exposed to the upward oriented SMF (Up group), and the third experimental group was exposed to the downward oriented SMF (Down group). Note that the magnetic field above MADU stripes was measured. It is the sum of the MADU stripe SMF and the ambient magnetic field, the latter comprising only 3.25% of the total exposure field.

Except for the SMF, all three groups of experimental animals were kept under the same conditions. The animal Plexiglas cages were separated out by 10 cm, which was enough to avoid magnetic interference. Three MADU stripes of appropriate orientation, generating either upward or downward oriented SMF, were placed under the cages of the Up and Down groups for the entire duration of the experiment, i.e., continuously for 30 days. Food consumption was measured daily and body mass weekly. In the animal facilities, where animals were kept, all cages were marked with a code. A person in charge of feeding and wellbeing of animals was the only person aware of presence of magnets below some cages, but she did not know the code. At the end of the exposure, mice were transferred to the laboratory where tissues were collected for analyses that were performed blindly. Tissues were put in samples that were coded and analyzed by researchers who were not cognizant of group sample origin.

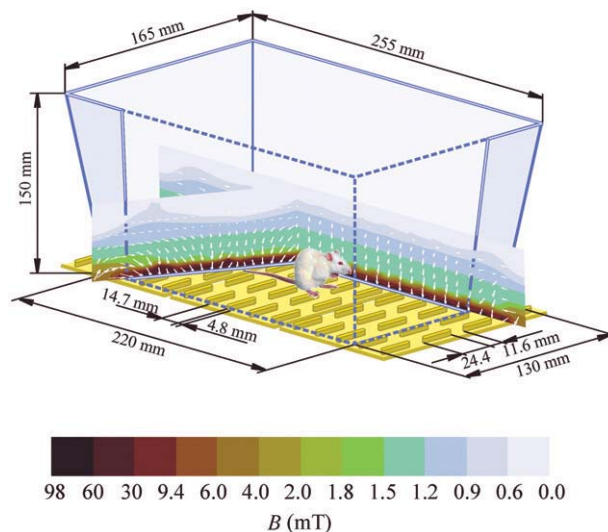


Figure 1. Experimental animal in cage with MADU stripes below. Static but spatially dependent magnetic field acts on animals moving freely within the experimental volume. The SMF distribution in vertical planes is shown for the two vertical cross sections of the cage. The first one coincides with the middle of the space between the two rows of ferromagnetic rods, while the second cross section is given at an angle of 60° in respect to the first one. The SMF intensity, indicated by different colors (shades of gray), varies much more with height than in the horizontal planes. The magnetic lines of force are almost vertical everywhere except at the edges of the stripes and the magnetic field can be characterized as vertically declining (Ilić et al. 2013).

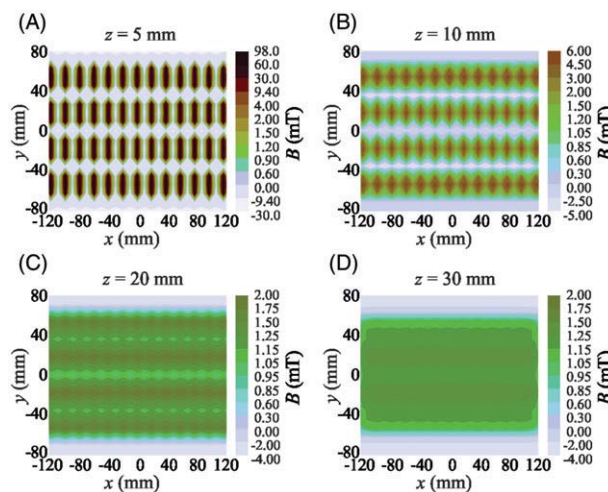


Figure 2. SMF variation in horizontal planes above the MADU type L stripes. Matrix arrangement of individual magnets produces the slowly decreasing SMF. Panels A, B, C, and D, show field variation in the planes parallel to the MADU surface. Detailed magnetic field description as well as more data is given by Ilić et al. (2013).

Table 1. Ten SMF dosage parameters (Colbert et al. 2009).

Magnet materials	Barium hexaferrite, $\text{BaFe}_{12}\text{O}_{19}$
Magnet dimensions	$W \times L \times H = 4.8 \times 24.4 \times 4.8 \text{ mm}^3$
Pole configuration	Same magnetic axes direction
Measured field strength	1–2 mT (magnet axis)
Frequency of application	Continuous application
Duration of application	30 days
Site of application	Whole body exposure
Magnet support device	Elastic rubber stripe
Target tissue	Brain, liver, spleen
Distance from the magnet surface	20–50 mm

Determination of copper and zinc

In order to determine the content of Zn and Cu in brain, liver, and spleen of the experimental animals, samples were microwave digested (ETHOS TC, Milestone S.r.l., Sorisole, Italy) according to manufacturer's recommendations. Tissue of interest (0.5 g) was treated with 8 ml of nitric acid (HNO₃) and 2 ml of hydrogen peroxide (30% H₂O₂); temperature program was as follows: 5 min from room temperature (20 °C) to 180 °C, then 10 min hold at 180 °C. After cooling, samples were transferred with deionized water in 50 ml volumetric flask. Analyses were carried out on atomic absorption spectrometer 'SpectrAA 220' (Varian, Palo Alto, CA, USA) according to Varian Atomic Absorption Spectrometers (AAS) Analytical Methods. Analytical quality control was achieved by analyzing certified reference material BCR-186 (Community Bureau of Reference – BCR, Brussels, Belgium), which is lyophilized pig kidney for determining trace elements (Institute for Reference Materials and Measurements, Geel, Belgium). Replicate analyses were undertaken within the range of certified values. Zinc and copper values were expressed as µg of Zn/Cu per mg of dried analyzed tissue.

Statistical analysis

Findings reported at this time correspond to a single subchronic continuous SMF exposure experiment. Each of the three experimental groups consisted of the same number of 10 animals per group. Except for the exposure SMF, experimental conditions were identical for all three groups. Simultaneous exposure was carried out while in the same facilities, and the subsequent analyses were performed blindly. Data is presented, in Figures 3 and 4, as mean ± SEM. Statistical analysis was performed using the SPSS Statistics software for Windows, version 16.0 (SPSS, Chicago, IL). Differences among groups were evaluated by the one-way ANOVA, followed by the Fischer's LSD test. The level of significance was set at $p < 0.05$.

Results

Experimental animals were, on average, exposed to 1 mT SMF, continuously, for the period of 30 days. Compared to the control group (13.36 ± 0.14 µg/mg), the animals in the Up group (14.46 ± 0.42 µg/mg) had statistically higher levels of Zn in brain tissue. The Zn increase in brain was even more pronounced in the Down group (15.00 ± 0.20 µg/mg). Brain Zn values in experimental groups are shown in Figure 3.

As for brain copper, the SMF produced significant decrease in both Up (3.66 ± 0.09 µg/mg) and Down (3.08 ± 0.09 µg/mg) groups, compared to the control group (4.25 ± 0.08 µg/mg). Even more, the level of Cu in the Down group was significantly decreased compared to the Up group. The brain Cu values for the three experimental groups are shown in Figure 4.

Zinc content in liver (Figure 3), as well as liver copper (Figure 4), decreased significantly following the exposure to 1 mT SMF. Specifically, zinc in the Up (46.07 ± 0.61 µg/mg) and Down (46.82 ± 0.75 µg/mg) groups experienced a drop of about 20% when compared to the control group

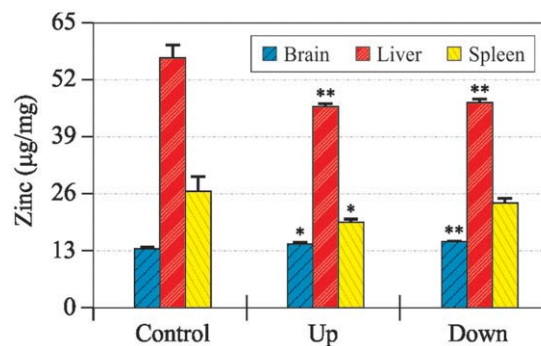


Figure 3. Zinc content in murine organs after exposure to SMF of different (Up and Down) orientation for 30 days. Data represent the mean ± SEM. * $p < 0.05$ compared to control; ** $p < 0.01$ compared to control.

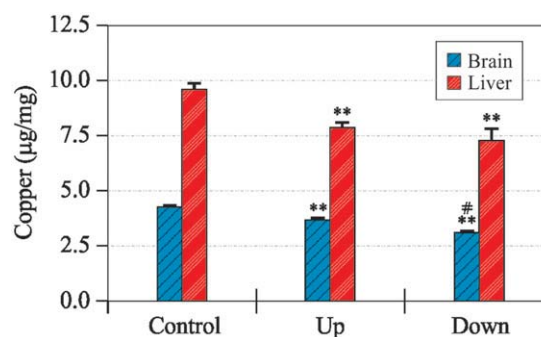


Figure 4. Copper values in murine organs after exposure to SMF of different (Up and Down) orientation for 30 days. Data represent the mean ± SEM. ** $p < 0.01$ compared to control; # $p < 0.01$ compared to Up.

(56.89 ± 3.30 µg/mg). Similarly, the liver Cu in the Up group was 7.88 ± 0.22 µg/mg and in the Down group was 7.33 ± 0.48 µg/mg, whereas for the control group it was 9.59 ± 0.30 µg/mg.

Exposure to the SMF for 30 days produced significant decrease in Zn content in spleen in the Up group (19.40 ± 0.78 µg/mg), while in the Down group (23.70 ± 1.20 µg/mg) decrease was not statistically significant (Figure 3). The control group zinc amounted to 26.48 ± 3.32 µg/mg. The copper levels in spleen were low (1.14 ± 0.81 µg/mg), disallowing for the precise determination of statistical differences between any two of the three groups of animals; therefore this data is not shown.

Discussion

The research data focusing on trace elements distribution after exposure to SMF is scarce (Salem et al. 2005, Miryam et al. 2010, Aida et al. 2014, Zhang et al. 2014). The impact to biological activities of imbalance in these elements, as well as the likelihood of being affected by magnetic fields, motivates further effort in this direction.

Numerous studies (Pourahmad et al. 2001, 2003, Tassabehji et al. 2005, Vanlandingham et al. 2005, Rana 2008, Annabi et al. 2013, Nunes et al. 2014, Waheed et al. 2014) showed toxic effects induced by Cu overload in tissues. Excess copper can, instead of iron, serve as a catalyst in Fenton-like reactions,

resulting in the production of ROS, responsible for lipid peroxidation in membranes, direct oxidation of proteins and cleavage of DNA and ribonucleic (RNA) molecules (Tapiero et al. 2003). A recent study (Singh et al. 2013) showed that in aging mice, accumulation of Cu in brain was associated with increased amyloid beta ($A\beta$) production and neuroinflammation. The pathological production of $\cdot OH$ from H_2O_2 and CuZn-SOD due to excess copper might play a role in Alzheimer's disease as well (Multhaup et al. 1997). Similar mechanism is known to be associated with the familial amyotrophic lateral sclerosis, resulting from CuZn-SOD gene mutations that lead to the zinc deficiency (Roberts et al. 2007).

Large amounts of zinc are normally present in the brain. Ten percent of the total brain zinc is localized to the lumen of glutamate containing synaptic vesicles, that may be released on excitation and may play role in modulation of synaptic signaling (Tapiero and Tew 2003). The dominant effect of zinc in the normal brain is to reduce excitability, thereby functioning as an endogenous anticonvulsant (Frederickson et al. 2005). The converse treatment, which involves intracranial administration of zinc salts, is directly cytolethal and proconvulsive. Since low Zn levels inhibit cell growth as well as division, and increase the possibility of seizures, whereas high Zn levels are toxic, cells must maintain cellular zinc content within a narrow window, which is estimated to be in a low picomolar range. Toxicity develops when the zinc concentration rises to nanomolar levels (Bozym et al. 2010).

Our results showed increased brain concentration of Zn upon exposure to SMF, as well as a decrease in the amount of brain Cu. From the standpoint of atomic physics, different result of the SMF influence on Zn and Cu could be attributed in part to their electron configurations. Zinc is diamagnetic with completely filled 3d orbital and no unpaired electron spins both in its atomic state and as a Zn^{2+} ion which is often a cofactor in complex molecules. In its atomic state, Cu is diamagnetic with completely filled 3d orbital and an unpaired spin in $4s^1$, whereas as a Cu^{2+} ion it becomes paramagnetic with an unpaired electron spin in 3d orbital. Therefore, Cu is much more likely to be directly affected by the externally applied SMF than Zn, whereas Zn can be affected indirectly through the chemical reactions involving Cu and possibly ROS. Moreover, in certain chemical reactions Zn and Cu act together, for example as cofactors in the CuZn-SOD, and any change in one or the other can influence the other one in the opposite way. In some disorders, for example, Zn deficiency and the excess of Cu can reinforce each other leading to the disruption of homeostasis (Dröge 2002, Roberts et al. 2007). It is important to assess whether these effects of 1 mT SMF on Zn and Cu are mostly beneficial, adversarial, or could be both depending on a situation.

Moderate increase in brain Zn could lead to anticonvulsive effect of Zn with preservation of its regulatory function for healthy brain (Serman et al. 1986, Elsas et al. 2009). However, zinc dysregulation is implicated as a contributing factor in two types of neuropathology: Alzheimer's disease and the so-called 'excitotoxicity' that injures neurons. It is widely accepted that free zinc in the extracellular fluid induces amyloid deposition and early-phase clinical trials indicate that zinc chelation inhibits $A\beta$ -plaque deposition (Ritchie et al. 2003). On the other

hand, while Cu and Fe binding to $A\beta$ induce O_2 -dependent H_2O_2 production and toxicity, co-incubation with zinc inhibits H_2O_2 production (Cuajungco and Faget 2003). Therefore, Zn^{2+} loading into plaque may represent an attempt at protective homeostatic response against Alzheimer's disease, where plaques form as the result of a more robust Zn antioxidant response to the underlying oxidative attack. Also, the $A\beta$ in the plaques has been redox-silenced by the high concentrations of zinc, whereas the diffuse and soluble $A\beta$ accumulations within the brain would be a source of H_2O_2 and oxidative damage (Frederickson and Bush 2001). Decreased Cu, as long as its level is sufficient to maintain normal brain functioning of exposed animals, protects the brain from oxidative injury or premature apoptosis. The increase of zinc in our experiment was diminutive, yet statistically significant, which, along with the decrease of copper, suggests probable protective effect against neuroinflammation.

Liver, as well as the brain, is an organ extremely vulnerable to the disturbed Cu metabolism and homeostasis. An observed decrease in liver Cu acts protectively against the ROS production, again if its level is still sufficient. We have also demonstrated the SMF induced decrease of Zn in the liver of exposed animals. A number of cited studies showed deleterious effects of zinc deficiency (Sullivan et al. 1980, Dardenne 2002). However, it was also shown (Phillips et al. 1996) that excess of zinc induced severe progressive cholestasis in children. Since the decrease of zinc concentration in liver of exposed animals was not very large, we can speculate that it did not disturb zinc homeostasis, but rather protected liver from possible damage. Interestingly, previous study of combined subchronic exposure to 128 mT SMF and Zn supplementation showed increased metallothionein synthesis in liver that has been suspected to control metal homeostasis and to maintain cell survival in response to various stimuli such as oxidative stress (Salem et al. 2005). As discussed for the RPM, weak SMF and moderately strong SMF can actually produce the opposite biological effects.

Studies performed on the Zn-deficient mice showed depressed responses to both the T-lymphocyte-dependent and the T-lymphocyte-independent antigens, as well as the decreased NK cell activity (Dardenne 2002). It cannot be stated with certainty if the observed decrease of zinc in the spleen in the Up group is sufficient to produce the above responses.

Conclusion

In our subchronic SMF exposure experiment, brain, liver and spleen were analyzed for Cu and Zn content. Specific changes were observed in the Cu and Zn content in examined organs, which presumably could be attributed to protective, rather than harmful effects of SMF. A decrease of copper in brain and liver, along with the increase of zinc in brain could, probably, represent positive consequences of the SMF exposure. It is worth pointing out that combined effect of decreased copper and increased zinc in brain was more statistically pronounced in the Down group. Potential employment of the SMF exposure against metal overload, instead of the standard chelator therapy, is a promising assumption adding to the importance of the observed results. Further studies with

chronic exposure and different SMF intensities could give better insight in the observed changes.

Acknowledgements

This study was supported by the grants No III-41013, No III-41019 and No III-45003 from the Ministry of Education, Science and Technological Development, Government of Serbia.

Disclosure statement

The authors report no conflict of interest. The authors alone are responsible for the content and writing of the paper.

Funding information

No funding body had any involvement in the preparation or content of this article or in the decision to submit it for publication.

References

- Aida L, Soumaya G, Myriam E, Mohsen S, Hafedh A. 2014. Effects of static magnetic field exposure on plasma element levels in rat. *Biol Trace Elem Res* 160:67–72.
- Allen KJ, Buck NE, Cheah DMY, Gazeas S, Bhathal P, Mercer JFB. 2006. Chronological changes in tissue copper, zinc and iron in the toxic milk mouse and effects of copper loading. *BioMetals* 19:555–564.
- Amara S, Abdelmelek H, Garrel C, Guiraud P, Douki T, Ravanat JL, Favier A, Sakly M, Ben Rhouma K. 2006. Effects of subchronic exposure to static magnetic field on testicular function in rats. *Arch Med Res* 37:947–952.
- Amara S, Douki T, Garel C, Favier A, Sakly M, Rhouma KB, Abdelmelek H. 2009. Effects of static magnetic field exposure on antioxidative enzymes activity and DNA in rat brain. *Gen Physiol Biophys* 28:260–265.
- Annabi A, Said K, Messaoudi I. 2013. Heavy metal levels in gonad and liver tissues – effects on the reproductive parameters of natural populations of *Aphanius fasciatus*. *Environ Sci Poll Res* 20:7309–7319.
- Bozym RA, Chimienti F, Giblin LJ, Gross GW, Korichneva I, Li Y, Libert S, Maret W, Parviz M, Frederickson CJ, Thompson RB. 2010. Free zinc ions outside a narrow concentration range are toxic to a variety of cells in vitro. *Exp Biol Med* 235:741–750.
- Brocklehurst B, McLauchlan KA. 1996. Free radical mechanism for the effects of environmental electromagnetic fields on biological systems. *Int J Radiat Biol* 69:3–24.
- Chasapis CT, Loutsidou AC, Spiliopoulou CA, Stefanidou ME. 2012. Zinc and human health: An update. *Arch Toxicol* 86:521–534.
- Colbert AP, Wahbeh H, Harling N, Connelly E, Schiffke HC, Forsten C, Gregory WL, Markov MS, Souder JJ, Elmer P, King V. 2009. Static magnetic field therapy: A critical review of treatment parameters. *Evidence-Based Complement Alternat Med* 6:133–139.
- Cuajungco MP, Faget KY. 2003. Zinc takes the central stage: Its paradoxical role in Alzheimer's disease. *Brain Res Rev* 41:44–56.
- Dardenne M. 2002. Zinc and immune function. *Eur J Clin Nutr* 56:S20–23.
- Djordjevic DM, De Luka SR, Milovanovich ID, Janković S, Stefanović S, Vesković-Moračanin S, Ćirković S, Ilić AŽ, Ristić-Djurović JL, Trbović AM. 2012. Hematological parameters' changes in mice subchronically exposed to static magnetic fields of different orientations. *Ecotoxicol Environ Saf* 81:98–105.
- Dröge W. 2002. Free radicals in the physiological control of cell function. *Physiol Rev* 82:47–95.
- Elsas SM, Hazany S, Gregory WL, Mody I. 2009. Hippocampal zinc infusion delays the development of after discharges and seizures in a kindling model of epilepsy. *Epilepsia* 50:870–879.
- Evans EW, Dodson CA, Maeda K, Biskup T, Wedge CJ, Timmel CR. 2015. Magnetic field effects in flavoproteins and related systems. *Interface Focus* 3:20130037.
- Frederickson CJ, Bush AI. 2001. Synaptically released zinc: Physiological functions and pathological effects. *BioMetals* 14:353–366.
- Frederickson CJ, Koh JY, Bush AI. 2005. The neurobiology of zinc in health and disease. *Nat Rev Neurosci* 6:449–462.
- Hashish AH, El-Missiry MA, Abdelkader HI, Abou-Saleh RH. 2008. Assessment of biological changes of continuous whole body exposure to static magnetic field and extremely low frequency electromagnetic fields in mice. *Ecotoxicol Environ Saf* 71:895–902.
- Ilić AŽ, Ćirković S, Djordjevic DM, De Luka SR, Milovanovich ID, Trbović AM, Ristić-Djurović JL. 2013. Analytical description of two-dimensional magnetic arrays suitable for biomedical applications. *IEEE Trans Magn* 49:5656–5663.
- Johnsen S, Lohmann KJ. 2008. Magnetoreception in animals feature article. *Phys Today* 61:29–35.
- Lahbib A, Ghodbane S, Sakly M, Abdelmelek H. 2014. Vitamins and glucose metabolism: The role of static magnetic fields. *Int J Radiat Biol* 90:1240–1245.
- László J, Reiczigel J, Székely L, Gasparics A, Bogár I, Bors L, Rácz B, Gyires K. 2007. Optimization of static magnetic field parameters improves analgesic effect in mice. *Bioelectromagnetics* 28:615–627.
- László JF, Farkas P, Reiczigel J, Vágó P. 2012. Effect of local exposure to inhomogeneous static magnetic field on stomatological pain sensation – a double-blind, randomized, placebo-controlled study. *Int J Radiat Biol* 88(5):430–438.
- Maeda K, Robinson AJ, Henbest KB, Hogben HJ, Biskup T, Ahmad M, Schleicher E, Weber S, Timmel CR, Hore PJ. 2012. Magnetically sensitive light-induced reactions in cryptochrome are consistent with its proposed role as a magnetoreceptor. *Proc Natl Acad Sci USA* 109:4774–4779.
- Mandić D, Patent No. (WO1999060581) Surface magnetised elastic magnetic strip and application. Available at: <http://patentscope.wipo.int/search/en/WO1999060581>
- Mészáros S, Tabák AG, Horváth C, Szathmári M, László JF. 2013. Influence of local exposure to static magnetic field on pain perception and bone turnover of osteoporotic patients with vertebral deformity – a randomized controlled trial. *Int J Radiat Biol* 89:877–885.
- Miryam E, Aida L, Samira M, Mohsen S, Hafedh A. 2010. Effects of acute exposure to static magnetic field on ionic composition of rat spinal cord. *Gen Physiol Biophys* 29:288–294.
- Multhaup G, Ruppert T, Schlicksupp A, Hesse L, Beher D, Masters CL, Beyreuther K. 1997. Reactive oxygen species and Alzheimer's disease. *Biochem Pharmacol* 54:533–539.
- Nunes B, Capela RC, Sergio T, Caldeira C, Goncalves F, Correia AT. 2014. Effects of chronic exposure to lead, copper, zinc and cadmium on biomarkers of the European eel, *Anguilla Anguilla*. *Environ Sci Poll Res* 21:5689–5700.
- Phillips MJ, Ackerley CA, Superina RA, Filler RM, Roberts EA, Levy GA. 1996. Excess zinc associated with severe progressive cholestasis in Cree and Ojibwa-Cree children. *The Lancet* 347:866–868.
- Pourahmad J, Ross S, O'Brien PJ. 2001. Lysosomal involvement in hepatocyte cytotoxicity induced by Cu²⁺ but not Cd²⁺. *Free Radical Biol Med* 30:89–97.
- Pourahmad J, O'Brien PL, Jokar F, Daraei B. 2003. Carcinogenic metal induced sites of reactive oxygen species formation in hepatocytes. *Toxicol In Vitro* 17:803–810.
- Prasad AS. 2008. Zinc in human health: Effect of zinc on immune cells. *Mol Med* 14:353–357.
- Ramirez DC, Gomez-Mejiba SE, Corbett JT, Deterding LJ, Tomer KB, Mason RP. 2009. Cu,Zn-superoxide dismutase-driven free radical modifications: Copper- and carbonate radical anion-initiated protein radical chemistry. *Biochem J* 417:341–353.
- Rana SVS. 2008. Metals and apoptosis: Recent developments. *J Trace Elem Med Biol* 22:262–284.
- Repacholi MH, Greenebaum B. 1999. Interaction of static and extremely low frequency electric and magnetic fields with living systems: Health effects and research needs. *Bioelectromagnetics* 20:133–160.
- Ritchie CW, Bush AI, Mackinnon A, Macfarlane S, Mastwyk M, MacGregor L, Kiers L, Cherny R, Li QX, Tammer A, Carrington D, Mavros C, Volitakis I, Xilinas M, Ames D, Davis S, Beyreuther K, Tanzi RE, Masters CL. 2003. Metal-protein attenuation with iodochlorhydroxyquin (Clioquinol) targeting Aβ amyloid deposition and toxicity in Alzheimer disease: A pilot phase 2 clinical trial. *Arch Neurol* 60:1685–1691.
- Roberts BR, Tainer JA, Getzoff ED, Malencik DA, Anderson SR, Bomben VC, Meyers KR, Karplus PA, Beckman JS. 2007. Structural characterization of

- zinc-deficient human superoxide dismutase and implications for ALS. *J Mol Biol* 373:877–890.
- Rodgers CT. 2009. Magnetic field effects in chemical systems. *Pure Appl Chem* 81:19–43.
- Rosen AD. 2003. Mechanism of action of moderate-intensity static magnetic fields on biological systems. *Cell Biochem Biophys* 39:163–173.
- Ryf S, Wolber T, Duru F, Luechinger R. 2008. Interference of neodymium magnets with cardiac pacemakers and implantable cardioverter-defibrillators: An in vitro study. *Technol Health Care* 16:13–18.
- Salem A, Hafedh A, Rached A, Mohsen S, Khemais BR. 2005. Zinc prevents hematological and biochemical alterations induced by static magnetic field in rats. *Pharmacol Rep* 57:616–622.
- Sato K, Akaike T, Kohno M, Ando M, Maeda H. 1992. Hydroxyl radical production by H₂O₂ plus Cu,Zn-superoxide dismutase reflects the activity of free copper released from the oxidatively damaged enzyme. *J Biol Chem* 267:25371–25377.
- Schenck JF. 2000. Safety of strong, static magnetic fields. *J Magn Reson Imaging* 12:2–19.
- Sies H. 2014. Role of metabolic H₂O₂ generation: Redox signalling and oxidative stress. *J Biol Chem* 289:8735–8741.
- Singh I, Sagare AP, Coma M, Perlmutter D, Gelein R, Bell RD, Deane RJ, Zhong E, Parisi M, Ciszewski J, Kasper RT, Deane R. 2013. Low levels of copper disrupt brain amyloid- β homeostasis by altering its production and clearance. *Proc Natl Acad Sci USA* 110:14771–14776.
- Sterman M, Shouse M, Fairchild M, Belsito O. 1986. Kindled seizure induction alters and is altered by zinc absorption. *Brain Res* 383:382–386.
- Sullivan JF, Jetton MM, Hahn HKJ, Burch RE. 1980. Enhanced lipid peroxidation in liver microsomes of zinc-deficient rats. *Am J Clin Nutr* 33:51–56.
- Tapiero H, Townsend DM, Tew KD. 2003. Trace elements in human physiology and pathology. Copper. *Biomed Pharmacother* 57:386–398.
- Tapiero H, Tew KD. 2003. Trace elements in human physiology and pathology: Zinc and metallothioneins. *Biomed Pharmacother* 57:399–411.
- Tassabehji NM, VanLandingham JW, Levenson CW. 2005. Copper alters the conformation and transcriptional activity of the tumor suppressor protein p53 in human HepG2 cells. *Exp Biol Med (Maywood)* 230:699–708.
- Turski ML, Thiele DJ. 2009. New roles for copper metabolism in cell proliferation, signaling and disease. *J Biol Chem* 284:717–721.
- VanLandingham JW, Tassabehji NM, Somers RC, Levenson CW. 2005. Expression profiling of p53-target genes in copper-mediated neuronal apoptosis. *Neuromolecular Med* 7:311–324.
- Vergallo C, Dini L, Szamosvölgyi Z, Tenuzzo BA, Carata E, Panzarini E, László JF. 2013. In vitro analysis of the anti-inflammatory effect of inhomogeneous static magnetic field-exposure on human macrophages and lymphocytes. *PLoS One* 8:e72374.
- Waheed S, Kamal A, Malik RN. 2014. Human health risk from organ-specific accumulation of toxic metals and response of antioxidants in edible fish species from Chenab River, Pakistan. *Environ Sci Poll Res* 21:4409–4417.
- Witeska M, Kosciuk B. 2013. The changes in common carp blood after short-term zinc exposure. *Environ Sci Poll Res* 10:284–286.
- Wolford JL, Chishti Y, Jin Q, Ward J, Chen L, Vogt S, Finney L. 2010. Loss of pluripotency in human embryonic stem cells directly correlates with an increase in nuclear zinc. *PLoS One* 5:1–7.
- Yamaguchi-Sekino S, Sekino M, Ueno S. 2011. Biological effects of electromagnetic fields and recently updated safety guidelines for strong static magnetic fields. *Magn Reson Med Sci* 10:1–10.
- Zhang J, Ding C, Shang P. 2014. Alterations of mineral elements in osteoblast during differentiation under hypo, moderate and high static magnetic fields. *Biol Trace Elem Res* 162:153–157.

Homogeneous static magnetic field of different orientation induces biological changes in subacutely exposed mice

Ivan D. Milovanovich¹ · Saša Ćirković² · Silvio R. De Luka¹ · Drago M. Djordjević¹ · Andjelija Ž. Ilić² · Tamara Popović³ · Aleksandra Arsić³ · Danilo D. Obradović⁴ · Dejan Oprić⁴ · Jasna L. Ristić-Djurović² · Alexander M. Trbović¹

Received: 26 January 2015 / Accepted: 21 July 2015
© Springer-Verlag Berlin Heidelberg 2015

Abstract It has been shown that static magnetic field (SMF) of moderate intensity produces considerable impact on biological systems. SMF can be homogeneous or inhomogeneous. In many studies, inhomogeneous SMF was employed. Aware that inhomogeneous SMF could result in experimental variability, we investigated the influence of a vertical homogeneous SMF of different orientation. Male Swiss-Webster 9- to 10-week-old mice were subacutely exposed to upward- and downward-oriented SMF of 128 mT generated by a cyclotron for 1 h/day during a 5-day period. We found that SMF affected various organs and that these effects were, to some degree, dependent on SMF orientation. Both upward- and downward-oriented SMF caused a reduction in the amount of total white blood cells (WBC) and lymphocytes in serum, a decrease of granulocytes in the spleen, kidney inflammation, and an increase in the amount of high-density lipoprotein (HDL). In addition, upward-oriented SMF caused

brain edema and increased spleen cellularity. In contrast, downward-oriented SMF induced liver inflammation and a decrease in the amount of serum granulocytes. These effects might represent a specific redistribution of pro-inflammatory cells in blood and among various organs. It appears that homogeneous SMF of 128 mT affected specific organs in the body, rather than simultaneously and equally influencing the entire body system.

Keywords Homogeneous static magnetic field of different orientation · Liver · Brain · Kidney · Spleen · Serum

Introduction

Two types of magnetic fields are widely present in the human environment—an alternating and a static magnetic field (SMF). Biological effects of alternating magnetic field have been extensively investigated since alternating electromagnetic fields are widely used in electrical power systems as well as in information and telecommunications technologies. In contrast, there is scarce data on SMF activity impact on human health (Heinrich et al. 2011). The main sources of SMF that is stronger than a geomagnetic field are found in various medical devices. SMF, which is difficult to shield and easily penetrates biological tissues, may be classified as weak (<1 mT), moderate (1 mT to 1 T), strong (1 to 5 T), and ultrastrong (>5 T). Unlike SMF of weak and, to some degree, SMF of strong intensity, SMF of moderate intensity has considerable effects on biological systems (Rosen 2003, Dini and Abbro 2005). These effects are mediated by interaction with moving charges (ions, proteins, etc.) and magnetic materials found in tissues as a consequence of several physical mechanisms (Schenck 2005, Saunders 2005). Homogeneous as well as inhomogeneous SMF was employed in many studies that report its

Responsible editor: Philippe Garrigues

Ivan D. Milovanovich and Saša Ćirković contributed equally to this work.

✉ Alexander M. Trbović
aleksandar.trbovic@mhub.bg.ac.rs;
alexander.m.trbovic@gmail.com

¹ Department of Pathological Physiology, School of Medicine, University of Belgrade, Dr Subotića 9, 11000 Belgrade, Serbia

² Institute of Physics, University of Belgrade, Pregrevica 118, 11080 Zemun-Belgrade, Serbia

³ Institute for Medical Research University of Belgrade, Laboratory for Nutrition and Metabolism, Tadeuša Košćuška 1, 11000 Belgrade, Serbia

⁴ Department of Pathology, School of Medicine, University of Belgrade, Dr Subotića 9, 11000 Belgrade, Serbia

significant effects (Abdelmelek et al. 2006, Elferchichi et al. 2007, Hashish et al. 2008, Amara et al. 2009, Elferchichi et al. 2010, Lahbib et al. 2010, László et al. 2007, Vergallo et al. 2013, Csillag et al. 2014, Kiss et al. 2015). Although it can be argued that spatial dependence introduced by field inhomogeneity is more likely to mimic realistic exposures to environmental fields, homogeneous magnetic fields offer an advantage for *in vivo* experiments with moving animals in that they ensure identical exposure conditions at every point of the experimental volume. Exposure dosage is equal at every point of animal body, regardless of animal position during the course of experiment. We therefore decided to employ a homogeneous SMF.

A significant influence of inhomogeneous SMF of moderate intensities with checkerboard configuration, i.e., of spatially alternating SMF with a period of 2 cm in both directions was reported (László et al. 2007, Vergallo et al. 2013, Csillag et al. 2014, Kiss et al. 2015). Thorough description, analysis, and optimization of the field (László et al. 2007) that was later used in a number of biomedical experiments (for example, in Vergallo et al. 2013, Csillag et al. 2014, Kiss et al. 2015) established justifiable cause-and-effect relationship between the applied field and the obtained results. Averaging of a spatially alternating field over the entire surfaces parallel to the magnetic checkerboard would result in zero magnetic flux density vector and mean field gradient. Therefore, the mean intensity of the applied SMF and strong local field gradients were the cause of the observed effects and the overall beneficial influence of SMF. Homogeneity of the cyclotron SMF that is used in our study is much better than that of the exposure systems commonly used in biomedical experiments. Consequently, any possible biological effect of field gradients is excluded and all observed results are due to the applied field intensity in the chosen direction. We exploited the possibilities of the cyclotron magnet to check if the field orientation as well as the field intensity applied throughout the experimental volume is of importance, the motivation for the former being the accounts of significance of field orientation in the inhomogeneous (Djordjevich et al. 2012) as well as in the homogeneous (Todorović et al. 2015) SMF. With the intention to single out the influence of the field orientation, we used downward as well as upward-oriented vertical, highly homogeneous SMF of moderate intensity. The intensity of the SMF was adjusted to 128 mT motivated by the existence of research data on the effects of the horizontal homogeneous SMF of the same intensity (Chater et al. 2006, Elferchichi et al. 2007, Amara et al. 2009, Lahbib et al. 2010, Elferchichi et al. 2010, Ghodbane et al. 2014), allowing for the comparison of the results.

The thorough study reported by Colbert et al. (2009) revealed that magnetic fields are often poorly described, lacking critical data on magnet characteristics, measured field strength, and estimated distance of the magnet from the target tissue. As a result, inferences drawn from such reports cannot

be precisely associated with the applied SMFs. To the contrary if, as suggested by Colbert et al. (2009), all ten SMF dosage and treatment parameters deemed necessary for the full description of the applied SMF were systematically reported, as for example, in our study and in László et al. (2007), replication of experiments by other investigators as well as comparison with the results of exposures to different magnetic fields is enabled.

Biological response to moderate SMF is wide-ranging, involving different types of cells in various tissues and organs. For example, it has been shown in *in vitro* system that exposure to SMF caused a significant initial decline in ROS production by human peripheral blood neutrophils that was reversible after longer incubation time (Poniedzialek et al. 2013). Moreover, it has been demonstrated that SMF exposure had beneficial effects in a murine model of allergic inflammation via mobilization of cellular ROS-eliminating mechanism (Csillag et al. 2014). It has been also shown that SMF of moderate intensity induces hematological changes in exposed mice that resemble hypoxia-like status (Elferchichi et al. 2010). In addition, the hypoxia-like status is associated with a sympathetic hyperactivity that could be attributed to stress reaction of exposed animals (Abdelmelek et al. 2006). Using an *in vivo* experimental model of mouse ear edema, it has been suggested that the place of SMF action may be in the lower spinal region (Kiss et al. 2015). *In vivo* experiments also demonstrated antinociceptive effects of SMF in invertebrate (László and Hernádi 2012), mice (László et al. 2007, László and Gyires 2009) and humans (László et al. 2012). *In vitro* analysis of the effects of SMF on human macrophages and lymphocytes provided a possible explanation for the effect observed *in vivo* (Vergallo et al. 2013). Namely, it was shown that SMF exposure (of 200 mT average intensity) suppresses inflammation by reducing release of pro-inflammatory cytokines IL-6, IL-8, and TNF- α from macrophages and by enhancing release of anti-inflammatory cytokine IL-10 from lymphocytes (Vergallo et al. 2013). SMF of 128 mT can also induce tissue changes in various organs such as the liver, kidney, and brain of exposed animals (Amara et al. 2007, Amara et al. 2009), as well as in cell culture (Sahebamei et al. 2007). These changes were attributed to oxidative stress. Another possibility is that the tissue changes induced by SMF were caused by the redistribution of inflammatory cells (Djordjevich et al. 2012). We were specifically interested to assess whether changes in hematological parameters could be directly related to changes observed in various organs from the same animals. Since changes in the blood may be specific to the hematological system and may not cause or reflect changes in the organs, we investigated whether changes in the blood corresponded to changes in selected organs, which had previously been studied by others in SMF of 128 mT. In our case, the spleen and kidney were selected for the experiment since they are involved in regulation of blood content.

On the other hand, the liver and brain were studied as target organs for possible redistribution of blood cells and consequent oxidative damage. In addition, we chose the liver as an example of a target body organ because of its central role in lipid metabolism, which we studied in-depth.

Phospholipids are a class of lipids in which a phosphate group replaces one of the fatty acids. They are a major structural component of all cell membranes where they are involved in forming lipid bilayers. Phospholipids are amphipathic molecules containing a hydrophilic phosphate group and a hydrophobic fatty acid tail. The four phospholipids that predominate in the plasma membrane of mammalian cells are phosphatidylcholine, phosphatidylethanolamine, phosphatidylserine, and sphingomyelin. Besides a structural role, phospholipids also have a metabolic role. They act as sources of intracellular signals in response to extracellular signals which interact with receptors on the outer layer of the plasma membrane. Phospholipid fatty acids of the cell membrane are precursors of lipid mediators, with eicosanoids (prostaglandins, thromboxanes, leukotrienes) being one of the most important. They, also, play a role in signal transduction and gene transcription pathways (Kremmyda et al. 2011). The liver plays an important role in the synthesis and metabolism of phospholipids. The structure of hepatocyte membrane phospholipids is dependent on nutritional intake and affects liver metabolic functions (Oguzhan et al. 2006). The fatty acid profile of liver phospholipids and triglycerides is known to be influenced by many factors, including dietary intake, age, gender, and endogenous metabolism (Oguzhan et al. 2006). However, magnetic field influence on the total fatty acids in an organism has been scarcely reported (Lahbib et al. 2010, Elferchichi et al. 2010). In the present study, we monitored the liver as a key representative organ of possible SMF influence on phospholipids.

We investigated the effects of homogeneous SMF on subacutely exposed animals by primary studying the hematological system and the liver, but we also monitored the brain, kidney, and spleen. Since literature analysis showed limited data regarding the interaction of differently oriented moderate SMF on biological systems, the present study was designed to investigate the effects of subacute exposure to differently oriented 128 mT SMF on mice.

Materials and methods

Animals

Male Swiss-Webster mice, weighing on average 23 ± 3 g, 9–10 weeks old, obtained from the Military Medical Academy Animal Research Facility (Belgrade, Serbia) were used. Mice were housed at four or five animals per cage and offered regular mouse feed and drinking water ad libitum. All

experimental protocols involving animals were reviewed and approved by the University of Belgrade, Faculty of Medicine Experimental Animals Ethics Committee. Furthermore, all experiments were conducted in accordance with procedures described in the National Institutes of Health Guide for Care and Use of Laboratory Animals (Washington, DC, USA), as well as in accordance with the US-NIH guidelines for conducting magnetic field experiments on animals.

Magnetic field

Customarily, experiments performed in accelerator facilities utilize ion beams. However, the VINCY Cyclotron located at the Vinča Institute of Nuclear Sciences is still under construction. Its ferromagnetic structure is fully assembled and operative but still accessible, allowing employment of a strong static magnetic field as an experimental tool.

The VINCY Cyclotron is a sector-focused isochronous multipurpose machine (Nešković et al. 2003). Special attention was devoted to an extremely precise design of sectors on pole tips of the electromagnet to enable acceleration of the widest possible range of ion beams (Ćirković et al. 2009). Power consumption is minimal in the most frequent operating mode, while an appropriate choice of electrical currents of main coils and ten pairs of trim coils results in different isochronous magnetic fields that could be used for various modes of operation (Ćirković et al. 2008). The produced magnetic field between the two poles is highly homogeneous in the sector regions and in the valley regions; however, it abruptly changes in the vicinity of sector edges and the gradient of the magnetic field in that narrow area is strong. The main coil current can be set up to 1000 A, whereas the maximum mean magnetic field may reach 2 T. The electromagnet pole diameter measures 2 m, and it has four sectors per pole whose azimuthal width is 42° .

Magnetic flux density of 128 mT, desired for our experiment, was produced by setting the main coil current to 36.5 A, without necessity to use trim coils for further field adjustment. Field intensity is larger between the sectors and smaller in the valleys. For our experiment, it was convenient to center cages with experimental animals in the middle of the valley, well away from sector edges to avoid high magnetic field gradients in this region, as shown in Fig. 1. Cages, 19 cm high, 35.5 cm long, and 20.5 cm wide, were placed inside the circle of radius 80 cm (from the center of the cyclotron) to avoid the stray field components at radii larger than 84 cm. The desired magnetic field was achieved with less than 0.68 % variation throughout the above described area; therefore, SMF was considered highly homogeneous throughout the experimental volume. Note that the field produced by solenoids often used for exposure setups is about an order of magnitude less homogenous than the field we used.

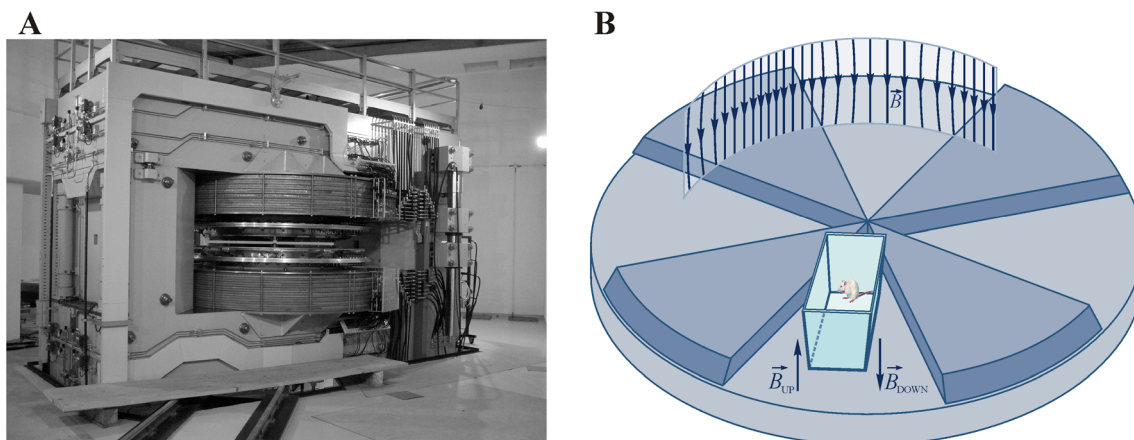


Fig. 1 The VINCY Cyclotron used as an experimental SMF exposure setup. **a** Photograph of the VINCY Cyclotron. **b** The lower pole of cyclotron magnet and position of the cage with animals in the middle of the cyclotron valley (drawn to scale). The produced magnetic field, depicted by the magnetic flux lines in the valley and above the sector, B , was vertical. The direction of the field was chosen to be directed

The geomagnetic field is directed downward in the northern hemisphere and upward in the southern hemisphere, i.e., in the same and the opposite direction to gravity, respectively. Therefore, experiments in two sets of magnetic field exposures were performed; in the first set, we used the magnetic field oriented in the same direction as gravity (down group), and in the second, the magnetic field oriented upwards (up group). The third group of animals was control (sham exposed).

Experimental design

Mice were randomly divided into three groups (9 mice per group). All three groups were kept under same conditions. The first experimental group was exposed to the upward-oriented 128 mT SMF (up group) for 1 h/day over a 5-day period. The second experimental group was exposed to the downward-oriented 128 mT SMF (down group) for 1 h/day over a 5-day period. The exposure period was always between 8 and 12 a.m. on a consecutive day under standard light exposure and constant temperature. The control group was sham exposed. Following a 5-day period, all mice were sacrificed and the blood, spleen, liver, brain, and kidney were collected for further analyses. These analyses were performed blindly, with material marked just with a code and people conducting the analyses unaware of sample group origin.

Blood and spleen parameters

Blood parameters [red blood cells (RBS), lymphocytes, neutrophils, basophils, eosinophils, platelets (Plt), hemoglobin (Hgb), hematocrit (Hct), mean corpuscular volume (MCV),

upwards or downwards for the two groups of SMF exposed animals, denoted as the up group and down group, and is represented by the vectors B_{UP} and B_{DOWN} , respectively. The variation of the magnetic field intensity was smaller than 0.68 % everywhere in the experimental volume. Magnetic flux density used was 128 mT

mean corpuscular hemoglobin (MCH), mean corpuscular hemoglobin concentration (MCHC)] were determined using hematological counter ABX Pentra 80X (Montpellier, France) according to the manufacturer's recommendations. The total number of granulocytes in blood and spleen samples was calculated by summing neutrophils with basophils and eosinophils. Total serum cholesterol, HDL, LDL, triglycerides, C-reactive protein (CRP), and alanine aminotransferase (ALT) were determined using BioSystems photometer type BTS-330 (Barcelona, Spain), according to manufacturer's recommendations.

Spleen cellularity was prepared and analyzed by the previously explained procedure (Djordjević et al. 2012).

Total lipid extraction from the liver

Obtained liver tissue was first homogenized using a 2:1 chloroform/methanol mixture and washed with a fivefold smaller volume of water or saline. The resulting mixture was separated into two phases. The lower phase was a total pure lipid extract. Liver tissue (1 g) was lyophilized and chloroform/methanol (2:1) and butylhydroxytoluene (BHT) as antioxidant were mixed. When the mixture was allowed to stand, a biphasic system was obtained. After evacuation, water was added. After centrifugation, the upper phase was put away until complete separation of the system was achieved. Further evacuation was done with 2:1 solvent systems: methanol/benzene, acetone/benzene, and ethanol/benzene. Addition and evacuation of chloroform and subsequent addition of hexane rendered the sample ready for thin liquid chromatography (TLC) (Tepšić et al. 2008).

Fatty acid analysis

The phospholipid fraction was isolated from the extracted lipids by one-dimensional (TLC) neutral lipid solvent system of hexane:diethyl ether:acetic acid (87:2:1) using Silica Gel GF plates (C. Merck, Darmstadt, Germany). The phospholipid fraction was scraped into glass tubes, and phospholipid fatty acids (FAs) methyl esters were prepared by transmethylation with sodium hydroxide (2 mol dm⁻³) in methanol (heated at 85 °C for 1 h) and after that with sulfuric acid (1 mol dm⁻³) in methanol (heated 85 °C for 2 h). After 30 min, samples of esters were centrifuged, upper phase were put into tubes and evaporated by technical nitrogen. FA methyl ester derivatives formed from isolated plasma phospholipids fraction were separated by gas chromatography (GC) using Shimadzu GC 2014 (Kyoto, Japan) equipped with a flame ionization detector and DB-23 fused silica gel capillary column. The flame ionization detector was set at 250 °C, the injection port at 220 °C, and the oven temperature programmed from 130 to 190 °C at the heating rate of 3 °C/min (Folch et al. 1957). Comparing sample peak retention times with authentic standards (Sigma Chemical Company) and/or the (PUFA)-2 standard mixtures (Restec) identified individual FAs methyl esters.

Estimated activities of desaturase system

Several fatty-acid indices, reflecting desaturase and elongase activity, were derived from primary data (Cvetković et al. 2010). The ratios of 20:4/20:3, 20:3/18:2, and 22:6/22:5 were used as a measure of estimated Δ 5-desaturase, Δ 6-desaturase, and Δ 4-desaturase activities, respectively, while 18:1/18:0 and 18:0/16:0 ratios represented estimated Δ 9-desaturase and elongase activities.

Histology analysis

Brain, liver, spleen, and kidney tissues were prepared for histological analysis by the procedure explained earlier (Bancroft and Gamble 2001). In short, tissues were fixated in formalin (10 % formaldehyde-water solution) for 24 h and then embedded in paraffin. Generated 5- μ m sections were mounted on slides and stained with hematoxylin (Bio-Optica, Milan, Italy) and eosin (MP Biomedicals LLC, Illkirch Cedex, France). Analysis of stained sections was conducted by two independent pathologists that used a light microscope Olympus BX41 (Tokyo, Japan) and made micrographs with Sony Exwave HAD digital camera, model SSC-DC50AP (Tokyo, Japan). Immunohistochemical (IHC) analysis was conducted with the CD3 (polyclonal rabbit anti-human CD3; Dako Denmark A/S; Glostrup, Denmark), CD15 (monoclonal mouse anti-human CD15 clone carb-3; Dako North America Inc., Camarillo, CA, USA), and CD20 (monoclonal mouse anti-human CD20cy clone L26; Dako Denmark A/S; Glostrup,

Denmark) antibodies. After exposing tissue to primary antibodies for 1 h, slides were rinsed with water and then the secondary antibody was applied for 15 min. Detection was conducted by employing a horse radish peroxidase kit (UltraVision Large Volume Detection System Anti-Polyvalent, HRP (Ready-To-Use); Thermo Fisher Scientific, (Cheshershire, UK). CD3 is a marker for T lymphocytes (Felgar et al. 1997), CD20 is a marker for B lymphocytes (Pinkus and Said 1988), and CD15 is a marker for granulocyte lineage (Barry et al. 2002).

Statistical analysis

Statistical analysis of obtained data was performed using software SPSS for Windows, version 16.0 (SPSS, Chicago, IL, USA). Differences among groups were evaluated by one-way ANOVA, followed by Fischer's LSD test. Distribution of non-parametric data was analyzed by chi-square test. The level of significance was set at $p < 0.05$.

Results

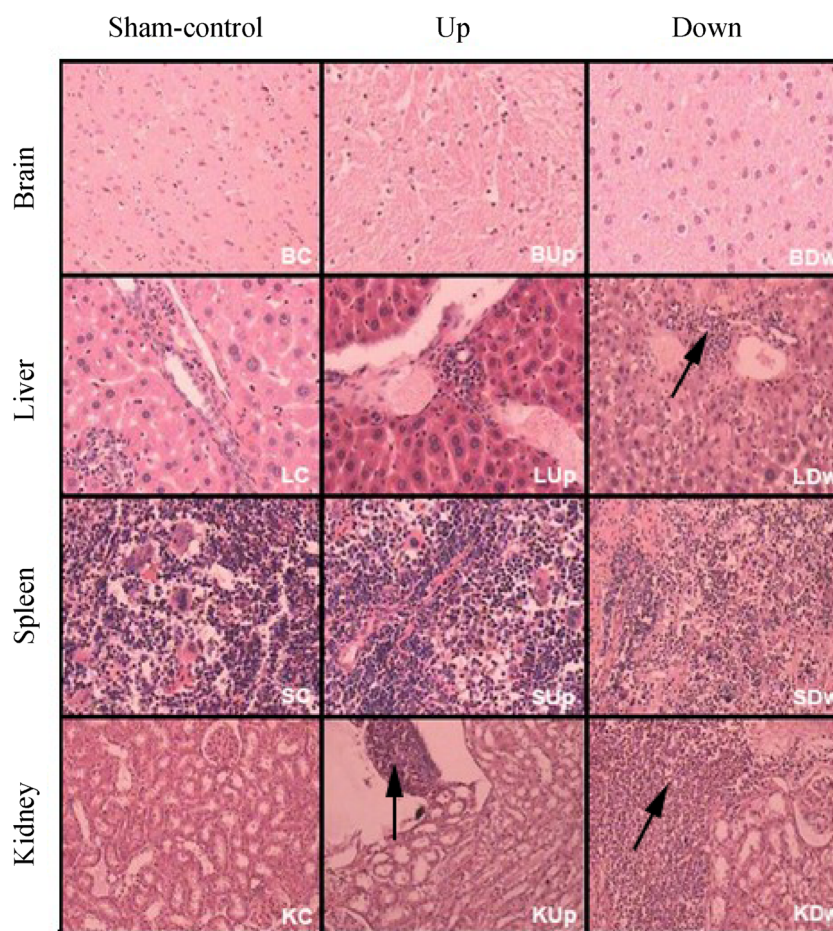
Histological characteristics

Tissue morphology of the liver, spleen, kidney, and brain is presented in Fig. 2. The liver in the down group showed significant inflammation. Liver infiltrate localization was periportal and predominantly made of granulocytes and lymphocytes. Edematous hepatocytes were also present. The spleen did not show any pathological changes among groups, though congestive hyperemia was visible in all three groups, which is a usual finding following sacrifice. The kidney showed increased inflammation (nonspecific pyelonephritis) in exposed animals, but not in sham animals. Brain edema characterized by edematous neurons was present in the up group, but not in the down and sham groups.

Histological analysis

Tissue characteristics of mice exposed to SMF of different orientations are presented in Table 1. The liver in the down group showed significant inflammatory characteristics when compared to up and sham groups ($p < 0.05$). The spleen did not show any pathological changes among groups ($p > 0.05$). The kidney showed increased inflammation in exposed animals (up and down group) when compared to control animals ($p < 0.05$). Brain tissue expressed significant edematous neurons in the up group when compared to the down and sham groups ($p < 0.05$).

Fig. 2 Histological characteristics of the brain, liver, spleen, and kidney in mice exposed (up group, down group) or unexposed (sham-control) to SMF of different orientations. *BC* brain tissue in unexposed mice (brain control), *BUp* brain tissue in mice exposed to up-oriented SMF, *BDw* brain tissue in mice exposed to down-oriented SMF. *LC* liver tissue in unexposed mice (liver control), *LUp* liver tissue in mice exposed to up-oriented SMF, *LDw* liver tissue in mice exposed to down-oriented SMF. *SC* splenic tissue in unexposed mice (spleen control), *SUp* splenic tissue in mice exposed to up-oriented SMF, *SDw* splenic tissue in mice exposed to down-oriented SMF. *KC* kidney tissue in unexposed mice (kidney control), *KUp* kidney tissue in mice exposed to up-oriented SMF, *KDw* kidney tissue in mice exposed to down-oriented SMF. Arrow shows inflammatory cells



Immunohistochemical analysis

Immunohistochemical (IHC) analysis of cell infiltrates in renal tissue is presented in Fig. 3. Initial determination of cell infiltrates in all affected organs was done by light microscopy. A confirmation of correct histological reading was conducted in a renal tissue by IHC analysis. In panel A, inflammatory cells are visible. In panel B, CD15 positive granulocytes are marked. In panel C, the CD3 positive T lymphocytes are shown. In panel D, the CD20 positive B lymphocytes are presented.

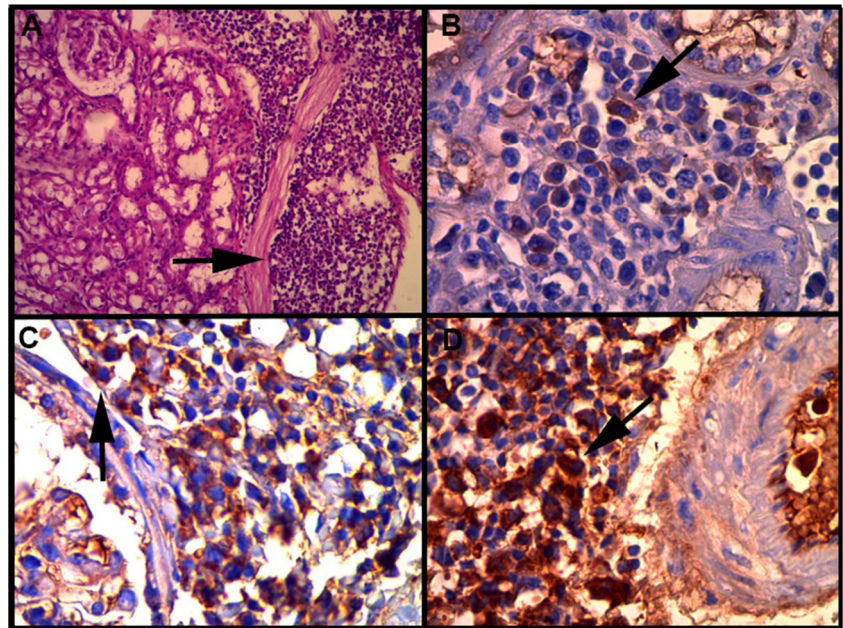
Table 1 Results of histological analysis of mice exposed (up group, down group) or unexposed (sham-control) to SMF of different orientation

	Histology	Sham-control	Up group	Down group
Liver	Normal [n(%)]	9 (100)	8 (88.9)	4 (44.4)
	Inflammation [n(%)]	0 (0)	1 (11.1)	5 (55.6)
Spleen	Normal [n(%)]	9 (100)	9 (100)	9 (100)
	Inflammation [n(%)]	0 (0)	0 (0)	0 (0)
Kidney	Normal [n(%)]	8 (88.9)	5 (55.6)	3 (33.3)
	Inflammation [n(%)]	1 (11.1)	4 (44.4)	6 (66.7)
Brain	Normal [n(%)]	8 (88.9)	1 (11.1)	9 (100)
	Edema [n(%)]	1 (11.1)	8 (88.9)	0 (0)

Blood parameters

Blood parameters in control mice and mice exposed to differently oriented SMF are shown in Table 2. Exposure of mice to differently oriented SMF did not alter the platelet count or Hgb, Hct, MCV, MCH, MCHC values among groups ($p > 0.05$). However, SMF of a different orientation influenced the serum lipids. There was a significant increase in serum values of HDL in exposed animals (up and down group) when compared to unexposed ones (61.50 ± 5.13 and 56.21 ± 2.38 vs. 41.77 ± 5.13 ; $p < 0.01$ and $p < 0.05$, respectively). Total serum cholesterol, LDL, and triglycerides did not change significantly among groups, but there was a trend of total cholesterol increase and LDL decrease in exposed groups (up and down group) ($p > 0.05$). C-reactive protein also did not change under the influence of differently oriented SMF (0.59 ± 0.09 and 0.64 ± 0.12 vs. 0.78 ± 0.32 ; $p > 0.05$), but we observed a significant increase of ALT in down group when compared to sham group (63.50 ± 8.17 vs. 42.33 ± 3.87 ; $p < 0.05$). In general, besides statistically significant results, the trend of increased values vs. sham group was more pronounced in the down group and the trend of decreased values vs. sham group was more pronounced in the up group.

Fig. 3 Immunohistochemical (IHC) analysis of cell infiltrates in renal tissue. **a** Renal tissue, magnification $\times 10$, hematoxylin-eosin staining. *Arrow* shows inflammatory cells. **b** Renal tissue, magnification $\times 40$, monoclonal mouse anti-human CD15 (granulocyte marker). *Arrow* shows CD15 positive granulocyte. **c** Renal tissue, magnification $\times 40$, polyclonal rabbit anti-human CD3 (T lymphocyte marker). *Arrow* shows CD3 positive T lymphocyte. **d** Renal tissue, magnification $\times 40$, monoclonal mouse anti-human CD20 (B lymphocyte marker). *Arrow* shows CD3 positive B lymphocyte



Blood cellularity

Blood cellularity in mice exposed (up, down) or unexposed to SMF of different orientation is shown in Fig. 4. Total serum white blood cells (WBC) count was found to be significantly lower in exposed (up and down group) when compared to unexposed animals (3.49 ± 0.50 and 3.31 ± 0.30 vs. 6.61 ± 0.70 ; $p < 0.01$) (panel A). This decrease in exposed groups was mainly due to a reduction in serum lymphocytes (2.74 ± 0.36 and 2.97 ± 0.27 vs. 5.47 ± 0.61 ; $p < 0.01$) (panel D) and to a decrease in

serum granulocytes, especially in down group (0.26 ± 0.03 vs. 0.87 ± 0.10 ; $p < 0.01$ compared to sham group and 0.26 ± 0.03 vs. 0.66 ± 0.14 ; $p < 0.05$ compared to up group) (panel C). While decrease in total WBC and serum lymphocytes were about the same in up and down groups, it is worth noting that statistically significant decrease in serum granulocytes occurred exclusively in the down group. This decrease in serum granulocytes was statistically significant not only versus the sham group but also versus the up group. SMF of a different orientation did not alter RBC count among groups ($p > 0.05$) (panel B).

Table 2 Blood parameters in mice exposed (up group, down group) or unexposed (sham-control) to SMF of different orientations

Blood parameter	Sham-control	Up group	Down group
Plt ($10^9/L$)	1311.86 \pm 59.99	1140.60 \pm 80.24	1266.25 \pm 41.49
Hgb (g/L)	125.42 \pm 5.39	130.00 \pm 3.52	132.00 \pm 6.50
Hct (L/L)	0.41 \pm 0.02	0.42 \pm 0.09	0.43 \pm 0.02
MCV (fl)	48.29 \pm 1.30	48.62 \pm 0.65	48.71 \pm 0.94
MCH (pg)	15.00 \pm 0.49	15.12 \pm 0.23	15.29 \pm 0.36
MCHC (g/L)	308.14 \pm 4.97	309.75 \pm 3.53	309.86 \pm 1.84
Total cholesterol (mg/dL)	76.17 \pm 3.97	78.73 \pm 6.79	89.48 \pm 5.71
HDL (mg/dL)	41.77 \pm 5.13	56.21 \pm 2.38*	61.50 \pm 6.19**
LDL (mg/dL)	25.81 \pm 6.61	10.74 \pm 6.31	16.16 \pm 7.26
Triglycerides (mg/dL)	52.94 \pm 3.53	48.88 \pm 4.37	59.13 \pm 5.35
ALT (IU/L)	42.33 \pm 3.87	51.29 \pm 7.94	63.50 \pm 8.17*
CRP (mg/dL)	0.78 \pm 0.32	0.59 \pm 0.09	0.64 \pm 0.12

Data are presented as mean \pm SEM

Plt platelets, *Hgb* hemoglobin, *Hct* hematocrit, *MCV* mean corpuscular volume, *MCH* mean corpuscular hemoglobin, *MCHC* mean corpuscular hemoglobin concentration, *HDL* high-density lipoprotein, *LDL* low-density lipoprotein, *ALT* alanine-aminotransferase, *CRP* C-reactive protein

* $p < 0.05$ compared to control; ** $p < 0.01$ compared to control

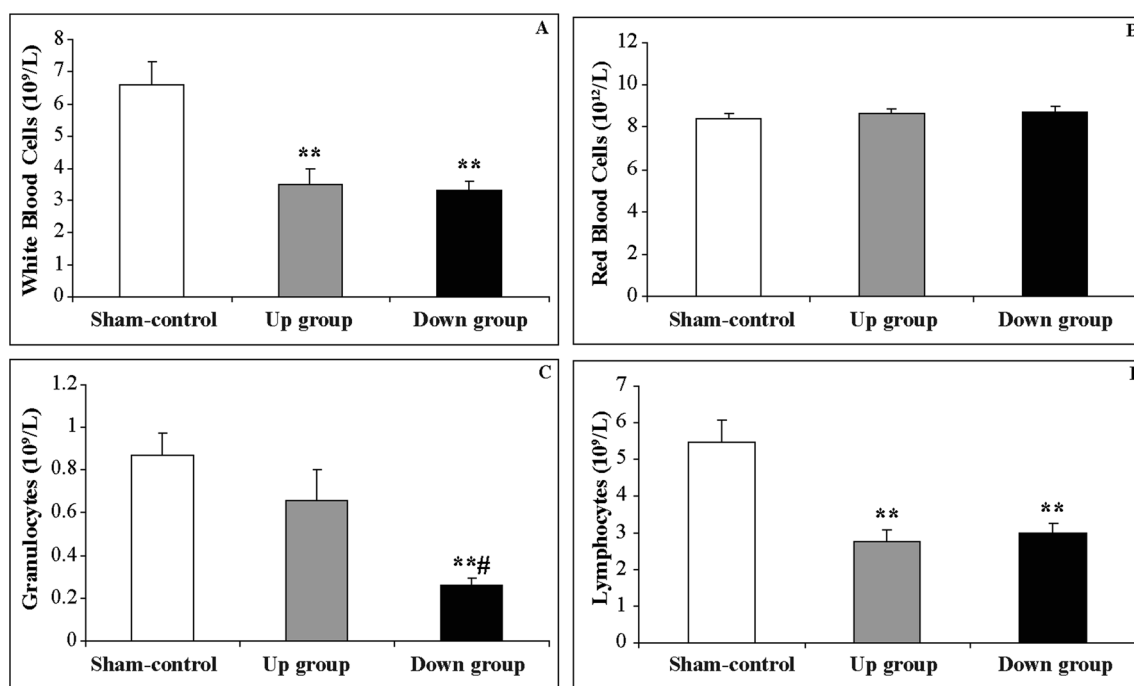


Fig. 4 Blood cellularity in mice exposed (up group, down group) or unexposed (sham-control) to SMF of a different orientation. Data are presented as mean±SEM. **a** Total serum white blood cells in mice exposed (up group, down group) or unexposed (sham-control) to SMF of a different orientation; **b** serum red blood cells in mice exposed (up group, down group) or unexposed (sham-control) to SMF of a different

orientation; **c** total serum granulocytes in mice exposed (up group, down group) or unexposed (sham-control) to SMF of a different orientation; **d** serum lymphocytes in mice exposed (up group, down group) or unexposed (sham-control) to SMF of a different orientation; ** $p < 0.01$ compared to control; # $p < 0.05$ compared to up group

Spleen cellular parameters

Spleen cellular parameters in mice exposed to SMF of a different orientation are presented in Fig. 5. Total spleen cellularity in mice exposed to upward-oriented SMF was significantly higher when compared to those exposed to downward-oriented SMF (1.08 ± 0.05 vs. 0.69 ± 0.03 ; $p < 0.01$) and to control mice (1.08 ± 0.05 vs. 0.73 ± 0.05 ; $p < 0.01$) (panel A). However, there was no difference in spleen red blood cell count among groups (30.54 ± 3.26 vs. 34.51 ± 1.4 vs. 34.71 ± 1.05 ; $p > 0.05$, respectively) (panel B). Spleen granulocytes in the up group were significantly lower when compared to the sham group (2.2 ± 0.28 vs. 8.26 ± 1.30 ; $p < 0.01$) and spleen granulocytes in the down group were also significantly lower when compared to the sham group (1.64 ± 0.19 vs. 8.26 ± 1.30 ; $p < 0.01$) (panel C). In contrast, spleen lymphocytes did not alter among groups under the influence of SMF of different orientation ($p > 0.05$) (panel D).

Liver phospholipid profile

Liver phospholipid profile in mice exposed to SMF of a different orientation is presented in Table 3. There was no difference in total saturated fatty acids (SFA). However, in mice exposed to downward-oriented SMF, there was a significant increase in content of palmitic acid (16:0) when compared to

control mice (24.54 ± 0.19 vs. 22.90 ± 0.70 ; $p < 0.01$). There was also an increase of palmitic acid in the upward-oriented group when compared to sham group, but this increase was on the border of significance (24.01 ± 0.13 vs. 22.90 ± 0.70 ; $p = 0.05$). Stearic acid (18:0) content showed tendency of decrease in exposed groups, but without statistical significance ($p > 0.05$). There was no difference in monounsaturated fatty acids (MUFA) in general. However, content of palmitoleic acid (16:1n-7) showed a significant, twofold increase in exposed animals (up and down group) when compared to sham group (0.82 ± 0.06 and 0.84 ± 0.07 vs. 0.40 ± 0.04 ; $p < 0.01$). On the other hand, oleic acid (18:1n-9) did not show alterations among the groups ($p > 0.05$). The amount of vaccenic acid (18:1n-7) significantly increased in the down group, but not in the up group, when compared to sham group (2.49 ± 0.14 vs. 1.97 ± 0.17) and also in the down group when compared to the up group (2.49 ± 0.14 vs. 1.96 ± 0.18). Not only that polyunsaturated fatty acids (PUFA) did not alter, but neither did the sum of omega-3 fatty acids (n-3), the sum of omega-6 fatty acids (n-6), or the ratio of omega-6 to omega-3 (n-6/n-3). However, dihomo- γ -linolenic acid (20:3n-6) was reduced in the exposed groups (up and down) when compared to sham group (1.06 ± 0.08 and 1.12 ± 0.02 vs. 1.40 ± 0.11 ; $p < 0.01$). In addition, α -linolenic acid (18:3n-3) was reduced in the down group when compared to both sham group (0.40 ± 0.04 vs. 0.62 ± 0.07 ; $p < 0.05$) and the up group (0.40 ± 0.04 vs. $0.67 \pm$

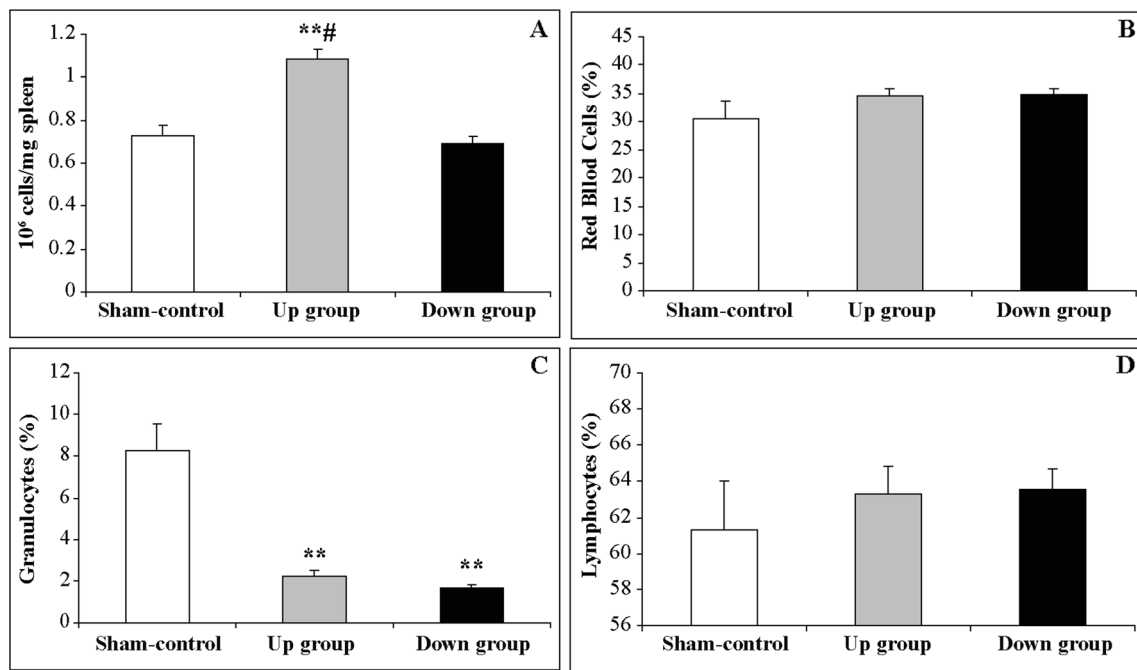


Fig. 5 Spleen cellularity in mice exposed (up group, down group) or unexposed (sham-control) to SMF of a different orientation. Data are presented as mean±SEM. **a** Total spleen cellularity in mice exposed (up group, down group) or unexposed (sham-control) to SMF of different orientation; **b** spleen red blood cells in mice exposed (up group, down group) or unexposed (sham-control) to SMF of a different orientation; **c**

spleen granulocytes in mice exposed (up group, down group) or unexposed (sham-control) to SMF of different orientation; **d** spleen lymphocytes in mice exposed (up group, down group) or unexposed (sham-control) to SMF of different orientation; ** $p < 0.01$ compared to control; # $p < 0.01$ compared to down group

0.08; $p < 0.01$). At the same time, α -linolenic acid from the up group did not change when compared to sham group ($p > 0.05$). Overall, in both up and down groups, there was a statistically significant change in content of palmitoleic (16:1n-7) and dihomo- γ -linolenic acid (20:3n-6) that occurred in the same direction. Namely, both the amount of palmitoleic acid and the dihomo- γ -linolenic acid decreased when compared to sham group. However, in three situations, a change in the amount of fatty acids was observed exclusively in the down group. Namely, palmitic (16:0) and vaccenic (18:1n7) acids increased and α -linolenic acid (18:3n-3) decreased in the down group when compared to sham group.

Desaturase and elongase activities

Desaturase and elongase activities in the liver in mice exposed to SMF of a different orientation are presented in Table 4. Delta 9 ($\Delta 9$) desaturase activity did not change in groups of exposed or unexposed animals ($p > 0.05$). Elongase activity decreased in the liver of exposed animals (up and down groups) when compared to sham group (0.73 ± 0.03 and 0.70 ± 0.01 vs. 0.81 ± 0.03 ; $p < 0.05$ and $p < 0.01$, respectively). Delta 6 ($\Delta 6$) desaturase and elongase also showed significant decrease in livers of exposed animals (up and down groups) when compared to control animals (0.07 ± 0.01 and 0.07 ± 0.003 vs. 0.09 ± 0.01 ; $p < 0.05$). Delta 5 ($\Delta 5$) desaturase

showed significant increase in the up group compared to sham group (13.52 ± 0.88 vs. 10.64 ± 1.02 ; $p < 0.05$) but did not differ when compared to the down group (13.52 ± 0.88 vs. 12.27 ± 0.32 ; $p > 0.05$).

Animal weight

There was no significant difference in animal weight or food intake among the groups at the beginning and at the end of the experiment (data not shown).

Discussion

In this study, we investigated the influence of a homogeneous, differently oriented static magnetic field (SMF) of 128 mT on hematological parameters, tissue characteristics, and lipid content in subacutely exposed mice. Aiming to single out the influence of field orientation, we used downward- as well as upward-oriented vertical homogeneous SMF (Fig. 1). SMF affected various organs and these effects were, to some degree, dependent on the SMF orientation. Since the field gradients were negligible, any possible biological effect of varying field gradients was excluded and all the observed effects were appropriated to the applied field intensity in the chosen direction.

Table 3 Fatty acid profiles of liver phospholipids in mice exposed (up group, down group) or unexposed (sham-control) to SMF of different orientation

Fatty acids (%)	Sham-control	Up group	Down group
SFA	41.42±0.97	41.60±0.72	41.79±0.26
16:0	22.90±0.70	24.01±0.13	24.54±0.19**
18:0	18.51±0.64	17.60±0.68	17.25±0.25
MUFA	10.26±0.98	11.21±0.71	10.90±0.60
16:1 n-7	0.40±0.04	0.82±0.06**	0.84±0.07**
18:1 n-9	7.89±0.83	8.43±0.82	7.58±0.51
18:1 n-7	1.97±0.17	1.96±0.18	2.49±0.14 ^a
PUFA	48.33±0.61	47.19±0.88	47.31±0.48
n-6	31.88±0.32	31.14±0.60	30.80±0.49
18:2 n-6	15.97±0.16	15.94±0.63	15.74±0.43
20:3 n-6	1.40±0.11	1.06±0.80**	1.12±0.02*
20:4 n-6	14.30±0.39	13.91±0.53	13.72±0.11
22:4 n-6	0.21±0.01	0.23±0.01	0.22±0.01
n-3	16.44±0.74	16.05±1.11	16.50±0.81
18:3 n-3	0.62±0.07	0.67±0.08	0.40±0.04***
20:5 n-3	0.52±0.15	0.56±0.16	0.72±0.16
22:5 n-3	0.70±0.08	0.75±0.06	0.82±0.04
22:6 n-3	14.61±0.66	14.07±1.18	14.56±0.78
n-6/n-3	1.96±0.10	2.01±0.17	1.91±0.12
MUFA/SFA	0.25±0.07	0.27±0.05	0.26±0.04
PUFA/SFA	1.17±0.09	1.14±0.09	1.13±0.03

Values are presented as means±SEM

SFA saturated fatty acids, MUFA monounsaturated fatty acids, PUFA polyunsaturated fatty acids

p*<0.05 compared to control; *p*<0.01 compared to control

^a*p*<0.05 compared to Up group

Both upward- and downward-oriented magnetic field caused a decrease in the amount of total WBC and lymphocytes in serum, a decrease of granulocytes in the spleen, kidney inflammation, and an increase in the amount of HDL. In addition, upward-oriented SMF caused brain edema and increased spleen cellularity. In contrast, downward-oriented SMF induced liver inflammation and a decrease in the amount of serum granulocytes. It appears that SMF of 128 mT affected

specific organs in the body, rather than simultaneously and equally influencing the entire body system.

We initially found inflammation in the liver after exposure to the down-oriented SMF of 128 mT (Fig. 2; Table 1). These histological findings were confirmed by an increase of serum ALT in the down group only (Table 2). Enzyme ALT is found in the highest concentration in the liver, and it is typically used to detect liver injury. Moreover, we have been the first to discover specific changes in fatty acid profile following SMF exposure. We observed exclusively in the down group an increase in pro-inflammatory palmitic fatty acid (16:0) (Soto-Vaca et al. 2013, Wu et al. 2014) and a decrease in anti-inflammatory α-linolenic fatty acid (18:3 n-3) (Ren et al. 2007, Erdinest et al. 2012) (Table 3). It has been shown that palmitic acid increases the level of pro-inflammatory TNF-alpha and IL-6 (Staiger et al. 2004, Zhou et al. 2013). An increase in palmitic fatty acid that we observed could be a consequence of a reduced activity of the enzyme elongase 18:0/16:0 that converts palmitic fatty acid into stearic fatty acid (18:0) (Table 4). In the case of α-linolenic acid, which is an essential fatty acid, we can speculate that employed SMF affected its metabolism in the liver. SMF of 128 mT may directly affect activity of enzymes by inducing their conformational changes. Alternatively, SMF may act through the rearrangement of membrane phospholipids, leading to a flux of ions (Rosen 1993) that alters enzyme functions. Observing that 128 mT SMF affected differently the two enzymes that contain the same metal, magnesium (enzyme Δ6 desaturase and elongase 20:3n-6/18:2n-6 and enzyme Δ5 desaturase 20:4n-6/20:3n-6), while at the same time, enzyme Δ9 desaturase 18:1n-9/18:0 that contains a different metal, iron, was not affected (Table 4), we conclude that SMF influence was probably at the membrane level, rather than at the level of enzymes' conformational change. This explanation is based on the important role of the liver in synthesis and degradation of phospholipids that are a major component of cell membranes (Rigotti et al. 1994). Alteration of membrane fatty acids changes membrane fluidity and ion flux and, consequently, the function of various enzymes (McGarry 2002). The ratio of unsaturated to saturated fatty acids influences membrane fluidity in bacteria (Mihoub et al. 2012) and in mammals (Perona et al. 2007). Moderate intensity SMF

Table 4 Estimated activities of desaturases and elongases in the liver in mice exposed (up group, down group) or unexposed (sham-control) to SMF of different orientations

Enzyme	Sham-control	Up group	Down group
Δ9 desaturase 18:1n-9/18:0	0.43±0.14	0.49±0.15	0.44±0.10
elongase 18:0/16:0	0.81±0.03	0.73±0.03*	0.70±0.01**
Δ6 desaturase and elongase 20:3n-6/18:2n-6	0.09±0.01	0.07±0.01*	0.07±0.003*
Δ5 desaturase 20:4n-6/20:3n-6	10.64±1.02	13.53±0.88*	12.28±0.32

Values are presented as means±SEM

Significantly different from control: **p*<0.05 compared to control; ***p*<0.01 compared to control

influences cell membrane ratio of unsaturated versus saturated fatty acids in bacteria, representing an adaptive reaction (Mihoub et al. 2012). However, in our study, although some fatty acids increased and some decreased, the total ratio of MUFA/SFA and PUFA/SFA of liver phospholipids did not change (Table 3), probably because of different intensity and duration of SMF exposure.

Various studies have shown an increase in free radical production and degradation of lipid bilayers in liver cells in SMF exposed animals (Watanabe et al. 1997, Amara et al. 2007, Hashish et al. 2008). This disruption of lipid membranes causes cellular edema and loss of functional integrity, which leads to histological changes and decreased liver function. In our experiments, we observed a tendency of a decrease in direct cholesterol transport via LDL and significant increase in reverse cholesterol transport via HDL (Table 2). An explanation for these findings could be that cholesterol synthesis, uptake, and degradation in liver decreased under SMF influence. As a consequence, there was a tendency of serum total cholesterol increase in exposed animals, mainly due to HDL increase. HDL is a major serum lipoprotein in rodents and its fluctuation affects total serum cholesterol to a significant extent (Lizenko et al. 2008). In previously conducted experiments, increased serum total cholesterol was accompanied by an increase in serum triglycerides (Lahbib et al. 2010), which we did not observe. The increase in serum triglycerides observed in their experiment could be due to different duration of applied SMF.

In the kidney, as in the liver, an inflammatory infiltrate was present in SMF exposed animals, causing nonspecific pyelonephritis (Fig. 2). The extent of this infiltrate was more pronounced in the down group. Other studies showed that besides the liver, SMF of 128 mT can also cause decreased activity of anti-oxidative enzymes in the kidney that leads to increased lipid peroxidation and oxidative stress (Amara et al. 2007, Ghodbane et al. 2011). We reported here morphological changes in the kidney as reflected by infiltration of various inflammatory cells (Fig. 3). Furthermore, we showed that morphological changes, observed in the kidney and liver of exposed animals, were more profound in the down group (Table 1). The specificity of our findings in the liver and kidney was confirmed by histological analysis of spleen, where no inflammation was observed (Fig. 2, Table 1).

In contrast to the liver and kidney, the brain showed edematous changes in upward exposed animals (Table 1, Fig. 2). Various animal studies showed that SMF causes increased blood-brain permeability (Saunders 2005). SMF can also induce changes in Na/K pump redistribution especially in the cytoplasm of affected neurons (Nikolić et al. 2013). Increased permeability of the blood-brain barrier and functional changes in Na/K pump can cause neuron swelling. It was shown that 128 mT SMF induces hypoxia-like status in exposed rats (Elferchichi et al. 2007). When hypoxia develops, one of the

first organs that are affected is the brain, with intraneuronal edema that we observed in the up group (Fig. 2).

Spleen cellularity is bound to the amount of RBC and WBC in serum. WBC consists of granulocytes and lymphocytes. Lymphocytes make the majority of WBC in mice (Green 1966). Analysis of the spleen has revealed a significant increase in spleen total cellularity (RBC and WBC together) in the up group (Fig. 5, panel A). This is a consequence of a fact that even a small increase in percentage of lymphocytes could cause a large increase in total spleen cellularity. We also observed a significant decrease in spleen granulocyte count in exposed animals (up and down) (Fig. 5, panel C) with concomitant decrease in serum granulocytes found mainly in the down group (Fig. 4, panel C). Previous research also showed a decrease in splenic granulocytes under the influence of SMF that was explained by increased phagocytosis and oxidative stress followed by death of granulocytes (Elferchichi et al. 2007). In our case, serum WBC and lymphocytes were also decreased in both exposed groups (Fig. 4, panel A and panel D). The total serum WBC reduction was probably a consequence of lymphocyte redistribution among the serum and various tissues. Namely, a decrease in serum lymphocytes in both groups of exposed animals (Fig. 4, panel D) was followed by an increase in lymphocyte content in the liver and kidney (Fig. 2 and Fig. 3).

Red blood cell count did not statistically change in the blood or in the spleen between exposed and unexposed animals. Additionally, there were no changes in hemoglobin content or in MCV, MCH, and MCHC values among groups (Table 2). This is in accordance with findings that rats exposed to a magnetic field of extremely low frequency for 50 and 100 days did not show alteration in RBC count (Cakir et al. 2009). Additionally, a previous study also showed that SMF of moderate intensity do not influence plasma red blood cell count (Elferchichi et al. 2007). We concluded that various intensities of magnetic fields and different exposure times do not influence RBC count in the blood and spleen of experimental animals. This is probably due to diamagnetic property of RBC and fast recovery of RBC after exposure to SMF (Schenck 2005).

Previous research showed that SMF influences the biological system by causing pro-inflammatory changes and an increase in production of reactive oxygen species (Sahebjamei et al. 2007, Hashish et al. 2008, Zhao et al. 2011, Todorović et al. 2015). Namely, these studies stated that SMF increased phagocytosis and death of granulocytes, associated with production of free radicals. Our experiments showed a redistribution of granulocytes and lymphocytes that was dependent upon SMF orientation. In addition, previous studies (Bras et al. 1998, Chionna et al. 2003) demonstrated cytoskeleton reorganization and modulation of orientation of lymphocytes following exposure to moderate static magnetic field. They hypothesized that some sublethal damage persists in the cells, even

when the cell morphology still seems to be normal, since it is known that SMF interferes with DNA repair processes (Ghodbane et al. 2013). Our observed inflammatory changes in the liver and kidney of exposed animals may not be connected to the previously observed oxidative stress (Amara et al. 2007). It has been suggested that SMF increases the level of acetylcholine by enhancing its release and by decreasing its degradation (Xu et al. 2011). Increased level of acetylcholine induces blood vessel dilatation and permeability that leads to granulocyte and lymphocyte infiltration of the surrounding tissue. However, another study showed that inhomogeneous SMF could inhibit the release of pro-inflammatory cytokines IL-6, IL-8, and TNF- α from leukocytes (Vergallo et al. 2013). The inhibition of release of pro-inflammatory cytokines from granulocytes and lymphocytes could be the factor explaining the absence of CRP increase in our experiment despite inflammatory changes in the observed tissue (Pepys and Hirschfield 2003). Here, presented results have been obtained in a very controlled environment with the outbred strain, which renders them even more significant.

Conclusion

We investigated the influence of downward- and upward-oriented homogeneous SMF of 128 mT on subacutely exposed mice. Our results suggested that SMF of moderate intensity produced pro-inflammatory effects that depended on its orientation. We discovered that upward-oriented SMF caused changes in the serum, spleen, kidney, and brain, while downward-oriented SMF influenced the serum, kidney, and liver. Observed changes varied from brain edema and alterations in blood total WBC count and spleen granulocyte count to inflammation of the liver and kidney. Mechanisms that led to inflammation of affected organs were direct infiltration of inflammatory cells, whereas, in the case of liver, we also found an increase of pro-inflammatory palmitic fatty acid and a decrease in anti-inflammatory α -linolenic fatty acid. Further studies are needed to fully understand these processes.

Acknowledgment This study was supported by the grant numbers III-41013, III-41019, III-41030, III-45003, and III-45006 from the Ministry of Education, Science and Technological Development, Government of Serbia. The experiment was performed at the Vinča Institute of Nuclear Sciences, Laboratory of Physics (010) to whose staff we thank for enabling access to the Cyclotron, as well as for their assistance and support.

Conflict of interest The authors declare that they have no competing interests.

Role of funding source No funding body had any involvement in the preparation or content of this article or in the decision to submit it for publication.

References

- Abdelmelek H, Molnar S, Servais S, Cottet-Emard JM, Pequignot JM, Favier R, Sakly M (2006) Skeletal muscle HSP72 and norepinephrine response to static magnetic field in rat. *J Neural Transm* 113: 821–827
- Amara S, Abdelmelek H, Garrel C, Guiraud P, Douki T, Ravanat J, Favier A, Sakly M, Ben Rhouma K (2007) Zinc supplementation ameliorates static magnetic field-induced oxidative stress in rat tissues. *Environ Toxicol Pharmacol* 23:193–197
- Amara S, Douki T, Garel C, Favier A, Sakly M, Ben Rhouma K, Abdelmelek H (2009) Effects of static magnetic field exposure on antioxidative enzymes activity and DNA in rat brain. *Gen Physiol Biophys* 28:260–265
- Bancroft JD, Gamble M (2001) *Theory and practice of histological techniques*. 5th ed. Churchill Livingstone, Edinburgh
- Barry SM, Condez A, Johnson MA, Janossy G (2002) Determination of bronchoalveolar lavage leukocyte populations by flow cytometry in patients investigated for respiratory disease. *Cytometry* 50(6): 291–297
- Bras W, Diakun GP, DíazJF MG, Kramer H, Bordas J, Medrano FJ (1998) The susceptibility of pure tubulin to high magnetic fields: a magnetic birefringence and X-ray fiber diffraction study. *Biophys J* 74:1509–1521
- Cakir DU, Yokus B, Akdag MZ, Sert C, Mete N (2009) Alterations of hematological variations in rats exposed to extremely low frequency magnetic fields (50 Hz). *Arch Med Res* 40:352–356
- Chater S, Abdelmelek H, Douki T, Garrel C, Favier A, Sakly M, Ben Rhouma K (2006) Exposure to static magnetic field of pregnant rats induces hepatic GSH elevation but not oxidative DNA damage in liver and kidney. *Arch Med Res* 37:941–946
- Chionna A, Dwikat M, Panzarini E, Tenuzzo B, Carlà EC, Verri T, Pagliara P, Abbro L, Dini L (2003) Cell shape and plasma membrane alterations after static magnetic fields exposure. *Eur J Histochem* 47(4):299–308
- Colbert AP, Wahbeh H, Harling N, Connelly E, Schiffke HC, Forsten C, Gregory WL, Markov MS, Souder JJ, Elmer P, King V (2009) Static magnetic field therapy: a critical review of treatment parameters. *Evid-Based Complement Alternat Med* 6:133–139
- Csillag A, Kumar BV, Szabó K, Szilasi M, Papp Z, Szilasi ME, Pázmándi K, Boldogh I, Rajnavölgyi É, Bácsi A, László JF (2014) Exposure to inhomogeneous static magnetic field beneficially affects allergic inflammation in a murine model. *J R Soc Interface* 11:20140097
- Cvetković Z, Vučić V, Cvetković B, Petrović M, Ristić-Medić D, Tepšić J, Glibetić M (2010) Abnormal fatty acid distribution of the serum phospholipids of patients with non-Hodgkin lymphoma. *Ann Hematol* 89:775–782
- Ćirković S, Ristić-Djurović JL, Ilić AŽ, Vujović V, Nešković N (2008) Comparative analysis of methods for isochronous magnetic field calculation. *IEEE Trans Nucl Sci* 55(6):3531–3538
- Ćirković S, Ristić-Djurović JL, Vorozhtsov AS, Ilić AŽ, Nešković N (2009) Method for fine magnet shaping in cyclotrons. *IEEE Trans Nucl Sci* 56(5):2821–2827
- Dini L, Abbro L (2005) Bioeffects of moderate-intensity static magnetic fields. *Micron* 36:195–217
- Djordjević DM, De Luka SR, Milovanovich ID, Janković S, Stefanović S, Vesković-Moračanin S, Ćirković S, Ilić AŽ, Ristić-Djurović JL, Trbović AM (2012) Hematological parameters' changes in mice subchronically exposed to static magnetic fields of different orientations. *Ecotoxicol Environ Saf* 81:98–105
- Elferchichi M, Abdelmelek H, Sakly M (2007) Effects of sub-acute exposure to static magnetic field on iron status and hematopoiesis in rats. *Turk J Hematol* 24:64–68
- Elferchichi M, Mercier J, Coisy-Quivy M, Metz L, Lajoix A, Rene Gross R, Belguith H, Abdelmelek H, Sakly M, Lambert K (2010) Effects

- of exposure to a 128-mT static magnetic field on glucose and lipid metabolism in serum and skeletal muscle of rats. *Arch Med Res* 41: 309–314
- Erdines N, Shmueli O, Grossman Y, Ovadia H, Solomon A (2012) Anti-inflammatory effects of alpha linolenic acid on human corneal epithelial cells. *Invest Ophthalmol Vis Sci* 53(8):4396–406
- Felgar RE, Macon WR, Kinney MC, Roberts S, Pasha T, Salhany KE (1997) TIA-1 expression in lymphoid neoplasms. Identification of subsets with cytotoxic T lymphocyte or natural killer cell differentiation. *Am J Pathol* 150:1893–1900
- Folch J, Lees M, Sloane Stanley GH (1957) A simple method for the isolation and purification of total lipids from animal tissues. *J Biol Chem* 226(1):497–509
- Ghodbane S, Amara S, Garrel C, Arnaud J, Ducros V, Favier A, Sakly M, Abdelmelek H (2011) Selenium supplementation ameliorates static magnetic field-induced disorders in antioxidant status in rat tissues. *Environ Toxicol Pharmacol* 31:100–106
- Ghodbane S, Lahbib A, Sakly M, Abdelmelek H (2013) Bioeffects of static magnetic fields: oxidative stress, genotoxic effects and cancer studies. *Biomed Res Int* 2013:602987. doi:10.1155/2013/602987
- Ghodbane S, Amara S, Lahbib A, Louchami K, Sener A, Sakly M, Abdelmelek H (2014) Vitamin E prevents glucose metabolism alterations induced by static magnetic field in rats. *Environ Sci Poll Res* 21(22):12731–12738
- Green EL (1966) *Biology of the laboratory mouse*. Dover publications, New York
- Hashish AH, El-Missiry MA, Abdelkader HI, Abou-Saleh RH (2008) Assessment of biological changes of continuous whole body exposure to static magnetic field and extremely low frequency electromagnetic fields in mice. *Ecotoxicol Environ Saf* 71:895–902
- Heinrich A, Szostek A, Nees F, Meyer P, Semmler W, Flor H (2011) Effects of static magnetic fields on cognition, vital signs, and sensory perception: a meta analysis. *J Magn Reson Imaging* 34(4):758–763
- Kiss B, László JF, Szalai A, Pórszász R (2015) Analysis of the effect of locally applied inhomogeneous static magnetic field-exposure on mouse ear edema—a double blind study. *PLoS ONE* 10(2), e0118089
- Kremmyda L-S, Tvrzicka E, Stankova B, Zak A (2011) Fatty acids as biocompounds: their role in human metabolism, health and disease—a review. Part 2: fatty acid physiological roles and applications in human health and disease. *Biomed Pap Med Fac Univ Palacky Olomouc Czech Repub* 155(3):195–218
- Lahbib A, Elferchichi M, Ghodbane S, Belguith H, Chater S, Sakly M, Abdelmelek H (2010) Time-dependent effects of exposure to static magnetic field on glucose and lipid metabolism in rat. *Gen Physiol Biophys* 29:390–395
- László J, Reiczgel J, Székely L, Gasparics A, Bogár I, Bors L, Rác B, Gyires K (2007) Optimization of static magnetic field parameters improves analgesic effect in mice. *Bioelectromagnetics* 28:615–627. doi:10.1002/bem.20341
- László J, Gyires K (2009) 3 T homogeneous static magnetic field of a clinical MR significantly inhibits pain in mice. *Life Sci* 84:12–17
- László JF, Hernádi L (2012) Whole body static magnetic field exposure increases thermal nociceptive threshold in the snail, *Helix pomatia*. *Acta Biol Hung* 63(4):441–452
- László JF, Farkas P, Reiczgel J, Vágó P (2012) Effect of local exposure to inhomogeneous static magnetic field on stomatological pain sensation—a double-blind, randomized, placebo-controlled study. *Int J Radiat Biol* 88(5):430–438
- Lizenko MV, Regerand TI, Bakhirev AM, Lizenko EI (2008) Comparative biochemical analysis of lipids of blood serum-lipoproteins of human and some animal species. *J Evol Biochem Physiol* 44(5):581–590
- McGarry JD (2002) Lipid metabolism I. In: Devlin TM (ed) *Textbook of biochemistry with clinical correlations*, 5th edn. Wiley-Liss, New York, pp 693–726
- Mihoub M, El May A, Aloui A, Chatti A, Landoulsi A (2012) Effects of static magnetic fields on growth and membrane lipid composition of *Salmonella typhimurium* wild-type and dam mutant strains. *Int J Food Microbiol* 157:259–266
- Nešković N, Ristić-Djurović J, Vorojtsov SB, Beličev P, Ivanenko IA, Čirković S, Vorozhtsov AS, Bojović B, Dobrosavljević A, Vujović V, Čomor JJ, Pajović SB (2003) Status report of the VINCY Cyclotron, *Nukleonika* vol. 48 suppl. 2 (2003),—Special Issue—Proc. of the XXXIII European Cyclotron Progress Meeting, Warsaw and Krakow, Poland, September, 17–21, 2002, S135–S139
- Nikolić L, Batavejčić D, Andjus PR, Nedeljković M, Todorović D, Janać B (2013) Changes in the expression and current of the Na⁺/K⁺ pump in the snail nervous system after exposure to a static magnetic field. *J Exp Biol* 216(18):3531–3541
- Oguzhan B, Sancho V, Acitores A, Villanueva-Peñacarrillo M-L, Portois L, Chardigny J-M, Sener A, Carpentier YA, Malaisse WJ (2006) Alteration of adipocyte metabolism in ω 3 fatty acid-depleted rats. *Horm Metab Res* 38(12):789–798
- Pepys MB, Hirschfield GM (2003) C-reactive protein: a critical update. *J Clin Invest* 111:1805–1812
- Perona JS, Vögler O, Sánchez-Domínguez JM, Montero E, Escribá PV, Ruiz-Gutiérrez V (2007) Consumption of virgin olive oil influences membrane lipid composition and regulates intracellular signaling in elderly adults with type 2 diabetes mellitus. *J Gerontol A Biol Sci Med Sci* 62(3):256–263
- Pinkus GS, Said JW (1988) Hodgkin's disease, lymphocyte predominance type, nodular-further evidence for a B cell derivation. L & H variants of Reed-Sternberg cells express L26, a pan B cell marker. *Am J Pathol* 133:211–217
- Poniedziałek B, Rzymiski P, Karczewski J, Jaroszyk F, Wiktorowicz K (2013) Reactive oxygen species (ROS) production in human peripheral blood neutrophils exposed in vitro to static magnetic field. *Electromagn Biol Med* 32(4):560–568
- Ren J, Han EJ, Chung SH (2007) In vivo and in vitro anti-inflammatory activities of alpha-linolenic acid isolated from *Actinidia polygama* fruits. *Arch Pharm Res* 30(6):708–714
- Rigotti A, Marzolo MP, Nervi F (1994) Lipid transport from the hepatocyte into the bile. *Curr Top Memb* 40:579–615
- Rosen AD (1993) A proposed mechanism for the action of strong static magnetic fields on biomembranes. *Int J Neurosci* 73:115–119
- Rosen AD (2003) Mechanism of action of moderate-intensity static magnetic fields on biological systems. *Cell Biochem Biophys* 39(2): 163–173
- Sahebamei H, Abdolmaleki P, Ghanati F (2007) Effects of magnetic field on the antioxidant enzyme activities of suspension-cultured tobacco cells. *Bioelectromagnetics* 28:42–47
- Saunders R (2005) Static magnetic fields: animal studies. *Prog Biophys Mol Biol* 87:225–239
- Schenck JF (2005) Physical interactions of static magnetic fields with living tissues. *Prog Biophys Mol Biol* 87:185–204
- Soto-Vaca A, Losso JN, McDonough K, Finley JW (2013) Differential effect of 14 free fatty acids in the expression of inflammation markers on human arterial coronary cells. *J Agric Food Chem* 61(42):10074–10079
- Staiger H, Staiger K, Stefan N, Wahl HG, Machicao F, Kellerer M, Häring HU (2004) Palmitate-induced interleukin-6 expression in human coronary artery endothelial cells. *Diabetes* 53:3209–3216
- Tepšić V, Pavlović M, Ristić-Medić D, Ristić V, Lekić N, Tepšić J, Debeljak-Martačić J, Milićević M, Glibetić M (2008) Influence of dietary fats on serum phospholipid fatty acid composition and its relation to obesity in animals. *Acta Vet* 58:33–41
- Todorović D, Perić-Mataruga V, Mirčić D, Ristić-Djurović J, Prolić Z, Petković B, Savić T (2015) Estimation of changes in fitness components and antioxidant defense of *Drosophila subobscura* (Insecta, Diptera) after exposure to 2.4 T strong magnetic field. *Environ Sci Pollut Res* 22:5305–5314. doi:10.1007/s11356-014-3910-8

- Vergallo C, Dini L, Szamosvölgyi Z, Tenuzzo BA, Carata E, Panzarini E, László JF (2013) In vitro analysis of the anti-inflammatory effect of inhomogeneous static magnetic field-exposure on human macrophages and lymphocytes. *PLoS ONE* 8(8), e72374
- Watanabe Y, Nakagawa M, Miyakoshi Y (1997) Enhancement of lipid peroxidation in the liver of mice exposed to magnetic field. *Industrial Health* 35:285–230
- Wu D, Liu J, Pang X, Wang S, Zhao J, Zhang X, Feng L (2014) Palmitic acid exerts pro-inflammatory effects on vascular smooth muscle cells by inducing the expression of C-reactive protein, inducible nitric oxide synthase and tumor necrosis factor- α . *Int J Mol Med* 34(6):1706–12
- Xu S, Okano H, Tomita N, Ikada Y (2011) Recovery effects of a 180 mT static magnetic field on bone mineral density of osteoporotic lumbar vertebrae in ovariectomized rats. *eCAM* 2011:ID620984:1–8
- Zhao G, Chen S, Wang L, Zhao Y, Wang J, Wang X, Zhang WW, Wu R, Wu L, Wu Y, Xu A (2011) Cellular ATP content was decreased by a homogeneous 8.5 T static magnetic field exposure: role of reactive oxygen species. *Bioelectromagnetics* 32:94–101
- Zhou BR, Zhang JA, Zhang Q, Permatasari F, Xu Y, Wu D, Yin ZQ, Luo D (2013) Palmitic acid induces production of proinflammatory cytokines interleukin-6, interleukin-1 β , and tumor necrosis factor- α via a Nf- κ B-dependent mechanism in HaCaT keratinocytes. *Mediators Inflamm* 2013:530429. doi:10.1155/2013/530429

3. K. Guven, M.D. Caliskan, and E. Ozbay, Experimental observation of left-handed transmission in a bilayer metamaterial under normal-to-plane propagation, *Opt Express* 14 (2006), 8685–8693.
4. M. Kafesaki, I. Tsiapa, N. Katsarakis, Th. Koschny, C.M. Soukoulis, and E.N. Economou, Left-handed metamaterials: The fishnet structure and its variations, *Phys Rev B* 75 (2007), 235114.
5. Z. Li, M. Mutlu, and E. Ozbay, Chiral metamaterials: From optical activity and negative refractive index to asymmetric transmission, *J Opt* 15 (2013), 1.
6. W. Bingnan, Z. Jiangfeng, T. Koschny, M. Kafesaki, and C.M. Soukoulis, Chiral metamaterials: simulations and experiments, *J Opt A: Pure Appl Opt* 11 (2009), 114003.
7. N. Papisimakis, V.A. Fedotov, K. Marinov, and N.I. Zheludev, Gyrotropy of a metamolecule: Wire on a torus, *Phys Rev Lett* 103 (2009), 093901.
8. L. Wu, Z.Y. Yang, Y. Cheng, Z. Lu, P. Zhang, M. Zhao, R. Gong, X. Yuan, Y. Zheng, and J. Duan, Electromagnetic manifestation of chirality in layer-by-layer chiral metamaterials, *Opt Express* 21 (2013), 5239–5246.
9. J.A. Kong, *Electromagnetic wave theory*, EMW Publishing, Cambridge, 2008.
10. J. Haiping and Z. Baoing, A double-layer metamaterial with negative refractive index originating from chiral configuration, *Microwave Opt Technol Lett* 53 (2011), 163–166.
11. R. Marques, L. Jelinek, and F. Mesa, Negative refraction from balanced quasi-planar chiral inclusions, *Microwave Opt Technol Lett* 49 (2007), 2606.
12. J.D. Baena, L. Jelinek, and R. Marques, Towards a systematic design of isotropic bulk magnetic metamaterials using the cubic point groups of symmetry, *Phys Rev B* 76 (2007), 245115.
13. B. Wang, J. Zhou, T. Koschny, and C.M. Soukoulis, Nonplanar chiral metamaterials with negative index, *Appl Phys Lett* 94 (2009), 151112.
14. E. Plum, J. Zhou, J. Dong, V.A. Fedotov, T. Koschny, C.M. Soukoulis, and N.I. Zheludev, Metamaterial with negative index due to chirality, *Phys Rev B* 79 (2009), 035407.
15. J. Zhou, J. Dong, B. Wang, T. Koschny, M. Kafesaki, and C.M. Soukoulis, Negative refractive index due to chirality, *Phys Rev B* 79 (2009), 121104.
16. J. F. Dong, J. F. Zhou, T. Koschny, and C. Soukoulis, Bi-layer cross chiral structure with strong optical activity and negative refractive index, *Opt Express* 17 (2009), 14172.
17. R. Zhao, L. Zhang, J. Zhou, T. Koschny, and C. M. Soukoulis, Conjugated gammadion chiral metamaterial with uniaxial optical activity and negative refractive index, *Phys Rev B* 83 (2011), 035105.
18. D. Zarifi, M. Soleimani, and V. Nayyeri, Dual- and multiband chiral metamaterial structures with strong optical activity and negative refraction index, *IEEE Antennas Wireless Propag Lett* 11 (2012), 334–337.
19. J. Li, F.Q. Yang, Z. Wang, and J.F. Dong, Design and simulation of chiral negative refractive structure based on folded-wire, *Acta Phys Sin* 60 (2011), 114101.
20. Z. Li, R. Zhao, T. Koschny, M. Kafesaki, and C.M. Soukoulis, Chiral metamaterials with negative refractive index based on four U split ring resonators, *Appl Phys Lett* 97 (2010), 081901.
21. H. Jiaming, Y. Yu, R. Lixin, J. Tao, J.A. Kong, C.T. Chan, and Z. Lei, Manipulating electromagnetic wave polarizations by anisotropic metamaterials, *Phys Rev Lett* 99 (2007), 063908.
22. M. Multu, and E. Ozbay, A transparent 90° polarization rotator by combining chirality and electromagnetic wave tunneling, *Appl Phys Lett* 100 (2012), 051909.
23. B. Wang, T. Koschny, and C.M. Soukoulis, Wide-angle and polarization-independent chiral metamaterial absorber, *Phys Rev B* 80 (2009), 033108.
24. D.K. Rongas, S.A. Amanatiadis, A.I. Dimitriadis, and N.V. Kantartzis, Directivity-enhanced log-spiral antenna through a chiral metamaterial superstrate, In: 7th European conference on antennas and propagation (EuCAP), 2007, p 2079.
25. D. Zarifi, H. Oraizi, and M. Soleimani, Improved performance of circularly polarized antenna using semi-planar chiral metamaterial covers, *Prog Electromagn Res* 123 (2012), 337–354.
26. M. Huang, M. Lv, J. Huang, and Z. Wu, A new type of combined element multiband frequency selective surface, *IEEE Trans Antennas Propag* 57 (2009), 1798–1803.
27. M.H. Li, S.Y. Liu, L.Y. Guo, H. Lin, H.L. Yang, B.X. Xiao, Influence of the dielectric-spacer thickness on the dual-band metamaterial absorber, *Opt Commun* 295 (2013), 262.
28. C. Menzel, C. Rockstuhl, and F. Lederer, Advanced jones calculus for the classification of periodic metamaterials, *Phys Rev A* 82 (2010), 053811.
29. M. Pu, P. Chen, Y. Wang, Z. Zhao, C. Huang, C. Wang, X. Ma, and X. Luo, Anisotropic meta-mirror for achromatic electromagnetic polarization manipulation, *Appl Phys Lett* 102 (2013), 131906.
30. Y. Yuqian, L. Xuan, Z. Fei, and C. Shuwei, Homogeneous circular polarizers using a bilayered chiral metamaterial, *Appl Phys Lett* 99 (2011), 031111.
31. R. Zhao, T. Koschny, and C.M. Soukoulis, Chiral metamaterials: Retrieval of the effective parameters with and without substrate, *Opt Express* 18 (2010), 14553.
32. L. Xie, H.L. Yang, X. Huang, and Z. Li, Multi-band circular polarizer using archimedean spiral structure chiral metamaterial with zero and negative refractive index, *Prog Electromagn Res* 141 (2013), 645–657.
33. J.F. Wang, S. Qu, Z. Xu, J. Zhang, H. Ma, Y. Yang, and C. Gu, Broadband planar left-handed metamaterials using split-ring resonator pairs, *Photonics Nanostruct Fundam Appl* 7 (2009), 108–113.

© 2014 Wiley Periodicals, Inc.

ELECTROMAGNETIC ANALYSIS OF GRAPHENE BASED TUNABLE WAVEGUIDE RESONATORS

Andjelija Ž. Ilić^{1,2} and Djurdj Budimir³

¹Innovation Center, School of Electrical Engineering, University of Belgrade, 11120, Belgrade, Serbia

²Wireless Communication Research Group, University of Westminster, London, W1W 6UW, United Kingdom

³Faculty of Science and Technology, Wireless Communication Research Group, University of Westminster, London, W1W 6UW, United Kingdom; Corresponding author: d.budimir@wmin.ac.uk

Received 8 February 2014

ABSTRACT: *The electromagnetic analysis of the proposed graphene based tunable waveguide resonators for submillimeter-wave applications is presented. Simple design based on the conventional E-plane resonator is considered. The desired tunability up to 5% is provided by the change of the effective resonator length. Simulation results are presented to validate the argument.* © 2014 Wiley Periodicals, Inc. *Microwave Opt Technol Lett* 56:2385–2388, 2014; View this article online at wileyonlinelibrary.com. DOI 10.1002/mop.28603

Key words: *tunable waveguide resonators; tunable circuits and devices; submillimeter-wave devices; graphene*

1. INTRODUCTION

Expected trends for the multigigabit wireless communications require usage of large bandwidth available in the submillimeter frequency range [1–3]. In addition to the existing satellite and remote sensing applications as well as specialized biomedical and security purposes [4], plans for commercial wireless applications will likely motivate rapid technological progress in this area. Accordingly, there is a significant recent progress in the development of submillimeter-wave components [5–11]. Size, complexity, and cost of high frequency components are reduced when the tunable and/or reconfigurable components are used. Tunability and reconfigurability can be achieved through the

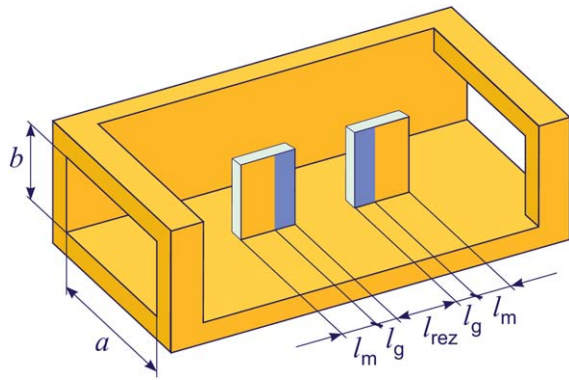


Figure 1 Inside view of a WR-3 (WG32) waveguide section with *E*-plane graphene based septa discontinuities. All-graphene and combined graphene-metal waveguide discontinuities are considered. [Color figure can be viewed in the online issue, which is available at wileyonlinelibrary.com]

usage of electronic tuning, magnetic tuning, optical switching, or microelectromechanical systems. For a particular application, selection of an approach is governed by the major limiting factor for each of the above groups, such as the inability of operation at higher frequencies (e.g., PIN diodes) or incapability of handling high power (e.g., MEMS, micro-electrical mechanical system). Relative shortage of naturally occurring materials with significant THz response left this frequency range, including the low THz and submillimeter-waves, largely unexplored. Recently, graphene emerged as an optimal solution in the design of tunable plasmonic antennas and other devices operating in the terahertz range [12–14]. It is already reported to be inefficient for the patch antenna design at microwaves (X–Ka band), and all our findings up to date were similar. The submillimeter and low terahertz frequency ranges have not yet been investigated in detail.

This investigation is focused on the 300 GHz frequency, likely to be much more used in the near future. We propose a novel class of tunable waveguide resonators incorporating graphene based waveguide discontinuities rather than switches made out of graphene. Graphene complex conductivity can be controlled electrostatically, magnetically, or optically, with the electrostatic tuning resulting in linear material response. Standard WR-3 (WG32) waveguide section is considered. A conventional *E*-plane resonator is replaced either with a conducting, two-dimensional graphene sheet, or with metal-graphene combined septa, with the graphene vertical stripe of length l_g located at the septa inner edges, that is, toward the center of a resonator structure as shown in Figure 1. Table 1 summarizes the relevant data, with the resonant frequency and attenuation levels given for the conventional *E*-plane resonator made out of copper with septa length $(l_m + l_g)$.

TABLE 1 Waveguide Resonator Dimensions and Frequency Range

Resonator Dimensions (μm)				
<i>A</i>	<i>B</i>	l_{rez}	l_g	l_m
863.6	431.8	360.0	120.0	200.0
Frequencies (GHz)			Attenuation (dB)	
$f_{\text{LO}} - f_{\text{HI}}$	f_{cutoff}	f_{rez}	$A_{\text{Cu,dc}}$	$A_{\text{Cu,smm}}$
220 – 325	173.28	300.0	0.43	0.60

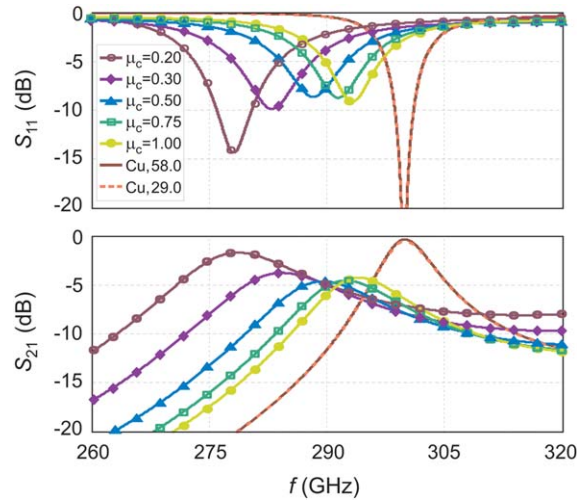


Figure 2 All-graphene based waveguide resonator. Significant tunability of 5% at 300 GHz can be achieved by varying graphene chemical potential via electrostatic biasing. [Color figure can be viewed in the online issue, which is available at wileyonlinelibrary.com]

Electromagnetic modeling and simulation of the structure is performed using the commercially available WIPL-D three-dimensional Electromagnetic Solver, CAE/CAM tool based on the higher order method of moments.

2. GRAPHENE BASED WAVEGUIDE RESONATORS

At 300 GHz, modeling of the structure must be performed with caution, that is, special care must be taken in the description of high frequency material properties to obtain highly accurate and reliable results. In our design, all of the metallic parts are assumed to consist of copper whose DC conductivity equals 58.0 MS/m. As the difference between the classical skin-effect model and Drude dispersion model for metals can become significant at higher terahertz frequencies, the relative error of the skin-effect model at 300 GHz is checked taking Drude dispersion as exact model. Conductivity error equals 0.8% resulting in the 0.4% impedance discrepancy. Surface roughness can reduce effective conductivity up to a factor of two at frequencies above 10 GHz [15], therefore, the analysis of an all-copper resonator of the given dimensions is repeated taking the effective conductivity of 29.0 MS/m. Both results, for 58.0 and 29.0 MS/m conductivity, are repeated as reference in Figure 2 through Figure 5 (shown in dark red and red, respectively). Numerical values in Table 1 correspond to the total simulated waveguide section length of 2.8 mm. The rest of the simulations are performed taking the DC conductivity for the skin-effect in copper. Losses in graphene prove dominant in comparison with copper as well as dielectric.

Due to its very good compatibility with graphene sheets, as well as high frequency properties, quartz is used as the needed dielectric holder material in all the simulations. Where a septum part is to be covered by the thin film of copper, that is, in graphene-metal resonators, a special technological process, such as preplating the quartz substrate with titanium would be needed to increase the thin film adhesivity. Thickness of the quartz holder is taken to be 50 μm , which is about the thinnest quartz wafer that is currently produced. Its relative dielectric constant equals 3.8 and high frequency loss tangent is 6×10^{-5} .

Frequencies of interest here are well below the graphene plasma roll-off frequency. Surface conductivity of graphene thus stems solely from the intraband contributions [16, 17]:

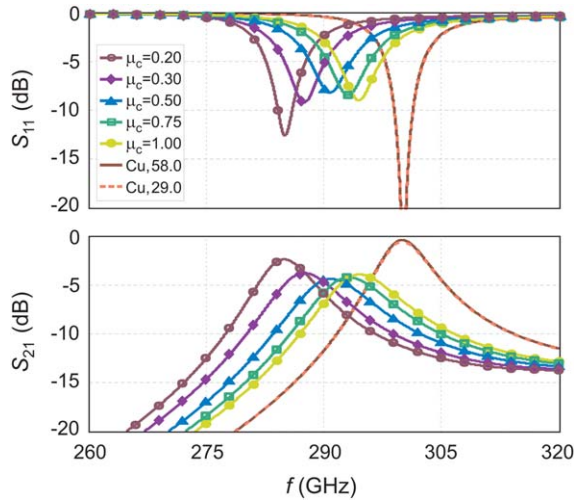


Figure 3 Graphene-metal combined waveguide resonator. Substantial quality factor improvement is obtained using the copper septa with the vertical inner-edge graphene stripes. [Color figure can be viewed in the online issue, which is available at wileyonlinelibrary.com]

$$\sigma(\omega, \mu_c, \Gamma, T) = \frac{-jq_c^2 k_B T}{\pi \hbar^2 (\omega - j2\Gamma)} \left(\frac{\mu_c}{k_B T} + 2 \ln \left(e^{-\frac{\mu_c}{k_B T}} + 1 \right) \right). \quad (1)$$

Therefore, the surface impedance of the graphene stripe or sheet equals $Z_S = R_S + j\omega L_S$, where the surface resistance and surface inductance can be calculated as

$$R_S = 2\Gamma \frac{q_c}{\hbar} L_S, \quad L_S = \frac{\pi \hbar^2}{q_c^2 k_B T \left(\frac{q_c \mu_c}{k_B T} + 2 \ln \left(e^{-\frac{q_c \mu_c}{k_B T}} + 1 \right) \right)}. \quad (2)$$

Electron charge, reduced Planck constant, and Boltzmann constant are denoted as $q_c, \hbar,$ and k_B . Angular electromagnetic field frequency is ω and the temperature is $T = 300$ K. The resistance to inductance ratio is constant and proportional to the phenomenological scattering rate $\Gamma = (2\tau)^{-1}$, that depends on the doping levels. Typical relaxation time $\tau = 1$ ps is taken here. There is one-to-one correspondence between the applied electrostatic bias voltage and the chemical potential μ_c , that can be used to tune the resonant frequency.

3. RESULTS AND DISCUSSION

3.1. All-Graphene Waveguide Resonators

Electrostatic tuning of graphene's surface conductivity produces an effect equivalent to varying the effective septum length on both edges. We assume $(l_m + l_g)$ long septum to be completely covered with atomically thin graphene sheet. Results shown in Figure 2 confirm that the desired 5% tunability can be easily achieved, with the acceptable losses. This tunability range is determined by the inductance to resistance ratio, that is, by the relaxation time τ . Higher levels of graphene doping are, therefore, more desirable.

3.2. Graphene-Metal Combined Waveguide Resonators

Coating only the septum inner edge, toward the center of the structure, with vertical graphene stripe of length, l_g , and covering the rest of the septum with the thin film of copper, we obtain combined graphene-copper resonators. Structure geometry is shown in Figure 1. As a result, effective resonator length is

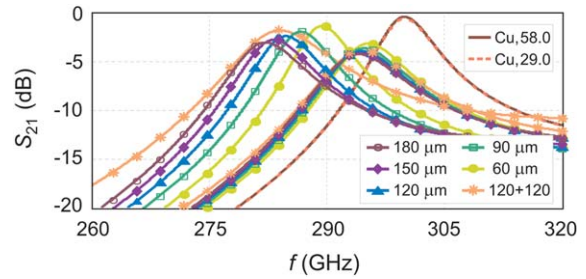


Figure 4 Effect of varying graphene stripe length l_g to the device tunability range. Graphene stripe should be taken as long as possible. Single example with two identical stripes at both septum ends is given for comparison. [Color figure can be viewed in the online issue, which is available at wileyonlinelibrary.com]

affected by varying the chemical potential μ_c , while the total resonator plus septa length is kept fixed. Due to the field distribution different from the previous case, losses corresponding to the $120 \mu\text{m}$ long graphene stripe are virtually the same as for the whole length of $320 \mu\text{m}$ graphene sheet. As seen from Figure 3, Q -factor is increased almost twice, that is, the change in S -parameters with frequency roughly follows the one corresponding to the all-copper case. Resonator tunability of 3.5% is obtained.

3.3. Effects of Varying Structure Parameters

Variation in resonator tunability range and graphene loss with the modification of the inner edge graphene stripe length, l_g , is illustrated in Figure 4. In conclusion, graphene stripe should be taken as long as possible. An example with two identical stripes at both septum ends with its central part covered with copper is shown as well (denoted by $120 + 120$). Comparing the two curves, for 120 and $120 \mu\text{m} + 120 \mu\text{m}$, we observe little impact in terms of loss and tunability, however, the Q -factor is significantly reduced in the second case. Finally, the effect of increasing total septum length while keeping constant the length of graphene stripe is shown in Figure 5. Along with some improvement in the loaded Q -factor, loss is significantly increased. This suggests that a trade-off between the Q -factor and tunability, if necessary, can be performed by increasing $(l_m + l_g)$ and simultaneously decreasing the graphene stripe length l_g .

4. CONCLUSIONS

The graphene based tunable waveguide resonators for the WR-3 (WG32) frequency range have been investigated using the full-wave electromagnetic analysis. Depending on the requirements,

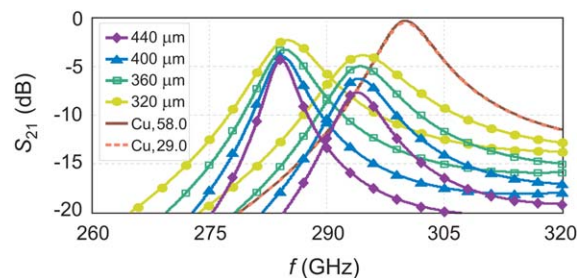


Figure 5 Effect of increasing septum length by increasing parameter l_m (keeping constant $l_g = 120 \mu\text{m}$). Trade-off between Q -factor, loss, and tunability can be achieved by simultaneously increasing $(l_m + l_g)$ and decreasing l_g . [Color figure can be viewed in the online issue, which is available at wileyonlinelibrary.com]

resonator can be all-graphene based or graphene-metal combined. Effects of varying structure parameters have been discussed. We have achieved tunability up to 5% with acceptable losses. More detailed analysis and filter design is under way.

ACKNOWLEDGMENT

This work was supported by the Serbian Ministry of Education, Science, and Technological Development under grant III-45003 and by the EU—Erasmus Mundus Action 2 project EUROWEB.

REFERENCES

1. T. Kleine-Ostmann and T. Nagatsuma, A review on terahertz communications research, *J Infrared Millim Terahertz Waves* 32 (2011), 143–171.
2. R. Piesiewicz, M. Jacob, M. Koch, J. Schoebel, and T. Kurner, Performance analysis of future multigigabit wireless communication systems at THz frequencies with highly directive antennas in realistic indoor environments, *IEEE J Sel Top Quantum Electron* 14 (2008), 421–430.
3. S. Priebe, C. Jastrow, M. Jacob, T. Kleine-Ostmann, T. Schrader, and T. Kurner, Channel and propagation measurements at 300GHz, *IEEE Trans Antennas Propag* 59 (2011), 1688–1698.
4. H. J. Hansen, Standoff detection using millimeter and submillimeter wave spectroscopy, *Proc IEEE* 95 (2007), 1691–1704.
5. H.-J. Song, K. Ajito, Y. Muramoto, A. Wakatsuki, T. Nagatsuma, and N. Kukutsu, 24 Gbit/s data transmission in 300 GHz band for future terahertz communications, *Electron Lett* 48 (2012), 953–954.
6. X. Shang, M. Ke, Y. Wang, and M.J. Lancaster, WR-3 band waveguides and filters fabricated using SU8 photoresist micromachining technology, *IEEE Trans Terahertz Sci Technol* 2 (2012), 629–637.
7. J. Hu, S. Xie, and Y. Zhang, Micromachined terahertz rectangular waveguide bandpass filter on silicon-substrate, *IEEE Microwave Wireless Compon Lett* 22 (2012), 636–638.
8. Z. Chen, Y. Zheng, X. Kang, B. Lu, and B. Cui, WR-2.8 band micromachined rectangular waveguide filter, *J Infrared Millim Terahertz Waves* 34 (2013), 847–855.
9. V. Furtula, H. Zirath, and M. Salewski, Waveguide bandpass filters for millimeter-wave radiometers, *J Infrared Millim Terahertz Waves* 34 (2013), 824–836.
10. V. Radisic, D. Sawdai, D. Scott, W.R. Deal, L. Dang, D. Li, J. Chen, A. Fung, L. Samoska, T. Gaier, and R. Lai, Demonstration of a 311 GHz fundamental oscillator using InP HBT technology, *IEEE Trans Microwave Theory Tech* 55 (2007), 2329–2335.
11. A. Maestrini, J.S. Ward, C. Tripon-Canseliet, J.J. Gill, C. Lee, H. Javadi, G. Chattopadhyay, and I. Mehdi, In-phase power-combined frequency triplers at 300 GHz, *IEEE Microwave Wireless Compon Lett* 18 (2008), 218–220.
12. M. Tamagnone, J.S. Gomez-Diaz, J.R. Mosig, and J. Perruisseau-Carrier, Reconfigurable terahertz plasmonic antenna concept using a graphene stack, *Appl Phys Lett* 101 (2012), 214102.
13. M. Dragoman, A.A. Muller, D. Dragoman, F. Coccetti, and R. Plana, Terahertz antenna based on graphene, *J Appl Phys* 107 (2010), 104313.
14. E. Carrasco, M. Tamagnone, and J. Perruisseau-Carrier, Tunable graphene reflective cells for THz reflectarrays and generalized law of reflection, *Appl Phys Lett* 102 (2013), 104103.
15. T. Liang, S. Hall, H. Heck, and G. Brist, A practical method for modeling PCB transmission lines with conductor surface roughness and wideband dielectric properties, In: *IEEE MTT-S International Microwave Symposium Digest*, San Francisco, CA, 2006, pp. 1780–1783.
16. G.W. Hanson, Dyadic Green's functions and guided surface waves for a surface conductivity model of graphene, *J Appl Phys* 103 (2008), 064302.
17. J.S. Gomez-Diaz, J. Perruisseau-Carrier, P. Sharma, and A. Ionescu, Non contact characterization of graphene surface impedance at micro and millimeter waves, *J Appl Phys* 111 (2012), 114908.

© 2014 Wiley Periodicals, Inc.

BROADBAND MONOPOLE ANTENNA WITH SPLIT RING RESONATOR LOADED SUBSTRATE FOR GOOD IMPEDANCE MATCHING

Ramasamy Pandeewari and Singaravelu Raghavan

Department of Electronics and Communication Engineering, National Institute of Technology, Tiruchirappalli, 620 015, Tamil Nadu, India; Corresponding author: rpands@nitt.edu

Received 15 February 2014

ABSTRACT: A coplanar waveguide-fed monopole antenna with split ring resonator (SRR) loaded substrate is introduced to obtain good impedance matching over a wide band of frequency. SRR is loaded on the backside of the substrate used to obtain a wideband covering from 3.87 to 7.63 GHz, which covers the 5 GHz WLAN and 5.8 GHz RFID applications. The size of the antenna is $31 \times 24.57 \times 1.6 \text{ mm}^3$. A prototype of the proposed antenna has been fabricated and measured. The radiation pattern measured at resonance is omnidirectional in the H-plane and bidirectional in the E-plane. Details of the proposed antenna design and measured results are presented and discussed. The measured peak antenna gain is 2.51 dBi. SRR characteristics are also discussed to validate the results and parametric study of SRR is also done. © 2014 Wiley Periodicals, Inc. *Microwave Opt Technol Lett* 56:2388–2392, 2014; View this article online at wileyonlinelibrary.com. DOI 10.1002/mop.28602

Key words: broadband antenna; impedance matching; metamaterial; monopole antenna; split ring resonator

1. INTRODUCTION

An exponential growth in the field of communication has created a great demand for broadband antennas for various wireless communication applications. Coplanar waveguide (CPW)-fed monopole antennas are appropriate for wideband wireless applications due to their attractive features like low profile, widebandwidth, good impedance matching, and omnidirectional radiation pattern. Impedance matching over a broad range of frequencies is a challenging one. Good impedance matching was obtained by changing the size of the ground plane, dimensions of the antenna, distance between feed point and ground [1–10]. Reactive lumped elements can also be used for good impedance matching [1]. Varactor diode was inserted in the monopole to make it resonate at low frequency and also for frequency reconfigurability. Reactive impedance substrate (RIS) for planar antenna increases the bandwidth and also reduces the size of the antenna [2]. RIS with proper choice of surface reactance is a key component for size miniaturization and bandwidth enhancement of the antenna. The interaction between the antenna and its image on the substrate was minimized by RIS which leads to good impedance matching. Substrate with high permittivity can also be used for size reduction but it reduces the efficiency of the antenna.

In the past decade, metamaterial with unusual properties were used for the enhancement of antenna parameters like bandwidth, gain, directivity, and size miniaturization [2–10]. Split ring resonator (SRR) is a basic component of metamaterial, which is designed to exhibit negative permeability over a certain range of microwave frequency. The various forms of SRR and their equivalent circuits were discussed [11]. Metamaterial substrate for antenna was constructed using array of SRR [12]. Metamaterial substrate reduces the size to a large extent but it decreases the gain and efficiency. This is mainly due to ohmic

IEEE TRANSACTIONS ON NUCLEAR SCIENCE

A PUBLICATION OF THE IEEE NUCLEAR AND PLASMA SCIENCES SOCIETY



DECEMBER 2013

VOLUME 60

NUMBER 6

IETNAE

(ISSN 0018-9499)

PART II OF TWO PARTS

SYMPOSIUM ON RADIATION MEASUREMENTS AND APPLICATIONS (SORMA WEST 2012)
OAKLAND, CA, USA, MAY 14–17, 2012

Development of an Ultrahigh Resolution Block Detector Based on 0.4 mm Pixel Ce:GAGG Scintillators and a Silicon
Photomultiplier Array *S. Yamamoto, J. Y. Yeom, K. Kamada, T. Endo, and C. S. Levin* 4582

18TH REAL TIME CONFERENCE (RT2012)
BERKELEY, CA, USA, JUNE 11-15, 2012

Time Measurement System Based on Waveform Digitization for Time-of-Flight Mass Spectrometer
..... *X. Hu, L. Zhao, C. Feng, W. Zheng, S. Liu, and Q. An* 4588

A Comprehensive Zero-Copy Architecture for High Performance Distributed Data Acquisition Over Advanced Network
Technologies for the CMS Experiment
..... *G. Bauer, U. Behrens, J. Branson, S. Bukowiec, O. Chaze, S. Cittolin, J. A. Coarasa Perez,
C. Deldicque, M. Dobson, A. Dupont, S. Erhan, D. Gigi, F. Glege, R. Gomez-Reino, C. Hartl, A. Holzner, L. Masetti,
F. Meijers, E. Meschi, R. K. Mommsen, C. Nunez-Barranco-Fernandez, V. O'Dell, L. Orsini, C. Paus, A. Petrucci,
M. Pieri, G. Polese, A. Racz, O. Raginel, H. Sakulin, M. Sani, C. Schwick, A. C. Spataru, F. Stoeckli, and K. Sumorok* 4595

Feedback Control of Loaded Q Values of the Superconducting Cavities at FLASH
..... *W. Cichalewski, J. Branlard, H. Schlarb, J. Carwardine, and A. Napieralski* 4603

19TH INTERNATIONAL WORKSHOP ON ROOM-TEMPERATURE SEMICONDUCTOR DETECTORS (RTSD)
ANAHEIM, CA, USA, OCTOBER 27–NOVEMBER 3, 2012

Tiled Array of Pixelated CZT Imaging Detectors for *ProtoEXIST2* and *MIRAX-HXI*
.. *J. Hong, B. Allen, J. Grindlay, B. Rodrigues, J. R. Ellis, R. Baker, S. Barthelmy, P. Mao, H. Miyasaka, and J. Apple* 4610

(Contents Continued on Page 4581)



REGULAR PAPERS

ACCELERATOR TECHNOLOGY

Magnet with Uncoupled Combined Functions	<i>J. L. Ristić-Djurović, S. Ćirković, and Ilić</i>	4618
Importance of Accurate Static Equilibrium Orbit Calculation in Cyclotron Design <i>A. Z. Ilić, J. L. Ristić-Djurović, and S. Ćirković</i>	4627

DIGITAL SIGNAL PROCESSING

Noise Analysis in Pulse-Processing Discrete-Time Filters	<i>D. Avila, E. Alvarez, and A. Abusleme</i>	4634
--	--	------

DOSIMETRY

Characterization and Simulation of a New Design Parallel-Plate Ionization Chamber for CT Dosimetry at Calibration Laboratories	<i>A. P. Perini, L. P. Neves, A. F. Maia, and L. V. E. Caldas</i>	4641
--	---	------

GAS DETECTORS

A Bi-Dimensional Multi-Wire Cathode Strip Detector for Fission Fragments	<i>R. P. Vind, D. C. Biswas, Y. K. Gupta, A. L. Inkar, R. V. Jangale, G. K. Prajapati, B. N. Joshi, B. V. John, B. K. Nayak, and R. K. Choudhury</i>	4650
Induced Charge Profile in a Glass RPC Operated in Avalanche Mode <i>S. Narita, Y. Hoshi, K. Neichi, and A. Yamaguchi</i>	4656

RADIATION EFFECTS

Atmospheric Radiation Environment Analyses Based-on CCD Camera, Neutron Spectrometer and Multi-Physics Modeling	<i>G. Hubert, A. Cheminet, T. Nuns, and V. Lacoste</i>	4660
Single-Event Transient Effect on a Self-Biased Ring-Oscillator PLL and an LC PLL Fabricated in SOS Technology <i>S. Guo, J. Li, P. Gui, Y. Ren, L. Chen, and B. L. Bhuva</i>	4668
Total and Partial Fragmentation Cross-Section of 500 MeV/nucleon Carbon Ions on Different Target Materials <i>B. Alpat, E. Pilicer, S. Blasko, D. Caraffini, F. D. Capua, V. Postolache, G. Saltanocchi, M. Menichelli, L. Desorgher, M. Durante, R. Pleskac, and C. L. Tessa</i>	4673
Field Oxide n-channel MOS Dosimeters Fabricated in CMOS Processes <i>J. Lipovetzky, M. A. García-Inza, S. Carbonetto, M. J. Carra, E. Redin, L. Sambuco Salomone, and A. Faigon</i>	4683
Neutron Induced Single Event Upset Dependence on Bias Voltage for CMOS SRAM With BPSG <i>A. Vázquez-Luque, J. Marín, J. A. Terrón, M. Pombar, R. Bedogni, F. Sánchez-Doblado, and F. Gómez</i>	4692
A New Method for Extracting the Radiation Induced Trapped Charge Density Along the STI Sidewall in the PDSOI NMOSFETs	<i>C. Peng, Z. Hu, Z. Zhang, H. Huang, B. Ning, D. Bi, and S. Zou</i>	4697
Characterization of an Innovative p-type Epitaxial Diode for Dosimetry in Modern External Beam Radiotherapy <i>A. Aldosari, A. Espinoza, D. Robinson, I. Fuduli, C. Porumb, S. Alshaikh, M. Carolan, M. Lerch, V. Perevertaylo, A. Rosenfeld, and M. Petasecca</i>	4705

RADIATION IMAGING

Charge Summing in Spectroscopic X-Ray Detectors With High-Z Sensors	<i>T. Koenig, E. Hamann, S. Procz, R. Ballabriga, A. Cecilia, M. Zuber, X. Llopart, M. Campbell, A. Fauler, T. Baumbach, and M. Fiederle</i>	4713
Characterization of a High Spatial Resolution γ Camera for Scanning HPGe Segmented Detectors <i>A. Hernández-Prieto and B. Quintana</i>	4719

RADIATION INSTRUMENTATION

Simulation Study of Using High-Z EMA to Suppress Recoil Protons Crosstalk in Scintillating Fiber Array for 14.1 MeV Neutron Imaging	<i>Q. Jia, H. Hu, F. Zhang, T. Zhang, W. Lv, Y. Zhan, and Z. Liu</i>	4727
---	--	------

READOUT ELECTRONICS

LAr TPC Electronics CMOS Lifetime at 300 K and 77 K and Reliability Under Thermal Cycling <i>S. Li, J. Ma, G. De Geronimo, H. Chen, and V. Radeka</i>	4737
---	---	------

2013 INDEX		4744
------------------	--	------

Importance of Accurate Static Equilibrium Orbit Calculation in Cyclotron Design

Andjelija Ž. Ilić, *Member, IEEE*, Jasna L. Ristić-Djurović, and Saša Ćirković

Abstract—Knowledge of the static equilibrium orbit properties is crucial for cyclotron design and development. With the increase of computational speed, numerical orbit calculations are more and more often employed as a part of other methods. Direct numerical integration of the canonical equations of motion is used most often for orbit calculations. We propose an original method for the calculation of static equilibrium orbit properties by direct trajectory tracking in the real, configuration space, and compare it with the method most commonly used.

Index Terms—Cyclotrons, magnetic fields, optimization methods, particle beam dynamics, static equilibrium orbit properties.

I. INTRODUCTION

STATIC EQUILIBRIUM ORBIT (SEO) calculations are an indispensable tool in the design and development of modern cyclotrons [1]–[7]. Since the cyclotron magnetic field has the double role in the process of acceleration, of guiding the ion beam bunch toward the field regions corresponding to the energies of ions and focusing the trajectories of ions, much of the accelerated orbit behavior can be deduced from the analysis of the field itself. Analytical expressions of different levels of complexity and accuracy [8], [9], developed over time, are nowadays almost completely abandoned in favor of numerical techniques. Numerical calculation of orbits for a large number of ion energy values gives a measure of quality of the designed magnetic field through its level of isochronism as well as the focusing properties. Computer codes for the simulation of ion beam acceleration using the well-known ray tracing method also rely on the SEO calculations. Namely, the transition matrix parameters used to transform the non-central trajectories about the central ray are determined from SEO analysis [10], [11].

Computational speed improvements over the last decades led us, as well as other authors, to employ the orbital frequency criterion as an error assessment tool in the iterative process of isochronous magnetic field calculation [12], [13], and iterative cyclotron magnet shimming [14]–[16]. We have also employed

the SEO calculation as a subroutine, used in the centering of trajectories, in the program module devoted to the optimization of accelerated equilibrium orbits (AEO) [17]. Precise SEO positioning played important role in determining of the focusing limit of a cyclotron using the beam dynamics simulation [18]. Whereas accurate calculation is important in the field analysis, it becomes an imperative when the SEO determination routines are used in the optimization process.

The SEO determination technique most commonly found in literature is based on direct numerical integration of the canonical equations of motion and is described in [1]. Static equilibrium orbit is defined as the closed orbit possessing the same N -fold symmetry as the guiding magnetic field, where N corresponds to the number of cyclotron magnetic sectors. It is unique for every considered particle energy. In numerical SEO analysis, there may be more than one appropriate closed orbit, concordant with numerical criteria, in the vicinity of the actual SEO. Highly accurate two-parameter optimization, used in [1] to locate the optimal closed orbit, is based on the well-known Newton iterative method. One of the major benefits of such iteration scheme is its rapid convergence when the error has been sufficiently reduced. On the other hand, the selected orbit is always the one closest to the initial guess, taken approximately for the first considered energy point and later extrapolated from the already obtained results.

During the design of the self-written software packages for ion beam dynamics VINDY and VINDY-A [17]–[20], we developed original algorithms for SEO determination. Same as the rest of the program modules written over time, the SEO calculation routines use the direct trajectory tracking in the real, configuration space, rather than solving the canonical equations of motion. Here we propose and describe the SEO determination method of a remarkable accuracy, used for different optimization purposes as described in [13], [14], and [17]. Two-parameter optimization of the SEO, used by our method, searches over the range of parameters in the vicinity of the optimal SEO in order to position it more precisely.

All of the presented examples use the layout and magnetic field maps given in [21]–[24]. The calculated isochronized magnetic field map corresponding to the H^- ion is used as an input in the evaluation of method performance. This particular field map is chosen due to the availability of data on the corresponding static equilibrium orbits calculated by CYCLOPS code described in [1]. Therefore, the method we propose is compared with the method most commonly used in literature. The accuracy of the method in dealing with the more realistic measured isochronized magnetic field is examined as well.

Manuscript received July 12, 2013; revised September 11, 2013; accepted September 27, 2013. Date of publication November 05, 2013; date of current version December 11, 2013. This work was supported in part by the Ministry of Education, Science and Technological Development of Serbia through the project III-45003.

The authors are with the Innovation Center, School of Electrical Engineering, University of Belgrade, 11120 Belgrade, Serbia (e-mail: andjelija.ili@ieee.org; jasna@stanfordalumni.org; kosjera@beotel.net).

Color versions of one or more of the figures in this paper are available online at <http://ieeexplore.ieee.org>.

Digital Object Identifier 10.1109/TNS.2013.2284194

II. METHOD DESCRIPTION

Two distinct numerical techniques need to be combined to provide the SEO analysis tool. The first one is the numerical integration of the trajectory of an ion, i.e., trajectory tracking. The other one is the optimization method used to determine the SEO. The insufficient accuracy of numerical integration directly translates into inaccurate orbit positioning regardless of optimization method used. This can be avoided easily, by setting stringent accuracy requirements. Optimization itself becomes a limiting factor for the SEO positioning in that case. The complete method description is built by treating its various parts in the following subsections.

A. Numerical Integration

The charged particle motion inside a cyclotron is described by general equations of particle motion in an electromagnetic field of electric field strength \mathbf{E} and magnetic induction \mathbf{B} :

$$\frac{d\mathbf{r}(t)}{dt} = \frac{1}{m_0} \sqrt{1 - \left(\frac{v(t)}{c}\right)^2} \mathbf{p}(t) \quad (1)$$

$$\frac{d\mathbf{p}(t)}{dt} = \frac{q}{m_0} \left(m_0 \mathbf{E}(t, \mathbf{r}) + \sqrt{1 - \left(\frac{v(t)}{c}\right)^2} \mathbf{p}(t) \times \mathbf{B}(\mathbf{r}) \right). \quad (2)$$

The position of the particle is \mathbf{r} , its momentum is \mathbf{p} , and v is the velocity intensity. The rest-mass of the particle is m_0 , q is the electric charge, and c is the speed of light. Equations (1) and (2) are solved using the adaptive time step Runge-Kutta method of the fourth order. The time step is chosen to comply with the two accuracy requirements: the maximal allowed local error of position calculation is x_{err} , while the local error of the momentum calculation must not exceed p_{err} , given as a fraction of the initial momentum. In the SEO analysis, the parameter p_{err} is recalculated for each considered energy. The two accuracy requirements are not fully independent from each other. High accuracy of position calculation inherently sets bounds on the momentum calculation error. As opposed to that, the local momentum error bound p_{err} alone is not limiting enough in the regions where the electric field is close to zero, which is the case with SEO analysis. In such cases it controls the momentum direction, as well as the constancy of the momentum intensity, important since the Runge-Kutta method is not symplectic. Combined, the two requirements result in an excellent control of the size of the time step.

B. Two-Parameter Optimization Requirements

The positioning of the SEO, for any given test ion energy T , comprises the optimization of exactly two parameters: the initial radial position and the initial momentum direction in the median plane of a cyclotron, where the SEO is located. Any initial azimuthal position is acceptable in the search for a closed orbit; therefore, a point at the midline of a sector or at the midline of a valley is often taken for simplicity. Due to the N -fold symmetry of orbits, radial coordinate as well as momentum direction angle of an ideal SEO should have identical values at the

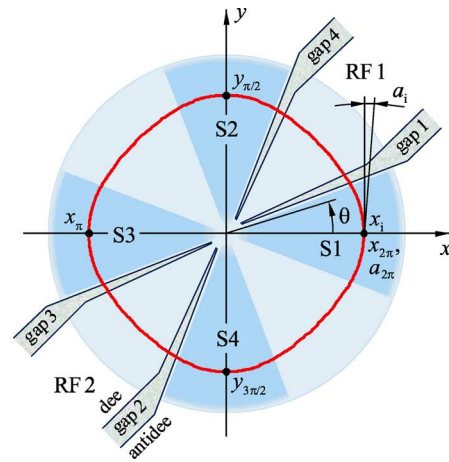


Fig. 1. The layout of a cyclotron and the coordinate system used. The control points along the integration path as well as the direction angles of the initial and final momentum vectors, used by our optimization criterion, are denoted on an example static equilibrium orbit.

cross-sections with all radial semi-axes, obtained by the rotation of positive x -axis by $360^\circ/N$. This requirement is virtually the same as the one imposed in [1]. If checked after a full turn, it defines the compliance with the perfectly closed orbit. The ideal closed orbit also has to be centered in the x - and y -direction in case of even N , or one of the two directions if N is odd. In the realistic magnetic fields, which are not perfectly symmetric, combinations of different requirements yield different results. It can be useful to define a number of control parameters, comprising ion position and momentum direction angle at various points along the path of integration. Weighting coefficients are used to choose among the predefined parameters of a flexible optimization criterion.

C. Optimization Criterion

For $N = 4$, as in our examples, it is convenient to take the cross-sections of the tracked orbits with the coordinate axes as the control points along the path of integration. Therefore, we employ the following optimization criterion:

$$f_{\text{oc}}(x_i, a_i) = w_1 \cdot (x_i + x_\pi)^2 + w_2 \cdot (y_{\pi/2} + y_{3\pi/2})^2 + w_3 \cdot (y_{\pi/2} + x_\pi)^2 + w_4 \cdot (x_i - x_{2\pi})^2 + w_5 \cdot (\sin(a_i) - \sin(a_{2\pi}))^2, \quad (3)$$

where x_i and a_i represent the considered initial radial position and initial momentum direction angle, respectively. Angle a_i is measured clockwise from the positive y -axis in the xy -plane. The coordinate system as well as the direction of increase of the azimuthal coordinate θ is defined in Fig. 1. Azimuth $\theta = 0$ coincides with the first sector midline. Test ion coordinates $y_{\pi/2}$, x_π , $y_{3\pi/2}$, $x_{2\pi}$ and $a_{2\pi}$, used as the control parameters, are obtained from the full-turn of the test ion trajectory tracking starting from (x_i, a_i) . The $\sin(a_i)$ and $\sin(a_{2\pi})$ in (3) correspond to the normalized momentum x -components, $P_{x,i}$ and $P_{x,2\pi}$. Optimization criterion is defined in a separate procedure, allowing simple addition of different criteria customized for various cases. As stated in the Subsection B, if N is odd orbit

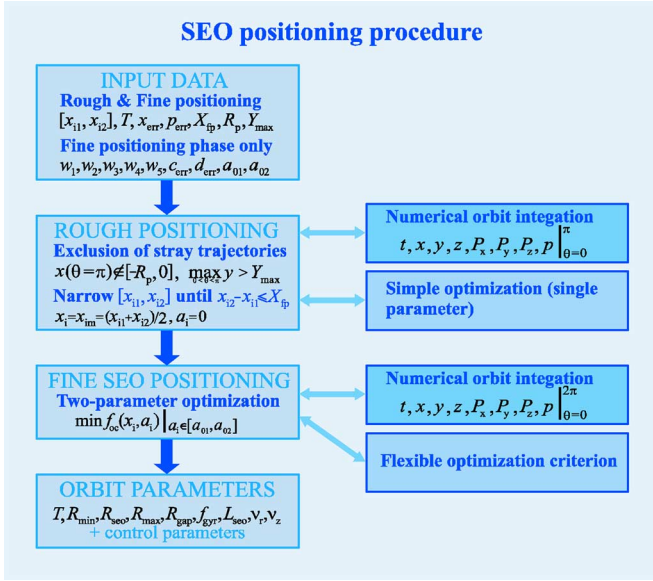


Fig. 2. The schematic representation of the optimization algorithm used to determine the static equilibrium orbits. Flexible optimization criterion results in a remarkable accuracy, while the division into the rough and the fine positioning phase makes the method efficient.

is centered in one of the two directions, here it is the y -direction. Inclusion of radial semi-axes is desired. In the case of spiral sectors, it is advisable to include both position and momentum direction angle at several points along the path of integration as the control parameters. Weighting coefficients w_1, w_2, w_3, w_4 , and w_5 are specified in the input file. Although each of them can be an arbitrary real number, we investigated the effect to the finally obtained SEO of setting each of the weighting coefficients either equal to zero or equal to one. The obtained binary arrays (w_1, w_2, w_3, w_4, w_5) correspond to different optimization criteria.

D. Rough SEO Positioning

In order to make the whole procedure as much user-friendly as possible, arbitrarily broad range of input radii $[x_{i1}, x_{i2}]$ can be specified. First, we exclude the trajectories that either exit the cyclotron pole region or never cross the y -axis. Then, the single parameter, x_i , optimization is used to further narrow the $[x_{i1}, x_{i2}]$ interval, until it reaches a given X_{fp} limit. The two just described parts of the SEO positioning comprise the rough positioning phase. The precise two-parameter optimization is referred to as the fine positioning phase of an algorithm schematically represented in Fig. 2. Exclusion of stray trajectories is performed as long as at least one of the three conditions is met: the final radial position x_f , after the half-turn ($\theta = 0$ to $\theta = \pi$) of the test ion trajectory tracking with initial radius x_{i1} and initial angle $a_i = 0$, exceeds the cyclotron pole radius, R_p ; nonnegative x_f is obtained after the half-turn starting from x_{i2} and $a_i = 0$; y -coordinate anywhere along the orbit exceeds $Y_{max} = 1.5 \cdot R_p$, ($R_p = 1$ m here). Iterative adjustment of the lower and upper limit radii, x_{i1} and x_{i2} , by a relatively large Δx_i , ($\Delta x_i = 10$ cm here), has computational cost negligible in comparison to the fine positioning phase. Further interval $[x_{i1}, x_{i2}]$ narrowing also proceeds fast: starting from

$x_{im} = (x_{i1} + x_{i2})/2$ and $a_i = 0$, we track the half-turn of the trajectory. Based on positive or negative $x_{im} + x_f$, or $x_{im} + x_f = 0$, we replace $x_{i2} = x_{im}$, $x_{i1} = x_{im}$, or $x_{i1} = (x_{i1} + x_{im})/2$, $x_{i2} = (x_{i2} + x_{im})/2$, respectively. The process is repeated until the $x_{i2} - x_{i1} \leq X_{fp}$ condition is reached. For the odd number of sectors, negative radial coordinate at the last cross-section of half-turn particle trajectory with one of the coordinate semi-axes has to be used instead of x_f . In order for the method to be applicable to cyclotrons with spiral sectors, analytical estimate of the initial momentum direction angle, $\alpha(x_i)$, would be necessary. Instead of $a_i = 0$, the initial angle $a_i = \alpha(x_i)$ is to be used throughout the rough positioning phase. However, detailed analysis of spiral sectors is beyond the scope of this paper. The described procedure alone would be sufficient for the SEO positioning, if the input magnetic field were ideally symmetric and its change with radius ideally smooth. In reality, this can not be fully achieved and the procedure moves on to the two-parameter adjustment.

E. Fine SEO Positioning

In the fine SEO positioning phase, each of the values x_{i1}, x_{i2} , and x_{im} is kept fixed, while the optimal a_i that minimizes the quality criterion f_{oc} for each of them is searched for. Thus, we obtain a_{i1}, a_{i2} , and a_{im} , as well as f_{oc1}, f_{oc2} , and f_{ocim} . Upon that, the pair of initial parameters (x_i, a_i) characterized by the larger f_{oc1} , or f_{oc2} , is being replaced by (x_{im}, a_{im}), and the corresponding f_{oc} value by f_{ocim} . Optimal a_i for the fixed value of x_i is searched for as long as the interval of the remaining momentum angles is larger than some predefined allowed direction error d_{err} . Similarly, new pairs (x_i, a_i) are found until the search interval becomes smaller than c_{err} , the allowed SEO positioning error.

F. Choice of Weighting Coefficients

Binary arrays of weighting coefficients, (w_1, w_2, w_3, w_4, w_5), correspond to different optimization criteria, several of them compared in Table I, for the symmetric calculated magnetic field map and the realistic measured magnetic field map for the same H^- ion. We assess the orbit shape quality through the compliance of all radial position coordinates at the crossing points with coordinate axes, as well as the compliance of initial and final momentum direction angle, shown in Table I. Formally, the same norm as the one given in (3) can be used, with all weighting coefficients set to 1.0. A larger number of control points along the path of integration can be used if desired. As opposed to what we might expect, the requirement that the orbit is x -centered and y -centered produces better overall orbit shape than the requirement on closeness in terms of equality of initial and final (x, a). That can be seen by the inspection of the first and second column of Table I. As shown in the next two columns, y -centeredness requirement inclusion gives excellent orbit for the calculated field map and significantly improves the orbit obtained with the measured field map. It is enough, in that case, to only control the initial and final momentum, since omitting the fourth term in (3) results in no changes. The last two columns investigate the effect of the requirement that the radial coordinates at the midlines of the second and third sector

TABLE I
VARIATION OF SEO CONTROL PARAMETERS FOR DIFFERENT CHOICES OF INPUT WEIGHTING COEFFICIENTS

$(w_1, w_2, w_3, w_4, w_5)$	(1, 1, 0, 0, 0)	(0, 0, 0, 1, 1)	(0, 1, 0, 1, 1)	(0, 1, 0, 0, 1)	(1, 0, 1, 0, 0)	(0, 1, 1, 0, 0)
Calculated isochronized magnetic field						
x_i (mm)	769.4690	769.4711	769.4690	769.4690	769.4825	769.4736
x_π (mm)	769.4690	769.4769	769.4690	769.4690	769.4659	769.4745
$x_{2\pi}$ (mm)	769.4690	769.4515	769.4690	769.4690	769.4616	769.4538
$y_{\pi/2}$ (mm)	769.4690	769.4284	769.4690	769.4690	769.4270	769.4281
$y_{3\pi/2}$ (mm)	769.4690	769.5076	769.4690	769.4690	769.5118	769.5085
a_i (°)	0.002662	0.000000	0.002662	0.002662	0.000000	0.000000
$a_{2\pi}$ (°)	0.002662	0.000253	0.002662	0.002662	0.000101	0.000175
Measured isochronized magnetic field						
x_i (mm)	769.5574	769.5519	769.5525	769.5525	769.6300	769.5557
x_π (mm)	769.5574	769.5625	769.5625	769.5625	769.5416	769.5593
$x_{2\pi}$ (mm)	769.5562	769.5519	769.5513	769.5512	769.5142	769.5544
$y_{\pi/2}$ (mm)	769.5595	769.5613	769.5590	769.5588	769.5302	769.5593
$y_{3\pi/2}$ (mm)	769.5595	769.5564	769.5587	769.5588	769.7887	769.5593
a_i (°)	0.014286	0.014362	0.014212	0.014202	0.000000	0.014256
$a_{2\pi}$ (°)	0.014118	0.014362	0.014211	0.014202	0.000697	0.014148

be equal, combined with the x -centeredness or y -centeredness of the orbit. The obtained results are inferior to the previously obtained ones even for the symmetric field map. We may notice from the presented data the difference in the maximal radial coordinates of an orbit in x - and y -direction for the measured field. Therefore, the usage of the third term in (3) is not practical. We set $w_1 = w_2 = 1.0, w_3 = w_4 = w_5 = 0.0$, and use the requirement on x -centeredness and y -centeredness of the orbit throughout the rest of this paper.

G. Determination of Orbit Parameters

Once the initial parameters (x_{im}, a_{im}) minimizing the quality criterion f_{oc} are found, the full turn of the test ion trajectory tracking is performed to gather most of the orbit data and a few more turns are tracked with the trajectory off-centered by $\Delta r_0 = 0.1$ mm radially or $\Delta z_0 = 0.1$ mm axially. Additional turns serve to calculate the frequencies of betatron oscillations from the time intervals between each two passes of radial and axial perturbation functions, Δr and Δz , through zero. The gyration frequency, just calculated as the inverse of time needed to perform a single turn starting from (x_{im}, a_{im}), is multiplied by twice the averaged zero-crossing intervals and the reciprocal of the product equals betatron tune. The output data comprises the ion test energy, T , minimal, mean, maximal radii of the SEO, $R_{min}, R_{seo}, R_{max}$, radial coordinate while traversing the accelerating gap, R_{gap} , gyration frequency, f_{gyr} , orbit circumference, i.e., the single turn trajectory length, L_{seo} , radial and axial betatron tunes, ν_r and ν_z , as well as the control parameters listed in Table II.

III. RESULTS AND THEIR UTILIZATION

The obtained gyration frequency and betatron oscillation frequencies (tunes) for the calculated H^- ion magnetic field map are shown in Figs. 3 and 4, respectively. The results of our calculations are compared to the results previously obtained using the code CYCLOPS [22], [25]. Calculation accuracy in [25] was set to $\varepsilon = 5 \cdot 10^{-5}$, and the accuracy requirements controlling the numerical integration in our method were set to $x_{err} = 100$ nm, $p_{err} = 0.1$ ppm. The accuracy requirements on the SEO positioning were set to $c_{err} = 10^{-5}$ nm, $d_{err} = 10^{-6}$ rad. Static

TABLE II
COMPARISON OF CHARACTERISTIC CONTROL PARAMETERS ALONG THE ORBIT FOR THE TWO METHODS, FOR THREE ENERGIES

	VINDY-A	CYCLOPS
$T = 10$ MeV		
x_i (mm)	353.83458206	353.81400000
x_π (mm)	-353.83458196	-353.85438956
$x_{2\pi}$ (mm)	353.83458254	353.81568188
$y_{\pi/2}$ (mm)	353.83458187	353.84420425
$y_{3\pi/2}$ (mm)	-353.83458184	-353.82336024
a_i (°)	0.0158096126	0.0145456797
$a_{2\pi}$ (°)	0.0158096541	0.0140864955
R_{seo} (mm)	343.615504	343.466858
f_g (MHz)	20.035898	20.035924
$T = 30$ MeV		
x_i (mm)	604.32695793	604.32900000
x_π (mm)	-604.32695849	-604.32497597
$x_{2\pi}$ (mm)	604.32695828	604.32882352
$y_{\pi/2}$ (mm)	604.32695795	604.32660361
$y_{3\pi/2}$ (mm)	-604.32695777	-604.32765372
a_i (°)	0.0041450369	0.0041598455
$a_{2\pi}$ (°)	0.0041451272	0.0042163061
R_{seo} (mm)	585.802025	585.205190
f_g (MHz)	20.038663	20.038660
$T = 50$ MeV		
x_i (mm)	769.46900599	769.46910000
x_π (mm)	-769.46900616	-769.46913179
$x_{2\pi}$ (mm)	769.46900547	769.46867637
$y_{\pi/2}$ (mm)	769.46900614	769.46813324
$y_{3\pi/2}$ (mm)	-769.46900619	-769.46984645
a_i (°)	0.0026619722	0.0027189712
$a_{2\pi}$ (°)	0.0026619340	0.0027150101
R_{seo} (mm)	744.240292	743.715520
f_g (MHz)	20.040972	20.040973

equilibrium orbit data is calculated for test ion energies from 0.2 MeV to 68.0 MeV, with the data step 0.2 MeV. The agreement of the two sets of results is excellent; in Fig. 4 we had to use rather thick line to represent the CYCLOPS data, since the two sets of data completely overlap. The general shape of the two gyration frequency curves in Fig. 3 is identical as well; however, there is somewhat larger amount of small oscillations

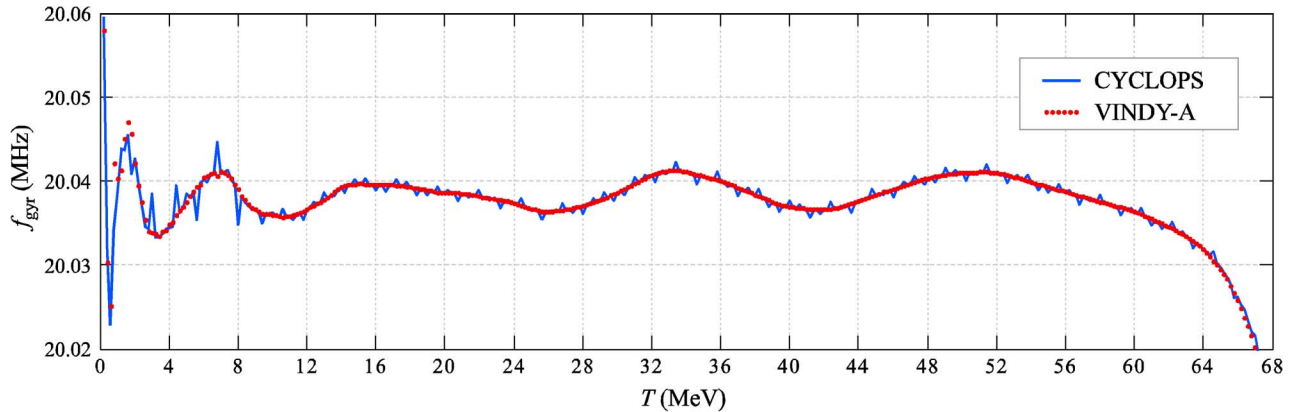


Fig. 3. Orbital gyration frequencies for the calculated H^- ion magnetic field map. Comparison of newly obtained results (VINDY-A) with those obtained using the CYCLOPS code [25] gives excellent agreement, except for the small oscillations in the CYCLOPS result. Such oscillations are due to slight variations in the obtained initial parameters (x_i, a_i) in the vicinity of the optimal closed orbit, where a number of orbits meet the numerical accuracy requirements (see Table I). The calculation accuracy of $\varepsilon = 5 \cdot 10^{-5}$ in [25] might be insufficient if the data is to be used as input of other procedures.

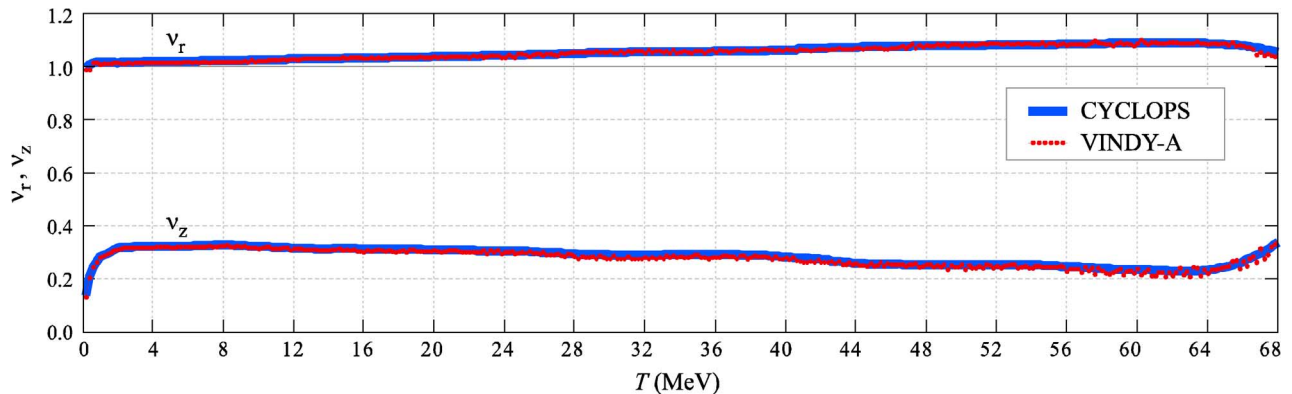


Fig. 4. Radial and axial betatron oscillation frequencies (tunes), ν_r and ν_z , for the calculated H^- ion magnetic field map. Betatron tunes are found by determining the zero-crossing periods, a method commonly used in signal processing. The two sets of results overlap in almost all points, therefore the CYCLOPS data is represented by a very thick line and our data as smaller dots.

in the CYCLOPS data. There is more than one orbit concordant with the numerical algorithm accuracy requirements in the vicinity of the orbit adopted as SEO, and such small oscillations can be attributed to finding a pair of initial parameters (x_i, a_i) slightly astray from the optimal. This problem could be removed in part, or even completely, by adopting better computation accuracy. The consistency in the gyration frequency calculation shown by our method is probably due to the fact that x - and y -centeredness combined in an optimization criterion actually produce better overall orbit shape, than the usual requirement on orbit closeness, as illustrated in Table I. The comparison of characteristic control parameters along the orbit is given in Table II, for initial parameters (x_i, a_i) determined by the two methods, for three energies. Fig. 5 compares the realistic measured with the calculated isochronous magnetic field map. In the following, examples of the recent utilization of described procedures as subroutines in other methods are given.

A. Isochronous Field Calculation Using Gyration Frequencies

The constancy of the ion gyration frequency checked by the use of numerical methods is the ultimate quality measure for an isochronous magnetic field. A step further is to employ the

gyration frequency adjustment in the process of isochronous field calculation. In the method suggested in [13], we choose to adjust the magnetic field source rather than the field itself in order to guarantee the magnet capability to produce the calculated field. Cyclotron magnet responds to the joint effect of the main and the trim coils as an effective main coil current inducing the desired magnetic field at a given radius, termed in [13] the effective induction current. The measured response of the magnet was available for the twenty values of the main coil current, at the measurement grid points in the median plane defined by $R_m = 0, 1, 2, \dots, 100$ cm, $\theta = 0, 1, 2, \dots, 359^\circ$. Alternatively, simulated magnetic fields for a number of main coil currents can be used. The gyration frequency dependence on the mean orbit radius is obtained from the SEO simulation in each of the field maps at a number of energy points. It is used to obtain the set of values corresponding to the mean orbit radii R_m . The effective induction current producing the desired gyration frequency is found for each radius separately, using the cubic spline interpolation. The azimuthal variation of the magnetic field corresponding to the considered effective current is determined in the same way. Azimuthal variations at different radii are merged into the isochronized field and the corresponding gyration frequency distribution over the radii is obtained. If the

TABLE III
COMPARISON OF MEAN ORBIT RADIUS, R_{seo} , AND THE NORMALIZED ORBIT
CIRCUMFERENCE, $L_{seo}/(2\pi)$

T (MeV)	R_{seo} (mm)	$L_{seo}/(2\pi)$ (mm)	ΔR (mm)	$\Delta R/R_{seo}$ (%)
10.0	343.616	344.745	1.130	0.329
20.0	481.963	483.672	1.709	0.355
30.0	585.802	587.803	2.001	0.342
40.0	671.529	673.622	2.093	0.312
50.0	744.240	747.308	3.068	0.412
60.0	808.868	812.731	3.863	0.477

desired isochronism level is not yet achieved, the solution is re-fined iteratively, although only few (even one) iterations result in a remarkable accuracy. As shown by comparison of methods given in [13], deviation of the realistic from the calculated magnetic field, due to the finite number of trim coils, is the least for the suggested method. Our method, as well as the CYCLOPS, calculates the mean orbit radius, R_{seo} , by the standard definition of the mean value of a physical variable. It should be noted that another parameter often used in the cyclotron community, the average radius based on the arc length, $L_{seo}/(2\pi)$, is always larger than R_{seo} by an amount depending on the angle between the arc tangent and the circle tangent in each integration step, $\xi(\theta)$.

$$\begin{aligned}
 R_{seo} &= \frac{1}{2\pi} \int_0^{2\pi} r(\theta) d\theta < \frac{1}{2\pi} \int_0^{2\pi} \frac{r(\theta)}{\cos \xi(\theta)} d\theta \\
 &= \frac{1}{2\pi} \int_0^{2\pi} dl = \frac{L_{seo}}{2\pi}.
 \end{aligned} \quad (4)$$

As shown in Table III, the discrepancy between the two in our case is less than 0.5%; however, for orbits with the more pronounced scalloping it can be much larger.

B. Fine Magnet Shaping by Azimuthal and Axial Shimming

The method for fine magnet shaping described in [14] uses the three-dimensional computer modeling of the magnet in combination with static equilibrium orbit calculations to relate the particular magnetic sector shape and the corresponding radial dependence of the ion gyration frequency. The gyration frequency is treated as a function of the sector shape and the equation linking the two is solved numerically by the regula falsi method. The pre-calculated magnetic field criterion and the empirical weight factors for the shape estimate are avoided by relying directly on the gyration frequency adjustment. The method is applicable to all radially dependent types of sector shimming, namely the azimuthal, axial-polar and axial-median shimming. It works equally well with straight as well as with spiral sectors and can be used to determine the pole thickness in the cyclotrons with azimuthally non-varying magnetic fields. Two initial limiting sector shapes are required, the two corresponding gyration frequency dependencies on the mean equilibrium orbit radius, R_{seo} , defined by (4), and the desired gyration frequency. The method is characterized by the excellent accuracy and fast convergence.

C. Accelerated Equilibrium Orbit (AEO) Centering

Accelerated equilibrium orbit centering based on the hard edge gap approximation customarily uses approximate analytical formulas to relate the relative increase in radius with the relative energy gain while traversing the accelerating gap. The very efficient orbit centering method is proposed in [17], relying on tabulated orbit parameters from the SEO analysis. Orbit centering starts from the middle of the valley on the SEO corresponding to the test ion energy. The amount of energy gained at each accelerating gap is numerically integrated. We use the cubic spline interpolation and the tabulated dependence of gap radial coordinate, R_{gap} , on the test ion energy to obtain the five values of R_{gap} . Differences in R_{gap} after and before each gap correspond to the orbit center movement. The barycenter of an outlined parallelogram-like contour corresponds to the shift of the initial ion coordinates required for the single turn centering. Although the procedure can be used iteratively, for medium to large energy values a single step of this single turn centering is adequate.

D. Betatron Tunes Calculation Using the AEO

Determination of the zero crossing periods, a method commonly used in signal processing and applied here to calculate the betatron tunes from the SEO analysis, is readily adapted to the AEO analysis. The test ion travelling along the optimized or presumed AEO is tracked simultaneously with the two other ions, one off-centered radially and the other elevated from the median plane. The radial and axial perturbations of the trajectories of the two ions with respect to the one following the AEO are considered almost sinusoidal signals whose frequency is to be found. For each time interval between the two zero-crossings, the averaged test ion energy during that interval is found, and the corresponding gyration frequency interpolated from the SEO analysis data using the cubic spline method. Betatron tunes obtained using the AEO are shown in part (b) of Fig. 5 by the solid red (dark gray) line. Consistent with the result obtained by the SEO analysis, the newly calculated tunes are found along the orbit that is not perfectly centered at all radii and that accounts for realistic energy gains during the acceleration.

E. Focusing Limit of a Cyclotron

The maximal obtainable energy of ions accelerated in a cyclotron is determined either by the bending capabilities or by the focusing capabilities of the machine, depending on the bending and focusing constants and ion specific charge. The focusing limit represents the ion energy at which the axial defocusing caused by the radial field growth overpowers focusing introduced by azimuthally varying fields. It is most often determined using the axial beam instability criterion based on the approximate analytical expressions for betatron tunes. In [18], critical SEO for axial instability is determined as the one whose maximal orbit radius corresponds to the maximum of radial magnetic field gradient in the considered limiting magnetic field. This is the orbit characterized by the maximal degree of axial beam defocusing, out of all orbits in the vicinity of extraction radius. Beam dynamics simulations along the critical SEO are employed to assess the extent of the beam defocusing as the maximal half-envelope achieved along the several simulated turns on the SEO. The focusing limit is taken to be the ion

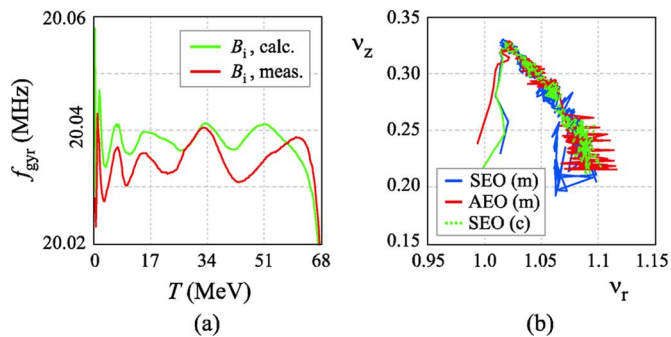


Fig. 5. Comparison of orbit properties for the measured and calculated H⁻ ion magnetic field map. Measured magnetic field map is obtained with the set of main and trim coil currents providing the field closest to the desired calculated field. (a) There is a significant gyration frequency difference between the two field maps. (b) The betatron oscillation frequencies seem to be much less affected by the field differences. The two cases, denoted as SEO (m) for the measured and SEO (c) for the calculated field map, are best discerned from the ν_z versus ν_r plot. The betatron tunes calculated from the radial and axial perturbations of accelerated equilibrium orbit in the measured magnetic field map, denoted as AEO (m), are shown as well. Large oscillations of the ν_r tune calculated using the AEO can be contributed to additional radial perturbation due to the imperfect orbit centering.

extraction energy corresponding to the maximal half-envelope reaching 135% of the initial vertical beam size. It is shown that the obtained focusing limit can be more than 9% smaller than that obtained from the approximate expressions. Focusing limit obtained by means of beam dynamics simulations is not only more accurate; it is actually achievable in reality, unlike the one from the approximate expressions that corresponds to the infinitely large beam size.

IV. CONCLUSION

During the creation of our self-written software packages for ion beam dynamics, highly accurate original method for the calculation of static equilibrium orbits was developed. It has been used in many other program modules we developed, but the method itself was not previously described. It is proposed here and compared in terms of accuracy with the method prevalent in existing literature, showing excellent agreement. In its many applications as a subroutine, it has proven to be robust and fast as well. The flexible quality criterion utilizing several weighting coefficients is used in the optimization process. A comparison given in Section II, using different combinations of weighting coefficients, corresponds to investigating several different optimization criteria. Except for the usual analysis of already obtained magnetic field maps, several examples of recent utilization of the proposed method within other methods are outlined. Remarkable consistency in finding the initial parameters (x_i, a_i) of each SEO is identified as the major factor contributing to the high accuracy and fast convergence of all outlined methods.

REFERENCES

- [1] M. M. Gordon, "Computation of closed orbits and basic focusing properties for sector focused cyclotrons and the design of "CYCLOPS", *Part. Accel.*, vol. 16, pp. 39–62, 1984.
- [2] A. Goswami, P. Sing Babu, and V. S. Pandit, "Behavior of space charge dominated beam in a high-current compact cyclotron," *Nucl. Instrum. Methods Phys. Res. A*, vol. 562, no. 1, pp. 34–40, Jun. 2006.

- [3] T. Zhang, H. Yao, J. Yang, J. Zhong, and S. An, "The beam dynamics study for the CYCIAE-100 cyclotron," *Nucl. Instrum. Methods Phys. Res. A*, vol. 676, pp. 90–95, June 2012.
- [4] B. Wang *et al.*, "Computer design of a compact cyclotron," *Phys. Part. Nucl. Lett.*, vol. 9, no. 3, pp. 288–298, May 2012.
- [5] J. X. Zhang, T. A. Antaya, and R. E. Block, "Beam dynamics of a compact SC isochronous cyclotron—Preliminary study of central region," in *Proc. 2nd Int. Particle Accel. Conf.*, San Sebastian, Spain, 2011, pp. 643–645.
- [6] J. Kang *et al.*, "Design study on magnet and RF systems of a 5 MeV H⁻ cyclotron," in *Proc. 17th Int. Conf. Cyclotrons and Their Applications*, Tokyo, Japan, 2005, pp. 378–380.
- [7] M. K. Craddock and Y.-N. Rao, "Cyclotron and FFAG studies using cyclotron codes," in *Proc. 19th Int. Conf. Cyclotrons and Their Applications*, Lanzhou, China, 2011, pp. 395–397.
- [8] H. L. Hagedoorn and N. F. Verster, "Orbits in an AVF cyclotron," *Nucl. Instrum. Methods*, vol. 18–19, pp. 201–228, 1962.
- [9] M. M. Gordon and D.-O. Jeon, "Improved formulas for calculating cyclotron orbit properties," *Nucl. Instrum. Methods Phys. Res. A*, vol. 301, no. 2, pp. 182–190, Mar. 1991.
- [10] C. J. Kost and G. H. Mackenzie, "COMA—A linear motion code for cyclotrons," *IEEE Trans. Nucl. Sci.*, vol. 22, no. 3, pp. 1922–1925, Jun. 1975.
- [11] B. M. Bardin, J. H. Hettner, W. P. Jones, and C. J. Kost, "Orbit dynamics of the Indiana University cyclotron," *IEEE Trans. Nucl. Sci.*, vol. 18, no. 3, pp. 311–314, Jun. 1971.
- [12] B. Qin *et al.*, "A pythonic integrated solution for virtual prototyping of cyclotrons," *Nucl. Instrum. Methods Phys. Res. B*, vol. 261, no. 1–2, pp. 56–59, Aug. 2007.
- [13] S. Ćirković, J. L. Ristić-Djurović, A. Ž. Ilić, V. Vujović, and N. Nešković, "Comparative analysis of methods for isochronous magnetic-field calculation," *IEEE Trans. Nucl. Sci.*, vol. 55, no. 6, pp. 3531–3538, Dec. 2008.
- [14] S. Ćirković, J. L. Ristić-Djurović, A. S. Vorozhtsov, A. Ž. Ilić, and N. Nešković, "Method for fine magnet shaping in cyclotrons," *IEEE Trans. Nucl. Sci.*, vol. 56, no. 5, pp. 2821–2827, Oct. 2009.
- [15] B. Qin *et al.*, "Precise isochronous field shimming using correlation matrix for compact cyclotrons," *Nucl. Instrum. Methods Phys. Res. A*, vol. 691, pp. 129–134, Nov. 2012.
- [16] P. Sing Babu, A. Goswami, P. R. Sarma, and V. S. Pandit, "Optimization of sector geometry of a compact cyclotron by random search and matrix methods," *Nucl. Instrum. Methods Phys. Res. A*, vol. 624, no. 3, pp. 560–566, Dec. 2010.
- [17] A. Ž. Ilić, J. L. Ristić-Djurović, S. Ćirković, A. Dobrosavljević, and N. Nešković, "Optimal acceleration in isochronous straight sector cyclotrons," *IEEE Trans. Nucl. Sci.*, vol. 56, no. 3, pp. 1498–1506, Jun. 2009.
- [18] S. T. Ćirković, J. L. Ristić-Djurović, A. Ilić, N. Nešković, A. S. Vorozhtsov, and S. B. Vorozhtsov, "Focusing limit of a cyclotron: Axial betatron instability against beam dynamics approach," *Nucl. Technol. Radiat. Protect.*, vol. 21, no. 2, pp. 40–46, Dec. 2006.
- [19] J. L. Ristić-Djurović, N. Nešković, and S. Ćirković, "Compound particle tracking algorithm: Application to the foil stripping extraction system design," in *Proc. 6th Int. Computational Accelerator Phys. Conf.*, 2000 [Online]. Available: <http://www.icap2000.de/frames/index.htm>
- [20] A. Ž. Ilić, J. L. Ristić-Djurović, and S. T. Ćirković, "Preliminary results of ion trajectory tracking in the acceleration region of the VINCY cyclotron," *Nucl. Technol. Radiat. Protect.*, vol. 21, no. 1, pp. 29–33, Jun. 2006.
- [21] N. Nešković *et al.*, "Status report of the VINCY cyclotron," *Int. J. Nucl. Res. NUKLEONIKA*, vol. 48, no. suppl. 2, pp. s135–s139, 2003.
- [22] A. Ž. Ilić, "Optimal acceleration of particles in multipurpose isochronous cyclotrons," Ph.D. dissertation, School of Elect. Eng., Univ. of Belgrade, Belgrade, Serbia, Oct. 2010, (in Serbian).
- [23] S. T. Ćirković, "Determining of the operating magnetic field and operating diagram of a multipurpose cyclotron," Ph.D. dissertation, School of Elect. Eng., Univ. of Belgrade, Belgrade, Serbia, Jun. 2009, (in Serbian).
- [24] S. T. Ćirković, "Measurement and calculation of the isochronous magnetic fields of the VINCY cyclotron," M.Sc. thesis, School of Elect. Eng., Univ. of Belgrade, Belgrade, Serbia, Jul. 2000, (in Serbian).
- [25] S. B. Vorozhtsov, A. S. Vorozhtsov, and P. Beličev, "Isochronous Field and Equilibrium Orbit Dynamical Properties of the VINCY Cyclotron Belgrade, Serbia, Internal Rep., Jul. 2005.

Magnet with Uncoupled Combined Functions

Jasna L. Ristić-Djurović, Saša Ćirković, and Andjelija Ž. Ilić, *Member, IEEE*

Abstract—Efficient extraction by ion stripping of a number of ion beams from a multipurpose cyclotron through the same transport line could be achieved with a combined function magnet. Characteristics of a combined magnet used for this purpose are significantly different from those of commonly used combined function magnets. For example, bending and focusing functions must be independently adjustable, beam paths are not centered to the device's axis, only one device is needed per cyclotron, and requirements regarding maximal achievable quadrupole and dipole fields as well as field linearity are not as demanding as for combined function magnets used for other applications. Using two analytical models as well as a simple numerical model, it is shown that two independently powered slanted dipoles, off-centered and arranged symmetrically with respect to the beam area, could efficiently serve as a combined function magnet in the stripping extraction system of a multipurpose cyclotron.

Index Terms—Accelerators, combined function magnets, cyclotrons, stripping extraction.

I. INTRODUCTION

A MULTIPURPOSE cyclotron provides a number of ion beams for different applications for the cost of a single machine. However, diversity of operating modes a machine delivers increases the difficulties encountered during its design and construction. Extraction of more than one beam from a multipurpose cyclotron into a single transport line is often achieved with the stripping extraction system [1]–[4]. In a cyclotron which accelerates negative as well as positive ion beams beam paths and transverse emittances after stripping extraction significantly depend on the sign of ion charge during acceleration [5]–[8]. Directions of ion beams accelerated as positive do not differ very much; however, these beams need to be focused in the horizontal direction as soon as they leave the cyclotron. Directions after extraction of ion beams accelerated as negative, although close to each other, significantly differ from those of ion beams which are accelerated as positive. After extraction ion beams accelerated as negative usually do not need to be focused because they change their sign, i.e., they become positive, during stripping and are therefore not defocused by the pole-edge field. Consequently, to efficiently prepare all the extracted beams for further transport through the same transport line a device providing adjustable strong

horizontal focusing combined with weak horizontal bending for beams accelerated as positive as well as strong horizontal bending in the opposite direction for beams accelerated as negative is needed. Due to the limited available space in the extraction region, these functions should preferably be delivered by a single device—the combined function magnet.

Combined function magnets are commonly used in storage rings, synchrotrons, beam lines, linear accelerators, as well as in cancer therapy devices, see for example [9]–[16] and references therein. General practical and theoretical approaches to designing a combined function magnets for these purposes are given in [17]–[19], whereas some important questions that need to be considered for their effective operation are addressed in [20]–[22].

Requirements for the combined function magnet suitable for the stripping extraction system of a multipurpose cyclotron significantly differ from those of the magnets used for the mentioned purposes. If it is a part of a cyclotron extraction system, the combined function magnet needs only dipole and quadrupole components of the magnetic field; however, these components must be independently adjustable. For this type of application, not only that the beam paths through the magnet are not centered to the device's axis, but are in fact widely horizontally distributed over the aperture in the first half of the magnet's length [7]. The tolerable levels of field components other than the bending and focusing components as well as of the fringe field are fairly high. Consequently, the linearity of the achieved field in the beam area as well as the sharp fringe field decrease does not have to be met as rigorously as is the case with other types of applications. In [7], for example, the focusing magnetic field gradients are determined using the step size of 0.05 T/m which is 5% of the strongest gradient needed. In addition, the sizes of the beams which require strong focusing are two times smaller than the considered beam area. On the other hand, the beams which require strong bending travel through the entire horizontal range of the considered beam area and the bending fields needed for different ion beams were calculated in [7] with five significant digits. However, these beams do not require focusing and their horizontal size is more than five times smaller than the considered beam area. Therefore, the linearity offset close to the beam area borders as high as 5% will not cause significant defocusing problems. If necessary, bending offsets in the beam area can be accounted for by using achieved shape of the field instead of the assumed linear dependence in the calculation of the bending field required for a particular beam. Finally, only a single combined function magnet is needed in the stripping extraction system of a multipurpose cyclotron.

The most common way to provide focusing is with a quadrupole structure of a magnet, whereas for independent adjustability of focusing and bending functions two uncoupled

Manuscript received July 10, 2013; revised August 23, 2013; accepted November 06, 2013. Date of publication December 03, 2013; date of current version December 11, 2013. This work was supported by the Serbian Ministry of Education, Science and Technological Development under Grant III45003.

The authors are with the Innovation Center, School of Electrical Engineering, University of Belgrade, 11120 Belgrade, Serbia (e-mail: jasna@stanfordalumni.org; sasa.cirkovic@ic.etf.bg.ac.rs; andjelija@ic.eee.org).

Color versions of one or more of the figures in this paper are available online at <http://ieeexplore.ieee.org>.

Digital Object Identifier 10.1109/TNS.2013.2290309

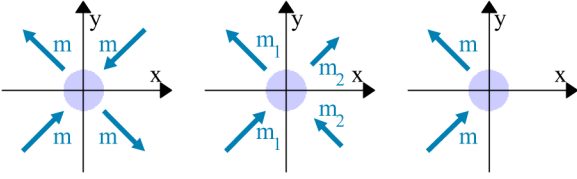


Fig. 1. Concept evolution. In each of the three sketches the ion beam area is indicated by a shaded circle, whereas the poles are represented by their magnetic moment vectors. The leftmost sketch corresponds to a typical quadrupole. If its poles are independently powered in pairs, as shown in the middle sketch, values of the two magnetic moments, m_1 and m_2 , serve to adjust bending as well as focusing of an ion beam. This concept will work if the two slanted as well as off-centered poles shown in the rightmost sketch provide linear field in the beam area.

input parameters must be available. Both of these requirements are met if a quadrupole is composed of two independently powered slanted dipoles, see Fig. 1. Initially, we assume that each of the dipoles can affect the other one only by the effective change in the field levels, rather than by the major qualitative field changes such as the field linearity. The magnetic moments of a slanted dipole's poles are not parallel, instead they are both inclined with respect to the y -axis by the same angle but in the opposite directions. In a typical quadrupole all four poles are azimuthally equidistant, whereas above described slant angle of a pole can have an arbitrary value. In addition, unlike a typical dipole whose target area is around its axis, the slanted dipole outlined in the right sketch in Fig. 1 is off-centered with respect to the beam area, i.e., the coordinate system origin. If a quadrupole composed of a slanted off-centered dipole and its independently powered mirror image is to be used as a combined function magnet, each of the slanted dipoles has to produce approximately linear field in the beam area in the vertical direction, i.e., $B_y = G \cdot x + B_{st}$. Linear field of the slanted dipole ensures that when two such fields are added in the proposed combined function magnet, the resulting sum is linear as well, regardless of the excitation current intensities which cause the two components.

Asymmetric excitation of a quadrupole by shunting part of the current from one pair of the coils is described in [23]. Our generalization of the problem to slanted dipoles is aimed at providing the dependence between the slanted dipole geometry and the achieved field quality. Note that the asymmetrically excited quadrupole is a special case of the combined function magnet composed of two slanted dipoles.

Operation of five devices with respect to bending and focusing is illustrated in Fig. 2. The left graph is devoted to a typical quadrupole, Q, a typical dipole, D, a slanted dipole shifted to the left of the beam area, LD, and its mirror image, i.e., a slanted dipole displaced to the right of the beam area, RD. The fifth device, the combined magnet composed of the two slanted dipoles is represented in the right graph. To enable comparison of the devices, bending and focusing factors, k_B and k_G , which define bending and focusing properties of a device, are expressed with respect to the device's maximal steering field and focusing gradient, B_{max} and G_{max} , respectively. Therefore, a particular operating mode of a device is defined by k_B and k_G , which can, in general, take any value between -1 and 1 . For a typical quadrupole $k_B = 0$, whereas for a typical dipole $k_G = 0$. If

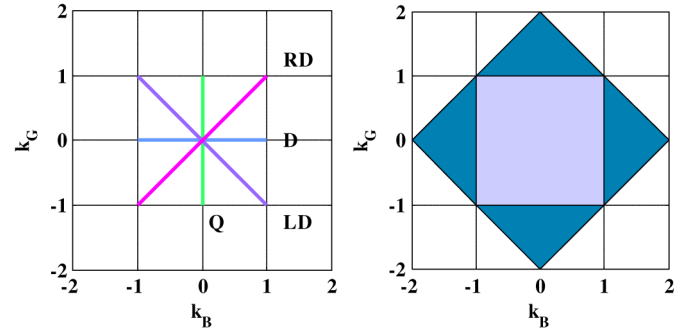


Fig. 2. Available sets of bending and focusing factors. The bending and focusing factors, k_B and k_G , scale the fields of a considered device to their maximums, i.e., $B_y = k_G \cdot G_{max} \cdot x + k_B \cdot B_{max}$. The line segments in the left graph represent a typical quadrupole, Q, dipole, D, and two slanted dipoles displaced to the left and to the right of the beam line, LD and RD. When independently powered slanted dipoles LD and RD are combined into a single device, their bending and focusing factors of the new device as $k_B = k_{BL} = -k_{GL} = k_1$ and $k_{BR} = k_{GR} = k_2$, determine bending and focusing factors of the new device as $k_B = k_1 + k_2$ and $k_G = k_2 - k_1$. Consequently, the two line segments representing each slanted dipole as a single device in the left graph expand into the area shown in the right graph in Fig. 2. The original ranges of bending and focusing factors, $[-1, 1]$, are uncoupled and are shown as lighter inner square. In addition, four sets of factors depicted as the darker triangles are now available.

a slanted off-centered dipole is displaced to the right of the coordinate system origin its bending and focusing factors are equal, $k_G = k_B$, whereas for its mirror image, denoted as shifted to the left of the beam area, $k_G = -k_B$. When the two independently powered slanted off-centered dipoles are composed into a combined function magnet the operating area expands from the two line segments shown in the left graph into the square depicted in the right graph in Fig. 2. For ion beams accelerated as negative, operating conditions of the device will be chosen from the most-right dark triangle, i.e., from the area where $k_B > 1$ and $k_G \approx 0$. After extraction, ion beams accelerated as positive need strong focusing as well as weak bending and both bending and focusing factors should be negative. Consequently, the operating mode of the combined function magnet is most likely to be chosen from the left half of the lower dark triangle, i.e., from the area defined by $k_B < 0$ and $k_G < -1$.

A single value of $k_B \in (-2, 2)$ or $k_G \in (-2, 2)$ in the combined function magnet can be achieved by multiple combinations of the field scaling factors of the left and right slanted dipole, k_1 and k_2 , see Fig. 3. Even though k_B as well as k_G is not governed by a single parameter k_1 or k_2 , the mapping of sets of pairs $(k_B, k_G) \leftrightarrow (k_1, k_2)$ is of one-to-one type. Consequently, the values of k_B and k_G can be adjusted independently.

The problem comes down to ensuring that a single slanted off-centered dipole can provide approximately linear magnetic field in the beam area. The concept is validated by modeling the slanted off-centered dipole with two analytical models as well as with one numerical model.

II. ANALYTICAL MODELS

A. Ideal Dipoles

In the first approximation of a slanted off-centered dipole each of its poles is modeled with an ideal dipole, as shown in Fig. 4. The diameter of the beam area as well as the horizontal pole offset from the coordinate system origin is fixed and taken

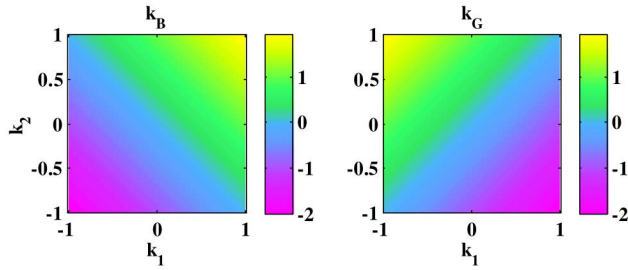


Fig. 3. Input/output mapping. The bending and focusing factors of the combined function magnet are uncoupled because the mapping $(k_B, k_G) \leftrightarrow (k_1, k_2)$ is a one-to-one mapping.

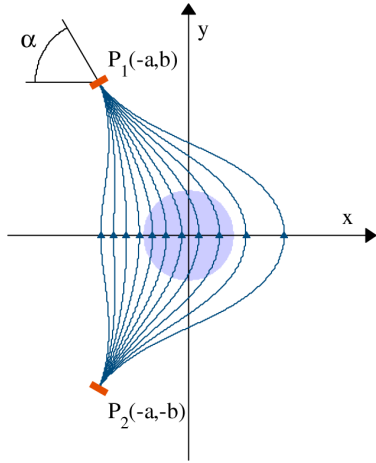


Fig. 4. Ideal dipoles model. Each pole of the slanted off-centered dipole is modeled by an ideal dipole inclined with respect to the horizontal axis by a slant-angle, α . The distance between the ideal dipoles is $2b$ and they are both shifted to the left of the beam axis by a . The diameter of the considered beam area is taken to be a , as well; therefore, this parameter is further used as the scaling factor for distances.

to be a . Consequently, a is used as the scaling factor, whereas the spatial parameters expected to shape the resulting magnetic field are α and b/a .

Magnetic field of an ideal dipole positioned at the origin of the coordinate system and aimed along the z -axis is defined in [24] as

$$\begin{aligned} B_x &= \frac{\mu_0 m}{4\pi} \cdot \frac{3xz}{R^5} \\ B_y &= \frac{\mu_0 m}{4\pi} \cdot \frac{3yz}{R^5} \\ B_z &= \frac{\mu_0 m}{4\pi} \cdot \left[\frac{3z^2}{R^5} - \frac{1}{R^3} \right], \end{aligned} \quad (1)$$

where $R = \sqrt{x^2 + y^2 + z^2}$, $\mu_0 = 4\pi \cdot 10^{-7}$ H/m and m is ideal dipole magnetic moment. After appropriate coordinate transformation for each of the two poles of the slanted off-centered dipole and summation, these formulas lead to the vertical magnetic field component along the horizontal axis, i.e., for $y = 0$:

$$\begin{aligned} B_y(x) &= B_0 \cdot \left[\left(1 + \frac{x}{a}\right)^2 + \frac{b^2}{a^2} \right]^{-5/2} \\ &\cdot \left[3 \frac{b}{a} \left(1 + \frac{x}{a}\right) \cos \alpha + \left(2 \frac{b^2}{a^2} - \left(1 + \frac{x}{a}\right)^2\right) \sin \alpha \right], \end{aligned} \quad (2)$$

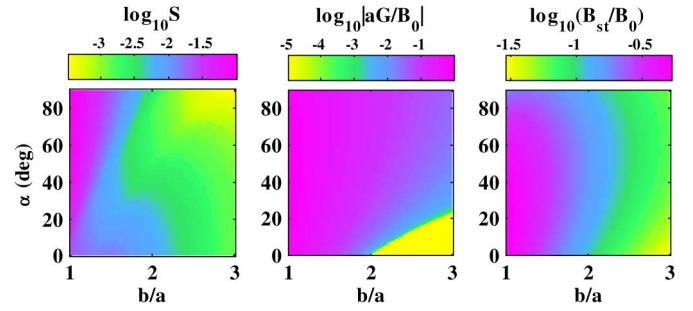


Fig. 5. Influence of slant-angle, α , and pole distance, b/a , on device properties. The dependence of the field linearity coefficient, S , as well as of normalized focusing and bending capabilities, aG/B_0 and B_{st}/B_0 , on α and b/a is shown in the right, middle and left graph, respectively. In general, small values of S and large values of aG/B_0 and B_{st}/B_0 are desired; however, the values of α and b/a which correspond to any desired optimization criterion can be determined from the depicted data.

where $B_0 = \mu_0 m / (2\pi a^3)$, whereas α , a and b are defined in Fig. 4. The values of B_y and of its derivative at $x = 0$ are used to define steering and focusing capabilities of the device, B_{st} and G as

$$\begin{aligned} B_{st} &\equiv B_y(0) = B_0 \cdot \left(1 + \frac{b^2}{a^2}\right)^{-5/2} \\ &\cdot \left[3 \frac{b}{a} \cos \alpha + \left(2 \frac{b^2}{a^2} - 1\right) \sin \alpha \right] \\ G &\equiv \left. \frac{\partial B_y}{\partial x} \right|_{x=0} = B_0 \frac{3}{a} \cdot \left(1 + \frac{b^2}{a^2}\right)^{-7/2} \\ &\cdot \left[\frac{b}{a} \left(\frac{b^2}{a^2} - 4\right) \cos \alpha + \left(1 - 4 \frac{b^2}{a^2}\right) \sin \alpha \right]. \end{aligned} \quad (3)$$

These are used to linearly approximate B_y along the line segment $x \in [-a/2, a/2]$ as $Gx + B_{st}$, as well as to further quantitatively express linearity coefficient of B_y as

$$S = \frac{1}{aB_0} \int_{-a/2}^{a/2} |B_y - Gx - B_{st}| dx. \quad (4)$$

The influence of the slant angle, α , and vertical pole distance expressed as b/a , on the linearity, focusing and bending coefficients of the resulting field is given in Fig. 5. To broaden the applicability of the results, bending and focusing coefficients are scaled to B_0 and are defined as B_{st}/B_0 and aG/B_0 , respectively.

Since the discrepancy between the achieved field and its linear approximation does not have to be very small if the combined function magnet is used as a part of the cyclotron stripping extraction system, the geometry of the ideal dipole model is optimized using the optimization criterion $\max(|B_{st}/B_0| \cdot |aG/B_0|)$ and the restriction $S \leq 0.004$. The corresponding optimized geometry of the ideal dipoles model has $\alpha = 60^\circ$ and $b/a = 1.7$. The normalized horizontal and vertical components of the magnetic field obtained with this geometry in the beam area are given in Fig. 6. The values of the focusing and bending parameters as well as field linearity

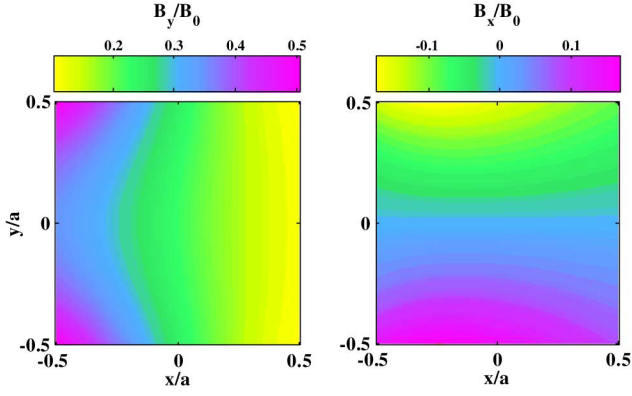


Fig. 6. Normalized magnetic field components. For the ideal dipoles model with $\alpha = 60^\circ$ and $b/a = 1.7$, the magnetic field in the beam area follows the desired pattern along x -axis as well as along y -axis. Namely, B_y is approximately linear and $B_x \cong 0$ for $y = 0$, whereas for $x = 0$ it is the other way around, i.e., $B_y \cong \text{const.}$ and B_x is approximately linear. However, the contour lines noticeably deviate from straight lines away from the axes.

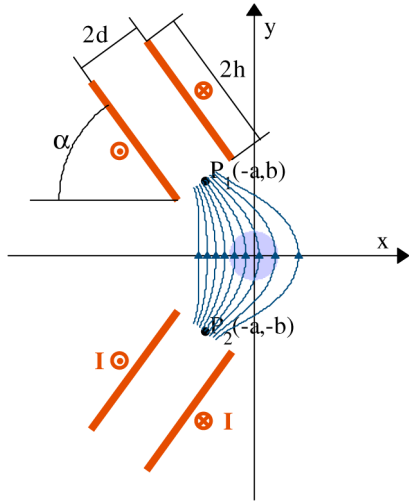


Fig. 7. Current stripes model. Infinite current stripes are expected to be a better model of a lengthy device. In addition to the slant angle, α , and pole distance expressed as b/a , which were used to define an ideal dipoles model, two new parameters, the stripe distance and width, expressed as d/a and h/a , respectively, must be considered as well. Following the principle established for the ideal dipoles model, all the distances, including the additional parameters are normalized to the beam area diameter i.e. the horizontal offset of the poles, a .

coefficient, as defined by (3) and (4) are $aG/B_0 = -0.26$, $B_{st}/B_0 = 0.22$, and $S = 0.0039$.

Despite promising results regarding the shape of the field the ideal dipoles model must be taken with caution because it does not take into account considerable length of a combined function magnet suitable for cyclotron extraction system, which is of the order of 0.5 m [7].

B. Infinitely Long Current Stripes

With the aim to obtain a more realistic model of a lengthy slanted off-centered dipole its poles are represented each with two infinitely long current stripes, Fig. 7. There are four parameters whose influence on the field must be considered: the slant angle, α , normalized half-distance between the poles, b/a , normalized half-width of the poles, d/a , and normalized half-width of the current stripes, h/a .

Magnetic field of the current stripes model is examined using the same parameters that were used in the case of the ideal dipoles model, i.e., the scaled bending and focusing parameters, B_{st}/B_0 and aG/B_0 , as well as the linearity coefficient, S . An infinitely long current stripe is treated as a collection of infinitely long wires; therefore, its magnetic field is calculated by integrating magnetic fields of infinite wires over the stripe width. Using the expression given in [24] for the strength of the magnetic field at a distance r from an infinitely long wire with current dI ,

$$dB = \frac{\mu_0 dI}{2\pi r}, \quad (5)$$

the magnetic field of an infinitely long current stripe defined by $y \in [-h, h]$ and its uniformly distributed total current, I , is calculated to be

$$B_x = \frac{\mu_0 I}{8\pi h} \ln \frac{x^2 + (y-h)^2}{x^2 + (y+h)^2}$$

$$B_y = \frac{\mu_0 I}{8\pi h} \left(\arctan \frac{y+h}{x} - \arctan \frac{y-h}{x} \right). \quad (6)$$

Using formulas (6) for the magnetic field of a single infinitely long current stripe, characterized by its width, $2h$, and uniformly distributed total current, I , after appropriate coordinate transformation for different stripes within the model and summation, the vertical magnetic field component of the slanted off-centered dipole along the horizontal axis, i.e., for $y = 0$, is calculated to be

$$B_y(x)/B_0 = \frac{a}{h} \sum_{i=1,2} \sum_{j=3,4} \{(-1)^{i+j-1} \cdot [\cos \alpha \ln(x_i^2 + x_j^2) + 2 \sin \alpha \arctan(x_j/x_i)]\} \quad (7)$$

where

$$x_1 = (x/a + 1) \sin \alpha - b/a \cos \alpha + d/a$$

$$x_2 = (x/a + 1) \sin \alpha - b/a \cos \alpha - d/a$$

$$x_3 = (x/a + 1) \cos \alpha + b/a \sin \alpha$$

$$x_4 = (x/a + 1) \cos \alpha + b/a \sin \alpha + 2h/a, \quad (8)$$

$B_0 = \mu_0 I / (4\pi a)$, $\mu_0 = 4\pi \cdot 10^{-7}$ H/m, and I is stripe current, whereas α , a , b , d , and h are defined in Fig. 7. Since $B_{st}/B_0 = B_y(0)/B_0$, the formula for the scaled bending parameter, B_{st}/B_0 , is identical to (7); however, the values for x_1 , x_2 , x_3 , and x_4 are now

$$x_1 = \sin \alpha - b/a \cos \alpha + d/a$$

$$x_2 = \sin \alpha - b/a \cos \alpha - d/a$$

$$x_3 = \cos \alpha + b/a \sin \alpha$$

$$x_4 = \cos \alpha + b/a \sin \alpha + 2h/a. \quad (9)$$

These values, defined by (9), should be used to calculate scaled focusing parameter, aG/B_0 , as well:

$$aGB_0 \equiv \frac{a}{B_0} \left. \frac{\partial B_y}{\partial x} \right|_{x=0} = \frac{2a}{h} \sum_{i=1,2} \sum_{j=3,4} \{(-1)^{i+j-1} \cdot [x_i \sin(2\alpha) + x_j \cos(2\alpha)] / (x_i^2 + x_j^2)\}. \quad (10)$$

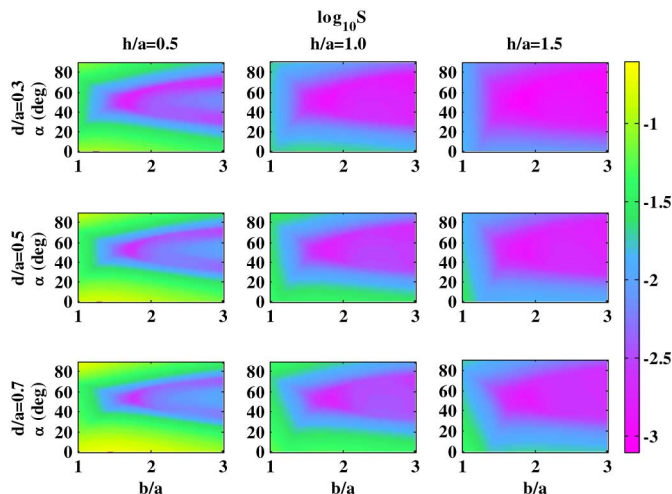


Fig. 8. Field linearity coefficient. Each of the nine graphs gives the dependence of S on α and b/a for a particular pair of values of d/a and h/a . The first, second and third row of graphs corresponds to d/a value of 0.3, 0.5, and 0.7, respectively. Each graph in the first, second and third column represents a set of current stripes models with the value of h/a equal to 0.5, 1.0, and 1.5, respectively. The areas corresponding to the desirable low values of S are larger for smaller d/a and larger h/a .

Further, B_y calculated with (7) and (8), G determined by (10) and (9), as well as B_{st} defined with (7) and (9) are used in (4) to obtain S , the linearity coefficient of B_y along the line segment $x \in [-a/2, a/2]$, which corresponds to the current stripes model.

In the ideal dipoles model each of the three considered characteristics of the magnetic field depends on the two parameters, α and b/a ; therefore, the dependence is illustrated with a single contour plot per magnetic field characteristics, see Fig. 5. In the current stripes model there are four parameters whose influence has to be investigated, α , b/a , d/a , and h/a . Consequently, the dependence of the linearity coefficient, S , focusing parameter, aG/B_0 , and bending parameter, B_{st}/B_0 , on these four parameters is each depicted with the nine contour plots in Figs. 8, 9, and 10, respectively.

Comparison of the results shown in Figs. 8, 9, and 10 reveals that the process of defining the four model parameters, α , b/a , d/a , and h/a , must be a trade-off between small values of the linearity coefficient and large values of the focusing and bending coefficients. The optimization criterion and restrictions should be chosen in accordance with the desired field linearity as well as with the focusing and bending strengths needed in a particular design of the device. For the sake of consistency, the optimization criterion, $\max(|B_{st}/B_0| \cdot |aG/B_0|)$, and the restriction, $S \leq 0.004$, used here as an example are the same as those used for the ideal dipoles model. The obtained optimized geometry of the current stripes model has $\alpha = 51^\circ$, $b/a = 1.65$, $d/a = 0.7$, and $h/a = 0.5$. The scaled horizontal and vertical components of the magnetic field obtained with this geometry in the beam area are given in Fig. 11. The values of the corresponding focusing, bending and field linearity coefficients are $aG/B_0 = -0.62$, $B_{st}/B_0 = 0.81$, and $S = 0.004$.

Table I lists the considered optimized example in the first row and compares it with the models resulting from three other optimization conditions. The two models with $\alpha = 45^\circ$ and

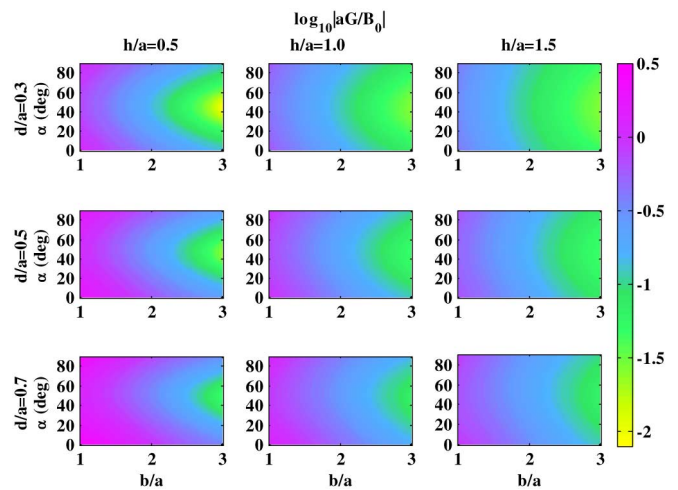


Fig. 9. Beam focusing coefficient. The format of the figure is the same as for Fig. 8. The areas corresponding to the desirable large values of aG/B_0 are larger for larger d/a and smaller h/a . The models with smaller values of b/a provide stronger focusing.

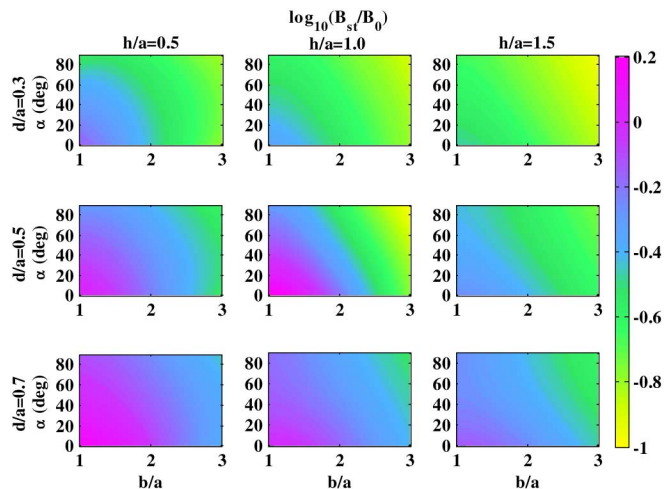


Fig. 10. Beam bending coefficient. The format of the figure is the same as for Fig. 8. The areas corresponding to the desirable large values of B_{st}/B_0 are larger for larger d/a and smaller h/a . The models with smaller values of α and b/a provide stronger steering.

$b/a = 1$ are the limiting examples of an independently powered quadrupole. The model in the second row represents a typical quadrupole with the minimal linearity coefficient, whereas the one in the third row is characterized by the maximal bending coefficient. Comparison of these two models with other models of a typical quadrupole revealed that the two limiting models are such with respect to all three considered coefficients. Namely, the model with the minimal linearity coefficient also has the minimal values of the focusing and bending coefficients, whereas the one with the maximal bending coefficient is characterized with the maximal linearity and focusing coefficients, as well. The typical quadrupole model with the most linear field, i.e., the smallest S , is inferior to our optimized model in all respects. The typical quadrupole model with the maximal values of the coefficients does provide 2.2 times stronger focusing as well as 1.2 stronger bending than our optimized model; however, it is 13 times less linear. In addition, there

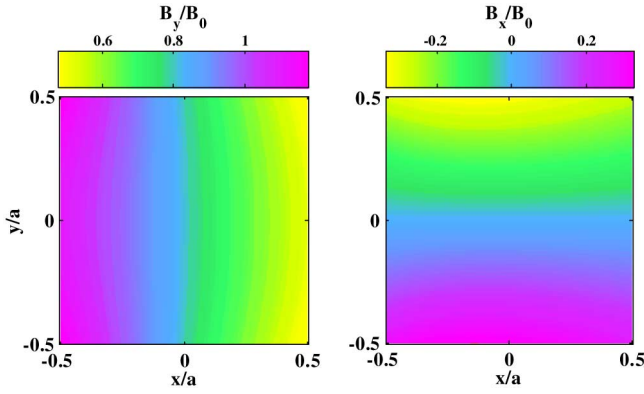


Fig. 11. Normalized magnetic field components. The scaled vertical (left graph) and horizontal (right graph) magnetic field components correspond to the current stripes model with $\alpha = 51^\circ$, $b/a = 1.65$, $d/a = 0.7$, and $h/a = 0.5$. The contour lines do not deviate very much from the desired vertical and horizontal straight lines pattern for B_y and B_x , respectively. The deviation from the desired pattern is more pronounced at larger distances from the axes.

TABLE I
COMPARISON OF FOUR MODEL GEOMETRIES

α ($^\circ$)	b/a	d/a	h/a	S	aG/B_0	B_{st}/B_0
51	1.65	0.7	0.5	0.004	-0.62	0.81
45	1	0.3	1.5	0.014	-0.34	0.27
45	1	0.7	0.5	0.053	-1.36	1.00
30	1.15	0.7	0.5	0.050	-1.40	1.10

are examples of other models which provide stronger focusing as well as bending even with slightly better linearity than the independently powered typical quadrupole, as can be seen from the third and fourth row of Table I.

The field linearity, focusing as well as bending coefficients predicted by the infinite current stripes model satisfy the requirements set for the combined function magnet used in the extraction system of a multipurpose cyclotron. Validity of this analytical model as well as of the concept of slanted off-centered dipoles is further tested by a numerical model.

III. NUMERICAL MODEL

The numerical model whose geometry is given in Fig. 12 is constructed and its magnetic field is calculated with MERMAID—a 3-D software package based on the first order finite elements method [25]. A 3-D mesh of the model is constructed from a non-uniform 2-D triangular mesh in $z = const.$ planes and a non-uniform 1-D grid in the z -direction.

Having in mind comparison of the analytical and numerical models, the geometry of the numerical model is chosen to resemble as closely as possible the geometry of the infinite current stripes model. In order to also relate the numerical model to the existing example given in [7], it was assumed that $a = 10$ cm and that the coils are powered by $NI = 100$ kA. The resulting magnetic flux density at the mid-length of the device is given in Fig. 13. The obtained values of the steering field and focusing field gradient at the coordinate system origin are $B_{st} = 0.36$ T and $G = 2.3$ T/m.

The fields obtained with the numerical model and two analytical models are compared in Fig. 14. Unlike in Figs. 6 and

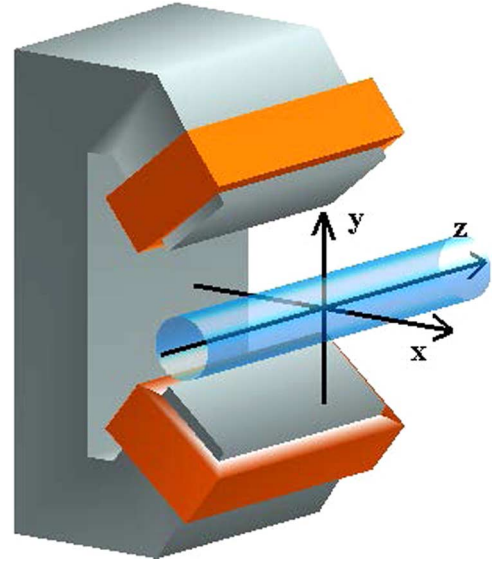


Fig. 12. Numerical model. The placement and width of the inner layers of the coils, i.e., next to the iron, in the $z = 0$ plane are identical to those of the infinite current stripes in the optimized current stripes model, namely, $\alpha = 51^\circ$, $b/a = 1.65$, $d/a = 0.7$, and $h/a = 0.5$. The coil thickness and length in the z -direction is taken to be $w/a = 0.3$ and $L/a = 4$, respectively. The magnetic properties of the iron are defined with one of the $B - H$ curves embedded in the numerical modeling software.

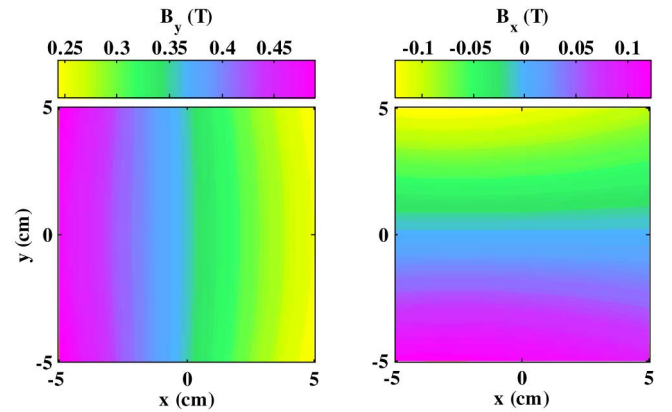


Fig. 13. Magnetic field components. The vertical and horizontal magnetic flux density components in the mid-plane, i.e., for $z = 0$, of the numerical model are given in the left and right graph, respectively. The longitudinal field component, B_z , is negligible. The contour lines do not deviate very much from the desired vertical straight lines for B_y and horizontal lines for B_x .

11, where B_0 is used for field normalization, the fields are here normalized to B_{st} in order to enable quantitative as well as qualitative comparison of the models.

The slanted dipole off-centered to the left of the beam area depicted in Fig. 12 is combined with its mirror image, referred to earlier as the slanted dipole displaced to the right of the beam line. Both dipoles are assumed to have the same maximal values of steering and focusing components of their fields, $B_{max} = 0.36$ T and $G_{max} = 2.3$ T/m, obtained from Fig. 13; however, the dipoles are independently powered to broaden the range of the resulting field according to Fig. 2. As stated earlier, the two input parameters, k_1 and k_2 , are not independently responsible one for the focusing and the other for the bending function of the combined magnet. Fortunately, the needed excitation levels of

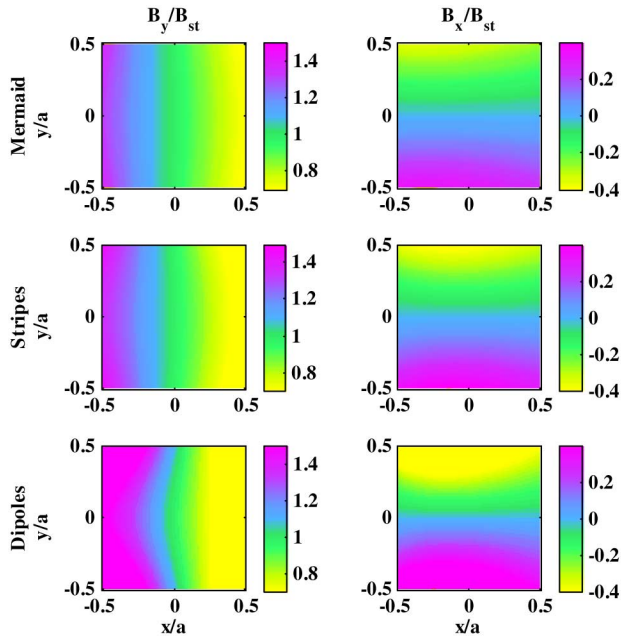


Fig. 14. Model comparison. The vertical, B_y (left column of graphs), and horizontal, B_x (right column of graphs), magnetic field components in the plane $z = 0$, of the numerical, current stripes, and ideal dipoles model are depicted in the first, second, and third row of graphs, respectively. To enable comparison, the field components are scaled to the steering field of the corresponding model. Note the good qualitative as well as quantitative agreement between the numerical model and the analytical model with infinite current stripes.

the two slanted dipoles are easily determined from the desired focusing and bending coefficients as $k_1 = (k_B - k_G)/2$ and $k_2 = (k_B + k_G)/2$.

To illustrate applicability of the described device in the stripping extraction system of multipurpose cyclotrons the limiting requirements for the combined function magnet from [7] are considered. For the beam of protons which are accelerated to the energy of 55 MeV as H^- ions the field needed in the combined function magnet is $B_y = 0.70$ T. Consequently, $k_B = k_1 + k_2 = 1.97$ and $k_G = k_2 - k_1 = 0$, which correspond to the scaling factors of the left and right off-centered dipoles $k_1 = 0.98$ and $k_2 = 0.98$, see Fig. 2 caption. For the ion beam accelerated as H_2^+ ions to 44 MeV, which are extracted as 22 MeV protons, the field in the combined magnet needs to be $B_y = -1$ T/m \cdot $x - 0.15$ T. Therefore, $k_B = -0.42$, $k_G = -0.43$, $k_1 = 0.01$, and $k_2 = -0.43$. The needed fields and those achieved in the numerical model of the proposed combined function magnet are shown in Fig. 15.

The purpose of the presented numerical model is to validate the analytical model and the principle of device's operation as well as to illustrate their applicability. In an engineering design of a particular device this numerical model can serve only as a first step in the design process. The good agreement between the numerical model and the analytical current stripes model ensures that Figs. 8, 9, and 10 can be used to determine the first estimate of the geometry of a device with the desired focusing and bending characteristics. Even though a simplified numerical model similar to the one presented here provides validation of the desired performance of a device, during the engineering design further steps towards a more realistic model as well as

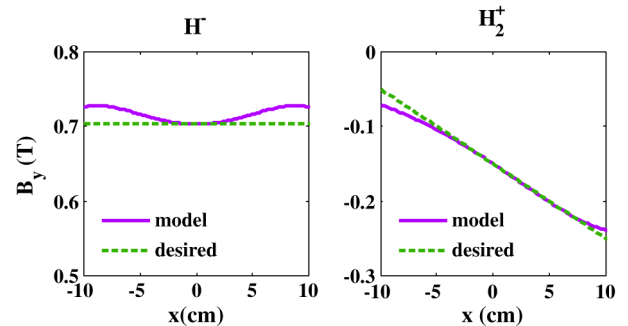


Fig. 15. Comparison of achieved and desired fields. To illustrate the applicability of the proposed design of the combined function magnet its fields are compared with the two limiting fields needed by the stripping extraction system described in [7]. The maximal relative errors of the achieved fields in the beam area, i.e. between -5 cm and 5 cm, are 1.87% for the H^- ions and 3.00% for the beam accelerated as H_2^+ ions, whereas for the two times larger interval, $x \in [-10$ cm, 10 cm], the maximal relative errors are 3.24% and 13.84%, respectively.

better field quality are due. For example, field linearity could be improved by changing the pole profile from the simple flat surface to the shape determined analytically using the method similar to the one described in [17] or numerically using the approach analogous to the one shown in [26]. Unlike the numerical model discussed here, in designing a particular device numerical modeling will focus on fulfilling engineering requirements rather than on resembling the analytical model. For example, the coil thickness as well as magnetomotive force would be adjusted in accordance with the resulting current density rather than with the similarity to the analytical model.

To illustrate a more realistic numerical modeling we use the same limiting requirements represented by the fields $B_y = 0.70$ T and $B_y = -1$ T/m \cdot $x - 0.15$ T, as for the simplified numerical model. The currents needed to achieve the field of 0.35 T or the gradient of 0.5 T/m with the slanted dipole modeled by the analytical, optimized infinite current stripes model are 432 kA and 80 kA, respectively. Consequently, the critical, the larger value of the two, $I_{\max} = 432$ kA, is used further for rough estimates of the realistic numerical model parameters. Unlike the analytical, the numerical model takes into account iron core, which enlarges the field due to magnetization. In addition, iron pole shape, which can follow any of the equipotential surfaces, enables field enhancement resulting from the decrease of the distance between the dipole poles. At the same time, since the two slanted dipoles in our example of the combined magnet are closer to each other than are the two poles within a dipole, the coupling between the two dipoles is expected to cause the field decrease as well as the field gradient increase. Namely, the iron cores of both slanted dipoles affect the resulting field even if only one of the dipoles is powered. The analytical infinite stripes model can be used to roughly estimate this effect as $C_C = B(a, b)/B(-a, b) = 9.84\%$, where $B(-a, b)$ and $B(a, b)$ are, respectively, the field produced by the one slanted dipole at its pole tip and at the mirror image of its pole tip, i.e., at the point where the pole of the mirror dipole within the combined magnet would be. In order to take this effect into account the realistic numerical

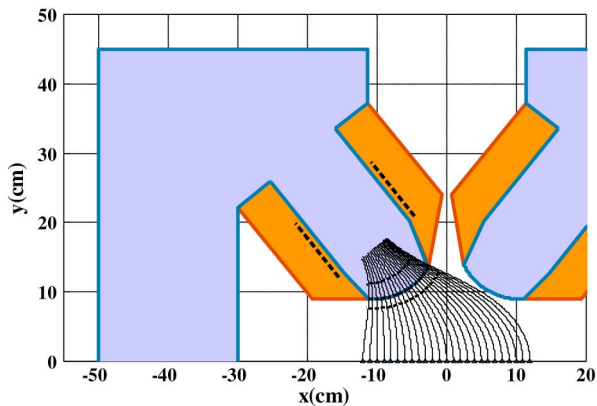


Fig. 16. Realistic numerical model. The infinite current stripes of the analytical model are indicated by the dashed straight line segments. The magnetic field lines corresponding to the analytical model are used to calculate three equipotential surfaces depicted with dashed black curves, the middle of which is used as a pole profile for the realistic numerical model. The coil width is taken to be $w = 6$ cm. The coil's outer height is extended to 17 cm compared to 10 cm wide current stripes, whereas on the inside the coils match the pole length. The iron core is 80 cm long along the z -axis.

model must include both slanted dipoles, unlike the simplified numerical model discussed previously. In a realistic numerical model the desired fields have to be achieved with a reasonable value of the induction current, i.e. the coil current density should not exceed $J_{\max} = 10$ A/mm². The mentioned estimates can be related to the coil's cross-section, S_{coil} , and field enhancement provided by the iron cores, C_{Fe} , as $S_{\text{coil}} \cdot C_{\text{Fe}} = (1 + C_c) \cdot I_{\max} / J_{\max} = 474.5$ cm². For example, if the iron core provides field enhancement factor equal to 4, the cross-section of the coils needs to be approximately 120 cm². The outline of a numerical model based on these estimates is shown in Fig. 16. Since the estimates are based on the analytical model the obtained outline of the numerical model should be treated as the second step in the design process. When designing a particular combined function magnet gap size, dipole coupling, as well as induction current density have to be carefully considered and further numerical model adjustments must follow.

IV. CONCLUSION

The proposed design of a combined function magnet offers simple and cost-effective way to improve extraction from multipurpose cyclotrons. Using two analytical models and one numerical model, it is shown that two independently powered, slanted, as well as off-centered dipoles form a combined function magnet suitable for use in the stripping extraction system of a multipurpose cyclotron. Bending and focusing functions of the magnet are uncoupled and each of them can be independently chosen to have any value between the two values which correspond to the limiting excitations of a single slanted off-centered dipole. In addition, each function of the combined magnet can have a value as high as double its limiting value corresponding to the slanted dipole. These additional values of one of the coefficients, bending or focusing, are achieved at the expense of the corresponding available range of the other coefficient. Although the bending as well as the focusing coefficient of the combined

magnet is not governed by a single input parameter, the needed excitation coefficients of the two slanted dipoles are easily calculated using two linear expressions.

Applicability of the proposed combined function magnet is illustrated using the limiting fields of an example stripping extraction system and acceptable discrepancy between the desired and achieved fields is obtained. Nevertheless, the considered very simplified numerical model with its straight edges leaves numerous possibilities for field improvements. For example, the pole shape could be refined using a method similar to the one described in [17]. The shape and size of the numerical model is chosen to match the optimized analytical current stripes model. Therefore, optimization of the numerical model similar to the optimizations of the two analytical models performed using the data in Fig. 5 and Figs. 8, 9, and 10, is likely to improve the obtained field as well.

On the other hand, due to not so tight field accuracy requirements it seems worthwhile not only to optimize the geometry of the combined magnet, but to explore the possibility of obtaining a combined function magnet using the geometry of a typical quadrupole, as well. In [27] and [28] it was shown that a simple cost-effective change of the powering scheme of an existing device can lead to qualitatively different device. Similarly, extending the asymmetric excitation of a typical quadrupole, suggested in [23], to fully independent powering of its two-by-two poles can produce a combined function magnet suitable for ion beam extraction from a multipurpose cyclotron.

REFERENCES

- [1] S. Z. An, F. P. Guan, H. D. Guan, S. M. Wei, H. J. Yao, Y. J. Bi, J. Q. Zhong, X. L. Jia, T. J. Zhang, Y. L. Lü, G. F. Song, B. Ji, and T. Ge, "Stripping extraction calculation and simulation for CYCIAE-100," *Chinese Phys. C (HEP & NP)*, vol. 33, no. 2, pp. 42–46, Jun. 2009.
- [2] D. Vandeplasse, W. Beeckman, W. Kleeven, S. Zarella, J. L. Delvaux, L. Medeiros-Romao, J. C. Amélia, Y. Jongen, and J. Fermé, "Extraction simulations for the IBA C70 cyclotron," in *Proc. 18th Int. Conf. Cyclotrons Their Applications*, Giardini Naxos, Italy, Oct. 1-5, 2007, pp. 63–65.
- [3] D. Solivajs, O. N. Borisov, A. Gall, G. G. Gulbekian, J. Keníž, J. Kliman, S. Králik, and M. Pavlović, "A study of charge-exchange beam extraction from the multi-purpose isochronous cyclotron DC-72," *J. Elect. Engrg.*, vol. 55, no. 7–8, pp. 201–206, 2004.
- [4] D. H. An, J. S. Chai, H. S. Chang, B. H. Hong, S. Hong, I. S. Jung, J. Kang, Y. Kim, M. Y. Lee, C. S. Park, J. Y. Suk, and T. K. Yang, "The stripping extraction system in the KIRAMS-13 cyclotron," in *Proc. 3rd Asian Particle Accelerator Conf.*, Gyeongju, Korea, Mar. 22-26, 2004, pp. 111–112.
- [5] J. L. Ristić-Djurović and N. Nešković, "Analytical prediction of ion stripping extraction from isochronous cyclotrons," *IEEE Trans. Nucl. Sci.*, vol. 59, no. 2, pp. 268–271, Apr. 2012.
- [6] J. L. Ristić-Djurović and N. Nešković, "Influence of cyclotron magnet gap size on stripping extraction," *IEEE Trans. Nucl. Sci.*, vol. 58, no. 3, pp. 1188–1195, Jun. 2011.
- [7] J. L. Ristić-Djurović and S. Čirković, "Unidirectional stripping extraction from a cyclotron which accelerates light as well as heavy ions," *Phys. Rev. Special Topics—Accel. Beams*, vol. 6, p. 033501, Mar. 2003.
- [8] J. L. Ristić-Djurović, "Stripping extraction of positive ions from a cyclotron," *Phys. Rev. Special Topics—Accel. Beams*, vol. 4, p. 123501, Dec. 2001.
- [9] V. V. Kashikhin, Y. I. Alexahin, N. V. Mokhov, and A. V. Zlobin, "High-field combined-function magnets for a 1.5×1.5 TeV muon collider storage ring," in *Proc. 3rd Int. Particle Accelerator Conf.*, New Orleans, LA, USA, May 20-25, 2012, pp. 3587–3589.
- [10] S. C. Leemann, J. Ahlbäck, Å. Andersson, M. Eriksson, M. Johansson, L. -J. Lindgren, M. Sjöström, and E. Wallén, "Status of the MAX IV storage rings," in *Proc. 1st Int. Particle Accelerator Conf.*, Kyoto, Japan, May 23-28, 2010, pp. 2618–2620.

- [11] A. Madur, D. Arbelaez, S. Marks, S. Prestemon, D. Robin, R. Schlueter, C. Steier, and W. Wan, "Harmonic sextupoles for the Advanced Light Source low emittance upgrade," *Nucl. Instrum. Meth. A*, vol. 649, pp. 39–41, 2011.
- [12] S. P. Möller, H. Bach, F. Bødker, T. G. Christiansen, A. Elkjær, S. Friis-Nielsen, N. Hauge, J. Kristensen, L. Kruse, and B. R. Nielsen, "Status of the injection system for the Australian synchrotron project," in *Proc. 21st Particle Accelerator Conf.*, Knoxville, TN, USA, May 16–20, 2005, pp. 3271–3273.
- [13] T. Nakamoto, N. Higashi, T. Ogitsu, A. Terashima, Y. Ajima, M. Anerella, R. Gupta, H. Hattori, T. Ichihara, Y. Iwamoto, N. Kimura, Y. Makida, T. Obana, K. Tanaka, P. Wanderer, and A. Yamamoto, "Design of superconducting combined function magnets for the 50 GeV proton beam line for the J-PARC neutrino experiment," *IEEE Trans. Appl. Supercond.*, vol. 14, no. 2, pp. 616–619, Jun. 2004.
- [14] C. M. Spencer, C. Adolphsen, M. Berndt, D. R. Jensen, R. Rogers, J. C. Sheppard, S. St. Lorant, T. B. Weber, J. Weisend, II, H. Brueck, and F. Toral, "Measuring the magnetic center behavior and field quality of an ILC superconducting combined quadrupole-dipole prototype," *IEEE Trans. Appl. Supercond.*, vol. 20, no. 3, pp. 1964–1968, Jun. 2010.
- [15] D. S. Robin, D. Arbelaez, S. Caspi, C. Sun, A. Sessler, W. Wan, and M. Yoon, "Superconducting toroidal combined-function magnet for a compact ion beam cancer therapy gantry," *Nucl. Instrum. Meth. A*, vol. 659, pp. 484–493, 2011.
- [16] A. Morita, Y. Iwashita, A. Noda, T. Shirai, H. Tongu, M. Umezawa, K. Hiramoto, and M. Tadokoro, "Design and measurement of a combined function magnet intended for a cancer therapy accelerator," *Phys. Rev. Special Topics—Accel. Beams*, vol. 4, p. 122401, Dec. 2001.
- [17] G. Sinha and G. Singh, "Design and characterization of combined function multipole magnet for accelerators," *Rev. Sci. Instrum.*, vol. 79, p. 123302, Dec. 2008.
- [18] P. R. Sarma, "Ideal coil shape for combined function superconducting magnets," *J. Phys. D: Appl. Phys.*, vol. 40, pp. 3056–3059, 2007.
- [19] P. R. Sarma, S. K. Pattanayak, and R. K. Bhandari, "New method of designing pole profile in combined function magnets of high field quality," *Rev. Sci. Instrum.*, vol. 70, no. 6, pp. 2655–2660, Jun. 1999.
- [20] S. Koscielniak, "Analysis of orbits in combined function magnets," in *Proc. 23rd Particle Accelerator Conf.*, Vancouver, Canada, May 4–8, 2009, pp. 5038–5040.
- [21] M. Yoon, J. Corbett, M. Cornacchia, J. Tanabe, and A. Terebilo, "Analysis of a storage ring combined-function magnet: Trajectory calculation and alignment procedure," *Nucl. Instrum. Meth. A*, vol. 523, pp. 9–18, 2004.
- [22] M. Seidl, "Identification and correction of antisymmetric field components in combined function magnets," *Phys. Rev. Special Topics—Accel. Beams*, vol. 5, p. 062402, Jun. 2002.
- [23] V. N. Litvinenko, Y. Wu, B. Burnham, J. M. J. Madey, and S. H. Park, "Performance of achromatic lattice with combined function sextupoles at Duke storage ring," in *Proc. 16th Particle Accelerator Conf.*, Dallas, Texas, USA, May 1–5, 1995, pp. 796–798.
- [24] R. P. Feynman, R. B. Leighton, and M. Sands, *The Feynman Lectures on Physics*. Menlo Park, CA: Addison-Wesley, 1977, vol. 2, ch. 13, 6th printing.
- [25] *Mermaid 2-D and 3-D User's Guide*. Novosibirsk, Russia: SIM, 1994.
- [26] S. Čirković, J. L. Ristić-Djurović, A. S. Vorozhtsov, A. Ž. Ilić, and N. Nešković, "Method for fine magnet shaping in cyclotrons," *IEEE Trans. Nucl. Sci.*, vol. 56, no. 5, pp. 2821–2827, Oct. 2009.
- [27] J. L. Ristić-Djurović, S. Čirković, and A. Ž. Ilić, "Optimization of equally charged quadrupole parameters," *IEEE Trans. Nucl. Sci.*, vol. 60, no. 3, pp. 2161–2169, Jun. 2013.
- [28] J. L. Ristić-Djurović, S. Čirković, and A. Ž. Ilić, "Ion beam acceleration with radio frequency powered rainbow lens," *IEEE Trans. Nucl. Sci.*, vol. 60, no. 2, pp. 1272–1279, Apr. 2013.

Higher-Order Frequency-Domain FEM Analysis of EM Scattering Off a Moving Dielectric Slab

Andjelija Ž. Ilić, *Member, IEEE*, and Milan M. Ilić, *Member, IEEE*

Abstract—A higher-order one-dimensional (1-D) finite element method for analysis of electromagnetic wave scattering off of a moving dielectric slab is proposed and developed. The numerical results are verified by comparison to analytical solutions.

Index Terms—Electromagnetic analysis, finite element methods, higher-order methods, Lorentz transformation, moving media, scattering.

I. INTRODUCTION

THE FINITE element method (FEM) is one of the most versatile techniques for electromagnetic (EM) analysis [1]. However, traditional FEM techniques and commercial high-frequency software tools solve macroscopic electromagnetic (EM) problems in the presence of stationary media. In this letter, we propose a novel higher-order FEM for EM analysis of scattering off a moving dielectric slab. The method supports modeling of slabs with arbitrarily (continuously) inhomogeneous layers and oblique angles of incidence and can be a useful tool in one-dimensional (1-D) analyses of relativistic plasmas with complex media parameter profiles, where analytical solutions are difficult or impossible to obtain. For a stationary slab, analytical solution (for the piecewise homogeneous slab) and a low-order FEM solution can be found in [1], whereas a higher-order FEM solution (for the normal incidence) can be found in [2]. For a moving slab, analytical solutions for homogeneous lossless non-magnetic slabs can be found in [3] and [4], and for a slab with linearly varying permittivity in [5]. Comparative full-wave numerical solutions are hard to find, they are usually in the time domain and often limited to perfect electric conductor (PEC) mirrors (e.g., [6]), whereas general frequency-domain FEM solutions could not be found.

II. THEORY AND IMPLEMENTATION

Consider a uniform linearly polarized plane EM wave impinging obliquely on a flat dielectric slab situated in vacuum, as shown in Fig. 1. The slab is stationary in its rest frame S' , which is moving at a constant velocity with respect to laboratory

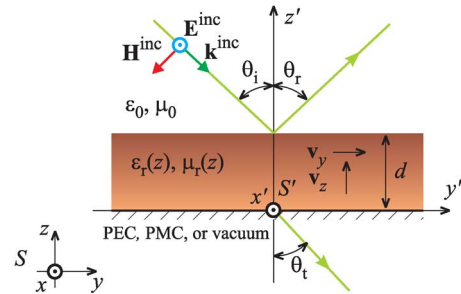


Fig. 1. Uniform plane wave scattering off a moving dielectric slab backed by a PEC, perfect magnetic conductor (PMC), or vacuum.

frame S . We consider a 1-D case, for which the incident wave polarization remains unchanged under Lorentz transformations, hence the slab can only move in the yOz -plane (plane of incidence) with velocity vector components v_y and v_z . In its rest frame, the slab is infinite in the $x'O'y'$ -plane, its (proper) thickness is d , and it can generally be inhomogeneous with relative permittivity ϵ_r and relative permeability μ_r , varying only as functions of z' . (Lossless frequency-independent parameters are assumed, noting that this assumption can easily be removed with minor modifications of the method.)

Fig. 1 shows an example of a TE incident wave, represented by its complex electric field intensity vector in S frame as

$$\mathbf{E}^{\text{inc}} = E_0 e^{-j\mathbf{k}^{\text{inc}} \cdot \mathbf{r}} \mathbf{i}_x \quad (1)$$

E_0 , $\mathbf{k}^{\text{inc}} = k_y \mathbf{i}_y + k_z \mathbf{i}_z$, and $\mathbf{r} = x \mathbf{i}_x + y \mathbf{i}_y + z \mathbf{i}_z$ being the complex field intensity at the origin, the incident-wave wave vector, and the position vector, respectively, where $|\mathbf{k}^{\text{inc}}| = \omega/c$ is the wavenumber, $c = 1/\sqrt{\epsilon_0 \mu_0}$ is the speed of light, and ω is the angular frequency of the implied time-harmonic excitation. The angles of the incident, reflected, and transmitted waves, θ_i , θ_r , and θ_t (which can be computed from respective wave vector components), are also shown in the figure. TM polarization is considered by means of dual expressions obtained by exciting the slab with a wave whose complex magnetic field intensity vector is given as $\mathbf{H}^{\text{inc}} = H_0 e^{-j\mathbf{k}^{\text{inc}} \cdot \mathbf{r}} \mathbf{i}_x$. However, these expressions are omitted to maintain conciseness of the letter. Note also that in case of normal incidence, the TE or TM polarizations still remain distinct as they are different with respect to the plane of movement.

We next introduce the normalized slab velocity components

$$\beta_y = \frac{v_y}{c} \quad \beta_z = \frac{v_z}{c} \quad (2)$$

and Lorentz-transformation factors

$$\beta = \sqrt{\beta_y^2 + \beta_z^2} \quad \gamma = \frac{1}{\sqrt{1 - \beta^2}} \quad (3)$$

Manuscript received June 14, 2013; accepted July 06, 2013. Date of publication July 10, 2013; date of current version August 01, 2013. This work was supported by the Serbian Ministry of Education, Science, and Technological Development under Grants III-45003 and TR-32005.

A. Ž. Ilić is with the Innovation Center, School of Electrical Engineering, University of Belgrade, 11120 Belgrade, Serbia (e-mail: andjelija@iee.org).

M. M. Ilić is with the University of Belgrade, School of Electrical Engineering, 11120 Belgrade, Serbia, and also with the Department of Electrical and Computer Engineering, Colorado State University, Fort Collins, CO 80523-1373 USA (e-mail: milanilic@etf.rs).

Color versions of one or more of the figures in this letter are available online at <http://ieeexplore.ieee.org>.

Digital Object Identifier 10.1109/LAWP.2013.2272717

To facilitate FEM computation, all incident-wave parameters, initially given in the S rest frame, are first transformed by means of the Lorentz transformation as seen from the S' frame, yielding [7]

$$\omega' = \gamma(\omega - ck_y\beta_y - ck_z\beta_z), \quad k'_x = 0 \quad (4)$$

$$k'_y = k_y \left(1 + (\gamma - 1)\beta_y^2/\beta^2\right) + k_z(\gamma - 1)\beta_y\beta_z/\beta^2 - \gamma\beta_y\omega/c \quad (5)$$

$$k'_z = k_z \left(1 + (\gamma - 1)\beta_z^2/\beta^2\right) + k_y(\gamma - 1)\beta_y\beta_z/\beta^2 - \gamma\beta_z\omega/c \quad (6)$$

$$E'_x = \gamma(E_x + \beta_y c B_z - \beta_z c B_y) \quad E'_y = 0 \quad E'_z = 0 \quad B'_x = 0 \quad (7)$$

$$B'_y = B_y \left(1 + (\gamma - 1)\beta_z^2/\beta^2\right) - B_z(\gamma - 1)\beta_y\beta_z/\beta^2 - \gamma\beta_z E_x/c \quad (8)$$

$$B'_z = B_z \left(1 + (\gamma - 1)\beta_y^2/\beta^2\right) - B_y(\gamma - 1)\beta_y\beta_z/\beta^2 + \gamma\beta_y E_x/c \quad (9)$$

noting that, for the given example, from Maxwell's equations we have

$$\omega B_y = k_z E_x \quad \omega B_z = -k_y E_x. \quad (10)$$

Disregarding the propagation term in the y' direction, $e^{-jk'_y y'}$, the incident field becomes

$$E'_x{}^{\text{inc}}(z') = E'_0 e^{-jk'_z z'} \quad (11)$$

the total field in front of the slab ($z' > d$) is represented as

$$E'_x(z') = E'_0 e^{-jk'_z z'} + E'_R e^{jk'_z z'} \quad (12)$$

and the Cauchy boundary condition, obtained by taking the first derivative of (12) and eliminating unknown E'_R , becomes

$$\left[\frac{\partial E'_x}{\partial z'} - jk'_z E'_x \right]_{z'=d^+} = -2jk'_z E'_0 e^{-jk'_z z'} \Big|_{z'=d^+}. \quad (13)$$

Behind the slab ($z' < 0$), the total transmitted field (in vacuum) is

$$E'_x(z') = E'_T e^{-jk'_z z'} \quad (14)$$

and the Cauchy boundary condition, obtained similarly as (13), becomes

$$\left[\frac{\partial E'_x}{\partial z'} + jk'_z E'_x \right]_{z'=0^-} = 0. \quad (15)$$

Under given circumstances, the electric field vector wave equation reduces to

$$\frac{\partial}{\partial z'} \left(\alpha_F \frac{\partial E'_x}{\partial z'} \right) + \alpha_F \beta_F E'_x = 0 \quad (16)$$

where

$$\alpha_F = \frac{1}{\mu_r}, \quad \beta_F = \left(\frac{\omega'}{c} \right) \varepsilon_r \mu_r - k_y'^2. \quad (17)$$

All natural boundary conditions, between the finite elements into which the slab can be subdivided, or on the slab outer boundaries, are imposed and enforced in the S' rest frame, thus on the front slab boundary we have

$$E'_x \Big|_{z'=d^+} = E'_x \Big|_{z'=d^-}, \quad \alpha_F \frac{\partial E'_x}{\partial z'} \Big|_{z'=d^+} = \alpha_F \frac{\partial E'_x}{\partial z'} \Big|_{z'=d^-} \quad (18)$$

and similarly on all boundaries between the elements and on the back boundary.

To solve (16), we next set up the higher-order 1-D FEM in the S' rest frame (where the slab is stationary) employing the higher-order field expansion, formally presented as

$$E'_x = \sum_{e=1}^M \sum_{j=1}^{n^e+1} a_j^e f_j^e \quad (19)$$

where M is the number of nonoverlapping uniformly sized 1-D elements, n^e is the order of the polynomial field-expansion in the e th element (we use $n^e = n$ for all elements in this letter), f^e are polynomial basis functions locally defined on each element, and a^e are unknown complex coefficients. Standard discretization of (16), employing (19), yields

$$\sum_{j=1}^{n^e} a_j \left[- \int_{z_i^e}^{z_r^e} \alpha_F \frac{df_i}{dz'} \frac{df_j}{dz'} dz' + \int_{z_i^e}^{z_r^e} \alpha_F \beta_F f_i f_j dz' \right] = \int_{z_i^e}^{z_r^e} f_i g dz' - f_i \alpha_F \frac{dE'}{dz'} \Big|_{z_i^e}^{z_r^e} \quad (20)$$

in each element. The details on the polynomial basis functions, global matrix assembly, and enforcement of the boundary conditions can be found in the weak formulation in [2]. Continuous variation of media parameters is implemented by means of Lagrange interpolation as a 1-D version of [8].

Once the FEM solution, valid for $z' \in [0^+, d^-]$, is obtained in the S' rest frame, tangential field components at $z' = d^+$ are first obtained as in (18), and similarly for $z' = 0^-$, and then transformed by the (inverse) Lorentz transformation [7] into S rest frame, together with the corresponding angular frequencies and wave vectors, thus finally yielding

$$E_x^{\text{ref}}(y, z) = E_x(d^+) e^{-j(k_{y,\text{ref}} y + k_{z,\text{ref}} z)} \quad (21)$$

$$\omega_{\text{ref}} = \gamma_z^2 [\omega (1 + \beta_z^2) - 2\beta_z c k_z] \quad (22)$$

$$k_{z,\text{ref}} = -\gamma_z^2 [k_z (1 + \beta_z^2) - 2\beta_z \omega/c] \quad k_{y,\text{ref}} = k_y \quad (23)$$

$$E_x^{\text{tr}}(y, z) = E_x(0^-) e^{-j(k_{y,\text{tr}} y + k_{z,\text{tr}} z)} \quad (24)$$

$$\omega_{\text{tr}} = \omega \quad k_{z,\text{tr}} = k_z \quad k_{y,\text{tr}} = k_y. \quad (25)$$

The reflection and transmission coefficients (which can be defined differently), also firstly found in the S' rest frame as

$$|R'| = \left| \frac{E'_x - E_x{}^{\text{inc}}}{E_x{}^{\text{inc}}} \right|_{z'=d^+} \quad |T'| = \left| \frac{E'_x}{E_x{}^{\text{inc}}} \right|_{z'=0^-} \quad (26)$$

respectively, are transformed into S rest frame (as electric field components), yielding $|R|$ and $|T|$. It is interesting to note the

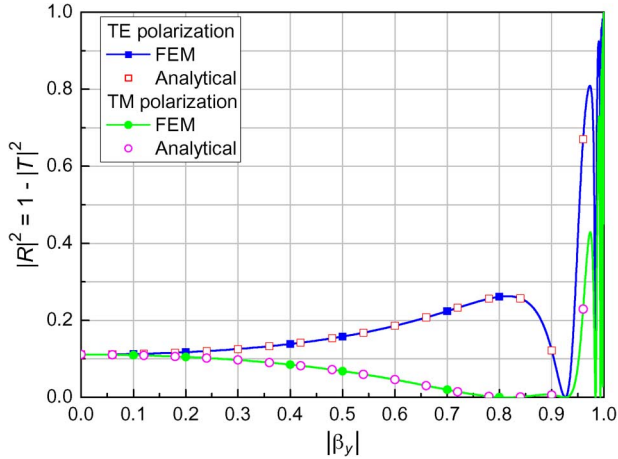


Fig. 2. Reflection (and transmission) coefficients for the slab moving transversally to direction of propagation of the normally incident plane wave: comparison of the FEM solution and analytical solutions from [3] and [4].

possible frequency shift in the reflected wave $\omega_{\text{ref}} \neq \omega$ (Doppler effect), not present in the transmitted wave, where $\omega_{\text{tr}} = \omega$.

III. NUMERICAL RESULTS AND DISCUSSION

As a numerical example, consider a uniform plane wave normally incident ($\theta_i = 0$) on a homogeneous lossless dielectric slab ($\epsilon_r = 2$, $\mu_r = 1$). The (proper) thickness of the slab, d , is such that $|\mathbf{k}^{\text{inc}}|d\sqrt{\epsilon_r} = \pi/2$, i.e., $d = \lambda_d/4$, λ_d being the wavelength in the dielectric. This particular example facilitates straightforward comparison of our numerical results with the analytical solutions from [3] and [4]. Note that the power reflection and transmission coefficients defined in [3] and [4] correspond to $|R|^2$ and $|T|^2$ defined in this letter (at normal incidence). We model the slab with four elements ($M = 4$) and employ the eight-order polynomial field expansion ($n = 8$), which is more than sufficient to obtain very accurate solution (for a stationary slab), considering that the slab is a quarter of a wavelength thick and optimal solutions are obtained utilizing six to seven unknowns per wavelength [2].

Shown in Fig. 2 are the power reflection (and transmission) coefficients computed for the slab moving transversally to direction of propagation of the plane wave. In the figure, higher-order FEM results are compared to analytical solutions from [3] and [4]. (Note that there are many typographical errors in the analytical expressions in cited papers. However, the plots presented therein are reasonably accurate.) We can conclude from the figure that the agreement of the FEM and analytical solutions is excellent.

Shown in Fig. 3 are the power reflection and transmission coefficients of a dielectric slab moving in direction of propagation of the plane wave normally incident on the slab. Note that polarizations are indistinguishable in this case. Again, the results obtained by the higher-order FEM (utilizing the same model as described above) are compared to the analytical solution [3] in the figure, and we can conclude that the agreement of the results is excellent. Due to energy transfer between the wave and the slab, $|R|$ can exceed unity in this example (analogously to a moving mirror in optics [9]).

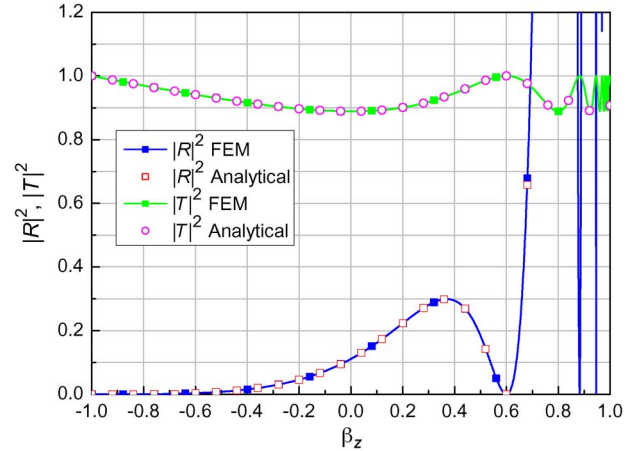


Fig. 3. Reflection and transmission coefficients for the slab moving in direction of propagation of the normally incident plane wave: comparison of FEM and analytical solutions from [3].

We next investigate the convergence of the FEM results at high slab speeds, where both $|R|$ and $|T|$ coefficients are highly oscillatory due to resonances occurring as effects of extreme and quick apparent changes in the transformed space-time. These changes influence the slab apparent dimensions and/or relevant EM quantities (e.g., frequency and wave vectors), critical for numerical computations within the FEM.

Fig. 4 shows the relative error $||R_{\text{FEM}}| - |R_{\text{An.}}||/|R_{\text{An.}}|$ with respect to analytical solution, for the reflection coefficient (TE polarization) at high transversal slab normalized velocities. Convergence of the FEM solutions under p -refinement and h -refinement are shown in Fig. 4(a) and (b), respectively. In Fig. 4(a), a single-element FEM model is p -refined, employing polynomial expansions of orders 1–8, and it can be concluded that highly accurate solutions (e.g., with errors smaller than 10^{-4}) can be obtained for the normalized velocities up to $|\beta_y| = 0.99$ with monotonic (except close to resonances) convergence with p -refinement.

If high accuracy of the solution is required at higher speeds, h -refinement has to be performed as well, and the convergence can be sustained, as shown in Fig. 4(b), where accurate solution for velocities higher than $|\beta_y| = 0.999$ is obtained with $n = 8$ and $M = 4$ uniformly sized elements.

For the slab moving at high longitudinal velocities β_z (errors not shown for brevity), similar conclusions hold, with the errors being higher than errors in Fig. 4 due to difference in nature of numerical problems associated with the two types of movement. Namely, after Lorentz transformations, the (propagation) coefficient β_F reduces to $\beta_F = \gamma^2 |\mathbf{k}^{\text{inc}}|^2 (2 - \beta_y^2)$, when $\beta_z = 0$, i.e., the FEM computation is affected as if the frequency of the excitation were increased γ times (the slab is becoming electrically thicker as velocity increases, becoming infinitely thick when $\beta_y \rightarrow 1$). Conversely, when $\beta_y = 0$, $\beta_F = 2|\mathbf{k}^{\text{inc}}|^2 (1 - \beta_z)/(1 + \beta_z)$, i.e., $\beta_F \rightarrow 0$ when $\beta_z \rightarrow 1$, and the FEM encounters a low-frequency breakdown.

As the final example, consider a TE wave scattering off a moving (in y -direction) inhomogeneous slab with linear permittivity variation $\epsilon_r = 2(1+z/d)$ at oblique incidence ($\theta_i = 60^\circ$), as shown in the inset of Fig. 5. There is no length contraction

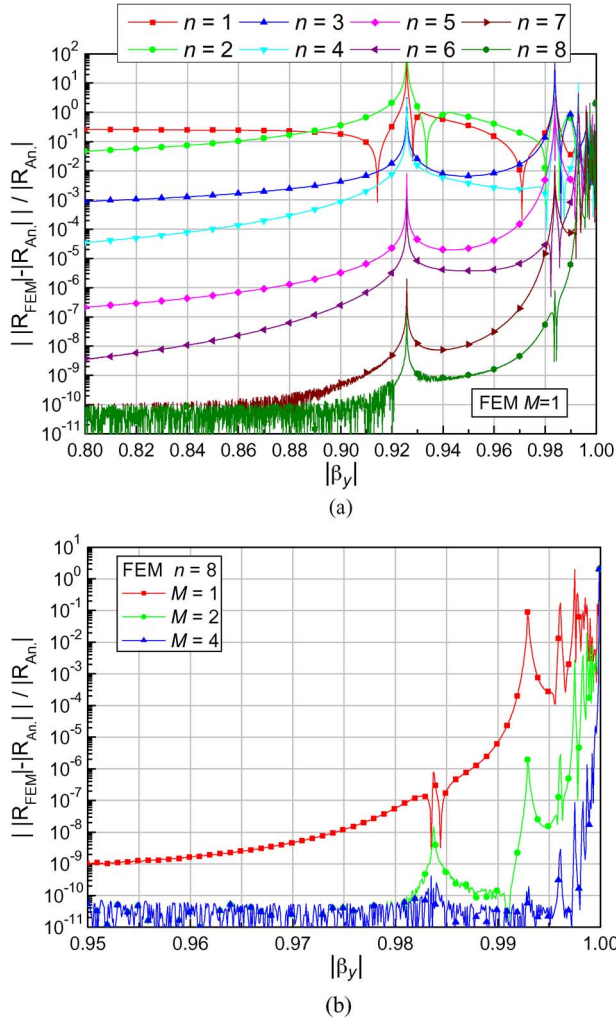


Fig. 4. Error of $|R|$ computed by FEM with respect to analytical solution versus normalized slab transversal velocity at velocities close to the speed of light: convergence of the FEM solutions with (a) p -refinement and (b) h -refinement.

in the z -direction, thus $z = z'$ in this case. The slab is modeled using $M = 2$ elements with polynomial expansion orders $n = 6$. Continuously inhomogeneous permittivity profile is modeled exactly, using Lagrange interpolation [8]. To account for the permittivity of the media in the front and in the back of the slab, permittivity of the background medium in FEM computation is changed from ε_0 to $\varepsilon_r \varepsilon_0 = 4\varepsilon_0$. To account for the movement of the medium behind the slab, with no changes in the described method and computer code, the slab is backed by a PEC and three thin homogeneous layers, constituting an artificial absorber optimized to yield minimal reflections [1] at the operating (Lorentz-transformed) frequency.

Shown in Fig. 5 are the power reflection coefficients computed for the stationary slab, $\beta_y = 0$, and for the slab moving with normalized velocity $\beta_y = 0.9$. In the figure, higher-order FEM results are compared to analytical solutions from [5], obtained after tedious derivations from the Maxwell–Minkowsky equations, and are valid only for the linearly varying permittivity profiles. We can conclude based on the figure that the agreement of the FEM and analytical solutions is excellent.

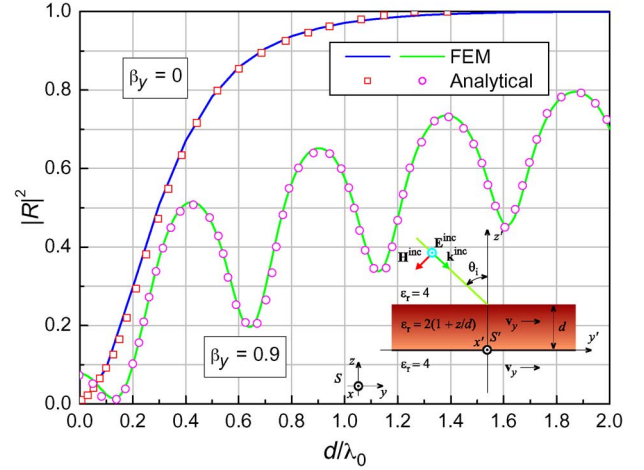


Fig. 5. Reflection coefficients for the inhomogeneous slab—stationary and moving transversally to direction of propagation of the obliquely incident plane wave: comparison of FEM and analytical solutions from [5].

IV. CONCLUSION

The numerical results obtained by the proposed higher-order FEM, appearing to be the first full-wave higher-order frequency-domain method of its kind, show excellent agreement with analytical solutions and monotonic and quick convergence with h -, p -, and hp -refinements, required for analysis when slab velocities approach the speed of light. The method can be extended to enable scattering analysis for slabs composed of layers moving with different transversal velocities. These cases and related practical applications will be studied in our future work.

REFERENCES

- [1] J. M. Jin, *The Finite Element Method in Electromagnetics*, 2nd ed. New York, NY, USA: Wiley, 2002.
- [2] V. V. Petrović and B. D. Popović, "Optimal FEM solutions of one-dimensional EM problems," *Int. J. Numer. Model., Electron. Netw., Devices Fields*, vol. 14, pp. 49–68, 2001.
- [3] C. Yeh and K. F. Casey, "Reflection and transmission of electromagnetic waves by a moving dielectric slab," *Phys. Rev.*, vol. 144, no. 2, pp. 665–669, Apr. 1966.
- [4] C. Yeh, "Reflection and transmission of electromagnetic waves by a moving dielectric slab. II. Parallel polarization," *Phys. Rev.*, vol. 167, no. 3, pp. 875–877, Mar. 1968.
- [5] K. Tanaka and K. Hazama, "Reflection and transmission of electromagnetic waves by a moving inhomogeneous medium," *Radio Sci.*, vol. 7, no. 10, pp. 973–978, Oct. 1972.
- [6] F. Harfoush, A. Taflove, and G. A. Kriegsmann, "A numerical technique for analyzing electromagnetic wave scattering from moving surfaces in one and two dimensions," *IEEE Trans. Antennas Propag.*, vol. 37, no. 1, pp. 55–63, Jan. 1989.
- [7] J. D. Jackson, *Classical Electrodynamics*, 3rd ed. New York, NY, USA: Wiley, 1998.
- [8] M. M. Ilić, A. Ž. Ilić, and B. M. Notaroš, "Continuously inhomogeneous higher order finite elements for 3-D electromagnetic analysis," *IEEE Trans. Antennas Propag.*, vol. 57, no. 9, pp. 2798–2803, Sep. 2009.
- [9] G. Goedecke, V. Toussaint, and C. Cooper, "On energy transfers in reflection of light by a moving mirror," *Amer. J. Phys.*, vol. 80, no. 8, pp. 684–687, Aug. 2012.

IEEE TRANSACTIONS ON MAGNETICS

A PUBLICATION OF THE IEEE MAGNETICS SOCIETY

DECEMBER 2013

VOLUME 49

NUMBER 12

IEMGAQ

(ISSN 0018-9464)

- 5595 **Structure and Magnetism of MnGa Ultra-Thin Films on GaAs(111)B**
A. W. Arins, H. F. Jurca, J. Zarpellon, J. Varalda, I. L. Graff, W. H. Schreiner, and D. H. Mosca
- 5599 **Optimization of Temperature Coefficient of Remanence and Magnetic Properties of Sintered $\text{Sm}_{0.7}\text{Dy}_{0.1}\text{Gd}_{0.2}(\text{Co}_{\text{bal}}\text{Fe}_{0.2}\text{Cu}_{0.08}\text{Zr}_{0.025})_{7.2}$ Magnets Prepared by Strip-Casting Technique**
Z. Liu, L. Liu, R. J. Chen, Y. L. Sun, D. Lee, and A. R. Yan
- 5603 **Co–Pt–Cr–CoSi–CoO Sintered Target for Low Ar-gas-pressure Deposition of CoPtCr–SiO₂ Granular Film with Stoichiometric SiO₂ Phase**
S. Sasaki, S. Saito, and M. Takahashi
- 5610 **Magnetic Dimensionality of Metal Formate $M[(\text{H}_2\text{O})_2(\text{HCOO})_2]$ Compounds ($M = \text{Co(II)}, \text{Cu(II)}$)**
L. L. L. Sousa, G. F. Barbosa, F. L. A. Machado, L. R. S. Araujo, P. Brandão, M. S. Reis, and D. L. Rocco
- 5616 **Cross-Track Pulse Shape and Nonlinear Loss as a Function of Frequency and Side Track Erasure in Perpendicular Magnetic Recording Systems**
O. B. Tarun and M. A. Nichols
- 5620 **Reliability Analysis and Comparison of Implication and Reprogrammable Logic Gates in Magnetic Tunnel Junction Logic Circuits**
H. Mahmoudi, T. Windbacher, V. Sverdlov, and S. Selberherr
- 5629 **Characterization and Implementation Methods of Multilayer Inductors with Ni-Zn Ferrite and Carbonyl SF Powder Iron on Ceramic Substrates for RF Amplifiers**
A. Eroglu
- 5635 **Magnetic Polarization of the Tunneling Current**
I. L. Fernandes and G. G. Cabrera
- 5639 **Influence of Wire-Connecting With Ni Electro-Plating on GMI Output Stability of Co-Rich Amorphous Microwires**
J.-S. Liu, D.-W. Xing, D.-Y. Zhang, F.-Y. Cao, X. Xue, and J.-F. Sun
- 5645 **A Design Tool for Magnetic Resonance Imaging Gradient Coils Using DUCAS with Weighted Nodes and Initial Current Potentials**
M. Abe
- 5656 **Analytical Description of Two-Dimensional Magnetic Arrays Suitable for Biomedical Applications**
A. Ž. Ilić, S. Ćirković, D. M. Djordjevic, S. R. De Luka, I. D. Milovanovich, A. M. Trbovich, and J. L. Ristić-Djurović

(Contents Continued on Page 5594)

- 5664 **Design and Demonstration of a Test-Rig for Static Performance-Studies of Permanent Magnet Couplings**
S. Högberg, B. B. Jensen, and F. B. Bendixen
- 5671 **High Speed Characterization of the Magnetolectric Hysteresis Loop**
Z. Shi, L. Z. Chen, Y. S. Tong, H. Xue, S. Y. Yang, Y. Lu, C. P. Wang, and X. J. Liu
- 5675 **Eddy Current Analysis Using a Nyström-Discretization of the Volume Integral Equation**
J. C. Young, S. D. Gedney, and R. J. Adams
- 5682 **Active Control of Magnetic Field by Manipulating Induced Currents in Two-Dimensional Switch-Mounted Loop Array**
H. Tanaka and H. Iizuka
- 5687 **Analytic Nonlinear Correction to the Impedance Boundary Condition**
R. M. Del Vecchio and R. Ahuja
- 5692 **Flux Linkage in Helical Windings and Application to Pick-up Coils**
A. Quercia
- 5698 **Three-Dimensional Analytical Modeling Technique of Electromagnetic Fields of Air-Cored Coils Surrounded by Different Ferromagnetic Boundaries**
J. P. C. Smeets, T. T. Overboom, J. W. Jansen, and E. A. Lomonova
- 5709 **Optimal Design of Electromagnetic Devices Using a Black-Hole-Based Optimization Technique**
H. R. E. H. Bouchekara
- 5715 **Residual and Equilibrated Error Estimators for Magnetostatic Problems Solved by Finite Element Method**
Z. Tang, Y. Le Menach, E. Creusé, S. Nicaise, F. Piriou, and N. Nemitz
- 5724 **An Adaptive Degrees-of-Freedom Finite-Element Method for Transient Magnetic Field Analysis**
Y. Zhao, S. L. Ho, and W. N. Fu
- 5730 **Multiphysical Analysis of Moving-Magnet Planar Motor Topologies**
J. M. M. Rovers, J. W. Jansen, and E. A. Lomonova
- 5742 **Optimal Design and Multifield Coupling Analysis of Propelling Motor Used in a Novel Integrated Motor Propeller**
J. Liang, X. Zhang, M. Qiao, P. Zhu, W. Cai, Y. Xia, and G. Li
- 5749 **Characteristic Analysis and Design of a Thomson Coil Actuator Using an Analytic Method and a Numerical Method**
D.-K. Lim, D.-K. Woo, I.-W. Kim, D.-K. Shin, J.-S. Ro, T.-K. Chung, and H.-K. Jung
- 5756 **Analytical Modeling of Air-Gap Field Distributions in Permanent Magnet Embedded Salient Pole Wind Generator**
Y. Guo, H. Lin, P. Jin, J. Yan, J. Wang, and Z. Jia

Analytical Description of Two-Dimensional Magnetic Arrays Suitable for Biomedical Applications

Andjelija Ž. Ilić¹, Saša Ćirković¹, Drago M. Djordjević², Silvio R. De Luka², Ivan D. Milovanovich², Alexander M. Trbović², and Jasna L. Ristić-Djurović¹

¹Innovation Center, School of Electrical Engineering, University of Belgrade, Belgrade 11120, Serbia

²Department of Pathological Physiology, School of Medicine, University of Belgrade, Belgrade 11000, Serbia

Two-dimensional magnetic arrays are used to generate a magnetic field that pervades a layer of volume above the array's surface, often creating regions of high magnetic flux density gradients. We have recently employed an array with equally oriented magnetic moments of individual elements in several biomedical experiments. We have chosen this type of array because of the slowly decreasing magnetic field it produces, which extends far from the array's surface and permeates the experimental volume. In order to fully define experimental conditions related to the applied magnetic field, we derive exact closed-form expressions for the magnetic flux density. Based on these analytical expressions and exploiting the array periodicity, a method is proposed for the approximate assessment of the main magnetic field parameters of interest—mean magnetic flux density and mean gradient of its component perpendicular to the array's surface. The obtained approximate assessment can further serve as a tool for the design of arrays with the desired mean field parameters. All the results are verified and validated by comparison with the finite element modeling as well as measurements.

Index Terms—Analytical modeling, finite element methods, magnetic arrays, magnetic field measurement, permanent magnets.

I. INTRODUCTION

TWO-DIMENSIONAL magnetic arrays are used in a number of applications including optical switching (electromagnetic mirror arrays) and other microactuator systems, microsensors, acoustic transducers, magnetic bearings, unique microscale components self-assembly, synchronous permanent magnet planar motors, and magnetic levitation [1]–[11]. A primary goal in these applications is to create regions of high magnetic flux density gradients. Array configurations using alternating magnetic axes of the neighboring elements, or magnetic axes rotated as suggested by Halbach [12], seem to be utilized more often. In that case, the obtained magnetic fields exert their influence mainly in the narrow region close to the array's surface, with the magnetic flux lines predominantly parallel to the surface and alternating in direction between the adjacent elements. When the array elements all have identically oriented magnetic moments perpendicular to the array's surface, the resultant field extends further from the surface. Field distribution at the surface is wavy, since the magnetic flux lines partially close in between the adjacent elements. The majority of the magnetic flux lines, however, add up together to form a resultant predominantly perpendicular magnetic flux density, always positive after some boundary distance.

The latter type of the magnetic array, with equally oriented magnetic axes, can be used to generate static magnetic fields suitable for biomedical research. Permanent magnets as well as their combinations in a form of small arrays are already used in the field of physical therapy and rehabilitation. Although the underlying mechanisms of action are not fully understood, experimental data suggests beneficial therapeutic effects in treating arthritis, reducing inflammation and wound

Manuscript received March 15, 2013; revised July 10, 2013; accepted August 06, 2013. Date of publication August 08, 2013; date of current version November 20, 2013. Corresponding author: A. Ž. Ilić (e-mail: andjelija.lic@iee.org).

Color versions of one or more of the figures in this paper are available online at <http://ieeexplore.ieee.org>.

Digital Object Identifier 10.1109/TMAG.2013.2277831

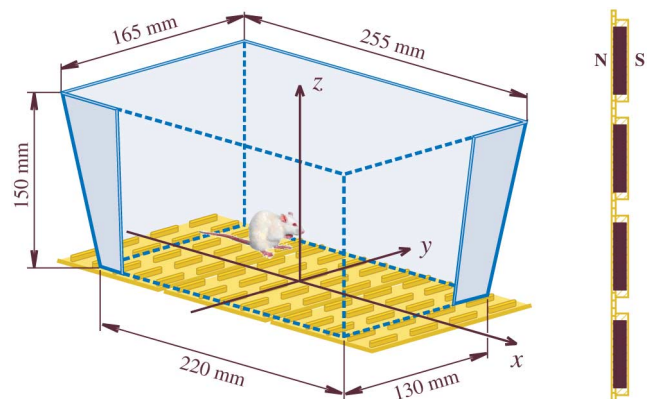


Fig. 1 Two-dimensional magnetic array used in biomedical research and referent coordinate system. The produced slowly decreasing magnetic field extends far from the surface of an array. Vertical cross-section of an array, corresponding to the plane $x = 0$ and halving the magnets along the y -axis, is shown on the right. Small permanent ferromagnetic rods are embedded into an elastic but firm rubber sheet that in no way disrupts the magnetic field.

healing, pain and stress relief and improving microcirculation [13]–[17]. However, according to [18], poor field description is the major flaw in a large number of publications investigating the biomedical effects of field exposure. Recently, we utilized the two-dimensional magnetic arrays with equally oriented magnetic axes in our experiments described in [19], [20]. Magnetic arrays were assembled using the appropriate number of the so-called type L (large) MADU stripes, five-by-four equidistant permanent magnet arrangements used in the field of physical therapy and rehabilitation [21]. These smaller magnetic arrays were readily available to us and we placed them side by side to ensure optimal magnetic field coverage throughout the experimental volume. Three MADU stripes, i.e., the total of fifteen-by-four individual ferromagnetic rods are placed below the small standard animal cages, as shown in Fig. 1. For the large cages, six stripes arranged as an array of twelve-by-ten ferromagnetic rods are needed.

The Fourier series expansion seems to be the method of choice in the analysis of large magnetic arrays [6], [7], while the smaller, non-periodic arrays are often analyzed using

the finite-element method (FEM) [1], [11]. Use of equivalent sources, i.e., magnetization currents or surface magnetic charges to represent the material properties, accordingly with the theorem of equivalence [22], [23], results in field integrals that can be solved either analytically or numerically. One choice of equivalent sources may result in expressions that are easier to solve, or only solvable [24]. The flat sided individual magnets lead to analytically solvable integrals. Expressions for the magnetic field of a single cuboid magnet, based on the magnetic charges, were first given in [25]. We derive easy to implement closed-form expressions for the two-dimensional magnetic array, i.e., the magnetic flux density in an arbitrary field point, based on the equivalent magnetization currents and field derivation for a single current sheet. We discuss how to adapt these complete expressions to the case of alternating magnetic axes as well as non-periodic arrays.

For arrays with equally oriented magnetic axes, magnetic flux density, \mathbf{B} , after some distance from the array's surface is predominantly perpendicular to the surface, i.e., the vector \mathbf{B} is approximately parallel to the z -axis in Fig. 1 ($B_x, B_y \ll B_z$). Disregarding the much smaller variations of the vector \mathbf{B} in planes parallel to the array's surface ($\frac{\partial B_x}{\partial x}, \frac{\partial B_y}{\partial y} \ll \frac{\partial B_z}{\partial z}$), we consider only its pronounced change in the z -axis direction and introduce the "magnetic flux density gradient" as the negative z -component of the gradient of $B_z(x, y, z)$:

$$G_z(x, y, z) = -\text{grad}_z B_z(x, y, z) = -\frac{\partial B_z(x, y, z)}{\partial z}. \quad (1)$$

The mean magnetic flux density and the mean gradient of its z -component in horizontal planes, as well as their dependence on the z -coordinate, are the main parameters of interest in describing these arrays. We propose a method for the fast preliminary assessment of these two parameters, based on the periodicity of the z -component of magnetic field. Both the detailed field expressions and the fast estimate are verified and validated by comparison with the finite-element calculations as well as the measured data. Further, the magnetic flux density variation throughout the experimental volume, including the stray magnetic field, is studied using the finite-element calculations. Possible optimization strategies, using the approximate analytical expressions as a tool to adjust the mean field parameters in the experimental volume, are briefly discussed. We expect this work to be useful both to researchers and to practitioners in the fields of two-dimensional magnetic array design and biomedical applications.

II. ANALYTICAL MODEL

The development of analytical expressions starts with considering the basic building block of the two-dimensional array, the single ferromagnetic rod. Remanent magnetization is either known in advance or it can be determined using the material characterization by measurements as explained in Section III. For the array we analyzed as an example the value of remanent magnetization was unavailable. Using the magnetic field measurements, we obtained $M_r = 60.0 \text{ A} \cdot \text{m}^2/\text{kg}$.

Due to the principal role of the considered stripes to easily conform to parts of the human body, magnetic array is created by embedding $4.8 \text{ mm} \times 24.4 \text{ mm} \times 4.8 \text{ mm}$ sized ferromagnetic rods into an elastic rubber stripe or sheet. The influence of the rubber can be completely neglected in all calculations. For a different substrate, care should be taken of its influence.

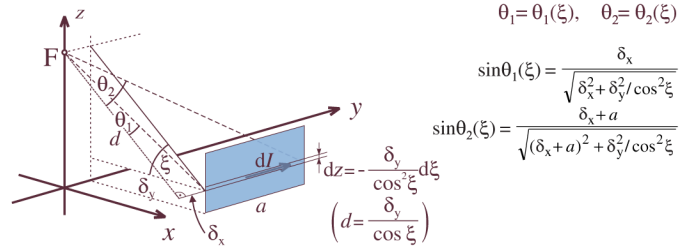


Fig. 2 Magnetic flux density calculation for a single current sheet. Defining the angle ξ as the field point elevation above the horizontal plane that contains the elemental current segment dI , we can express all other parameters as a function of ξ in order to simplify the analytical integration.

Assuming the uniform magnetization over the volume of a ferromagnetic rod, the produced magnetic field is identical to that corresponding to a short solenoid of rectangular cross-section. The surface current density vector, \mathbf{J}_{mS} , is given by

$$\mathbf{J}_{\text{mS}} = \mathbf{M} \times \mathbf{n} \quad (2)$$

where the magnetization vector is denoted by \mathbf{M} and \mathbf{n} represents the surface normal, i.e., the unit vector perpendicular to the magnet-air boundary surface, directed from the magnet outwards. We obtain $J_{\text{mS}} = \rho \cdot M_r = 294.0 \cdot 10^3 \text{ A/m}$.

Each of the four sides of rectangular cross-section solenoid is a flat current sheet that can be considered as a collection of very thin wires carrying the elemental currents dI . Magnetic flux density, \mathbf{B} , is perpendicular to the plane defined by the straight finite wire and the field point F , shown in Fig. 2, and related to dI by the right-hand rule. Magnitude is evaluated directly from the Biot-Savart law [22]:

$$B = \frac{\mu_0 dI}{4\pi d} (\sin \theta_2 - \sin \theta_1). \quad (3)$$

Above, d represents the shortest (perpendicular) distance from the arbitrary considered field point F to the conductor axis and also defines the referent axis for the measurement of angle θ . Angles θ_1 and θ_2 correspond to the point of current entrance into the conductor and its exit, respectively.

Due to cancellation of other field components, vector \mathbf{B} on the single solenoid axis has only the component in the axis direction. Defining the angle ξ as the field point elevation above the plane parallel to the xOy that contains the elemental current segment dI , we can express all other parameters as a function of ξ in order to simplify the integration. Throughout this work the plane $z = 0$ coincides with the top surface of the magnetic array, including the rubber wrap whose thickness on each side is $t = 0.8 \text{ mm}$. Therefore, $z_1 = z + t + h$ and $z_2 = z + t$ correspond to the field point vertical distance from the bottom and top surface of the ferromagnetic rods whose sides are $a = 24.4 \text{ mm}$ and $b = 4.8 \text{ mm}$, and height is $h = b$. Angles ξ_{a1} , ξ_{a2} , and ξ_{b1} , ξ_{b2} , match z_1 and z_2 . The elemental currents equal $dI_a = -J_{\text{mS}} \frac{b}{2\cos^2 \xi_a} d\xi_a$ and $dI_b = -J_{\text{mS}} \frac{a}{2\cos^2 \xi_b} d\xi_b$, for the sides a and b , respectively. Integrating $dB_z = dB \cos \xi$ we obtain

$$B_1 = -\frac{\mu_0 J_{\text{mS}}}{\pi} \left(\int_{\xi_{a1}}^{\xi_{a2}} \frac{a \cos \xi_a d\xi_a}{\sqrt{a^2 \cos^2 \xi_a + b^2}} + \int_{\xi_{b1}}^{\xi_{b2}} \frac{b \cos \xi_b d\xi_b}{\sqrt{a^2 + b^2 \cos^2 \xi_b}} \right),$$

$$B_1(z) = \frac{\mu_0 J_{\text{mS}}}{\pi} \left(\arcsin \left(\frac{2 \frac{a}{\sqrt{a^2 + b^2}} z}{\sqrt{b^2 + 4z^2}} \right) + \arcsin \left(\frac{2 \frac{b}{\sqrt{a^2 + b^2}} z}{\sqrt{a^2 + 4z^2}} \right) \right) \Bigg|_{z_2}^{z_1}. \quad (4)$$

The magnetic flux density at the array's surface equals $B_1(z = 0) = 103.08$ mT, and at the center of each magnet $B_1(z = -3.2$ mm) = 189.11 mT.

Two-dimensional magnetic array is constructed by placing M_a individual ferromagnetic rods in each of the N_a parallel rows in the xOy plane, the magnetic axes all in the z -direction. Magnets are spaced equidistantly with a center-to-center shift $x_d = 19.5$ mm and $y_d = 36.0$ mm in the x - and y -direction. Due to the periodicity of the problem, the Fourier series expansion is frequently used in literature. Analytical integration over the heights of all the current sheets involved, as explained above, results in the exact expressions for all three components of the magnetic flux density in an arbitrary considered field point. The obtained expressions are valid for small as well as large arrays, and can be applied to the non-periodic arrays if a set of masking coefficients is properly introduced. However, the array periodicity is exploited to obtain the simple but effective analytical assessment of magnetic field parameters of interest, based on the exact field values at two vertical axes.

With the increase in the number of individual magnets in both dimensions, the magnetic flux density approaches a limiting, final-state distribution of an infinite array, which is periodic with a period of x_d in the x -, and y_d in the y -direction. The magnetic flux density distribution in the central part of a finite array has to be approximately periodic as well, with the hills of the distribution located directly above the magnet centers and the lowest values (valleys) at vertical axes going through the cross-sections of midlines between the rows of magnets. Horizontal vector \mathbf{B} components are small enough in comparison with the z -component to be excluded from the assessment. Therefore, the magnetic flux density on the axes through the points H and V in Fig. 3, denoted $B_H(z)$ and $B_V(z)$, represents maxima and minima in horizontal planes. The mean magnetic flux density in a horizontal plane, $\bar{B}_z(z)$, may in the first approximation be replaced by the arithmetic mean of B_H and B_V . Such an approach will be justified by comparison with measurements and finite-element modeling. In our example, number of array elements is rather small, while the size of individual magnets, their aspect ratio and mutual spacing are considerable. It is, therefore, somewhat of a worst-case scenario for validation of the proposed approach. Vector \mathbf{B} mean value and variation,

$\bar{B}_z(z)$ and $\Delta B_z(z)$, and its gradient defined by (1), $\bar{G}_z(z)$ and $\Delta G_z(z)$, become

$$\begin{aligned}\bar{B}_z(z) &= \frac{B_H(z) + B_V(z)}{2}, \\ \Delta B_z(z) &= \frac{B_H(z) - B_V(z)}{2}, \\ \bar{G}_z(z) &= -\text{grad}_z \bar{B}_z = -\frac{1}{2} \left(\frac{\partial B_H(z)}{\partial z} + \frac{\partial B_V(z)}{\partial z} \right) \\ &= \frac{G_H(z) + G_V(z)}{2}, \\ \Delta G_z(z) &= \frac{G_H(z) - G_V(z)}{2}, \\ G_H &= -\frac{\partial B_H(z)}{\partial z}, \quad G_V = -\frac{\partial B_V(z)}{\partial z}.\end{aligned}\quad (5)$$

Without loss of generality, we assume the odd number of elements, $M_a = 2M + 1$, in the x -direction and even, $N_a = 2N$, in the y -direction. Integrating $dB_z = dB \cos \xi$ over all the current sheets we obtain $B_z(x, y, z)$. Current sheets parallel to the yOz plane contribute $dB_x = \pm dB \sin \xi$ to vector \mathbf{B} , and those parallel to the xOz plane generate y -component, $dB_y = \pm dB \sin \xi$. After representing $dI = J_{mS} \cdot dz$, $\sin \theta_1$, $\sin \theta_2$, d and dz as a function of angle ξ , as shown in Fig. 2, two integrals that need to be solved for each current sheet become

$$\begin{aligned}\int_{\sin \xi_1}^{\sin \xi_2} \frac{d(\sin \xi)}{\sqrt{P^2 - \sin^2 \xi}} &= \arcsin \left(\frac{\sin \xi}{P} \right) \Big|_{\sin \xi_1}^{\sin \xi_2}, \\ \int_{\cos \xi_1}^{\cos \xi_2} \frac{d(\cos \xi)}{\sqrt{\cos^2 \xi + R^2}} &= \ln \left(\cos \xi + \sqrt{\cos^2 \xi + R^2} \right) \Big|_{\cos \xi_1}^{\cos \xi_2}.\end{aligned}\quad (6)$$

Therefore, we obtain (7), shown at the bottom of the page. The parameters p and q correspond to the sines of angles θ_0 and ξ , respectively, with θ_0 being the projection of the angle θ to the xOy plane. Upper indices $tp = 0$ and $tp = 1$ correspond to the point of current entrance into the current sheet and its exit, respectively. Upper indices $tq = 0$ and $tq = 1$ denote the bottom surface or the top surface of the ferromagnetic rod, i.e.,

$$\begin{aligned}B_z(x, y, z) &= \frac{\mu_0 J_{mS}}{4\pi} \sum_{i=-M}^M \sum_{j=-N}^{N-1} \sum_{k=1}^4 \sum_{tp=0}^1 \sum_{tq=0}^1 (-1)^{(tp+tq+1)} \arcsin(p_{i,j,k}^{tp} \cdot q_{i,j,k}^{tq}), \\ p_{i,j,k}^{tp} &= \frac{\left(i \cdot x_d + (-1)^{\lfloor \frac{k}{2} \rfloor + tp} \frac{b}{2} - x \right)^{m_2} \cdot \left((j + \frac{1}{2}) \cdot y_d + (-1)^{\lfloor \frac{k-1}{2} \rfloor + tp} \frac{a}{2} - y \right)^{m_1}}{\sqrt{\left(i \cdot x_d + (-1)^{\lfloor \frac{k}{2} \rfloor + 1 + (tp-1)m_2} \frac{b}{2} - x \right)^2 + \left((j + \frac{1}{2}) \cdot y_d + (-1)^{\lfloor \frac{k-1}{2} \rfloor + 1 + (tp-1)m_1} \frac{a}{2} - y \right)^2}}, \\ q_{i,j,k}^{tq} &= \frac{\frac{\text{sgn}(i \cdot x_d + (-1)^{m_s} \frac{b}{2} - x)^{m_1}}{(-\text{sgn}((j + \frac{1}{2}) \cdot y_d + (-1)^{m_s} \frac{a}{2} - y))^{m_2}} \cdot (z + t + (1 - tq) \cdot h)}{\sqrt{\left(i \cdot x_d + (-1)^{m_s} \frac{b}{2} - x \right)^{2m_1} \left((j + \frac{1}{2}) \cdot y_d + (-1)^{m_s} \frac{a}{2} - y \right)^{2m_2} + (z + t + (1 - tq) \cdot h)^2}}, \\ m_1 &= (1 + (-1)^{k-1}) / 2, \quad m_2 = (1 + (-1)^k) / 2, \quad m_s = \left(1 - \text{sgn} \left(k - \frac{5}{2} \right) \right) / 2.\end{aligned}\quad (7)$$

the considered current sheet. Lower indices (i, j) correspond to the i -th element in the j -th row of the magnetic array, while k denotes one of the four current sheets formed by the considered element. For k equal to 1, 2, 3, and 4, current sheet is located at $\Delta x = -b/2$, $\Delta y = -a/2$, $\Delta x = b/2$, and $\Delta y = a/2$, with respect to the center of the considered ferromagnetic rod, respectively. Operator $[\cdot]$ stands for the integer division. As pointed out in [26], expressions describing permanent magnets of rectangular cross-section depend only on the magnet corner positions, which simplifies the calculations. Using (7), $B_H(z) = B_z(0, y_d/2, z)$, $B_V(z) = B_z(x_d/2, 0, z)$, $B_O(z) = B_z(0, 0, z)$, and $B_P(z) = B_z(x_d/2, y_d/2, z)$ are calculated at four characteristic axes through the points H , V , O , and P , denoted in Fig. 3. In our example $M = 7$ and $N = 2$. The magnetic flux density at the top surface of an individual magnet in the central part of a stripe is decreased from $B_1(0)$ to $B_H(0) = 95.80$ mT. At larger z , there is an increase in both $B_H(z)$ and $B_V(z)$ due to the contributions of surrounding rods.

The estimate (5) is based only on the dominant z -component of the magnetic flux density. For the sake of completeness, as well as possible extension of this analytical description to the non-periodic arrays, exact expressions for the horizontal field components are also given in (8), shown at the bottom of the page. Exact description of arrays with alternating magnetic moments of the neighboring elements is obtained easily by multiplying each element of the sums by $(-1)^{i+j}$, or just $(-1)^i$, i.e., $(-1)^j$. For the arrays with rotated magnetic axes, expressions get more complicated. Magnetization currents exist at the top and bottom sides of the magnets as well. Starting from the general expression $\mathbf{J}_{mS} = J_x^{i,j,k} \mathbf{i}_x + J_y^{i,j,k} \mathbf{i}_y + J_z^{i,j,k} \mathbf{i}_z$, $k \in \{1, 2, 3, 4, 5, 6\}$, where \mathbf{i}_x , \mathbf{i}_y , and \mathbf{i}_z represent the unit vectors in the x -, y - and z -direction, every term in (7) and (8) is replaced by the three terms, each multiplied by appropriate $J^{i,j,k}$, and the summation over k now includes $k = 5$ and $k = 6$ as

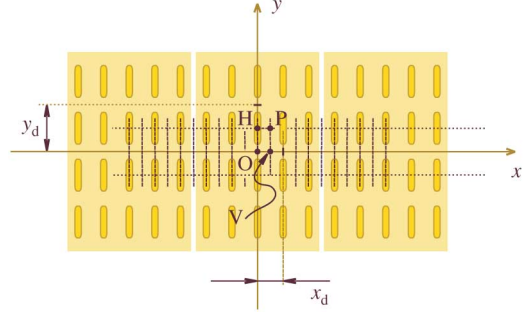


Fig. 3 Characteristic points used in approximate assessment of the mean magnetic field parameters. Mean magnetic flux density in the horizontal planes and its mean gradient given in (5), are approximated using the exact analytically obtained values at the vertical axes going through the points H and V . Magnetic flux density at axes through the points O and P , as well as H and V , is validated by comparisons with the finite-element calculations and measurements performed for nine values of z coordinate. Measurement grid is denoted by the crossings of the dashed lines, along the x -axis and along the two lines parallel to the x -axis.

well. For the non-periodic arrays a set of masking coefficients $M^{i,j} \in \{0, 1\}$ is introduced, describing the existence of a particular element in an array's matrix.

III. MEASUREMENTS

Measurements performed on the example two-dimensional array, using Digital Teslometer DTM-151, serve two purposes. Firstly, remanent magnetization is determined from the measured maxima and minima of the vector \mathbf{B} in horizontal planes. Secondly, analytical expressions as well as the finite-element model are validated against the measured data.

As shown in Fig. 3, we used a set of three stripes and a measurement grid, consisting of 21-by-3 points in planes parallel to the xOy plane. Grid step in x - and y -direction equals $x_d/2 = 9.75$ mm and $y_d/2 = 18.0$ mm, which agrees with

$$\begin{aligned}
 B_x(x, y, z) &= \frac{\mu_0 J_{mS}}{4\pi} \sum_{i=-M}^M \sum_{j=-N}^{N-1} \sum_{k=1,3}^1 \sum_{tp=0}^1 \sum_{tq=0}^1 \frac{(-1)^{(tp+tq+1)}}{\operatorname{sgn}((j + \frac{1}{2}) \cdot y_d + (-1)^{m_s+tp+1} \frac{a}{2} - y)} \\
 &\quad \cdot \ln \left(-|u_{i,j,k}^{a,tq}| + \sqrt{(u_{i,j,k}^{a,tq})^2 + (r_{i,j,k}^{a,tp})^2} \right), \\
 B_y(x, y, z) &= \frac{\mu_0 J_{mS}}{4\pi} \sum_{i=-M}^M \sum_{j=-N}^{N-1} \sum_{k=2,4}^1 \sum_{tp=0}^1 \sum_{tq=0}^1 \frac{(-1)^{(tp+tq)}}{\operatorname{sgn}(i \cdot x_d + (-1)^{m_s+tp} \frac{b}{2} - x)} \\
 &\quad \cdot \ln \left(-|u_{i,j,k}^{b,tq}| + \sqrt{(u_{i,j,k}^{b,tq})^2 + (r_{i,j,k}^{b,tp})^2} \right), \\
 r_{i,j,k}^{a,tp} &= \frac{(i \cdot x_d + (-1)^{m_s} \frac{b}{2} - x)}{((j + \frac{1}{2}) \cdot y_d + (-1)^{m_s+tp+1} \frac{a}{2} - y)}, & r_{i,j,k}^{b,tp} &= \frac{((j + \frac{1}{2}) \cdot y_d + (-1)^{m_s} \frac{a}{2} - y)}{(i \cdot x_d + (-1)^{m_s+tp} \frac{b}{2} - x)}, \\
 u_{i,j,k}^{a,tq} &= \frac{(i \cdot x_d + (-1)^{m_s} \frac{b}{2} - x)}{\sqrt{(i \cdot x_d + (-1)^{m_s} \frac{b}{2} - x)^2 + (z + t + (1 - tq) \cdot h)^2}}, \\
 u_{i,j,k}^{b,tq} &= \frac{((j + \frac{1}{2}) \cdot y_d + (-1)^{m_s} \frac{a}{2} - y)}{\sqrt{((j + \frac{1}{2}) \cdot y_d + (-1)^{m_s} \frac{a}{2} - y)^2 + (z + t + (1 - tq) \cdot h)^2}}, & m_s &= \frac{1 - \operatorname{sgn}(k - \frac{5}{2})}{2}. \tag{8}
 \end{aligned}$$

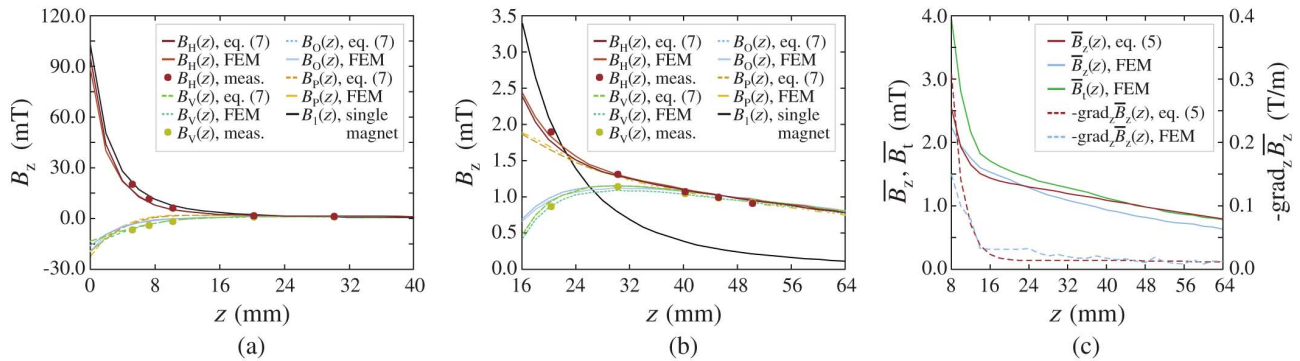


Fig. 4 Agreement of the three sets of results for the magnetic flux density above the array. Due to large magnetic flux density variations with the z coordinate, the same results are shown in parts (a) and (b), but for two different z -ranges. Values of B_z calculated analytically, using (7), and numerically (FEM) agree well and fully correspond to the realistic, measured magnetic flux density data (dots) at eight heights. At larger z , $B_H(z)$ and $B_V(z)$ converge and show slow and almost linear decrease, opposed to rapidly decreasing $B_1(z)$. Analytical estimates, using (5), for $\bar{B}_z(z)$ and its mean gradient defined by (1) are compared to the numerically obtained values in part (c). The difference between the two is mainly a consequence of the finite number of elements comprising the magnetic array. Analytical estimates are good enough to be used for fast parameter assessment or preliminary design. Mean total magnetic flux density, $\bar{B}_t(z)$, where $B_t = \sqrt{B_x^2 + B_y^2 + B_z^2}$, is obtained from finite-element calculations. It is mainly contributed by B_z , and the analytical estimate for $\bar{B}_z(z)$ lies between \bar{B}_z and \bar{B}_t .

the hills and valleys of the magnetic flux density distribution. Measurement resolution is 0.005 mT and the reading precision is 0.01%, for the utilized range of up to 0.3 T [27].

Hexagonal barium hexaferrite ($\text{BaFe}_{12}\text{O}_{19}$), the material out of which the individual magnets are made, is a type of robust ceramics that is generally stable to moisture and resistant to corrosion. One of the most important hard magnetic materials, it is widely used for permanent magnets, magnetic recording media and microwave devices. Its production cost is low, whereas its magnetic properties are very good, e.g., high Curie temperature and high saturation magnetization. These are the material intrinsic properties, unaffected by the microstructure. Theoretical values $T_C = 450^\circ\text{C}$ and $B_r = 480$ mT are reported in [28]. Given the barium hexaferrite density reported in [29], $\rho = 4.9 \cdot 10^3$ kg/m³, the corresponding saturation magnetization is $M_s = 78.0$ A · m²/kg. However, other magnetic properties can vary a lot as a function of production process, e.g., sintering time and temperature [29]–[31]. Therefore, a trial value of M_r is used to calculate $B_H(z)$ and $B_V(z)$ according to (7) and the scaling constant for M_r giving the actual field levels is obtained by field measurement in several hill points. Since we collected a large amount of measured data to verify the models, averaged hill and valley magnetic field data for five planes, $z \in \{19.4, 29.4, 39.4, 44.4, 49.4\}$ mm, was used as a reference to find a multiplicative constant that minimizes the mean square difference between the calculated and measured data. However, it is sufficient to measure $B_H(z)$ in three to five points above one of the most central hills, at a distance from the array's surface. Upon the correction, $M_r = 60.0$ A · m²/kg.

In total, three sets of measurements were performed. Firstly, we measured magnetic field at the array's surface, considering only hills. Values of (55.70 ± 7.22) and (54.34 ± 7.22) mT, given as (mean value \pm standard deviation), are obtained from the repeated measurements for the 'north' and 'south' side of the stripes, respectively. We attribute the differences to the stronger or lighter adhesion to the soft rubber surface or slight tilt of the Hall probe measuring only the perpendicular field component, during the manually conducted measurements. Measured values are somewhat lower than the theoretically predicted 59.62 mT at the height of the active measurement area of the Hall probe, $z = 1.2$ mm.

Second set of measurements followed the measurement grid described above, marked out on a thin glass plate. Data was taken for $z \in \{4.4, 6.5, 9.4, 19.4, 29.4, 39.4, 44.4, 49.4\}$ mm. Estimates for $B_V(z)$ and $B_H(z)$ are obtained by averaging the ten out of 21 values taken along the x -axis, and 22 hill values taken for $y = \pm y_d/2$, respectively. The relative variability of measurements, assessed as the ratio of the standard deviation and the mean value, is twice smaller for the second set of measurements than for the first one.

The third set of measurements was taken following the same procedure as for the second one, with the two and three layers of arrays on top of each other. Its purpose was to verify the analytical expressions for the layered arrays.

IV. FINITE ELEMENT MODELING

The finite-element calculations can be used to validate the analytical expressions, as well as study the magnetic flux density variation in the experimental volume, including the stray magnetic field. Any software package for magnetostatic analysis and modeling could be used for the two-dimensional magnetic array modeling. We employed the Mermaid FEM suite for magnetostatics [32], [33]. It is a universal tool for the design of permanent and electro-magnets, utilizing first-order scalar elements to solve for the magnetostatic potential. For the best accuracy of the results, the basic two-dimensional triangular mesh is iteratively refined to better conform to the equipotential lines. It is then repeated in the third dimension to form layers of triangular prisms. We used 202 by 208 nodes out of maximal 223 by 223 in this software version, covering a 125.0 mm by 172.4 mm surface, to model a third of an array; the rest of the data is obtained from the symmetry requirements. A total of 61 vertical layers is used, resulting in the total number of nodes equal to 2 562 976. Material properties input, as the remanent magnetic flux density in elements designated as ferromagnetic, $B_r = \mu_0 \cdot M_r = 4\pi \cdot 10^{-7} \cdot M_r$, corresponds to a piece of material very long in the direction of magnetization (compare to 189.11 mT in the centers of our magnets). This is accounted for by considering the actual dimensions of the magnets. Requiring the relative accuracy of the final results of 10^{-4} , the solution is obtained after 2.16 minutes on an Intel Pentium 4 machine at 2.2 GHz.

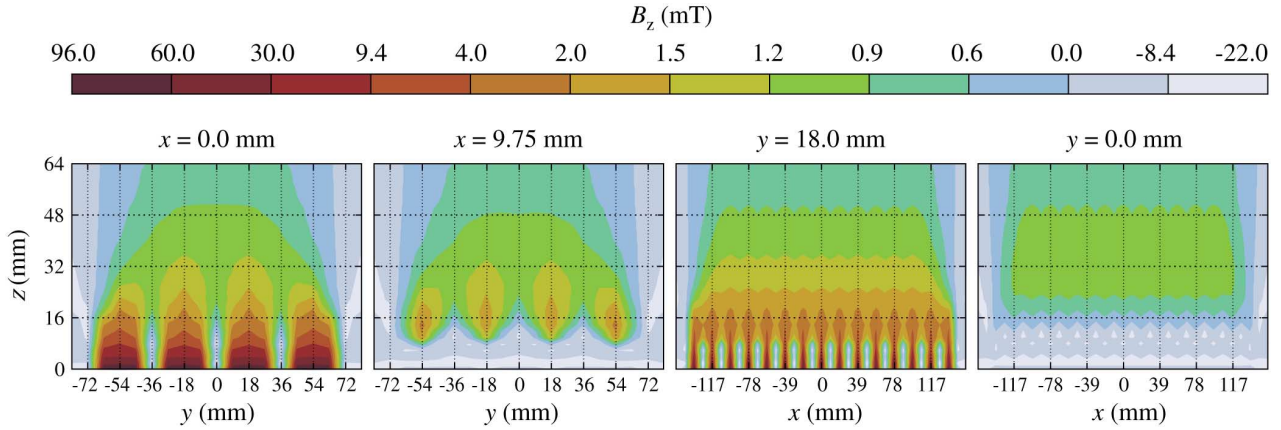


Fig. 5 The magnetic flux density variation in vertical planes obtained using the finite-element calculations. The dominant, B_z component, is shown for the four cross-sections: two parallel to the yOz plane and two parallel to the xOz plane, one of each halving the magnets and the other halving the space between the two rows of magnets. For the cross-sections parallel to the xOz plane the stray magnetic field lies outside the experimental volume, so that the assumptions of the magnetic flux density periodicity are justified. In the cross-sections parallel to the yOz plane that is not the case due to the small number of magnets in y -dimension and large spacing between them. This is the reason for the discrepancies between the approximate analytical estimates and finite-element calculations of $\vec{B}_z(z)$ and $-\text{grad}_z \vec{B}_z(z)$ in Fig. 4.

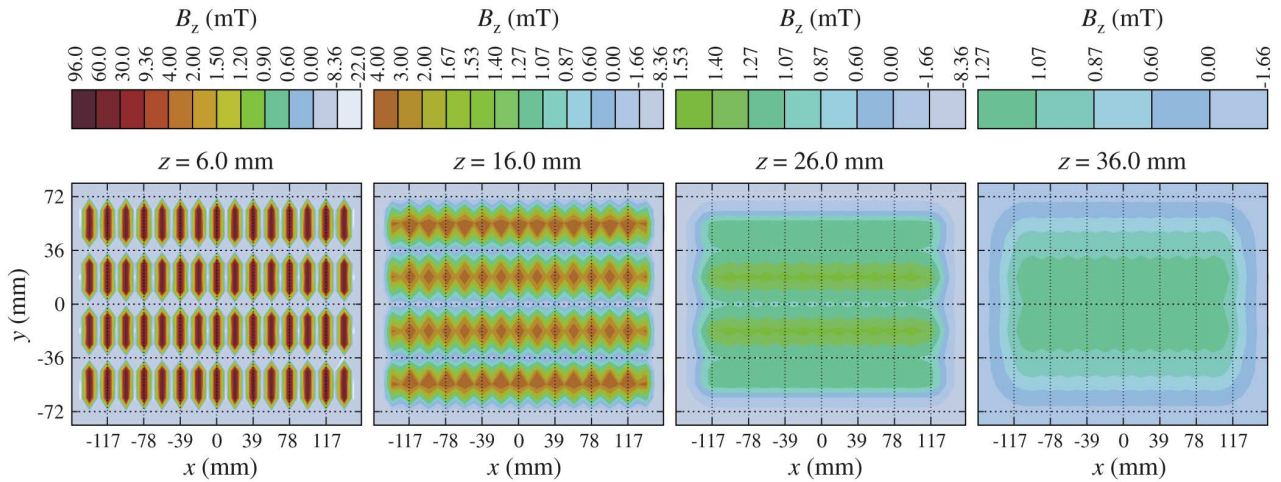


Fig. 6 The magnetic flux density variation in horizontal planes obtained using the finite-element calculations. The magnetic flux density of up to 96 mT is produced right above the ferromagnetic rods, however, flux lines close between the rows of magnets and the variations are large. Above the height of 14 mm flux lines act to increase a resultant field whose distribution in horizontal planes varies much less than with the height above the array. Mean magnetic flux density in the experimental volume is obtained by averaging within the z -ranges of interest.

Obtained results are compared in parts (a) and (b) of Fig. 4 with the analytically calculated data corresponding to the four characteristic axes, through the points H , V , O , and P , denoted in Fig. 3. Both the analytical and the FEM model are validated by comparison with measurements. The agreement of the three sets of results is excellent. The magnetic array field extends much further from the surface and decreases slowly, almost linearly, as opposed to the $B_1(z) \sim z^{-3}$ of a single ferromagnetic rod. Part (c) of Fig. 4 illustrates usefulness of the approximate analytical estimates given by (5) for the fast parameter assessment and preliminary design of magnetic arrays. It compares the analytical estimates with the exact numerically obtained values, which took into account effects caused by the finite number of array elements. Horizontal field components were included in the numerical model. However, the stray fields at the very edges of the stripes were excluded when taking mean values. Numerically obtained z -component mean, $\vec{B}_z(z)$, is somewhat lower than its analytical estimate.

The results are also used to study the magnetic flux density variation throughout the experimental volume, including stray

magnetic fields. The two experimental volume cross-sections parallel to the xOz plane, shown in Fig. 5, give evidence of an almost periodic magnetic flux density distribution. For these planes, the regions of the stray field are actually located outside the experimental volume, see Fig. 1. Therefore, the field description suggested by (5) is quite realistic. However, due to the small number of elements (four) in the y -direction and relatively large magnet spacing, the z -component of the vector \mathbf{B} is significantly lower for the two non-central “hills” and “valleys” in the planes parallel to the yOz . The results of analytical calculations and those obtained with FEM are studied using B_z . The FEM data shows that the z -component constitutes more than 96% of the total magnetic flux density in the central hill region and more than 80% everywhere in the hill region. The same amount of 96% is obtained for the “central valley” along the x -axis, by comparing minima of B_z and B_t from $y = -y_d/2$ to $y = y_d/2$ for every considered z . In the other two valleys this quantity decreases with height going as low as 47%. Significant horizontal field components are to be expected when there are three rows of magnets on one side versus only one row on the

TABLE I
MEAN MAGNETIC FIELD PARAMETERS IN THE EXPERIMENTAL VOLUME
OBTAINED USING THE FINITE ELEMENT CALCULATIONS

h_1 (mm)	h_2 (mm)	\bar{B}_z (mT)	\bar{B}_t (mT)	\bar{G}_z (T/m)
0.0*	10.0	15.4394	16.1613	1.8549
0.0*	20.0	9.1341	9.6192	1.0302
0.0*	30.0	6.6632	7.0497	0.7165
16.0	46.0	1.1371	1.3127	0.0223
24.0	54.0	0.9719	1.1476	0.0176
32.0	62.0	0.8442	1.0122	0.0141

* for the first three rows $|\bar{B}|$ was used

other and having in mind closure of the flux lines around the edges. The total magnetic flux density, however, does not suffer much of a decline when three valleys are compared: it is exactly the same up to the height of 4 cm and at larger z it does not fall below 80% with respect to the central valley. The total exposure field therefore does not change too much in horizontal planes.

From the FEM data and Fig. 5, it follows that $z = 14$ mm is the limiting height where the magnetic flux lines start to add together to form a resultant positive, slowly decreasing, magnetic flux density ($B_V(14 \text{ mm}) = 0.05$ mT). Fig. 6 shows four horizontal cross-sections of the experimental volume, right above the surface of an array, at 16 mm showing small but positive B_V , and the next two at larger z , where the field is predominantly vertical and vertically decreasing. Therefore, it is reasonable to perform parameter averaging in the horizontal planes to get the mean magnetic flux density and its mean gradient defined by (1) as a function of z -coordinate. The actual experimental volume is located between the delimiting planes $z = h_1$ and $z = h_2$, determined by the type of experiment to be conducted. The mean parameters for the experimental magnetic field description are calculated by further averaging between the heights h_1 and h_2 . Several cases are presented as an example in Table I.

V. POSSIBLE OPTIMIZATION STRATEGIES

Specific ranges of mean magnetic flux density and its mean gradient as defined by (1) may be required for a certain application. It is worthwhile to briefly discuss two ways of magnetic field modification. Firstly, the slowly decreasing magnetic field of the considered array type allows for the significant field amplification if the heights of equivalent current sheets are increased by stacking the layers of arrays on top of each other. This is illustrated in Fig. 7 and Table II. Whereas a rapid decrease of the single element magnetic flux density prevents effective field increase by stacking magnets, distributed placement of magnets over the surface imposes the linear field decrease with distance and the effect is considerable. It is important that the nonmagnetic support between array elements in no way disrupts the fields produced by other layers. Placement of a large ferromagnetic plate beneath the lowest layer could be used to produce an effect equivalent to doubling the number of layers [22], [23].

The increase in the height of current sheets can be combined with the adjustments of magnet spacings in x - and y -direction to obtain different combinations of mean magnetic flux density, $\bar{B}_z(z)$, and its mean gradient defined by (1), $-\text{grad}_z \bar{B}_z$. Expressions (5) can be used as a design tool for this type of magnetic arrays. As an illustration, in Fig. 8 we present the results of the

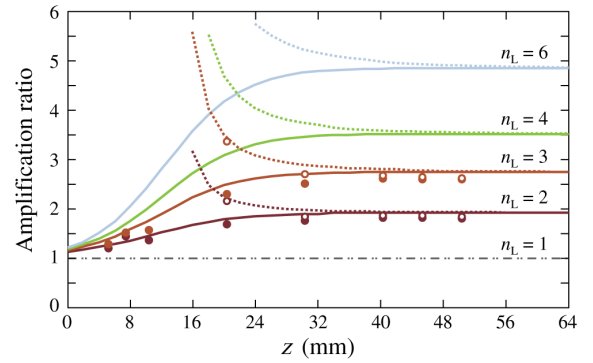


Fig. 7 The magnetic flux density amplification using several layers of arrays on top of each other. The magnetic flux density above the ferromagnetic rods (hills) and in between the rows of magnets (valleys) is obtained analytically, using (7). It is depicted by the solid lines in the case of rods (hills) and by the dashed lines for the valleys. Validity of our assumptions is checked for the number of layers, n_L , equal to two and three, and the results measured for eight heights at the hill points and at the valleys are given by the full and unfilled dots, respectively. Due to the slowly decreasing magnetic field, the superposition results in an amplification ratio of almost n_L , although every additional layer is shifted by the height of one layer with respect to the others.

TABLE II
MEAN MAGNETIC FIELD PARAMETERS FOR LAYERS OF ARRAYS OBTAINED
USING THE ANALYTICAL EXPRESSIONS

h_1 (mm)	h_2 (mm)	\bar{B}_z (mT)	\bar{B}_t (mT)	\bar{G}_z (T/m)
Two layers				
16.0	46.0	2.1932	2.5316	0.0431
24.0	54.0	1.8715	2.2096	0.0350
32.0	62.0	1.6214	1.9442	0.0276
Three layers				
16.0	46.0	3.4402	3.9597	0.0636
24.0	54.0	2.7465	3.2406	0.0518
32.0	62.0	2.3294	2.7931	0.0402

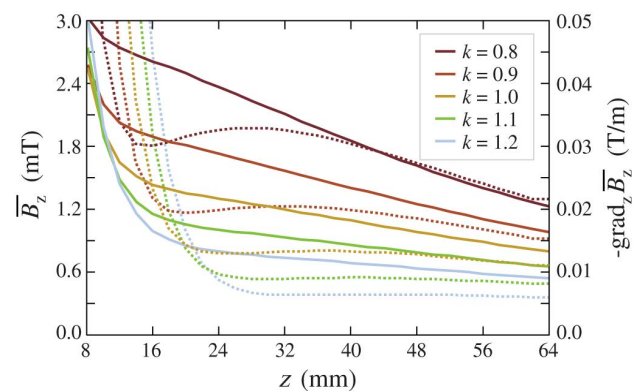


Fig. 8 Possible increase in mean magnetic flux density and its mean gradient given in (5) with the magnet spacing adjustment. The effect to the mean field parameters of the modification in the array element spacing by a factor k is determined using the approximate analytical estimates given in (5). Different combinations of mean magnetic flux density, \bar{B}_z , and mean gradient defined by (1), $-\text{grad}_z \bar{B}_z(z)$, are depicted by solid and dashed curves, respectively.

modification in the array element spacing by a factor k , here taken to be the same for x - and y -direction. Were the individual array elements cylindrical instead of brick-shaped, we would obtain the elliptic integrals. If the numerical integration is to be avoided, they can be represented using some of the various expansions, as it was done in [34]. Expressions (7) and (8) become more complicated, but the validity and usefulness of estimates (5) remain unaffected.

VI. CONCLUSION

We have considered the general case of two-dimensional magnetic arrays with the same orientation of magnetic axes perpendicular to the array's surface. Exact closed-form expressions are derived for the magnetic flux density in an arbitrary field point. An extension to the case of alternating magnetic moments is straightforward, whereas additional terms have to be included for the most general case of an array with different vectors of magnetization from element to element. Exploiting the array periodicity, we propose an approximate assessment of main magnetic field parameters of interest, that can serve as a design tool. Finite-element analysis served for the verification of analytical model, as well as more detailed magnetic field analysis. Both models are validated by comparison with measurements.

ACKNOWLEDGMENT

This work was supported by the Ministry of Education, Science and Technological Development of Serbia through the projects (grants) no. III-45003, III-41013, and III-41019. The authors have no conflict of interest regarding the material and information presented in the article.

REFERENCES

- [1] W. P. Taylor, J. J. Bernstein, J. D. Brazzle, and C. J. Corcoran, "Magnet arrays for use in a 3-D MEMS mirror array for optical switching," *IEEE Trans. Magn.*, vol. 39, no. 5, pp. 3286–3288, Sep. 2003.
- [2] T. M. Liakopoulos, W. Zhang, and C. H. Ahn, "Micromachined thick permanent magnet arrays on silicon wafers," *IEEE Trans. Magn.*, vol. 32, pp. 5154–5156, Sep. 1996.
- [3] I. Zana and G. Zangari, "Electrodeposited Co–Pt permanent micro-magnet arrays on Cu(111)–Si(110) substrates," *IEEE Trans. Magn.*, vol. 38, no. 5, pp. 2544–2546, Sep. 2002.
- [4] H. J. Cho and C. H. Ahn, "A bidirectional magnetic microactuator using electroplated permanent magnet arrays," *J. Microelectromech. Syst.*, vol. 11, no. 1, pp. 78–84, Feb. 2002.
- [5] S. B. Shetye, J. S. Agashe, and D. P. Arnold, "Investigation of microscale magnetic forces for magnet array self-assembly," *IEEE Trans. Magn.*, vol. 43, no. 6, pp. 2713–2715, Jun. 2007.
- [6] D. L. Trumper, W. Kim, and M. E. Williams, "Design and analysis framework for linear permanent-magnet machines," *IEEE Trans. Ind. Applicat.*, vol. 32, no. 2, pp. 371–379, Mar. 1996.
- [7] J. Cao, Y. Zhu, J. Wang, W. Yin, and G. Duan, "Analysis and comparison of two-dimensional permanent-magnet arrays for planar motor," *IEEE Trans. Magn.*, vol. 40, no. 6, pp. 3490–3494, Nov. 2004.
- [8] J. Cao, Y. Zhu, J. Wang, W. Yin, and G. Duan, "A novel synchronous permanent magnet planar motor and its model for control applications," *IEEE Trans. Magn.*, vol. 41, no. 6, pp. 2156–2163, Jun. 2005.
- [9] M. G. Lee and D-G. Gweon, "Optimal design of a double-sided linear motor with a multi-segmented trapezoidal magnet array for a high precision positioning system," *J. Magn. Magn. Mater.*, vol. 281, pp. 336–346, Oct. 2004.
- [10] D. Golda and M. L. Culpepper, "Modeling 3D magnetic fields for precision magnetic actuators that use non-periodic magnet arrays," *Precision Eng.*, vol. 32, no. 2, pp. 134–142, Apr. 2008.
- [11] G. G. Sotelo, A. C. Ferreira, and R. de Andrade, Jr, "Halbach array superconducting magnetic bearing for a flywheel energy storage system," *IEEE Trans. Appl. Supercond.*, vol. 15, no. 2, pp. 2253–2256, Jun. 2005.
- [12] K. Halbach, "Design of permanent multipole magnets with oriented rare earth cobalt material," *Nucl. Instrum. Methods*, vol. 169, no. 1, pp. 1–10, Feb. 1980.
- [13] M. I. Weintraub, G. I. Wolfe, and R. A. Barohn *et al.*, "Static magnetic field therapy for symptomatic diabetic neuropathy: A randomized, double-blind, placebo-controlled trial," *Arch. Phys. Med. Rehab.*, vol. 84, no. 5, pp. 736–746, May 2003.
- [14] N. A. Segal, Y. Toda, and J. Huston *et al.*, "Two configurations of static magnetic fields for treating rheumatoid arthritis of the knee: A double-blind clinical trial," *Arch. Phys. Med. Rehab.*, vol. 82, no. 10, pp. 1453–1460, Oct. 2001.
- [15] C. Vallbona, C. F. Hazlewood, and G. Jurida, "Response of pain to static magnetic fields in postpolio patients: A double-blind pilot study," *Arch. Phys. Med. Rehab.*, vol. 78, no. 11, pp. 1200–1203, Nov. 1997.
- [16] H. N. Mayrovitz and E. E. Groseclose, "Effects of a static magnetic field of either polarity on skin microcirculation," *Microvasc. Res.*, vol. 69, no. 1–2, pp. 24–27, Jan. 2005.
- [17] Y. Yan, G. Shen, and K. Xie *et al.*, "Wavelet analysis of acute effects of static magnetic field on resting skin blood flow at the nail wall in young men," *Microvasc. Res.*, vol. 82, no. 3, pp. 277–283, Nov. 2011.
- [18] A. P. Colbert, H. Wahbeh, and N. Harling *et al.*, "Static magnetic field therapy: A critical review of treatment parameters," *Evidence Based Complem. Altern. Med.*, vol. 6, no. 2, pp. 133–139, Jun. 2009.
- [19] D. M. Djordjević, S. R. De Luka, I. D. Milovanović, S. Janković, S. Stefanović, S. Vesković-Moračanin, S. Ćirković, A. Ž. Ilić, J. L. Ristić-Djurović, and A. M. Trbović, "Hematological parameters' changes in mice subchronically exposed to static magnetic fields of different orientations," *Ecotoxicol. Environ. Safety*, vol. 81, pp. 98–105, Jul. 2012.
- [20] S. R. De Luka, D. M. Djordjević, and I. D. Milovanović *et al.*, "Sub-chronic exposure to static magnetic field affects zinc and copper content in mice brain and liver," *Cell Biochem. Biophys.*, submitted for publication.
- [21] D. Mandić, "Surface magnetized elastic magnetic stripe and application," (WO1999060581) [Online]. Available: <http://patentscope.wipo.int/search/en/WO1999060581>.
- [22] B. M. Notaroš, *Electromagnetics*. Upper Saddle River, NJ, USA: Prentice Hall/Pearson Education, 2010.
- [23] C. A. Balanis, *Advanced Engineering Electromagnetics*. Hoboken, NJ, USA: Wiley, 1989.
- [24] R. Ravaut and G. Lemarquand, "Comparison of the Coulombian and Amperean current models for calculating the magnetic field produced by radially magnetized arc-shaped permanent magnets," *Progr. Electromagn. Res.*, vol. 95, pp. 309–327, Jul. 2009.
- [25] G. Akoun and J. P. Yonnet, "3D analytical calculation of the forces exerted between two cuboidal magnets," *IEEE Trans. Magn.*, vol. MAG-20, no. 5, pp. 1962–1964, Sep. 1984.
- [26] F. Bancel, "Magnetic nodes," *J. Phys. D: Appl. Phys.*, vol. 32, no. 17, pp. 2155–2161, Sep. 1999.
- [27] "DTM-151 Digital Teslameter with serial communications," Group3, User's Manual.
- [28] I. R. Harris and A. J. Williams, "Magnetic materials," in *Materials Science and Engineering*, R. D. Rawlings, Ed. Oxford, U.K.: Eolss Publishers, 2009 [Online]. Available: <http://www.eolss.net>, in Encyclopedia of Life Support Systems (EOLSS), under the auspices of the UNESCO
- [29] P. Shepherd, K. K. Mallick, and R. J. Green, "Magnetic and structural properties of M-type barium hexaferrite prepared by co-precipitation," *J. Magn. Magn. Mater.*, vol. 311, no. 2, pp. 683–692, Apr. 2007.
- [30] S. Ram, H. Krishnan, K. N. Rai, and K. A. Narayan, "Magnetic and electrical properties of Bi₂O₃ modified BaFe₁₂O₁₉ hexagonal ferrite," *Jpn. J. Appl. Phys.*, vol. 28, no. 4, pp. 604–608, Jan. 1989.
- [31] S. R. Janasi, M. Emura, F. J. G. Landgraf, and D. Rodrigues, "The effects of synthesis variables on the magnetic properties of coprecipitated barium ferrite powders," *J. Magn. Magn. Mater.*, vol. 238, no. 2–3, pp. 168–172, Jan. 2002.
- [32] MERMAID 2D and 3D User's Guide, SIM, Novosibirsk, Russia, 1994.
- [33] N. A. Dubrovina, E. A. Simonov, and S. B. Vorozhtsov, "MERMAID 3D code in ATLAS applications," CERN, Geneva, ATLAS Note ATL-TECH-2001-003, 2001.
- [34] J. S. Agashe and D. P. Arnold, "A study of scaling and geometry effects on the forces between cuboidal and cylindrical magnets using analytical force solutions," *J. Phys. D: Appl. Phys.*, vol. 41, no. 10, p. 105001(9), May 2008.

IEEE TRANSACTIONS ON NUCLEAR SCIENCE

A PUBLICATION OF THE IEEE NUCLEAR AND PLASMA SCIENCES SOCIETY



JUNE 2013

VOLUME 60

NUMBER 3

IETNAE

(ISSN 0018-9499)

PART III OF THREE PARTS

SYMPOSIUM ON RADIATION MEASUREMENTS AND APPLICATIONS (SORMA WEST 2012)
OAKLAND, CA, USA, MAY 14–17, 2012

Evaluation of Effective Dose using TLDs With Different Weighted PMMA Phantoms Undergoing Coronary Artery Calcium Computed Tomography Examination	<i>S.-Y. Tsai, C.-Y. Chen, J.-S. Lee, and J.-C. Chen</i>	2147
Microscopic SEM Texture Analysis of NIPAM Gel Dosimeters	<i>C.-T. Shih, Y.-J. Chang, B.-T. Hsieh, and J. Wu</i>	2155

REGULAR PAPERS

ACCELERATOR TECHNOLOGY

Optimization of Equally Charged Quadrupole Parameters	<i>J. L. Ristić-Djurović, S. Ćirković, and A. Z. Ilić</i>	2161
The Effect of 2-Directional Magnetic Biasing Used for Tuning of a Ferrite-Loaded Re-entrant Cavity	<i>C. Vollinger, F. Caspers, and E. Jensen</i>	2170
Fast and Accurate Magnetic Field Shimming for A Compact Cyclotron	<i>D. Chen, K. Liu, J. Yang, Z. Chen, D. Li, B. Qin, J. Huang, Y. Q. Xiong, and M. Fan</i>	2175

ANALOG AND DIGITAL CIRCUITS

A 1.6-Gsps High-Resolution Waveform Digitizer Based on a Time-Interleaved Technique	<i>L. Zhao, X. Hu, C. Feng, S. Tang, S. Liu, and Q. An</i>	2180
FSDR16—Fast and Low Noise Multichannel ASIC With 5th Order Complex Shaping Amplifier	<i>R. Kleczek and P. Grybos</i>	2188
A Compact, Flexible, High Channel Count DAQ Built From Off-the-Shelf Components	<i>M. Heffner, V. Riot, and L. Fabris</i>	2196

(Contents Continued on Page 2145)



A 19.6 ps, FPGA-Based TDC With Multiple Channels for Open Source Applications	<i>M. W. Fishburn, L. H. Menninga, C. Favi, and E. Charbon</i>	2203
---	--	------

COMPUTING, SIMULATION, ALGORITHMS, AND SOFTWARE

Kernel-Based Machine Learning for Background Estimation of NaI Low-Count Gamma-Ray Spectra	<i>M. Alamaniotis, J. Mattingly, and L. H. Tsoukalas</i>	2209
Pareto-Optimal Gamma Spectroscopic Radionuclide Identification Using Evolutionary Computing	<i>M. Alamaniotis, J. Mattingly, and L. H. Tsoukalas</i>	2222

GAS DETECTORS

Performance Characteristics of the OSMOND Neutron Detector	<i>J. E. Bateman, T. R. Charlton, R. Dalglish, D. M. Duxbury, C. J. Kinane, N. J. Rhodes, E. M. Schooneveld, and E. J. Spill</i>	2232
--	--	------

HOMELAND SECURITY APPLICATIONS

Performance of the Roadside Tracker Portal-Less Portal Monitor	<i>K. P. Ziock, E. C. Bradley, A. Cheriyyadat, M. Cunningham, L. Fabris, C. L. Fitzgerald, J. S. Goddard, D. E. Hornback, R. A. Kerekes, T. P. Karnowski, W. T. Marchant, and J. Newby</i>	2237
--	--	------

PHOTODETECTORS

New Developments of Near-UV SiPMs at FBK	<i>T. Pro, A. Ferri, A. Gola, N. Serra, A. Tarolli, N. Zorzi, and C. Piemonte</i>	2247
--	---	------

RADIATION DAMAGE EFFECTS

Exploring Various Isolation Techniques to Develop Low Noise, Radiation Hard Double-Sided Silicon Strip Detectors for the CBM Silicon Tracking System	<i>S. Chatterji, M. Singla, W. F. J. Müller, and J. M. Heuser</i>	2254
--	---	------

RADIATION EFFECTS

Total Dose Effects: A New Approach to Assess the Impact of Radiation on Device Reliability	<i>N. Martinez, O. Gilard, and G. Quadri</i>	2266
A Wide Temperature, Radiation Tolerant, CMOS-Compatible Precision Voltage Reference for Extreme Radiation Environment Instrumentation Systems	<i>B. M. McCue, B. J. Blalock, C. L. Britton, J. Potts, J. Kemerling, K. Isihara, and M. T. Leines</i>	2272
Prediction of CMOS Image Sensor Dark Current Distribution and Noise in a Space Radiation Environment	<i>E. Martin, O. Gilard, T. Nuns, J.-P. David, and C. Virmondois</i>	2280
Electronic Transport Transition of Hydrogenated Amorphous Silicon Irradiated With Self Ions	<i>S. Sato and T. Ohshima</i>	2288

RADIATION IMAGING

A Modulating Liquid Collimator for Coded Aperture Adaptive Imaging of Gamma-Rays	<i>J. G. M. FitzGerald, L. W. Burggraf, B. R. Kowash, and E. L. Hull</i>	2300
Experimental Benchmark of Electron Trajectory Reconstruction Algorithm for Advanced Compton Imaging	<i>B. Plimley, D. Chivers, A. Coffey, and K. Vetter</i>	2308

READOUT ELECTRONICS

VMM1—An ASIC for Micropattern Detectors *G. De Geronimo, J. Fried, S. Li, J. Metcalfe, N. Nambiar, E. Vernon, and V. Polychronakos* 2314

SCINTILLATION DETECTORS

Effects of Photonic Crystals on the Light Output of Heavy Inorganic Scintillators *A. Knapitsch, E. Auffray, C. W. Fabjan, J.-L. Leclercq, X. Letartre, R. Mazurczyk, and P. Lecoq* 2322

Development of Transparent Ceramic Ce-Doped Gadolinium Garnet Gamma Spectrometers *N. J. Cherepy, Z. M. Seeley, S. A. Payne, P. R. Beck, O. B. Drury, S. P. O'Neal, K. M. Figueroa, S. Hunter, L. Ahle, P. A. Thelin, T. Stefanik, and J. Kindem* 2330

A Study on Radiation Damage in PWO-II Crystals *F. Yang, R. Mao, L. Zhang, and R. Zhu* 2336

SOLID STATE DETECTORS

Monolithic Pixel Sensors for Fast Silicon Vertex Trackers in a Quadruple Well CMOS Technology *S. Zucca, L. Gaioni, L. Ratti, V. Re, G. Traversi, S. Bettarini, F. Forti, F. Morsani, G. Rizzo, L. Bosisio, and I. Rashevskaya* 2343

Characterizing the Timing Performance of a Fast 4H-SiC Detector With an ²⁴¹Am Source *X. Zhang, J. W. Cates, J. P. Hayward, G. Bertuccio, D. Puglisi, and P. A. Hausladen* 2352

Development of Double-Sided Full-Passing-Column 3D Sensors at FBK *G. Giacomini, A. Bagolini, M. Boscardin, G.-F. Dalla Betta, F. Mattedi, M. Povoli, E. Vianello, and N. Zorzi* 2357

TRIGGERS AND FRONT END SYSTEMS

An Analog Trigger System for Atmospheric Cherenkov Telescope Arrays *L. A. Tejedor, M. Barceló, J. Boix, D. Herranz, G. Martínez, J. A. Barrio, O. Blanch Bigas, C. Delgado, and R. López* 2367

Optimization of Equally Charged Quadrupole Parameters

Jasna L. Ristić-Djurović, Saša Ćirković, and Andjelija Ž. Ilić, *Member, IEEE*

Abstract—A quadrupole with equally charged electrodes could be used to focus as well as to accelerate ion beams. The equality of electrode charges causes the driving electric field of this device to be qualitatively different from that of other devices with a similar structure composed of four rod-like electrodes. For the same reason, the area of strong field influence on the beam is shifted towards the entrance and exit of the device. Consequently, it is expected that the device's performance depends on the shapes of its entrance and exit regions. The device parameters whose influence is studied are aperture radius, gap size, and rod length. Performance of the device is quantified with accelerating and focusing potentials, which are obtained as integrals of axial and radial electric fields. These variables are further used to choose optimal values of the device parameters for desired operation of the device.

Index Terms—Electrostatic focusing, field description, linear accelerators, performance estimates, quadrupoles.

I. INTRODUCTION

THE operation of an electrostatic quadrupole whose poles are all positively charged is first studied in [1] and [2], using the helical shape of the electrodes. Here, an equally charged quadrupole (ECQ) is taken to have straight rod-like electrodes, which are parallel to the device's axis and are equidistantly distributed around it. If the voltage used to power the electrodes is electrostatic, the ECQ device can operate as a lens [3], [4]. If the driving electric force alternates in time with appropriately chosen radio frequency (RF), the ECQ device could produce significant ion beam acceleration, as shown by the ion beam dynamics simulations in [5] and [6].

The ECQ device is analyzed in [6] with the intent to increase available ion beam energy of the existing low energy ion beam facility by applying electrode voltages equal in sign rather than alternating in sign to the existing device with the quadrupole-like structure. The obtained results indicated that the described low-cost changes of electrode polarity and use of grounded cylindrical shield may lead to further application

Manuscript received December 15, 2012; revised February 16, 2013; accepted March 16, 2013. Date of publication April 30, 2013; date of current version June 12, 2013. This work was supported by the Ministry of Education, Science and Technological Development of Serbia through the project "Physics and Chemistry with Ion Beams," no. III45006 and was performed while the authors were at the Vinča Institute of Nuclear Sciences, University of Belgrade 11001 Belgrade, Serbia.

The authors were with the Vinča Institute of Nuclear Sciences, University of Belgrade 11001 Belgrade, Serbia. They are now with the Innovation Center, School of Electrical Engineering, University of Belgrade 11120 Belgrade, Serbia (e-mail: jasna@stanfordalumni.org; kosjera@vinca.rs; andjelija@iee.org).

Color versions of one or more of the figures in this paper are available online at <http://ieeexplore.ieee.org>.

Digital Object Identifier 10.1109/TNS.2013.2253618

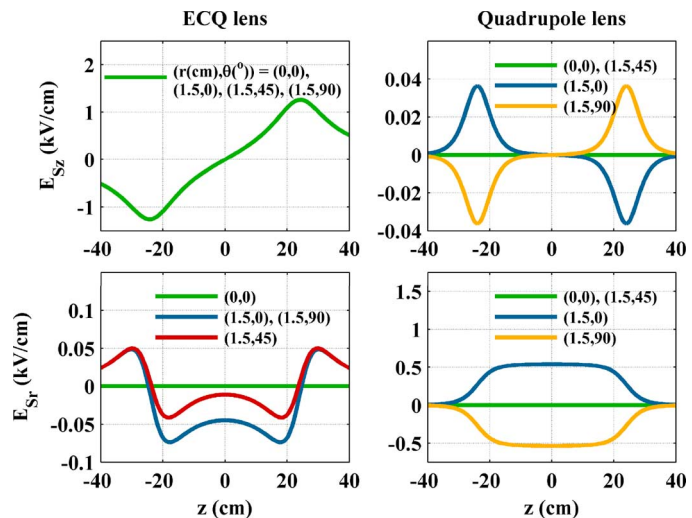


Fig. 1. Comparison of electric fields corresponding to simple analytical models of ECQ and quadrupole lens. The axial and radial electric field components, E_{S_z} and E_{S_r} , are given along the lines parallel to the z -axis, which are defined by their radial and azimuthal coordinates, r and θ . Four rod-like electrodes are approximated with four uniformly charged finite wires. The wires are positioned along the edges of imaginary quadratic prism. The wire length and the sides of quadratic prism bases are taken to be $L_w = 48$ cm and $d_w = 12$ cm, respectively. For the ECQ lens specific charges of the wires are all equal, $Q'_{w1} = Q'_{w2} = Q'_{w3} = Q'_{w4} = 0.36 \mu\text{C/m}$, whereas for the quadrupole lens $Q'_{q1} = Q'_{q3} = -0.36 \mu\text{C/m}$ and $Q'_{q2} = Q'_{q4} = 0.36 \mu\text{C/m}$.

span broadening of the considered ion beam facility as well as of other similar facilities if the ECQ device parameters are adequately adjusted. Note that, as in [4] and [6], the rod radius and the distance between the rods are chosen to be equal to the values corresponding to the existing device, here as well. Consequently, the ratio between the rod radius and the radius of the aperture amongst the rods has the value of 8/9.

Even though the geometry of an ECQ device is similar to a number of other devices or device components, for example those described in [7]–[15], the equality of electrode voltages in an ECQ device produces qualitatively different electric fields. To illustrate the difference, electric fields within the ECQ and quadrupole lenses with the same geometry are compared in Figs. 1 and 2.

The axial and radial components of the field are chosen for comparison because they could serve as an estimate of accelerating and focusing capability of a device. In the simplest analytical model the ECQ lens as well as the quadrupole lens is approximated with four uniformly charged finite wires. The devices are situated in the cylindrical coordinate system whose origin is in the middle of the lens and whose z -axis is coinciding with the device's axis. The positions of the wires are

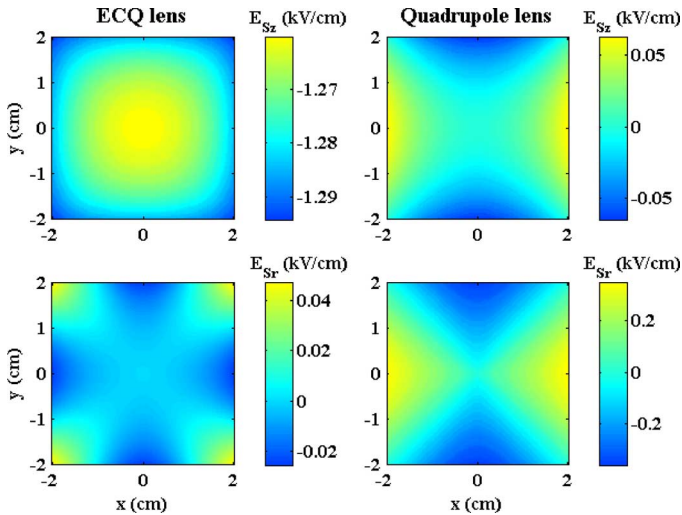


Fig. 2. Electric fields in transverse plane. The axial and radial electric field components, E_{S_z} and E_{S_r} , are given in the plane $z = -24$ cm. The simple analytical finite wires models used to represent the ECQ and the quadrupole lens are the same as those in Fig. 1. The depicted shape of the fields justifies the use of the line segments in the half-planes $\theta = 0^\circ$ and $\theta = 45^\circ$ for data analysis.

defined with radial and azimuthal coordinates given as pairs $(r_{wi}, \theta_{wi}) = (d_w/\sqrt{2}, 0^\circ), (d_w/\sqrt{2}, 90^\circ), (d_w/\sqrt{2}, 180^\circ),$ and $(d_w/\sqrt{2}, 270^\circ)$ for $i = 1, 2, 3,$ and $4,$ respectively, where d_w is the distance between the two neighboring wires. The axial and radial electric fields within the simplest (subscript S) analytical models E_{S_z} and E_{S_r} are calculated using analytical formulas for finite wires

$$E_{S_z}(r, \theta, z) = \frac{Q'}{4\pi\epsilon_0} \sum_{i=1}^4 (-1)^{i-C_q} \cdot \left(\frac{1}{r_{2i}} - \frac{1}{r_{1i}} \right)$$

$$E_{S_r}(r, \theta, z) = \frac{Q'}{4\pi\epsilon_0} \sum_{i=1}^4 (-1)^{i-C_q} \cdot \left(\frac{r - r_{wi} \cos(\theta - \theta_{wi})}{r_{2i}(p_2 + r_{2i})} - \frac{r - r_{wi} \cos(\theta - \theta_{wi})}{r_{1i}(p_1 + r_{1i})} \right) \quad (1)$$

where

$$r_{1i} = \sqrt{r^2 + r_{wi}^2 - 2rr_{wi} \cos(\theta - \theta_{wi}) + p_1^2},$$

$$r_{2i} = \sqrt{r^2 + r_{wi}^2 - 2rr_{wi} \cos(\theta - \theta_{wi}) + p_2^2},$$

$$p_1 = z + \frac{L_w}{2},$$

$$p_2 = z - \frac{L_w}{2},$$

Q' is charge density, and constant C_q adjusts the sign of the charge, i.e., $C_q = 1$ for the quadrupole lens, whereas for the ECQ lens, $C_q = 0$. Note that finite wires are an approximation of somewhat shorter rods. For example, for $d_w = 12$ cm, and the rod radius of 4 cm, good agreement between the simplest analytical field corresponding to $L_w = 48$ -cm-long finite wires and numerically modeled field of $L_r = 40$ -cm-long rods is obtained in [6].

The azimuthal positions of lines along which the calculated fields are given in Fig. 1 are chosen to correspond to the limiting

fields in one of the devices or both of them. The field components along the lines in $\theta = 0^\circ$ and $\theta = 90^\circ$ planes have limiting values for the quadrupole lens, whereas, for the ECQ device, the limiting radial fields are in $\theta = 0^\circ$ and $\theta = 45^\circ$ planes. This is consistent with twofold and fourfold symmetry of the quadrupole and ECQ device, respectively. The radial component of the field, i.e., the focusing capability, in the ECQ lens is an order of magnitude smaller than in the quadrupole lens. However, the limiting radial fields have the same sign and shape for the ECQ lens compared to the opposite effects, i.e., focusing and defocusing, in the two mutually perpendicular transverse directions of the quadrupole lens. On the other hand, the axial component of the field, i.e., the accelerating capability of the ECQ device is practically equal along all considered line segments and is more than an order of magnitude larger than that of the standard quadrupole device. In the quadrupole device, the radial as well as axial field components fall to zero much faster with distance from the device's entrance and exit than is the case for the ECQ device.

The axial and radial electric fields shown in Fig. 2 are calculated in the transverse plane containing wire tips, using simple analytical models of the ECQ and quadrupole lenses. In the vicinity of the z -axis, the contour plots corresponding to the ECQ lens reveal similarities with the contour plots of the einzel lens fields. The further away the transverse plane is from the wire tips and coordinate system origin, the broader is the area around the z -axis where the contour lines of the ECQ lens fields resemble circles.

The simplest estimates of the ECQ device fields shown in Figs. 1 and 2 indicate that, despite of its quadrupole structure, operation of this device is more similar to the einzel lens if it is used for focusing and to the drift tube Sloan-Lawrence accelerator if it is used for acceleration.

The simplest analytical estimate given with (1) predicts very slow fringe field decay for an ECQ device. In order to gain control of the field shape in the entrance as well as exit region, a grounded cylindrical shield around four rod-like electrodes is introduced. It is to be expected that parameters that define the geometry of the entrance and exit, e.g., the size of the apertures on the grounded cylinder and the distance between the apertures and electrode ends, will play an important role in shaping the field as well as in the device's performance. Consequently, additional effort is due in order to describe the field in the entrance and exit region of the device.

II. FINITE WIRES MODEL

In the finite wires model of an ECQ device, the rod-like electrodes are modeled with finite wires, as in the simplest analytical model. In addition, the grounded cylindrical shield is modeled with two grounded conducting planes. It is assumed that the grounded cylinder has an infinite outer radius, i.e., that the cylinder bases are extended into planes. The influence of these two conducting surfaces is calculated by first adding the fields of the two images of four finite wires (see Fig. 3) and then by subtracting the fields resulting from the missing parts of the planes due to apertures. Therefore, the axial and radial components of approximated field are obtained as $E_z = E_{S_z} + E_{I1z} + E_{I2z} - E_{A1z} - E_{A2z}$ and $E_r = E_{S_r} + E_{I1r} + E_{I2r} -$

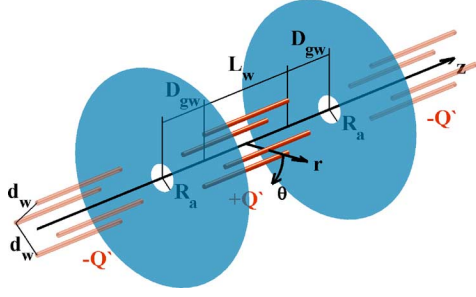


Fig. 3. Finite wires model of ECQ device. In addition to four $L_w = 48$ -cm-long wires uniformly charged with charge density $+Q'$, and each two adjacent positioned $d_w = 12$ cm apart, two infinite grounded planes are introduced. The planes have apertures with radius R_a and are placed at the distance D_{gw} from each end of the wires. The influence of the two planes is modeled using the method of images.

$E_{A1r} - E_{A2r}$, where E_{Sz} and E_{Sr} are components of the simplest (subscript S) analytical electric field defined with (1). The fields corresponding to the two images (subscripts $i1$ and $i2$) are $E_{i1z}(r, \theta, z) = -E_{Sz}(r, \theta, z - z_{i1})$, $E_{i1r}(r, \theta, z) = -E_{Sr}(r, \theta, z - z_{i1})$, $E_{i2z}(r, \theta, z) = -E_{Sz}(r, \theta, z - z_{i2})$, and $E_{i2r}(r, \theta, z) = -E_{Sr}(r, \theta, z - z_{i2})$, where $z_{i1} = -L_w - 2D_{gw}$ and $z_{i2} = L_w + 2D_{gw}$ are axial shifts of the two images with respect to the original. The axial and radial field components corresponding to the apertures (subscript A), i.e., to the missing parts of grounded planes, are numerically integrated as

$$\begin{aligned}
 E_{Aiz}(r, \theta, z) &= \int_{\rho=0}^{R_a} \int_{\varphi=0}^{2\pi} \frac{E_{Sz}(\rho, \varphi, z_{Ai})}{4\pi d_i^2} \frac{\vec{d}_i \cdot \vec{z}}{d_i z} \rho d\varphi d\rho \\
 &= \int_{\rho=0}^{R_a} \int_{\varphi=0}^{2\pi} \frac{E_{Sz}(\rho, \varphi, z_{Ai}) (z - z_{Ai}) \rho d\varphi d\rho}{4\pi (r^2 + \rho^2 - 2r\rho \cos(\varphi - \theta) + (z - z_{Ai})^2)^{3/2}} \\
 E_{Air}(r, \theta, z) &= \int_{\rho=0}^{R_a} \int_{\varphi=0}^{2\pi} \frac{E_{Sz}(\rho, \varphi, z_{Ai})}{4\pi d_i^2} \frac{\vec{d}_i \cdot \vec{r}}{d_i r} \rho d\varphi d\rho \\
 &= \int_{\rho=0}^{R_a} \int_{\varphi=0}^{2\pi} \frac{E_{Sz}(\rho, \varphi, z_{Ai}) (r - \rho \cos(\varphi - \theta)) \rho d\varphi d\rho}{4\pi (r^2 + \rho^2 - 2r\rho \cos(\varphi - \theta) + (z - z_{Ai})^2)^{3/2}} \quad (2)
 \end{aligned}$$

where $z_{Ai} = (-1)^i (L_w/2 + D_{gw})$ and $i = 1, 2$, for the entrance and exit aperture (subscripts A1 and A2), respectively.

After completion of all the calculations, the field within the finite wires model depends on the spatial coordinates r , θ , and z , as well as on R_a , D_{gw} , and L_w . The parameters of the finite wires model D_{gw} and L_w are related to the rod length L_r and distance between apertures and rods, D_g , in the real device through the equation $L_w + 2D_{gw} = L_r + 2D_g$, i.e., the distance between the grounded planes in Fig. 3 is equal to the length of the real device's grounded cylinder. Consequently, $z_{i1} = (-1)^i (L_r + 2D_g) = 2z_{Ai}$, for $i = 1, 2$. In order to enable comparison, the results are sorted using the same set of parameters, namely, L_r and D_g , in this section for the finite wires model

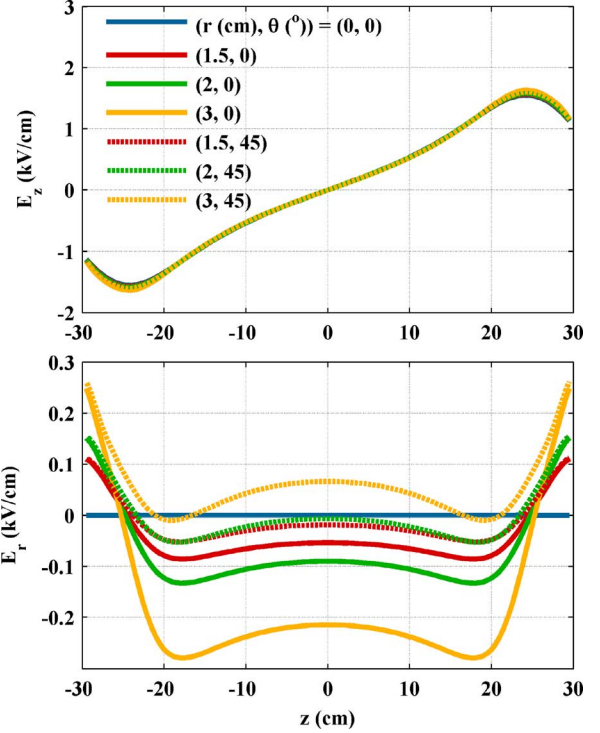


Fig. 4. Electric field of finite wires model. The aperture radius and gap size of the model are taken to be $R_a = 4.5$ cm and $D_g = 10$ cm. The axial and radial electric field components E_z and E_r are given along seven line segments. The line segments stretch between the two grounded planes, $z \in [-30 \text{ cm}, 30 \text{ cm}]$, they are parallel to the z -axis and are determined by their radial and azimuthal coordinates, (r_i, θ_i) , equal to $(0 \text{ cm}, 0^\circ)$, $(1.5 \text{ cm}, 0^\circ)$, $(1.5 \text{ cm}, 45^\circ)$, $(2 \text{ cm}, 0^\circ)$, $(2 \text{ cm}, 45^\circ)$, $(3 \text{ cm}, 0^\circ)$, and $(3 \text{ cm}, 45^\circ)$, for $i = 1, 2, 3, 4, 5, 6$, and 7 .

as well as in the following sections for data corresponding to the cylindrical rods model.

If the fields of the finite wires model and the cylindrical rods model, which will be described later, are to be comparable, special attention must be paid to adjusting the voltages in the two models. For all examples of the cylindrical rods model, the voltage of the electrodes is set to 20 kV. Consequently, the charge density in each sample finite wires model is calculated from the equations $V(R_a, 0, L_r/2 + D_g) = 0$ kV and $V(d_w/\sqrt{2} - R_r, 0, L_r/2) = 20$ kV, where $V(r, \theta, z)$ is electrostatic potential derived from the electric field of the finite wires model and $R_r = 4$ cm is radius of the electrodes in the cylindrical rods model.

Rather than being uniformly distributed, the charge is piling up at wire tips. Therefore, the shape of the fields around $z = 0$ cm predicted by the finite wires model is not expected to be accurate. Consequently, the influence of L_r on the approximated fields is not investigated; instead, it was taken that $L_r = 40$ cm, and $L_w = 48$ cm.

The dependence of the field on the spatial parameters r , θ , and z within the volume around the device's axis for sample values of aperture radius R_a and gap size D_g is illustrated in Fig. 4. The axial field component practically does not depend on the radial as well as on the azimuthal position. The limiting radial field components, which correspond to $\theta = 0^\circ$ and $\theta = 45^\circ$, form wider range at larger radii.

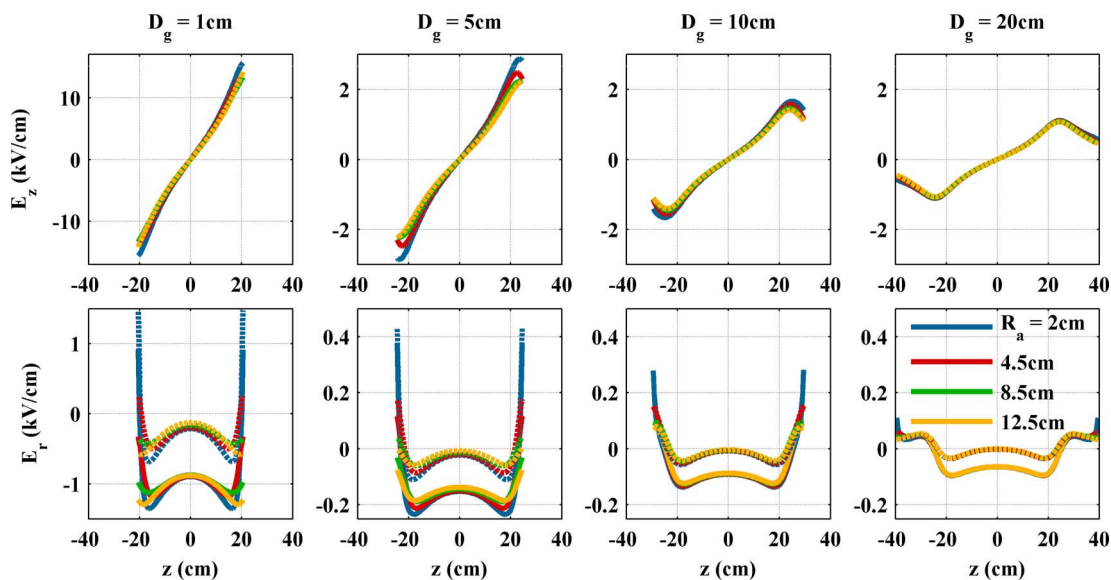


Fig. 5. Dependence of fields in finite wires model on R_a and D_g . The field components are given between the grounded planes along line segments parallel to the z -axis at $r = 1.5$ cm. The data corresponding to azimuthal line segment positions $\theta = 0^\circ$ and $\theta = 45^\circ$ are depicted with solid and dashed lines, respectively. The axial and radial components of the field E_z and E_r are given in the first and second row of graphs, respectively. Each column of graphs corresponds to the gap value, D_g , indicated in its title. In each graph, different line colors are dedicated to different values of R_a .

The dependence of the field components on the aperture radius as well as on the size of the gap between the rods and the grounded cylinder's bases is given in Fig. 5. The approximated field depends much more strongly on the gap size D_g than on the aperture radius R_a . Further, the field change is much steeper for smaller values of D_g . Although small, the influence of R_a is larger for smaller values of D_g and R_a . The graphs in the first column, for $D_g = 1$ cm, have larger scales compared to the scales of the corresponding graphs in the remaining three columns. Note that the value of D_{gw} corresponding to $D_g = 1$ cm is negative, i.e., $D_{gw} = -3$ cm; therefore, the finite wires and their images overlap and the resulting field is equal to the one corresponding to $L_w = 36$ cm and $D_g = 3$ cm.

Analysis of the finite wires model has shown that performance of the ECQ device can be modified by adjusting the geometry of its entrance and exit regions. However, due to unrealistic assumption of uniform charge distribution along wires, a better numerical model of the device must be used in order to prove the hypothesis as well as to obtain quantitative device performance predictions.

III. CYLINDRICAL RODS MODEL

In order to obtain highly accurate electric fields usable for device performance predictions, the geometry of the ECQ device is numerically modeled, and its fields are calculated with the commercially available software package WIPL-D [16]. The electromagnetic solver incorporated in this package models arbitrarily shaped structures with wires and plates as basic building blocks. Electrically large bilinear generalized quadrilaterals are used for modeling metallic plates, lossy or lossless dielectrics as well as magnetic surfaces. The surface integral equations are solved with the method of moments and surface sources as unknowns. For the ECQ device, the boundary conditions come down to the requirement that the

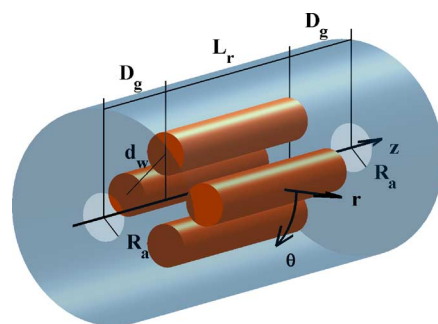


Fig. 6. Numerically modeled structure of ECQ device. Four cylindrical rods with base radius $R_r = 4$ cm replace the wires used in the finite wires model. The distance between axes of each two neighboring rods is equal to the distance between the wires in the finite wires model, $d_w = 12$ cm, i.e., the rods are positioned at $(r_{r1}, \theta_{r1}) = (6\sqrt{2} \text{ cm}, 0^\circ)$, $(r_{r2}, \theta_{r2}) = (6\sqrt{2} \text{ cm}, 90^\circ)$, $(r_{r3}, \theta_{r3}) = (6\sqrt{2} \text{ cm}, 180^\circ)$, and $(r_{r4}, \theta_{r4}) = (6\sqrt{2} \text{ cm}, 270^\circ)$. The rods are housed in a grounded cylinder with base radius of 20 cm. The values of aperture radius R_a , gap between rods and grounded cylinder base D_g , as well as rod length L_r , vary and are different for different examples of the model.

electric field components tangential to the metallic surfaces of the rods and of the grounded cylinder are equal to zero.

The device is modeled with four cylindrical rods used as electrodes and a surrounding grounded cylinder with entrance and exit apertures (Fig. 6). The electrostatic potential of the rods is taken to be 20 kV.

The dependences of axial E_z and radial E_r components of calculated field on spatial coordinates r , θ , and z in a sample cylindrical rods model are given in Fig. 7. These results can be compared with those corresponding to the finite wires model shown in Fig. 4, because the values of model parameters R_a , D_g , and L_r are taken to be the same in both cases. The qualitative behavior of the fields corresponding to the two models agrees well. As is the case for the finite wires model, for the cylindrical model, as well, the axial field component is practically dependent only on z , whereas the radial field component

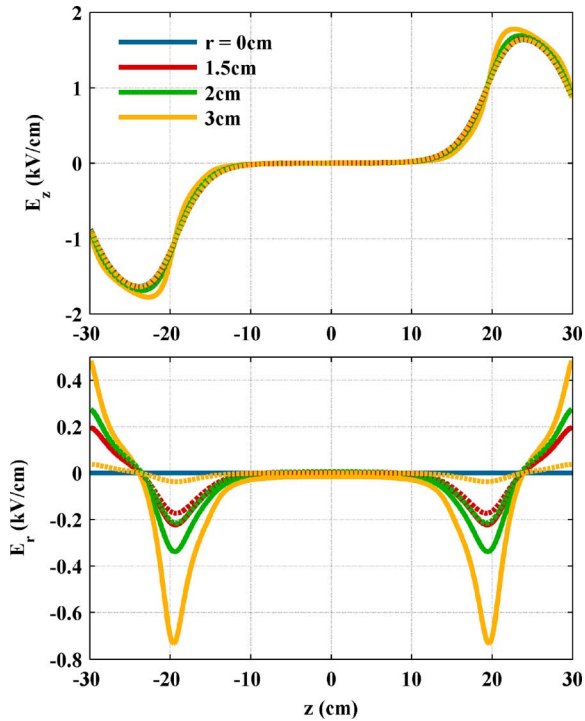


Fig. 7. Electric field of cylindrical rods model. The figure format is identical to the one of Fig. 4. The aperture radius, gap size, and rod length of the model are, as well, taken to be equal to those of finite wires model in Fig. 4, i.e., $R_a = 4.5$ cm, $D_g = 10$ cm, and $L_r = 40$ cm. Data given along line segments with different radial positions are depicted by different colors. The azimuthal line segments positions $\theta = 0^\circ$ and $\theta = 45^\circ$ are indicated by solid and dashed lines, respectively.

is more azimuthally dependent at larger radii. The shapes of the fields in the entrance and exit regions of the device are similar for both models. However, outside the entrance and exit regions, the discrepancy between the fields corresponding to the two models is large. This is a consequence of the assumption taken in the finite wires model that charge is uniformly distributed along the wires. Inside the cylindrical rods model, away from the rods ends, the field is negligible; therefore, it seems that the field does not depend on the rods length.

The dependence of fields in the cylindrical rods model on R_a and D_g is illustrated in Figs. 8 and 9 for $L_r = 40$ cm and $L_r = 20$ cm, respectively. From both of these figures, the conclusions regarding the influences of the parameters R_a and D_g on the field are similar to the ones drawn for the finite wires model from Fig. 5. Namely, the dependence of field components on the gap size D_g is stronger than on the aperture radius R_a . The data in Figs. 5 and 8 cannot be quantitatively compared despite the equality of all three device parameters in the corresponding graphs because of different radial positions of line segments used, i.e., $r = 1.5$ cm for the finite wires model, whereas for the cylindrical rods model, $r = 2$ cm. For the finite wires model the line segments with radial position $r = 1.5$ cm are chosen in order to stay clear from the apertures for all model examples with $R_a = 2$ cm. The finite wires model is an approximate model and, as such, it does not describe reality well around edges. Examples of the cylindrical rods model are designed in WIPL-D; therefore, field calculations around edges

are performed with high accuracy. However, unlike the finite wires model where the model parameters R_a , D_g , and L_r are easily changed by adjusting the appropriate values in an input file, changing the model parameters values, as well as field calculation, for the cylindrical rods model is more time consuming. To speed up the process, the fields in the cylindrical rods models are calculated only along the selected line segments, rather than in the entire model volume. The line segments with larger value of r are chosen because obtained data are intended to be used primarily for device performance prediction, and focusing properties are more pronounced at larger r . The anomalies that occur close to the apertures in the example models with $R_a = 2$ cm and that are the most noticeable in E_z curves corresponding to $D_g = 5$ cm and $D_g = 10$ cm models in both Figs. 8 and 9 reflect the edge position $r = R_a = 2$ cm.

A comparison of the results shown in Figs. 8 and 9 reveals that the rod length does not influence the shape of the fields in the important entrance and exit regions. Closer inspection shows that the graphs in Fig. 8, which correspond to $L_r = 40$ cm, can be obtained by cutting the corresponding graphs in Fig. 9, which correspond to $L_r = 20$ cm, at $z = 0$ cm and inserting straight lines equal to zero from $z = -10$ cm to $z = 10$ cm. Although L_r cannot directly influence ECQ device performance, it may serve to adjust synchronization between an ion beam and a quasi-static RF voltage. However, it should be noted that the zero field region in the models with $L_r = 20$ cm is very short. Therefore, this value of L_r is very close to the lower limit after which the entrance and exit regions of the device overlap and are likely to no longer have entrance and exit region fields equal to those corresponding to larger values of L_r .

The electric fields obtained for a number of sample cylindrical rods models illustrated in Figs. 8 and 9 confirm the conclusion drawn from the study performed with the finite wires model. Namely, the model parameters D_g and, to much lesser extent R_a , can influence the electric field of an ECQ device and, consequently, its performance. Further, electric field shape is more sensitive on D_g as well as R_a for smaller values of D_g . Influence of R_a increases with its decrease, as well.

To justify the approach of analyzing electric fields along the chosen line segments as well as to illustrate similarities with the einzel lens and the drift tube accelerator, axial and radial electric fields of an ECQ device are given in four transverse planes in Fig. 10. The shown results confirm that the device acts upon an ion beam primarily around the rod tips as well as inside the gaps between the grounded cylinder and the rod tips. Note that the ratio between the rod radius R_r and the rod aperture radius, $R_{ra} = d_w/\sqrt{2} - R_r$, is equal to 8/9 for all the considered examples. For larger values of this ratio, the fields along the $\theta = 45^\circ$ line will be less different from the ones along the $\theta = 0^\circ$ direction, and, consequently, the corresponding dashed curves will be closer to the solid curves in Figs. 7–9. Fig. 10 also verifies that focusing capabilities of the ECQ device depend more on R_{ra} than on R_r , as well as that the radial and azimuthal dependence of accelerating abilities of the device are negligible compared to their axial dependence. Therefore, in order to apply the obtained results to other devices, for small D_g and focusing estimates, the rod aperture radius R_{ra} should be used as the

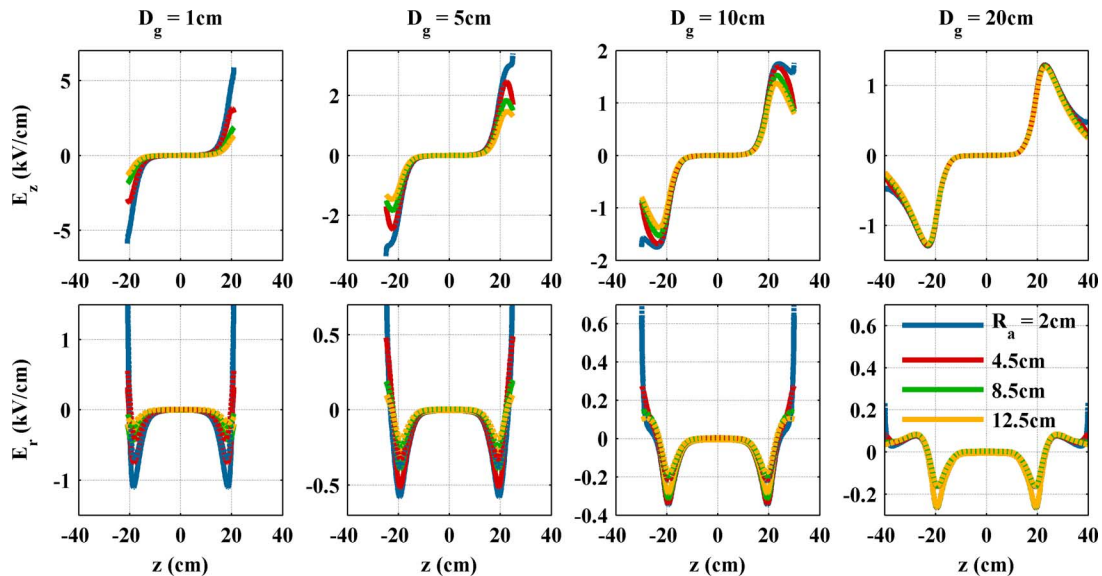


Fig. 8. Dependence of fields in cylindrical rods model on R_a and D_g for $L_r = 40$ cm. The format of the figure is equal to the one of Fig. 5. Here, the rod length is taken to be $L_r = 40$ cm, as well; however, the line segments along which the field components are given are parallel to the z -axis at $r = 2$ cm. The data corresponding to the azimuthal line segment positions $\theta = 0^\circ$ and $\theta = 45^\circ$ are depicted with solid and dashed lines, respectively.

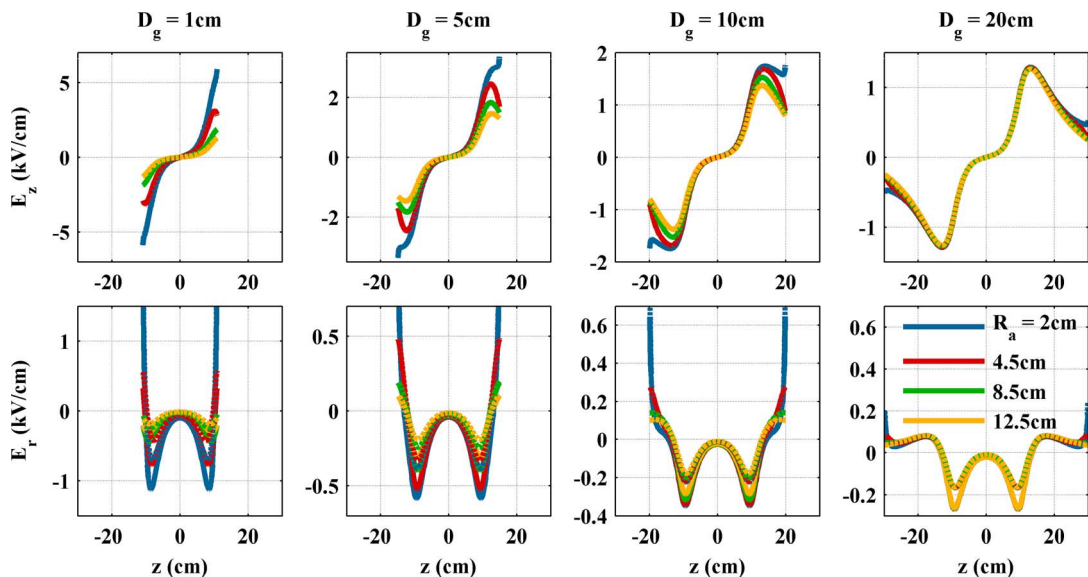


Fig. 9. Dependence of fields in cylindrical rods model on R_a and D_g for $L_r = 20$ cm. The format of the figure is equal to the one of Fig. 8. The results shown in Figs. 8 and 9 correspond to two examples of the cylindrical rods model which differ only in the value of L_r .

scaling factor, whereas, for large D_g and acceleration estimates, d_w is a better choice for the scaling factor.

As mentioned earlier, axial E_z and radial E_r electric fields can be used as indicators of accelerating and focusing capabilities of a device. Due to the high computational accuracy of WIPL-D used to calculate the fields in a number of sample cylindrical rod models, these fields can be further used to quantitatively estimate ECQ device performance for different values of model parameters D_g and R_a .

IV. DEVICE PERFORMANCE

Accurate performance of a device is usually obtained with ion beam dynamics simulations. However, interaction between

a device and an ion beam depends not only on the device parameters but on the ion beam parameters as well, e.g., ion energy, charge, and mass. If the device performance is to be evaluated independently, the forces acting on a beam within the fully extended beam path volume must be evaluated. Focusing/defocusing as well as accelerating/decelerating effects accumulate along the path of a test ion through a device. Consequently, integrals of radial and axial components of electric field could be used to evaluate device performance.

Instead of integration over the complete, fully extended beam path volume, we integrate over the line segments corresponding to the limiting fields. For the ECQ device, limiting electric fields occur in the $\theta = 0^\circ$ and $\theta = 45^\circ$ planes due to the fourfold symmetry of the device. Therefore, we establish parameters f_A

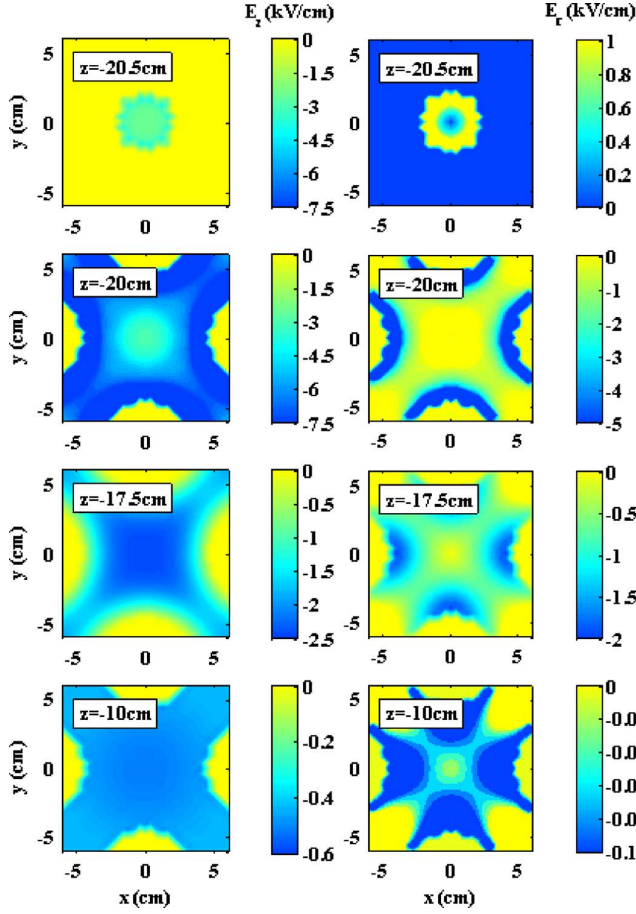


Fig. 10. Axial and radial electric fields in sample transverse planes. The parameters of the cylindrical rods model are $D_g = 0.5$ cm, $R_a = 2$ cm, and $L_r = 40$ cm. Consequently, the transverse planes chosen for the field sampling, $z = -20.5$ cm, -20 cm, -17.5 cm, and -10 cm, correspond to the axial positions of the grounded cylinder entrance aperture, electrode tips, maximal focusing plane, and quarter-length of the device, respectively. The fields at $z = -10$ cm are an order of magnitude smaller than those within the entrance region of the device, i.e., at the remaining three axial positions.

and f_F as measures of ECQ device accelerating and focusing capabilities:

$$\begin{aligned}
 f_A(D_g, R_a, r, \theta) &= \int_{z=-L_r/2-D_g}^{z=0} E_z(z) dz = (-1) \\
 &\quad \cdot \int_{z=0}^{z=L_r/2+D_g} E_z(z) dz \\
 f_F(D_g, R_a, r, \theta) &= \int_{z=-L_r/2-D_g}^{z=0} E_r(z) dz \\
 &= \int_{z=0}^{z=L_r/2+D_g} E_r(z) dz \quad (3)
 \end{aligned}$$

where r and θ are coordinates of the line segment along which the integrals are computed. Because of their units, we refer to f_A and f_F as accelerating and focusing potential, respectively. These parameters are used to quantitatively express performance of the ECQ device in Fig. 11. To achieve smoother dependencies on D_g , a number of sample models in addition to those represented by corresponding data in Figs. 8 and 9 are created.

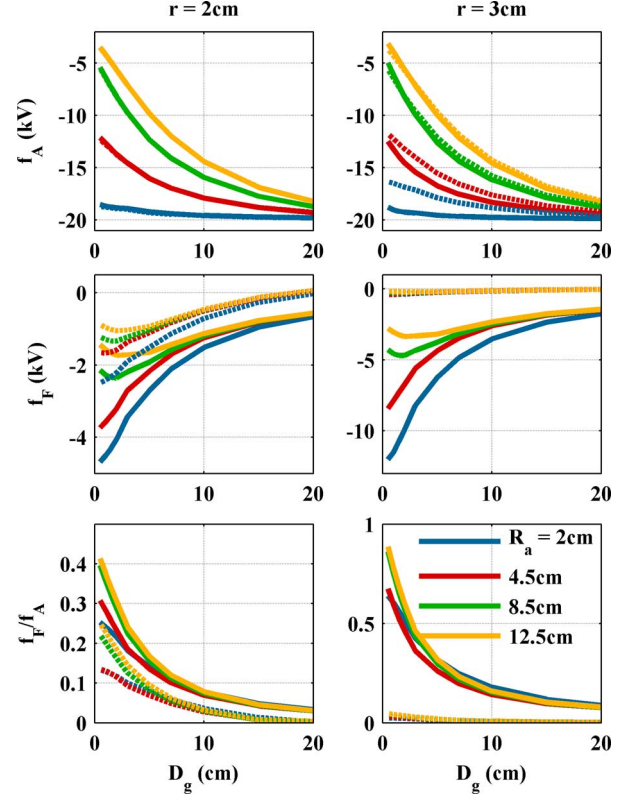


Fig. 11. ECQ device performance. The dependence of the ECQ device's accelerating f_A and focusing f_F potentials, as well as of their ratio f_F/f_A , on the gap size, D_g and aperture radius R_a is shown. The accelerating and focusing potentials are calculated using (3). The data corresponding to the two values of line segment radius, $r = 2$ cm and 3 cm are given in the first and second column of graphs, respectively. The limiting values occurring in the $\theta = 0^\circ$ plane are given as solid lines, whereas those in the $\theta = 45^\circ$ plane are depicted as dashed lines. Different values of R_a are marked with different line colors. The results are obtained for sample models with $L_r = 20$ cm; however, the figure is identical for $L_r = 40$ cm, as can be seen from Fig. 12.

Even though the performance parameters shown in Fig. 11 are calculated for sample models with $L_r = 20$ cm, the results are practically equal to those for $L_r = 40$ cm, as can be seen from Fig. 12. This confirms the conclusion drawn earlier that the ECQ device acts upon a beam in the vicinity of device's entrance and exit, whereas the region in between is the drift space. Note that this independence of Fig. 11 on L_r is valid for $L_r \geq 20$ cm, because entrance and exit region fields overlap around $z = 0$ for lower values of L_r .

The accelerating potential does not depend significantly on r or on θ . Since f_A changes its sign at $z = 0$ cm, a beam is decelerated in the entrance region and accelerated in the exit region. The focusing potential is negative along both $\theta = 0^\circ$ and 45° line segments for $r = 2$ cm. For $r = 3$ cm and $\theta = 0^\circ$, the absolute value of the focusing potential is larger than for $r = 2$ cm. Consequently, for $\theta = 0^\circ$, focusing is stronger for larger distances from the devices axis, as it should be for a focusing device. For $r = 3$ cm and $\theta = 45^\circ$, the focusing potential is approximately equal to zero, i.e., a beam is neither being focused nor defocused. Excellent focusing properties are somewhat shaded by the fact that the ratio f_F/f_A is smaller than 1, which means that more power is spent on acceleration/deceleration than on focusing. On the other hand, this indicates

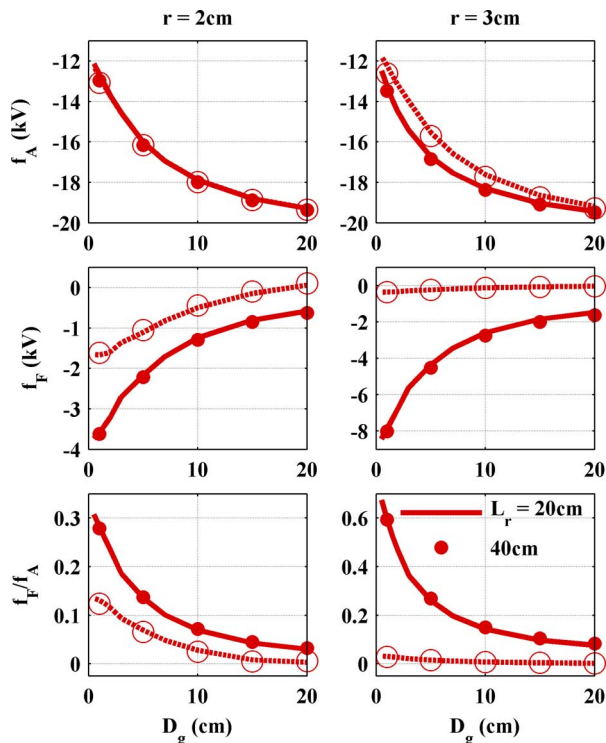


Fig. 12. Dependence of focusing and accelerating potentials on L_r . The figure format is identical to the one of Fig. 11. The solid line and filled symbols represent data in the $\theta = 0^\circ$ plane, whereas dashed line and open symbols correspond to the $\theta = 45^\circ$ plane. For clarity, only data corresponding to $R_a = 4.5$ cm is shown; the agreement between the results corresponding to the two different values of L_r is excellent for other values of R_a , as well.

that the device could work more efficiently as an accelerator if its voltage is reversed for $z < 0$. These conclusions prove that the initial estimates arisen from Fig. 1 are correct.

If the device is to serve as an accelerator, E_z must change its sign for $z < 0$. This can be achieved either by applying RF voltage, as illustrated in [6], or by altering the device's geometry, as shown in Fig. 13. In the former case, the field is quasi-static; therefore, at any given moment, E_z still has different signs for $z < 0$ and for $z > 0$. The test ion ideally synchronized with the applied RF field only perceives E_z as positive throughout the device. Regardless of whether the change of E_z 's sign for $z < 0$ is real or fictitious, it is accompanied by the E_r 's change of sign in the same region. As a result, an ion beam will be defocused in the entrance region and focused in the exit region of the device. Due to a favorable value of f_F/f_A , more energy is spent on acceleration than on defocusing.

The dependencies in Fig. 11 can be used to adjust the device parameters to achieve desired performance. If the device is to be used as an ECQ lens, D_g should be chosen to be as small as possible. The value for R_a is a tradeoff between stronger focusing achieved with smaller values of R_a and larger f_F/f_A obtained with larger R_a .

In the ECQ accelerator, D_g should be as large as possible, although gain in performance decays with the increase in D_g . Smaller values of R_a provide somewhat stronger acceleration, whereas for larger R_a , defocusing in the entrance region is slightly weaker. If entering defocusing is to be overcome by

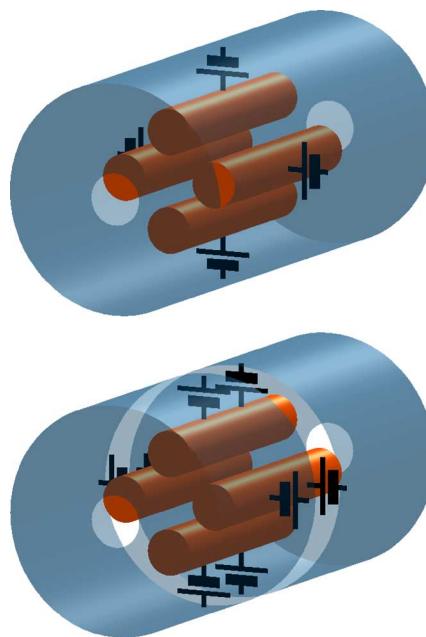


Fig. 13. Geometries of ECQ device. The upper figure gives the geometry of the ECQ lens and RF ECQ accelerator. Four dc power supplies correspond to the ECQ lens. For the RF ECQ accelerator, these are replaced with four ac power supplies. The lower figure depicts the dc ECQ accelerator. The missing stripe in the grounded cylinder and four additional properly connected dc power supplies enable the desired change of axial field orientation in the entrance region.

exit focusing, medium values of D_g as well as R_a should be chosen.

Note that R_r/R_{ra} is equal to 8/9 for all the considered examples, which is smaller than the typical value of 8/7. Larger values of this ratio will cause dashed curves in Figs. 11 and 12 to be closer to those depicted by solid lines. The strongest interaction between the ECQ device and a beam occurs in the vicinity and within the gaps between the rod tips and the bases of the surrounding cylinder. Consequently, R_{ra} and d_w should be considered as scaling parameters when using data in Figs. 11 and 12 for performance estimates of other devices with a similar structure. For acceleration estimates and large D_g , a good choice is d_w , whereas R_{ra} is more suitable for focusing estimates and small D_g .

V. CONCLUSION

The ECQ device acts upon an ion beam within its entrance and exit regions, i.e., in the regions between the apertures and electrodes. If the electrode length is above the limiting value, the acting entrance and exit regions are separated by the drift space spreading out on both sides of the middle of device length. Therefore, the device parameters influencing its performance are the aperture radius and the aperture-electrode gap size. If it is above the lower limit, the electrode length does not influence device performance; however, it plays a role in synchronization with a beam if device operates in RF mode. The parameter whose value should be chosen with most care is the gap size. The aperture radius is used for fine adjustments of the device performance. If the device is to serve as a lens, the gap size should be small, whereas efficient acceleration is achieved

with large gap sizes. The roles of the entrance and exit regions may be adjusted to be different by choosing different values of the corresponding gap sizes and aperture radii. For example, the combination of large entrance and small exit gap size provides neutralization of entrance defocusing, although less efficient acceleration. In the ECQ device, the percentage of driving power used for focusing is always smaller than the one spent on deceleration/acceleration. Nevertheless, the ECQ lens may be appealing for weak focusing because its focusing potential along a fixed radial position oscillates between the strongest focusing at the azimuthal positions of electrodes and either weaker focusing or no action at the azimuths corresponding to the midline between electrodes.

REFERENCES

- [1] L. Xiu, L. Dong, S. Ohnuma, and C. D. Meitzler, "A new design of helical electrostatic quadrupole and its quasi-octupole mode of operation," in *Proc. 3rd Eur. Particle Accelerator Conf.*, Berlin, Germany, Mar. 24–28, 1992, pp. 1533–1535.
- [2] L. Xiu, S. Ohnuma, K. Wang, C. D. Meitzler, and Y. Xu, "Test of the transport properties of a helical electrostatic quadrupole and quasi-octupole," in *Proc. 15th Particle Accelerator Conf.*, Washington, DC, USA, May 17–20, 1993, pp. 3148–3150.
- [3] N. Nešković, I. Telečki, B. Bojović, and S. Petrović, "A square electrostatic rainbow lens: Catastrophic ion beam focusing," *Nucl. Instrum. Methods A*, vol. 635, no. 1, pp. 1–7, Apr. 2011.
- [4] I. Telečki, S. Petrović, P. Beličev, B. Radenović, R. Balvanović, B. Bojović, and N. Nešković, "Focusing properties of a square electrostatic rainbow lens," *Nucl. Instrum. Methods A*, vol. 694, pp. 224–233, 2012.
- [5] J. L. Ristić-Djurović and A. Ž. Ilić, "Role and significance of uniform distribution in a study of ensemble of particles," *IEEE Trans. Nucl. Sci.*, vol. 60, no. 1, pp. 236–245, Feb. 2013.
- [6] J. L. Ristić-Djurović, S. Čirković, and A. Ž. Ilić, "Ion beam acceleration with radio frequency powered rainbow lens," *IEEE Trans. Nucl. Sci.*, vol. 60, no. 2, pt. 2, pp. 1272–1279, 2013.
- [7] D. A. Swenson, "Status of the RFD linac structure development," in *Proc. 20th Int. LINAC Conf.*, Monterey, CA, USA, Aug. 21–25, 2000, pp. 935–937.
- [8] C. P. Welsch, M. Grieser, J. Ullrich, A. Wolf, and C. Gläbner, "An electrostatic quadrupole doublet with an integrated steerer," in *Proc. 9th Eur. Particle Accelerator Conf.*, Lucerne, Switzerland, Jul. 5–9, 2004, pp. 1234–1236.
- [9] F. M. Bieniosek, C. M. Celata, E. Henestroza, J. W. Kwan, L. Prost, P. A. Seidl, A. Friedman, D. P. Grote, S. M. Lund, and I. Haber, "2-MV electrostatic quadrupole injector for heavy-ion fusion," in *Phys. Rev. Special Topics—Accel. Beams*, Jan. 2005, vol. 8, p. 010101.
- [10] C. P. Welsch, M. Grieser, J. Ullrich, and A. Wolf, "An ultra-low-energy storage ring at FLAIR," *Nucl. Instrum. Methods A*, vol. 546, pp. 405–417, 2005.
- [11] A. J. Kreiner, J. W. Kwan, A. A. Burlón, H. Di Paolo, E. Henestroza, D. M. Minsky, A. A. Vlada, M. E. Debray, and H. Somacal, "A tandem electrostatic-quadrupole for accelerator-based BNCT," *Nucl. Instrum. Methods B*, vol. 261, pp. 751–754, 2007.
- [12] A. J. Kreiner, H. Di Paolo, A. A. Burlon, J. M. Kesque, A. A. Valda, M. E. Debray, Y. Giboudot, P. Levinas, M. Fraiman, V. Romeo, H. R. Somacal, and D. M. Minsky, "Accelerator-based boron neutron capture therapy and the development of a dedicated tandem-electrostatic-quadrupole," in *Proc. 7th Latin Amer. Symp. Nucl. Phys. Appl.*, Cusco, Peru, Jun. 11–16, 2007, pp. 17–24.
- [13] G. A. Westenskow, D. Grote, F. Bieniosek, and J. W. Kwan, "A multi-beamlet injector for heavy ion fusion reactor: Experiments and modeling," in *Proc. 22nd Particle Accelerator Conf.*, Albuquerque, NM, USA, Jun. 25–29, 2007, pp. 3777–3781.
- [14] D. A. Swenson, "CW proton LINAC for the BNCT application," in *Proc. 24th Linear Accelerator Conf.*, Victoria, BC, Canada, Sep.–Oct. 29–3, 2008, pp. 220–222.
- [15] M. J. King, G. T. Miller, J. Reijonen, Q. Ji, N. Andresen, F. Gicquel, T. Kalvas, K.-N. Leung, and J. W. Kwan, "Initial evaluation of a pulsed white spectrum neutron generator for explosive detection," *IEEE Trans. Nucl. Sci.*, vol. 56, no. 3, pt. 2, pp. 1283–1287, 2009.
- [16] "WIPL-D Microwave," Software and User's Manual. Belgrade, Serbia, WIPL-D d.o.o, 2005.

IEEE TRANSACTIONS ON NUCLEAR SCIENCE

A PUBLICATION OF THE IEEE NUCLEAR AND PLASMA SCIENCES SOCIETY



APRIL 2013

VOLUME 60

NUMBER 2

IETNAE

(ISSN 0018-9499)

PART II OF TWO PARTS

17TH REAL TIME CONFERENCE (RT2010) LISBON, PORTUGAL, MAY 24–28, 2010

Design of the Front-End Readout Electronics for ATLAS Tile Calorimeter at the sLHC	1255
..... <i>F. Tang, K. Anderson, G. Drake, J.-F. Genat, M. Oreglia, J. Pilcher, and L. Price</i>	
CMS Silicon Strip Tracker Monitoring	1260
..... <i>S. Mersi</i>	
Pixel Advisor: An Expert System for the ATLAS Pixel Detector Control System	1265
..... <i>T. Henss, D. Huning, S. Kersten, P. Maettig, M. Mechtel, and N. Wulff</i>	

REGULAR PAPERS

ACCELERATOR TECHNOLOGY

Ion Beam Acceleration With Radio Frequency Powered Rainbow Lens	1272
..... <i>J. L. Ristić-Djurović, S. Ćirković, and A. Z. Ilić</i>	
ISHN Ion Source Control System. First Steps Toward an EPICS Based ESS-Bilbao Accelerator Control System	1280
..... <i>M. Eguiraun, J. Jugo, I. Arredondo, M. del Campo, J. Feuchtwanger, V. Etxebarria, and F. J. Bermejo</i>	

ANALOG AND DIGITAL CIRCUITS

Super-Altro 16: A Front-End System on Chip for DSP Based Readout of Gaseous Detectors	1289
..... <i>P. Aspell, M. De Gaspari, H. França, E.G. García, and L. Musa</i>	
Analog Circuit for Timing Measurements With Large Area SiPMs Coupled to LYSO Crystals	1296
..... <i>A. Gola, C. Piemonte, and A. Tarolli</i>	
Radiation-Tolerant Code-Density Calibration of Nyquist-Rate Analog-to-Digital Converters	1303
..... <i>C. R. Grace, P. Denes, D. Gnani, H. von der Lippe, and J.-P. Walder</i>	

(Contents Continued on Page 1253)



ASTROPHYSICS AND SPACE INSTRUMENTATION

- Ultra-Thin Silicon Nitride X-Ray Windows *P. T. Törmä, H. J. Sipilä, M. Mattila, P. Kostamo, J. Kostamo, E. Kostamo, H. Lipsanen, N. Nelms, B. Shortt, M. Bavdaz, and C. Laubis* 1311
-

COMPUTING, SIMULATION, ALGORITHMS, AND SOFTWARE

- Iterative Estimation of Location and Trajectory of Radioactive Sources With a Networked System of Detectors *B. Deb* 1315
-

GAS DETECTORS

- SPRINTER: A New Detector System for the INTER Neutron Reflectometer *D. M. Duxbury, N. J. Rhodes, E. M. Schooneveld, E. J. Spill, and J. R. P. Webster* 1327
-

NUCLEAR POWER INSTRUMENTATION AND CONTROL

- Nonlinear Adaptive Power-Level Control for Modular High Temperature Gas-Cooled Reactors *Z. Dong* 1332
An Innovative Acoustic Sensor for In-Pile Fission Gas Composition Measurements *E. Rosenkrantz, J. Y. Ferrandis, F. Augereau, T. Lambert, D. Fourmentel, and X. Tiratay* 1346
-

RADIATION EFFECTS

- Total Dose Irradiation-Induced Degradation of Hysteresis Effect in Partially Depleted Silicon-on-Insulator NMOSFETs *H. Huang, D. Bi, B. Ning, Y. Zhang, Z. Zhang, and S. Zou* 1354
Circuit and Measurement Technique for Radiation Induced Drift in Precision Capacitance Matching *S. Prasad and K. G. Shankar* 1361
Stimulation of Radiation Damage Recovery of Lead Tungstate Scintillation Crystals Operating in a High Dose-Rate Radiation Environment *A. E. Borisevitch, V. I. Dormenev, A. A. Fedorov, M. V. Korjik, T. Kuske, V. Mechinsky, O. V. Mishevitch, R. W. Novotny, R. Rusack, and A. V. Singovski* 1368
Total-Dose Radiation Response of HfLaO Films Prepared by Plasma Enhanced Atomic Layer Deposition *D. Cao, X. Cheng, T. Jia, L. Zheng, D. Xu, Z. Wang, C. Xia, Y. Yu, and D. Shen* 1373
Displacement Damage in TiO₂ Memristor Devices *E. DeIonno, M.D. Looper, J. V. Osborn, and J.W. Palko* 1379
Memory Reliability Analysis for Multiple Block Effect of Soft Errors *S. Lee, S. H. Jeon, S. Baeg, and D. Lee* 1384
-

RADIATION IMAGING

- 3D Millimeter Event Localization in Bulk Scintillator Crystals *K. P. Ziock, M. A. Blackston, and T. Van Vuure* 1390
-

RADIATION INSTRUMENTATION

- Design and Implementation of a Mobile Radiological Emergency Unit Integrated in a Radiation Monitoring Network .. *A. Baeza, J. A. Corbacho, and J. Miranda* 1400
-

SCINTILLATION DETECTORS

- High Resolution Gamma Ray Spectroscopy at MHz Counting Rates With LaBr₃ Scintillators for Fusion Plasma Applications *M. Nocente, M. Tardocchi, A. Olariu, S. Olariu, R. C. Pereira, I. N. Chugunov, A. Fernandes, D. B. Gin, G. Grosso, V. G. Kiptily, A. Neto, A. E. Shevelev, M. Silva, J. Sousa, and G. Gorini* 1408
Comparison of Lithium Gadolinium Borate Crystal Grains in Scintillating and Nonscintillating Plastic Matrices *K. Kazkaz, N. S. Bowden, and M. Pedretti* 1416
Improving of LSO(Ce) Scintillator Properties by Co-Doping *N. G. Starzhinskiy, O. T. Sidletskiy, G. Tamulaitis, K. A. Katrunov, I. M. Zenya, Y. V. Malyukin, O. V. Viagin, A. A. Masalov, and I. A. Rybalko* 1427
-

SOLID STATE DETECTORS

Electrical Characteristics and Fast Neutron Response of Semi-Insulating Bulk Silicon Carbide	1432
..... <i>P. A. Bryant, A. Lohstroh, and P. J. Sellin</i>	
X- γ Ray Spectroscopy With Semi-Insulating 4H-Silicon Carbide	1436
..... <i>G. Bertuccio, D. Puglisi, A. Pullia, and C. Lanzieri</i>	
Effect of Temperature Variation on the Energy Response of a Photon Counting Silicon CT Detector	1442
..... <i>H. Bornefalk, M. Persson, C. Xu, S. Karlsson, C. Svensson, and M. Danielsson</i>	
High-Purity CdMnTe Radiation Detectors: A High-Resolution Spectroscopic Evaluation	1450
..... <i>R. Rafiei, M. I. Reinhard, K. Kim, D. A. Prokopovich, D. Boardman, A. Sarbutt, G. C. Watt, A. E. Bolotnikov, L. J. Bignell, and R. B. James</i>	
DEPFET Active Pixel Detectors for a Future Linear e^+e^- Collider	1457
..... <i>O. Alonso, R. Casanova, A. Dieguez, J. Dingfelder, T. Hemperek, T. Kishishita, T. Kleinohl, M. Koch, H. Krüger, M. Lemarenko, F. Lütticke, C. Marinas, M. Schnell, N. Wermes, A. Campbell, T. Ferber, C. Kleinwort, C. Niebuhr, Y. Soloviev, M. Steder, R. Volkenborn, S. Yaschenko, P. Fischer, C. Kreidl, I. Peric, J. Knopf, M. Ritzert, E. Curras, A. Lopez-Virto, D. Moya, I. Vila, M. Boronat, D. Esperante, J. Fuster, I. G. Garcia, C. Lacasta, A. Oyanguren, P. Ruiz, G. Timon, M. Vos, T. Gessler, W. Kühn, S. Lange, D. Münchow, B. Spruck, A. Frey, C. Geisler, B. Schwenker, F. Wilk, T. Barvich, M. Heck, S. Heindl, O. Lutz, T. Müller, C. Pulvermacher, H. J. Simonis, T. Weiler, T. Krausser, O. Lipsky, S. Rummel, J. Schieck, T. Schlüter, K. Ackermann, L. Andricek, V. Chekelian, V. Chobanova, J. Dalseno, C. Kiesling, C. Koffmane, L. L. Gioi, A. Moll, H. G. Moser, F. Müller, E. Nedelkovska, J. Ninkovic, S. Petrovics, K. Prothmann, R. Richter, A. Ritter, M. Ritter, F. Simon, P. Vanhoefer, A. Wassatsch, Z. Dolezal, Z. Drasal, P. Kodys, P. Kvasnicka, and J. Scheirich</i>	

Ion Beam Acceleration With Radio Frequency Powered Rainbow Lens

Jasna L. Ristić-Djurović, Saša Ćirković, and Andjelija Ž. Ilić, *Member, IEEE*

Abstract—The electrostatic quadrupole lens, quadrupole accelerator and square rainbow lens as well as radio frequency quadrupole accelerator all have similar structure with four rod-like electrodes. Unlike the last one, which is powered by the alternating voltage, the first three are electrostatic devices. Each two adjacent electrodes of a common electrostatic lens have equal magnitude and opposite signs of their electric potentials, whereas, electric potentials of rainbow lens's electrodes are all equal in magnitude as well as in sign. If powered by the appropriate radio frequency instead of a DC voltage, the rainbow lens transforms into an ion beam accelerator which could cost-effectively broaden the available energy range of low energy ion beam facilities.

Index Terms—Electrostatic quadrupoles, ion beam dynamics, linear accelerators.

I. INTRODUCTION

THE electrostatic quadrupole accelerator has been introduced in [1]–[3]. More recently electrostatic accelerating gaps and focusing electrostatic quadrupole lenses are combined, for example, in [4], [5]. Another electrostatic device similar to the electrostatic quadrupole lens, the electrostatic square rainbow lens is shown to have focusing properties as well [6], [7]. Unlike the electrostatic quadrupole lens whose four electrodes are powered by static electric voltages equal in intensity but alternating in sign with respect to the azimuthal position of the electrodes [8]–[10], the electrode voltages of electrostatic rainbow lens are all equal in sign. Contrary to these electrostatic devices, four electrodes in a radio frequency quadrupole accelerator are powered by radio frequency (RF) voltage, see, for example, [11]–[13] and references therein. The RF voltage, four rods and focusing quadrupole field resulting from independent operation at different electric potential of two pieces each supporting two electrodes are combined in the RF-Focused Interdigital (RFI) and RF-Focused Drift tube (RFD) linac structures [14], [15]. With the aim to broaden the application scope of the low energy FAMA facility [16], in what follows we show that a rainbow lens can be transformed into an accelerator by relatively small, low cost changes.

The accelerating axial electric field created by slanting the electrodes of electrostatic rainbow lens with respect to its axis

Manuscript received October 25, 2012; revised November 24, 2012; accepted November 25, 2012. Date of publication February 11, 2013; date of current version April 10, 2013. This work was supported in part by the Ministry of Education and Science of Serbia through the project “Physics and Chemistry with Ion Beams,” no. III45006.

The authors are with the Vinča Institute of Nuclear Sciences, Laboratory of Physics (010), University of Belgrade, 11001 Belgrade, Serbia (e-mail: jasna@stanfordalumni.org; kosjera@vinca.rs; andjelijailic@ieee.org).

Color versions of one or more of the figures in this paper are available online at <http://ieeexplore.ieee.org>.

Digital Object Identifier 10.1109/TNS.2012.2230452

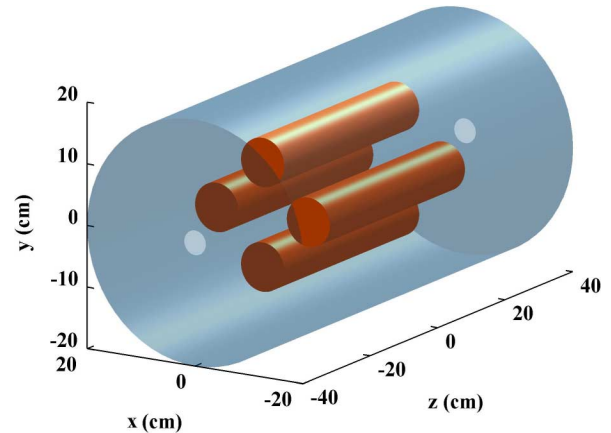


Fig. 1. Electric quadrupole accelerator. Four $L_r = 40$ cm long cylindrical rods with base radius $R_r = 4$ cm are positioned between $z = -20$ cm and $z = 20$ cm at $(x_{r1}, y_{r1}) = (6\sqrt{2}$ cm, 0 cm), $(x_{r2}, y_{r2}) = (0$ cm, $6\sqrt{2}$ cm), $(x_{r3}, y_{r3}) = (-6\sqrt{2}$ cm, 0 cm), and $(x_{r4}, y_{r4}) = (0$ cm, $-6\sqrt{2}$ cm). The rods are housed in a grounded cylinder with base radius, $R_g = 20$ cm, aperture radius, $R_a = 2$ cm, and length, $L_g = 80$ cm.

[17] turned out to be insufficiently effective [18]. Consequently, for noticeable acceleration the acceleration method had to be changed. Namely, if its DC voltage source is replaced with the medium to high RF power supply, the rainbow lens becomes a quasi electrostatic instead of an electrostatic device and can efficiently accelerate ion beams.

If the four rods housed in a grounded cylinder are all powered by the same properly adjusted RF voltage an ion beam would be accelerated through the entrance as well as exit accelerating gap between the rods and the base of grounded cylinder, see Fig. 1. To validate the principle as well as to illustrate its efficiency, interaction between a test proton beam and the described device is used. In the first approximation the electric field of the device is replaced by the analytical electric field of uniformly charged finite wires. Once the principle is proven to work it is further tested with the realistic electromagnetic field obtained by modeling the device with the commercially available software package WIPL-D [19]. Test ion trajectories within the proton beam are simulated using the self-made software package VINDY [20].

II. ANALYTICAL ESTIMATE

In order to test the idea an analytical model of the device is composed. Four parallel, equally charged finite wires are positioned along the edges of imaginary quadratic prism which coincide with the axes of the rods shown in Fig. 1. The distance between two adjacent wires, $d_w = 12$ cm, is equal to the distance between the axes of neighboring rods; however, in order

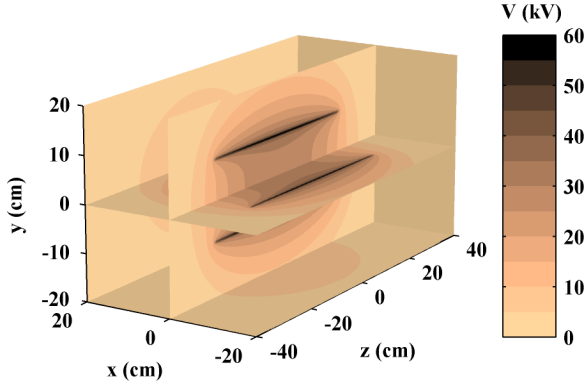


Fig. 2. Electric potential of four uniformly charged finite wires. The wires are each charged with the uniform charge density $Q' = 0.36 \mu\text{C}/\text{m}$. The resulting potential of the electrostatic field is shown in the $x = 0$, $y = 0$, $z = 40$ cm, $x = 20$ cm, and $y = -20$ cm planes.

to better match the electric potential of the rods, the length of the wires is extended to $L_w = 48$ cm compared to the length of the rods, $L = 40$ cm. Electric field is calculated using analytical formulas for uniformly charged finite wires

$$\begin{aligned} E_x(x, y, z) &= \frac{Q'}{4\pi\epsilon_0} \sum_{i=1}^4 \left(\frac{(x - x_{wi})}{r_{2i}(p_2 + r_{2i})} - \frac{(x - x_{wi})}{r_{1i}(p_1 + r_{1i})} \right) \\ E_y(x, y, z) &= \frac{Q'}{4\pi\epsilon_0} \sum_{i=1}^4 \left(\frac{(y - y_{wi})}{r_{2i}(p_2 + r_{2i})} - \frac{(y - y_{wi})}{r_{1i}(p_1 + r_{1i})} \right) \\ E_z(x, y, z) &= \frac{Q'}{4\pi\epsilon_0} \sum_{i=1}^4 \left(\frac{1}{r_{2i}} - \frac{1}{r_{1i}} \right), \end{aligned} \quad (1)$$

where

$p_1 = z + L_w/2$, $r_{1i} = \sqrt{(x - x_{wi})^2 + (y - y_{wi})^2 + p_1^2}$, $p_2 = z - L_w/2$, $r_{2i} = \sqrt{(x - x_{wi})^2 + (y - y_{wi})^2 + p_2^2}$, Q' is charge density and pairs (x_{wi}, y_{wi}) are wire coordinates equal to $(d_w/\sqrt{2}, 0)$, $(0, d_w/\sqrt{2})$, $(-d_w/\sqrt{2}, 0)$, and $(0, -d_w/\sqrt{2})$ for $i = 1, 2, 3$, and 4 , respectively. The wires stretch between $z = -24$ cm and $z = 24$ cm. Being a vector, electric field is not easy to visualize; therefore, it is the electric potential corresponding to the calculated electric field that is given in five sample planes in Fig. 2. Better matching between the electrostatic potentials of the four wires and of the four rods is achieved if the wire length is extended at each end by $R_r = 4$ cm because the equipotential ellipsoid of a wire, which contains the circumference of the rod's base, is than not only longer but is thinner as well and therefore closer to the rod's cylinder. Adjusted length of the wires together with the charge density of $Q' = 0.36 \mu\text{C}/\text{m}$ provide that the analytical field of finite wires and the field corresponding to the real device given in Fig. 1, have the same values of electrostatic potential of 0 kV at $x = 0$ cm, $y = 0$ cm, $z = L_r = 40$ cm, and 20 kV at $x = d_w/\sqrt{2} - R_r = 6.5$ cm, $y = 0$ cm, $z = L_r/2 = 20$ cm. Note that, unlike in [6], the point of zero potential is chosen to be within the beam path volume; therefore, the agreement between the ion beam simulations in the approximated and in the realistic field is expected to be reasonably good.

A beam of protons traveling along the z -axis from $z = -40$ cm to $z = 40$ cm is first decelerated until it

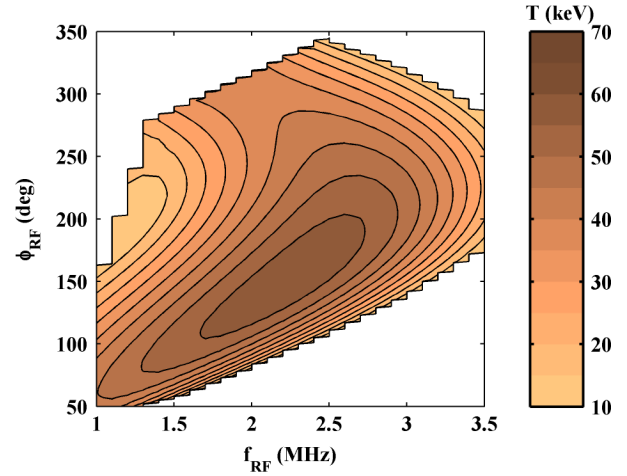


Fig. 3. Output energy dependence on frequency and phase of power supply. The initial proton energy of 10 keV is increased to $T = 58.5$ keV with $f_{\text{RF}} = 2.3$ MHz and $\phi_{\text{RF}} = 156.0^\circ$.

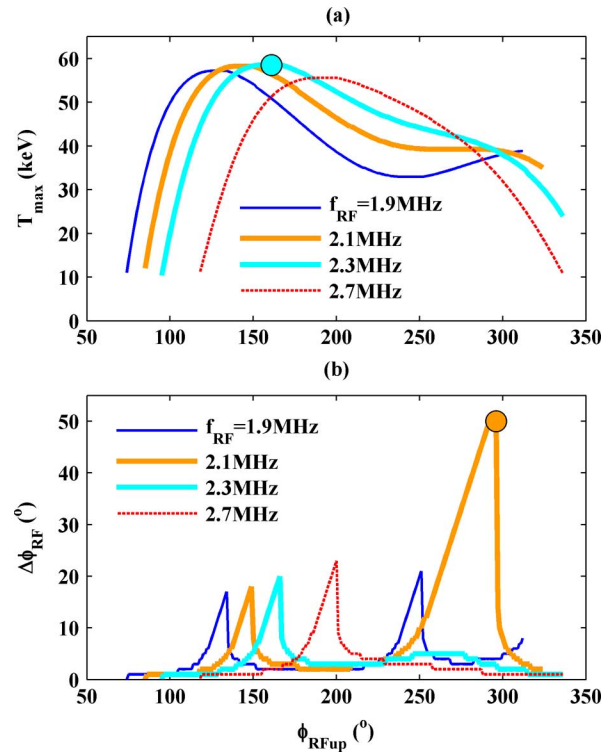


Fig. 4. Optimal acceleration conditions. Maximal proton energy within a beam bunch, T_{max} , and phase width of a beam bunch, $\Delta\phi_{\text{RF}} = \phi_{\text{RFup}} - \phi_{\text{RFdown}}$, are shown in graphs (a) and (b), respectively. Each point corresponds to a beam bunch traveling along the z -axis whose energy spread after acceleration is 1%. The optimal accelerations corresponding to the global maxima $\max(T_{\text{max}})$ and $\max(\Delta\phi_{\text{RF}})$ are marked with circles in graphs (a) and (b), respectively.

reaches $z = 0$ cm and then accelerated for the rest of the path. A proton could be accelerated throughout its path if the electric potential of the wires is time varying and changing its sign when the proton reaches $z = 0$ cm. If the charge, uniform along wire's length, is alternating in time with radio frequency f_{RF} , i.e.,

$$Q'(t) = Q'_0 \sin(2\pi f_{\text{RF}} t - \phi_{\text{RF}}), \quad (2)$$

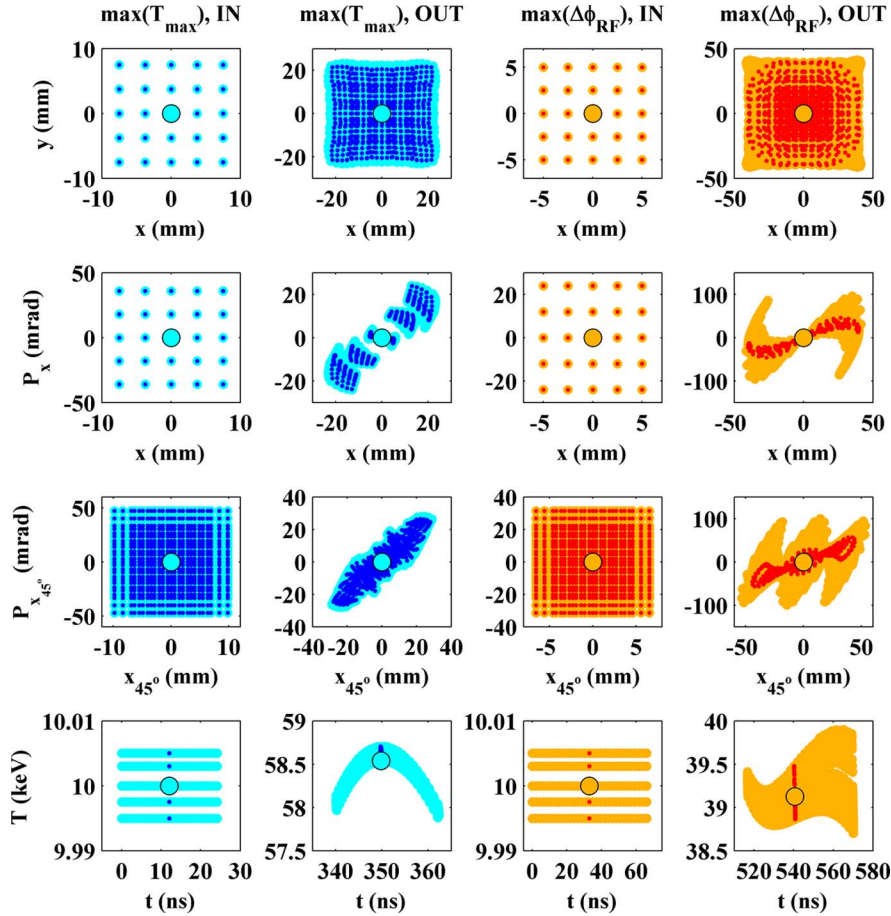


Fig. 5. Optimal accelerations. The graphs in the first and second column correspond to the optimal acceleration with respect to the maximal achieved ion energy within a bunch, $\max(T_{\max})$, and, consequently, to the conditions given in the first row of Table I. The optimal acceleration depicted by the graphs in the third and fourth column correspond to the maximal phase width criterion, $\max(\Delta\phi_{\text{RF}})$, and to the second row of Table I. The first and third columns of graphs show the initial proton bunches at the device entrance $z = -40$ cm, whereas the output bunches at $z = 40$ cm are given in the second and fourth columns. In each graph, the total of 96 875 simulated test particles is shown. The graphs in the first row give transverse, i.e., $x - y$, images of the simulated beam. Due to the fourfold symmetry, the transverse emittances along mutually perpendicular axes, e.g., along x - and y -axis, are identical. Therefore, in order to fully represent the beam its transverse emittances are given along the two axes which are 45° apart. Consequently, the second and third row of graphs is devoted to the $x - P_x$ and $x_{45^\circ} - P_{x_{45^\circ}}$ emittances of the beam, respectively. The images of the beam bunch in the longitudinal phase space, $t - T$, are given in the fourth row of graphs. The central ion within the bunch is depicted by a circle on all graphs. The test ions within the bunch which are in phase with the accelerating voltage are depicted by dark dots. Angular as well as spatial spreads of the beam caused by the normalized momentum are much larger than those induced by the spatial coordinate. The output energy depends mostly on the timing between the test ion and the accelerating RF voltage. The least influential parameter is the initial ion energy.

the electric field defined with (1) will resume the same time dependence. Note that for our example $Q'_0 = 0.36 \mu\text{C/m}$. Given the size of the device, the time dependent electric field can be treated as quasi static as long as the condition $f_{\text{RF}} \ll (2\pi L_g \sqrt{\epsilon\mu})^{-1} \cong 60 \text{ MHz}$ is satisfied.

The energy a proton gains during its interaction with the field defined with (1) and (2) depends on the synchronization between the two, i.e., it depends on the field's frequency and phase, f_{RF} , ϕ_{RF} , as well as on the initial energy of a proton, T_0 . The dependence of the output proton energy, T , on f_{RF} and ϕ_{RF} is given in Fig. 3 for the initial proton energy of $T_0 = 10 \text{ keV}$. The data is obtained by simulating proton trajectories along z -axis for different values of f_{RF} and ϕ_{RF} .

In order to determine optimal conditions for acceleration of a beam bunch rather than a single proton, the data in Fig. 3 is further analyzed. Acceleration of a beam bunch whose energy spread after acceleration is 1 % is investigated using four criteria: maximal output energy of a single proton within a bunch, T_{\max} , phase width of a bunch, $\Delta\phi_{\text{RF}}$, averaged energy, T_{av} , and

total energy of a bunch, T_{tot} . Since the chosen energy spread of 1 % is rather small, the shapes of the curves defining the dependence of the maximal proton energy within a bunch and the averaged energy are very similar and the values of f_{RF} and ϕ_{RF} corresponding to the maxima of these curves are practically equal. The same is true for the second and fourth criteria, i.e., for the bunch width and total energy. Therefore, only two out of four dependencies are shown in Fig. 4. The values corresponding to the optimal acceleration with respect to all four criteria are given in Table I. Note that the maxima of curves $\Delta\phi_{\text{RF}}(\phi_{\text{RFup}})$ in graph (b) in Fig. 4 correspond to the intervals with local minimum, local maximum or inflection point of curves $T_{\max}(\phi_{\text{RFup}})$ in graph (a). In particular, the global maximum in graph (b) corresponds to the phase interval which contains inflection point of the corresponding curve, $f_{\text{RF}} = 2.1 \text{ MHz}$, in graph (a).

Using the data from the first two rows of Table I as initial conditions for ion beam dynamics simulations, the two optimal accelerations marked with circles in Fig. 4 are further investi-

TABLE I
OPTIMAL ACCELERATION CONDITIONS IN ANALYTICAL ELECTRIC FIELD CORRESPONDING TO FINITE WIRES

criterion	f_{RF} (MHz)	ϕ_{ow} ($^\circ$)	ϕ_{up} ($^\circ$)	T_{max} (keV)	$\Delta\phi_{\text{RF}}$ ($^\circ$)	T_{av} (keV)	T_{tot} (MeV)
$\max(T_{\text{max}})$	2.3	146	166	58.5	20	58.3	1.2
$\max(\Delta\phi_{\text{RF}})$	2.1	244	294	39.1	50	38.9	2.0
$\max(T_{\text{av}})$	2.3	146	161	58.5	15	58.4	0.9
$\max(T_{\text{tot}})$	2.1	243	293	39.2	50	38.9	2.0

gated and the results are shown in Fig. 5. A proton bunch is represented with the spatial coordinates x and x_{45° , normalized momentums, P_x and $P_{x_{45^\circ}}$, energy, T , and time, t . Because of the fourfold symmetry of the device and axial beam symmetry $x - P_x$ and $y - P_y$ graphs are identical. Therefore, for data presentation purposes $y - P_y$ graphs are replaced with $x_{45^\circ} - P_{x_{45^\circ}}$ graphs, where x_{45° is the axis rotated clockwise 45° with respect to the x -axis in the $x - y$ plane.

The limits of initial test ion phase space coordinates are chosen in accordance with the proton beam obtained with the p-VINIS ion source [21]. The ion source provides a beam whose spatial as well as angular distribution is Gaussian with $2\sigma = 2.5$ mm and $2\sigma = 12$ mrad, respectively. The energy spread within the ion source plasma is smaller than 1 eV. However, input variables should be distributed over sufficiently wider intervals if the simulated input-output mapping is to be used to interpolate the output corresponding to any desired distribution of input variables, as described in [22]. Therefore, in our optimal acceleration study, the initial spatial as well as angular beam spread is taken to be 6σ for the optimal acceleration with $\max(T_{\text{max}})$, and 4σ for the $\max(\Delta\phi_{\text{RF}})$ example. In both cases it was taken that the initial energy spread is 10 eV. Further, all input parameters are taken to be equally spaced as well as uniformly distributed. Consequently, ion beam simulations are performed once and the output corresponding to any desired distribution of input variables is obtained much faster by the method described in [22]. Note that the spatial beam spreads in Fig. 5 exceed grounded cylinder aperture of $R_a = 2$ cm at $z = -40$ cm as well as at $z = 40$ cm; therefore, the depicted results could be used to determine the acceptance of the device, as well.

As can be seen from the last row of graphs in Fig. 5, the analytical quasi static electric field of four finite wires can efficiently accelerate a proton beam. The maximal ion energy achieved in the examples of proton beam acceleration with finite wires shown in [22] and [23] is 37 % larger because the wires were 8 cm shorter and the applied charge density was almost two times larger.

III. NUMERICAL MODEL

Encouraging results shown in Fig. 5 must be validated by a more realistic approximation of electromagnetic field. The structure shown in Fig. 1 is modeled using the commercially available software package WIPL-D [19]. The three-dimensional electromagnetic solver incorporated in this package models arbitrarily shaped structures with wires and plates as basic building blocks. Because it is a frequency domain solver based on the higher order method of moments it is well-suited for closed region problems and the method of choice for open

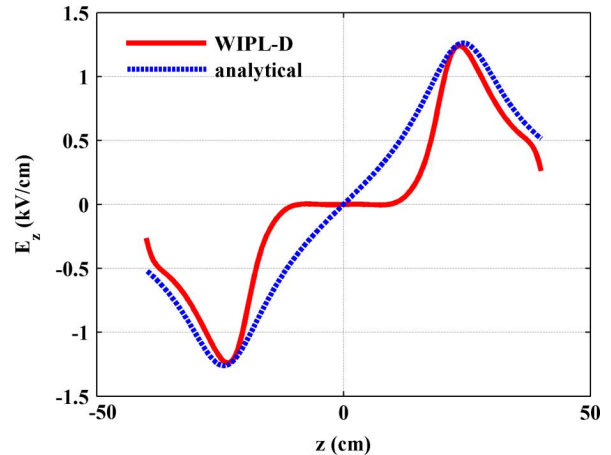


Fig. 6. Comparison between realistic and analytical electric field. Due to the difference between the numerically modeled and approximate analytical electric field along the axis of the device maximal achievable energy of a test proton is expected to be lower than the value predicted for the analytically computed field. Note that, along the z -axis, the total electric field has only axial component, i.e., $E = E_z$ if $x = y = 0$ cm.

regions modeling. Metallic plates, lossy or lossless dielectric as well as magnetic surfaces are modeled with electrically large bilinear generalized quadrilaterals, which provide very good flexibility and geometrical accuracy. The higher order numerical engine ensures that highly accurate results are achieved efficiently.

If proton beam accelerations in the analytically approximated and numerically modeled field are to be compared the appropriate parameters corresponding to the two cases have to be adjusted. In order to preserve field symmetry, power lines are attached to the four electrodes and the grounded cylinder in the middle of the device. To match the approximated field electrostatic potential of 20 kV at $x = d_w/\sqrt{2} - R_r = 6.5$ cm, $y = 0$ cm, $z = L_r/2 = 20$ cm, the amplitude of the voltage applied to the rod electrodes is taken to be 20 kV as well.

The shape of the real electric field is reasonably well approximated in the previous section with the field corresponding to uniformly charged finite wires because the length of wires is extended and the points with zero and driving electrostatic potential are chosen carefully. However, for the analytical finite wires approximation it was assumed that charge distribution along the wires is uniform; therefore, the largest discrepancy between the realistic and approximated field is caused by the charge pile up at the edges of the device, see Fig. 6. Note that the fields are given at their peaks, i.e., the value of sine in (2) as well as in the appropriate expression for total field obtained with WIPL-D are taken to be 1.

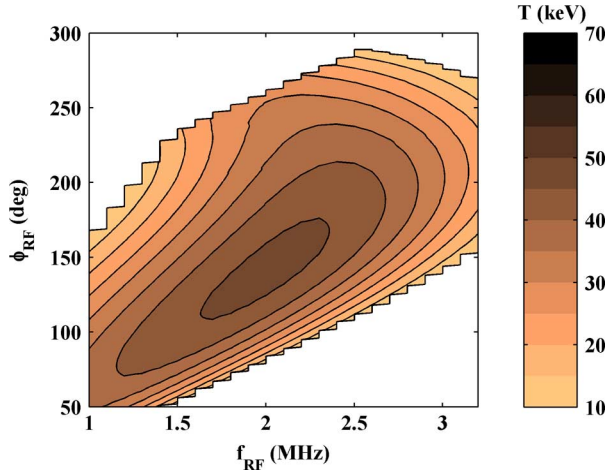


Fig. 7. Output energy dependence on frequency and phase of power supply for numerically modeled field. The initial proton energy of 10 keV is increased to $T = 46.6$ keV with $f_{\text{RF}} = 2.0$ MHz and $\phi_{\text{RF}} = 140.0^\circ$. As expected, the maximal achieved energy is 20 % smaller compared to the value predicted by the simulation in analytically approximated field, see Fig. 3.

The device dimensions and the considered frequencies provide that the corresponding electromagnetic field is quasi static; therefore, the influences on ion beam dynamics of the real and imaginary magnetic as well as imaginary electric parts of the modeled electromagnetic field are negligible. Regardless, all components of the realistic electromagnetic field obtained with numerical modeling are used in ion beam dynamics simulations. The ion beam dynamics simulations performed with the analytical field shown in Figs. 3 and 4 and Table I are repeated using the numerically modeled electromagnetic field and the results are given in Figs. 7 and 8 and Table II, respectively.

In the analytically calculated field, optimal accelerations with respect to the $\max(T_{\text{max}})$ and $\max(\Delta\phi_{\text{RF}})$ conditions correspond to the phase intervals which contain local maximum and inflection point of the matching $T_{\text{RF}}(\phi_{\text{RFup}})$ curve, respectively, see Fig. 4. However, in the modeled field both considered optimal accelerations correspond to the local maxima of the matching $T_{\text{RF}}(\phi_{\text{RFup}})$ curve. Consequently, beam bunch dynamics of the two optimal accelerations in the modeled field are more alike than is the case for the analytically approximated field, see Figs. 5 and 9. For the same reason, the beam bunch dynamics simulations shown in Fig. 9 are performed using equally wide intervals of spatial as well as angular coordinates of 6σ for the both considered cases of optimal acceleration, i.e., the simulation intervals for the $\max(\Delta\phi_{\text{RF}})$ case are extended from 4σ to 6σ .

Wide ranges of input as well as output variables in Figs. 5 and 9 are chosen to illustrate the acceptances of the studied devices, i.e., of the finite wires and of the rods housed in the grounded cylinder, respectively. In order to depict a realistic optimal acceleration, the method described in [22] and n -dimensional linear interpolation are applied to the input-output mapping shown in first and second column of Fig. 9, to obtain the output which corresponds to realistically distributed initial parameters of a proton bunch. The result is given in Fig. 10. The initial distribution of the bunch is chosen in accordance with the output of the p-VINIS ion source [21]. After the interaction with

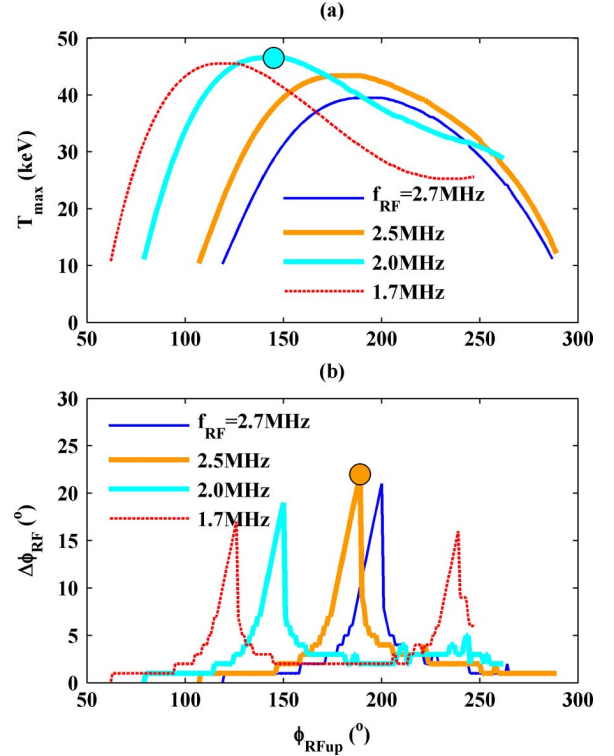


Fig. 8. Optimal acceleration conditions in numerically modeled field. The figure format is identical to the one of Fig. 4. Each point corresponds to a beam bunch traveling along the z -axis whose energy spread after acceleration is 1 %. The optimal accelerations corresponding to the global maximum $\max(T_{\text{max}})$ and $\max(\Delta\phi_{\text{RF}})$ are depicted with circles in graphs (a) and (b), and fully defined in the first and second row in Table II, respectively.

the device, the proton beam bunch is defocused and is twice as wide in the transverse direction as before the interaction. While time distribution does not change significantly, energy distribution seems to evolve from the random uniform into a log-normal distribution.

IV. DEVICE PROPERTIES

When used as an electrostatic piece of equipment the rainbow lens is intended to be a focusing device. However, as a side effect, in the vicinity of lens's entrance a beam is decelerated and farther along its path close to the exit it is accelerated, see Fig. 11. The focusing strength, i.e., the radial component of electric field is limited by the beam energy, which has to be large enough to overcome entering deceleration. The ratio between the driving, focusing and the side effect, accelerating/decelerating force is unfavorable because $|E_r| < |E_z|$.

If the device is used as quasi static the sign of the sine multiplier is negative roughly for $z < 0$; consequently, a beam is accelerated through the entering as well as exit gap. The side effect is distributed first as undesired defocusing through the first half and then favorable focusing later along the second half of beam path through the device. The net side effect is unfortunately undesired defocusing due to larger beam energy and consequently shorter path along the radial direction for $z > 0$. The ratio $|E_z/E_r| > 1$ indicates that the device is more efficient as an accelerator than as a lens. Note that these relations depend on the size of accelerating gaps, $(L_g - L_r)/2$, rod length, L_r , as

TABLE II
OPTIMAL ACCELERATION CONDITIONS IN NUMERICALLY MODELED ELECTROMAGNETIC FIELD CORRESPONDING TO ROD ELECTRODES

criterion	f_{RF} (MHz)	ϕ_{low} ($^\circ$)	ϕ_{up} ($^\circ$)	T_{max} (keV)	$\Delta\phi_{\text{RF}}$ ($^\circ$)	T_{av} (keV)	T_{tot} (MeV)
$\max(T_{\text{max}})$	2.0	131	150	46.6	19	46.4	0.9
$\max(\Delta\phi_{\text{RF}})$	2.5	167	189	43.4	22	43.2	1.0
$\max(T_{\text{av}})$	2.0	131	145	46.5	14	46.4	0.7
$\max(T_{\text{tot}})$	2.4	160	182	44.7	22	44.5	1.0

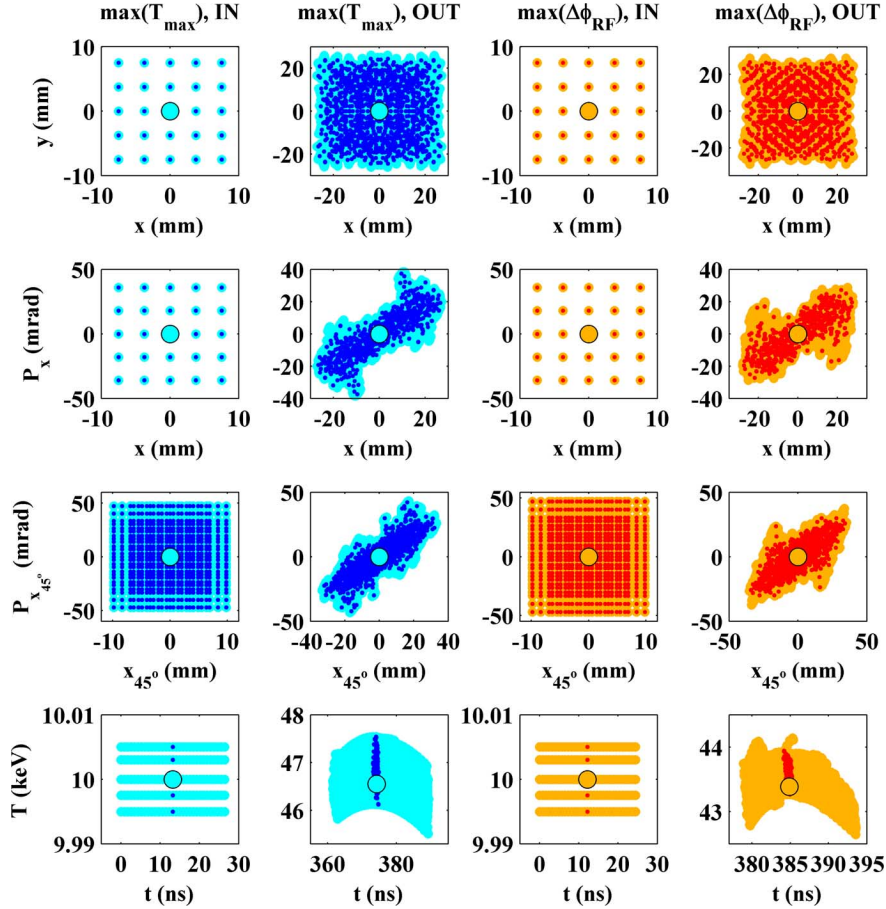


Fig. 9. Optimal accelerations in numerically modeled field. The figure format and the number of simulated test ions are equal to those in Fig. 5. The optimal RF frequency values are $f_{\text{RF}} = 2.0$ MHz and 2.5 MHz for $\max(T_{\text{max}})$ and $\max(\Delta\phi_{\text{RF}})$ criterion, as given in the first and second row of Table II, respectively. One of these two non-random uniform input-output mappings, the one corresponding to $\max(T_{\text{max}})$, is used to obtain the optimal acceleration of realistically distributed beam bunch shown in Fig. 10.

well as aperture radius, R_a , see Fig. 1. The values used in our study are chosen in accordance with the existing device; however, in order to achieve maximal efficiency of either focusing or accelerating task, a thorough study of these dependencies should be performed.

As can be seen from Fig. 11, acceleration occurs primarily within the gaps between the electrode tips and the grounded cylinder bases. Consequently, acceleration achieved with the rainbow accelerator is of the drift tube type, as is the case for the RF focused drift tube (RFD) and RF focused interdigital (RFI) linac structures, see [14], [15] and references therein. However, the electrodes in these devices are divided in two pairs and each pair operates at different electric potential. Consequently, the resulting quadrupole-like field produces opposite effects along the two mutually perpendicular transverse axes which contain electrode centers, in our example these are x - and

y -axis, and no effect along the axes rotated for 45° , i.e., along x_{45° - and y_{45° -axis. On the other hand, equal polarity of the rainbow accelerator electrodes provides equal effect along the x - and y -axis, as well as less intense but still the same type of effect along the x_{45° - and y_{45° -axis.

In order to fully describe the device, its capabilities to accelerate various ion beams to different energies should be investigated and relationships between the desired beam characteristics and device parameters should be defined. As the first step in this direction, for protons with initial energy of 10 keV, we give Table III which relates the final energy of accelerated proton, T_{max} , with the required RF voltage parameters: amplitude, V_0 , frequency, f_{RF} , and phase limits, ϕ_{low} and ϕ_{up} .

Illustration of the rainbow effect, detailed technical parameters of the rainbow accelerator as well as more thorough discussion about its capabilities will be given in [24].

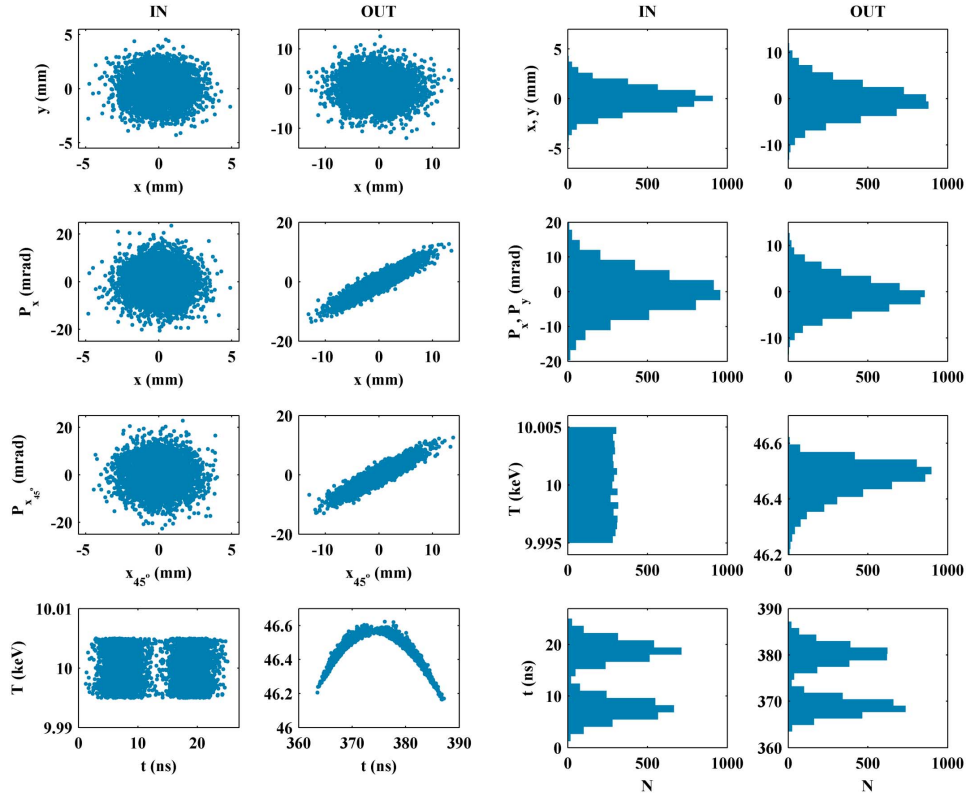


Fig. 10. Optimal acceleration of realistically distributed proton bunch. Only optimal acceleration with respect to $\max(T_{\max})$ criterion is considered. The initial and final phase space coordinates of 5000 test particles shown in the first and second column of graphs follow the form accepted in Figs. 5 and 9. The initial spatial coordinates, x and y , as well as normalized momenta, P_x and P_y , follow Gaussian distribution, initial test ion energy, T , is taken to have random uniform distribution, whereas time of arrival at $z = -40$ cm plane, t , has a distribution typical for the output of a device known as the beam buncher. The initial distributions are defined by the histograms in third column. After the interaction with the device the output parameters are distributed according to the histograms in fourth column.

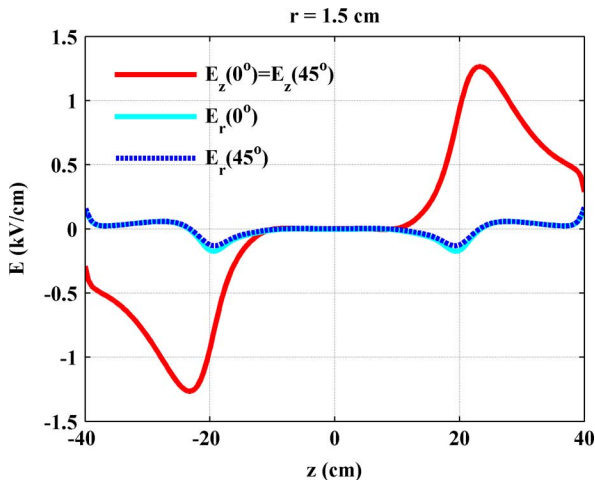


Fig. 11. Peak axial and radial components of electric field. The peak values of axial and radial electric field components, E_z and E_r , are given along two straight segments parallel to the z -axis at the distance $r = 1.5$ cm. The field components $E_z(0^\circ)$ and $E_r(0^\circ)$ correspond to $x = 1.5$ cm and $y = 0$ cm, whereas $E_z(45^\circ)$ and $E_r(45^\circ)$ are given along the line defined with $x_{45^\circ} = 1.5$ cm and $y_{45^\circ} = 0$ cm.

V. CONCLUSION

By changing its power supply from DC to RF voltage the electrostatic rainbow lens can be transformed into an ion beam accelerator. It is efficient and inexpensive way to broaden available

TABLE III
OPTIMAL ACCELERATION CONDITIONS FOR $\max(T_{\max})$ CRITERION

V_0 (kV)	f_{RF} (MHz)	ϕ_{low} ($^\circ$)	ϕ_{up} ($^\circ$)	T_{\max} (keV)
20	2.0	131	150	46.6
40	2.5	138	157	82.6
60	2.9	142	161	118.4
80	3.3	148	169	154.0
100	3.6	151	172	189.6

beam energy span of the existing low energy ion beam facilities. Despite of physical as well as functional similarities between the RF rainbow accelerator, electrostatic quadrupole accelerator, and RF quadrupole accelerator, the acceleration achieved with the RF rainbow accelerator is in its nature the most similar to the one of the drift tube Sloan-Lawrence accelerator. Due to the equal polarity of the electrodes the resulting effects are identical along the transverse x - and y -axis and are of the same type but lesser intensity along the x_{45° - and y_{45° -axis. The RFD as well as RFI linac structures apply the same drift tube type acceleration; however, the quadrupole-like field in these devices produce opposite effects along the x - and y -axis and no effect along the x_{45° - and y_{45° -axis. It seems worthwhile to further investigate the dependence of the RF rainbow accelerator operation on the size of its aperture radius, accelerating gap and electrode length, as well as to accordingly perform consequent optimization of its operation.

ACKNOWLEDGMENT

The authors thank N. Nešković for numerous fruitful discussions.

REFERENCES

- [1] E. A. Abramyan, "Transformer type accelerators for intense electron beams," *IEEE Trans. Nucl. Sci.*, vol. 18, pp. 447–455, 1971.
- [2] D. A. Goldberg *et al.*, "A multi-aperture electrostatic quadrupole (MESQ) accelerator for neutral beam injection," *Bull. Am. Phys. Soc.*, vol. 27, p. 1142, 1982.
- [3] O. A. Anderson, L. Soroka, C. H. Kim, R. P. Wells, C. A. Matuk, P. Purgalis, J. W. Kwan, M. C. Vella, W. S. Cooper, and W. B. Kunkel, "Applications of the constant-current variable-voltage dc accelerator," *Nucl. Instrum. Meth. B*, vol. 40–41, pt. 2, pp. 877–880, 1989.
- [4] F. M. Bieniosek, C. M. Celata, E. Henestroza, J. W. Kwan, L. Prost, P. A. Seidl, A. Friedman, D. P. Grote, S. M. Lund, and I. Haber, "2-MV electrostatic quadrupole injector for heavy-ion fusion," *Phys. Rev. Special Topics-Accel. Beams*, vol. 8, p. 010101, Jan. 2005.
- [5] A. J. Kreiner, J. W. Kwan, A. A. Burlón, H. Di Paolo, E. Henestroza, D. M. Minsky, A. A. Vlada, M. E. Debray, and H. Somacal, "A tandem-electrostatic-quadrupole for accelerator-based BNCT," *Nucl. Instrum. Meth. B*, vol. 261, pp. 751–754, 2007.
- [6] N. Nešković, I. Telečki, B. Bojović, and S. Petrović, "A square electrostatic rainbow lens: Catastrophic ion beam focusing," *Nucl. Instrum. Meth. A*, vol. 635, no. 1, pp. 1–7, Apr. 2011.
- [7] I. Telečki, S. Petrović, P. Beličev, B. Rađenović, R. Balvanović, B. Bojović, and N. Nešković, "Focusing properties of a square electrostatic rainbow lens," *Nucl. Instrum. Meth. A*, vol. 694, pp. 224–233, 2012.
- [8] J. J. Livingood, *Principles of Cyclic Particle Accelerators*. New York: Van Nostrand, 1961, pp. 311–313.
- [9] E. Close and W. B. Herrmannsfeldt, "Numerical simulation of the transport of intense beams of heavy ions in an electrostatic quadrupole system," *IEEE Trans. Nucl. Sci.*, vol. 28, no. 3, pp. 2425–2427, 1981.
- [10] M. Reiser, "Comparison of Gabor lens, gas focusing, and electrostatic quadrupole focusing for low-energy ion beams," in *Proc. 1989 IEEE Particle Accelerator Conf. Accelerator Science Technol.*, 1989, pp. 1744–1747.
- [11] J. W. Staples, RFQ's—An Introduction CA, Sept. 1990, LBL-29472, Lawrence Berkeley Lab., Univ. California Berkeley.
- [12] M. Weiss, "Introduction to RF linear accelerators," *CAS School: Fifth General Accelerator Physics Course*, pp. 913–953, 1994, CERN-94-01.
- [13] R. Gaur and P. Shrivastava, "Beam dynamics and electromagnetic design studies of 3 MeV RFQ for SNS programme," *J. Electromagn. Anal. Appl.*, vol. 2, pp. 519–528, 2010.
- [14] D. A. Swenson, "CW proton linac for the BNCT application," in *Proc. 24th Linear Accelerator Conf.*, Victoria, BC, Canada, Sept. 29–Oct. 3 2008, pp. 220–222.
- [15] D. A. Swenson, "Status of the RFD linac structure development," in *Proc. 20th Int. Linac Conf.*, Monterey, CA, Aug. 21–25, 2000, pp. 935–937.
- [16] A. Dobrosavljević, P. Beličev, V. Jocić, N. Nešković, I. Trajić, V. Vujović, and L. J. Vukosavljević, "Facility for modification and analysis of materials with ion beams (FAMA)," in *Proc. 19th Int. Conf. Cyclotrons Their Applications*, Lanzhou, China, Sep. 6–10, 2010, pp. 108–110.
- [17] N. Nešković, Vinča Institute for Nuclear Sciences. Belgrade, Serbia, Jan. 2011, private communication.
- [18] J. L. Ristić-Djurović, "Acceleration with four uniformly charged finite wires," unpublished.
- [19] Software and User's Manual WIPL-D Microwave. Belgrade, Serbia, 2005, WIPL-D d.o.o.
- [20] J. Ristić-Djurović, N. Nešković, and S. Ćirković, "Compound particle tracking algorithm: Application to the foil stripping extraction system design," in *Proc. 6th Int. Computational Accelerator Physics Conf.*, Darmstadt, Germany, Sep. 11–14, 2000 [Online]. Available: <http://www.icap2000.de/frames/index.htm>, Available:
- [21] P. Beličev, B. Bojović, M. Rajčević, and N. Y. Kazarinov, "Injection transport line of the VINCY Cyclotron," in *Proc. 17th Int. Conf. Cyclotrons Their Appl.*, Tokyo, Japan, Oct. 18–22, 2004, pp. 489–491.
- [22] J. L. Ristić-Djurović and A. Ž. Ilić, "Role and significance of uniform distribution in a study of ensemble of particles," *IEEE Trans. Nucl. Sci.*, DOI: 10.1109/TNS.2012.2225153, to be published.
- [23] J. L. Ristić-Djurović, A. Ilić, and S. Ćirković, Finite Wire Accelerator INN Vinča, Dec. 2011, Internal report.
- [24] N. Nešković, J. L. Ristić-Djurović, S. Petrović, P. Beličev, B. Rađenović, S. Ćirković, A. Ž. Ilić, and A. Dobrosavljević, in preparation.

IEEE TRANSACTIONS ON NUCLEAR SCIENCE

A PUBLICATION OF THE IEEE NUCLEAR AND PLASMA SCIENCES SOCIETY



FEBRUARY 2013

VOLUME 60

NUMBER 1

IETNAE

(ISSN 0018-9499)

PART II OF TWO PARTS

18TH INTERNATIONAL WORKSHOP ON ROOM-TEMPERATURE SEMICONDUCTOR DETECTORS (RTSD)
VALENCIA, SPAIN, OCTOBER 23–29, 2011

CZT AND CdTe GROWTH AND CHARACTERIZATION

Effects of Dislocation Walls on Image Quality When Using Cadmium Telluride X-Ray Detectors	199
..... C. Buis, G. Marrakchi, T. A. Lafford, A. Brambilla, L. Verger, and E. Gros d'Aillon	
SAFEGUARDS, MONITORING, AND INTERNATIONAL SECURITY	
Source Detection Performance Prediction for a CdZnTe Array ... D. J. Lingenfelter, J. A. Fessler, C. D. Scott, and Z. He	204

NUCLEAR AND SPACE RADIATION EFFECTS CONFERENCE (NSREC)
MIAMI, FL, JULY 16–20, 2012

Effects of Neutron-Induced Well Potential Perturbation for Multiple Cell Upset of Flip-Flops in 65 nm	213
..... J. Furuta, R. Yamamoto, K. Kobayashi, and H. Onodera	
Experimental Study of Defect Formations in GaAs Devices Using Gain, Photoluminescence and Deep Level Transient Spectroscopy	219
..... E. Bielejec, G. Vizkelethy, R. M. Fleming, D. K. Serkland, J. K. McDonald, G. A. Patrizi, and D. B. King	
Analysis of the TID Induced Failure Modes in NOR and NAND Flash Memories	224
..... Y. Yan, W. Chen, R. Fan, X. Guo, H. Guo, F. Zhang, L. Ding, K. Zhang, D. Lin, and Y. Wang	
Applicability of Redundant Pairs of SOI Transistors for Analog Circuits and Their Applications to Phase-Locked Loop Circuits	230
..... A. Makihara, T. Yokose, Y. Tsuchiya, Y. Miyazaki, H. Abe, H. Shindou, T. Ebihara, A. Maru, K. Morikawa, S. Kuboyama, and T. Tamura	

REGULAR PAPERS

ACCELERATOR TECHNOLOGY

Role and Significance of Uniform Distribution in a Study of Ensemble of Particles	236
..... J. L. Ristić-Djurović and A. Ilić	

(Contents Continued on Page 197)



ANALOG AND DIGITAL CIRCUITS

Multiplexed Oversampling Digitizer in 65 nm CMOS for Column-Parallel CCD Readout	246
..... C. R. Grace, J.-P. Walder, P. Denes, and H. von der Lippe	
An Analog Level 1 Trigger Prototype for CTA L. A. Tejedor, J. A. Barrio, J. L. Lemus, C. Delgado, and J. I. Alonso	251

CALORIMETERS

Upgrade of the CMD-3 BGO Endcap Calorimeter	259
..... D. N. Grigoriev, R. R. Akhmetshin, V. F. Kazanin, A. E. Kuzmenko, and Y. V. Yudin	

CHERENKOV DETECTORS

Studies of the Effects of CO ₂ Contamination of the Neon Gas Radiator on the Performance of the NA62 RICH Detector ..	
..... G. Anzivino, A. Bizzeti, F. Bucci, A. Cassese,	
P. Cenci, R. Ciaranfi, E. M. Gersabeck, E. Iacopini, M. Lenti, M. Pepe, R. Piandani, M. Piccini, A. Sergi, and M. Veltri	265

COMPUTING, SIMULATION, ALGORITHMS, AND SOFTWARE

A Gamma-Ray Identification Algorithm Based on Fisher Linear Discriminant Analysis D. Boardman and A. Flynn	270
Criticality of Oklo Natural Reactors: Realistic Model of Reaction Zone 9	
..... S. E. Bentrudi, B. Gall, F. Gauthier-Lafaye, A. Seghour, A. Pape, and D. E. Medjadi	278

DIGITAL SIGNAL PROCESSING

Probing the Merits of Different Event Parameters for the Identification of Light Charged Particles in CHIMERA CsI(Tl) Detectors With Digital Pulse Shape Analysis	
..... L. Acosta, F. Amorini, R. Bassini, C. Boiano, G. Cardella, E. De Filippo, L. Grassi,	
C. Guazzoni, P. Guazzoni, M. Kiš, E. La Guidara, Y. Leifels, I. Lombardo, T. Minniti, A. Pagano, M. Papa, S. Pirrone,	
G. Politi, F. Porto, F. Riccio, F. Rizzo, P. Russotto, S. Santoro, W. Trautmann, A. Trifirò, G. Verde, P. Zambon, and L. Zetta	284
Adaptive Filters for Digital Spectroscopy With Gaussian Peaks Preservation, Enhanced Rate and Low Frequency Noise Rejection	
..... G. Ripamonti, A. Abba, F. Caponio, and A. Geraci	293

DOSIMETRY

Neutron Dosimetry in Quasi-Monoenergetic Fields of 244 and 387 MeV	
..... V. Mares, C. Pioch, W. Rühm, H. Iwase,	
Y. Iwamoto, M. Hagiwara, D. Satoh, H. Yashima, T. Itoga, T. Sato, Y. Nakane, H. Nakashima, Y. Sakamoto, T. Matsumoto,	
A. Masuda, H. Harano, J. Nishiyama, C. Theis, E. Feldbaumer, L. Jaegerhofer, A. Tamii, K. Hatanaka, and T. Nakamura	299

INDUSTRIAL APPLICATIONS

Fluorescence-Assisted Gamma Spectrometry for Surface Contamination Analysis	
..... S. Ihtola, J. Sand, K. Peräjärvi, J. Toivonen, and H. Toivonen	305

NUCLEAR POWER INSTRUMENTATION AND CONTROL

Dynamic Compensation of Vanadium Self Powered Neutron Detectors for Use in Reactor Control	
..... A. K. Mishra, S. R. Shimjith, T. U. Bhatt, and A. P. Tiwari	310
Linear Representation and Sparse Solution for Transient Identification in Nuclear Power Plants	
..... Y. Chang, X. Huang, Y. Hao, and C.-W. Li	319
Nuclear Heating Measurements in Material Testing Reactor: A Comparison Between a Differential Calorimeter and a Gamma Thermometer	
..... D. Fourmentel,	
C. Reynard-Carette, A. Lyoussi, J. F. Villard, J. Y. Malo, M. Carette, J. Brun, P. Guimbal, and Y. Zerega	328

PHOTODETECTORS

Simulating Silicon Photomultiplier Response to Scintillation Light *A. K. Jha, H. T. van Dam, M. A. Kupinski, and E. Clarkson* 336

RADIATION DAMAGE EFFECTS

Development, Design and Characterization of a Novel Protocol and Interfaces for the Control and Readout of Front-End Electronics in High Energy Physics Experiments *N. Costantino, G. Borgese, S. Saponara, L. Fanucci, J. Incandela, and G. Magazzù* 352

RADIATION EFFECTS

Comparison of Radiation Induced Noise Levels in Two Ion Detectors for Shielded Space Instruments in High Radiation Fields *R. R. Benke, D. M. White, J. A. Trevino, and K. S. Pickens* 365

Design Techniques for Xilinx Virtex FPGA Configuration Memory Scrubbers *I. Herrera-Alzu and M. López-Vallejo* 376

Component and System Level Studies of Radiation Damage Impact on Reflective Electroabsorption Modulators for Use in HL-LHC Data Transmission *S. Papadopoulos, S. Seif El Nasr-Storey, J. Troska, I. Papakonstantinou, F. Vasey, and I. Darwazeh* 386

Non-Monotonic γ -Ray Influence on Mo/n-Si Schottky Barrier Structure Properties *O. Y. Olikh* 394

Total Ionizing Dose Radiation Effects in Al₂O₃-Gated Ultra-Thin Body In_{0.7}Ga_{0.3}As MOSFETs *X. Sun, F. Xue, J. Chen, E. X. Zhang, S. Cui, J. Lee, D. M. Fleetwood, and T. P. Ma* 402

RADIATION IMAGING

Fast CdTe and CdZnTe Semiconductor Detector Arrays for Spectroscopic X-Ray Imaging *A. Brambilla, P. Ouvrier-Buffet, G. Gonon, J. Rinkel, V. Moulin, C. Boudou, and L. Verger* 408

Phase Contrast X-Ray Imaging Signatures for Security Applications *E. A. Miller, T. A. White, B. S. McDonald, and A. Seifert* 416

RADIATION INSTRUMENTATION

GATE Simulation of ¹²C Hadrontherapy Treatment Combined With a PET Imaging System for Dose Monitoring: A Feasibility Study *S. Jan, T. Frisson, and D. Sarrut* 423

A Multichannel Integrated Readout Circuit for High Throughput X-Ray Spectroscopy With Silicon Drift Detectors *L. Bombelli, R. Quaglia, C. Fiorini, R. Alberti, and T. Frizzi* 430

READOUT ELECTRONICS

Evaluation of a Second-Generation Ultra-Fast Energy-Resolved ASIC for Photon-Counting Spectral CT *C. Xu, M. Persson, H. Chen, S. Karlsson, M. Danielsson, C. Svensson, and H. Bornefalk* 437

VERITAS: A 128-Channel ASIC for the Readout of pnCCDs and DEPFET Arrays for X-Ray Imaging, Spectroscopy and XFEL Applications *M. Porro, D. Bianchi, G. De Vita, R. Hartmann, G. Hauser, S. Herrmann, L. Strüder, and A. Wassatsch* 446

SCINTILLATION DETECTORS

A Phoswich Detector With Compton Suppression Capability for Radioxenon Measurements *A. T. Farsoni, B. Alemayehu, A. Alhawsawi, and E. M. Becker* 456

SOLID STATE DETECTORS

Tests With Soft X-rays of an Improved Monolithic SOI Active Pixel Sensor *S. G. Ryu, T. G. Tsuru, G. Prigozhin, S. Kissel, M. Bautz, B. LaMarr, S. Nakashima, R. F. Foster, A. Takeda, Y. Arai, T. Imamura, T. Ohmoto, and A. Iwata* 465

Role and Significance of Uniform Distribution in a Study of Ensemble of Particles

Jasna L. Ristić-Djurović and Andjelija Ž. Ilić, *Member, IEEE*

Abstract—Dynamics of an ensemble of particles is often studied by tracking a large number of test particles from a chosen initial state to an adequately defined final state. Random distributions of particles over considered parameters are frequently used to describe an initial state of studied ensemble. Randomness of input data insures that there is no overlapping in test particles visualization; however, it hides the dependencies between various input and output parameters. If non-random, uniformly distributed input data is used, relationships between the input and output variables are revealed. Further, mapping of such an input into its output together with an appropriate interpolation scheme contains description of an output corresponding to any desired distribution of input data. A mapping of non-random uniformly distributed input into its output is combined with n -dimensional linear interpolation into a method for studying dynamics of an ensemble of particles. Advantages and efficiency of the method are illustrated using an ion beam interaction with two devices: the four parallel, equally spaced finite wires and the spiral inflector. The method is applicable if interactions between particles within an ensemble are negligible compared to other forces involved.

Index Terms—Distribution functions, nonlinear systems, particle beams.

I. INTRODUCTION

HERE are numerous scientific studies of interactions between an ensemble of particles and various devices, fields or ambiances [1]–[7]. Often, equations describing the problem of interest are solved numerically, resulting in computer tracking of an ensemble in time or space. Input data for these problems can be divided into variables which define the initial state of an ensemble and those related to a device or ambient interacting with an ensemble. Device related input parameters are usually fixed or adjusted by using several discrete values. On the other hand, in order to describe an ensemble of particles as realistically as possible, values of variables defining individual particles within an ensemble are often chosen randomly. Further, these random numbers are usually selected to follow uniform or normal, Gaussian distribution. As a result, every particle within an ensemble is visible regardless of variables chosen for visualization. Unfortunate consequence is that much information is buried in the randomness of input data.

If initial values of all input variables are not random, but are evenly spaced over the considered ranges of variables, a number

Manuscript received July 30, 2012; revised September 20, 2012; accepted October 12, 2012. Date of publication January 09, 2013; date of current version February 06, 2013. This work was supported by the Ministry of Education and Science of Serbia through the project “Physics and Chemistry with Ion Beams”, no. III45006.

The authors are with the Vinča Institute of Nuclear Sciences, Laboratory of Physics (010), University of Belgrade 11001 Belgrade, Serbia (e-mail: jasna@stanfordalumni.org; andjelijailic@ieee.org).

Color versions of one or more of the figures in this paper are available online at <http://ieeexplore.ieee.org>.

Digital Object Identifier 10.1109/TNS.2012.2225153

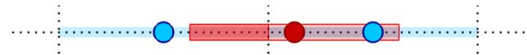


Fig. 1. 1D linear interpolation. The grid nodes and grid cells are lighter (blue). The data point and data cell are darker (red). The data cell and grid cells are equal in size and are centered on the data point and grid nodes, respectively. Only the two grid nodes surrounding the data point are drawn. The data cell segments falling into different grid cells are different in shade.

of dependencies and relationships can be studied. Influence of a single variable as well as of its gradient is revealed from the output data corresponding to the part of input data where all other variables each have a single value. Coupling of variables is uncovered by extending the considered part of the input and the corresponding output to include variable input of two variables.

Response of the studied system to a realistic, random distribution of input parameters can be obtained by combining the input-output mapping corresponding to the uniform non-random input with a suitable interpolation scheme. Consequently, computer simulation of the studied process is performed only once and the output corresponding to any desired input is interpolated from the once obtained uniform input-output mapping. If the interpolation is properly chosen and implemented, it provides substantial decrease in required computational time. The suggested method can be used to obtain the full space or time variation of the studied process as well. This is achieved by considering any intermediate state of the system as the output. Note, however, that the outlined approach is limited to ensembles of particles within which forces between particles are much smaller than the outer forces acting upon the ensemble. Consequently, the suggested method is not applicable, for example, to problems requiring inclusion of space charge effects or strong beam currents.

II. METHOD DESCRIPTION

Over the years we have combined uniform distribution of input variables with n -dimensional linear interpolation to investigate several problems [8]–[12]. The uniform distribution, input-output mapping and linear interpolation are explained in numerous textbooks, for example in [13]–[16]. In what follows we combine the three methods and adjust their representation to our needs.

Our intention is to lay out the concept and illustrate its usefulness rather than to solve a particular problem. Therefore, the linear interpolation scheme emerges as a reasonable option due to its simplicity and speed. When solving a particular problem the accuracy of our approach can be improved by using a higher-order interpolation scheme as well as by decreasing the step sizes of the non-random, uniformly distributed data.

A. Uniform Input-Output Mapping

An output of any process can be conceived as a function of input parameters. Equations which define a process very rarely

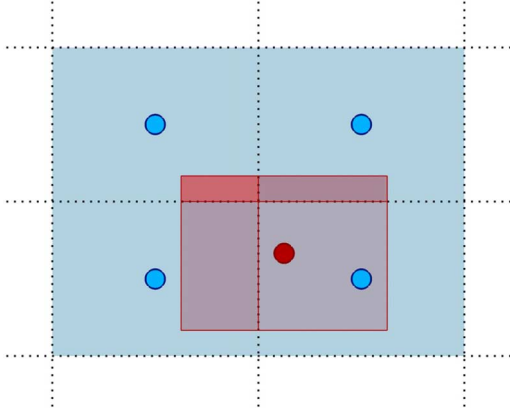


Fig. 2. 2D linear interpolation. The grid nodes and grid cells are lighter (blue). The data point and data cell are darker (red). The data cell and grid cells are equal in size and are centered on the data point and grid nodes, respectively. Four grid nodes surround the data point and are the ones relevant for the linear interpolation. The data cell areas falling into different grid cells are different in shade.

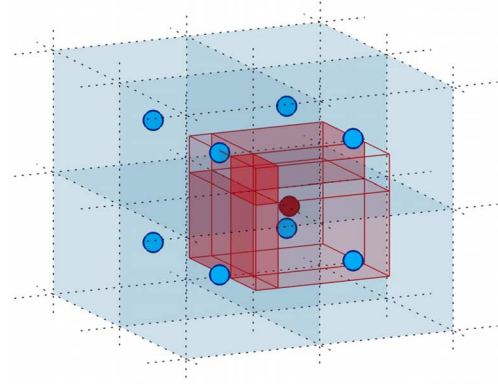


Fig. 3. 3D linear interpolation. The grid nodes and grid cells are lighter (blue). The data point and data cell are darker (red). The data cell and grid cells are equal in size and are centered on the data point and grid nodes, respectively. There are $8 = 2^3$ grid nodes around the data point. Consequently, the data cell is composed of eight volumes each falling into a different surrounding grid cell. The data cell volumes corresponding to different grid cells are depicted by different shades.

have analytical solution; therefore, they are solved numerically using computer simulation. Consequently, the process is defined by the mapping

$$(p_{1,l}, p_{2,l}, \dots, p_{i,l}, \dots, p_{n,l}) \rightarrow (f_{1,l}, f_{2,l}, \dots, f_{k,l}, \dots, f_{m,l}), \quad (1)$$

where $p_i, i = 1, 2, \dots, n$ are n input parameters, $f_k, k = 1, 2, \dots, m$ are m output parameters, $l = 1, 2, \dots, s$ are s simulated input-output state transfers, and $p_{i,l}$ and $f_{k,l}$ are the values of i -th input and k -th output parameters corresponding to the l -th state transfer. The input-output state transfer described by (1) can be written as the input-output matrix mapping

$$\mathbf{P}_{s \times n} \rightarrow \mathbf{F}_{s \times m}. \quad (2)$$

There are no restrictions regarding the choice of input and output parameters. Namely, input parameters are not necessarily test particle coordinates; they could be device or ambient related. Also, input parameters could be chosen for monitoring

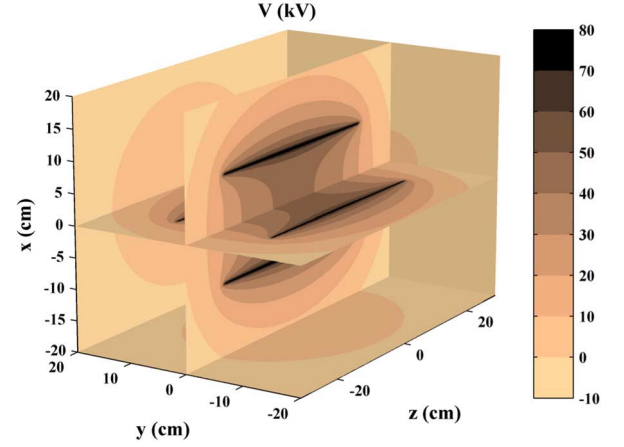


Fig. 4. Electric potential of four wires. The wires are each charged with charge density $Q' = 0.7 \mu\text{C}/\text{m}$. The resulting potential of the electrostatic field is shown in the $x = 0, y = 0, z = 30 \text{ cm}$, $x = -20 \text{ cm}$, and $y = 20 \text{ cm}$ planes.

the interaction process, i.e., they could be used as output parameters as well.

In order to enable interpolation, values of the input parameters cannot be chosen randomly. Each input variable, p_i , is represented by s_i values equally separated by Δp_i . Therefore, volume in the n -dimensional input variables phase space is sampled by $s_u = s_1 \cdot s_2 \cdot \dots \cdot s_n$ uniformly distributed points. For $s = s_u$, (2) becomes uniform input-output matrix mapping, which fully describes the investigated process.

B. N-Dimensional Linear Interpolation

Linear interpolation is a widespread method of obtaining the value of a function for the data point within a grid cell by using the function values corresponding to the grid cell nodes. The common formula for one-dimensional linear interpolation can be expressed in a way that at first seems less simple, but in fact enables simpler extension to the higher dimensions

$$f(x) = f(n_1) \cdot L_1(x)/L + f(n_2) \cdot L_2(x)/L. \quad (3)$$

The data point x falls between the nodes n_1 and n_2 , the length of the grid cell as well as of the cell drawn around the data point is L , whereas L_1 and L_2 are the segments of data point cell that fall into the grid cells corresponding to the nodes n_1 and n_2 , respectively. Fig. 1 illustrates one-dimensional linear interpolation.

If a function depends on two variables the data point is surrounded by four nodes, n_1, n_2, n_3 , and n_4 and the data cell area, P , is divided into four areas falling into four surrounding grid cells, P_1, P_2, P_3 , and P_4 . The value of a function in the data point is the sum of function values in the four nodes, $f(n_1), f(n_2), f(n_3)$, and $f(n_4)$, each scaled by the normalized data cell areas distributed in the four corresponding grid cells, $P_1(x, y)/P, P_2(x, y)/P, P_3(x, y)/P$, and $P_4(x, y)/P$, see Fig. 2,

$$f(x, y) = f(n_1) \cdot \frac{P_1(x, y)}{P} + f(n_2) \cdot \frac{P_2(x, y)}{P} + f(n_3) \cdot \frac{P_3(x, y)}{P} + f(n_4) \cdot \frac{P_4(x, y)}{P}. \quad (4)$$

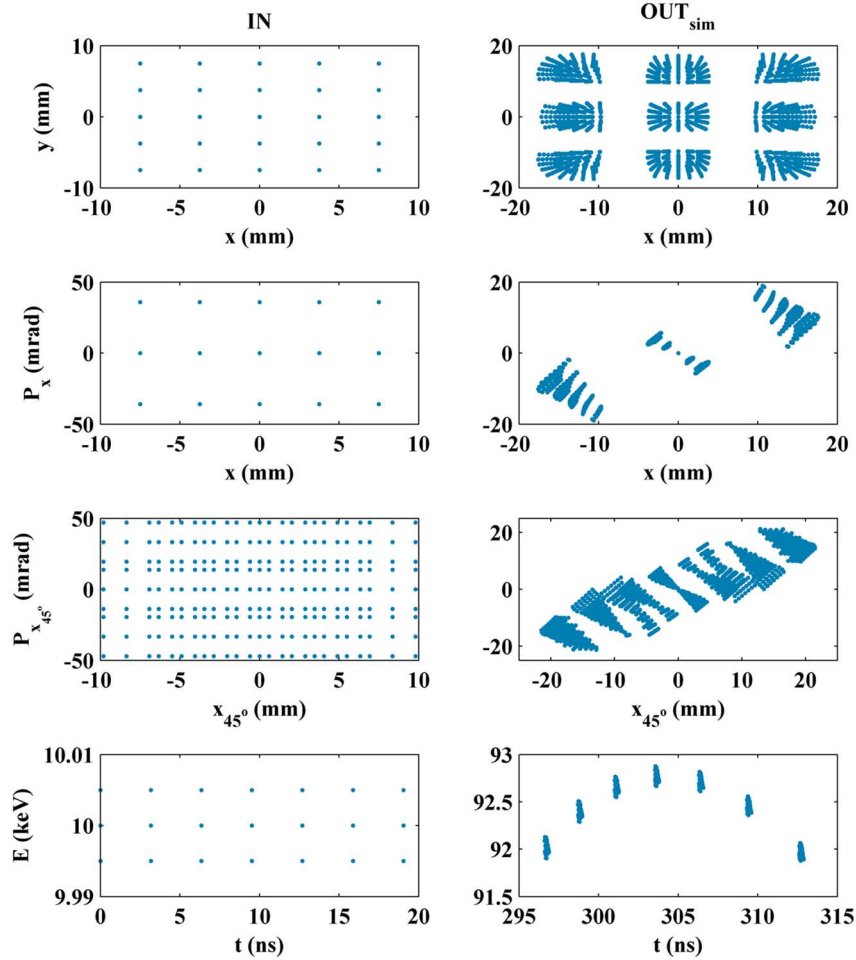


Fig. 5. Uniform input-output mapping. Six test particle's phase space coordinates used as input parameters, $n = 6$, are the spatial coordinates $x = p_1$ and $y = p_2$, normalized momentums, $P_x = p_3$ and $P_y = p_4$, energy, $E = p_5$, and time, $t = p_6$. The total of $s_u = s_1 \cdot s_2 \cdot s_3 \cdot s_4 \cdot s_5 \cdot s_6 = 5 \cdot 5 \cdot 3 \cdot 3 \cdot 3 \cdot 7 = 4725$ test particles is simulated. The same set of six variables is used as the output parameters, i.e., $m = n = 6$, $f_k = p_i$, for $k = i = 1, 2, \dots, 6$. Angular as well as spatial spreads of the beam caused by the normalized momentum are much larger than those induced by the spatial coordinate. The output energy depends mostly on the timing between the test ion and the accelerating RF voltage. The least influential parameter is the initial ion energy.

For a three dimensional function, $f(x, y, z)$, the areas become volumes, $V_j(x, y, z)$ and V , the number of nodes surrounding the data point increases to eight, $j = 1, 2, \dots, 8$, as shown in Fig. 3, and the linear interpolation formula becomes

$$f(x, y, z) = \sum_{j=1}^8 \left(f(n_j) \cdot \frac{V_j(x, y, z)}{V} \right). \quad (5)$$

Even though it is impossible to visualize further increase of phase space dimension it is easy to follow the sequence of (3)–(5) with the formula for n -dimensional linear interpolation

$$\begin{aligned} & f(p_1, \dots, p_i, \dots, p_n) \\ &= \frac{\sum_{j=1}^{2^n} \left(f(p_1(n_j), \dots, p_i(n_j), \dots, p_n(n_j)) \cdot V_j^{(n)} \right)}{V^{(n)}}, \quad (6) \end{aligned}$$

where

$$V_j^{(n)} = \prod_{i=1}^n (\Delta p_i - |p_i - p_i(n_j)|) \quad (7)$$

are parts of the n -dimensional volume of data point cell which fall into the j -th's node cell and

$$V^{(n)} = \prod_{i=1}^n \Delta p_i \quad (8)$$

is the n -dimensional volume of a node cell as well as of the data cell. Δp_i is the width of the cell corresponding to the i -th phase space coordinate, p_i ; $p_i(n_j)$ is the i -th coordinate of the j -th node, n_j .

The phase space coordinates, p_i , where $i = 1, 2, \dots, n$, are further treated as the input variables, whereas function f , is the output variable. Equations (6)–(8) are valid for any desired number of output variables, f_k , $k = 1, 2, \dots, m$; namely

$$\begin{aligned} & f_k(p_1, \dots, p_i, \dots, p_n) \\ &= \frac{\sum_{j=1}^{2^n} \left(f_k(p_1(n_j), \dots, p_i(n_j), \dots, p_n(n_j)) \cdot V_j^{(n)} \right)}{V^{(n)}}. \quad (9) \end{aligned}$$

Since j -th node, n_j , is defined by its n coordinates in the n -dimensional phase space, $n_j = (p_{1,j}, p_{2,j}, \dots, p_{n,j})$, expressions $f_k(p_1(n_j), \dots, p_n(n_j))$ under the sum in (9) are actually

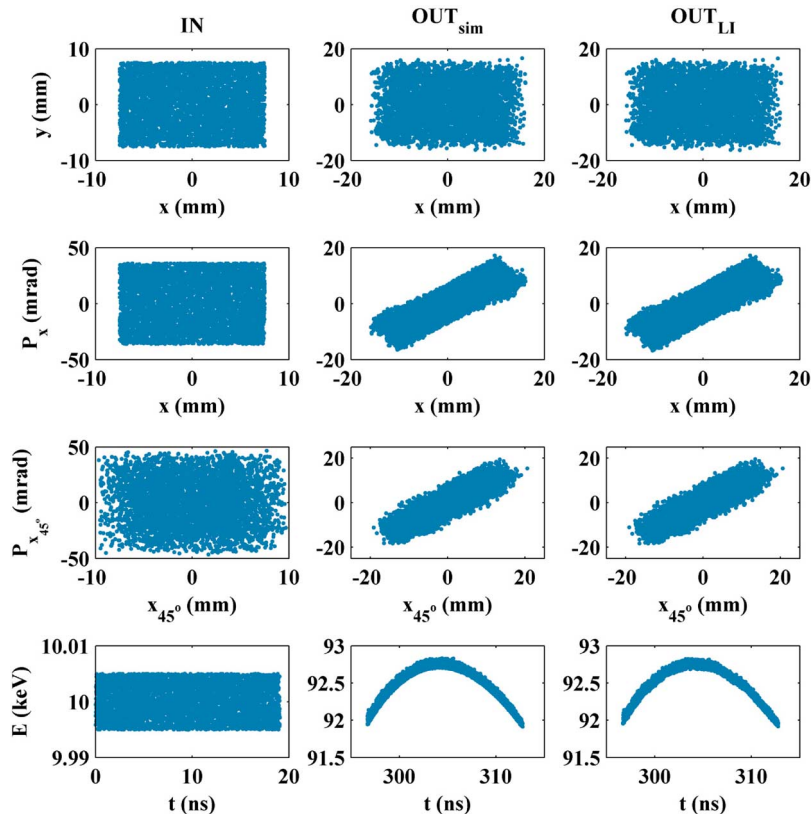


Fig. 6. Comparison between simulated and interpolated output. The same number of test particles, $s = s_u = 4725$, non-randomly distributed in Fig. 5, is randomly distributed here over the same intervals of input coordinates, as shown in the first column. The output depicted in the second column is the result of test ion trajectory simulations. Due to input data randomness all dependencies clearly visible in Fig. 5 are indistinguishable here. The results in the third column are obtained using the uniform input-output mapping depicted in Fig. 5, six-dimensional linear interpolation, and input data from the first column. The CPU time needed for linear interpolation is 24 times shorter than the one used up for trajectory simulations. The largest mean error of the interpolated results is 0.9 %, see Table I.

$f_k(p_{1,j}, p_{2,j}, \dots, p_{n,j})$, i.e., they are each equal to (1). Consequently, $f_k(p_{1(n_j)}, \dots, p_{n(n_j)})$ are 2^n out of s rows in (2) and represent a bound between the uniform input-output matrix mapping given by (2) and the n -dimensional linear interpolation defined by (9).

III. RESULTS

To illustrate the method as well as to obtain quantitative validation of its efficiency, interaction of ion beams with two devices is used. The first device is composed of four parallel, equally charged wires positioned along the edges of imaginary quadratic prism. Ion beam travels parallel to the wires along the prism axis. In the second example ion beam direction is changed from vertical to horizontal using a device known in cyclotron physics as the spiral inflector.

Test ion trajectories are simulated using the self-made software package VINDY [17], n -dimensional linear interpolation and post-processing is done in MATLAB, whereas electric field

of the spiral inflector is determined with the commercially available software package WIPL-D [18]. All computations are performed on a PC with 1.86 GHz CPU and 1.98 GB of RAM.

A. Four Finite Wires

Interaction between a proton beam and an electric field of finite wires whose charge varies in time is used as an illustration of the proposed method. Four parallel, $L_w = 40$ cm long wires, each two adjacent positioned $d_w = 12$ cm apart are shown in Fig. 4.

Electric field is calculated using analytical formulas for uniformly charged finite wires. However, because of its scalar nature, electric potential is easier to represent graphically and formula it is defined with is shorter. Consequently, instead of for the electric field, we give the formula for the electric potential of four finite wires in (10), shown at the bottom of the page, where Q' is charge density and pairs (x_{wi}, y_{wi}) are wire coordinates equal to $(d_w/\sqrt{2}, 0)$, $(0, d_w/\sqrt{2})$, $(-d_w/\sqrt{2}, 0)$, and $(0, -d_w/\sqrt{2})$ for $i = 1, 2, 3$, and 4, respectively. In Fig. 4 five

$$V(x, y, z) = \frac{Q'}{4\pi\epsilon_0} \cdot \sum_{i=1}^4 \ln \frac{(z + L_w/2) + \sqrt{(x - x_{wi})^2 + (y - y_{wi})^2 + (z + L_w/2)^2}}{(z - L_w/2) + \sqrt{(x - x_{wi})^2 + (y - y_{wi})^2 + (z - L_w/2)^2}}, \quad (10)$$

TABLE I
INTERPOLATION ERRORS FOR FINITE WIRES EXAMPLE

k	$\max(f_k^{\text{LI}} - f_k^{\text{sim}})$	$\frac{\max(f_k^{\text{LI}} - f_k^{\text{sim}})}{\max(f_k^{\text{sim}}) - \min(f_k^{\text{sim}})}$	$(f_k^{\text{LI}} - f_k^{\text{sim}})$	$\frac{(f_k^{\text{LI}} - f_k^{\text{sim}})}{\max(f_k^{\text{sim}}) - \min(f_k^{\text{sim}})}$
1	0.181 mm	0.564 %	0.027 mm	0.086 %
2	0.194 mm	0.591 %	0.027 mm	0.083 %
3	0.738 mrad	2.191 %	0.122 mrad	0.362 %
4	0.792 mrad	2.387 %	0.121 mrad	0.363 %
5	0.029 keV	3.183 %	0.008 keV	0.920 %
6	0.061 ns	0.382 %	0.034 ns	0.213 %

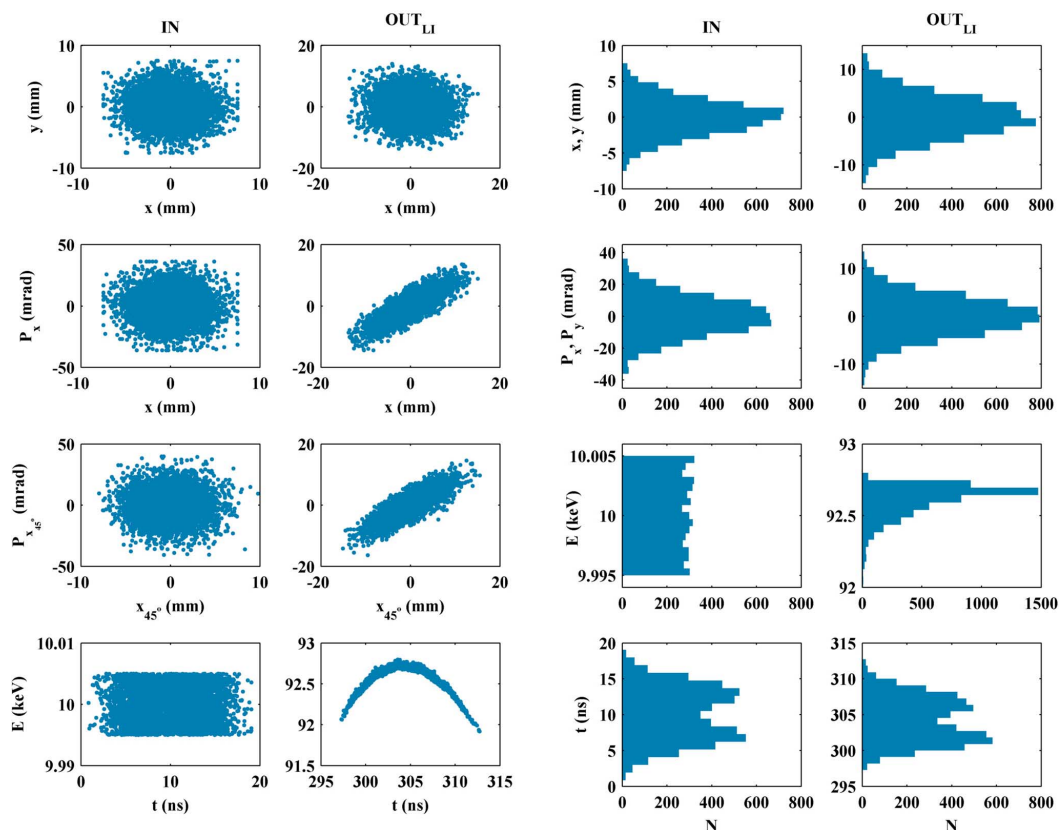


Fig. 7. Interpolated output from desired input. The uniform input-output mapping depicted in Fig. 5 is used to linearly interpolate output corresponding to $s = 5000$ sets of input parameters. The obtained non-uniform input-output mapping is shown in first two columns following the form accepted in Figs. 5 and 6. Each of the six input parameters is chosen to follow its own realistic distribution defined by the histograms in third column. After the interaction with the device the output parameters are distributed according to the histograms in fourth column. Note that this six-dimensional linear interpolation is performed in less than 11 s.

sample planes are used to illustrate this electric potential. It is assumed that the voltage alternating in time with radio frequency $f_{\text{RF}} = 2.8$ MHz at its peak provides equal charge density along each wire, $Q' = 0.7 \mu\text{C}/\text{m}$. The resulting time dependent electric field can be treated as quasi static. A beam of protons travels along the z -axis from $z = -40$ cm to $z = 40$ cm. The described device acts as an ion beam accelerator; it increases ion energy more than nine times [19].

Six test particle's phase space coordinates used as input parameters are the spatial coordinates x and y , normalized momentums, P_x and P_y , energy, E , and time, t . Because of the fourfold symmetry of the device and axial beam symmetry $x - P_x$ and $y - P_y$ graphs are identical. Therefore, for data presentation purposes $y - P_y$ graphs are replaced with $x_{45^\circ} - P_{x_{45^\circ}}$ graphs, where x_{45° is the axis rotated clockwise 45° with respect to the x -axis in the $x - y$ plane. The same set of variables is used as the output parameters, as well.

The uniform input-output mapping obtained with computer simulation of test ion trajectories traveling through the de-

scribed device is shown in Fig. 5. Due to overlapping of test ion images, the number of considered test ions appears to be much smaller than it is. However, more importantly, the results reveal relationships between input and output variables essential for understanding ion beam acceleration and focusing caused by the considered device.

If the initial coordinates of the same number of test ions are random numbers uniformly distributed over the same ranges of initial coordinates as in Fig. 5, the test ions images do not overlap and are all visible; consequently, the graphical presentation of the studied interaction is much richer as seen in the first two columns in Fig. 6. However, all the dependencies that are so clear for non-random input become invisible when randomness of input data is introduced.

The same uniformly distributed random input is used to obtain simulated output as well as linearly interpolated output. The obtained results are compared in Fig. 6. The CPU time used up for trajectory simulations is 244.4 s compared to 10.1 s needed for six-dimensional linear interpolation corresponding to the

same input data. Consequently, it can be concluded that once the uniform non-random input-output mapping is simulated, the linear interpolation of the outcome of any subsequent interaction between the ion beam and the four finite wires is roughly 24 times faster than is the simulation of the same interaction. If the simulated results are taken as accurate the errors of the interpolated output are given in Table I. The uniform input-output mapping which is the basis for six-dimensional linear interpolation is performed for $s_{in} = 4725$ sets of input parameters. Therefore, the initial phase space volume is on average sampled with less than 4.1 samples per coordinate.

The suggested method can be used to obtain the response of the system to any desired input. For the example shown in Fig. 7 initial coordinates are chosen to be random numbers whose density follows common distributions. The spatial and angular input coordinates follow Gaussian distribution, initial energy is distributed uniformly, whereas time, i.e., the moment of arrival of a test particle at the initial plane, $z = -40$ cm, follows the distribution with two peaks which resembles the characteristic output of the device known as the ion beam buncher.

B. Spiral Inflector

The spiral inflector is commonly used in cyclotrons to inflect an ion beam from the vertical injection channel to the horizontal median plane between the poles of a cyclotron magnet [20]–[23]. This device has two electrodes whose electric potentials have the same value but are of opposite sign. Due to a complex form of its electrodes spiral inflector can be viewed as an extravagantly shaped capacitor. Five parameters used to define this complicated geometry are the height, A , radius, R_m , tilt parameter, k' , distance between electrodes d_0 , and electrodes' width, a . The first three parameters define the spiral inflector axis, i.e., the analytical central ion trajectory through the inflector [21]:

$$\begin{aligned} x(b) &= \frac{A}{2} \left[\frac{2}{1 - (A/R_m + k')^2} + \frac{\cos((A/R_m + k' - 1)b)}{A/R_m + k' - 1} - \frac{\cos((A/R_m + k' + 1)b)}{A/R_m + k' + 1} \right], \\ y(b) &= \frac{A}{2} \left[\frac{\sin((A/R_m + k' + 1)b)}{A/R_m + k' + 1} - \frac{\sin((A/R_m + k' - 1)b)}{A/R_m + k' - 1} \right], \\ z(b) &= A \sin(b) - A \end{aligned} \quad (11)$$

where $0 \leq b \leq \pi/2$ is an angle between z -axis and ion velocity along the trajectory. These equations, d_0 , and a define the surfaces of spiral inflector electrodes, which are used in WIPL-D [18] to calculate electric field of the device in the nodes of a 3D grid. Further, the electric field in an arbitrary point along a test particle trajectory is interpolated by the three-dimensional linear interpolation. The spiral inflector shown in Fig. 8 is designed for D^- ions and magnetic field of $B = 1.84$ T. As was the case with the finite wires example, for graphical presentation purposes electric field is replaced by the corresponding electric potential because of its easier visualization.

In reality the central trajectory through the spiral inflector does not follow its analytical path and it usually ends up slightly off the median plane of a cyclotron. The vertical coordinate of the real central trajectory after it leaves the inflector is adjusted

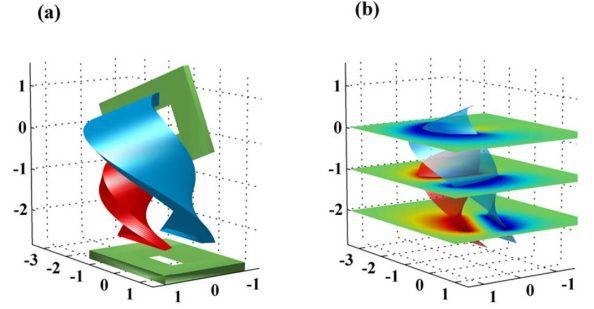


Fig. 8. Spiral inflector electrodes and potential. (a) Electrodes. The two electrodes are defined by the height, $A = 2.27$ cm, and exit radius, $R_m = 1.61$ cm, of analytical central trajectory, tilt parameter, $k' = 0.43$, gap between electrodes, $d_0 = 0.8$ cm, and electrodes' width expressed with respect to the gap between them, $a = 2$. The two grounded plates positioned $d_0/2$ away from the inflector entrance and exit have rectangular openings parallel to the inflector entrance and exit. (b) Potential. The potentials of the electrodes are $+V_0$ and $-V_0$. The signs of the electrodes are adjusted according to the electric charge sign of the ion beam that is being inflected. The electric potential corresponding to the electric field calculated with WIPL-D is given in three horizontal planes, $z = -1.9$ cm, -0.9 cm, and 0.1 cm. The inflector electrodes are indicated as their transparent inner surfaces.

to be in the median plane by fine-tuning the inflector voltage. This procedure causes the inflector voltage, V_0 , to emerge as one of the input parameters in a study of ion beam interaction with the inflector. In the finite wires example input as well as output variables were all related to an ensemble of particles. Here, in the spiral inflector example, a device parameter, the inflector voltage, is used as an input parameter. Since the median plane of a cyclotron coincides with $z = 0$, z coordinate of test ions is the output parameter used for monitoring the proper placement of the inflected beam.

Because of the problem geometry, phase space coordinates of a test ion used as input as well as output parameters are given with respect to the inflector axis, i.e., with respect to the analytical central trajectory. The h and u axes, which are tied up to the analytical central trajectory are perpendicular to it as well as to each other. Additionally, h -axis is perpendicular whereas, u -axis is parallel to the electric field of the inflector. The initial and final positions of test ions are at the inflector entrance and exit, respectively. The inflector voltage does not change in time; therefore, the output does not depend on the initial time and consequently, time is not amongst the input parameters. However, a spiral inflector does affect the time a test ion spends inside this device; therefore, time is one of the considered output parameters.

The uniform input-output mapping corresponding to the spiral inflector example is shown in the first two columns in Fig. 9. The obtained uniform input-output mapping and six-dimensional linear interpolation are used further to attain the interpolated output, which is then compared to the simulated output in Fig. 9 as well. The input parameters for the two sets of compared results are chosen in such a way to insure the largest interpolation error. For linear interpolation the largest discrepancy between the accurate and the interpolated value is most likely to occur at the midpoint of interpolation interval. Consequently, the input parameters used to obtain the two outputs for the comparison are equally spaced as well as those input parameters corresponding to the uniform input-output mapping; however, the spacing in the former is half the one used for the later. The output corresponding to the simulated test ion trajectories is taken to be accurate and the errors of the interpolated output are given in Table II. The averaged errors

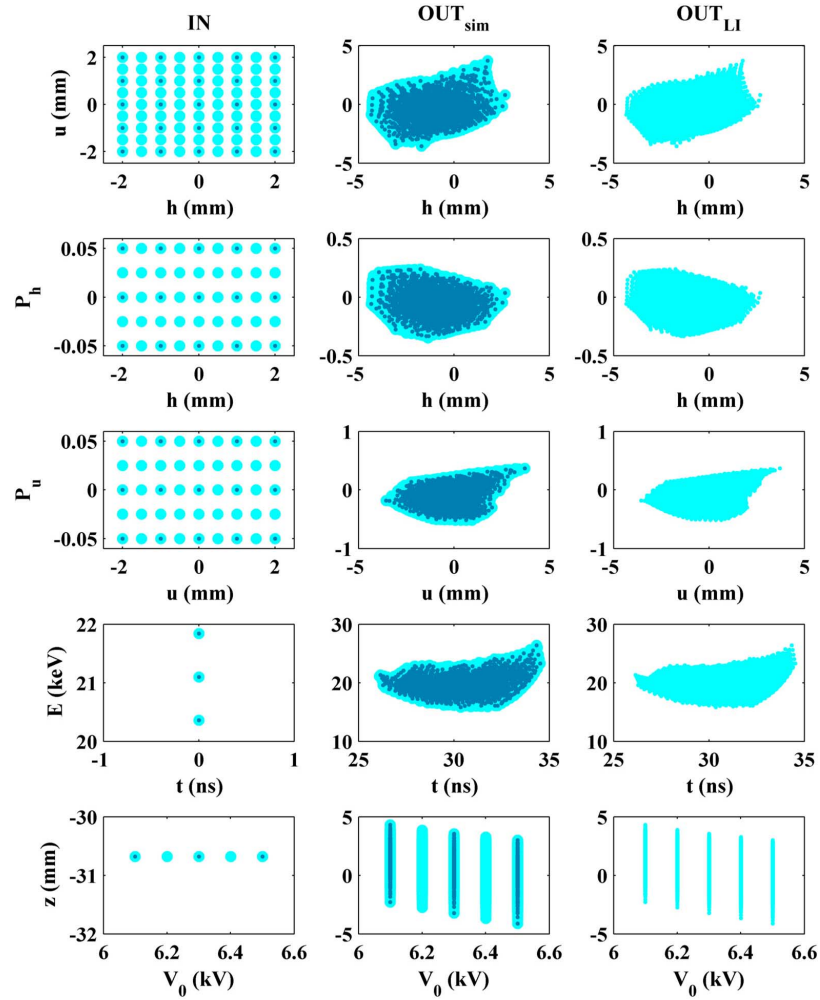


Fig. 9. Uniform input-output mapping and comparison between simulated and interpolated output. Six variables are used as input parameters, $n = 6$. Five of them are test particle related coordinates: the spatial coordinates $h = p_1$ and $u = p_2$, normalized momentums, $P_h = p_3$ and $P_u = p_4$, and energy, $E = p_5$. The sixth input parameter, the spiral inflector voltage, $V_0 = p_6$ is device related. The first five out of seven output parameters, $m = 7$, are equal to the first five input parameters, i.e., $f_k = p_i$, for $k = i = 1, 2, \dots, 5$. The sixth and seventh output variables are the duration of interaction, $t = p_6$, and vertical coordinate of a test ion, $z = p_7$. The uniform input-output mapping depicted in the first and second column with dark dots corresponds to the total of $s_u = s_1 \cdot s_2 \cdot s_3 \cdot s_4 \cdot s_5 \cdot s_6 = 5 \cdot 5 \cdot 3 \cdot 3 \cdot 3 \cdot 3 = 2025$ simulated test particles. The simulated and linearly interpolated output shown with light dots in the second and third column, respectively, correspond to uniformly distributed $s = s_1 \cdot s_2 \cdot s_3 \cdot s_4 \cdot s_5 \cdot s_6 = 9 \cdot 9 \cdot 5 \cdot 5 \cdot 3 \cdot 5 = 30375$ sets of input parameters depicted by light dots in the first column. The CPU time needed for linearly interpolated output is 62.3 s. This is 17.0 times less than 1058.4 s used up to track 30375 test ion trajectories for the simulated output. The largest mean error of the interpolated results is 0.7 %, see Table II.

given in the last two columns are calculated after the exclusion of the accurate interpolated results that correspond to the input data sets identical to those of the uniform input-output mapping. Consequently, the number of data sets considered in error calculations is $s - s_u = 28350$. The six-dimensional linear interpolation of interpolated output is based on the uniform input-output mapping corresponding to less than 3.6 samples per coordinate.

The dependence $z(V_0)$ given in the graph in the fifth row of second column in Fig. 9 is used to determine that the inflector second value which provides the best horizontality of the beam after the inflector is $V_0 = 6.4$ kV. Once the proper value of the inflector voltage is determined the number of input and output parameters as well as the degree of linear interpolation in further studies decreases. The inflector voltage, V_0 , and vertical position of a test ion, z , are not observed anymore; therefore, the number of input and output variables is now $n = 5$ and $m = 6$, respectively. The uniform input-output mapping now has $s_u = s_1 \cdot s_2 \cdot s_3 \cdot s_4 \cdot s_5 = 5 \cdot 5 \cdot 3 \cdot 3 \cdot 3 = 675$ sets of

data, which is less than 3.7 sample values per coordinate. This smaller set of simulated data is used to illustrate various dependencies between input and output variables in Fig. 10.

Comparison between Figs. 9 and 5 reveals that dependencies between input and output variables in the spiral inflector example are not nearly as easily distinguishable as is the case with the four finite wires example. Therefore, in Fig. 10 relationships between variables are visually set apart by using different colors as well as different symbols for specifically chosen subsets of data. The template data depicted with the smallest dots in Fig. 10 in the first and second column is identical to the data in the third and fourth column, respectively. Larger symbols of different colors are simply used to emphasize chosen parts of the existing data set. The similarities between the second row of the first two columns and the third row of the last two columns as well as between the third row of the first two columns and the second row of the last two columns indicate that the spatial and angular coordinates in h and u direction are coupled. Further, vague similarities in shapes between the graphs $g_{1,1}$

TABLE II
 INTERPOLATION ERRORS FOR SPIRAL INFLECTOR EXAMPLE

k	$\max(f_k^{\text{LI}} - f_k^{\text{sim}})$	$\frac{\max(f_k^{\text{LI}} - f_k^{\text{sim}})}{\max(f_k^{\text{sim}}) - \min(f_k^{\text{sim}})}$	$(f_k^{\text{LI}} - f_k^{\text{sim}})$	$\frac{(f_k^{\text{LI}} - f_k^{\text{sim}})}{\max(f_k^{\text{sim}}) - \min(f_k^{\text{sim}})}$
1	1.283 mm	17.648 %	0.048 mm	0.664 %
2	0.680 mm	9.688 %	0.031 mm	0.444 %
3	0.115 rad	12.975 %	2.346 mrad	0.266 %
4	0.064 rad	10.871 %	1.271 mrad	0.216 %
5	1.474 keV	13.981 %	0.078 keV	0.744 %
6	0.928 ns	11.021 %	0.020 ns	0.244 %
7	1.371 mm	16.285 %	0.056 mm	0.659 %

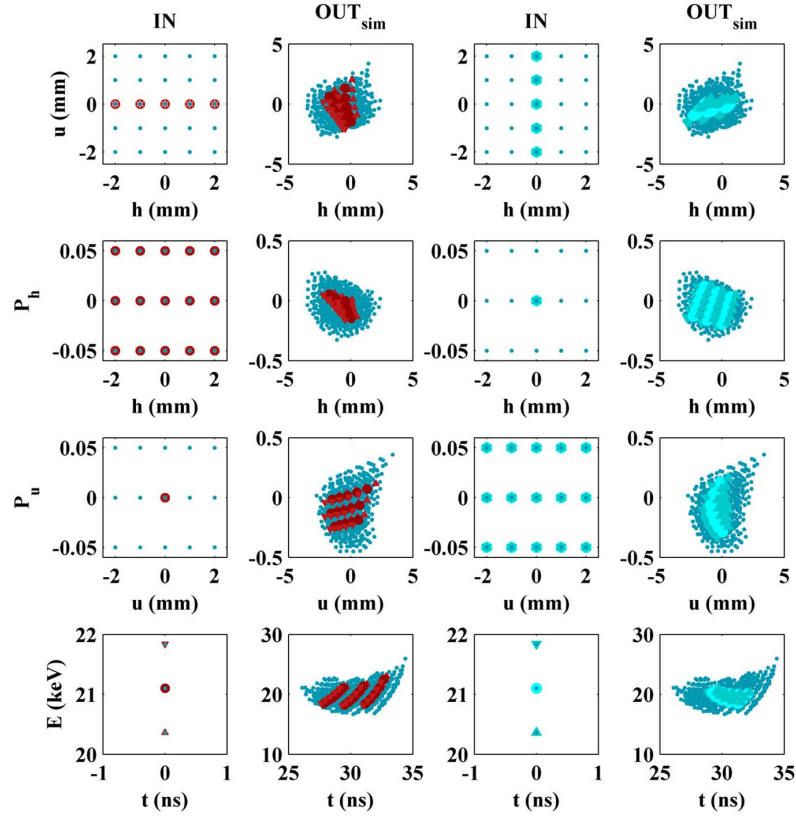


Fig. 10. Uniform input-output mapping for $n = 5$ and $m = 6$. Five test particle phase space coordinates used as input parameters, $n = 5$, are the spatial coordinates $h = p_1$ and $u = p_2$, normalized momenta, $P_h = p_3$ and $P_u = p_4$, and energy, $E = p_5$. The first five of six output variables, $m = 6$, are equal to the input parameters, i.e., $f_k = p_i$, for $k = i = 1, 2, \dots, 5$. The sixth output parameter is time, $t = f_6$. The total of $s_u = s_1 \cdot s_2 \cdot s_3 \cdot s_4 \cdot s_5 = 5 \cdot 5 \cdot 3 \cdot 3 \cdot 3 = 675$ test particles is marked with the smallest dots in all four columns. Subset of data defined by $(p_2 = u = 0 \text{ mm} \wedge p_4 = P_u = 0)$ is emphasized by larger darker (red) symbols in first and second column. The condition $(p_1 = h = 0 \text{ mm} \wedge p_3 = P_h = 0)$ determines the second subset of data highlighted by larger lighter (cyan) symbols in third and fourth column. Each of these two subsets is further divided into three subsets defined with $p_5 = E = 20.4 \text{ keV}$, 21.1 keV , and 21.8 keV , marked by upper triangle, circle, and lower triangle, respectively. The influences of input variables on the output variables are all of comparable intensity. Angular as well as spatial coordinates in the h direction are coupled with those directed along the u -axis.

and $g_{1,4}$, as well as $g_{1,3}$ and $g_{1,2}$, may indicate that the coordinates h and u exchange their roles in the input and output planes, where $g_{c,r}$ represents the graph in the c -th column and r -th row in Fig. 10. Similarly, vague resemblances in shapes between the graphs $g_{2,1}$ and $g_{3,2}$, as well as $g_{3,3}$ and $g_{2,4}$, may point toward role exchange in the input and output planes not only between h and u , but between P_h and P_u , as well. Note that the results shown in Fig. 10 are obtained by test ion trajectory simulations and are a subset of the results depicted by dark dots in Fig. 9.

As was the case with the finite wires example, here as well we illustrate the applicability of our method to realistically distributed test particles within an ensemble. An ensemble of $s = 50000$ test ions randomly distributed over their input parameters is used to perform the five-dimensional output interpolation

from the uniform input-output mapping of $s_u = 675$ test ions depicted in Fig. 10. The results are shown in Fig. 11. In addition, to demonstrate the flexibility of the method, the ion beam parameters tied up to the central trajectory are transformed from, h, u, P_h , and P_u , given in the Cartesian coordinate system into r, θ, P_r and P_θ given in the polar coordinate system.

The data related to the performance of our method in all examples considered so far is summarized in Table III. The performances of simulation and linear interpolation are expressed as CPU times, t_{sim} and t_{LI} , as well as CPU times per number of test particles, t_{sim}/s and t_{LI}/s , respectively. The uniform input-output mapping used to perform n -dimensional linear interpolation has n input parameters, m output parameters, s_u state transfers and $\sqrt{s_u}$ sample values per input parameter. The efficiency

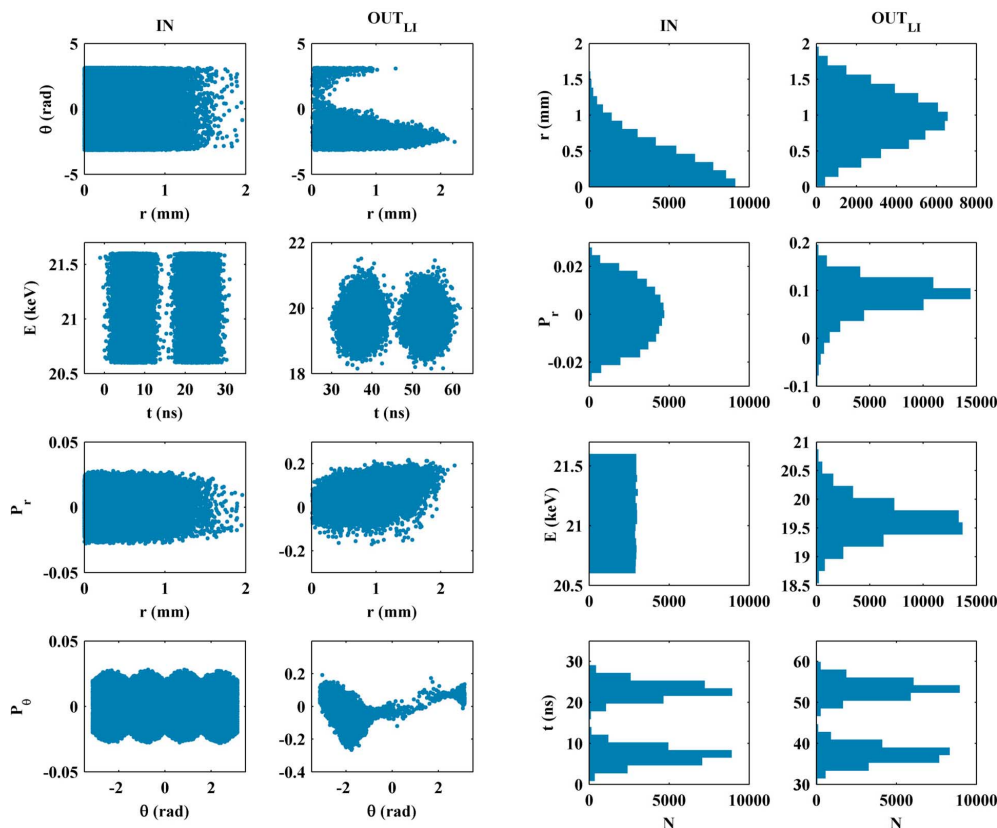


Fig. 11. Interpolated output corresponding to desired input. The uniform input-output mapping with $s_u = 675$ depicted in Fig. 10 is used to linearly interpolate output corresponding to $s = 50000$ sets of input parameters. The obtained mapping of the desired input into the corresponding output is shown in the first two columns. The input parameters are chosen to follow realistic distributions defined by the histograms in third column. After the interaction with the spiral inflector the output parameters are distributed according to the histograms in fourth column. Note that this five-dimensional linear interpolation and coordinate transformation from the Cartesian to the polar system is performed in less than 90 s.

TABLE III
PERFORMANCE AND EFFICIENCY OF PROPOSED METHOD

Example	n	m	s_u	$n\sqrt{s_u}$	s	t_{sim} (s)	t_{sim}/s (ms)	t_{LI} (s)	t_{LI}/s (ms)	t_{sim}/t_{LI}	
1	wires	6	6	4725	4.1	4725	244.4	51.7	10.1	2.1	24.2
2	wires	6	6	4725	4.1	5000	—	—	10.7	2.1	—
3	inflector	6	7	2025	3.6	30375	1058.4	34.8	62.3	2.1	17.0
4	inflector	5	6	675	3.7	50000	—	—	89.7	1.8	—

of the proposed method is measured by the ratio t_{sim}/t_{LI} . The data in rows 1, 2, 3, and 4 correspond to the results shown in Figs. 6, 7, 9 and 11, respectively.

In order to investigate the influence of various parameters on the performance and efficiency of the proposed method a number of additional examples are considered and the obtained results are shown in Fig. 12. The value of s_u chosen for solving a particular problem is a tradeoff between the accuracy and the efficiency of the interpolation. For both of the two discussed devices $s_u = 2025$ seems to be a reasonable choice. Consequently, it is safe to conclude that n -dimensional linear interpolation is approximately 20 times faster than test particle trajectory simulations in the spiral inflector study, whereas for the finite wires example this efficiency indicator is larger than 30.

Our intention was not to solve the two problems but rather to use the two examples to illustrate usefulness of the proposed method. When solving a particular problem the accuracy of our approach can be improved by decreasing the step sizes of the non-random, uniformly distributed data as well as by using a higher-order interpolation scheme. A systematic approach for constructing high order spline interpolation methods used to in-

terpolate fields given at rectangular spatial grids is presented in [24]. Similar schemes can be used to obtain more accurate output data for any chosen initial distribution based on evenly spaced input data mapping. Nevertheless, the trade-off between the gain in calculation accuracy and the resulting increase in computational times imposes that the order of the interpolation scheme should be kept as low as practical.

IV. CONCLUSION

It is shown that, unlike commonly used random distribution, non-random, uniform distribution of input variables is very efficient in studying dependencies between variables. Its disadvantage of being unrealistic is overcome by interpolating output corresponding to any desired distribution of input variables from once obtained non-random uniform input-output mapping. A multidimensional interpolation had been used in simulations of spatial and/or temporal advances of a studied system to provide more accurate ambient conditions given in equally spaced grid points of a 3D spatial grid. To the best of our knowledge, our extension of this application of a multidimensional interpolation to interpolating output data

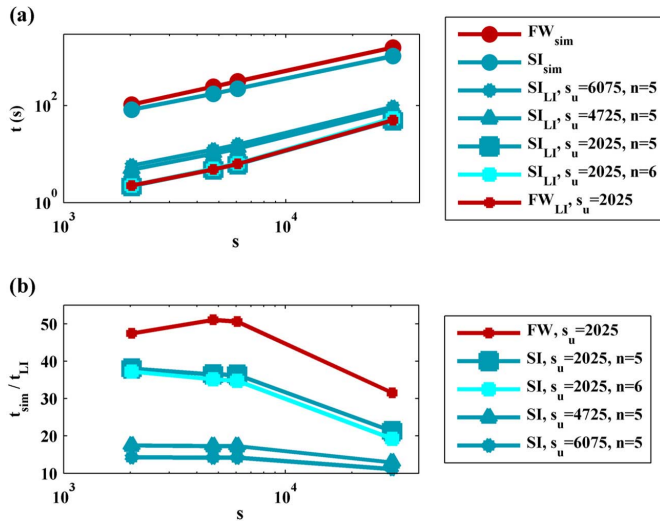


Fig. 12. Performance and efficiency of proposed method. Interactions between s test ions and the four finite wires, FW, as well as the spiral inflector, SI, are simulated, sim, and linearly interpolated, LI. The n -dimensional linear interpolation is based on s_u uniform input-output state transfers. The performance given as CPU time, t , is shown in the upper graph, (a). For FW as well as SI examples t is more than an order of magnitude larger for sim than for LI. It increases with s as well as with s_u and seems to be unaffected by n . Note that the three curves corresponding to $s_u = 2025$ are approximately equal. The lower graph, (b), gives the efficiency of the proposed method expressed as the ratio between the CPU time needed for n -dimensional linear interpolation and the CPU time used up to simulate trajectories of the same number of test particles, t_{sim}/t_{LI} . Efficiency for FW is larger than for SI, it decreases with the increase of s_u and slightly decreases for larger n .

corresponding to any chosen distribution of input data from the evenly spaced input-output data mapping has not been discussed before. The order of the interpolation is equal to the number of input variables. We used the simplest and fastest of all interpolation schemes, the linear interpolation, to illustrate application of five- as well as six-dimensional interpolation to solving two sample problems. It is shown that the efficiency of the method is more than an order of magnitude larger compared to the simulation of input-output transfer. If the sampling grid is as coarse as less than four samples per dimension the accuracy achieved in the two considered examples is better than 1%. The accuracy of our approach can be improved by decreasing the step sizes of the non-random, uniformly distributed data as well as by using a higher-order interpolation scheme. Although the proposed approach to solving problems is illustrated using interactions between ion beams and two devices, the method could be implemented in state transfer studies of wide varieties of systems. However, it should be emphasized that the method is applicable only if internal forces between particles within an ensemble are negligible compared to the forces caused by external fields, devices or ambiances. Therefore, further improvement could include development of a similar method for problems with strong internal forces within the studied ensemble as well as application of n -dimensional non-linear interpolation.

REFERENCES

[1] A. Kponou, A. Pikin, E. Beebe, J. Alessi, and L. Liljebj, "Determining the acceptance of the Brookhaven EBIS test stand for primary ions by computer simulation," in *Proc. Ninth Int. Symp. on Electron Beam Ion Sources and Traps*, Japan, 2004, vol. 2, no. 1, pp. 165–172, 2004.

[2] P. N. Ostroumov and K. W. Shepard, "Multiple-charge beam dynamics in an ion linac," *Phys. Rev. ST—Accelerators and Beams*, vol. 3, no. 3, p. 030101, Mar. 2000.

[3] T. Zhang, Z. Li, and C. Chu, "CYCIAE-100, a 100 MeV H^- cyclotron for RIB production," *Nucl. Instrum. Meth. Phys. Res. Sec. B*, vol. 261, no. 1–2, pp. 1027–1031, Aug. 2007.

[4] A. A. Geraci and D. H. Whittum, "Transverse dynamics of a relativistic electron beam in an underdense plasma channel," *Phys. Plasmas*, vol. 7, no. 8, pp. 3431–3440, Aug. 2000.

[5] T. Furukawa and K. Noda, "Compensation of the asymmetric phase-space distribution for a slowly extracted beam from a synchrotron," *Nucl. Instrum. Meth. Phys. Res. Sec. A*, vol. 565, no. 2, pp. 430–438, Sept. 2006.

[6] E. Henestroza, S. Yu, M. C. Vella, and W. M. Sharp, "Simulations of channel-based final beam transport," *Nucl. Instrum. Meth. Phys. Res. Sec. A*, vol. 415, no. 1, pp. 186–192, Sept. 1998.

[7] S. A. Bogacz and V. A. Lebedev, "Recirculating linacs for a neutrino factory—Arc optics design and optimization," *Nucl. Instrum. Meth. Phys. Res. Sec. A*, vol. 472, no. 3, pp. 528–532, Oct. 2001.

[8] J. L. Ristić-Djurović, "Gyroresonant Scattering of Radiation Belt Electrons by Oblique Whistler Waves," Ph.D. dissertation, Dept. Elect. Eng., Stanford Univ., Stanford, CA, May 1993.

[9] J. L. Ristić-Djurović, T. F. Bell, and U. S. Inan, "Precipitation of radiation belt electrons by magnetospherically reflected whistlers," *J. Geophys. Res.*, vol. 103, no. A5, pp. 9249–9260, May 1998.

[10] J. Ristić-Djurović and N. Nešković, "Energy and time spreads of the ion beam caused by the spiral inflector," *Nucl. Instrum. Meth. Phys. Res. Sec. A*, vol. 406, no. 1, pp. 172–176, Mar. 1998.

[11] J. L. Ristić-Djurović and S. Ćirković, "Unidirectional stripping extraction from a cyclotron which accelerates light as well as heavy ions," *Phys. Rev. ST—Accelerators and Beams*, vol. 6, no. 3, p. 033501, Mar. 2003.

[12] A. Ž. Ilić, J. L. Ristić-Djurović, S. Ćirković, and N. Nešković, "Enhancement of ion beam acceleration efficiency in isochronous cyclotrons," *IEEE Trans. Nucl. Sci.*, vol. 59, no. 2, pp. 272–280, Apr. 2012.

[13] A. Papoulis, *Probability, Random Variables, and Stochastic Processes*. Tokyo: McGraw-Hill Kogakusha, Ltd, 1965, ch. 4.

[14] W. J. Rugh, *Linear System Theory*, 2nd ed. Upper Saddle River, NJ: Prentice Hall, 1996.

[15] D. Sundararajan, *A Practical Approach to Signals and Systems*. Singapore: Wiley, 2008.

[16] W. H. Press, S. A. Teukolsky, W. T. Vetterling, and B. P. Flannery, *Numerical Recipes in C: The Art of Scientific Computing*. Cambridge: Cambridge Univ. Press, 1993.

[17] J. Ristić-Djurović, N. Nešković, and S. Ćirković, "Compound particle tracking algorithm: Application to the foil stripping extraction system design," in *Proc. of the Sixth International Computational Accelerator Physics Conference*, Darmstadt, Germany, Sep. 11–14, 2000 [Online]. Available: <http://www.icap2000.de/frames/index.htm>, Available:

[18] "WIPL-D microwave," Software and User's Manual. Belgrade, Serbia, 2005, WIPL-D d.o.o.

[19] J. L. Ristić-Djurović, A. Ilić, and S. Ćirković, Finite Wire Accelerator Dec. 2011, Internal report, INN Vinča.

[20] L. W. Root, "Design of an Inflector for the TRIUMF Cyclotron," M.Sc. thesis, Dept. of Phys., The Univ. British Columbia, Vancouver, Canada, Apr. 1972.

[21] L. W. Root, "Experimental and Theoretical Studies of the Behaviour of an H^- Ion Beam During Injection and Acceleration in the TRIUMF Central Region Model Cyclotron," Ph.D. dissertation, Dept. of Phys., The Univ. British Columbia, Vancouver, Canada, Apr. 1974.

[22] T. Zhang, H. Yao, F. Guan, C. Chu, Y. Lu, X. Jia, J. Zhong, J. Yang, J. Xing, and Y. Lin, "Spiral inflector and central region study for three cyclotrons at CIAE," *Nucl. Instrum. Meth. Phys. Res. Sec. B*, vol. 261, no. 1–2, pp. 60–64, Aug. 2007.

[23] Y. Zhang and G. D. Alton, "Electric field distribution in a spiral inflector for cyclotron injection applications," in *Proc. Particle Accelerator Conf.*, Portland, Oregon, May 12–16, 2003.

[24] C. C. Lalescu, B. Teaca, and D. Carati, "Implementation of high order spline interpolations for tracking test particles in discretized fields," *J. Comput. Phys.*, vol. 229, no. 17, pp. 5862–5869, Aug. 2010.



ELSEVIER

Contents lists available at [SciVerse ScienceDirect](http://www.sciencedirect.com)

Nuclear Instruments and Methods in Physics Research A

journal homepage: www.elsevier.com/locate/nima

Minimization of the measurement errors induced by the cyclotron magnetic field measurement system

Saša Ćirković*, Andjelija Ž. Ilić, Aleksandar Dobrosavljević, Roman Balvanović, Jasna L. Ristić-Djurović

Laboratory of Physics 010, Vinča Institute of Nuclear Sciences, University of Belgrade, PO Box 522, 11001 Belgrade, Serbia

ARTICLE INFO

Article history:

Received 15 December 2011

Received in revised form

27 February 2012

Accepted 4 March 2012

Available online 23 March 2012

Keywords:

Cyclotrons

Ion beams

Magnetic field measurement

Systematic error

Data analysis

ABSTRACT

Systematic errors caused by the deficiencies of the measurement equipment are occurring relatively often in the engineering practice. The magnetic field measurement system of the VINCY Cyclotron has been designed well; however, due to the practical limitations in the machining process fabrication errors are imminent. We present our experiences with the produced measurement system and the techniques used for the detection and correction of errors. A change in the measuring protocol is suggested in order to overcome otherwise unavoidable errors caused by measuring system machining imperfections.

© 2012 Elsevier B.V. All rights reserved.

1. Introduction

Magnetic field plays crucial role in the operation of an isochronous cyclotron. During the acceleration, beam ions are guided, focused, and synchronized with the accelerating radio-frequency voltage under the influence of the isochronous magnetic field. A lot of patience and care is taken to obtain the desired magnetic field as accurately as possible. Among other procedures, the precise magnetic field measurements must be conducted during the process of the magnetic field design and realization.

Magnetic field measurements represent an integral part of the iterative magnet shimming campaign. In the design of a multipurpose cyclotron, measurements are performed for the nominal as well as for a number of important non-nominal operating modes of the cyclotron. The obtained detailed maps of the magnetic fields additionally form a permanent database for the cyclotron control system and serve in the development of the future experimental programs as well.

VINCY Cyclotron is a compact multipurpose isochronous cyclotron for the acceleration of both light and heavy ions [1]. Three groups of magnetic field measurements are performed, the first one resulting in twenty magnetic field maps for different main coil currents, the second group summing up to a total of

hundred magnetic field maps for different combinations of the main and trim coils currents, and the third one comprised of the isochronized magnetic field maps corresponding to the four test ions of the VINCY Cyclotron. Acquisition of a large quantity of required data took a lot of time and manpower in spite of the automatized measurement procedures.

The magnetic field measurement system of the VINCY Cyclotron is custom built in accordance with the relevant cyclotron geometrical parameters as well as the basic accuracy and flexibility requirements [2]. Fabrication of the system parts is conducted within the specifications in all aspects except for the measurement arm, which in lack of long enough titanium rods was created from the two pieces welded together. It was only perceived as a problem during the measurement system exploitation, but it turned out to be of a little consequence. In spite of that, the usual machining process tolerances led to the small but consequential errors in the Hall probe positioning. The origin, effects, and detection of these errors are described. Their possible correction is investigated, but proven to be only partial with the planned approach to the system operation. It is shown that the complete avoidance of the noticed errors is possible with the modified measurement procedure, i.e., system utilization.

2. Cyclotron magnetic field measurement systems

Mostly contributing to the nonlinearities of the materials used, the cyclotron magnetic field design represents a cumbersome task. Starting with the approximate analytical estimates, followed by the accurate numerical magnetic field modeling, characterization of

* Corresponding author. Tel.: +381 11 2454965; fax: +381 11 2447963.

E-mail addresses: kosjera@vinca.rs (S. Ćirković), andjelijailic@ieee.org (A.Ž. Ilić), alextd@vinca.rs (A. Dobrosavljević), broman@vinca.rs (R. Balvanović), jasna@stanfordalumni.org (J.L. Ristić-Djurović).

materials and measurements on the reduced model of the cyclotron magnet, it is finalized through the iterative magnet shimming campaign. Availability of the sophisticated software tools for detailed three-dimensional modeling of magnet systems allows for the simulated magnetic field maps usage in the analysis and optimization of the magnet design, once the magnetic properties of the materials are well known. An excellent example of a measurement system for determination of material magnetic properties, primarily B-H curves, can be found in [3]. Most commonly used methods and instruments for magnetic measurements are described in [4].

As pointed out in [5], magnetic field mapping machines for cyclotron magnets belong to the special purpose equipment and are custom built to match the cyclotron being designed. An interesting example of such system realized with the flip-coil arrays mounted on a rotating beam is the magnetic field survey system for the TRIUMF Cyclotron magnet [6]. The choice of the flip coils was motivated by the troublesome control of temperature dependent output of the Hall probes of the time. The rotating beam was made out of aluminum and deflected naturally under its own weight; it was prebowed upwards to account for that problem. The Hall probe positioner, designed for the PSI Cyclotron a decade later, already utilized Hall probes with the much lower temperature coefficients, allowing the system operation without special thermostatic facilities [7]. It utilized two 110° circular segments and a radial bar moving in azimuthal direction on the segments, carrying two Hall probes mounted on the carriage which was moving in radial direction on the bar. Azimuthal positioning was performed by means of the two nonmagnetic stainless steel tapes with precisely drilled position holes and controlled by the two photo cells. Namely, a coincidence network connected with the photo cells assured that the virtual line, going through the centers of both Hall probes, always showed to the coordinate center.

Many of the recent measurement system designs use the method similar to that in [6], with the long measurement arm, fixed in the machine center, rotating azimuthally and carrying the Hall probe that can perform radial movement [8,9]. An example of especially robust and reliable magnetic field mapping system is described in [10]. Azimuthal accuracy in this system is obtained by mechanical indexation, i.e., the outer ring carries cogged segments with one cog for every 0.5°. Similar principle is used for radial positioning, i.e., to avoid any problems that can be related to the use of the synthetic belt for radial movement, the rack rail moved by a gear wheel and the shuttle fastened to it are used. A completely different approach to the magnetic field mapping is presented in [11], where the magnetic field mapping in the Cartesian coordinate system is performed and the measured data subsequently converted into the field data in the polar coordinates, required for further analysis. The presented measurement system is fast and very accurate, due to the high precision mechanical x-y stage with the two Hall probes, ensuring remarkably accurate alignment with the coordinate system of the machine. The in-depth analysis of the results obtained by measurements is a major part of the iterative magnetic field forming process [8–11]. It employs harmonic analysis, as well as the beam dynamics calculations.

3. Magnetic field measurement system of the VINCY Cyclotron

The realized magnetic field measurement system and its operation are illustrated in Fig. 1. Measurements are performed by the miniature ($14 \times 5 \times 2 \text{ mm}^3$) Hall probe MPT-141, whose small sensitive area of $1 \times 0.5 \text{ mm}^2$ enables high precision. A temperature sensor is included in the probe, allowing for the

corrections of all temperature dependent effects. Measured values are sent to the control unit using the DTM-141 Teslameter; the combined relative accuracy of the probe and the Teslameter is 0.01% [12].

The MPT-141 Hall probe is mounted on a movable cart and kept in place in its center by means of the small gap at its axis. The cart travels along the measurement arm made of titanium to be light and firm, and to ensure minimal side effects in the presence of a strong magnetic field. The arm is supported at the center of the magnet by the vertical shaft and at two points at the circumference of the supporting ring by the supporting wheels. It is located in the median plane of the VINCY Cyclotron.

Azimuthal positioning of the measurement arm, and thus the Hall probe, is performed by the OMRON servo motor with an optical incremental encoder of 8000 pulses/rev. It is supervised by another 15-bit optical absolute encoder. The theoretical precision of azimuthal positioning is 1.7" while the accuracy of the absolute encoder readout is 40". Radial Hall probe positioning is performed by the OMRON servo motor as well, acting upon the toothed belt gear made of Kevlar that advances the movable cart. Servo motor is equipped with an 8000 pulses/rev optical incremental encoder, but the reduction gear with zero clearance and gear reduction ratio 1:29 is used. The resulting theoretical precision of radial positioning is 0.6 μm .

In the fully automatized standard measurement procedure, the measurement arm rotates in the azimuthal direction from $\theta=0^\circ$ to $\theta=180^\circ$. The Hall probe, carried by the movable cart, travels along the measurement arm and scans the magnetic field from one to the other side of the pole (from $R=+100 \text{ cm}$ to $R=-100 \text{ cm}$). When the probe reaches the final position, the measurement arm moves in the azimuthal direction for one step and measurements are repeated. In this manner the whole circular surface in the median plane is covered and the complete magnetic field map obtained. The usual azimuthal step is 1° and the usual radial step 10 mm.

4. Systematic measurement error

Magnet shimming procedures are always iterative, proceeding from the coarse magnetic structure to the finer and finer one. At the beginning of the second phase of the VINCY Cyclotron magnetic field measurements the existence of relatively strong first harmonic component, equaling 3 mT, in the central region of the machine has been noticed [13]. The usual cause of deficiencies in the machining and construction of the ferromagnetic structure was suspected at first; however, additional examination as well as the most precise placement of the magnetic sectors resulted in no improvement at all. Such a result indicated that there is a systematic error brought in by the measurement equipment. We shall describe the techniques used for the detection and correction of errors on the example of magnetic field mapping for the main coil current of 256.5 A and the trim coils currents set to zero. The lower the main coil current, the larger the magnetic field flutter, so that the measurement errors are easier to perceive. The choice made above is especially convenient because it is the lowest of the four main coil currents corresponding to the four test ions of the VINCY Cyclotron. The main coil current of 256.5 A corresponds to the H^- test ion.

We presumed that there might be a problem with the Hall probe positioning. The control measurements, performed for the two different initial azimuthal positions of the Hall probe, confirmed the measurement grid off-centering. Completely different results obtained for the magnetic field first harmonic in the two cases, as shown in Fig. 2, can not be associated with a single considered ferromagnetic structure.

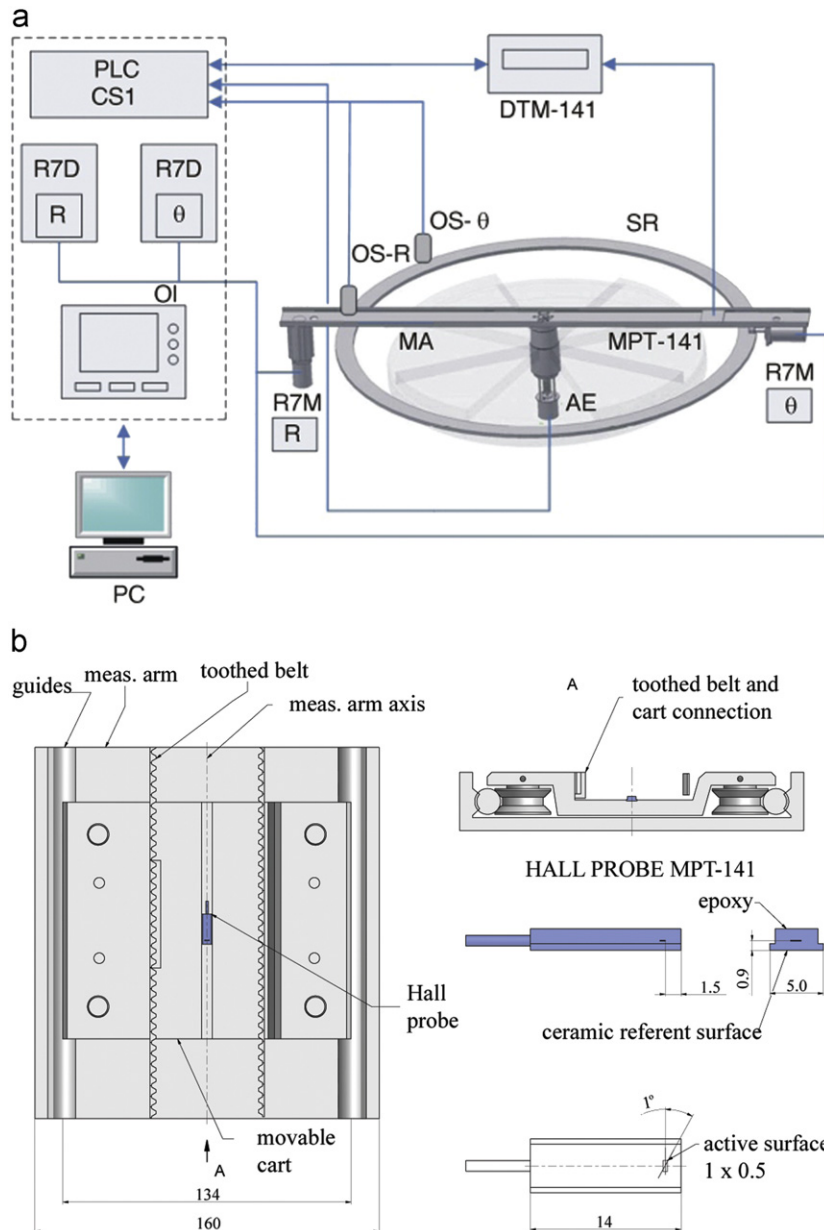


Fig. 1. Magnetic field measurement system of the VINCY Cyclotron (a) and the detailed view of the movable cart carrying the Hall probe (b). The measurement system is comprised of the mechanical subsystem, control unit and measurement instrumentation. (a) Mechanical subsystem elements are: MA – measurement arm, SR – supporting ring, R7M – OMRON servo motors for radial (R) and azimuthal (θ) positioning, AE – absolute encoder. Control unit includes OS-R and OS- θ -optical switches for radial (R) and azimuthal (θ) origin point, respectively, DTM-141 – Digital Hall-Effect Teslameter, PLC CS1 – OMRON servo drivers, OI – operator interface panel, and PC – personal computer with programs and archive of magnetic field maps. Miniature Hall probe MPT-141 acts as the measurement instrumentation. (b) Movable cart carrying the MPT-141 Hall probe. The Hall probe is kept in place in the center of the movable cart by means of the gap located at the cart axis. The cart travels along the measurement arm as guided by the toothed belt gear made of Kevlar. The accuracy of the probe positioning depends on the precision of the cart positioning with respect to the measurement arm as well as the measurement arm positioning with respect to the coordinate system of the VINCY Cyclotron.

The complete check up of all the components of the magnetic field measurement system was performed. The produced measurement arm did not comply with the project specifications. In lack of a long enough single titanium rod, it was created from the two pieces welded together and thus not perfectly straight. Although the manufacturer gave a satisfactory initial estimate of the measurement arm straightness, based on the laser interferometer system measurements, it turned out incorrect. Repeated measurements, using the precise DEA Epsilon 2304 coordinate measuring machine, revealed a misalignment of the two welded pieces by $0^{\circ}1'56''$. It is positioned at $R=750$ mm according to the standard measurement coordinate system. Due to the relatively long legs of an angle, misalignment resulted in a deviation from the straight

line of 0.561 mm at $R=1000$ mm, which is out of the ± 0.1 mm tolerance range. Fortunately, with the large enough (0.2–0.3 mm) clearance between the guides and the wheels and the sufficient tension of the belt, the toothed belt dictates the straight and centered trajectory to the movable cart. Angular displacement of the cart trajectory is thereby reduced approximately four times with respect to the misalignment of the two welded pieces. Even with the highest azimuthal magnetic field gradient equaling 330 mT° , the resulting error due to the misalignment angle would be about 2.5 mT. Influence of the measurement arm deformity itself to the errors is therefore insignificant in comparison to the observed error magnitudes, which can be as high as 220 mT [13].

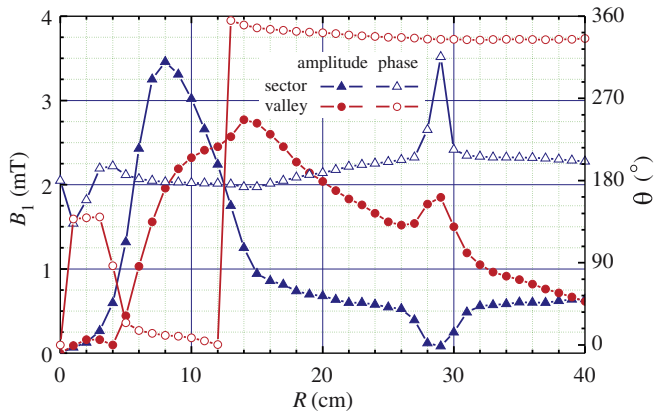


Fig. 2. Systematic error of the magnetic field measurement system. The control measurements are performed for the two different initial azimuthal positions of the Hall probe. The first one coincides with the usual initial azimuthal position, i.e., the midline of the first magnetic sector S1. The amplitude and phase of the first harmonic of the magnetic field in this case are depicted by the blue triangles. Another initial azimuthal position is moved clockwise by 45° with respect to the first one to fall at the midline of the fourth valley. The red circles represent the results for this case. Were the imperfections of the ferromagnetic structure of the VINCY Cyclotron the cause for the existence of the first harmonic component, the obtained first harmonic amplitudes ought to be the same, whereas the phases should be of the same shape only shifted by 45° . However, that is not the case, leading to the conclusion that the measurement system introduces the errors. (For interpretation of the references to colour in this figure legend, the reader is referred to the web version of this article.)

However, the very same clearance between the guides and the wheels, taken to ensure the motion with minimum friction important for radial positioning, as well as the trajectory straightness in case of the minor realization flaws, allows for the movable cart to slightly drift away from the arm symmetry axis. The active measuring surface of the Hall probe can be somewhat off-centered as well, i.e., the probe manufacturer declares the active surface placement tolerance of ± 0.2 mm. In addition to that, the measurement arm deformity may have played the role in the wear out of the wheels and guides by friction while the cart is moving in the vicinity of $R=750$ mm where the deformity occurs. The combination of these effects resulted in the Hall probe offset by a small amount Δs with respect to the measurement arm symmetry axis, occurring during the automatic probe positioning.

The magnetic field of an isochronous cyclotron changes very smoothly with both the radius and azimuth, except in the region around the magnetic sector edges. Very high azimuthal magnetic field gradients in that region provide strong focusing necessary for the isochronous acceleration. As explained in Fig. 3, even a small offset in the azimuthal Hall probe positioning in this region produces the significant amount of unwanted harmonics. The measurement errors corresponding to the two halves of the measurement arm are positively correlated introducing the false asymmetry in the results.

To further examine this assumption, we have introduced the auxiliary “manual” measurement, i.e., the measurement with the manually adjusted azimuthal positioning of the Hall probe. The radial position is kept fixed at $R=8$ cm, where the highest amount of unwanted harmonics was observed, while the measurement arm is rotating through the $[0^\circ, 360^\circ]$ range with the 1° step. The azimuthal positioning is achieved by the manual motion of the arm, with the precision of $40''$ given by the absolute encoder readout. Since the probe centering with respect to the arm symmetry axis is identical for all the azimuthal positions, any centering offset that might occur would result in the negatively correlated measurement errors corresponding to the each set of

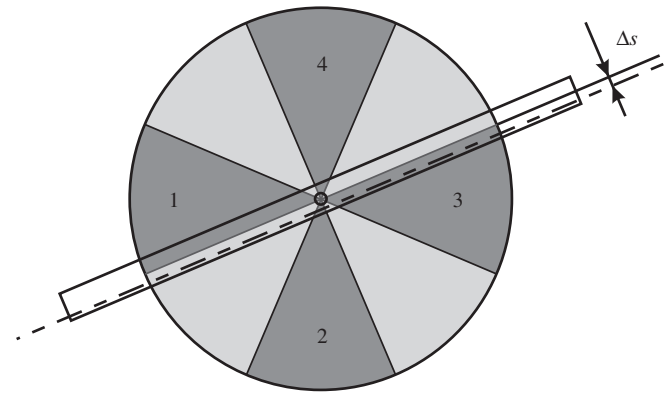


Fig. 3. The Hall probe offset with respect to the symmetry axis of the measurement arm. Measurement arm shaft is fixed in the center of the VINCY Cyclotron and the trajectory dictated by the guides and the toothed belt is straight and centered. Therefore, the arm itself is not the major cause for the measurement grid off-centering. However, the Hall probe travels together with the movable cart along the axis shifted by a small amount Δs with respect to the measurement arm symmetry axis. As a result, the actual measurements are taken at different azimuthal positions than intended. The azimuthal magnetic field gradient in the vicinity of the magnetic sector edges can be as high as $330 \text{ mT}/^\circ$. One of the measured magnetic field values corresponding to the two diametrically opposite azimuths is therefore larger than it should be and the other one is lower. The difference in measured values reaches 220 mT, producing the false asymmetry of the measured magnetic field and the large amounts of unwanted harmonics.

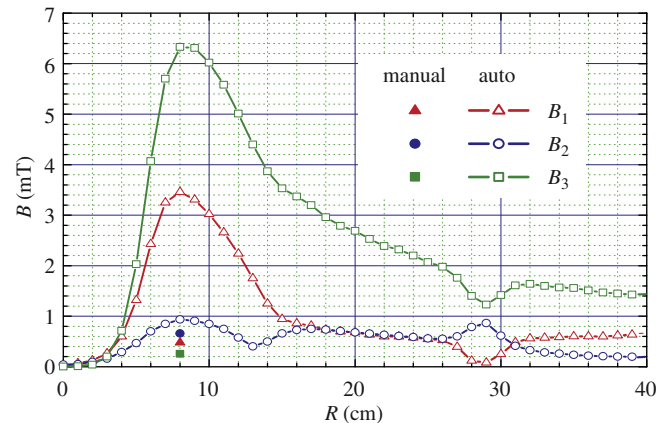


Fig. 4. The amplitudes of the first three measured magnetic field harmonics compared with the control values. Standard measurement procedure errors resulted in the highest amount of unwanted harmonics at the radius $R=8$ cm. The realistic estimates are therefore obtained for this radial position performing the time consuming but very accurate manual adjustment of the Hall probe azimuthal position. The amplitudes of the first and third harmonic are 7.25 and 24.73 times smaller, respectively, when the manual azimuth adjustment is performed. The drop in the second harmonic amplitude equals 29.7%. The obtained results confirm the assumption of the Hall probe offset being the major reason for the off-centering of the measurement grid.

diametrically opposite azimuths. The maximal difference of the measured magnetic field values is therefore the one corresponding to the optical absolute encoder reading precision. For the highest azimuthal magnetic field gradient equaling $330 \text{ mT}/^\circ$, it does not exceed 7.3 mT, a value negligible in comparison with the 220 mT difference obtained during the standard automatic measurement. Manual Hall probe position adjustment therefore provides the realistic control values of the magnetic field differences and field harmonics.

Fig. 4 compares the amplitudes of the first three magnetic field harmonics with the control values for the radius $R=8$ cm, where

the highest amount of unwanted harmonics is discovered. The control values confirm that the actual harmonics amplitudes are considerably smaller than the apparent ones. Therefore, the measurement grid off-centering is predominantly caused by the Hall probe offset Δs . The direct deduction of the actual probe offset at the time of measurement from the collected data, presented in Fig. 4, is not possible. First, the active measuring surface of the Hall probe becomes additionally offset from the center of the probe if there is any tilt with respect to the radial direction. Second, with the standard measurement procedure there is a positive correlation of errors for the diametrically opposite azimuths, which amplifies the effect. It is possible, however, to make a reasonable estimate of the joint effect of these factors, from the assessment of magnetic field gradients and errors shown in Fig. 4. Were all the other effects negligible, offset corresponding to the results in Fig. 4 would be 1 mm; therefore, we may define the estimate, effective Hall probe offset, as $\Delta s_e = 1$ mm.

5. Measurement error correction

The solution of the observed problem was attempted by the Hall probe alignment with respect to the measurement arm. Before the automatic measurement procedure is initiated, the Hall probe and the movable cart are positioned using the vernier caliper and the adjustment of the cart wheels. The probe is fixed and the measurement further performed using the standard procedure. The effect of the Hall probe alignment to the reduction of measurement errors is shown in Fig. 5. The maximal difference ΔB of the measured data obtained for the diametrically opposite azimuthal positions, θ and $\theta + 180^\circ$, is on average reduced four times with respect to the standard measurement without the probe alignment. However, at a new level of about 5 mT, it is still unacceptably high. The corresponding effective Hall probe offset equals $\Delta s_e = 0.15$ mm. During the lengthy radial motion along the measurement arm the movable cart, initially aligned with the arm symmetry axis, drifts slightly away. Additionally, perfect alignment is impossible and therefore the positive correlation of offset pertaining to the two diametrically opposite points can

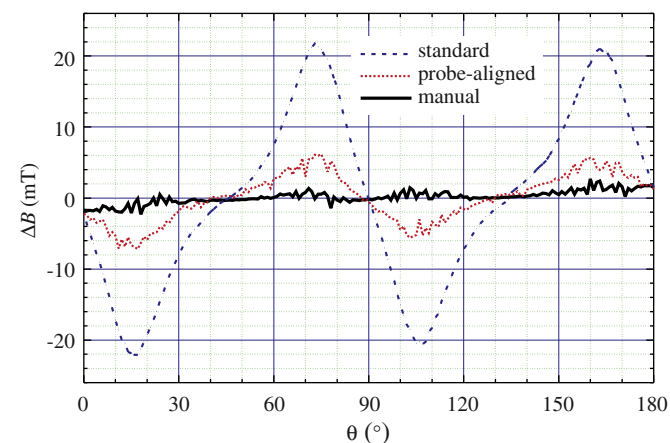


Fig. 5. The alignment of the Hall probe with respect to the measurement arm. The difference ΔB of the magnetic field measured in two diametrically opposite points, at azimuths θ and $\theta + 180^\circ$, is shown for the measurement arm azimuthal position θ ranging from 0° to 180° and the Hall probe radial position $R = 8$ cm. The results of the standard automatic measurement, standard probe-aligned automatic measurement and the measurement with the manual adjustment of the Hall probe position are compared. The systematic error of the standard measurement procedure is significantly reduced by the Hall probe alignment. However, it is still unacceptably high.

produce errors. The realistic control measurements prove that the difference of the magnetic field amplitudes for the opposite azimuths should in the worst case be limited to the $[-2 \text{ mT}, 2 \text{ mT}]$ interval.

To further lessen the measurement error and bring it to an acceptable level, we decided to modify the automatic measurements and use only one half of the measurement arm. In that manner, the measured data corresponding to the two opposite azimuthal positions is negatively correlated. As demonstrated in Fig. 6, we finally obtain a good agreement with the control manually measured data. With the modified automatic measurement, the asymmetry of the magnetic field at $R = 8$ cm is almost completely lost i.e., ΔB is confined to the $[-2 \text{ mT}, 2 \text{ mT}]$ interval. The agreement of the modified automatic measurements with the control manual measurements is easier to discern in the presence of actual magnetic structure imperfections. Therefore, we illustrate the precision of the modified procedure in Fig. 7, comparing it with the control manual measurements at two other radii. An excellent agreement of the results for the two cases is observed, while the standard measurement with the Hall probe alignment gives inadequate results. The amplitudes and phases of the low order magnetic field harmonics with the modified automatic measurement are shown in Fig. 8. The decrease in the level of the low order harmonics is substantial compared to the data in Fig. 4 corresponding to the standard measurement procedure. The low order harmonics are brought to a level concurrent with the manually determined control values shown in Fig. 4 for $R = 8$ cm. The harmonic components peak out for radii larger than $R = 92$ cm, presenting no problems for extraction since the radius of extraction equals $R_{\text{ex}} = 84$ cm.

The quality of the realized isochronized magnetic fields as well as the accuracy of measurement procedures can be further assessed from the beam dynamics parameters, such as the betatron oscillation frequencies, gyration frequency fluctuations from its ideal constant value and the corresponding phase excursion of an accelerated particle. The betatron oscillation frequencies can be calculated directly from the magnetic field properties, i.e., the magnetic field harmonic analysis, as well as from the beam dynamics simulations. We use both of these methods and compare

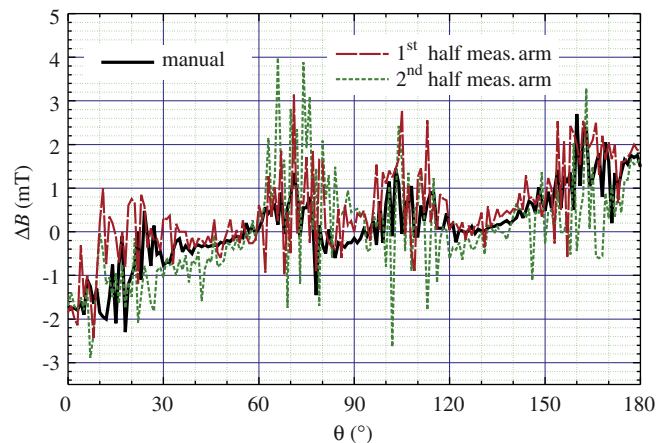


Fig. 6. The modified automatic measurement procedure. We suspected that the total amount of the Hall probe radial movement as well as the correlation of the azimuthal positioning errors for the two halves of the measurement arm play significant role in the buildup of the measurement errors. Therefore, a different approach in the magnetic field measurement is considered and as a result, the systematic measurement errors are finally brought to an acceptable level. The results of the modified measurements, with one and with the other half of the measurement arm, are compared with the manually performed measurement and the agreement of the results is excellent.

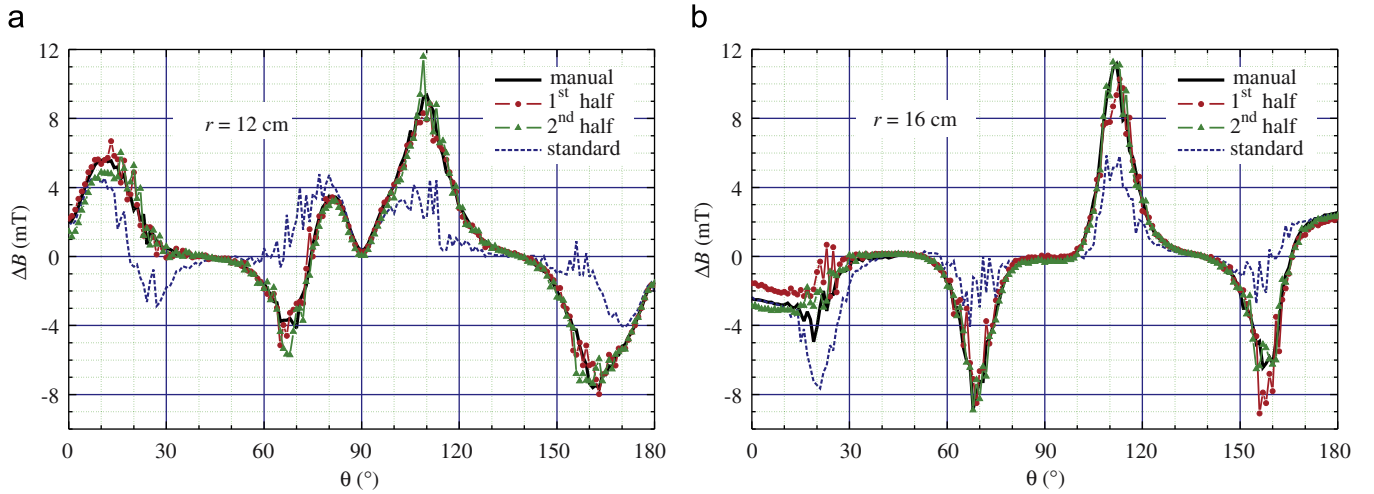


Fig. 7. The difference ΔB of the magnetic field values at diametrically opposite azimuthal points as a measure of the ferromagnetic structure imperfections. Utilizing the modified automatic measurement procedure the difference ΔB at $R=8$ cm is confined to the $[-2$ mT, 2 mT] interval. The remaining differences in the field values at azimuths θ and $\theta+180^\circ$ indicate the actual errors due to the magnetic structure imperfections. Such differences are shown for the measurement arm azimuthal position θ ranging from 0° to 180° and the radial positions $R=12$ cm (left) and $R=16$ cm (right). An excellent agreement of the two independent measurements using the modified automatic procedure with the control manually performed measurements at these radii is observed, while the standard measurement even with the Hall probe alignment (dashed blue line) gives an erroneous result. (For interpretation of the references to colour in this figure legend, the reader is referred to the web version of this article.)

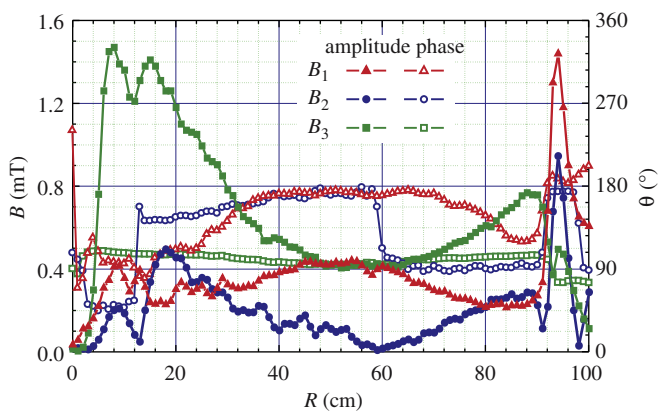


Fig. 8. The amplitudes and phases of the first three measured magnetic field harmonics after the correction of measurement errors. With the modified automatic measurement procedure, the amplitude of the first magnetic field harmonic, as well as the second one, is brought below the level of 0.5 mT. The third magnetic field harmonic shows peaks at the radii $R=8$ cm and $R=16$ cm, reaching the values of 1.5 mT and 1.4 mT, respectively. In the most part of the accelerating region, for radii larger than $R=30$ cm, it lies below 0.8 mT. The radius of extraction is $R_{\text{ex}}=84$ cm, therefore the peaks of the harmonic components for radii larger than $R=92$ cm are of no influence. The presented results are greatly improved in comparison to the ones shown in Fig. 4, corresponding to the standard measurement procedure.

the obtained results in Fig. 9 for the measured isochronized magnetic field map of the H^- test ion. The beam dynamics simulations are performed using the self-written software package VINDY-A [14]. The results verify the absence of harmful resonant behavior along the chosen accelerated orbit, and thus the well designed isochronized magnetic field. The ion kinetic energy dependence on the mean orbit radius, shown in green dash-dot-dot line, allows for the interpretation of the results in terms of energy.

The obtained level of isochronism is depicted in Fig. 10. The nominal gyration frequency used for the H^- test ion magnetic field design was $f_g^{\text{nom}}=20.037$ MHz, while the obtained mean gyration frequency equals $\bar{f}_g=20.035$ MHz. The relative error of the gyration frequency is shown by the dashed blue line in Fig. 10; it is rather small indicating the well-isochronized magnetic field. As a

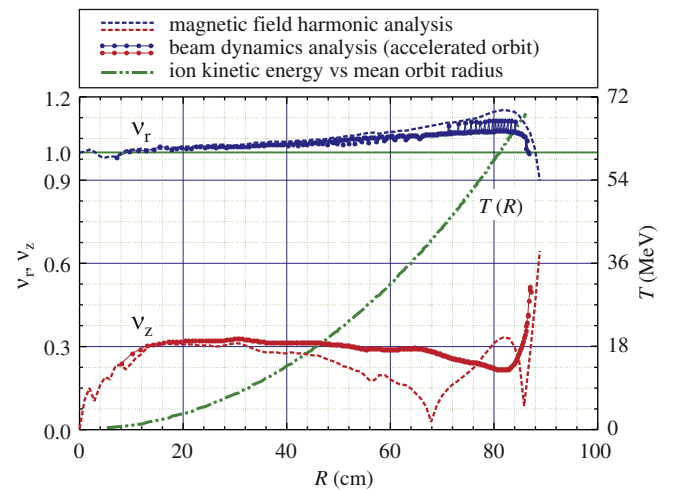


Fig. 9. Radial and axial betatron oscillation frequencies corresponding to the measured isochronized magnetic field map of the H^- test ion, after the measurement error correction. Two methods for the calculation of betatron oscillation frequencies are used, the magnetic field harmonic analysis and the beam dynamics analysis. The latter is performed along the accelerated orbit, resulting in actual betatron oscillation frequencies during the acceleration along the chosen orbit. The results agree well with each other and verify the absence of harmful resonant behavior during the acceleration. The ion kinetic energy dependence on the mean orbit radius is shown in green dash-dot-dot line in order to allow the interpretation of the results in terms of energy. (For interpretation of the references to colour in this figure legend, the reader is referred to the web version of this article.)

result of the gyration frequency fluctuations, the phase slip of a particle occurs during the acceleration. The radiofrequency system phase, ϕ_{RF} , has been monitored at the same azimuth ($\theta=45^\circ$) for different particle kinetic energy, i.e., corresponding to the different mean orbit radii along the accelerated orbit. Phase excursion of a particle during the acceleration, $\Delta\phi$, is obtained as the difference between the monitored radiofrequency system phase and its nominal value for the considered azimuth, $\phi_{\text{RF}}^{\text{nom}}(45^\circ)=90^\circ$. Phase excursion falls into the range of $\pm 5^\circ$, which can be considered an excellent result.

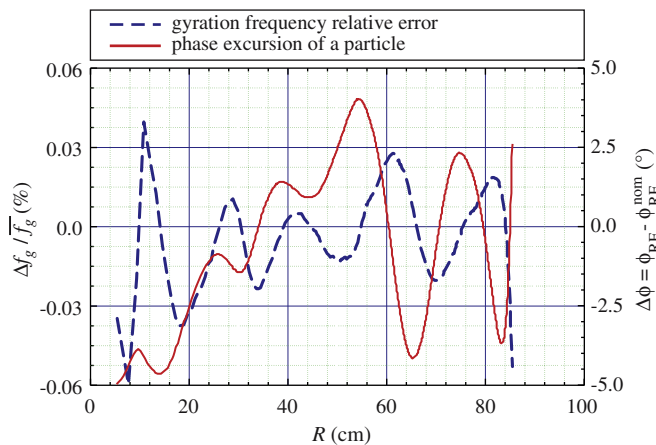


Fig. 10. The deviation from the isochronous acceleration as a result of the measured magnetic field imperfections for the H^- test ion. The magnetic field imperfections translate into the gyration frequency fluctuations i.e., the deviation from the isochronous motion, and further to the phase slip of an accelerated particle. The gyration frequency fluctuations are depicted through the relative error of the gyration frequency f_g , as represented by the dashed blue line. The solid red line shows the resultant phase excursion of a particle, $\Delta\phi$, versus mean orbit radius. The corresponding ion kinetic energy dependence on the mean orbit radius is shown in Fig. 9 (green dash-dot-dot line). The small level of the gyration frequency fluctuations, as well as the remarkably constrained phase excursion less than $\pm 5^\circ$, testify to the high quality of the measured isochronized magnetic field of the H^- test ion. (For interpretation of the references to colour in this figure legend, the reader is referred to the web version of this article.)

6. Conclusion

During the design and construction of the ferromagnetic structure of the multipurpose VINCY Cyclotron, we encountered several serious problems with the generally well devised magnetic field measurement system. One of them was the persisting systematic error stemming from the inability to realize the low friction precise radial movement along with the very rigid requirements on azimuthal precision due to the abrupt azimuthal changes of field amplitudes. We described the two procedures used to check for the amount of errors due to the measurement system and to localize the errors. The severity of the measurement system systematic error can be gauged by a small convenient change in the measurements, such as starting with the different initial position of the probe. The actual errors due to the magnetic structure imperfections can be estimated if the more time consuming but accurate manual measurements are performed in the regions of largest total measurement errors.

The solution of the problem was firstly attempted without the modifications of the original measurement procedure. The Hall probe azimuthal positioning is checked and aligned with the measurement arm prior to every new instance of field mapping. Although the measurement precision improved significantly, the described practice still remained insufficient in coping with the influence of the high azimuthal field gradients to the error buildup, as well as the problems in keeping the probe well aligned during the lengthy radial motion. The modified automatic measurement procedure is adopted that only uses one half of the measurement arm and thereby avoids the positive correlation of the measurement errors. The precision of the modified

measurement procedure is illustrated through the comparison with the control manual measurements, magnetic field harmonic analysis and using the beam dynamics simulations.

The main objective of describing our experiences and the problems encountered in the magnetic field measurements was to put them to use to the others dealing with the similar issues, where the precise measurements are of key interest to the final design and the custom built measurement systems are often subject to the rather small but highly consequential realization flaws.

Acknowledgement

This work was supported by Ministry of Education and Science of Serbia through project Physics and Chemistry with Ion Beams, no. III 45006.

References

- [1] N. Nešković, J. Ristić-Đurović, S.B. Vorozhtsov, P. Beličev, I.A. Ivanenko, S. Ćirković, A.S. Vorozhtsov, B. Bojović, A. Dobrosavljević, V. Vujović, J.J. Čomor, S.B. Pajović, Status Report on the VINCY Cyclotron, *Nukleonika* 48 (2) (2003) S135–S139. [Proc. XXXIII European Cyclotron Progress Meeting, Poland, 2002].
- [2] A. Dobrosavljević, S. Ćirković, Đ. Košutić, Lj. Vukosavljević, D. Vranić, Automatic system for mapping of the VINCY Cyclotron magnetic field, *Nuclear Technology and Radiation Protection*, XXI (1) (2006) 13–20.
- [3] V.M. Amoskov, V. Belyakov, T. Belyakova, S. Dmitriev, O.G. Filatov, A. Firsov, I. Franko, B. Gikal, G. Gulbekyan, O. Ilyasov, I. Ivanenko, V. Kostyrev, V. Kukhtin, V. Kutchinsky, E. Lamzin, M. Larionov, B. Maximov, A. Semchenkov, O. Semchenkova, S. Sytchevsky, Computerized system for magnetic measurements over extended field range, Preprint JINR P13-2004-153, Dubna, (2004).
- [4] K.N. Henrichsen, Classification of magnetic measurement methods, In: S. Turner (Ed.), *Proceedings of the CERN Accelerator School on Magnetic Measurement and Alignment*, 16–20 March, 1992, Montreux, Switzerland, pp. 70–83, CERN 92-05, Geneva, 1992.
- [5] A. Harvey, Mechanical equipment for magnet measurement and alignment. In: S. Turner (Ed.), *Proceedings of the CERN Accelerator School on Magnetic Measurement and Alignment*, 16–20 March, Montreux, Switzerland, 1992, pp. 228–239, CERN 92-05, Geneva, 1992.
- [6] E.G. Auld, D.L. Livesey, A.J. Otter, N. Rehlinger, The magnetic field survey system for the TRIUMF Cyclotron magnet, in: *Proceedings of the 4th International Conference on Magnet Technology*, 19–22 September, Upton, New York, 1972, pp. 767–772.
- [7] B. Berkes, O. Brombach, O. Szavits, Fast field mapping device for cyclotron magnets, *IEEE Transactions on Magnetics*, MAG, 17 (5) (1981), pp. 2121–2124.
- [8] M. Fan, X. Zhang, T. Zhang, C. Liang, Q. Tao, Z. Chao, C. Chu, T. Li, Y. Hu, Y. Chen, H. Zhang, H. Jia, C. Jiao, J. Liu, W. Zhang, C. Zhou, J. Jiao, Y. Hou, Measurement and adjustment of CIAE medical cyclotron magnet, in: *Proceedings of the IEEE Particle Accelerator Conference*, vol. 4, 17–20 May, Washington, D.C., 1993, pp. 2841–2843.
- [9] G. Yu., A.F. Alenitsky, S.A. Chesnov, L.M. Kostromin, E.V. Onischenko, Samsonov, N.L. Zaplatin, Modeling and forming the magnetic field of the heavy ion cyclotron, *Problems of Atomic Science and Technology*, series, *Nuclear Physics Investigations* 43 (2) (2004) 78–80.
- [10] Y. Paradis, D. Vandeplassche, W. Beeckman, J.-L. Delvaux, W. Kleeven, L. Medeiros-Romao, S. Zaremba, J.C. Amélia, F. Salicis, The magnetic field mapping system for the IBA C70 Cyclotron, in: *Proceedings of the 18th International Conference on Cyclotrons and their Applications*, 1–5 October, 2007, Giardini-Naxos, Sicily, Italy, 2007, pp. 78–80.
- [11] K.H. Park, Y.G. Jung, D.E. Kim, B.K. Kang, M. Yoon, J.S. Chai, Y.S. Kim, Field mapping system for cyclotron magnet, *Nuclear Instruments and Methods in Physics Research Section A* 545 (3) (2005) 533–541.
- [12] Group3, DTM-151 DIGITAL TESLAMETER with Serial Communications, User's Manual.
- [13] N. Grujić, S. Ćirković, D. Košutić, L. Vukosavljević, R. Balvanović, Results of the second phase of measurements of the VINCY Cyclotron, Internal Report, July 2007.
- [14] Anđelija Ž. Ilić, Jasna L. Ristić-Djurović, Saša T. Ćirković, Preliminary results of ion trajectory tracking in the acceleration region of the VINCY Cyclotron, *Nuclear Technology and Radiation Protection* XXI (1) (2006) 29–33.



ELSEVIER

Contents lists available at [SciVerse ScienceDirect](http://www.sciencedirect.com)

Ecotoxicology and Environmental Safety

journal homepage: www.elsevier.com/locate/ecoenv

Hematological parameters' changes in mice subchronically exposed to static magnetic fields of different orientations

Drago M. Djordjevich^{a,1,2}, Silvio R. De Luka^{a,1,2}, Ivan D. Milovanovich^{a,2}, Saša Janković^{b,3}, Srdjan Stefanović^{b,3}, Slavica Vesković-Moračanin^{b,3}, Saša Ćirković^{c,4}, Andjelija Ž. Ilić^{c,4}, Jasna L. Ristić-Djurović^{c,4}, Alexander M. Trbovich^{a,2,*}

^a Department of Pathological Physiology, School of Medicine, University of Belgrade, Dr Subotića 9, 11000 Belgrade, Serbia

^b Institute of Meat Hygiene and Technology, Kačanskog 13, 11000 Belgrade, Serbia

^c Laboratory of Physics (010), Vinča Institute of Nuclear Sciences, University of Belgrade, P.O. Box 522, 11001 Belgrade, Serbia

ARTICLE INFO

Article history:

Received 28 February 2012

Received in revised form

27 April 2012

Accepted 28 April 2012

Available online 23 May 2012

Keywords:

Static magnetic field

Hematology

Iron

ABSTRACT

Static magnetic fields (SMFs) are time independent fields whose intensity can be spatially dependent. This study investigates influence of subchronic continuous exposure to upward and downward directed SMF on hematological parameters and spleen cellularity in mice. The experiment is performed on the Northern hemisphere; consequently, the vertical component of geomagnetic field is directed downward. Male, Swiss-Webster, 6 weeks old mice were exposed to the vertically declining SMF. Mice were divided in three groups and continuously exposed or not exposed for 28 days to the SMF characterized by the averaged field of 16 mT and averaged field gradient of 10 mT/cm. Differently oriented SMF did not alter hemoglobin and hematocrit content among the groups. However, the groups exposed to the upward and downward fields had statistically significant higher levels of serum transferrin compared to the control. Moreover, spleen cellularity in animals in the downward group was significantly higher compared to the upward and control group. In addition, spleen lymphocytes in both of the exposed groups were significantly higher than in the control group. In contrast, spleen granulocytes in the exposed groups were significantly lower than in the control group. Significant decrease was also observed in brain and liver iron content with concomitant increase of iron in serum and spleen in exposed animals. Subchronic continuous exposure to 16 mT SMF caused lymphocyte and granulocyte redistribution between spleen and blood. This distribution is typical for stress induced hematological changes. These results suggest that observed changes were not due to an unspecific stress response, but that they were rather caused by specific adaptation to subchronic SMF exposure.

© 2012 Elsevier Inc. All rights reserved.

1. Introduction

Beneficial and adverse effects of magnetic fields on human body have been assessed for long time. The frequency of exposure to magnetic fields has increased with rapid advances in science and

* Corresponding author. Fax: +381 11 2685 340.

E-mail addresses: aleksandar.trbovich@mfub.bg.ac.rs, alexander.m.trbovich@gmail.com (A.M. Trbovich).

URLS: <http://www.mfub.bg.ac.rs> (D.M. Djordjevich),

<http://www.mfub.bg.ac.rs> (S.R. De Luka),

<http://www.mfub.bg.ac.rs> (I.D. Milovanovich),

<http://www.inmesbgd.com> (S. Janković), <http://www.inmesbgd.com>

(S. Stefanović), <http://www.inmesbgd.com> (S. Vesković-Moračanin),

<http://www.vinca.rs> (S. Ćirković), <http://www.vinca.rs> (A.Ž. Ilić),

<http://www.vinca.rs> (J.L. Ristić-Djurović),

<http://www.mfub.bg.ac.rs> (A.M. Trbovich).

¹ Equally contributed and, thus, share first authorship.

² Fax: +381 11 2685 340.

³ Fax: +381 11 2651 825.

⁴ Fax: +381 11 2447 963.

technology, such as magnetic resonance imaging (MRI) diagnosis, nuclear magnetic resonance (NMR) spectroscopy and passenger transport systems that are based on magnetic levitation (World Health Organization, 2006a). Therefore, it has become necessary to systematically elucidate the influence of magnetic fields on the body.

Static magnetic fields (SMFs) are time independent fields whose intensity could be spatially dependent. In our experiment, the magnetic field does not change in time; therefore it is static. However, it has different values in space so it is spatially dependent. There are four SMF parameters relevant for the interaction with a biological system: target tissue(s), magnet characteristics, magnet support device, and dosing regimen (Colbert et al., 2009). SMFs are difficult to shield and can freely penetrate biological tissues (Hashish et al., 2008). However, not only the field intensity, but also the gradient of the field has important role in biological effects of SMF (McLean et al., 1995; Markov, 2007a). SMF can interact directly with moving charges (ions, proteins, etc.) and magnetic materials found in tissues through several physical mechanisms (World Health Organization, 2006a).

Small artificial sources of SMFs are common, ranging from specialized (audio speakers components, battery-operated motors, microwave ovens) to trivial (refrigerator magnets) (Stuchly, 1986; Kowalczyk et al., 1991; World Health Organization 2006a; Hashish et al., 2008). These small magnets can produce fields of up to few mT within a centimeter or so of their magnetic poles that further decrease with square distance reaching levels of few μT (World Health Organization, 2006b; Hashish et al., 2008). A number of studies of *in vitro* biological response to applied magnetic field suggest the existence of biological “windows” (Markov et al., 1975; Ukolova et al., 1975; Bawin and Adey, 1976; Azanza and del Moral, 1994; Engstrom et al., 2002; Markov, 2007a, 2007b, 2011; Dini and Panzarini, 2010). These windows represent combinations of amplitude, frequency of exposure and exposure duration within which the optimal response is observed, and once outside this range, the response is found to be significantly smaller. This demonstrates the principle that more does not necessarily mean better (Markov 2007a). For SMFs, several windows have been reported, such as 0.5–2 mT, 15–20 mT and 45–50 mT (Markov et al., 1975; Zukov and Lazarovich, 1989; Markov, 2005, 2007a, 2011).

A large numbers of SMF studies have been performed on cells and cellular components, genetic material, reproduction and development, physiological and behavioral responses (World Health Organization, 2006a; Health Protection Agency, 2008). When taken as a whole, they do not suggest any acute detrimental effects on major development, behavioral or physiological parameters for short-term exposures (Schenck, 2000; Löscher, 2003; Hashish et al., 2008). However, some detrimental effects have been noticed in *in vitro* experiments with hippocampal slides. Namely, electromagnetic field of 2–3 mT caused small transient depression of excitatory postsynaptic potentials followed by a long-lasting amplification of the potentials, while electromagnetic field of 8–10 mT depressed excitatory postsynaptic potential (Trabulsi et al., 1996). This effect was attributed to the activity of intracellular calcium channels that were affected by SMF leading to fluctuations in the intracellular Ca^{2+} concentration (Wieraszko, 2000). Taken together, long-term experiments still need to be conducted to assess effects of subchronic and chronic exposure to SMF. There are several scientific articles concerning the biological effects of the 15–20 mT SMF *in vitro* (Markov, 2005; World Health Organization, 2006a; Tavasoli et al., 2009) or *in vivo* (World Health Organization, 2006a; Health Protection Agency, 2008). However, biological effects of 15 mT SMF on hematological samples were only investigated in *in vitro* experiments (Tavasoli et al., 2009; Elblbesy, 2010). Thus far, SMF studies showed that both extremely low frequency magnetic field and SMF alter hematological parameters in rats and mice (Schenck, 2000; Hashish et al., 2008). Spleen total lymphocyte count, as well as spleen T and B lymphocyte count are also affected by SMF in mice (Hashish et al., 2008).

On the basis of these results and the fact that the upward and downward directed magnetic fields have different effects on biological systems (Krylov and Tarakanova, 1960; Ružič et al., 1993; Yano et al., 2001; Eccles, 2005; World Health Organization, 2006a; Health Protection Agency, 2008), we decided to investigate influence of subchronic continuous exposure to 16 mT SMF oriented upwards as well as downwards on hematological parameters and spleen cellularity in mice. However, the magnetic field we used decreases vertically and ranges from 29.7 mT to 5.8 mT throughout the mice body. Consequently, different parts of animal bodies were exposed to different field intensity. The averaged value of the magnetic field throughout the experimental volume potentially occupied by the mice is 16 mT. To our knowledge, nobody else had previously compared separate biological effects of the upward and downward oriented SMF on hematological characteristics in experimental animals.

2. Materials and methods

2.1. Animals

Male Swiss-Webster mice, 6 weeks old, obtained from the Military Medical Academy Animal Research Facility (Belgrade, Serbia) were used. Mice were housed at four or five animals per cage and offered regular mouse feed and drinking water *ad libitum*.

All experimental protocols involving animals were reviewed and approved by the University of Belgrade School of Medicine Experimental Animals Ethics Committee. Furthermore, all experiments were conducted concordant to procedures described in the National Institutes of Health Guide for Care and Use of Laboratory Animals (Washington, DC, USA).

2.2. Magnetic field

As a source of spatially dependent SMF MADU stripes (The Mihailo Pupin Institute, Belgrade, Serbia; patent number YU 48907/02, Republic of Serbia Intellectual Property Office, Belgrade, Serbia; patent number WO 99/60581, World Intellectual Property Organization, Brussels, Belgium, EU) were used. The MADU stripes are designed to provide easy-to-carry magnetic field, whose aim is to penetrate into the body, rather than to affect just the body surface, when deployed to humans or animals. The type L MADU stripe (Fig. 1 Panel A) as well as the experimental setup (Fig. 1 Panel B) is depicted in Fig. 1. Due to the five rows of embedded permanent magnetic rods the width of the type L MADU stripe is comparable to its length; therefore, it is rather a sheet than a stripe. If the magnetic axes of the embedded rods alternate in direction throughout the sheet, the resulting magnetic field is predominantly horizontal, parallel to the sheet's surface and the volume of its influence is relatively thin layer above the sheet's surface. If the magnetic axes of the rods are all oriented in the same direction the resulting magnetic field is predominantly vertical, orthogonal to the sheet's surface and it spreads further away from the sheet. It has been shown that if the magnetic axes of the rods have the same direction, either upwards or downwards, the depth of the resulting magnetic field penetration through a tissue is in general 4–8 times larger than is the case if the upward and downward directions of the magnetic axes alternate throughout the sheet (Markov, 2007a). Consequently, the former can be used to study its influence on the body, whereas the latter is more likely to affect just the skin of an animal or a human. Since the experiment is performed on the Northern hemisphere, the vertical component of geomagnetic field is directed downwards and SMF of MADU stripes has the same or opposite direction to this field. The downward direction of vertical component of geomagnetic field is consistent with the geomagnetic reversal. Namely, the south pole of the Earth's magnetic field attracts the north pole of the compass magnet; therefore, the south geomagnetic pole is located in the northern Arctic region in the vicinity of the north geographic pole (Campbell, 2001). The field intensity of MADU stripes is measured using Digital Teslameter DTM-151 (Group 3 Technology, Auckland, New Zealand), whose resolution is 0.005 mT for the range of up to 0.3 T. The precision of the reading for the same range is 0.01%. The 3D simulation of the magnetic field of the MADU sheet is performed using Mermaid software (SIM, Novosibirsk, Russia). The obtained computer model gives the relative values of the magnetic field, i.e., these values must be multiplied by a multiplicative constant in order for the model to match the reality. The multiplicative constant is determined by the magnetic field calibration procedure, which uses magnetic field values measured at several chosen points. In our case, the field is measured in the four horizontal planes parallel to just at several points. Consequently, not only that the multiplicative constant is determined, but the validity of the computer model is also confirmed. The values of the obtained magnetic field are shown in Fig. 2 for the four planes parallel at four different distances to the XY-plane, $Z=0.5$ cm, 1 cm, 2 cm, and 4 cm. The XY-plane at $Z=0$ contains tops of the embedded magnetic rods. Origin 7.0 software (OriginLab, Northampton, MA, USA) was used for graphing the 3D calculations generated with Mermaid software. As explained earlier, the magnetic field calculated with the 3D Mermaid model is calibrated using the measured data.

Although static, the magnetic field we use in the experiment is spatially dependent. The farther away from the surface of the magnet, the smaller is the magnetic field. Spatial dependence of variables is described by the variable's gradient, i.e. its change per distance. The gradient is obtained by subtracting the values of the variables at two adjacent points and then dividing the difference by the distance between the two points. In our case not only the magnetic field but the gradient of the magnetic field has different values at different points of the experimental volume, i.e. the cage and mice body. To fully describe the field we used, we give the values of the field at different points in space (Fig. 2). In order to summarize the information given in the figure we provide two numbers. The averaged magnetic field is obtained by summing the values of the magnetic field at different points in the experimental volume and dividing the sum by the number of points. The averaging of the gradient of the magnetic field is performed in the same manner, i.e., all the values are summed and then divided by the number of points. The maximal value of magnetic field is 60 mT and it occurs immediately above the magnets, i.e. at $Z=0$ mm. In order to classify the experiment according to the common magnetic field window classification

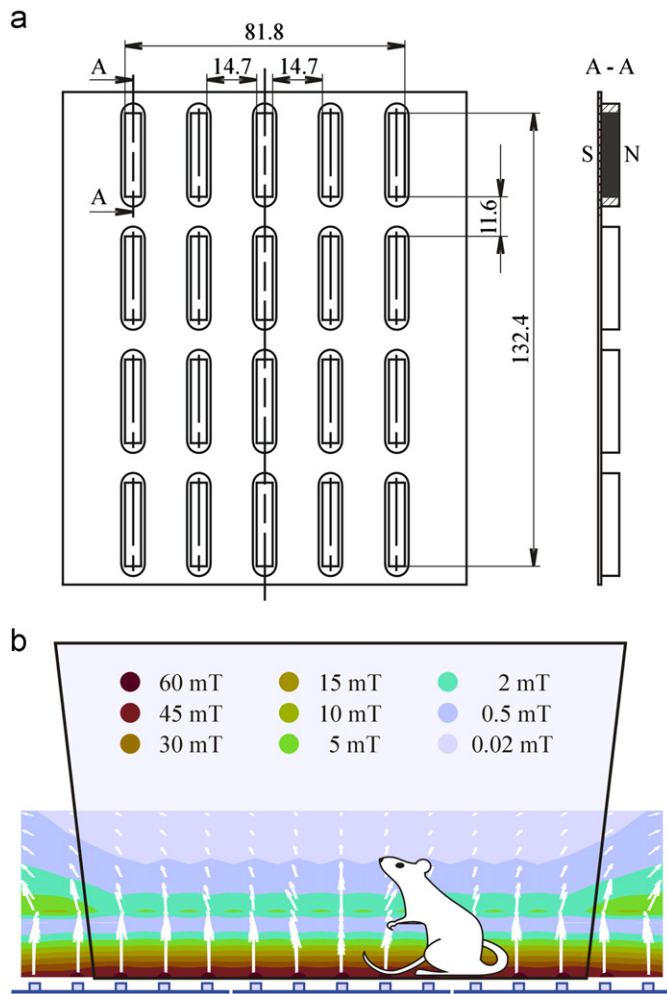


Fig. 1. Graphic presentation of MADU stripe (Panel A) and experimental setup (Panel B). Panel A The type L MADU stripe contains twenty ceramic ferromagnetic rods made of barium ferrite ($\text{BaFe}_{12}\text{O}_{19}$) embedded in a plastic sheet. The size of each rod is $4.8 \text{ mm} \times 24.4 \text{ mm} \times 4.8 \text{ mm}$. Magnetic rods are equidistantly distributed along X as well as along Y-axes, the distance between them being 14.7 mm and 11.6 mm, respectively. The magnetic axes of the rods are vertical and equally directed; the example shown corresponds to the upward directed magnetic field. Panel B Experimental setup. The vertical cross-section through the middle of the experimental setup is shown. The plastic cage with 4 or 5 animals is placed over MADU stripes. The magnetic field of MADU stripes is distributed throughout the experimental volume. The intensity of the magnetic field is indicated by different shades (colors). Also shown are magnetic lines of force. (For interpretation of the references to color in this figure legend, the reader is referred to the web version of this article.)

scheme (Markov et al., 1975; Zukov and Lazarovich, 1989; Markov, 2005, 2007a, 2011) the averaged values of the applied magnetic field and magnetic field gradient are used. The MADU stripes were placed directly beneath the two animal Plexiglas cages that were separated out by 10 cm. The animals were freely moving inside the cages; consequently, it seems reasonable to perform magnetic field averaging over the volume potentially occupied by the mice bodies. Since the height of a mice was 2 cm, we assumed that they were predominantly exposed to the part of SMF limited by the horizontal planes at $Z=0.5 \text{ cm}$ and $Z=2 \text{ cm}$. The averaged magnetic field and magnetic field gradient in the defined volume are calculated to be 15.63 mT and 9.8 mT/cm, respectively. Therefore, it can be concluded that the mice were exposed to the part of spatially dependant SMF of the MADU stripes characterized by the average magnetic field of 16 mT and average magnetic field gradient of 10 mT/cm.

2.3. Experimental design

Mice were randomly divided into three groups (9 per group). All three groups were kept under same conditions. The first experimental group was exposed to the upward oriented SMF (Up group). The second experimental group was exposed to the downward oriented SMF (Down group). The permanent magnets embedded in the MADU stripes cannot be removed or turned off. Therefore,

instead of using sham exposed animals we use a control group exposed to the ambient magnetic field. The ambient field is measured and the obtained value is $40 \mu\text{T}$, which is only 0.25% of the field to which Up and Down groups are exposed. Note that the magnetic field above MADU stripes is measured; therefore, it is the sum of the field produced by MADU magnets and the ambient magnetic field.

Exposure to SMF was conducted using three MADU stripes of different orientation that were placed under the plastic animal cage continuously for 28 days. Food consumption was measured daily and body mass weekly. Following the exposure period of 28 days, all mice were sacrificed and blood and spleen were collected for further analyses that were blindly performed.

2.4. Blood and spleen parameters

Blood parameters [erythrocytes, lymphocytes, monocytes, neutrophils, basophils, eosinophils, hemoglobin, hematocrit, MCV (mean corpuscular volume), MCH (mean corpuscular hemoglobin), MCHC (mean corpuscular hemoglobin concentration)] were determined using Hematological counter ABX Pentra 80X (Montpellier, France) according to manufacturer's recommendations. The total number of granulocytes in blood sample was calculated by summing neutrophils with basophils, and eosinophils.

Serum transferrin was analyzed using BioSystems photometer type BTS-330 (Barcelona, Spain) according to manufacturer's recommendations. Transferrin saturation was calculated from iron (Fe) and total iron binding capacity (TIBC) as serum $\text{Fe}/\text{TIBC} \times 100$.

Spleen was excised, connective and fat tissue were removed, and then spleen was weighted. A weighted part of the tissue was minced in 1 ml of saline and dispersed through 0.1 mm cell sieve (KDL, Anping, China) until only the remaining connective (white) tissue was visible. This cell suspension was additionally resuspended by pulling and pushing it 10 times through $0.45 \mu\text{m}$ needle placed on top of 5 ml syringe (Nipro, Zaventem, Belgium). Total cellular count was determined using counting chamber (Fein-Optik, Jena, Germany) and expressed as a number of nucleated cells per microliter of soluble homogenized tissue. A separate part of spleen tissue was macerated, dispersed through 0.1 mm cell sieve and smeared for hematological analysis. Spleen smears stained with May Grünwald–Giemsa (Carlo Erba, Rodano, Italy) were used to count erythrocytes, lymphocytes and granulocytes in ten visual fields by scoring 100 cells per one visual field of counting chamber and were expressed as a percentage of total number of counted cells (Vranic et al., 2000).

Iron was determined in serum, brain, liver and spleen tissue. Total serum iron was determined using BioSystems photometer type BTS-330 (Barcelona, Spain) according to manufacturer's recommendations. Transferrin-bound ferric ions in the serum samples were released by guadinium and reduced to ferrous by means of hydroxylamine. Ferrous ions reacted with ferrozine, forming a colored complex that was measured by spectrophotometer.

Brain, liver, and spleen tissue samples were prepared by microwave digestion (ETHOS TC, Milestone S.r.l., Sorisole, Italy) according to manufacturer's recommendations. Tissue of interest (0.5 g) was treated with 8 ml of nitric acid (HNO_3) and 2 ml of hydrogen peroxide (30% H_2O_2); temperature program was as follows: 5 min from room temperature to 180°C then 10 min hold at 180°C . After cooling, samples were transferred with deionised water in 50 ml volumetric flask. Analyses were carried out on atomic absorption spectrometer "SpectrAA 220" (Varian, Palo Alto, California, USA) according to Varian Atomic Absorption Spectrometers (AAS) Analytical Methods. Analytical quality control was achieved by analyzing certified reference material BCR-186 (Community Bureau of Reference—BCR, Brussels, Belgium), which is lyophilized pig kidney used for determining trace elements (Institute for Reference Materials and Measurements, Geel, Belgium). Replicate analyses were undertaken within the range of certified values. Iron values were expressed as μg of Fe per mg of dried analyzed tissue.

2.5. Statistical analysis

Statistical analysis was performed using software SPSS for Windows, version 10.0 (SPSS, Chicago, IL, USA). Difference between groups was evaluated by one-way ANOVA, followed by Fischer's LSD test. The level of significance was set at $p < 0.05$.

3. Results

3.1. Blood parameters

Blood parameters in control mice and mice exposed to differently oriented SMF are shown in Table 1. There was a trend in blood lymphocytes reduction and blood granulocytes increase in mice exposed to SMF. However, the exposure of mice to the differently oriented SMF did not alter erythrocytes and leukocytes count (lymphocytes, monocytes, neutrophils, basophils, granulocytes;

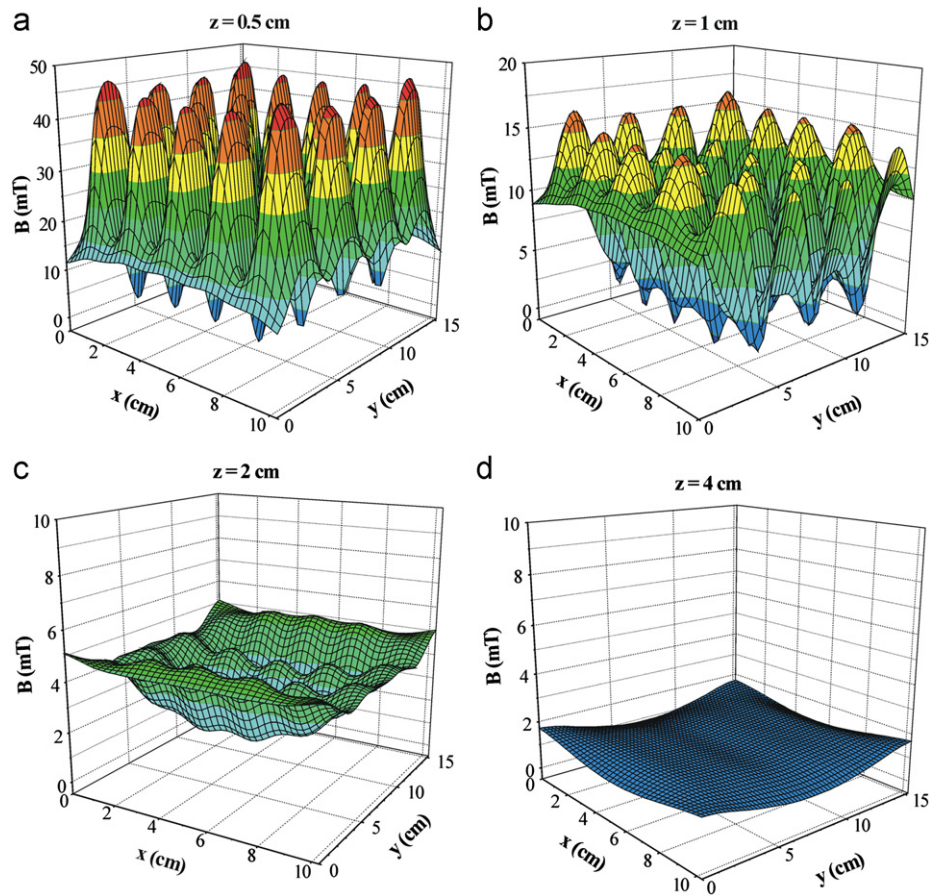


Fig. 2. Magnetic field of type L MADU stripe. Panels A, B, C, and D represent the magnetic field in the horizontal plane at $Z=0.5$ cm, 1 cm, 2 cm, and 4 cm, respectively. Panel A—The magnetic field in the horizontal plane at $Z=0.5$ cm; Panel B—The magnetic field in the horizontal plane at $Z=1$ cm; Panel C—The magnetic field in the horizontal plane at $Z=2$ cm; Panel D—The magnetic field in the horizontal plane at $Z=4$ cm.

Table 1

Blood parameters in mice exposed (Up group, Down group) or not exposed (Control group) to SMF of different orientation for 28 days.

Blood parameter	Up group	Down group	Control group
Erythrocytes ($\times 10^{12}/L$)	7.63 ± 0.39	6.93 ± 0.46	6.99 ± 0.55
Lymphocytes ($\times 10^9/L$)	2.03 ± 0.37	1.63 ± 0.20	4.19 ± 2.65
Monocytes ($\times 10^9/L$)	0.11 ± 0.04	0.12 ± 0.05	0.20 ± 0.14
Neutrophils ($\times 10^9/L$)	0.31 ± 0.06	0.29 ± 0.07	0.21 ± 0.04
Basophils ($\times 10^9/L$)	0.03 ± 0.01	0.04 ± 0.02	0.02 ± 0.01
Granulocytes ($\times 10^9/L$)	0.35 ± 0.07	0.33 ± 0.076	0.22 ± 0.056
Hemoglobin (g/L)	114.88 ± 4.89	101.38 ± 6.92	106.10 ± 7.54
Hematocrit (L/L)	0.38 ± 0.02	0.34 ± 0.02	0.35 ± 0.03
MCV (fL)	50.25 ± 1.28	48.67 ± 0.78	50.20 ± 1.21
MCH (pg)	15.13 ± 0.35	15.00 ± 0.29	15.40 ± 0.27
MCHC (g/L)	302.00 ± 2.96	306.33 ± 2.03	303.90 ± 2.31
Transferrin (mg/dL)	$47.96 \pm 2.78^{***,****}$	$37.99 \pm 2.58^*$	26.10 ± 3.83

Data are expressed as mean \pm SEM.

* $p < 0.05$ compared to control group.

** $p < 0.01$ compared to control group.

*** $p < 0.05$ compared to the down group.

$p > 0.05$). In addition, differently oriented SMF did not alter hemoglobin and hematocrit content, nor MCV, MCH or MCHC values among the groups ($p > 0.05$).

The up and down groups had statistically significant higher levels of serum transferrin compared to the control group (47.96 ± 2.78 and 37.99 ± 2.58 vs. 26.1 ± 3.83 ; $p < 0.01$ and $p < 0.05$, respectively). Additionally, animals exposed to the upward oriented SMF had higher levels of serum transferrin than those exposed to the downward field (47.96 ± 2.78 vs.

37.99 ± 2.58 ; $p < 0.05$). Taken together, both SMF exposed groups demonstrated statistically significant decrease in transferrin saturation, when compared to control animals, with more pronounced reduction in the down group (Fig. 3).

3.2. Spleen cellularity

Spleen cellular parameters in mice exposed to SMF of different orientation are shown in Fig. 4. Spleen cellularity in animals

exposed to the downward oriented SMF was significantly higher compared to those exposed to the upward oriented field (0.80 ± 0.02 vs. 0.60 ± 0.04 ; $p < 0.01$), and to control (0.80 ± 0.02 vs. 0.34 ± 0.02 ; $p < 0.01$). In addition, spleen cellularity in animals exposed to the upward oriented SMF (Fig. 4A) was significantly higher when compared to the control group (0.60 ± 0.04 vs. 0.34 ± 0.02 ; $p < 0.01$). However, there was no difference in spleen erythrocyte count (Fig. 4B) among the groups (20.49 ± 3.64 vs. 17.43 ± 1.76 vs. 20.12 ± 1.75 ; $p > 0.05$).

Spleen lymphocytes in the up group (Fig. 4C) were significantly higher than in the control group (75.90 ± 3.46 vs. 68.20 ± 1.38 ; $p < 0.05$) and spleen lymphocytes in the down group were also significantly higher when compared to control group (79.04 ± 1.71 vs. 68.20 ± 1.38 ; $p < 0.01$). In contrast, spleen granulocytes in the up (3.58 ± 0.72) and the down (3.52 ± 0.29) groups (Fig. 4D) were significantly lower than in the control group (11.66 ± 0.83 ; $p < 0.01$).

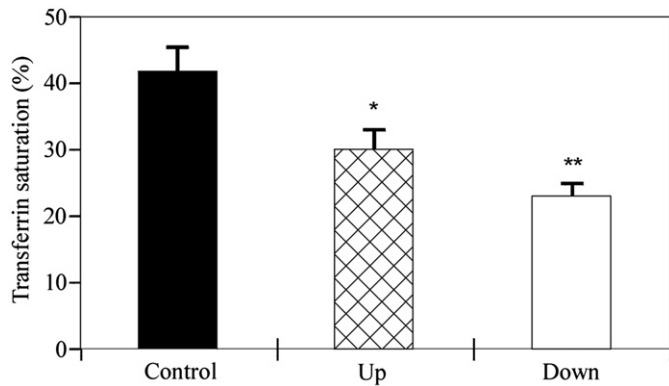


Fig. 3. Plasma transferrin saturation values in mice exposed (up, down) or not exposed (control) to SMF of different orientation for 28 days. Data are expressed as mean \pm SEM; * $p < 0.05$ compared to control group; ** $p < 0.01$ compared to control group.

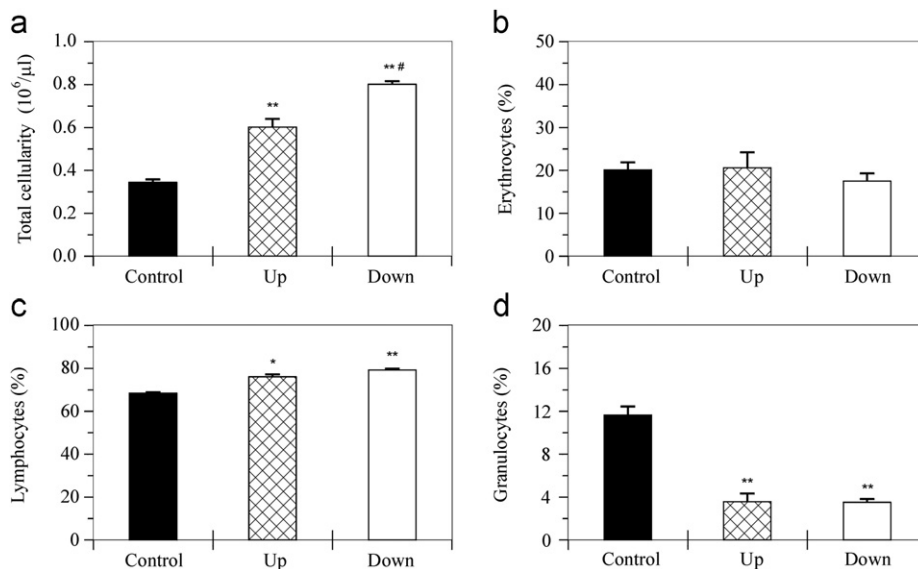


Fig. 4. Spleen cellular parameters in mice exposed to SMF of different orientation. Panel A—Total spleen cellularity in mice exposed (up, down) or not exposed (control) to SMF of different orientation for 28 days; Panel B—Spleen erythrocytes in mice exposed (up, down) or not exposed (control) to SMF of different orientation for 28 days; Panel C—Spleen lymphocytes in mice exposed (up, down) or not exposed (control) to SMF of different orientation for 28 days; Panel D—Spleen granulocytes in mice exposed (up, down) or not exposed (control) to SMF of different orientation for 28 days; Data are expressed as mean \pm SEM; * $p < 0.05$ compared to control group; ** $p < 0.01$ compared to control group; # $p < 0.01$ compared to the up group.

3.3. Serum and tissue iron content

Tissue and serum iron values in mice exposed to SMF of different orientation are shown in Fig. 5.

Brain showed significant decrease in iron content in the down group (15.75 ± 0.43) when compared to the up (18.92 ± 0.32) and the control group (19.92 ± 0.80 ; $p < 0.01$) (Fig. 5A).

Liver showed significant decrease in iron content in the up (261.73 ± 15.61) as well as in the down group (252.03 ± 10.96) when compared to the control group (310.30 ± 15.84 ; $p < 0.05$ and $p < 0.01$, respectively) (Fig. 5B).

Spleen showed significant increase in iron content in the up group (Fig. 5C) when compared to the control group (513.06 ± 35.79 vs. 394.85 ± 18.35 ; $p < 0.05$).

Serum showed significant increase in iron content in the up group (4.30 ± 1.40) compared to the down (2.22 ± 0.45) and the control group (2.83 ± 1.22 ; $p < 0.01$ and $p < 0.05$, respectively) (Fig. 5D).

3.4. Animal food intake and body mass

There was no difference in food intake between exposed and control animals. In addition, there was no difference in body mass between exposed and unexposed animals. (Data not shown)

4. Discussion

The applied static magnetic field was not uniform, but was vertically declining. In addition to vertical decrease the field variation in horizontal planes is intense and has local maxima and minima. The spatially averaged magnetic field of 16 mT is used as the closest approximation for the experiment classification by the magnetic field windows criteria.

Our investigation showed an increase in total spleen cellularity in mice exposed to 16 mT SMF of either orientation. In addition, total spleen cellularity was higher in the downward oriented SMF than in the upward oriented SMF or in the case of unexposed animals. The spleen lymphocyte count showed a statistically significant increase in SMF exposed animals, with a pronounced

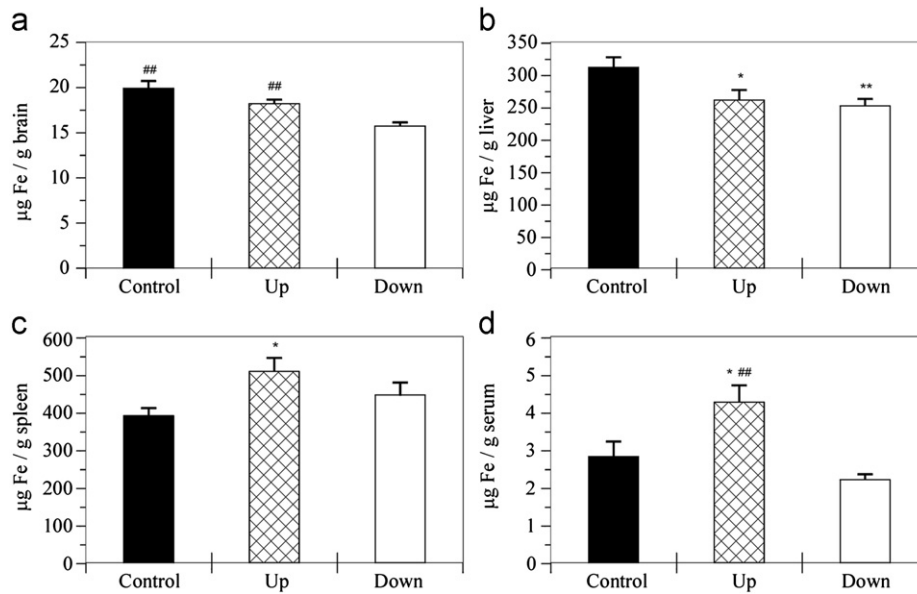


Fig. 5. Tissue and serum iron values in mice exposed to SMF of different orientation. Panel A—Brain iron values in mice exposed (up, down) or not exposed (control) to SMF of different orientation for 28 days; Panel B—Liver iron values in mice exposed (up, down) or not exposed (control) to SMF of different orientation for 28 days; Panel C—Spleen iron values in mice exposed (up, down) or not exposed (control) to SMF of different orientation for 28 days; Panel D—Serum iron values in mice exposed (up, down) or not exposed (control) to SMF of different orientation for 28 days; Data are expressed as mean \pm SEM; * p < 0.05 compared to control group; ** p < 0.01 compared to control group; *# p < 0.01 compared to the down group.

increase in the down group. We assumed that the increase in total spleen cellularity was due to the rise of lymphocyte count in exposed animals. This is additionally supported by the fact that majority of leukocytes in mice are lymphocytes (Green, 1966) and even a small increase in percent of lymphocytes could cause a large increase in total spleen cellularity. There was a simultaneous tendency of blood lymphocyte count decrease in SMF exposed animals. This result is in contrast to findings of decreased splenic lymphocytes in mice exposed to 2.9 μ T SMF (Hashish et al., 2008). The exposure time in that study (30 days) was similar to exposure period in our experiment, but the intensity of SMF in our experiment was around 5000 time higher, namely 16 mT. The difference in SMF intensities, strain of experimental animals (Swiss-Webster in our experiment and Swiss BALB/c in theirs) and type of used magnets (our magnetic stripes versus their classical magnetic disks) could account for the difference in splenic lymphocyte count. However, blood lymphocyte count showed similar patterns in both studies. We assumed that due to subchronic exposure and concurrent adaptation, the spleen, which is a main lymphopoietic organ in mice (Green, 1966), increased lymphocytes production and their preservation in the organ without statistically significantly decreasing blood lymphocytes.

Previous research showed that SMF influences biological system in a way that causes proinflammatory changes, as well as an increase in production of reactive oxygen species (Sahebamei et al., 2007; Hashish et al., 2008; Zhao et al., 2011). We found a statistically significant decrease in spleen granulocyte count and a tendency of blood granulocyte count to increase in SMF exposed animals. These findings are comparable to those from other studies, which demonstrate granulocyte count increase in blood of SMF exposed mice (Hashish et al., 2008). Explanation behind the observed changes in our study could be that phagocytosis and death of granulocytes, which are associated with production of free radicals, are increased in splenic tissue of animals exposed to either SMF orientation.

Red blood cells count did not change in blood or in spleen between exposed and unexposed group. This is in accordance with findings that mice exposed to SMF for 30 days and rats

exposed to extreme low frequency magnetic field for 50 and 100 days did not show alteration in red blood cell count (Hashish et al., 2008; Cakir et al., 2009). We concluded that various intensities of SMF and different exposure time do not influence red blood cells count in blood and spleen of experimental animals. This is probably due to fast recovery of the red blood cells after their exposure to the SMF.

Iron is an absolute requirement for most forms of life because of its unusual flexibility to serve both as an electron donor and an acceptor. It can be potentially toxic since free iron in the cell can catalyze conversion of hydrogen peroxide to free radicals. To prevent this scenario, all life forms that use iron bind that iron to proteins. This allows cells to benefit from iron while limiting its ability to harm. Majority of iron is located in hemoglobin molecules of red blood cells (RBCs), and the rest is stored in a form of ferritin in liver, spleen, and bone marrow. The liver's stores of ferritin are the primary physiologic source of reserve iron in the body. Macrophages also store iron as part of process of breaking down and processing hemoglobin. Once RBCs are degraded, macrophages recycle iron by putting it onto transferrin molecules that carry iron through the blood. In addition, macrophages require iron for their own antibacterial activity (Alford et al., 1991).

Main iron storage organs in mice are liver, heart and brain (Hahn et al., 2009). In our experiment, liver demonstrated a marked decrease of iron content in the up and in the down groups when compared to control animals. Besides liver, we have also determined the amount of iron in spleen and brain. While dynamics of iron in liver of animals in the exposed groups was the same, there was a difference in dynamics of iron in brain and spleen from the animals exposed to the upward or the downward directed field when compared to control. Namely, in the animals exposed to the upward magnetic field, the amount of iron did not change in the brain; it dropped in the liver and increased in spleen. On the other hand, in the animals exposed to the downward magnetic field, the amount of iron decreased both in the brain and liver while remaining unchanged in the spleen. Results from the animals exposed to the upward field may suggest

relocation of iron from storage in liver to spleen for possible lymphopoiesis. However, the effects of downward magnetic field on iron are harder to explain. Iron in brain is tightly regulated and its elimination is undesired. While too much iron can cause oxidative stress, too little iron can result in energy insufficiency. It was unclear where brain and liver iron relocates in animals exposed to the downward magnetic field. We considered macrophages to be a possible destination of this process. To test this hypothesis, we measured serum iron and transferrin in all animal groups.

Transferrins are iron-binding blood plasma proteins that control the level of free iron in biological fluids (Crichton and Charleaux-Wauters, 1987). The affinity of transferrin for iron is very high, but progressively decreases with pH going down below neutrality. Liver is a key source of the transferrin production but other places such as brain also produce transferrin. The main role of transferrin is in transport of iron from absorption center in duodenum or from RBCs recycling centers in reticuloendothelial macrophages to tissues. Transferrin is not only crucial for erythropoiesis and cell division (Macedo and de Sousa, 2008), but also plays a role in innate immunity. Transferrin is responsible for iron withholding that impedes bacterial survival. Consequently, the level of transferrin decreases in inflammation (Ritchie et al., 1999). However, in mice the level of transferrin increases in inflammation during acute phase response (Barnum-Huckins et al., 1997).

In our experiments, we have noticed different serum iron dynamics in animals exposed to the magnetic field while there was no difference in pattern of transferrin production or transferrin saturation between exposed groups. In the up group serum iron and production of transferrin increased, while transferrin saturation decreased when compared to control. In the down group serum iron did not change, transferrin saturation decreased and transferrin production increased compared to control. In both groups decreases in transferrin saturation could be explained by possible decrease of pH or by increases in transferrin production. The transferrin production in the case of the up group should have been larger than the surplus of iron. Serum iron in the up group could have increased due to transport from liver to spleen. Serum iron in the down group did not change. There is a possibility that iron in the down group ended up in the macrophages and this could be the reason that no changes in serum or spleen iron were detected there.

It has been recently shown that short-term exposure to SMF (128 mT/1 h/5 days) produced statistically significant decrease in serum iron (Elferchichi et al., 2007). The same experimental design demonstrated that SMF (128 mT/1 h/5 days) induced sympathetic hyperactivity in rats (Abdelmelek et al., 2006). This result has been explained through the high turnover of norepinephrine in the noradrenergic system that could negatively influence the peristaltic activity implicated in the assimilation of divalent elements such as iron (Abdelmelek et al., 2006). This could be true for acute exposure; however, after 28 days of exposure to SMF the level of serum iron increased in our experiment, most probably as a result of redistribution from other compartments rich in iron such as liver. The rise of spleen content showed the main end point of iron relocation. It is well established that through the Fenton reaction, ferro ion (Fe^{2+}) transforms the weak oxidant hydrogen peroxide into hydroxyl radical ($\text{HO}^{\cdot-}$), one of the most reactive species in nature (Arredondo and Nunez, 2005). Iron is important for immune response in several ways. Macrophages exhibit reduced bactericidal activity and neutrophils have reduced activity of the iron-containing enzyme myeloperoxidase when there is a lack of iron. Iron deficiency also results in decreased T-lymphocyte numbers and in decreased T-lymphocyte blastogenesis and mitogenesis (Kuvibidila et al., 1999). Therefore, our results are in line with the supposition that increased iron level in the spleen could contribute to the proinflammatory response. This result goes along

with the increase in the serum granulocytes and decreased lymphocytes, the findings that previously have been shown to contribute to the increase in immune response and oxidative stress (Hashish et al., 2008).

Alongside proinflammatory effect, our results lead us to assume that 16 mT SMF induced chronic stress. Static magnetic field exposure induces a common stress response in cell cultures, in spite of the differences related to exposure time and to the cell types (Dini and Abbro, 2005). In our study, the level of serum transferrin also changed under the influence of SMF. Namely, mice exposed to the upward oriented SMF had higher values of serum transferrin than mice exposed to the downward oriented SMF or unexposed animals. Mice exposed to the downward oriented SMF also had higher levels of transferrin when compared to unexposed animals. A similar finding was observed in study of mice exposed to 128 mT SMF and it was explained as an increase in iron metabolism induced by SMF (Elferchichi et al., 2007). In addition, transferrin in mice has a role in unspecific acute phase response to inflammation as its positive indicator (Barnum-Huckins et al., 1997). Since exposure period in our study was 28 days, increased transferrin level in treated animals is more likely specific adaptive reaction to subchronically induced SMF stress rather than an unspecific stress reaction. Transferrin saturation was reduced in both SMF groups when compared to control. However, the rise of serum transferrin was so immense (almost doubled in the up group), that it might surpass the need for saturation. Also, iron level in the spleen increased, and it may not be achieved with reduced transferrin saturation, so the saturation may be decreased, but not to extent to disturb iron distribution.

Our results have demonstrated that continuous exposure to 16 mT SMF has no effect on body mass and food intake. Various researchers had similar findings using SMF of different field intensity or different exposure times on rats and mice (Margonato et al., 1995; Robertson et al., 1996; High et al., 2000). The overall data on food consumption and body mass confirm that SMF cause adaptation to stress in subchronically exposed animals.

The validity and significance of our results is additionally substantiated by the fact that we worked with an outbred, genetically diverse strain of mice, since statistical significance is achieved more easily when using a genetically identical inbred strain of mice.

5. Conclusions

Our study is the first, to our knowledge, in vivo experiment that has simultaneously used separate upward and downward oriented magnetic fields. We employed spatially dependent SMF with the average intensity of 16 mT to investigate hematological parameters in our model. Obtained results showed significant increase in total spleen cellularity in SMF exposed animals, especially in animals exposed to the downward directed magnetic field. Moreover, subchronic continuous exposure to the spatially dependent SMF whose average intensity of 16 mT was found to cause lymphocyte and granulocyte redistribution between spleen and blood, in a way that is typical for stress induced hematological changes. Serum transferrin levels, body mass and food intake confirm that these changes are not due to an unspecific stress response, but rather that they are caused by specific adaptation to subchronic SMF exposure.

Conflict of interest

The authors have no conflict of interest regarding the material and information presented in the article.

Role of funding source

No funding body had any involvement in the preparation or content of this article or in the decision to submit it for publication.

Acknowledgment

This study was supported by the grants No III-41013 and No III-41019 from the Ministry of Education and Science, Government of Serbia

References

- Abdelmelek, H., Molnar, A., Servais, S., Cottet-Emard, J.M., Pequignot, J.M., Favier, R., Sakly, M., 2006. Skeletal muscle HSP72 and norepinephrine response to static magnetic field in rat. *J. Neural. Transm.* 113, 821–827.
- Alford, C.E., King Jr., T.E., Campbell, P.A., 1991. Role of transferrin, transferrin receptors, and iron in macrophage listericidal activity. *J. Exp. Med.* 174 (2), 459–466.
- Arredondo, M., Nunez, M.T., 2005. Iron and copper metabolism. *Mol. Asp. Med.* 26, 313–327.
- Azanza, M.J., del Moral, A., 1994. Cell membrane biochemistry and neurobiological approach to biomagnetism. *Prog. Neurobiol.* 44, 517–601.
- Bawin, S.M., Adey, W.R., 1976. Sensitivity of calcium binding in cerebral tissue to weak environmental electric fields oscillating at low frequency. *Proc. Natl. Acad. Sci. USA* 73, 1999–2003.
- Barnum-Huckins, K.M., Martínez, A.O., Rivera, E.V., Adrian Jr., E.K., Herbert, D.C., Weaker, F.J., Walter, C.A., Adrian, G.S., 1997. A comparison of the suppression of human transferrin synthesis by lead and lypopolysaccharide. *Toxicology* 118, 11–22.
- Cakir, D.U., Yokus, B., Akdag, M.Z., Sert, C., Mete, N., 2009. Alterations of hematological variations in rats exposed to extremely low frequency magnetic fields (50 Hz). *Arch. Med. Res.* 40, 352–356.
- Campbell, W.H., 2001. *Nature's magnetism, Earth Magnetism: A Guided Tour Through Magnetic Fields*. Harcourt/Academic Press, San Diego, pp. 1–23 (Chapter 1).
- Colbert, A.P., Souder, J., Markov, M., 2009. Static magnetic field therapy: methodological challenges to conducting clinical trials. *Environmentalist* 29, 177–185.
- Crichton, R.R., Charletoaux-Wauters, M., 1987. Iron transport and storage. *Eur. J. Biochem.* 164 (3), 485–506.
- Dini, L., Abbro, L., 2005. Bioeffects of moderate-intensity static magnetic fields on cell cultures. *Micron* 36, 195–217.
- Dini, L., Panzarini, E., 2010. The influence of a 6 mT static magnetic field on apoptotic cell phagocytosis depends on monocyte/macrophage differentiation. *Exp. Biol. Med.* 235, 1432–1441.
- Eccles, N.K., 2005. A critical review of randomized controlled trials of static magnets for pain relief. *J. Altern. Complement. Med.* 11 (3), 495–509.
- Elblbesy, M.A., 2010. Effect of static magnetic field on erythrocytes characterizations. *J. Biomed. Sci. Eng.* 3, 300–303.
- Elferchichi, M., Abdelmelek, H., Sakly, M., 2007. Effects of sub-acute exposure to static magnetic field on iron status and hematopoiesis in rats. *Turk. J. Hematol.* 24, 64–68.
- Engstrom, S., Markov, M.S., McLean, M.J., Holcomb, R.R., Markov, J.M., 2002. Effects of non-uniform static magnetic fields on the rate of myosin phosphorylation. *Bioelectromagnetics* 23, 475–479.
- Green, E.L., 1966. *Biology of the laboratory mouse*. Dover publications, New York.
- Hahn, P., Song, Y., Ying, G.S., He, X., Beard, J., Dunaief, J.L., 2009. Age-dependent and gender-specific changes in mouse tissue iron by strain. *Exp. Gerontol.* 44, 594–600.
- Hashish, A.H., El-Missiry, M.A., Abdelkader, H.I., Abou-Saleh, R.H., 2008. Assessment of biological changes of continuous whole body exposure to static magnetic field and extremely low frequency electromagnetic fields in mice. *Ecotoxicol. Environ. Saf.* 71, 895–902.
- Health Protection Agency, 2008. *Static Magnetic Fields*. Report of the independent Advisory Group on Non-ionising Radiation. RCE-6. Documents of the Health Protection Agency. Radiation, Chemical and Environmental Hazards. Chilton, U.K.
- High, W.B., Sikora, J., Ugurbil, K., Garwood, M., 2000. Subchronic in vivo effects of a high static magnetic field (9.4T) in rats. *J. Magn. Reson. Imaging* 12, 122–139.
- Kowalczyk, C.I., Sienkiewicz, Z.J., Saunders, R.D., 1991. *Biological Effects of Exposure to Non-ionizing Electromagnetic Fields and Radiation*. I. Static Electric and Magnetic Fields (NRPB-R238). National Radiation Protection Board, Chilton, U.K.
- Krylov, A.V., Tarakanova, G.A., 1960. Magnetotropism of plants and its nature. *Plant. Physiol.* 7, 156–160.
- Kuvibidila, S.R., Kitchens, D., Baliga, B.S., 1999. In vivo and in vitro iron deficiency reduces protein kinase C activity and translocation in murine splenic and purified T cells. *J. Cell. Biochem.* 74, 468–478.
- Löscher, W., 2003. Potential risks of magnetic fields: experimental studies on teratogenicity and carcinogenicity of static and extremely low frequency magnetic fields. In: McLean, M.J., Engström, S., Holcomb, R.R. (Eds.), *Magneto-therapy: Potential Therapeutic Benefits and Adverse Effects*. The Floating Gallery, New York, pp. 41–56.
- Macedo, M.F., de Sousa, M., 2008. Transferrin and the transferrin receptor: of magic bullets and other concerns. *Inflamm. Allergy—Drug Targets* 7 (1), 41–52.
- Maronato, V., Nicolini, P., Conti, R., Zecca, L., Veicsteinas, A., Cerretelli, P., 1995. Biologic effects of prolonged exposure to ELF electromagnetic fields in rats: II. 50 Hz magnetic fields. *Bioelectromagnetics* 16, 343–355.
- Markov, M.S., Todorov, S.I., Ratcheva, M.R., 1975. Biomagnetic effects of the constant magnetic field action on water and physiological activity. In: Jensen, K., Vassileva, Y. (Eds.), *Physical Bases of Biological Information Transfer*. Plenum Press, New York, pp. 441–445.
- Markov, M.S., 2005. "Biological windows": a tribute to W. Ross Adey. *Environmentalist* 25, 67–74.
- Markov, M.S., 2007a. Therapeutic application of static magnetic fields. *Environmentalist* 27, 457–463.
- Markov, M.S., 2007b. Magnetic field therapy: a review. *Electromagn. Biol. Med.* 26, 1–23.
- Markov, M.S., 2011. How living systems recognize applied electromagnetic fields. *Environmentalist* 31 (2), 89–96.
- McLean, M.J., Holcomb, R.R., Wamil, A.W., Pickett, J.D., Cavopol, A.V., 1995. Blockade of sensory neuron action potentials by a static magnetic field in the 10 mT range. *Bioelectromagnetics* 16, 20–32.
- Ritchie, R.F., Palomaki, G.E., Neveux, L.M., Navolotskaia, O., Ledue, T.B., Craig, W.Y., 1999. Reference distributions for the negative acute-phase serum proteins, albumin, transferrin and transthyretin: a practical, simple and clinically relevant approach in a large cohort. *J. Clin. Lab. Anal.* 13 (6), 273–279.
- Robertson, I.G., Wilson, W.R., Dawson, B.V., Zwi, L.J., Green, A.W., Boys, J.T., 1996. Evaluation of potential health effects of 10 kHz magnetic fields: a short-term mouse toxicology study. *Bioelectromagnetics* 17, 111–122.
- Ružič, R., Jerman, I., Jeglič, A., Fefer, D., 1993. Various effects of pulsed and static magnetic fields on the development of *Castanea sativa* Mill in tissue culture. *Electro-Magnetobiol* 12, 165–177.
- Sahebamei, H., Abdolmaleki, P., Ghanati, F., 2007. Effects of magnetic field on the antioxidant enzyme activities of suspension-cultured tobacco cells. *Bioelectromagnetics* 28, 42–47.
- Schenck, J.F., 2000. Safety of strong magnetic fields. *J. Magn. Reson. Imaging* 12, 2–19.
- Stuchly, M.A., 1986. Human exposure to static and time-varying magnetic fields. *Health Phys* 51, 215–225.
- Tavasoli, Z., Abdolmaleki, P., Mowla, S.J., Ghanati, F., Sarvestani, A.S., 2009. Investigation of the effects of static magnetic field on apoptosis in bone marrow stem cells of rat. *Environmentalist* 29 (2), 220–224.
- Trabulsi, R., Pawlowski, B., Wieraszko, A., 1996. The influence of steady magnetic fields on the mouse hippocampal evoked potentials in vitro. *Brain. Res.* 728 (1), 135–139.
- Ukolova, M.A., Kvakina, E.B., Garkavi, L.H., 1975. *Stages of Magnetic Field Action. Problems of Action of Magnetic Fields on Biological Systems*, vol. 1. Nauka, Moscow, pp. 57–71.
- Vranic, V., Savovski, K., Dedovic, N., Dimitrijevic, B., 2000. Hematological toxicity associated with tiazofurin-influence on erythropoiesis. *Toxicol. Lett.* 114, 81–90.
- Wieraszko, A., 2000. Dantrolene modulates the influence of steady magnetic fields on hippocampal evoked potentials in vitro. *Bioelectromagnetics* 21 (3), 175–182.
- World Health Organization, 2006a. *Static Fields (Environmental Health Criteria: 232)*. Geneva, Switzerland.
- World Health Organization, 2006b. *Electromagnetic Fields and Public Health: Static Electric and Magnetic Fields*. WHO Fact Sheet #299, Geneva, Switzerland.
- Yano, A., Hidaka, E., Fujiwara, K., Imoto, M., 2001. Induction of primary root curvature in radish seedlings in a static magnetic field. *Bioelectromagnetics* 22 (3), 194–199.
- Zhao, G., Chen, S., Wang, L., Zhao, Y., Wang, J., Wang, X., Zhang, W.W., Wu, R., Wu, L., Wu, Y., Xu, A., 2011. Cellular ATP content was decreased by a homogeneous 8.5 T static magnetic field exposure: role of reactive oxygen species. *Bioelectromagnetics* 32, 94–101.
- Zukov, B.N., Lazarovich, V.G., 1989. *Magneto-therapy in Angiology*. Zdorovie, Kiev, p. 111.

IEEE TRANSACTIONS ON NUCLEAR SCIENCE

A PUBLICATION OF THE IEEE NUCLEAR AND PLASMA SCIENCES SOCIETY

APRIL 2012

VOLUME 59

NUMBER 2

IETNAE

(ISSN 0018-9499)

17TH REAL TIME CONFERENCE (RT2010)
LISBON, PORTUGAL, MAY 24–28, 2010

Performance Analysis of a DWDM Optical Transmission System
..... A. Aloisio, F. Ameli, A. D'Amico, R. Giordano, G. Giovanetti, and V. Izzo 251

17TH INTERNATIONAL WORKSHOP ON ROOM-TEMPERATURE SEMICONDUCTOR X- AND GAMMA-RAY DETECTORS
KNOXVILLE, TN, OCTOBER 30–NOVEMBER 6, 2010

CZT AND CdTe DEVICE PERFORMANCE IMPROVEMENTS

Elimination of Te Inclusions in $Cd_{1-x}Zn_xTe$ Crystals by Short-term Thermal Annealing
..... P. Fochuk, R. Grill, O. Kopach, A. E. Bolotnikov, E. Belas, M. Bugar,
G. Camarda, W. Chan, Y. Cui, A. Hossain, K. H. Kim, I. Nakonechnyi, O. Panchuk, G. Yang, and R. B. James 256

CZT AND CdTe GROWTH AND CHARACTERIZATION

Crystal Defects in CdZnTe Crystals Grown by the Modified Low-Pressure Bridgman Method
..... L. Marchini, A. Zappettini, M. Zha, N. Zambelli, A. E. Bolotnikov, G. S. Camarda, and R. B. James 264

REGULAR PAPERS

ACCELERATOR TECHNOLOGY

Analytical Prediction of Ion Stripping Extraction From Isochronous Cyclotrons
..... J. L. Ristić-Djurović and N. Nešković 268
Enhancement of Ion Beam Acceleration Efficiency in Isochronous Cyclotrons
..... A. Ž. Ilić, J. L. Ristić-Djurović, S. Čirković, and N. Nešković 272

ANALOG AND DIGITAL CIRCUITS

High Voltage Power Supply With High Output Current and Low Power Consumption for Photomultiplier Tubes
..... J. P. V. S. Cunha, M. Begalli, and M. D. Bellar 281

(Contents Continued on Page 249)

A Tunable Delay Line for Fast Analog Pulses as Key Element of a New Sum-Trigger for Cherenkov Telescopes	289
..... <i>D. Haefner, T. Schweizer, M. Shayduk, R. Mirzoyan, and M. Teshima</i>	
A 10-Bit Multichannel Digitizer ASIC for Detectors in Particle Physics Experiments	294
..... <i>M. Idzik, K. Swientek, T. Fiutowski, S. Kulis, and D. Przyborowski</i>	

COMPUTING, SIMULATION, ALGORITHMS, AND SOFTWARE

The Plateau de Bure Neutron Monitor: Design, Operation and Monte Carlo Simulation	303
..... <i>S. Semikh, S. Serre, J. L. Aufran, D. Munteanu, S. Sauze, E. Yakushev, and S. Rozov</i>	
Computation of Neutron Multiplicity Statistics Using Deterministic Transport	314
..... <i>J. Mattingly</i>	
Estimating Transmission Curves of Primary X-Ray Beams Used in Diagnostic Radiology	323
..... <i>G. Hoff, S. F. Firmino, R. M. Papaléo, and M. T. M. B. de Vilhena</i>	
Improvement of Performance of Cardiac SPECT Camera Using Curved Detectors With Pinholes	334
..... <i>J. Dey</i>	

DIGITAL SIGNAL PROCESSING

The FastTracker Real Time Processor and Its Impact on Muon Isolation, Tau and b-Jet Online Selections at ATLAS	348
..... <i>A. Andreani, A. Andreatza, A. Annovi, M. Beretta, V. Bevacqua, G. Blazey, M. Bogdan, E. Bossini, A. Boveia, V. Cavaliere, F. Canelli, F. Cervigni, Y. Cheng, M. Citterio, F. Crescioli, M. Dell'Orso, G. Drake, M. Dunford, P. Giannetti, F. Giorgi, J. Hoff, A. Kapliy, M. Kasten, Y. K. Kim, N. Kimura, A. Lanza, H. L. Li, V. Liberali, T. Liu, D. Magalotti, A. McCarn, C. Melachrinou, C. Meroni, A. Negri, M. Neubauer, J. Olsen, B. Penning, M. Piendibene, J. Proudfoot, M. Riva, C. Roda, F. Sabatini, I. Sacco, M. Shochet, A. Stabile, F. Tang, J. Tang, R. Tripiccion, J. Tuggle, V. Vercesi, M. Villa, R. A. Vitillo, G. Volpi, J. Webster, K. Yorita, and J. Zhang</i>	
The DLED Algorithm for Timing Measurements on Large Area SiPMs Coupled to Scintillators	358
..... <i>A. Gola, C. Piemonte, and A. Tarolli</i>	
The Digital Processing System for the Soft X-Ray Spectrometer Onboard ASTRO-H—The Design and the Performance—	366
..... <i>H. Seta, M. S. Tashiro, Y. Ishisaki, M. Tsujimoto, Y. Shimoda, Y. Abe, T. Yasuda, S. Takeda, M. Asahina, Y. Hiyama, S. Yamaguchi, Y. Terada, K. R. Boyce, F. S. Porter, C. A. Kilbourne, R. L. Kelley, R. Fujimoto, Y. Takei, K. Mitsuda, K. Matsuda, and K. Masukawa</i>	

DOSIMETRY

Floating Gate CMOS Dosimeter With Frequency Output	373
..... <i>E. Garcia-Moreno, E. Isern, M. Roca, R. Picos, J. Font, J. Cesari, and A. Pineda</i>	

HIGH ENERGY PHYSICS DETECTORS

Development and Commissioning of the Timing Counter for the MEG Experiment	379
..... <i>M. De Gerone, D. Dussoni, K. Fratini, F. Gatti, R. Valle, G. Boca, P. W. Cattaneo, R. Nardò, M. Rossella, L. Galli, M. Grassi, D. Nicolò, Y. Uchiyama, and D. Zanella</i>	

HOMELAND SECURITY APPLICATIONS

The Application of High Energy Resolution Green's Functions to Threat Scenario Simulation	389
..... <i>G. G. Thoreson and E. A. Schneider</i>	

NUCLEAR POWER INSTRUMENTATION AND CONTROL

Fault Diagnosis of Helical Coil Steam Generator Systems of an Integral Pressurized Water Reactor Using Optimal Sensor Selection	403
..... <i>F. Li, B. R. Upadhyaya, and S. R. P. Perillo</i>	
On-Line Fault Recognition System for the Analogic Channels of VVER 1000/400 Nuclear Reactors	411
..... <i>M. Yazikov, G. Gola, O. Berg, J. Porsmyr, H. Valseth, D. Roverso, and M. Hoffmann</i>	

RADIATION DAMAGE EFFECTS

Annealing at Different Temperatures of Silicon Microstrip Detectors After Severe Hadron Irradiation 419
..... G. Casse, A. Affolder, P. P. Allport, V. Chmill, D. Forshaw, A. Greenall, T. Huse, I. Tsurin, and M. Wormald

RADIATION EFFECTS

Radiation Induced Absorption in Rare Earth Doped Optical Fibers M. Lezius, K. Predehl, W. Stöwer, A. Türler,
M. Greiter, Ch. Hoeschen, P. Thirolf, W. Assmann, D. Habs, A. Prokofiev, C. Ekström, T. W. Hänsch, and R. Holzwarth 425
SET Tolerant Dynamic Logic X. She, N. Li, and D. O. Erstad 434
Synergistic Radiation Effects on PNP Transistors Caused by Protons and Electrons
..... X. Li, C. Liu, H. Geng, E. Rui, D. Yang, and S. He 439
A Dynamic Model for the Validation of Cosmic Rays Anisotropy at Low Earth Orbit F. F. Badavi 447
Interactions of Energetic Particle Radiation With a MCT ($x = 0.48$) P on N Detector Array
..... C. F. Bruce, W. Kim, and B. Richardson 456

RADIATION IMAGING

Development of the X'tal Cube: A 3D Position-Sensitive Radiation Detector With All-Surface MPPC Readout
..... Y. Yazaki, N. Inadama, F. Nishikido,
T. Mitsuhashi, M. Suga, K. Shibuya, M. Watanabe, T. Yamashita, E. Yoshida, H. Murayama, and T. Yamaya 462
Maximum-Likelihood Deconvolution in the Spatial and Spatial-Energy Domain for Events With Any Number of
Interactions W. Wang, C. G. Wahl, J. M. Jaworski, and Z. He 469

SCINTILLATION DETECTORS

Investigation of Eu^{2+} Doped Barium Silicates as Scintillators
..... Y. Eagleman, E. Bourret-Courchesne, and S. E. Derenzo 479

Enhancement of Ion Beam Acceleration Efficiency in Isochronous Cyclotrons

Andjelija Ž. Ilić, *Member, IEEE*, Jasna L. Ristić-Djurović, Saša Ćirković, and Nebojša Nešković

Abstract—A novel method for efficient analysis of ion beam acceleration in an isochronous cyclotron is proposed. Numerical simulation is used to perform multiple beam dynamics analyses on the conveniently chosen subsets of data; consequently, the total quantity of studied data is significantly reduced. The obtained results provide direct insight into beam behavior and quality of acceleration. Therefore, the analysis is not only efficient, but detailed and systematic as well. It is used to assess the impact of the accelerated orbit optimization to the enhancement of acceleration efficiency when study is extended from a single test ion to the complete ion beam consideration.

Index Terms—Acceleration efficiency, cyclotrons, multipurpose, optimal acceleration, particle beam acceptances, particle beam dynamics.

I. INTRODUCTION

ISOCHRONOUS or AVF cyclotrons (“azimuthally varying field” cyclotrons) are currently following one of the two development routes. The manufacturers of commercial cyclotrons, facing market competition, are focused on the constant improvement of the small single purpose machines in terms of performances and price [1]–[3]. At the same time, advanced research centers and radioactive ion beam facilities throughout the world are being equipped by the ever larger and more powerful multipurpose isochronous cyclotrons [4]–[11]. Intended for acceleration of various ion beams in different operation regimes, multipurpose cyclotrons often serve for both research and commercial applications. They are used either separately or as elements in a chain of accelerating structures which deliver high energy ion beams.

The method to achieve optimal acceleration of a test ion in isochronized azimuthally varying magnetic fields, with all the imperfections due to machining, construction and field profile realization constraints, has been suggested in our previous work [12]. Although generally applicable, it is expected to be especially useful in the design of multipurpose machines, requiring the simultaneous optimization of more than one operation mode.

The obtained range of optimal accelerating conditions from [12] corresponds to single test ion acceleration. It is very narrow

in comparison with the typical beam emittances and can be matched only by a very small fraction of beam ions. However, with the appropriate choice of the referent test ion, the whole beam acceleration is expected to be optimized as well. Detailed beam tracking is required to assess the impact optimization has on the whole beam acceleration.

We propose to apply an accelerated orbit optimization for a referent test ion to the whole ion beam acceleration, so that the statistical center of a beam bunch coincides with the optimal accelerating conditions. In that case, the average variation of the phase space coordinates from their optimal values would be the least. The acceleration efficiency throughout the beam acceptance region is evaluated in order to quantify the overall impact of such optimization. Analysis efficiency results from the in-depth examination of beam dynamics on the conveniently chosen subsets of the initial six-dimensional phase space coordinates. Namely, numerical simulations offer the benefit of separate analysis on different subsets of data and only subsequent to this the joint interpretation of the results. The measurement systems observe all six phase space dimensions at once, and probably because of that, the beam tracking analyses as well are customarily conducted in the six-dimensional phase space as a whole. The computational power available nowadays allows for comprehensive and accurate beam dynamics simulations. Previous analysis of optimal accelerating conditions in very high intensity beams, employing millions of particles, can be found in [13]–[15]. Our primary goal was to perform accurate and systematic acceleration efficiency study when using a small personal computer. To obtain the accurate results, the coordinate coupling is constantly kept in mind and the data subsets are chosen accordingly. The total quantity of data is thereby significantly reduced, keeping the benefit of providing direct insight into the quality of the acceleration process. Beam acceptance, its distribution with respect to the acceleration efficiency, and the coupling of phase space coordinates are analyzed.

As an illustration of the method, and to yield general insight into the behavior of the beam as a whole, detailed beam tracking is performed for the input parameters corresponding to the VINCY Cyclotron [13] and the 65 MeV H^- test ion. The measured magnetic field used is the same as in [12]; it provides the best obtainable isochronism in the considered magnetic structure with the available ranges of main and trim coil currents [17], [18]. The first harmonic mode of the cyclotron operation corresponds to the H^- test ion acceleration. The accelerating region layout and the main characteristics of the VINCY Cyclotron are given in Fig. 1 and Table I, respectively.

The computer simulations are performed using the ion beam tracking module of the self written VINDY-A software package

Manuscript received November 01, 2011; revised December 13, 2011; accepted December 13, 2011. Date of publication February 07, 2012; date of current version April 13, 2012. This work was supported by the Serbian Ministry of Education and Science through the project “Physics and Chemistry with Ion Beams” (III45006).

The authors are with the Vinča Institute of Nuclear Sciences, Laboratory of Physics (010), 11001 Belgrade, Serbia (e-mail: andjelijailic@ieee.org).

Color versions of one or more of the figures in this paper are available online at <http://ieeexplore.ieee.org>.

Digital Object Identifier 10.1109/TNS.2011.2180737

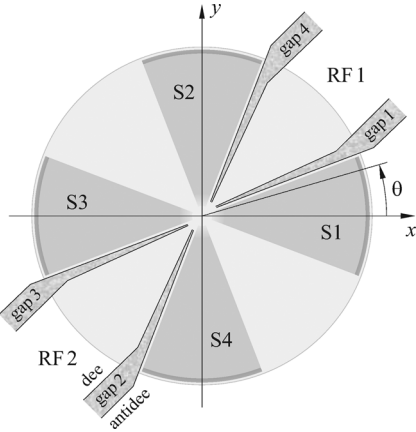


Fig. 1. The layout of the VINCY Cyclotron's accelerating region. Four straight sectors of the multipurpose compact isochronous Cyclotron VINCY are denoted as S1, S2, S3 and S4. Two radiofrequency resonators, denoted as RF1 and RF2, are located in the first and third valley of the VINCY Cyclotron. The average angular distance between the midlines of the accelerating gaps of each resonator equals 41° , allowing the acceleration in the first, second, third and fourth harmonic mode. The beam rotates clockwise, whereas the azimuthal angle θ is measured counterclockwise, as denoted.

TABLE I
MAIN CHARACTERISTICS OF THE VINCY CYCLOTRON

Type	compact isochronous, multipurpose
Ion specific charges	0.15 – 1.00
Number of sectors	4
Sector azimuthal width	42°
Spiral angle	0
Pole diameter	2 m
Maximal magnetic induction in the machine center	1.97 T
Hill gap	36 mm
Valley gap	190 mm
Bending constant	135 MeV
Focusing constant	69 MeV
Number of dees	2
Average angular width of the dee	34°
Aver. angular width of the antidee	48°
RF frequency range	17 MHz – 31 MHz
Harmonic modes	1, 2, 3, 4
Peak RF voltage	100 kV
Injection	spiral inflector
Ion sources	External
Extraction	stripping foil

[12], [19]. The fourth order Runge-Kutta method, with the adaptive time step algorithm, is employed. The calculation accuracy is kept within 1×10^{-5} when the backward tracking and then forward tracking through the complete accelerating region is performed. The beam acceptance analysis implies much wider range of the initial phase space coordinates than is the one corresponding to a typical ion beam bunch in a cyclotron. The particle-particle solver for space-charge effects is thus turned off and ion transmission and the corresponding acceleration efficiency assessed for each of the considered beam ions independently of the others.

II. OPTIMAL ACCELERATION OF A TEST ION

In [12], the ion acceleration is optimized by the adjustment of the radiofrequency (RF) electrode parameters and the acceler-

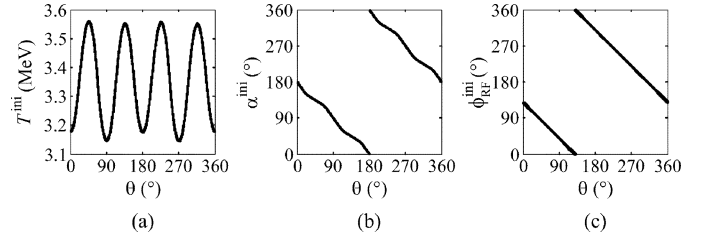


Fig. 2. The complete sets of initial conditions yielding the optimal acceleration of the H^- test ion in the VINCY Cyclotron. (a) The optimal initial energy, T^{ini} . (b) The optimal initial momentum vector direction angle, α^{ini} , measured clockwise with respect to the positive y -axis. (c) The optimal initial RF phase, $\phi_{\text{RF}}^{\text{ini}}$. For the considered radius R_a and an arbitrary azimuth θ , the phase space coordinates in the median plane of a cyclotron resulting in optimal acceleration are obtained by interpolation from the sets' elements. What appears to be a thick curve in each part of the figure is actually a strip; instead of a single value a range of acceptable values for each initial parameter is obtained for every azimuthal position. The method for defining the complete continuous sets of input parameters shown above is explained in [12].

ating orbit centering. The synchronization between the ion and the accelerating voltage depends on the achievable isochronism of the magnetic field and is addressed by the RF parameters adjustment. Orbit centering reduces the differences between the mean energy increments per gap for different gaps, which in ideal case should be equal. As a first step, the averaged discrepancy between the RF frequency and the gyration frequency is minimized, to account for the gyration frequency fluctuations. Next, the accelerating orbit is centered using the hard edge gap approximation with the numerical integration of the gap energy gains. The static equilibrium orbit (SEO) is taken as the initial guess at the large radii. A single iteration of this single turn centering is sufficient, contributing to the efficiency of the method. The optimal RF phase curve is then calculated, taking into account that a part of the RF phase fluctuations is induced by the insufficient isochronism and thus unavoidable. To separate it from the fluctuations due to improper trajectory centering or poor synchronization with the accelerating voltage, we assume the ideal acceleration during which the test ion moves along the SEOs and jumps from one SEO to another at the midlines of the accelerating gaps. With such an approximation, the impact of the unavoidable level of fluctuations is minimized by reducing the averaged RF phase deviation from nominal value for a considered azimuth. The optimized orbit obtained using these three steps is not unique; instead the method results in a number of accelerated orbits providing excellent quality of acceleration.

III. INITIAL CONDITIONS

The optimization procedure has been shown to be highly accurate and very efficient, and it is also fully automatized. For a given test ion, the corresponding magnetic field and harmonic mode of the cyclotron operation, the complete sets of optimal accelerating conditions at the beginning of the accelerating region are defined. The radius R_a denotes the beginning of the accelerating region. It is chosen so that the ion beam dynamics at larger radii is not affected by the possible electrode configuration changes in the central region. Fig. 2 shows optimal initial conditions for the 65 MeV H^- test ion, for $R_a = 200$ mm. The phase space coordinates for an arbitrary azimuth θ are obtainable by interpolation from the sets' elements, which cover the

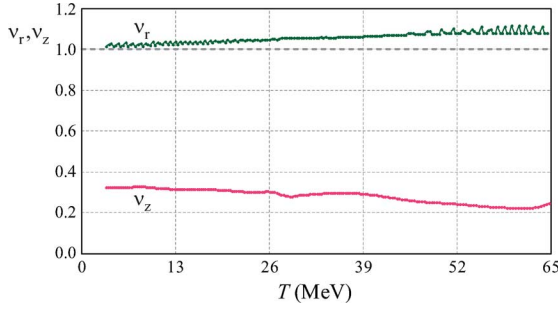


Fig. 3. Betatron tunes vs. energy in tracking along the chosen accelerated orbit. The variation of betatron oscillation frequencies during the acceleration confirms that the initial conditions for acceleration are properly chosen. The coupling between the radial and vertical oscillation modes $\nu_r = 5 \cdot \nu_z$ is quickly traversed at about 44 MeV. There are no dangerous resonant conditions.

range from zero to 360° . Here we take $\theta = 15^\circ$, as this azimuth does not coincide with any distinctive initial azimuth, such as the edge or the midline of the magnetic sector, the midline of the valley, the accelerating gap, etc. The chosen accelerated orbit is therefore representing the majority of the optimized accelerated orbits corresponding to the initial coordinates shown in Fig. 2. Betatron tunes during the acceleration along the chosen orbit are calculated and the results shown in Fig. 3 verify that no severe problems due to the coupling resonances are to be expected.

IV. ACCELERATING REGION ACCEPTANCES

The six-dimensional phase space volume of the ion beam emittance or the accelerating structure acceptance can not be visualized in a simple and comprehensible manner. The ion beam emittance, i.e., the phase space region occupied by the beam bunch, is usually represented by the two-dimensional distributions of particles obtained as the emittance projections to the radial, axial and longitudinal phase plane. It is not convenient to use the same approach for the representation of the structure acceptance, i.e., the range of permissible phase space coordinates resulting in the ion transmission through the structure. To keep the information on the coordinate coupling, we use the six-dimensional phase space volume cross sections resembling the “slices of the volume”, instead.

The phase space coordinates are denoted as $\Delta r, p_r, \Delta z, p_z, \Delta\phi$, and ΔT , corresponding to the ion position vector and ion momentum vector angle components in the radial and axial direction, relative to the central ion, to the ion phase relative to the central ion phase, and to the kinetic energy relative to the central ion kinetic energy, respectively. The ion phase, $\Delta\phi$, is measured in the direction of motion. The beam acceptance cross sections with the radial, Δr - p_r , axial, Δz - p_z , and longitudinal, $\Delta\phi$ - ΔT , phase plane, with the other four phase space coordinates coinciding with the corresponding central ion ones, are called the decoupled radial, axial and longitudinal acceptances. They are shown in Fig. 4. The corresponding Twiss parameters as well as the acceptance statistics are given in Table II.

Almost perfect centeredness of all the particles belonging to the decoupled acceptances about the origins of the three phase space planes in Fig. 4 verifies that the chosen accelerated orbit of

TABLE II
TWISS PARAMETERS AND BEAM ACCEPTANCE STATISTICS FOR THE DECOUPLED ACCELERATING REGION ACCEPTANCES

TWISS PARAMETERS *				
	α (1)	β (u_x/u_{p_x})	γ (u_{p_x}/u_x)	ε ($\pi u_x u_{p_x}$)
RADIAL	0.35	0.24	4.71	$3.19 \cdot 10^3$
AXIAL	-0.12	0.60	1.70	123.35
LONGITUDINAL	-0.26	$6.56 \cdot 10^{-3}$	$0.16 \cdot 10^3$	$5.11 \cdot 10^3$
BEAM ACCEPTANCE STATISTICS *				
	$\overline{\Delta x}$ (u_x)	$\overline{p_x}$ (u_{p_x})	$\sigma_{\Delta x}$ (u_x)	σ_{p_x} (u_{p_x})
RADIAL	0.00	2.86	24.44	108.52
AXIAL	0.00	0.00	7.61	12.84
LONGITUDINAL	-1.01	141.35	5.11	806.92

* The longitudinal units u_x and u_{p_x} are given in degrees and keV; the corresponding radial and axial units are mm and mrad, respectively. In the radial, axial and longitudinal direction the pair $(\Delta x, p_x)$ corresponds to the coordinate pair $(\Delta r, p_r)$, $(\Delta z, p_z)$ and $(\Delta\phi, \Delta T)$, respectively.

a referent, central particle is indeed the optimal one. The acceleration efficiency of an ion is measured by its averaged energy gain per accelerating gap, $\overline{\Delta T}_{\text{gap}}$, as in [12]. It is calculated for every point belonging to the decoupled acceptances and the resulting accelerating region acceptance distribution with respect to the acceleration efficiency is shown in Fig. 5.

The axial particle motion in an isochronous cyclotron is usually decoupled from both the radial and longitudinal motion, as shall be proven explicitly in the following sections. The axial acceptance area shown in Figs. 4 and 5, obtained for the optimal values of other four phase space coordinates, is the largest and beam ions outside of this area shall under no conditions reach the radius of extraction. It is limited by the small vertical distance between the sectors of the cyclotron magnet. The radial and longitudinal acceptance, on the other hand, are determined by the insufficient focusing or lost synchronization. As a result, the axial acceptance is small, while the acceleration efficiency is excellent for all the ions.

The acceleration efficiency is very good for about half of the transmitted beam ions in the radial and in the longitudinal phase plane. It is excellent ($\overline{\Delta T}_{\text{gap}} \geq 22.2$ keV) for about 10% of the input phase space coordinates in the center of the acceptance area for both phase space planes. Having in mind the usual beam emittances of the considered test ion in the VINCY Cyclotron [20]–[22], the following may be concluded. The axial emittance at the beginning of the accelerating region fits in the Δz and p_z coordinate ranges of ± 6 mm and ± 10 mrad, respectively; thus, it is much smaller than the corresponding beam acceptance. Even with the decrease in the acceptance area due to the deviations of other phase space parameters, the axial ion beam dynamics should still represent no problem at all. The radial ion beam emittance, with Δr and p_r within ± 10 mm and ± 20 mrad, respectively, allows for an excellent matching unless impeded by the inflector system or the central region design restrictions. The same holds true for the usual energy range at this point, ± 0.25 MeV; however, the input ion beam phase deviation with respect to the phase of an accelerating RF voltage is much wider than the $\pm 5.5^\circ$ phase interval seen to result in the best acceleration efficiency according to Fig. 5. It fits in the range of $\pm 25^\circ$. Due to the suboptimal accelerating conditions a part of

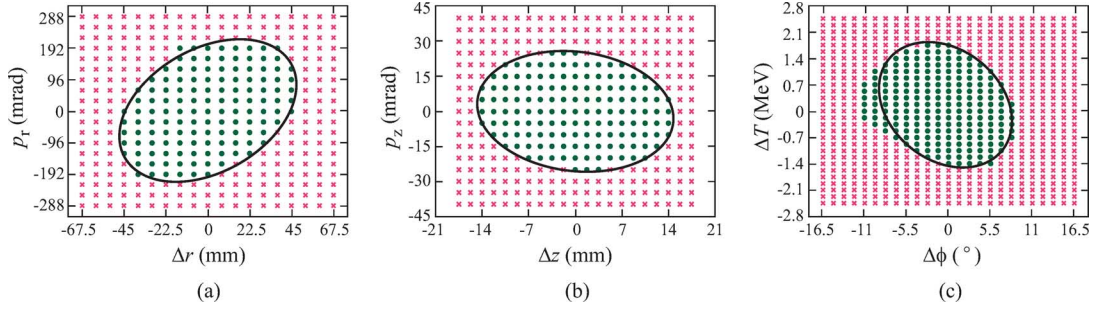


Fig. 4. Beam acceptance cross sections with the radial (a), axial (b) and longitudinal (c) phase plane, corresponding to the 65 MeV H^- ion beam motion in the accelerating region of the VINCY Cyclotron. The phase space coordinates belonging to the decoupled accelerating region acceptances are shown as green dots, whereas the other input guesses for the beam trajectory tracking simulation appear as red crosses. The origin of the six-dimensional phase space corresponds to the optimal initial conditions for acceleration shown in Fig. 2. The phase ellipses shown are determined so, as to best encompass the simulation results. Note that the accelerating region axial acceptance is about 25 times smaller than the radial acceptance.

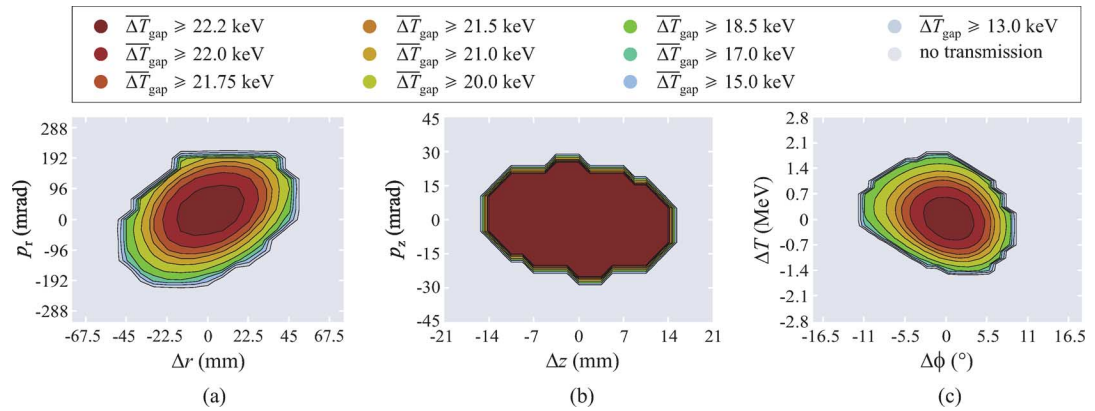


Fig. 5. The accelerating region acceptance distribution with respect to the acceleration efficiency for the 65 MeV H^- ion beam. The acceleration efficiency, measured by the averaged energy gain per accelerating gap, $\overline{\Delta T}_{\text{gap}}$, is excellent for about 10% of input phase space coordinates in the center of the acceptance area in the radial phase plane (a) and in the longitudinal phase plane (c). However, all of the input phase space coordinates in the axial phase plane, belonging to the acceptance area, are characterized by excellent acceleration efficiency (b). The latter is due to the small vertical distance between the sectors of the cyclotron magnet preventing the transmission of beam ions, as opposed to the insufficient focusing and synchronization responsible for stopping of beam ions in the other two cases. For the same reason, the accelerating region axial acceptance is significantly smaller than the radial acceptance.

the beam ions might lose synchronization with the accelerating voltage and leave the beam bunch.

V. COUPLING OF THE PHASE SPACE COORDINATES

In order to completely describe the six-dimensional beam acceptance ellipsoid we need to analyze the two-dimensional phase space volume cross sections corresponding to different nonzero combinations of other four phase space coordinates. The range of input guesses shown in Figs. 4 and 5 for the beam trajectory tracking is wide enough for the investigation of coordinate coupling. Randomly chosen initial phase space coordinates, as well as a reasonable number of equidistant ones, require an extremely lengthy simulation to provide enough data for the desired analysis. Moreover, a huge quantity of data resulting from such analysis is unnecessary. The radial acceptance is of a particular interest to the adjustment of initial conditions for acceleration. The radial emittance of an incoming ion beam bunch needs to be matched with the radial acceptance at a considered point. The initial range of input ion beam phase deviations can be reduced by introducing the ion beam buncher and ion beam chopper in the vertical channel guiding the ion beam to the spiral inflector. The initial energy range mostly depends

on the characteristics of the ion source employed. Because of the axial symmetry, the optimal initial conditions will always be in the median plane of a cyclotron. Therefore, the influence of other phase space coordinates to the radial acceptance and the acceleration efficiency in the radial phase plane has been investigated. For each of the parameters, equidistant initial guesses are taken, i.e., the distribution of test ions at start is uniform. The total number of initial guesses for the beam trajectory tracking is thus greatly reduced without any loss of relevant information.

Fig. 6 shows the influence of ion energy, its phase with respect to the RF voltage, axial position and axial momentum to the radial accelerating region acceptance. For a change in ion energy in the vicinity of optimal initial conditions from Fig. 2 the corresponding shift of the phase space ellipse is almost linear. In the first approximation, it is given by:

$$\Delta r^{\text{cen}} = 28.6 \cdot \Delta T, \quad p_r^{\text{cen}} = 2.86 + 16.0 \cdot \Delta T, \quad (1)$$

with the coordinates of the phase space ellipse center, Δr^{cen} and p_r^{cen} , given in mm and mrad, and ion energy deviation ΔT in MeV. Parameters Δr^{cen} and p_r^{cen} are obtained as the statistical mean values of the coordinates within the acceptance area.

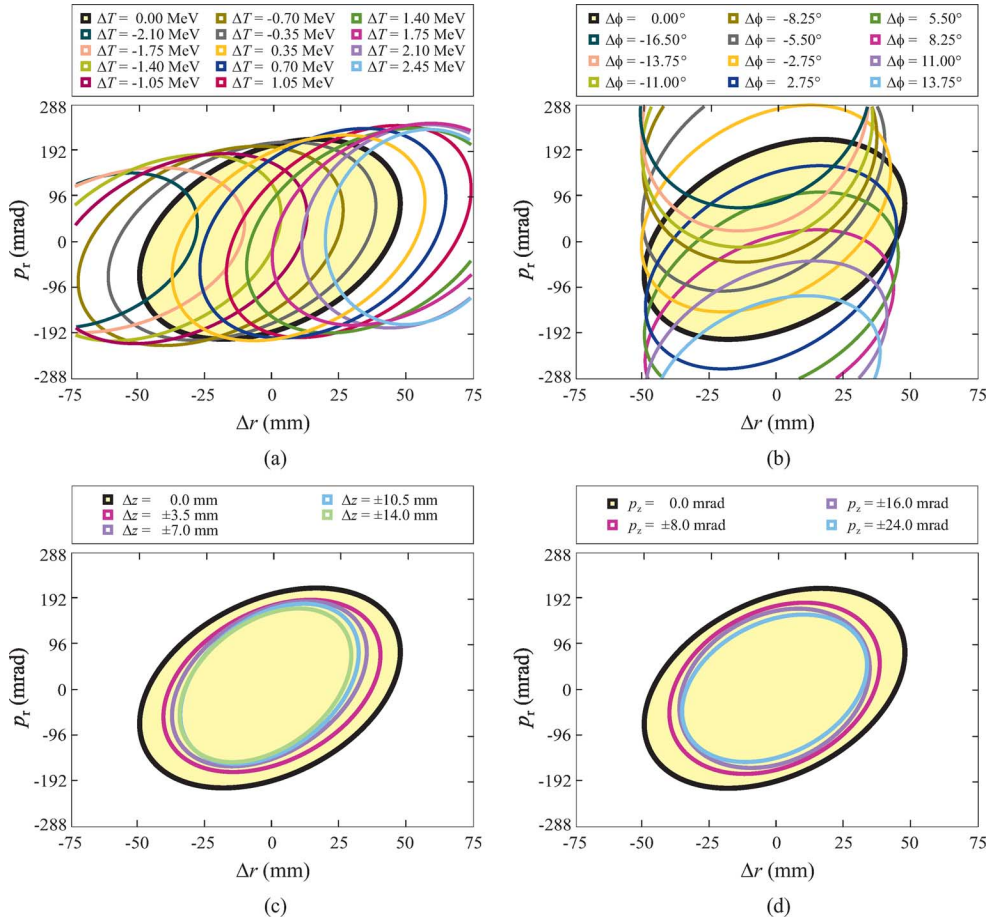


Fig. 6. The coupling of the accelerating region radial acceptance with other four phase space coordinates. The deviations from the optimal values of ion energy (a) or its phase with respect to the accelerating radiofrequency voltage (b), denoted by ΔT and $\Delta\phi$, lead to the almost linear shifts of the phase space ellipse defining the radial acceptance. The change of the phase space ellipse position is accompanied by very small variations in the ellipse shape and orientation, as well as the decrease in size of the acceptance area. The deviations from the optimal values of axial position (c) or axial momentum (d) of an ion, Δz and p_z , respectively, do not cause any significant changes of the phase space ellipse position, shape, or orientation, but the decrease in size of the acceptance area is pronounced. Therefore, the radial motion of an ion is not influenced by its axial motion, whereas the decrease of six-dimensional acceptance is the direct consequence of the accelerating region axial acceptance.

TABLE III

THE RADIAL ACCEPTANCE TWISS PARAMETERS DEPENDENCE ON ION ENERGY

ΔT (MeV)	α (1)	β ($\frac{\text{mm}}{\text{mrad}}$)	γ ($\frac{\text{mrad}}{\text{mm}}$)	ϵ ($\pi\text{-mm-mrad}$)
-1.05	0.3142	0.3930	2.7958	2.7563
-0.70	0.3232	0.3396	3.2521	3.1592
-0.35	0.3177	0.2770	3.9743	3.2134
0.00	0.3491	0.2384	4.7057	3.1876
0.35	0.3599	0.2513	4.4949	3.1607
0.70	0.3672	0.2887	3.9305	3.1585
1.05	0.3693	0.3353	3.3896	3.1351

The acceptance ellipse size, shape and slope change slightly as illustrated by the data in Table III.

Similarly, the ion phase deviation, $\Delta\phi$, with respect to the accelerating RF voltage leads to the almost linear shift of the phase space ellipse defining the radial acceptance:

$$\Delta r^{\text{cen}} \approx 0, \quad p_r^{\text{cen}} = 2.86 - 20.6 \cdot \Delta\phi, \quad (2)$$

TABLE IV

THE RADIAL ACCEPTANCE TWISS PARAMETERS DEPENDENCE ON ION PHASE DEVIATION

$\Delta\phi$ ($^\circ$)	α (1)	β ($\frac{\text{mm}}{\text{mrad}}$)	γ ($\frac{\text{mrad}}{\text{mm}}$)	ϵ ($\pi\text{-mm-mrad}$)
-5.50	0.0539	0.1550	6.4706	3.1066
-2.75	0.2554	0.2030	5.2479	3.1831
0.00	0.3491	0.2384	4.7057	3.1876
2.75	0.3853	0.2181	5.2657	3.0111
5.50	0.2947	0.1689	6.4355	2.9686

with Δr^{cen} and p_r^{cen} in mm and mrad, and $\Delta\phi$ in degrees. The comparison of Twiss parameters α , β , γ and ϵ , for several values of phase deviation is given in Table IV.

The analysis of the accelerating region radial acceptance coupling with the axial position and axial momentum gives qualitatively different results. There are no significant changes of the phase space ellipse position, shape, or orientation, but the decrease in size of the acceptance area as a consequence of the decreased axial acceptance is pronounced. The corresponding Twiss parameters for different values of Δz and p_z are given in Tables V and VI, respectively.

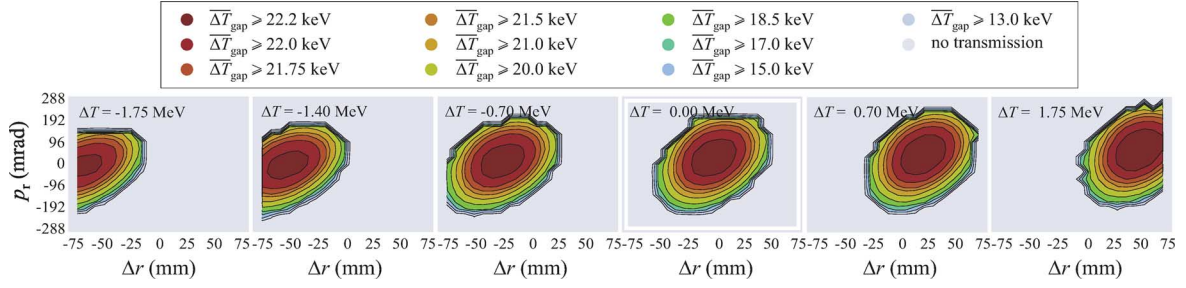


Fig. 7. The ion energy influence on the acceleration efficiency distribution over the radial acceptance. With an increase in ion energy, $\Delta T > 0$, there is no reduction in size of the acceptance area characterized by the largest acceleration efficiency. The set of coordinate pairs in the radial phase plane, $(\Delta r, p_r)$, which corresponds to the most efficient acceleration varies in accordance with the phase space ellipse shifts. The decrease in ion energy, $\Delta T < 0$, leads to the significant reduction in size of the most efficiently accelerated part of the acceptance, as well as to the decrease of overall radial acceptance. Therefore, ion energy lower than the optimal one cannot be accounted for merely by the convenient choice of radial phase space coordinates.

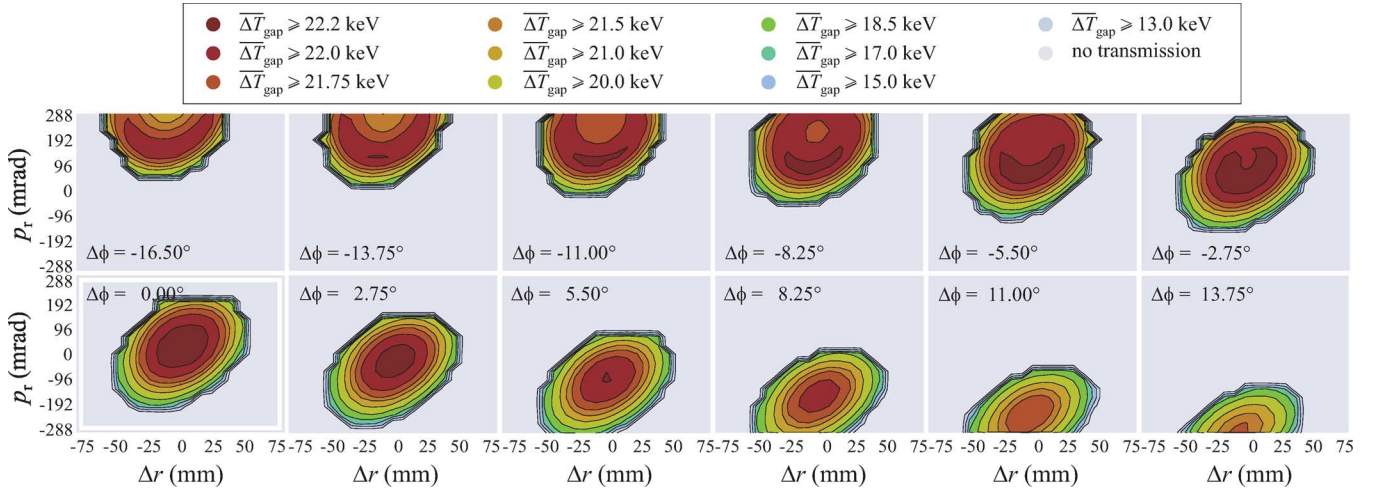


Fig. 8. The ion phase deviation influence on the acceleration efficiency distribution over the radial acceptance. Positive values of the ion phase offset, $\Delta\phi$, correspond to the ions leading in comparison with $\Delta\phi = 0$, whereas for $\Delta\phi < 0$ ions are lagging. Regardless of the sign of $\Delta\phi$, a decline of acceleration efficiency is considerable, rapid, and much more pronounced than the corresponding decrease of radial acceptance. The findings confirm that ion phase offset has the major influence on acceleration efficiency in cyclotrons.

TABLE V
THE RADIAL ACCEPTANCE TWISS PARAMETERS DEPENDENCE ON AXIAL POSITION

Δz (mm)	α (1)	β ($\frac{\text{mm}}{\text{mrad}}$)	γ ($\frac{\text{mrad}}{\text{mm}}$)	ϵ ($\pi\text{-mm}\cdot\text{mrad}$)
0.0	0.3491	0.2384	4.7057	3.1876
± 3.5	0.3574	0.2386	4.7264	2.1926
± 7.0	0.4139	0.2314	5.0609	2.0036
± 10.5	0.3343	0.2142	5.1901	1.8718
± 14.0	0.3599	0.2311	4.8880	1.7219

TABLE VI
THE RADIAL ACCEPTANCE TWISS PARAMETERS DEPENDENCE ON AXIAL MOMENTUM

p_z (mrad)	α (1)	β ($\frac{\text{mm}}{\text{mrad}}$)	γ ($\frac{\text{mrad}}{\text{mm}}$)	ϵ ($\pi\text{-mm}\cdot\text{mrad}$)
0.0	0.3491	0.2384	4.7057	3.1876
± 8.0	0.3170	0.2339	4.7057	2.1442
± 16.0	0.3093	0.2107	5.1997	1.8983
± 24.0	0.3611	0.2364	4.7817	1.7281

VI. INFLUENCE OF THE COUPLED INPUT PARAMETERS ON THE ACCELERATION EFFICIENCY

The key question when assessing the quality of acceleration is how much the changes in the coupled input parameters influence the acceleration efficiency. Fig. 7 shows that the increase in ion energy with respect to the optimal value results solely in the acceptance shift according to (1). However, the decrease in energy causes the reduction in size of the radial phase space area with the best acceleration efficiency. Fig. 8 demonstrates that the ion phase deviation, $\Delta\phi$, leads to the very pronounced deterioration in the acceleration efficiency, regardless of the sign of $\Delta\phi$. The overall decrease in the acceleration efficiency is larger than 10% for $\Delta\phi = \pm 5.5^\circ$. As shown in Fig. 9, the axial parameters have no impact on the acceleration efficiency in the radial phase space plane.

The presented analysis presumes a uniform distribution of particles in each of the six dimensions of a phase space. It is convenient since the distribution of ions within a beam bunch differs from case to case. Knowledge of the ion distribution for a particular case, along with the system acceptance for the uniform distribution, enables optimization of the beam parameters. It may happen that the central particle is not the one best suited

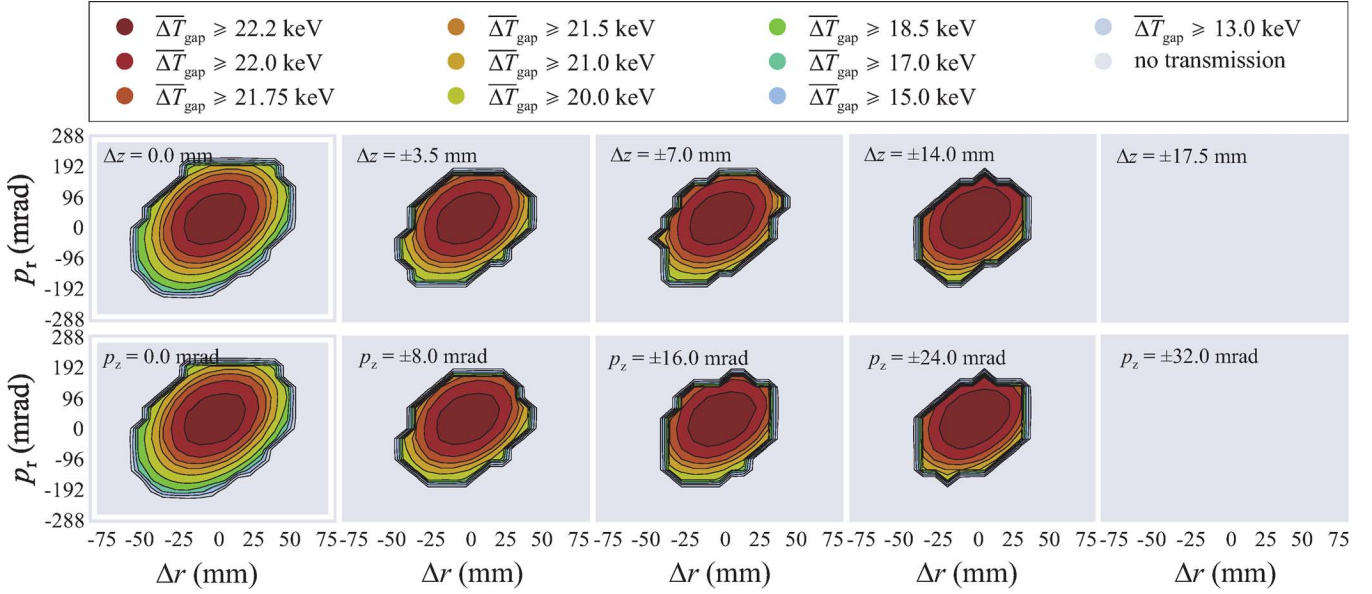


Fig. 9. The influence of the axial phase plane coordinates on the acceleration efficiency distribution over the radial acceptance. Acceleration efficiency within the radial acceptance, is influenced by neither the axial position, Δz , (top), nor by the axial momentum, p_z , (bottom). The area in the center of radial acceptance, corresponding to the excellent acceleration efficiency, is conserved with changes of both Δz and p_z , as long as the acceleration to the extraction energy is achievable. Beam ions characterized by lower values of acceleration efficiency are lost first, with the increase in magnitude of Δz or p_z .

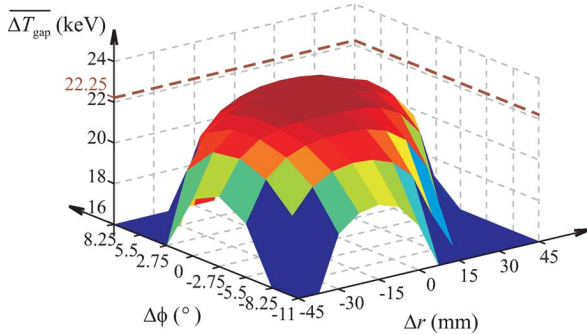


Fig. 10. The influence of the RF phase offset and orbit decentering on the acceleration efficiency. The acceleration efficiency for the 65 MeV H^- test ion is the highest and almost constant for $-20 \text{ mm} < \Delta r < 20 \text{ mm}$ and $-4^\circ < \Delta\phi < 4^\circ$. With further offset in the particle – RF voltage synchronization or larger orbit decentering, the acceleration efficiency rapidly decreases. While the radial dimension of the ion beam is usually much smaller than the acceptable range of Δr , the phase width of the accelerated test beam bunch is typically wider than its optimal range. This is why the RF phase offset is most often the critical parameter linked to the deterioration of acceleration efficiency.

for the accelerated orbit matching, i.e., that some other particle should be the referent one.

VII. INFLUENCE OF THE RF PHASE OFFSET AND ORBIT DECENTERING ON THE ACCELERATION EFFICIENCY

The obtained data can be further exploited to analyze the influence of the RF phase offset and orbit decentering on the acceleration efficiency. The upper limit of orbit decentering may be estimated as the initial radial deviation, Δr , for the ion trajectories characterized by the initial radial momentum $p_r = 0$. The RF phase offset is estimated by the initial beam ion phase deviation, $\Delta\phi$. The results shown in Fig. 10 emphasize once again the

critical impact of input range of phase deviations to the acceleration efficiency in an isochronous cyclotron. The radial dimension of the ion beam is usually much smaller than the acceptable beam decentering. A proper choice of initial conditions for acceleration can reduce the first problem and fully account for the second one.

VIII. COUPLING OF ALL SIX PHASE SPACE COORDINATES

Finally, for the sake of completeness and to confirm the above conclusions, the accelerating region acceptances have been analyzed using the randomly chosen input phase space coordinates for beam tracking. The range of input guesses is the same as in previous analysis, i.e., as in Figs. 4 and 5. Beam tracking analysis has been performed on a total of 20 000 ions, a number chosen to be comparable with the sum of 18 410 ions used in all the previous calculations together.

The six-dimensional beam acceptance projections to the radial, axial and longitudinal phase planes are shown in Fig. 11. The coupling between the motions in different directions can be analyzed, finding the particular ranges of input phase space coordinates shown in parts (a) and (c) in different symbols. As seen before, changes in only ΔT or only $\Delta\phi$ in the vicinity of optimal initial conditions, lead to almost linear shifts of the radial phase space ellipse given by (1) and (2). Due to such coupling of coordinates, projections of the six-dimensional acceptance are spread throughout the radial and the longitudinal phase planes. An excellent agreement of the axial acceptance projection and the decoupled axial acceptance verifies that the axial motion is decoupled from the other two. The equal distribution of the large dots in Fig. 11, whether they are surrounded by the green squares or not, testifies that the radial or longitudinal motion are not affected by the axial phase space coordinates either.

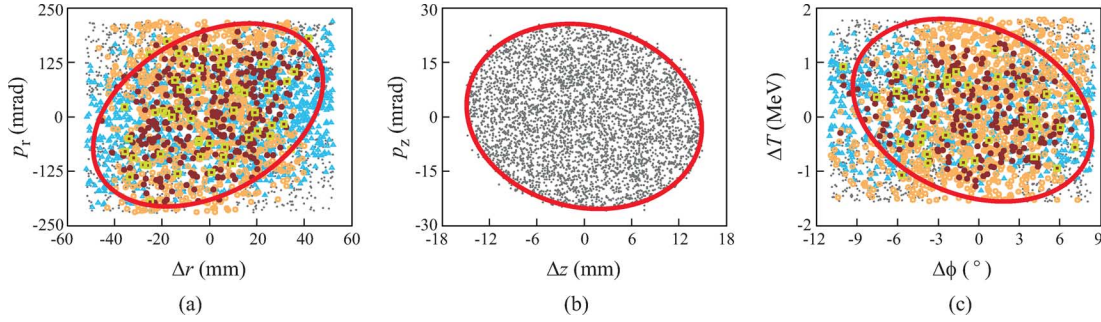


Fig. 11. Coupling between the radial (a), axial (b) and longitudinal (c) motion in the accelerating region of the VINCY Cyclotron. The agreement between the axial projection of the six-dimensional acceptance represented by dots and the decoupled axial acceptance ellipse from Fig. 4 is excellent (b), verifying that the axial motion is decoupled from the motion in radial and longitudinal directions. The other two motions are mutually coupled. The conditions $\Delta r \in \delta_r$, $p_r \in \delta_{p_r}$, $\Delta z \in \delta_z$, $p_z \in \delta_{p_z}$, $\Delta \phi \in \delta_\phi$, and $\Delta T \in \delta_T$, are approximated by $-10 \text{ mm} < \Delta r < 10 \text{ mm}$, $-50 \text{ mrad} < p_r < 50 \text{ mrad}$, $-5 \text{ mm} < \Delta z < 5 \text{ mm}$, $-8 \text{ mrad} < p_z < 8 \text{ mrad}$, $-2.75 < \Delta \phi < 2.75^\circ$, and $-350 \text{ keV} < \Delta T < 350 \text{ keV}$, respectively. Blue triangles and orange circles correspond to $\Delta \phi \in \delta_\phi$ and $\Delta T \in \delta_T$ in part (a), and to $\Delta r \in \delta_r$ and $p_r \in \delta_{p_r}$ in part (c). In part (a) they depict the radial phase ellipse movements defined by (1) and (2). Fulfillment of both conditions, shown by the large dark violet dots, defines the corresponding decoupled acceptances and completely agrees with the solid line ellipses copied from Fig. 4. Additionally, the ions complying with $\Delta z \in \delta_z$ and $p_z \in \delta_{p_z}$ as well are represented by the green squares. Their equal distribution throughout the corresponding phase space ellipses validates the assumption that the axial phase plane coordinates exhibit no influence to radial and longitudinal motion.

The axial phase plane is therefore fully decoupled from the other two planes.

IX. CONCLUSION

The novel method for detailed, systematic and efficient beam tracking analysis has been described. Its main benefit lies in the capability to obtain a lot of relevant results with a very limited quantity of input data. Separate analyses on the conveniently chosen subsets, i.e., subspaces, of input phase space coordinates were used. Care is taken to interpret the results correctly by accounting for the coordinate coupling. All the results in Sections III–V were obtained from beam tracking analyses on a total of 18 410 ions. However, they give much better insight into the improvement of the quality of acceleration than the results of Section VI, obtained with the total of 20 000 randomly chosen initial phase space coordinates.

It is confirmed that the ion beam motion in the axial phase plane is fully decoupled from both the radial and longitudinal motions. Further, it is shown that all of the beam ions within the axial acceptance have excellent acceleration efficiency. Axial input beam parameters do have impact on the beam ion transmission for those ions whose radial or longitudinal initial phase coordinates are non-optimal.

The acceleration efficiency for the 65 MeV H^- test ion is excellent ($\overline{\Delta T}_{\text{gap}} \geq 22.2 \text{ keV}$) for about 10% of the input phase space coordinates in the center of the decoupled acceptance area for both radial and longitudinal phase space planes. Therefore, although the range of optimal accelerating conditions for the referent particle, shown in Fig. 2, is relatively narrow, the regions of the phase space planes characterized by the excellent acceleration efficiency are very wide. For five out of six phase space coordinates the six-dimensional ion beam acceptance is wide enough to completely optimize the acceleration process. Only the RF phase range of accelerated beam is wider than the phase interval seen to result in the best acceleration efficiency.

The coupling of the phase space coordinates has been investigated from the point of view of the influence on the radial acceptance and the acceleration efficiency in the radial phase

plane of the other four phase space coordinates. It is of a particular interest to know the effects of coupling on the radial acceptance in order to adjust the radial emittance of an incoming ion beam bunch. It has been shown that changes in ion energy or ion phase deviation in the vicinity of optimal initial conditions lead to almost linear shifts of the radial phase space ellipse. The radial phase space area corresponding to the excellent acceleration efficiency is significantly reduced for the ion energy smaller than the optimal. The ion phase deviation leads to the very pronounced overall deterioration in the acceleration efficiency, whether an ion is leading or lagging. For the phase deviation of $\pm 5.5^\circ$, the overall decrease in the acceleration efficiency is larger than 10%.

The presented detailed analysis confirms that the method proposed in [12] is of a great importance for improvement of the quality of acceleration in an isochronous cyclotron. The accelerating region acceptance distribution with respect to the acceleration efficiency allows for optimal acceleration of the most of beam ions.

REFERENCES

- [1] Y. Jongen *et al.*, “High-intensity cyclotrons for radioisotope production and accelerator driven systems,” *Nucl. Phys. A*, vol. 701, pp. 100c–103c, Apr. 2002.
- [2] R. R. Johnson *et al.*, “Advances in intense beams, beam delivery, targetry, and radiochemistry at advanced cyclotron systems,” *Nucl. Instrum. Methods Phys. Res. B*, vol. 261, no. 1–2, pp. 803–808, Aug. 2007.
- [3] A. M. J. Paans, “Compact cyclotrons for the production of tracers and radiopharmaceuticals,” *Int. J. Nucl. Res. NUKLEONIKA*, vol. 48, no. Suppl. 2, pp. s169–s172, 2003.
- [4] M. Duval, M. P. Bourgarel, and F. Ripoubeau, “New compact cyclotron design for SPIRAL,” *IEEE Trans. Magn.*, vol. 32, no. 4, pp. 2194–2196, Jul. 1996.
- [5] R. E. Tribble *et al.*, “A facility upgrade at Texas A&M University for accelerated radioactive beams,” *Euro. Phys. J.–ST*, vol. 150, no. 1, pp. 255–258, Nov. 2007.
- [6] R. C. York *et al.*, “Proposed upgrade of the NSCL,” in *Proc. IEEE Particle Accelerator Conf.*, 1995, vol. 1, pp. 345–347.
- [7] S. Kurashima *et al.*, “Developments at JAEA AVF cyclotron facility for heavy-ion microbeam,” in *Proc. 18th Int. Conf. Cyclotrons and Their Applications*, Catania, Italy, 2008, pp. 131–133.
- [8] B. N. Gikal *et al.*, “DUBNA Cyclotrons – status and plans,” in *Proc. 17th Int. Conf. Cyclotrons and Their Applications*, Tokyo, Japan, 2005, pp. 100–104.

- [9] S. Brandenburg, "The superconducting cyclotron AGOR: Accelerator for light and heavy ions," in *1987 Proc. IEEE Particle Accelerator Conf.*, Washington, DC, 1987, pp. 376–378.
- [10] D. Rifuggiato, L. Calabretta, and G. Cuttone, "Ten years of operation with the LNS superconducting cyclotron," in *Proc. 17th Int. Conf. Cyclotrons and Their Applications*, Tokyo, Japan, 2005, pp. 118–120.
- [11] M. Fukuda *et al.*, "Design studies of the K900 JAERI superconducting AVF cyclotron for the research in biotechnology and materials science," in *Proc. 16th Int. Conf. Cyclotrons and Their Applications*, New York, 2001, pp. 189–191.
- [12] A. Ž. Ilić, J. L. Ristić-Djurović, S. Ćirković, A. Dobrosavljević, and N. Nešković, "Optimal acceleration in isochronous straight sector cyclotrons," *IEEE Trans. Nucl. Sci.*, vol. 56, no. 3, pp. 1498–1506, Jun. 2009.
- [13] A. Adelman *et al.*, "The object oriented parallel accelerator library (OPAL), design, implementation and application," in *Proc. Int. Computational Accelerator Physics Conf.*, San Francisco, CA, 2009, pp. 107–110.
- [14] Y. J. Bi *et al.*, "Challenges in simulating MW beams in cyclotrons," in *Proc. 46th ICFA Advanced Beam Dynamics Workshop*, Morschach, Switzerland, 2010, pp. 295–299.
- [15] Y. J. Bi *et al.*, "Towards quantitative simulations of high power proton cyclotrons," *Phys. Rev. ST, Accel. Beams*, vol. 14, no. 5, pp. 054402-1–9, May 2011.
- [16] N. Nešković *et al.*, "Status report of the VINCY Cyclotron," *Int. J. Nucl. Res. NUKLEONIKA*, vol. 48 (Suppl. 2), pp. s135–s139, 2003.
- [17] S. Ćirković, J. L. Ristić-Djurović, A. Ž. Ilić, V. Vujović, and N. Nešković, "Comparative analysis of methods for isochronous magnetic field calculation," *IEEE Trans. Nucl. Sci.*, vol. 55, no. 6, pp. 3531–3538, Dec. 2008.
- [18] N. Grujić, S. Ćirković, D. Košutić, L. Vukosavljević, and R. Balvanović, "Results of the second phase of measurements of the VINCY Cyclotron," Internal Rep., Jul. 2007.
- [19] A. Ž. Ilić, J. L. Ristić-Djurović, and S. T. Ćirković, "Preliminary results of ion trajectory tracking in the acceleration region of the VINCY Cyclotron," *Nucl. Technol. Radiat. Protect.*, vol. 21, no. 1, pp. 29–33, Jun. 2006.
- [20] P. Beličev *et al.*, "Ion beam dynamics in the central region of the VINCY Cyclotron," in *Proc. 34th Euro. Cyclotron Progress Meeting*, Belgrade, Serbia, Oct. 6–8, 2005.
- [21] P. Beličev *et al.*, "VINCY Cyclotron H⁻ ion beam dynamics: A new spiral inflector and the midplane acceleration," Internal Rep., Feb. 2006.
- [22] E. E. Perepelkin *et al.*, "Ion beam dynamics in the VINCY Cyclotron," in *Proc. 35th Euro. Cyclotron Progress Meeting*, Nice, France, Nov. 2–5, 2006.

IEEE

ANTENNAS AND WIRELESS PROPAGATION LETTERS

A PUBLICATION OF THE ANTENNAS AND PROPAGATION SOCIETY



2011

VOLUME 10

IAWPA7

(ISSN 1536-1225)

SPECIAL CLUSTER ON METAMATERIALS

EDITORIAL

Editorial: Status of AWPL	<i>G. Lazzi</i>	1
---------------------------------	-----------------	---

LETTERS

Wideband Omnidirectional and Compact Antenna for VHF/UHF Band	<i>S. Palud, F. Colombel, M. Himdi, and C. Le Meins</i>	3
Enhancing Frequency-Scanning Response of Leaky-Wave Antennas Using High-Impedance Surfaces	<i>M. García-Vigueras, J. L. Gómez-Tornero, G. Goussetis, A. R. Weily, and Y. J. Guo</i>	7
Tunable High-Impedance Surface With a Reduced Number of Varactors	<i>F. Costa, A. Monorchio, and G. P. Vastante</i>	11
Multiband and Compact WCDMA/WLAN Antenna for Mobile Equipment	<i>B. Yildirim</i>	14
Indoor Radio Noise Long-Term Measurements in Medium Wave Band in Buildings of City Areas in the North of Spain ...	<i>I. Landa, A. Arrinda, I. Fernández, and P. Angueira</i>	17
Physical Optics Scattering of Waves by a Half-Plane With Different Face Impedances	<i>Y. Z. Umul</i>	21
Multiband Antenna for Wireless USB Dongle Applications	<i>S.-H. Lee and Y. Sung</i>	25
A Simple CRLH LWA Circuit Condition for Constant Radiation Rate	<i>J. S. Gomez-Diaz, D. Cañete-Rebenaque, and A. Alvarez-Melcon</i>	29
Tunable Near-Field Focused Circular Phase-Array Antenna for 5.8-GHz RFID Applications	<i>R. Siragusa, P. Lemaître-Auger, and S. Tedjini</i>	33
Axisymmetric Resonant Lens Antenna With Improved Directivity in Ka-Band	<i>A. Rolland, M. Ettorre, A. V. Boriskin, L. Le Coq, and R. Sauleau</i>	37
Multimode Multiband (VHF/UHF/L/802.11a/b) Antennas for Broadcasting and Telecommunication Services	<i>J. Kim, C. Yang, T. Yun, and C. Jung</i>	41

(Contents Continued on Page 1667)

A Wideband Dual-Sleeve Monopole Antenna for Indoor Base Station Application	45
..... Z.-Y. Zhang, G. Fu, W.-J. Wu, J. Lei, and S.-X. Gong	
Dual-Band Circularly Polarized Stacked Annular-Ring Patch Antenna for GPS Application	49
..... X. Sun, Z. Zhang, and Z. Feng	
Modeling and Design of Millimeter-Wave High Q -Factor Parallel Feeding Scheme for Dielectric Resonator Antenna Arrays	53
..... W. M. Abdel-Wahab, S. Safavi-Naeini, and D. Busuioac	
Halved Vivaldi Antenna With Reconfigurable Band Rejection	56
..... X. Artiga, J. Perruisseau-Carrier, P. Pardo-Carrera, I. Llamas-Garro, and Z. Brito-Brito	
Filter-Antenna Module Using Substrate Integrated Waveguide Cavities	59
..... O. A. Nova, J. C. Bohórquez, N. M. Peña, G. E. Bridges, L. Shafai, and C. Shafai	
Compact Expressions for Efficiency and Bandwidth of Patch Antennas Over Lossy Magneto-Dielectric Materials	63
..... C. Niamien, S. Collardey, A. Sharaiha, and K. Mahdjoubi	
Miniaturized UWB Monopole Microstrip Antenna Design by the Combination of Giuseppe Peano and Sierpinski Carpet Fractals	67
..... H. Oraizi and S. Hedayati	
The Phoenix Cell: A New Reflectarray Cell With Large Bandwidth and Rebirth Capabilities	71
..... L. Moustafa, R. Gillard, F. Peris, R. Loison, H. Legay, and E. Girard	
Dual-Polarized Coupled Sectorial Loop Antennas for UWB Applications	75
..... A. Elsherbini and K. Sarabandi	
A Loaded Wideband Linearly Tapered Slot Antenna With Broad Beamwidth	79
..... F. Zhang, F.-S. Zhang, G. Zhao, C. Lin, and Y.-C. Jiao	
Application of the Active Element Pattern Method for Calculation of the Scattering Pattern of Large Finite Arrays	83
..... S. Zhang, S. Gong, Q. Gong, Y. Guan, and B. Lu	
Small Circularly Polarized U-Slot Wideband Patch Antenna	87
..... K. Y. Lam, K.-M. Luk, K. F. Lee, H. Wong, and K. B. Ng	
Experimental Investigation of New Radiating Mode in Rectangular Hybrid Dielectric Resonator Antenna	91
..... Y. Gao, Z. Feng, and L. Zhang	
Dual-Mode Loop Antenna With Compact Feed for Polarization Diversity	95
..... Y. Li, Z. Zhang, Z. Feng, and M. F. Iskander	
A Coordinate Transformation-Based Broadband Flat Lens via Microstrip Array	99
..... R. Yang, W. Tang, Y. Hao, and I. Youngs	
An Electrically Small Frequency Reconfigurable Antenna With a Wide Tuning Range	103
..... Y. Yu, J. Xiong, H. Li, and S. He	
Small Wideband Double-Loop Antennas Using Lumped Inductors and Coupling Capacitors	107
..... G. Mumcu, S. Gupta, K. Sertel, and J. L. Volakis	
Inkjet Printing of Ultrawideband (UWB) Antennas on Paper-Based Substrates	111
..... G. Shaker, S. Safavi-Naeini, N. Sangary, and M. M. Tentzeris	
Interwoven Spiral Array (ISPA) With a 10:1 Bandwidth on a Ground Plane	115
..... I. Tzanidis, K. Sertel, and J. L. Volakis	
Angular Resolution Improvement of Infrared Phased-Array Antennas	119
..... B. A. Slovick, J. A. Bean, and G. D. Boreman	
Passive UHF RFID Tag for Airport Suitcase Tracking and Identification	123
..... C. R. Medeiros, J. R. Costa, and C. A. Fernandes	
A Miniaturized Antipodal Vivaldi Antenna With Improved Radiation Characteristics	127
..... P. Fei, Y.-C. Jiao, W. Hu, and F.-S. Zhang	
A Spectral Rotation Approach for the Efficient Calculation of the Mutual Coupling Between Rectangular Apertures	131
..... G. Tiberi, S. Bertini, A. Monorchio, G. Mazzarella, and G. Montisci	
Antenna Placement for Minimizing Target Localization Error in UWB MIMO Noise Radar	135
..... W.-J. Chen and R. M. Narayanan	
Narrow-Size Multiband Inverted-F Antenna	139
..... L. Pazin and Y. Leviatan	
Comparative Study of FDTD-Adopted Numerical Algorithms for Kerr Nonlinearities	143
..... I. S. Maksymov, A. A. Sukhorukov, A. V. Lavrinenko, and Y. S. Kivshar	
Reducing Ground-Plane Effects on UWB Monopole Antennas	147
..... Y. Lu, Y. Huang, H. T. Chattha, and P. Cao	
Terrain Partial Obstruction LOS Path Loss Model for Rural Environments	151
..... H. El-Sallabi	
A Ground-Folded Slot Antenna for Imaging Radar Applications	155
..... W. Kang, S. Lee, and K. Kim	
Compact Broadband Printed Slot-Monopole-Hybrid Diversity Antenna for Mobile Terminals	159
..... G. Kang, Z. Du, and K. Gong	
FDTD Calculations of the Diffraction Coefficient of Vibrating Wedges	163
..... M. Madrid, J. J. Simpson, and M. M. Hayat	

An Omnidirectional Microstrip Antenna for WiMAX Applications	<i>J. Li</i>	167
Design of a Band-Notched UWB Monopole Antenna by Means of an EBG Structure	<i>M. Yazdi and N. Komjani</i>	170
Perturbation Analysis of a Planar Periodic Leaky-Wave Antenna Fed by Surface Waves	<i>S. F. Mahmoud, S. K. Podilchak, Y. M. M. Antar, and A. P. Freundorfer</i>	174
Signal Modeling and Analysis of a Planar Phased-Array FMCW Radar With Antenna Switching	<i>M.-S. Lee</i>	179
Multiplexing Efficiency of MIMO Antennas	<i>R. Tian, B. K. Lau, and Z. Ying</i>	183
On the Evaluation of Retarded-Time Potentials for SWG Bases	<i>H. A. Ülkü, A. A. Ergin, and F. Dikmen</i>	187
Understanding the Ultrawideband Channel Characteristics Within a Computer Chassis	<i>S. Redfield, S. Woracheewan, H. Liu, P. Chiang, J. Nejedlo, and R. Khanna</i>	191
A Novel Compact Double Exponentially Tapered Slot Antenna (DE TSA) for GPR Applications	<i>F. Zhang, G.-Y. Fang, Y.-C. Ji, H.-J. Ju, and J.-J. Shao</i>	195
Guidance Properties of Plasmonic Nanogrooves: Comparison Between the Effective Index Method and the Finite Integration Technique	<i>A. Polemi, A. Alù, and N. Engheta</i>	199
Miniaturized Design of Microstrip-Fed Slot Antennas Loaded With C-Shaped Rings	<i>R. H. Chen and Y.-C. Lin</i>	203
Efficient Spurious Rejection and Null Steering Using Slot Antennas	<i>M. J. Parihar, A. Basu, and S. K. Koul</i>	207
Circular Aperture Antenna With Conical Beam	<i>S. Qi, W. Wu, D.-G. Fang, and Z. Shen</i>	211
UWB High-Isolation Directive Coupled-Sectorial-Loops Antenna Pair	<i>A. Elsherbini and K. Sarabandi</i>	215
Multioctave Frequency Selective Surface Reflector for Ultrawideband Antennas	<i>Y. Ranga, L. Matekovits, K. P. Esselle, and A. R. Weily</i>	219
Bent Four-Leaf Antenna	<i>H. Nakano, Y. Ogino, and J. Yamauchi</i>	223
Band-Notched Small Square-Ring Antenna With a Pair of T-Shaped Strips Protruded Inside the Square Ring for UWB Applications	<i>M. Ojaroudi, S. Yazdanifard, N. Ojaroudi, and R. A. Sadeghzadeh</i>	227
Superluminal Waveguides Based on Non-Foster Circuits for Broadband Leaky-Wave Antennas	<i>D. F. Sievenpiper</i>	231
A Beam-Steering Broadband Microstrip Antenna for Noncontact Vital Sign Detection	<i>Z. Park and J. Lin</i>	235
Dual-Printed-Dipoles Reader Antenna for UHF Near-Field RFID Applications	<i>X. Li and Z. Yang</i>	239
Designing a Compact-Optimized Planar Dipole Array Antenna	<i>S. M. Hashemi, V. Nayyeri, M. Soleimani, and A.-R. Mallahzadeh</i>	243
High-Impedance-Surface-Based Antenna With Two Orthogonal Radiating Modes	<i>A. O. Karilainen, J. Vehmas, O. Luukkonen, and S. A. Tretyakov</i>	247
Design of an Ultrawideband Antipodal Tapered Slot Antenna Using Elliptical Strip Conductors	<i>J. Y. Siddiqui, Y. M. M. Antar, A. P. Freundorfer, E. C. Smith, G. A. Morin, and T. Thayaparan</i>	251
UWB Printed Slot Antenna With Bluetooth and Dual Notch Bands	<i>M. M. Samadi Taheri, H. R. Hassani, and S. Mohammad Ali Nezhad</i>	255
Dual-Band Circularly Polarized Pentagonal Slot Antenna	<i>Y. Sung</i>	259
Investigation of Rectenna Array Configurations for Enhanced RF Power Harvesting	<i>U. Olgun, C.-C. Chen, and J. L. Volakis</i>	262
A Compact GPS Antenna for Artillery Projectile Applications	<i>J.-H. Bang, B. Enkhbayar, D.-H. Min, and B.-C. Ahn</i>	266
A New Type of Macro-Elements for Efficient Two-Dimensional FEM Analysis	<i>G. Fotyga, K. Nyka, and L. Kulas</i>	270
Broadband CPW-Fed Circularly Polarized Square Slot Antenna With Three Inverted-L-Shape Grounded Strips	<i>N. Felegari, J. Nourinia, C. Ghobadi, and J. Pourahmadazar</i>	274
Vertically Integrated Three-Pole Filter/Antennas for Array Applications	<i>H. Cheng, Y. Yusuf, and X. Gong</i>	278
Experimental Demonstration of Complex Image Theory and Application to Position Measurement	<i>D. D. Arumugam, J. D. Griffin, and D. D. Stancil</i>	282
A Noninvasive Microwave Sensor and Signal Processing Technique for Continuous Monitoring of Vital Signs	<i>N. Celik, R. Gagarin, H. Youn, and M. F. Iskander</i>	286
Small Antenna With a Coupling Feed and Parasitic Elements for Multiband Mobile Applications	<i>K.-J. Kim, S. H. Lee, B.-N. Kim, J.-H. Jung, and Y. J. Yoon</i>	290
A Magnetic Field-Independent Absorbing Boundary Condition for Magnetized Cold Plasma ...	<i>Y. Yu and J. J. Simpson</i>	294
Miniaturized Triple-Band Antenna With a Defected Ground Plane for WLAN/WiMAX Applications	<i>J. Pei, A.-G. Wang, S. Gao, and W. Leng</i>	298
UWB Monopole Antenna With Stable Radiation Pattern and Low Transient Distortion	<i>F. Fereidoony, S. Chamaani, and S. A. Mirtaheri</i>	302

A Dual Circularly Polarized 2.45-GHz Rectenna for Wireless Power Transmission	306
..... Z. Harouni, L. Cirio, L. Osman, A. Gharsallah, and O. Picon	
Reducing Mutual Coupling of Closely Spaced Microstrip MIMO Antennas for WLAN Application	310
..... J. OuYang, F. Yang, and Z. M. Wang	
Suppression of Undesired Radiated Fields Based on Equivalent Currents Reconstruction From Measured Data	314
..... J. L. Araque Quijano, L. Scialacqua, J. Zackrisson, L. J. Foged, M. Sabbadini, and G. Vecchi	
Design of a 45°-Inclined SIW Resonant Series Slot Array Antenna for Ka-Band	318
..... D.-Y. Kim, W. Chung, C. Park, S. Lee, and S. Nam	
Wideband Self-Complementary Quasi-Yagi Antenna for Millimeter-Wave Systems	322
..... H. Chu, Y.-X. Guo, H. Wong, and X. Shi	
Directivity Enhancement to Vivaldi Antennas Using Compactly Anisotropic Zero-Index Metamaterials	326
..... B. Zhou and T. J. Cui	
Capacitive-Sensor-Induced Losses in 900-, 1800-, and 1900-MHz Antennas	330
..... S. Myllymaki, R. Valkonen, J. Holopainen, A. Huttunen, V. K. Palukuru, M. Berg, H. Jantunen, and E. Salonen	
Large Array Thinning by Means of Deterministic Binary Sequences	334
..... P. Rocca	
A Square-Loop Antenna With 4-Port Feeding Network Generating Semi-Doughnut Pattern for Vehicular and Wireless Applications	338
..... A. Pal, A. Mehta, D. Mirshekar-Syahkal, and H. Nakano	
Using GPU With CUDA to Accelerate MoM-Based Electromagnetic Simulation of Wire-Grid Models	342
..... T. Topa, A. Karwowski, and A. Noga	
Stripline-Fed Archimedean Spiral Antenna	346
..... T.-K. Chen and G. H. Huff	
Reconstruction of Unknown Surface Profiles in Multilayered Media by Complex Images Green's Functions Technique ..	350
..... B. Yektakhah and R. Faraji-Dana	
EM/Circuit Mixed Simulation Technique for an Active Antenna	354
..... G. Zakka El Nashef, F. Torrès, S. Mons, T. Reveyrand, T. Monédière, E. Ngoya, and R. Quéré	
Design of a New Printed Dipole Antenna Using in High Latitudes for Inmarsat	358
..... L. Wang, H.-C. Yang, and Y. Li	
Biologically Inspired Electrically Small Antenna Arrays With Enhanced Directional Sensitivity	361
..... N. Behdad, M. A. Al-Joumayly, and M. Li	
Design and Time-Domain Analysis for a Novel Pattern Reconfigurable Antenna	365
..... G.-M. Zhang, J.-S. Hong, B.-Z. Wang, G. Song, and P. Li	
Broadband CPW-Fed Circularly Polarized Square Slot Antenna With Inverted-L Strips for UWB Applications	369
..... J. Pourahmadazar, C. Ghobadi, J. Nourinia, N. Felegari, and H. Shirzad	
Low-Profile and Wideband Antenna	373
..... S.-G. Zhou and J.-Y. Li	
Wideband RFID Tag Antenna for Metallic Surfaces Using Proximity-Coupled Feed	377
..... H.-W. Son and S.-W. Jeong	
A Compact Filtering Microstrip Antenna With Quasi-Elliptic Broadside Antenna Gain Response	381
..... C.-K. Lin and S.-J. Chung	
A Study on Energetic Efficiency of Coil Antennas Used for RF Diathermy	385
..... M. Parise	
Efficiency Analysis of Magnetic Resonance Wireless Power Transfer With Intermediate Resonant Coil	389
..... J. Kim, H.-C. Son, K.-H. Kim, and Y.-J. Park	
Bandwidth Enhancement and Radiation Characteristics Improvement of Rectangular Dielectric Resonator Antenna	393
..... M. Khalily, M. K. A. Rahim, and A. A. Kishk	
Top-Hat Monopole Antenna for Conical-Beam Radiation	396
..... Z. Shen and J. Wang	
Analysis of Double-Negative (DNG) Bandwidth for a Metamaterial Composed of Magnetodielectric Spheres Embedded in a Matrix	399
..... J. Liu and N. Bowler	
Design and Analysis of Compact Printed Triple Band-Notched UWB Antenna	403
..... T. D. Nguyen, D. H. Lee, and H. C. Park	
A Dual-Layer T-Shaped Element for Broadband Circularly Polarized Reflectarray With Linearly Polarized Feed	407
..... L.-S. Ren, Y.-C. Jiao, F. Li, J.-J. Zhao, and G. Zhao	
Bandwidth Improvement in a Resonant Optical MST-Probe Applicable to Near-Field Imaging	411
..... H. Memarzadeh-Tehran, A. Diaz-Bolado, J.-J. Laurin, and R. Kashyap	
Passive UHF RFID Tag With Backscatter Diversity	415
..... H.-C. Liu, W.-C. Lin, M.-Y. Lin, and M.-H. Hsu	
A Novel Implementation of Discrete Complex Image Method for Layered Medium Green's Function	419
..... Y. P. Chen, W. C. Chew, and L. Jiang	

Investigation of the Influence of Reflective Insulation on Indoor Reception in Rural Houses	<i>J.-B. Yan and J. T. Bernhard</i>	423
A Novel Impedance Matched Mode Generator for Excitation of the TE ₂₁ Mode in Compact Dual-Mode Circular Waveguide Feeds	<i>Z. Allahgholi Pour and L. Shafai</i>	427
Dielectric Cap Loading Technique for Improving the Antenna Element Performance	<i>M. Hirvonen</i>	431
Compact Broadband Crescent Moon-Shape Patch-Pair Antenna	<i>J. Guo, Y. Zou, and C. Liu</i>	435
Ground Current Modification of Mobile Terminal Antennas and Its Effects	<i>M. R. Islam and M. Ali</i>	438
A Compact Yagi-Uda Antenna With Enhanced Bandwidth	<i>D. Arceo and C. A. Balanis</i>	442
Comparison of Ergodic Capacities From Wideband MIMO Antenna Measurements in Reverberation Chamber and Anechoic Chamber	<i>X. Chen, P.-S. Kildal, J. Carlsson, and J. Yang</i>	446
A Wideband VHF/UHF Discone-Based Antenna	<i>A. Chen, T. Jiang, Z. Chen, D. Su, W. Wei, and Y. Zhang</i>	450
Statistical Modeling of the “Antenna–Head” Interaction	<i>M. A. Mellah, A. Sibille, C. Roblin, M. Nedil, and T. A. Denidni</i>	454
Design of a Coplanar Integrated Microstrip Antenna for GPS/ITS Applications	<i>K. Wei, Z. Zhang, and Z. Feng</i>	458
Compact Triband Square-Slot Antenna With Symmetrical L-Strips for WLAN/WiMAX Applications	<i>W. Hu, Y.-Z. Yin, P. Fei, and X. Yang</i>	462
Reconfigurable Loaded Planar Inverted-F Antenna Using Varactor Diodes	<i>M. Ng Mou Kehn, O. Quevedo-Teruel, and E. Rajo-Iglesias</i>	466
Microwave and Millimeter-Wave Attenuation in Sand and Dust Storms	<i>X.-Y. Dong, H.-Y. Chen, and D.-H. Guo</i>	469
Improved Detection Scheme for Chipless RFIDs Using Prolate Spheroidal Wave Function-Based Noise Filtering	<i>W. Dullaert, L. Reichardt, and H. Rogier</i>	472
Aperture Efficiency Predictions in Symmetrical Paraboloidal Reflector Antennas With Nonplanar Log-Periodic-Type Feeds	<i>D. I. L. de Villiers</i>	476
Adapting MoM With RWG Basis Functions to GPU Technology Using CUDA	<i>T. Topa, A. Noga, and A. Karwowski</i>	480
Novel Modified Pythagorean Tree Fractal Monopole Antennas for UWB Applications	<i>J. Pourahmadazar, C. Ghobadi, and J. Nourinia</i>	484
A Compact Monopole Antenna for Super Wideband Applications	<i>K.-R. Chen, C.-Y.-D. Sim, and J.-S. Row</i>	488
Dual-Band Circularly Polarized Antennas Using Stacked Patches With Asymmetric U-Slots	<i>P. Nayeri, K.-F. Lee, A. Z. Elsherbeni, and F. Yang</i>	492
Target Detection With Impulse Radiating Antenna	<i>C. Bajracharya, S. Xiao, C. E. Baum, and K. H. Schoenbach</i>	496
A Slot-Monopole Antenna for Dual-Band WLAN Applications	<i>C.-Y. Huang and E.-Z. Yu</i>	500
The Poincaré–Steklov Operator in Hybrid Finite Element-Boundary Integral Equation Formulations	<i>P. Demarcke and H. Rogier</i>	503
A Triband Second-Order Frequency Selective Surface	<i>H. Zhou, S. Qu, Z. Xu, J. Wang, H. Ma, W. Peng, B. Lin, and P. Bai</i>	507
A Scalable Solar Antenna for Autonomous Integrated Wireless Sensor Nodes	<i>T. Wu, R. Li, and M. M. Tentzeris</i>	510
Single RF Channel Digital Beamforming Multibeam Antenna Array Based on Time Sequence Phase Weighting	<i>J. Zhang, W. Wu, and D.-G. Fang</i>	514
Concentric Annular-Ring Microstrip Antenna With Circular Polarization	<i>M. Ramírez, J. Parrón, J. M. González-Arbesú, and J. Gemio</i>	517
Chipless UWB RFID Tag Detection Using Continuous Wavelet Transform	<i>A. Lazaro, A. Ramos, D. Girbau, and R. Villarino</i>	520
A Wideband Uniplanar Polarization Independent Left-Handed Metamaterial	<i>N. Amiri, K. Forooghi, and Z. Atlasbaf</i>	524
Accurate and Conforming Mixed Discretization of the MFIE	<i>K. Cools, F. P. Andriulli, D. De Zutter, and E. Michielssen</i>	528
Vectorial Low-Frequency MLFMA for the Combined Field Integral Equation	<i>J. Aronsson and V. Okhmatovski</i>	532
A Novel Mathematical Model to Realizing Randomness in Full-Wave Simulations of Regularly Arranged Nanoparticles	<i>H. Jaradat and A. Akyurtlu</i>	536
Compact Inverted-F Antenna With Meander Shorting Strip for Laptop Computer WLAN Applications	<i>H.-W. Liu, S.-Y. Lin, and C.-F. Yang</i>	540
Compact CPW-Fed Dielectric Resonator Antenna With Dual Polarization	<i>Y. Gao, Z. Feng, and L. Zhang</i>	544
Design of Planar Crossed Monopole Antenna for Ultrawideband Communication	<i>S. Ghosh</i>	548

Increasing Isolation Between Colocated Antennas Using a Spatial Notch	<i>E. Janssen, D. Milosevic, M. Herben, and P. Baltus</i>	552
Radiation Q -Factors of Thin-Wire Dipole Arrangements	<i>P. Hazdra, M. Capek, and J. Eichler</i>	556
Efficient Modeling of Open Structures Using Nonuniform Leapfrog ADI-FDTD	<i>F. Jolani, Y. Yu, and Z. Chen</i>	561
MMW Antenna in IPD Process for 60-GHz WPAN Applications	<i>F.-J. Huang, C.-M. Lee, C.-Y. Kuo, and C.-H. Luo</i>	565
An Internal Triple-Band WLAN Antenna	<i>H. Wang and M. Zheng</i>	569
Micromachined 300-GHz SU-8-Based Slotted Waveguide Antenna	<i>Y. Wang, M. Ke, M. J. Lancaster, and J. Chen</i>	573
Planar Array of Electric- LC Resonators With Broadband Tunability	<i>W. Withayachumnankul, C. Fumeaux, and D. Abbott</i>	577
Omnidirectional Vest-Mounted Body-Worn Antenna System for UHF Operation	<i>G.-Y. Lee, D. Psychoudakis, C.-C. Chen, and J. L. Volakis</i>	581
Radiation Characteristics of Mushroom-Like PPW LWAs: Analysis and Experimental Verification	<i>J. S. Gomez-Diaz, A. Alvarez-Melcon, and T. Bertuch</i>	584
Novel Array EBG Structures for Ultrawideband Simultaneous Switching Noise Suppression	<i>Y. He, C.-H. Liang, and Q. H. Liu</i>	588
RF B_1 Field Calculation With Transmission-Line Resonator Analysis for High-Field Magnetic Resonance Systems	<i>H. Yoo, J. T. Vaughan, and A. Gopinath</i>	592
Using GTEM Cell to Measure RCS of Electrically Small Scatterers	<i>S. Xing, S. Li, W. Hong, and X. Liu</i>	596
On the Direct Evaluation of Surface Integral Equation Impedance Matrix Elements Involving Point Singularities	<i>A. G. Polimeridis and J. R. Mosig</i>	599
Miniature Long-Term Evolution (LTE) MIMO Ferrite Antenna	<i>J. Lee, Y.-K. Hong, S. Bae, G. S. Abo, W.-M. Seong, and G.-H. Kim</i>	603
Compact Modified Pentaband Meander-Line Antenna for Mobile Handsets Applications	<i>I.-F. Chen and C.-M. Peng</i>	607
Efficient IE-FFT and PO Hybrid Analysis of Antennas Around Electrically Large Platforms	<i>J. Ma, S.-X. Gong, X. Wang, Y.-X. Xu, W.-J. Zhao, and J. Ling</i>	611
Novel Broadband Artificial Magnetic Conductor With Hexagonal Unit Cell	<i>M. E. de Cos, Y. Álvarez, and F. Las-Heras</i>	615
Tuning a Hybrid GPU-CPU V-Cycle Multilevel Preconditioner for Solving Large Real and Complex Systems of FEM Equations	<i>A. Dziekonski, A. Lamecki, and M. Mrozowski</i>	619
Broadband Electromagnetic Radiation Modulated by Dual Memristors	<i>L. Wang, M. Yuan, T. Xiao, W. T. Joines, and Q. H. Liu</i>	623
A Compact Dual-Band Fork-Shaped Monopole Antenna for Bluetooth and UWB Applications	<i>S. K. Mishra, R. K. Gupta, A. Vaidya, and J. Mukherjee</i>	627
Theory and Experiment of the Hollow Rectangular Dielectric Resonator Antenna ...	<i>K. Lu, K. W. Leung, and Y. M. Pan</i>	631
Compact Printed Quadrifilar Helical Antenna With Iso-Flux-Shaped Pattern and High Cross-Polarization Discrimination	<i>S. Hebib, N. J. G. Fonseca, and H. Aubert</i>	635
Exact Imaging by an Elliptic Lens	<i>O. Akgol, D. Erricolo, and P. L. E. Uslenghi</i>	639
Realization of the D'/B' Boundary Condition	<i>I. V. Lindell, A. Sihvola, L. Bergamin, and A. Favaro</i>	643
Mutual Coupling Reduction of Fabry-Perot SIW Feeds Using a Double Partially Reflecting Pin-Made Grid Configuration	<i>E. Gandini, M. Ettorre, R. Sauleau, and A. Neto</i>	647
Planar Multiband Antenna for Compact Mobile Transceivers	<i>A. Dadgarpour, A. Abbosh, and F. Jolani</i>	651
Improved Formalism for the FDTD Analysis of Thin-Slot Penetration by Equivalence Principle	<i>R. Xiong, B. Chen, Q. Yin, and Z.-Y. Cai</i>	655
Enhanced Transmission and High-Directivity Radiation Based on Composite Right/Left-Handed Transmission Line Structure	<i>Y. Liu, H. Gu, and X. Zhao</i>	658
Investigation of Near-Field Wireless Power Transfer Under Multiple Transmitters	<i>I.-J. Yoon and H. Ling</i>	662
Compact Coplanar Waveguide Spiral Antenna With Circular Polarization for Wideband Applications	<i>N. Ghassemi, K. Wu, S. Claude, X. Zhang, and J. Bornemann</i>	666
Sparse Linear Array Synthesis With Multiple Constraints Using Differential Evolution With Strategy Adaptation	<i>S. K. Goudos, K. Siakavara, T. Samaras, E. E. Vafiadis, and J. N. Sahalos</i>	670
An Efficient Technique for the Evaluation of the Reduced Matrix in the Context of the CBFM for Layered Media	<i>G. Bianconi, C. Pelletti, R. Mittra, K. Du, and A. Monorchio</i>	674

Analysis of Arbitrary Frequency-Dependent Losses Associated With Conducting Structures in a Time-Domain Electric Field Integral Equation	<i>Z. Mei, Y. Zhang, T. K. Sarkar, M. Salazar-Palma, and B. H. Jung</i>	678
A Compact Hexagonal Wide-Slot Antenna With Microstrip-Fed Monopole for UWB Application	<i>M. R. Ghaderi and F. Mohajeri</i>	682
Performance of a Relay System for Two Extreme Ends of a Vessel at 2.4 GHz	<i>X. H. Mao and Y. H. Lee</i>	686
Performance Evaluation of Actual Multielement Antenna Systems Under Transmit Antenna Selection/Maximal Ratio Combining	<i>V. C. Papamichael and P. Karadimas</i>	690
PIFA–Top-Loaded-Monopole Antenna With Diversity Features for WBAN Applications	<i>T. Alves, B. Poussot, and J.-M. Laheurte</i>	693
Bandwidth Enhancement and Miniaturization of Fork-Shaped Monopole Antenna	<i>R. Zaker and A. Abdipour</i>	697
Triangular-Shaped Single-Loop Resonator: A Triple-Band Metamaterial With MNG and ENG Regions in S/C Bands	<i>O. Yurduseven, A. E. Yilmaz, and G. Turhan-Sayan</i>	701
24-GHz LTCC Fractal Antenna Array SoP With Integrated Fresnel Lens	<i>F. A. Ghaffar, M. U. Khalid, K. N. Salama, and A. Shamim</i>	705
Performance-Enhanced and Symmetric Full-Space Scanning End-Switched CRLH LWA	<i>H. V. Nguyen, S. Abielmona, and C. Caloz</i>	709
Design and Modeling of a Miniaturized Substrate Integrated Waveguide Using Embedded SRRs	<i>F. Farzami, K. Forooghi, and M. Noroozian</i>	713
A Dual-Band Tunable Ultra-Thin Cavity Antenna	<i>Y. Zhao, Z. Zhang, and Z. Feng</i>	717
Reconfigurable Slot-Array Antenna With RF-MEMS	<i>D. Sánchez-Escuderos, M. Ferrando-Bataller, M. Baquero-Escudero, and J. I. Herranz</i>	721
Miniaturized Parallel Coupled-Line Filter-Antenna With Spurious Response Suppression	<i>L. Yang, P. Cheong, L. Han, W.-W. Choi, K.-W. Tam, and K. Wu</i>	726
Analysis of WiMAX Radio Measurements and Comparison With Some Models Over Dense Urban Western India at 2.3 GHz	<i>C. Dalela, M. V. S. N. Prasad, P. K. Dalela, and R. Saraf</i>	730
New Single-/Dual-Mode Design Formulas of the Rectangular Dielectric Resonator Antenna Using Covariance Matrix Adaptation Evolutionary Strategy	<i>X. S. Fang, C. K. Chow, K. W. Leung, and E. H. Lim</i>	734
24-Element Antenna-in-Package for Stationary 60-GHz Communication Scenarios	<i>W. Hong, A. Goudelev, K.-H. Baek, V. Arkhipenkov, and J. Lee</i>	738
A Cross-Shaped Dielectric Resonator Antenna for Multifunction and Polarization Diversity Applications	<i>L. Zou and C. Fumeaux</i>	742
Size-Independent Prism Resonator Partially Filled With DNG Metamaterial	<i>P. L. E. Uslenghi</i>	746
Experimental Characterization and Statistical Analysis of the Pseudo-Dynamic Ultrawideband On-Body Radio Channel	<i>Q. H. Abbasi, A. Sani, A. Alomainy, and Y. Hao</i>	748
Experimental Investigation of MIMO Performance Using Passive Repeater in Multipath Environment	<i>L. Wang, S.-W. Qu, J. Li, Q. Chen, Q. Yuan, and K. Sawaya</i>	752
Elliptically Shaped Quad-Ridge Horn Antennas as Feed for a Reflector	<i>O. B. Jacobs, J. W. Odendaal, and J. Joubert</i>	756
Dual-Band Printed Fractal Monopole Antenna for LTE Applications	<i>L. Lizzi and A. Massa</i>	760
Planar Slotted Array Antenna Fed by Single Wiggly-Ridge Waveguide	<i>M. Moradian, M. Tayarani, and M. Khalaj-Amirhosseini</i>	764
Dual-Band UHF-RFID Tags Based on Meander-Line Antennas Loaded With Spiral Resonators	<i>F. Paredes, G. Zamora, F. J. Herraiz-Martínez, F. Martín, and J. Bonache</i>	768
Mobile Terminal Antenna Performance With the User’s Hand: Effect of Antenna Dimensioning and Location	<i>J. Ilvonen, O. Kivekäs, J. Holopainen, R. Valkonen, K. Rasilainen, and P. Vainikainen</i>	772
Mirror-Integrated Transparent Antenna for RFID Application	<i>C. C. Serra, C. R. Medeiros, J. R. Costa, and C. A. Fernandes</i>	776
Spatial Correlation Analysis of On-Body Radio Channels Considering Statistical Significance	<i>X. D. Yang, Q. H. Abbasi, A. Alomainy, and Y. Hao</i>	780
Design of a Microstrip Leaky-Wave Antenna for Two-Dimensional Bearing Tracking	<i>S.-T. Yang and H. Ling</i>	784
A Novel Harmonic Suppressed Coplanar Waveguide (CPW)-Fed Slot Antenna	<i>M. S. Ghaffarian and G. Moradi</i>	788
Radial Integration Scheme for Handling Weakly Singular and Near-Singular Potential Integrals	<i>M.-D. Zhu, X.-L. Zhou, and W.-Y. Yin</i>	792
Implementation of UWB MIMO Time-Reversal Radio Testbed	<i>Y. Song, N. Guo, and R. C. Qiu</i>	796

Very Low-Profile Top-Loaded UWB Coupled Sectorial Loops Antenna	<i>A. Elsherbini and K. Sarabandi</i>	800
Compact Dual-Band Printed Quadrifilar Antennas for UHF RFID/GPS Operations	<i>K.-S. Oh, W.-I. Son, S.-Y. Cha, M.-Q. Lee, and J.-W. Yu</i>	804
An Empirical Path Loss Model and Fading Analysis for High-Speed Railway Viaduct Scenarios	<i>R. He, Z. Zhong, B. Ai, and J. Ding</i>	808
Beam Synthesis Based on Inverse Discrete Radon Transform for Linear Pulsed Arrays	<i>N. Basta and A. Dreher</i>	813
Octaband Internal Antenna for 4G Mobile Handset	<i>C.-W. Yang, Y.-B. Jung, and C. W. Jung</i>	817
Equivalent Circuit Method for Analyzing Frequency Selective Surface With Ring Patch in Oblique Angles of Incidence ...	<i>X. Yao, M. Bai, and J. Miao</i>	820
A Dual-Band Printed Electrically Small Antenna Covered by Two Capacitive Split-Ring Resonators	<i>L. Wang, M. Q. Yuan, and Q. H. Liu</i>	824
Design of a CMOS On-Chip Slot Antenna With Extremely Flat Cavity at 140 GHz	<i>S. Pan and F. Capolino</i>	827
Wideband Dual-Frequency Dual-Polarized Dipole-Like Antenna	<i>X. L. Bao and M. J. Ammann</i>	831
Adaptive Frequency-Sampling Method for Wideband Electromagnetic Scattering of Precipitation Particles	<i>J. Chen, Z. Liu, P. Shen, D. Ding, and H. Peng</i>	835
Estimation of Rain Attenuation From Experimental Drop Size Distributions	<i>J. M. García-Rubia, J. M. Riera, A. Benarroch, and P. García-del-Pino</i>	839
Monopole Antenna Loaded by a Stepped-Radius Dielectric Ring Resonator for Ultrawide Bandwidth	<i>C. Ozzaim</i>	843
PML Absorbing Boundary Condition for Efficient 2-D WLP-FDTD Method	<i>Y.-T. Duan, B. Chen, H.-L. Chen, and D.-G. Fang</i>	846
Compact Open-Slot Antenna With Bandwidth Enhancement	<i>W. Liu, Y. Yin, W. Xu, and S. Zuo</i>	850
A Miniaturized Printed Slot Antenna for Six-Band Operation of Mobile Handsets	<i>B. Yuan, Y. Cao, and G. Wang</i>	854
High-Gain Patch Antennas Loaded With High Characteristic Impedance Superstrates	<i>H. Attia, L. Yousefi, and O. Ramahi</i>	858
Mutual Coupling Reduction Between Very Closely Spaced Patch Antennas Using Low-Profile Folded Split-Ring Resonators (FSRRs)	<i>A. Habashi, J. Nourinia, and C. Ghobadi</i>	862
An Efficient 2-D FDTD Method for Analysis of Parallel-Plate Dielectric Resonators	<i>B. Yao, Q. Zheng, J. Peng, R. Zhong, S. Li, and T. Xiang</i>	866
An Idea of Additional Modified Modes in Rectangular Patch Antennas Loaded With Metamaterial	<i>M. R. C. Mahdy, M. R. A. Zuboraj, A. A. N. Ovi, and M. A. Matin</i>	869
Design of Simple Multiband Patch Antenna for Mobile Communication Applications Using New E-Shape Fractal	<i>N. Bayatmaku, P. Lotfi, M. Azarmanesh, and S. Soltani</i>	873
A Fluidic Loading Mechanism for Phase Reconfigurable Reflectarray Elements	<i>S. A. Long and G. H. Huff</i>	876
Compact Printed Monopole Antenna With Chip Inductor for WLAN	<i>Q. Luo, J. R. Pereira, and H. M. Salgado</i>	880
Frequency-Tunable Differentially Fed Rectangular Dielectric Resonator Antennas	<i>C. X. Hao, B. Li, K. W. Leung, and X. Q. Sheng</i>	884
Accuracy Improvement of Cubic Polynomial Inter/Extrapolation of MoM Matrices by Optimizing Frequency Samples ...	<i>W.-D. Li, H.-X. Zhou, J. Hu, Z. Song, and W. Hong</i>	888
A Thin Wave Absorber Using Closely Placed Divided Conductive Film and Resistive Film	<i>Y. Tsuda, T. Yasuzumi, and O. Hashimoto</i>	892
Design and Characterization of a Wi-Fi Loop Antenna Suitable for in Vivo Experiments	<i>C. Merla, A. Paffi, A. D'Attis, R. Pinto, M. Liberti, G. A. Lovisolo, and F. Apollonio</i>	896
Analysis of Incident Field Modeling and Incident/Scattered Field Calibration Techniques in Microwave Tomography	<i>M. Ostadrahimi, P. Mojabi, C. Gilmore, A. Zakaria, S. Noghmanian, S. Pistorius, and J. LoVetri</i>	900
Dipole Antenna Above EBG Substrate for Local SAR Reduction	<i>R. Ikeuchi and A. Hirata</i>	904
Self-Generation of Circular Polarization Using Compact Fabry–Perot Cavity Antennas	<i>S. A. Muhammad, R. Sauleau, L. Le Coq, and H. Legay</i>	907
A Compact Multiband Open-Ended Slot Antenna for Mobile Handsets	<i>Y. Cao, B. Yuan, and G. Wang</i>	911
Dual-Band Dual-Sense Circularly Polarized Slot Antenna With a C-Shaped Grounded Strip	<i>Y.-Y. Chen, Y.-C. Jiao, G. Zhao, F. Zhang, Z.-L. Liao, and Y. Tian</i>	915
An Interleaved, Interelement Phase-Detecting/Phase-Shifting Retrodirective Antenna Array for Interference Reduction ...	<i>T. F. Chun, A. Zamora, B. J. Lei, R. T. Iwami, and W. A. Shiroma</i>	919

Antenna Modeling by Elementary Sources Based on Spherical Waves Translation and Evolutionary Computation	<i>J. F. Izquierdo and J. Rubio</i>	923
An FET-Based Unit Cell for an Active Magnetic Metamaterial	<i>L. Jelinek and J. Machac</i>	927
A Compact Single-Layer Dual-Band Microstrip Antenna for Satellite Applications	<i>S. H. S. Esfahlani, A. Tavakoli, and P. Dehkhoda</i>	931
Electrically Small GPS L1 Rectennas	<i>N. Zhu, R. W. Ziolkowski, and H. Xin</i>	935
Planar Wideband Polarization Diversity Antenna for Mobile Terminals	<i>M. Sonkki, E. Antonino-Daviu, M. Ferrando-Bataller, and E. T. Salonen</i>	939
Radiation From a Line Source Shielded by a Confocal Elliptic Layer of DNG Metamaterial	<i>O. Akgol, V. G. Daniele, D. Erricolo, and P. L. E. Uslenghi</i>	943
Offset Dual-Reflector Antenna System Efficiency Predictions Including Subreflector Diffraction	<i>D. I. L. de Villiers</i>	947
A New Magneto-Dielectric Material Loaded, Tunable UHF Antenna for Handheld Devices	<i>F. Ferrero, A. Chevalier, J. M. Ribero, R. Staraj, J. L. Mattei, and Y. Queffelec</i>	951
A Time-Domain Uniform Asymptotic Theory Applied to the Analysis of Pulse-Excited PEC Wedges	<i>C. G. Rego and F. J. V. Hasselmann</i>	955
Ultrawideband Antenna With Triple Band-Notched Characteristics Using Closed-Loop Ring Resonators	<i>M. Almalkawi and V. Devabhaktuni</i>	959
Metamaterial-Based Electrically Small Multiband Planar Monopole Antennas	<i>D. K. Ntaikos, N. K. Bourgis, and T. V. Yioultsis</i>	963
Impulse Radiating Log-Periodic Dipole Array Antenna Using Time-Reversal Technique	<i>A. Khaleghi, H. S. Farahani, and I. Balasingham</i>	967
Classification of Buried Targets Using Ground Penetrating Radar: Comparison Between Genetic Programming and Neural Networks	<i>J. S. Kobashigawa, H. Youn, M. F. Iskander, and Z. Yun</i>	971
Two-Way Propagation Modeling in Waveguides With Three-Dimensional Finite-Element and Split-Step Fourier-Based PE Approaches	<i>G. Apaydin and L. Sevgi</i>	975
A Dual-Band Diamond-Shaped Antenna for RFID Application	<i>M. I. Sabran, S. K. A. Rahim, A. Y. Abdul Rahman, T. Abdul Rahman, M. Zairil Muhammad Nor, and Evizal</i>	979
On the Uncertainty of Refractivity Height Profile Measurements	<i>O. Jicha, P. Pechac, V. Kvicera, and M. Grabner</i>	983
Dual-Polarized Printed S-Band Radar Array Antenna for Spacecraft Applications	<i>R. Di Bari, T. Brown, S. Gao, M. Notter, D. Hall, and C. Underwood</i>	987
Microstrip Antenna Arrays Fed by a Series-Parallel Slot-Coupled Feeding Network	<i>K. Wincza and S. Gruszczynski</i>	991
Wideband Operation of Amplifying Array Using Tunable Phase Shifters	<i>T.-P. Kuo and T.-G. Ma</i>	995
Magnetically Actuated Latching Waveguide Switch and Filters	<i>H. Ouassal and J.-J. Laurin</i>	999
Wide-Bandwidth 60-GHz Aperture-Coupled Microstrip Patch Antennas (MPAs) Fed by Substrate Integrated Waveguide (SIW)	<i>W. M. Abdel-Wahab and S. Safavi-Naeini</i>	1003
Gap Waveguides Using a Suspended Strip on a Bed of Nails	<i>A. Valero-Nogueira, M. Baquero, J. I. Herranz, J. Domenech, E. Alfonso, and A. Vila</i>	1006
Design of a Label-Typed UHF RFID Tag Antenna for Metallic Objects	<i>T.-W. Koo, D. Kim, J.-I. Ryu, H.-M. Seo, J.-G. Yook, and J.-C. Kim</i>	1010
Wideband Circularly Polarized Patch Antennas on Reactive Impedance Substrates	<i>L. Bernard, G. Chertier, and R. Sauleau</i>	1015
Accurate Approximation to the PDF of the Product of Independent Rayleigh Random Variables	<i>H. Lu, Y. Chen, and N. Cao</i>	1019
Implementation of Reconfigurable Patch Antennas Using Reed Switches	<i>C. Wu, T. Wang, A. Ren, and D. G. Michelson</i>	1023
An Integrated Dual-Band PIFA for DVB-T and WiMAX Applications	<i>R. Caso, A. D'Alessandro, A. A. Serra, P. Nepa, and G. Manara</i>	1027
A Frequency-Agile Compact Array With a Reconfigurable Decoupling and Matching Network	<i>Y. Cai and Y. J. Guo</i>	1031
Robust Beamformer Using Manifold Separation Technique for Semispherical Conformal Array	<i>P. Yang, F. Yang, Z. P. Nie, H. J. Zhou, B. Li, and X. F. Tang</i>	1035
A Novel Dual-Band MIMO Antenna Array With Low Mutual Coupling for Portable Wireless Devices	<i>X. Ling and R. Li</i>	1039
Comparisons of UTD-Based and FK Models for Propagation Through Windows	<i>M. Yang and A. K. Brown</i>	1043

Study of Thermal Noise Generated in a Vivaldi Antenna Using the Improved Wheeler Cap Method	1047
..... <i>L. Belostotski, A. Sutinjo, R. H. Johnston, M. Okoniewski, M. A. Petursson, and T. Burgess</i>	
A Linear Phased Array Antenna Composed of Inductive Loaded Patch Antennas	1051
..... <i>T.-Y. Kim, Y.-M. Yoon, G.-S. Kim, and B.-G. Kim</i>	
A Broadband Proximity-Coupled Stacked Microstrip Antenna With Cavity-Backed Configuration	1055
..... <i>D. Sun, W. Dou, L. You, X. Yan, and R. Shen</i>	
A Higher-Order Nyström Scheme for a Marching-On-in-Degree Solution of the Magnetic Field Integral Equation	1059
..... <i>Y. Shi and J.-M. Jin</i>	
Path Loss Measurements of HF/VHF Land Links in a Brazilian Atlantic Rainforest Urban Site	1063
..... <i>M. H. C. Dias, A. Rotava, F. G. Andrade, R. A. Alem, M. A. K. Melo, and J. C. A. Santos</i>	
Analysis and Design of Conformal Tapered Leaky-Wave Antennas	1068
..... <i>J. L. Gómez-Tornero</i>	
Reconstruction of Two-Dimensional Permittivity Distribution With Distorted Rytov Iterative Method	1072
..... <i>W. Zhang and A. Hoorfar</i>	
Performance Verification of a Multimodal Interferometric DOA-Estimation Antenna	1076
..... <i>E. Ben-Ari and J. Remez</i>	
An Accurate Technique for Calculation of Radiation From Printed Reflectarrays	1081
..... <i>M. Zhou, S. B. Sørensen, E. Jørgensen, P. Meincke, O. S. Kim, and O. Breinbjerg</i>	
Reactive-to-Radiating Near-Field Propagation Behavior Measured on a Ka-Band Horn Antenna	1085
..... <i>D.-J. Lee, J.-Y. Kwon, N.-W. Kang, and J. F. Whitaker</i>	
Effects of a Coplanar Waveguide Biasing Network Built Into the Ground Plane on the Dispersion Characteristics of a Tunable Unit Cell With an Elliptical Patch and Multiple Vias	1088
..... <i>L. Matekovits, A. De Sabata, and K. P. Esselle</i>	
High-Permittivity Substrate Multiresonant Antenna Inside Metallic Cover of Laptop Computer	1092
..... <i>Y. Li, Z. Zhang, Z. Li, J. Zheng, and Z. Feng</i>	
Heart Rate Tracking Using a Doppler Radar With the Reassigned Joint Time-Frequency Transform	1096
..... <i>C. Lee, C. Yoon, H.-J. Kong, H. C. Kim, and Y. Kim</i>	
Planar Near-Field RFID Reader Antenna for Item-Level Tagging	1100
..... <i>C. Cho, C. Lee, J. Ryoo, and H. Choo</i>	
Novel Compact Wide-Band EBG Structure Based on Tapered 1-D Koch Fractal Patterns	1104
..... <i>J. de Dios Ruiz, F. L. Martínez, and J. Hinojosa</i>	
Development of a Flexible SU-8/PDMS-Based Antenna	1108
..... <i>C.-P. Lin, C.-H. Chang, Y. T. Cheng, and C. F. Jou</i>	
Expansion of the Kronecker and Keyhole Channels Into Spherical Vector Wave Modes	1112
..... <i>A. Alayón Glazunov</i>	
X-Band Planar Rectenna	1116
..... <i>G. Monti, L. Tarricone, and M. Spartano</i>	
Design of a Multiband Quasi-Yagi-Type Antenna With CPW-to-CPS Transition	1120
..... <i>Y. Ding, Y. C. Jiao, P. Fei, B. Li, and Q. T. Zhang</i>	
A Modified CPW-Fed Slot Loop Antenna With Reduced Cross Polarization and Size	1124
..... <i>Y.-C. Chen, S.-Y. Chen, and P. Hsu</i>	
Characteristics of the NLoS Bias for an Outdoor-to-Indoor Scenario at 2.45 GHz and 5.2 GHz	1127
..... <i>W. Wang, T. Jost, and U.-C. Fiebig</i>	
A New Compact Filter-Antenna for Modern Wireless Communication Systems	1131
..... <i>W.-J. Wu, Y.-Z. Yin, S.-L. Zuo, Z.-Y. Zhang, and J.-J. Xie</i>	
Design of Near-Field Edge-Shorted Slot Microstrip Antenna for RFID Handheld Reader Applications	1135
..... <i>H.-W. Liu, C.-H. Weng, and C.-F. Yang</i>	
Measurements and Simulations of Wave Propagation for Wireless Sensor Networks in Jet Engine Turbines	1139
..... <i>M. Grudén, M. Jobs, and A. Rydberg</i>	
Effective HF Radar Installation in Challenging Terrain Environments for Homeland Security Applications	1143
..... <i>N. Omaki, Z. Yun, N. Celik, H.-S. Youn, and M. F. Iskander</i>	
Low-Profile Conformal UHF RFID Tag Antenna for Integration With Water Bottles	1147
..... <i>T. Björninen, A. Z. Elsherbeni, and L. Ukkonen</i>	
A Printed Band-Notched UWB Antenna Using Quasi-Self-Complementary Structure	1151
..... <i>C.-Y. Huang and J.-Y. Su</i>	
A Compact Frequency-Reconfigurable Metamaterial-Inspired Antenna	1154
..... <i>H. Mirzaei and G. V. Eleftheriades</i>	
UHF RFID Tag Antenna for Embedded Use in a Concrete Floor	1158
..... <i>S.-H. Jeong and H.-W. Son</i>	
Compact Heptaband Reconfigurable Loop Antenna for Mobile Handset	1162
..... <i>Y. Li, Z. Zhang, J. Zheng, and Z. Feng</i>	
Novel Compact Quasi-Dipole Diversity Antenna for Mobile Terminals	1166
..... <i>G. Kang, Z. Du, and K. Gong</i>	
Mode-Based Computation Method of Channel Characteristics for a Near-Field MIMO	1170
..... <i>Y. Tak and S. Nam</i>	

Influence of Multiantenna Tag on the Read Range of a Passive UHF RFID System	1174
..... <i>G. Seigneuret, E. Bergeret, C. Moreaux, T. Deleruyelle, and P. Pannier</i>	
A Compact UWB Band-Notched Printed Monopole Antenna With Defected Ground Structure	1178
..... <i>A. Nouri and G. R. Dadashzadeh</i>	
A CPW-Fed Broadband Circularly Polarized Regular-Hexagonal Slot Antenna With L-Shape Monopole	1182
..... <i>S.-W. Zhou, P.-H. Li, Y. Wang, W.-H. Feng, and Z.-Q. Liu</i>	
Compact Wideband Unidirectional Antenna With a Reflector Connected to the Ground Using a Stub	1186
..... <i>G.-M. Zhang, J.-S. Hong, B.-Z. Wang, G. Song, and P. Zhang</i>	
Compact Tapered-Shape Slot Antenna for UWB Applications	1190
..... <i>R. Azim, M. T. Islam, and N. Misran</i>	
Cloud-Cover Statistics and Cloud Attenuation at Ka- and V-Bands for Satellite Systems Design in Tropical Wet Climate ..	1194
..... <i>T. V. Omotosho, J. S. Mandeep, and M. Abdullah</i>	
An ODDM-Based Solution to CFIE With Impedance Boundary Condition	1197
..... <i>W.-D. Li, H.-X. Zhou, J. Hu, Z. Song, and W. Hong</i>	
Threshold Receiver Model for Throughput of Wireless Devices With MIMO and Frequency Diversity Measured in Reverberation Chamber	1201
..... <i>P.-S. Kildal, A. Hussain, X. Chen, C. Orlenius, A. Skårbratt, J. Åsberg, T. Svensson, and T. Eriksson</i>	
Multicircular Monopole Antenna for Multiband Applications	1205
..... <i>R. Eshtiaghi, M. G. Shayesteh, and N. Zad-Shakooian</i>	
Triband Inverted-F Antenna With Stacked Branched Monopoles and a Parasitic Strip	1208
..... <i>K. Huang and T. Chiu</i>	
Compact LTCC Dual-Band Circularly Polarized Perturbed Hexagonal Microstrip Antenna	1212
..... <i>K. Qian and X. Tang</i>	
Quality Factor of an Antenna With Closely Spaced Resonances	1216
..... <i>O. B. Vorobyev</i>	
A Dual-Band High-Gain Resonant Cavity Antenna With Orthogonal Polarizations	1220
..... <i>H. Moghadas, M. Daneshmand, and P. Mousavi</i>	
Compact and Broadband Antenna for LTE and Public Safety Applications	1224
..... <i>H. Mopidevi, D. Rodrigo, O. Kaynar, L. Jofre, and B. A. Cetiner</i>	
Reconfigurable Beam Steering Using a Microstrip Patch Antenna With a U-Slot for Wearable Fabric Applications	1228
..... <i>S.-J. Ha and C. W. Jung</i>	
Optimum Design of Linear Antenna Arrays Using a Hybrid MoM/GA Algorithm	1232
..... <i>A. H. Hussein, H. H. Abdullah, A. M. Salem, S. Khamis, and M. Nasr</i>	
WCS-FDTD Algorithm for Periodic Structures	1236
..... <i>Y.-F. Mao, B. Chen, R. Xiong, H.-J. Geng, and J.-Z. Tang</i>	
Isofrequency-Reconfigurable 8-Bit RF Repeater	1239
..... <i>E. Diaz, A. Grau, J. R. De Luis, F. De Flaviis, and L. Jofre</i>	
Compressive Sensing for Fast Analysis of Wide-Angle Monostatic Scattering Problems	1243
..... <i>M. S. Chen, F. L. Liu, H. M. Du, and X. L. Wu</i>	
A Radon Transform Interpretation of Contour Integral in Time-Domain Equivalent Edge Currents	1247
..... <i>Y. Guan, S.-X. Gong, S. Zhang, and Y.-X. Xu</i>	
Wireless RF Energy Propagation in Multiply-Connected Reverberant Spaces	1251
..... <i>J. S. Giuseppe, C. Hager, and G. B. Tait</i>	
Input Impedance of Horizontal Dipole Located Above Lossy Metamaterial Half-Space	1255
..... <i>Y. Radi, S. Nikmehr, and S. Hosseinzadeh</i>	
An Inverse Fast Multipole Method for Imaging Applications	1259
..... <i>Y. Álvarez, J. A. Martínez, F. Las-Heras, and C. M. Rappaport</i>	
Isolation Enhancement Between Two Packed Antennas With Coupling Element	1263
..... <i>J.-N. Hwang and S.-J. Chung</i>	
An Analytical Convolution Method Combined With the Conformal Fourier Transform for Solving 1-D Integral Equations	1267
..... <i>C. H. Zhu, Q. H. Liu, Y. Shen, and L. Liu</i>	
Development of a <i>Ka</i> -Band Wideband Circularly Polarized 64-Element Microstrip Antenna Array With Double Application of the Sequential Rotation Feeding Technique	1270
..... <i>A. Chen, Y. Zhang, Z. Chen, and C. Yang</i>	
UHF RFID Reader Antenna for Near-Field and Far-Field Operations	1274
..... <i>B. Shrestha, A. Elsherbeni, and L. Ukkonen</i>	
Circularly Polarized Beam-Steering Antenna Array With Butler Matrix Network	1278
..... <i>C. Liu, S. Xiao, Y.-X. Guo, M.-C. Tang, Y.-Y. Bai, and B.-Z. Wang</i>	
Reconstruction of Antenna Radiation Patterns From Phaseless Measurements in Nonanechoic Chambers	1282
..... <i>S. Loredó, G. León, R. G. Aycstarán, and F. Las-Heras</i>	
Fast and Accurate Analysis of Homogenized Metamaterials With the Surface Integral Equations and the Multilevel Fast Multipole Algorithm	1286
..... <i>O. Ergül</i>	
Wideband Beam-Steerable Flat Reflectors via Transformation Optics	1290
..... <i>R. Yang, W. Tang, and Y. Hao</i>	

A Stepwise Nicolson–Ross–Weir-Based Material Parameter Extraction Method	1295
..... <i>O. Luukkonen, S. I. Maslovski, and S. A. Tretyakov</i>	
Infrared Linear Tapered Slot Antenna	1299
..... <i>L. A. Florence, B. A. Slovick, E. C. Kinzel, J. A. Bean, and G. D. Boreman</i>	
Bowtie-Feed Broadband Monopole Antenna for Laptop Applications	
..... <i>I.-F. Chen, C.-M. Peng, S.-M. Shen, D.-B. Lin, and K.-Y. Lee</i>	1302
A Singly Fed Wideband Circularly Polarized Dielectric Resonator Antenna Using Concentric Open Half-Loops	
..... <i>M. I. Sulaiman and S. K. Khamas</i>	1305
Computational Estimates of Electrically Small Antenna High-Contrast Polarizabilities	
..... <i>J. Ethier and D. A. McNamara</i>	1309
A Study of the Impedance and Pattern Bandwidths of Probe-Fed Cylindrical Dielectric Resonator Antennas	
..... <i>A. P. Huynh, D. R. Jackson, S. A. Long, and D. R. Wilton</i>	1313
High-Efficiency Periodic Sparse Patch Array Based on Mutual Coupling	
..... <i>S.-W. Qu, D.-J. He, M.-Y. Xia, Z.-P. Nie, and C. H. Chan</i>	1317
Reflection Coefficient Measurement for North American House Flooring at 57–64 GHz	
..... <i>J. Ahmadi-Shokouh, S. Noghianian, and H. Keshavarz</i>	1321
A Circularly Polarized Switched-Beam Antenna Array	1325
..... <i>J. Ouyang</i>	
Multilayer Integration of Low-Cost 60-GHz Front-End Transceiver on Organic LCP	
..... <i>D. J. Chung, A. L. Amadjikpè, and J. Papapolymerou</i>	1329
Achieving Ratio Bandwidth of 25:1 From a Printed Antenna Using a Tapered Semi-Ring Feed	
..... <i>J. Liu, K. P. Esselle, S. G. Hay, and S. Zhong</i>	1333
MIMO Performance of Realistic UE Antennas in LTE Scenarios at 750 MHz	
..... <i>F. Athley, A. Derneryd, J. Fridén, L. Manholm, and A. Stjernman</i>	1337
Coherent MIMO Array Design With Periodical Physical Element Structures	
..... <i>F. Belfiori, W. van Rossum, and P. Hoogeboom</i>	1341
Measurements of RFID Tag Sensitivity in Reverberation Chamber	
..... <i>J. H. Rudander, Ikram-e-Khuda, P.-S. Kildal, and C. Orilenius</i>	1345
Compact Dual-Band Antenna With Electronic Beam-Steering and Beamforming Capability	
..... <i>H. Liu, S. Gao, and T. H. Loh</i>	1349
Enhancement of Wireless Power Transmission by Using Novel Multitone Approaches for Wireless Recharging	
..... <i>C.-L. Yang, C.-L. Tsai, Y.-L. Yang, and C.-S. Lee</i>	1353
Broadband Circularly Polarized Microstrip Antenna Array Using Sequentially Rotated Technique	
..... <i>Y.-J. Hu, W.-P. Ding, and W.-Q. Cao</i>	1358
Wide Bandwidth, High-Gain, and Low-Profile EBG Prototype for High Power Applications	
..... <i>M. Salah Toubet, M. Hajj, R. Chantalat, E. Arnaud, B. Jecko, T. Monediere, H. Zhang, and J.-C. Diot</i>	1362
Chipless RFID System Based on Group Delay Engineered Dispersive Delay Structures	
..... <i>S. Gupta, B. Nikfal, and C. Caloz</i>	1366
Application of Invasive Weed Optimization to Design a Broadband Patch Antenna With Symmetric Radiation Pattern ..	
..... <i>F. Mohamadi Monavar, N. Komjani, and P. Mousavi</i>	1369
A Reconfigurable Antenna With Frequency and Polarization Agility	
..... <i>P.-Y. Qin, Y. J. Guo, Y. Cai, E. Dutkiewicz, and C.-H. Liang</i>	1373
A Compact Zeroth-Order Resonant Antenna Employing Novel Composite Right/Left-Handed Transmission-Line Unit-Cells Structure	
..... <i>H.-M. Lee</i>	1377
Rain Attenuation Time Series Synthesizer Based on the Gamma Distribution	
..... <i>F. J. A. Andrade and L. A. R. da Silva Mello</i>	1381
A Compact Dual-Band Bow-Tie Slot Antenna for 900-MHz and 2400-MHz ISM Bands	
..... <i>L. A. Berge, M. T. Reich, and B. D. Braaten</i>	1385
Design of a Dual-Band Orthogonally Polarized L-Probe-Fed Fractal Patch Antenna Using Modal Methods	
..... <i>J. Eichler, P. Hazdra, M. Čapek, T. Kořínek, and P. Hamouz</i>	1389
Potentials of an Adaptive Rectenna Circuit	1393
..... <i>V. Marian, C. Vollaïre, J. Verdier, and B. Allard</i>	
A Unidirectional Cylindrical Conformal Monopole Antenna Designed for Impulse Radar System	
..... <i>Y.-T. Li, X.-L. Yang, Z.-B. Li, L. Wang, and H.-C. Yang</i>	1397
Characterization of MB-OFDM-Based Ultrawideband Systems for Body-Centric Wireless Communications	
..... <i>Q. H. Abbasi, A. Alomainy, and Y. Hao</i>	1401

Planar Broadband Tag Antenna Mounted on the Metallic Material for UHF RFID System	<i>J.-H. Lu and G.-T. Zheng</i>	1405
Lightweight Portable Planar Slot Array Antenna for Satellite Communications in X-Band	<i>J. M. Fernández González, P. Padilla, G. Expósito-Domínguez, and M. Sierra-Castañer</i>	1409
Bandwidth and Gain Enhancement of an Aperture Antenna With Modified Ring Patch	<i>M. M. Honari, A. Abdipour, and G. Moradi</i>	1413
Dual-Beam Directional Modulation Technique for Physical-Layer Secure Communication	<i>T. Hong, M.-Z. Song, and Y. Liu</i>	1417
Wideband Passband Transmission Line Based on Metamaterial-Inspired CPW Balanced Cells	<i>A. L. Borja, A. Belenguer, J. Cascón, H. Esteban, and V. E. Boria</i>	1421
Comparison of Spherical Antennas Fabricated via Conformal Printing: Helix, Meanderline, and Hybrid Designs	<i>J. J. Adams, S. C. Slimmer, T. F. Malkowski, E. B. Duoss, J. A. Lewis, and J. T. Bernhard</i>	1425
Printed UWB Antenna Operating Over Multiple Mobile Wireless Standards	<i>L. Lizzi, R. Azaro, G. Oliveri, and A. Massa</i>	1429
UHF RFID Tag for Integration Into a Cigarette Pack	<i>S. Wang, Y. Tao, and G. Wang</i>	1433
Estimation of Average Rician K-Factor and Average Mode Bandwidth in Loaded Reverberation Chamber	<i>X. Chen, P.-S. Kildal, and S.-H. Lai</i>	1437
Theory and Generation of Circularly Polarized Waves by Antenna Arrays With N -Fold Rotational Symmetry	<i>M. E. Marhic, A. Mehta, and A. Pal</i>	1441
A Multiprobe-Per-Collector Modulated Scatterer Technique for Microwave Tomography	<i>M. Ostadrahimi, P. Mojabi, S. Noghianian, J. LoVetri, and L. Shafai</i>	1445
Application of Transmission-Line Model to Dual-Band Stepped Monopole Antenna Designing	<i>M.-T. Wu and M.-L. Chuang</i>	1449
Radiation Pattern Characteristics of a Wideband Novel Modified Archimedean Spiral Antenna Array Covering DCS/PCS/WLAN and LTE Wireless Communication Bands	<i>S. K. Sharma and B. Shanmugam</i>	1453
Constant Speed Parametrization Mapping of Curved Boundary Surfaces in Higher-Order Moment-Method Electromagnetic Modeling	<i>M. M. Ilić, S. V. Savić, A. Ž. Ilić, and B. M. Notaroš</i>	1457
An Electrically Large Metallic Cavity Antenna With Circular Polarization for Satellite Applications	<i>Y. Zhao, Z. Zhang, and Z. Feng</i>	1461
Design of CPW-Fed Circularly Polarized Slot Antenna With a Miniature Configuration	<i>J.-Y. Sze and S.-P. Pan</i>	1465
Ultrawide Bandwidth (UWB) Planar Monopole Antenna Backed by Novel Pyramidal-Shaped Cavity Providing Directional Radiation Patterns	<i>R. A. Moody and S. K. Sharma</i>	1469
Vertical Dependence of Refractive Index Structure Constant in Lowest Troposphere	<i>M. Grabner, V. Kvicera, P. Pechac, and O. Jicha</i>	1473

SPECIAL CLUSTER LETTERS

Guest Editorial: Special Cluster on Metamaterials	<i>D. Schurig, G. V. Eleftheriades, D. R. Smith, and S. A. Tretyakov</i>	1476
Effective Permittivity of Heterogeneous Substrates With Cubes in a 3-D Lattice	<i>C. C. Njoku, W. G. Whittow, and J. C. Vardaxoglou</i>	1480
Analysis of Double-Negative (DNG) Bandwidths for Metamaterials Composed of Three-Dimensional Periodic Arrays of Two Different Magnetodielectric Spheres Arbitrarily Arranged on a Simple Tetragonal Lattice ...	<i>Y. Li and N. Bowler</i>	1484
Chiral Metamaterials With Negative Refractive Index Composed by an Eight-Cranks Molecule	<i>G. J. Molina-Cuberos, A. J. García-Collado, I. Barba, and J. Margineda</i>	1488
Effective-Medium Properties of Cylindrical Transmission-Line Metamaterials	<i>J. G. Pollock and A. K. Iyer</i>	1491
Experimental Verification of the Effective Medium Properties of a Transmission-Line Metamaterial on a Skewed Lattice	<i>M. Selvanayagam and G. V. Eleftheriades</i>	1495
Metasurfing: Addressing Waves on Impenetrable Metasurfaces (<i>Invited Paper</i>)	<i>S. Maci, G. Minatti, M. Casaletti, and M. Bosiljevac</i>	1499
Mushroom-Type High-Impedance Surface With Loaded Vias: Homogenization Model and Ultra-Thin Design	<i>C. S. R. Kaipa, A. B. Yakovlev, S. I. Maslovski, and M. G. Silveirinha</i>	1503
Characterizing Metasurfaces/Metafilms: The Connection Between Surface Susceptibilities and Effective Material Properties (<i>Invited Paper</i>)	<i>C. L. Holloway, E. F. Kuester, and A. Dienstfrey</i>	1507
Surface-Wave Waveguides	<i>D. J. Gregoire and A. V. Kabakian</i>	1512

Nonlinear Grounded Metasurfaces for Suppression of High-Power Pulsed RF Currents (<i>Invited Paper</i>)	D. F. Stevenpiper	1516
A Low-Cost Compact Patch Antenna With Beam Steering Based on CSRR-Loaded Ground	W. Cao, Y. Xiang, B. Zhang, A. Liu, T. Yu, and D. Guo	1520
Split-Ring Resonator Loading for the Slotted Waveguide Antenna Stiffened Structure	K. J. Nicholson, W. S. T. Rowe, P. J. Callus, and K. Ghorbani	1524
Multiband Printed Monopole Antennas Loaded With OCSRRs for PANs and WLANs	F. J. Herraiz-Martínez, G. Zamora, F. Paredes, F. Martín, and J. Bonache	1528
A Compact Omnidirectional Self-Packaged Patch Antenna With Complementary Split-Ring Resonator Loading for Wireless Endoscope Applications	X. Cheng, D. E. Senior, C. Kim, and Y.-K. Yoon	1532
Direct Use of the High Impedance Surface as an Antenna Without Dipole on Top	C. Guclu, J. Sloan, S. Pan, and F. Capolino	1536
Miniaturization of a Microstrip Antenna Using a Compact and Thin Magneto-Dielectric Substrate	F. Farzami, K. Forooghi, and M. Noroozfar	1540
A Broadband Monopole Antenna Enabled by an Ultrathin Anisotropic Metamaterial Coating (<i>Invited Paper</i>)	Z. H. Jiang, M. D. Gregory, and D. H. Werner	1543
Triple-Band Microstrip-Fed Monopole Antenna Loaded With CRLH Unit Cell	A. A. Ibrahim, A. M. E. Safwat, and H. El-Hennawy	1547
Nonreciprocal Magnetless CRLH Leaky-Wave Antenna Based on a Ring Metamaterial Structure (<i>Invited Paper</i>)	T. Kodera, D. L. Sounas, and C. Caloz	1551
Metamaterial Spiral Antenna	H. Nakano, J. Miyake, M. Oyama, and J. Yamauchi	1555
Evolutionary Generation of Subwavelength Planar Element Loaded Monopole Antenna	M. Ohira, H. Ban, and M. Ueba	1559
Nature-Inspired Optimization of High-Impedance Metasurfaces With Ultrasmall Interwoven Unit Cells	Z. Bayraktar, J. P. Turpin, and D. H. Werner	1563
A Quick and Easy Simulation Procedure to Aid in Metamaterial Unit-Cell Design	L. I. Babilio, L. K. Warne, W. L. Langston, W. A. Johnson, and M. B. Sinclair	1567
RF Limiter Metamaterial Using p-i-n Diodes (<i>Invited Paper</i>)	A. R. Katko, A. M. Hawkes, J. P. Barrett, and S. A. Cummer	1571
A Controllable Bandwidth Filter Using Varactor-Loaded Metamaterial-Inspired Transmission Lines	A. L. Borja, J. Carbonell, J. D. Martínez, V. E. Boria, and D. Lippens	1575
Tunable Phase Shifter Using Composite Right/Left-Handed Transmission Line With Mechanically Variable MIM Capacitors	N. Michishita, H. Kitahara, Y. Yamada, and K. Cho	1579
Active Metamaterial-Inspired Broad-Bandwidth, Efficient, Electrically Small Antennas (<i>Invited Paper</i>)	N. Zhu and R. W. Ziolkowski	1582
Wideband Artificial Magnetic Conductors Loaded With Non-Foster Negative Inductors	D. J. Gregoire, C. R. White, and J. S. Colburn	1586
A Grounded Slim Luneburg Lens Antenna Based on Transformation Electromagnetics	A. Demetriadou and Y. Hao	1590
Transmission-Line Cloak as an Antenna	J. Vehmas, P. Alitalo, and S. A. Tretyakov	1594
Suppressing the Electromagnetic Scattering With an Helical Mantle Cloak (<i>Invited Paper</i>)	P.-Y. Chen, F. Monticone, and A. Alù	1598
Silver-Gelatine Metal-Dielectric Composites Made From Developed X-Ray Films	J. Krupka, J. Parka, P. Łoś, J. G. Hartnett, and K. Naguszewska	1602
Analysis of a Gradient Index Metamaterial Blazed Diffraction Grating	D. R. Smith, Y.-J. Tsai, and S. Larouche	1605
<hr/>		
CORRECTIONS		
Corrections to “Application of Novel Cavity-Backed Proximity-Coupled Microstrip Patch Antenna to Design Broadband Conformal Phased Array”	D. Sun, W. Dou, and L. You	1609
Correction to “Efficiency Analysis of Magnetic Resonance Wireless Power Transfer With Intermediate Resonant Coil”	J. Kim, H.-C. Son, K.-H. Kim, and Y.-J. Park	1609
<hr/>		
2011 List of Reviewers		1610
<hr/>		
2011 INDEX		1615

Constant Speed Parametrization Mapping of Curved Boundary Surfaces in Higher-Order Moment-Method Electromagnetic Modeling

Milan M. Ilić, *Member, IEEE*, Slobodan V. Savić, Andjelija Ž. Ilić, *Member, IEEE*, and Branislav M. Notaroš, *Senior Member, IEEE*

Abstract—A constant speed parametrization (CSP) mapping of boundary surfaces is proposed for moment-method analysis of antennas and scatterers, along with its approximation using large higher-order Lagrange-type curved quadrilateral patches. The importance of the proper placement of interpolation nodes that ensures minimum mapped parametric space distortion (arc-length parametrization) is explained and demonstrated on simple examples. The CSP mapping results in on average five times lower radar cross section (RCS) error for a spherical scatterer than with the ray casting (central projection) parametrization mapping. The extension of the CSP concept to arbitrary surfaces is illustrated in modeling of the double-ogive target.

Index Terms—Curved parametric elements, electromagnetic analysis, geometrical mapping, higher-order modeling, moment methods, scattering.

I. INTRODUCTION

RELATIVELY recently, the computational electromagnetics (CEM) community has started to extensively investigate and employ curvilinear elements for geometrical modeling of antennas and scatterers [1]–[9] because they offer greater modeling flexibility and enable larger elements to be used in meshes of arbitrary structures, particularly when combined with higher-order basis functions for currents and fields. Most frequently used curved parametric elements for CEM modeling by far are those involving polynomial parametrization (e.g., Lagrange interpolating polynomials, Bézier curves, and splines) [1]–[7], but more complex parametrization based on rational polynomial functions (e.g., rational Bézier curves

and nonuniform rational B-splines or NURBS) has also been adopted in a number of works [8], [9]. Rational polynomial parametrization allows exact modeling of all conical sections (e.g., a circle) and can ensure constant surface tangents across element interconnects, but it comes at the cost of more complex implementation and impairing the overall polynomial structure, and thus the resulting opportunities for efficient nonredundant calculations of field integrals and generalized impedances (inner products) [3], when polynomial basis functions in parametric coordinates are used.

However, practically all works in curvilinear CEM modeling focus on definitions and implementations of particular basis functions on curved elements, as well as on evaluations of associated generalized impedances, i.e., integrals in the curvilinear space, and it appears that none of them address the problem of how to actually position the interpolation (control) nodes that guide the geometry of curved elements. On the other hand, the mapping from the element parent domain to its curvilinear form, typically done by some kind of projection, can be performed in an infinite number of ways. This problem, which apparently has not been adequately investigated and documented by CEM researchers, turns out to be especially important when higher-order large curvilinear elements are constructed and applied (e.g., Lagrange elements of orders higher than two, when more than three interpolation nodes per edge drive the element geometry).

This letter focuses on Lagrange-type generalized parametric quadrilaterals as basic geometrical boundary elements in the method of moments (MoM) analysis of metallic and dielectric antennas and scatterers within the surface integral equation (SIE) approach [3] and points out the importance of proper placement of interpolation nodes such that the resulting mapping introduces the least amount of parametric coordinate distortion in the mapped domain, i.e., it keeps the differential arc lengths as constant as possible at all points of the mapped surface. The goal of this work is to introduce the constant speed parametrization mapping of MoM-SIE surfaces and its approximation using large Lagrange quadrilateral patches, and to explain and emphasize the importance, in general, of achieving the constant speed parametrization (arc-length parametrization) along the surface coordinate lines, in an exact or approximate fashion, in order to obtain final analysis results with the best possible accuracy, considering the degrees of freedom used to describe the geometry. Note that an interesting example of a CEM application of the arc-length parametrization can be found

Manuscript received November 09, 2011; accepted December 08, 2011. Date of publication December 16, 2011; date of current version January 02, 2012. This work was supported by the National Science Foundation under Grants ECCS-0650719 and ECCS-1002385 and the Serbian Ministry of Science and Technological Development under Grant TR-32005.

M. M. Ilić is with the School of Electrical Engineering, University of Belgrade, 11120 Belgrade, Serbia, and also with the Department of Electrical and Computer Engineering, Colorado State University, Fort Collins, CO 80523-1373 USA (e-mail: milanilic@etf.rs).

S. V. Savić is with School of Electrical Engineering, University of Belgrade, 11120 Belgrade, Serbia (e-mail: ssavic@etf.rs).

A. Ž. Ilić is with the Laboratory of Physics 010, Vinča Institute of Nuclear Sciences, 11001 Belgrade, Serbia (e-mail: andjelijaalic@iee.org).

B. M. Notaroš is with the Department of Electrical and Computer Engineering, Colorado State University, Fort Collins, CO 80523-1373 USA (e-mail: notaros@colostate.edu).

Color versions of one or more of the figures in this letter are available online at <http://ieeexplore.ieee.org>.

Digital Object Identifier 10.1109/LAWP.2011.2180354

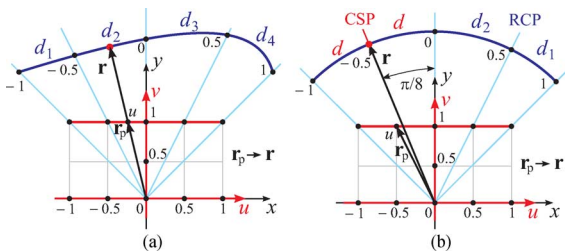


Fig. 1. Parent-line to parametric-curve mapping for (a) an arbitrary curve and (b) a quarter of a circular arc.

in [10], where it is adopted in the context of directivity and impedance optimizations of planar curved wire antennas. This letter also derives simple formulas for the exact mapping of parent line segments and squares to circular arcs and spherical sections, respectively, which result in uniformly or almost uniformly spaced interpolation nodes in the projected domain, thus keeping the least amount of distortion, and which, in that respect, differ from conventional mapping formulas based on the central projection parametrization (ray casting). Furthermore, it demonstrates the general applicability of the constant speed parametrization (CSP) mapping to more complex curved surfaces by positioning the Lagrange interpolation nodes so that the equidistant points in the parent domain are also equidistant along the corresponding projected arcs in the child domain through a numerical solution to a set of resulting CSP equations in the parametric space.

II. RAY CASTING AND CONSTANT SPEED PARAMETRIZATION GEOMETRICAL MAPPINGS

Consider an arbitrary curve that needs to be parametrized for the purposes of CEM simulation, as shown in Fig. 1(a). To this end, we start from the parametric equation for the line segment in the parent domain, $\mathbf{r}_p = u\mathbf{i}_x + \mathbf{i}_y$, $-1 \leq u \leq 1$, $v = 1$, and seek a transformation in the form $\mathbf{r}(u) = x(u)\mathbf{i}_x + y(u)\mathbf{i}_y$. Conventionally, the mapping of the line segment is done by projecting it onto the curve with the common center as the projection center (an analogous procedure for square-to-surface mapping is given in [11] and [12]). This type of mapping can be referred to as the ray-casting parametrization (RCP) mapping, given the analogy with ray-casting applications in computer graphics [13], [14]. Applied to a quarter of a circular arc of radius a , shown in Fig. 1(b), the RCP mapping is then easily derived as

$$\mathbf{r}(u) = a \frac{\mathbf{r}_p(u)}{|\mathbf{r}_p(u)|} = a \frac{u\mathbf{i}_x + \mathbf{i}_y}{\sqrt{1+u^2}} \quad (1)$$

and the rate of change of differential arc lengths on the curve comes out to be $dl/du = \sqrt{(\partial x/\partial u)^2 + (\partial y/\partial u)^2} = a/(1+u^2)$, so that it can be clearly seen in the right-hand half of Fig. 1(b) that the RCP yields nonequidistant projections of parent interpolation nodes ($d_1 < d_2$). However, we introduce here a different mapping, as depicted in the left-hand half of Fig. 1(b), where the interpolation node at $u = -0.5$ is mapped to the middle of the left-hand half of the arc, which

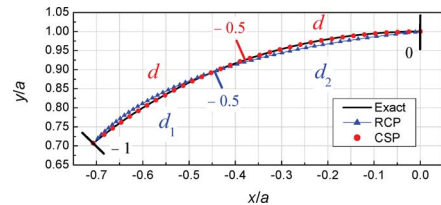


Fig. 2. Geometrical modeling of an eighth of a circular arc based on approximations of the RCP and CSP mappings, respectively, using second-order Lagrange parametric curves. Distances between interpolation nodes according to RCP and CSP mappings are also indicated.

results in uniformly spaced nodes on the parametric curve. The associated $\mathbf{r}_p \rightarrow \mathbf{r}$ transformation is given by

$$\mathbf{r}(u) = a \sin\left(\frac{\pi u}{4}\right) \mathbf{i}_x + a \cos\left(\frac{\pi u}{4}\right) \mathbf{i}_y \quad (2)$$

for which $dl/du = a\pi/4$ is constant. We call this type of mapping the CSP mapping, as the speed with which the mapped point traces the curve, expressed in terms of the parameter (u), is constant along the curve (for $-1 \leq u \leq 1$).

To demonstrate the difference resulting from approximations of the mappings in (1) and (2) by Lagrange elements, we model the left-hand half of the circular arc in Fig. 1(b) by a second-order ($K_u = 2$) Lagrange curve using three equidistant interpolation nodes obtained by RCP and CSP mappings, respectively, and plot the results in Fig. 2. It can be seen that the CSP curve approximates the arc geometrically almost exactly, whereas the RCP curve deviates from it, albeit only slightly. Thus, it is to be expected that any models with the CSP mapping will yield better results. Furthermore, the computed dl/du is much more uniform for the CSP curve. Hence, in addition to a higher geometrical accuracy, we expect better solutions with the CSP mapping than with the RCP one because the surface-current densities in MoM modeling are expressed as functions of coordinates in the parent domain, i.e., u and v (on generalized quadrilaterals), in which integrations and testing are performed as well, and with respect to which the approximation of the CSP mapping introduces less distortion.

We next consider mapping from a square parent domain to one-sixth of a sphere (of radius a). The exact RCP mapping, found analogously to (1) [11], [12], is illustrated in the left inset of Fig. 3, where similar problems as in Fig. 1 with distortion of the projected parametric space are observed. The use of the CSP mapping, with keeping the points uniformly distributed along the corresponding parts of the two great circles on the spherical patch, again can overcome the problems. As a generalization of (2), the resulting exact CSP mapping is given by

$$h(u, v) = \sqrt{1 + \tan^2\left(\frac{\pi u}{4}\right) + \tan^2\left(\frac{\pi v}{4}\right)} \\ x = \frac{a \tan\left(\frac{\pi u}{4}\right)}{h} \quad y = \frac{a \tan\left(\frac{\pi v}{4}\right)}{h} \quad z = \frac{a}{h} \quad (3)$$

and this is depicted in the right inset of Fig. 3.

In general, explicit analytical expressions for the CSP mappings are difficult or impossible to find. Instead, positioning the Lagrange interpolation nodes such that the equidistant points in the parent domain are also equidistant along the corresponding

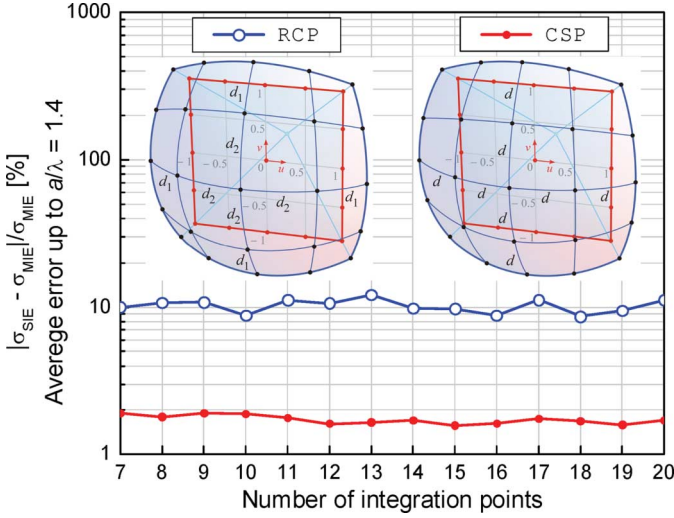


Fig. 3. MoM-SIE analysis of a dielectric ($\epsilon_r = 4$) spherical scatterer (six quadrilaterals, $K_u = K_v = 4$, and $N_u = N_v = 6$), using RCP and CSP mapping models: absolute relative RCS error averaged over multiple values of a/λ versus the number of integration points in the Gauss–Legendre formula (with details of RCP and CSP square-to-surface mappings depicted in the insets).

projected arcs in the child domain is sufficient and can be carried out numerically along an arbitrary parametric line, as will be demonstrated in an example in Section III.

Finally, note that although the CSP mapping is presented in this letter in conjunction with Lagrange curvilinear parametric elements, it can as well be applied to any curve or surface defined by mathematical equations, including those using NURBS [15]. Namely, any curve can be reparametrized to achieve constant speed parametrization [16], which, in general, must be done numerically [15].

III. NUMERICAL RESULTS OF 3-D MoM-SIE EM MODELING USING RCP AND CSP MAPPINGS

As the first example of 3-D MoM-SIE EM modeling using RCP and CSP mapping approaches, consider a dielectric ($\epsilon_r = 4$, $\mu_r = 1$) spherical scatterer of radius a in free space. The spherical surface is modeled by means of six Lagrange quadrilateral patches of the fourth geometrical order ($K_u = K_v = 4$), and with polynomial divergence-conforming hierarchical basis functions [3] of order $N_u = N_v = 6$ in both directions (u and v) for electric and magnetic surface current density vectors on all patches. It is found that the CSP model, which gives accurate results for the monostatic radar cross section (RCS) up to the frequency at which $a/\lambda = 2$, λ being the wavelength in the dielectric, performs much better than the RCP model, which results in noticeable errors even starting from relatively low frequencies (where $a/\lambda \approx 0.42$) and definitely performs poorly at frequencies where $a/\lambda > 1.4$. In addition, Fig. 3 presents the respective percentage errors of the RCS calculation [with respect to the analytical solution (Mie’s series)] averaged over the frequency range up to where $a/\lambda = 1.4$ versus the number of integration points (using the Gauss–Legendre integration formula) in each direction of quadrilateral patches in MoM-SIE solutions. We conclude from the figure that while both models

produce numerically stable solutions, the CSP model gives five times lower average error in the considered frequency span.

As the second example, in order to independently identify the sole influence of the parametrization on the solution accuracy, we consider a metallic square plate scatterer (of side length $a = 1$ m), which is geometrically exactly represented by a flat quadrilateral. While the computed RCS at a frequency of $f = 550$ MHz for the CSP model (standard quadrilateral with $K_u = K_v = 1$) agrees very well with a completely hp -refined reference solution by WIPL-D, the result for a non-CSP quadrilateral with $K_u = K_v = 4$ for which we offset the control points at $v = \pm 0.5$ by ± 0.1 m differs by 46%. The accuracy gain in the current distribution over the plate is even more pronounced.

As the last example and a demonstration of the general applicability of the CSP mapping to more complex curved surfaces (arbitrarily defined by some sort of mathematical equations), we perform CSP modeling and scattering analysis of the metallic double ogive, a benchmark target established by the Electromagnetic Code Consortium (EMCC), at a frequency of $f = 1.57$ GHz [17]. First, the ogive is meshed (based on geometrical equations from [17]) using 24 MoM quadrilateral patches with $K_u = K_v = 4$, and the model appears in the inset of Fig. 4. Next, the CSP algorithm is applied to parameter ranges -2.5 in $< t < 0$ and $0 < t < 5$ in, respectively. For a parametric line defined by $x(t)$, $y(t)$, $z(t)$, we stipulate that the partial arc lengths between any two points are equal to one another, and equal to $1/N$ of the total arc length spanned by t , where N is the number of segments required within the parameter span. This is done by numerically solving the set of equations

$$\int_{t=t_0}^{t_{xOy,i}} \sqrt{\left(\frac{\partial x}{\partial t}\right)^2 + \left(\frac{\partial y}{\partial t}\right)^2 + \left(\frac{\partial z}{\partial t}\right)^2} dt = \frac{i}{8} \int_{t=t_0}^{t_8} \sqrt{\left(\frac{\partial x}{\partial t}\right)^2 + \left(\frac{\partial y}{\partial t}\right)^2 + \left(\frac{\partial z}{\partial t}\right)^2} dt, \quad i = 0, 1, \dots, 7 \quad (4)$$

$$\int_{t=t_{xOy,i}}^{t_{24}} \sqrt{\left(\frac{\partial x}{\partial t}\right)^2 + \left(\frac{\partial y}{\partial t}\right)^2 + \left(\frac{\partial z}{\partial t}\right)^2} dt = \frac{24-i}{16} \int_{t=t_8}^{t_{24}} \sqrt{\left(\frac{\partial x}{\partial t}\right)^2 + \left(\frac{\partial y}{\partial t}\right)^2 + \left(\frac{\partial z}{\partial t}\right)^2} dt, \quad i = 9, 10, \dots, 24 \quad (5)$$

where $t_0 = -2.4925$ in and $t_{24} = 4.9925$ in (the very tip points of the two half-ogives are excluded), and $t_{xOy,8} = 0$ (there is a jump discontinuity at the $t = 0$ plane), using a standard secant method for numerical root finding and evaluating all the integrals numerically as well. The solutions are parameters t arranged in the CSP manner in the xOy -plane ($t_{xOy,i}$, $i = 0, 1, \dots, 24$). On the other hand, as the ogive is rotationally symmetric, the CSP distribution of the ψ parameter ($0 < \psi < 2\pi$) is given by $\psi_j = j2\pi/16$, $j = 0, 1, \dots, 15$. Finally, interpolation nodes (that define MoM patches) are obtained by substituting parameters t_{xOy} and ψ into geometrical equations of the ogive in [17]. Higher-order MoM CSP results with $N_u = N_v = 3$ (total number of unknowns is 420) for the RCS of the double ogive are compared in Fig. 4 with simulation

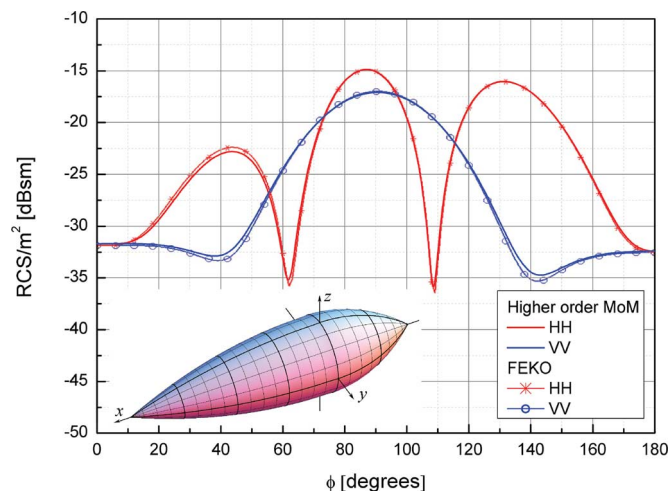


Fig. 4. RCS of the metallic double ogive at $f = 1.57$ GHz [17] as a function of the azimuthal angle (the elevation angle is zero) for the horizontal (HH) and vertical (VV) polarizations, respectively: comparison of the higher-order MoM-SIE solution using CSP parametrization with results obtained by FEKO [18]; geometrical model with 24 curved ($K_u = K_v = 4$) quadrilateral elements is shown in the figure inset.

results obtained by FEKO [18], and an excellent agreement of the two sets of results is observed.

IV. CONCLUSION

This letter has introduced a constant speed parametrization mapping of MoM-SIE boundary surfaces in analysis of antennas and scatterers and its approximation using large Lagrange-type quadrilateral patches and has demonstrated the importance of achieving, at least approximately, the constant speed parametrization (arc-length parametrization) along the surface coordinate lines. The proper placement of interpolation nodes that ensures minimum mapped parametric space distortion is especially important when large high-order curvilinear elements are constructed and applied. In 3-D MoM-SIE analysis of a spherical scatterer, the CSP cube-to-sphere mapping has resulted in on average five times lower percentage error in RCS computations than with the ray-casting parametrization mapping. The RCS results have confirmed all conclusions and expectations derived from the analysis of geometrical results in Fig. 2. Moreover, we realize that what appeared as slight geometrical inaccuracies in the model actually translates into rather considerable errors in the RCS, which emphasizes even more the importance of proper geometrical mapping, namely, CSP mapping in the higher-order MoM-SIE case. The proposed CSP mapping concept has been extended to arbitrary curves

and surfaces (defined by some sort of parametric equations) employing a numerical solution to a set of resulting CSP equations in the parametric space, which has been demonstrated in 3-D MoM-SIE modeling of the EMCC double-ogive target.

REFERENCES

- [1] P. P. Silvester and R. L. Ferrari, *Finite Elements for Electrical Engineers*. Cambridge, U.K.: Cambridge Univ. Press, 1996.
- [2] B. M. Notaroš, "Higher order frequency-domain computational electromagnetics," *IEEE Trans. Antennas Propag.*, vol. 56, no. 8, pp. 2251–2276, Aug. 2008.
- [3] M. Djordjevic and B. M. Notaros, "Double higher order method of moments for surface integral equation modeling of metallic and dielectric antennas and scatterers," *IEEE Trans. Antennas Propag.*, vol. 52, no. 8, pp. 2118–2129, Aug. 2004.
- [4] J. P. Swartz and D. B. Davidson, "Curvilinear vector finite elements using a set of hierarchical basis functions," *IEEE Trans. Antennas Propag.*, vol. 55, no. 2, pp. 440–446, Feb. 2007.
- [5] G. Kang, J. Song, W. C. Chew, K. C. Donepudi, and J. M. Jin, "A novel grid-robust higher order vector basis function for the method of moments," *IEEE Trans. Antennas Propag.*, vol. 49, no. 6, pp. 908–915, Jun. 2001.
- [6] W. Ding and G. Wang, "Treatment of singular integrals on generalized curvilinear parametric quadrilaterals in higher order method of moments," *IEEE Antennas Wireless Propag. Lett.*, vol. 8, pp. 1310–1313, 2009.
- [7] M. S. Tong and W. C. Chew, "A higher-order Nyström scheme for electromagnetic scattering by arbitrarily shaped surfaces," *IEEE Antennas Wireless Propag. Lett.*, vol. 4, pp. 277–280, 2005.
- [8] E. Martini, G. Pelosi, and S. Selleri, "A hybrid finite-element-modal-expansion method with a new type of curvilinear mapping for the analysis of microwave passive devices," *IEEE Trans. Microw. Theory Tech.*, vol. 51, no. 6, pp. 1712–1717, Jun. 2003.
- [9] L. Valle, F. Rivas, and M. F. Catedra, "Combining the moment method with geometrical modelling by NURBS surfaces and Bézier patches," *IEEE Trans. Antennas Propag.*, vol. 42, no. 3, pp. 373–381, Mar. 1994.
- [10] J. Kataja and K. Nikoskinen, "The parametric optimization of wire dipole antennas," *IEEE Trans. Antennas Propag.*, vol. 59, no. 2, pp. 350–356, Feb. 2011.
- [11] B. M. Kolundzija and B. D. Popovic, "Entire-domain Galerkin method for analysis of metallic antennas and scatterers," *Proc. Inst. Elect. Eng. H*, vol. 140, no. 1, pp. 1–10, Feb. 1993.
- [12] B. M. Kolundzija and A. R. Djordjević, *Electromagnetic Modeling of Composite Metallic and Dielectric Structures*. Norwood, MA: Artech House, 2002.
- [13] *An Introduction to Ray Tracing*, A. S. Glassner, Ed. San Francisco, CA: Morgan Kaufmann, 1989.
- [14] A. De Cusatis Jr., L. H. De Figueiredo, and M. Gattass, "Interval methods for ray casting implicit surfaces with affine arithmetic," in *Proc. 12th Brazilian Symp. Comput. Graphics Image Process.*, 1999, pp. 65–71.
- [15] G. Casciola and S. Morigi, "Reparametrization of NURBS curves," *Int. J. Shape Model.*, vol. 2, no. 2 & 3, pp. 103–116, 1996.
- [16] B. O'Neill, *Elementary Differential Geometry*, 2nd ed. Amsterdam, The Netherlands: Elsevier, 2006.
- [17] A. C. Woo, H. T. G. Wang, M. J. Schuh, and M. L. Sanders, "Benchmark radar targets for the validation of computational electromagnetics programs," *IEEE Antennas Propag. Mag.*, vol. 35, no. 1, pp. 84–89, Feb. 1993.
- [18] "FEKO," EM Software & Systems-S.A. (Pty) Ltd., Stellenbosch, South Africa, 2011 [Online]. Available: <http://feko.info/applications/RCS>

EVALUATION OF SMF EXPOSURE FIELD LEVELS AND GRADIENTS OBTAINABLE USING THE 2D MAGNETIC ARRAYS*

Andjelija Ž. Ilić **, Saša Ćirković, Jasna L. Ristić-Djurović

Institute of Physics, University of Belgrade, Zemun-Belgrade, Serbia

Abstract. Two-dimensional magnetic arrays have been proven useful as exposure setups for biomedical experiments with static magnetic fields. Different static magnetic field levels as well as vertical field gradients can be attained from these exposure setups by means of varying the geometrical parameters of an array and the type of magnetic material employed. Evaluation of obtainable field and gradient values has been conducted by varying one by one parameter. Several relevant parameters were chosen to represent the effects of input parameter changes on the magnetic flux density above the array. Calculations were conducted using the exact analytical expression.

Key words: Non-ionizing radiation exposures, exposure setups, static magnetic field (SMF), two-dimensional magnetic arrays, parameter adjustment

DOI: 10.21175/RadJ.2016.02.027

1. INTRODUCTION

Effects of electromagnetic (EM) fields on biological systems can be either beneficial or adversarial. Static magnetic fields (SMF) of low and moderate intensity are shown to have mainly beneficial effects, based on empirical and collected experimental data. Observed therapeutic effects include those related to treating arthritis [1], healing bone fractures [2], and improving microcirculation [3]. Mechanisms of action of SMFs are not yet fully understood.

Experimental magnetic fields are generated using various arrangements of current coils or permanent magnets. Certain types of two-dimensional (2D) magnetic arrays have been successfully employed as exposure setups for SMF generation as well [4], [5]. The type of the array described in [4], with the magnetic axes of individual magnets equally oriented and perpendicular to the array's surface, produces the slowly decreasing magnetic field. In the considered case, individual magnets were distributed across a flat surface periodically at equal distances x_d and y_d in two orthogonal directions. The dominant field component is perpendicular to the surface of the array and an order of magnitude larger than other magnetic field components, provided that individual magnets are not too sparsely placed across the surface. Magnetic flux density variation in planes parallel to the array's surface is significantly smaller than the field decrease with distance from the surface. This allows for the definition of the field gradient perpendicular to the array's surface. This exposure setup therefore produces inhomogeneous magnetic field whose magnetic flux density as well as gradient vary predominantly in the direction perpendicular to the array's surface, with very slight variations in planes parallel to the surface. This

configuration enables studying the effects of both magnetic flux density and its gradient.

Different SMF field levels as well as field gradients can be attained by means of varying the geometrical parameters of an array and the type of magnetic material employed. We investigate the effects to the magnetic flux density and its gradient of varying several parameters, with the aim to define the range of SMF exposure field levels and gradients available for conducting experiments.

2. TWO-DIMENSIONAL MAGNETIC ARRAYS WITH EQUALLY ORIENTED MAGNETIC MOMENTS OF ARRAY ELEMENTS

In the investigation of obtainable exposure field levels and gradients we assume an array of N -by- N identical square cross-section magnets, equally spaced on a flat horizontal surface and kept in place by a non-magnetic substrate. We assume equal and vertical orientation of magnetic moments of all magnets. Were the magnets mounted on a ferromagnetic plate instead, similar analysis would apply, with the height of the magnets doubled due to the image theorem.

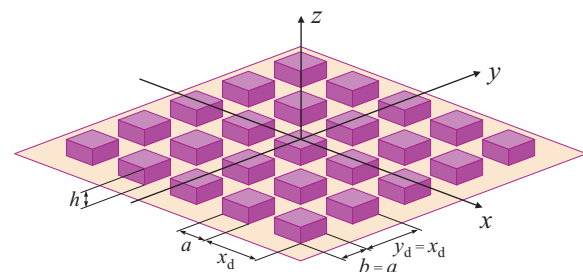


Figure 1. Two-dimensional magnetic array

* The paper was presented at the Third International Conference on Radiation and Applications in Various Fields of Research (RAD 2015), Budva, Montenegro, 2015.

**andjelija@iee.org

Vertical axis is denoted as the z -axis and the whole array is assumed to be symmetrical with respect to the x - and y -direction, as shown in Fig. 1. Rows of magnets are parallel to the x -axis, with the magnet centers spaced by x_d . Distance between the adjacent rows is $y_d = x_d$. Magnetic flux density distribution at the array's surface varies periodically from negative to positive B_z , since the magnetic flux lines partially close between the adjacent elements. With the increase in height, z , above the array's surface the majority of the magnetic flux lines add up together to form a resultant magnetic flux density B_z . Above a low-limit height for conducting experiments, $z = z_0$, magnetic flux density is positive everywhere except for the stray field above the array edges. With the further increase in height, magnetic flux density variation in horizontal planes decreases. We define parameter $z_{1\%}$, as the height above the array above which field variation in the horizontal planes is less than 1%, and $\overline{B_z}_{1\%}$ as the corresponding mean magnetic flux density. Magnetic field vertical gradient decreases with height as well, with magnetic field decrease almost linear at larger heights.

Basic properties of several magnetic materials most commonly used for permanent magnets [6], [7] are listed in Table 1. Material remanent magnetization, B_r , and Curie temperature, T_c , as well as the maximum energy product, $(BH)_m$, must all be accounted for when choosing the right magnets for a particular application. Improved energy product is accompanied by the increased cost of permanent magnets, ranging from about 5 USD per kg for ferrites (BaFe₁₂O₁₉), to about 50 USD/kg for Alnico, and to about 120 USD/kg for samarium-cobalt and neodymium magnets [8]. High quality neodymium magnets are more expensive, up to about 200 USD/kg. Remanent magnetic flux density corresponds to bulk material, i.e., to a piece of material very long in the direction of magnetization. It is related to the magnetization per unit density, M_r , by the equation $B_r = \mu_0 \cdot \rho \cdot M_r$, where ρ represents the material density. Considering equivalent surface currents resulting from magnetization and real magnet dimensions, actual magnetic flux density is obtained analytically. For the magnetization in the z -direction, four vertical sides of each magnet can be replaced by the current sheets carrying the surface current density $J_{ms} = \rho \cdot M_r$.

Vertical component of the magnetic flux density, $B_z(x, y, z)$, is calculated as the sum of the contributions of all vertical sides of all the magnets comprising the array. For a single square cross-section magnet of side length a and height h magnetic flux density is given by:

$$B_{z1}(x_1, y_1, z) = \frac{\mu_0 J_{ms}}{4\pi} \sum_{k=1}^4 \sum_{ip=0}^1 \sum_{tq=0}^1 (-1)^{(ip+tq+1)} \arcsin(p_k^{ip} \cdot q_k^{tq}),$$

$$p_k^{ip} = \frac{((-1)^{\lfloor \frac{k}{2} \rfloor} \frac{a-x_1}{2})^{m_2} \cdot ((-1)^{\lfloor \frac{k-1}{2} \rfloor} \frac{a-y_1}{2})^{m_1}}{\sqrt{((-1)^{\lfloor \frac{k}{2} \rfloor} \frac{a-x_1}{2})^{2m_2} + ((-1)^{\lfloor \frac{k-1}{2} \rfloor} \frac{a-y_1}{2})^{2m_1}}},$$

$$q_k^{tq} = \frac{\frac{\text{sgn}((-1)^{m_s} \frac{a-x_1}{2})^{m_1}}{(-\text{sgn}((-1)^{m_s} \frac{a-y_1}{2}))^{m_2}}}{\sqrt{((-1)^{m_s} \frac{a-x_1}{2})^{2m_1} + ((-1)^{m_s} \frac{a-y_1}{2})^{2m_2} + (z+(1-tq)h)^2}},$$

$$m_1 = (1+(-1)^{k-1})/2, \quad m_2 = (1+(-1)^k)/2, \quad m_s = (1-\text{sgn}(k-\frac{5}{2}))/2.$$

In the above, x_1 and y_1 are the distances, measured in the direction of x -axis and y -axis, from the magnet center to the field point. Magnet side is denoted by k , numbers 1, 2, 3 and 4 corresponding to the negative x -axis, negative y -axis, positive x -axis and positive y -axis with respect to the magnet center. Square brackets stand for the integer division. Point of current entrance into the current sheet corresponds to $tp = 0$, and the point of current exit to $tp = 1$. Indices $tq = 0$ and $tq = 1$ denote the bottom surface or the top surface of the magnet. Derivation of the above equation, as well as the expressions for x -component and y -component of the magnetic flux density, are given in [4]. It has been shown in [4] that the B_z field component is dominant. Therefore, this evaluation considers only the dominant field component.

Table 1. Basic properties of typical commercial magnetic materials

Material	B_r (T)	$(BH)_m$ (kJ/m ³)	T_c (°C)	M_r (Am ² /kg)	J_{ms} (A/m)
BaFe ₁₂ O ₁₉	0.40	34	450	65.0	318.3
Alnico	1.25	43	860	142.1	994.7
SmCo ₅	0.88	150	720	85.4	700.3
Sm ₂ Co ₁₇	1.08	220	820	102.3	859.4
Nd ₂ Fe ₁₄ B	1.28	300	400	135.8	1018.6

3. RESULTS AND DISCUSSION

The surface current density, J_{ms} , enters the magnetic flux density equation as the multiplicative factor to scale the expression depending exclusively on the geometrical parameters of an array. Therefore, for a fixed given geometry of an array, difference in the achieved field levels for different magnetic materials corresponds to the ratio of remanent magnetization of materials. This is illustrated by the example shown in Fig. 2, where moderately sized magnets ($a = 8$ mm, $h = 5$ mm) were arranged with the gap between every two magnets equal to the magnet length a ($k_d = 1$). Please note that the parameter k_d is introduced as the ratio of the gap size to the magnet size. Corresponding center-to-center magnet spacing equals $x_d = (k_d+1) \cdot a$. Number of individual magnets in a row is taken equal to $N = 15$ in this as well as in the all other examples.

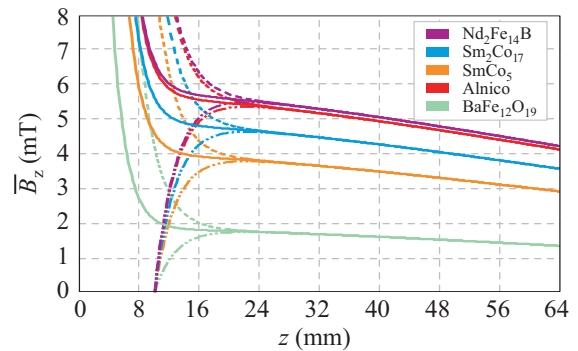


Figure 2. Magnetic flux density along the magnet axis, along the magnet gap axis, and mean magnetic flux density in

horizontal planes above the array, for magnetic materials listed in Table 1 ($a = 8 \text{ mm}$, $h = 5 \text{ mm}$, $x_d = 16 \text{ mm}$)

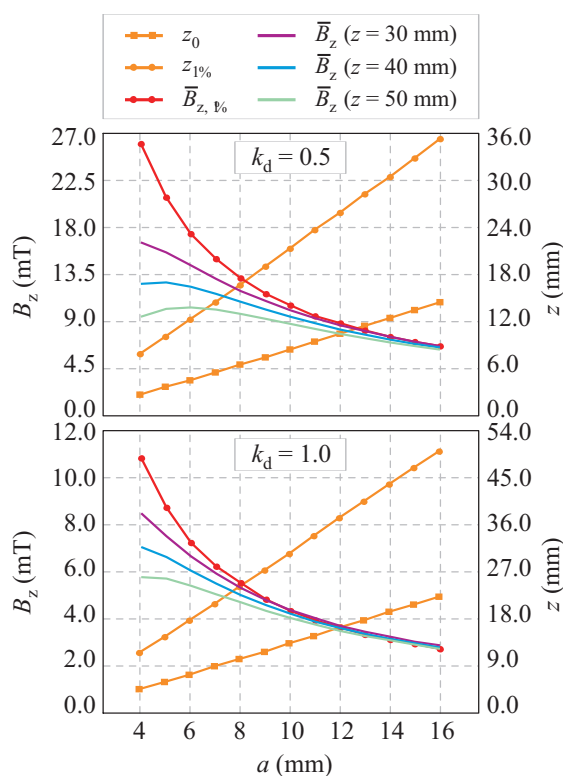


Figure 3. Influence of the magnet side length, a , on several parameters describing the magnetic field above the array, with the relative spacing between the magnets kept fixed at half the side length (upper plot) and whole side length (lower plot)

In Fig. 2, magnetic flux density at the vertical axes through the magnet centers is represented by the dashed lines, and the one between every four magnets (axes where the x -spacings and y -spacings cross) is shown by the dash-dot-dot lines. Mean magnetic flux density in horizontal planes above the array is well approximated as the average of the two (depicted by the solid lines). Up to some low-limit height magnetic flux density along the magnet gap axis is negative as the flux lines close between the magnets. At the same height, right above the magnets the field is strong, so that all in all next to the surface the field intensity is strong, direction of magnetic flux lines alternates, and field gradients are very pronounced. After the limiting height, z_0 , magnetic flux densities above the magnets and between the magnets start converging to fast reach the height where the field variation everywhere in the horizontal planes lies below 1% of the mean field level in that plane. For the considered example, magnetic flux density is positive everywhere above the plane $z_0 = 10.2 \text{ mm}$. The 1% threshold is $z_{1\%} = 24.0 \text{ mm}$, and the B_z value for the strongest neodymium magnets at that height equals $B_{z,1\%} = 5.5 \text{ mT}$. In this particular example, field further decreases almost linearly.

Having in mind average mice height of about 30 mm, experimental volume for *in vivo* experiments can be taken from the height of about 25 mm to

55 mm. For *in vitro* experiments, a range of different field intensities is available by appropriate placement of specimens at different heights above the array. Mean magnetic flux density and its mean gradient in the experimental volume are determined by field averaging between the two limiting horizontal planes.

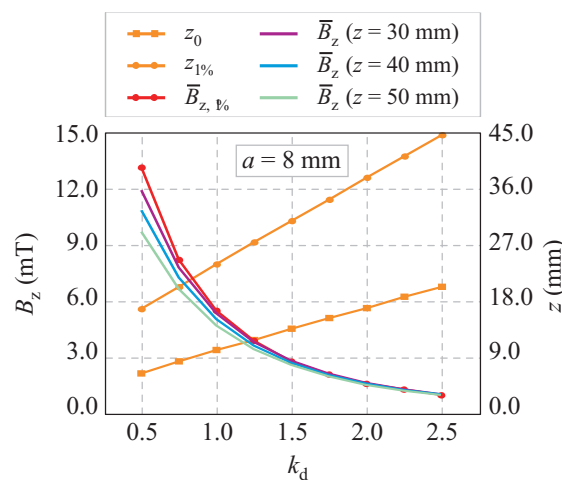


Figure 4. Influence of the gap size, $ka \cdot a$, between the two neighboring magnets on the parameters describing the magnetic field above the array

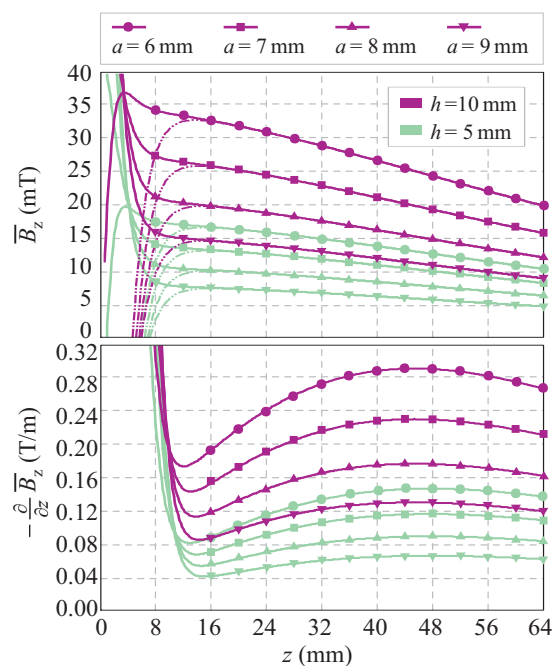


Figure 5. Mean magnetic flux density and its mean gradient for the fixed center-to-center magnet spacing of $x_d = 12 \text{ mm}$, for different ratios a versus $ka \cdot a$, for two magnet heights h

Since the amount of data that could be depicted in Fig. 3 and Fig. 4 is limited, three heights, $z = 30 \text{ mm}$, $z = 40 \text{ mm}$, and $z = 50 \text{ mm}$, were chosen to represent field variations resulting from the changes of input parameters.

Provided that the height of the magnets is relatively small with respect to the size of an array in lateral

directions, doubling the magnet height results in twice the magnetic flux density. Height of the magnets can therefore be used to adjust the field levels. If the more homogeneous magnetic flux density is desired for the experiment, one magnetic array is placed below the experimental volume, and the other one on top. Resultant magnetic flux density is fairly homogeneous. Height of the magnets in Fig. 3 and Fig. 4 is fixed at $h = 5$ mm and in Fig. 5 it is compared with $h = 10$ mm.

Data presented in Fig. 3 analyze what are the effects to the field of the changes in magnet side length, a . The ratio gap size versus magnet size is kept fixed at $k_d = 0.5$ (upper plot) and $k_d = 1$ (lower plot). Both the low-limit height z_0 and the 1% threshold $z_{1\%}$ show linear dependence on the lateral size of the magnets. Magnetic field is higher and the two limiting heights, z_0 and $z_{1\%}$, are lower for the smaller magnets. Data shown in Fig. 3, Fig. 4 and Fig. 5 correspond to $\text{Nd}_2\text{Fe}_{14}\text{B}$ magnets. For other types of magnetic materials, data need to be scaled by the relative ratio of remanent magnetizations.

Parameters of interest are presented in Fig. 4 as a function of k_d , with the fixed values of other input data. Size of the magnets is kept at moderate $a = 8$ mm. Similar conclusions are drawn as in the previous example – smaller magnet spacing results in the stronger and higher quality magnetic field (in terms of field homogeneity in horizontal planes).

Figure 5 shows mean magnetic flux density and its mean gradient for the fixed center-to-center magnet spacing of $x_d = 12$ mm, value of x_d resulting in almost constant gradient about 40 to 48 mm height. Magnetic flux density decrease in that case shows the least variation from the linear one inside the experimental volume recommended for *in vivo* experiments (25 to 55 mm height above the array). It is demonstrated that the increase in height of the magnets results in almost the same relative increase in field intensity.

4. CONCLUSIONS

Generic example of the symmetrical two-dimensional magnetic array has been studied using the analytical expressions describing the magnetic flux density above the array. Evaluation of obtainable static magnetic field levels as well as vertical field gradients has been conducted by varying one by one parameter.

Input parameters comprised magnet size and spacing (the geometrical parameters) and the type of magnetic material used. The collection of data and results presented can be used for preliminary design of 2D magnetic arrays.

Acknowledgement: This work was supported by the Ministry of Education, Science and Technological Development of Serbia through the project III-45003.

REFERENCES

1. N. Taniguchi, S. Kanai, M. Kawamoto, H. Endo and H. Higashino, "Study on application of static magnetic field for adjuvant arthritis rats", *Evid. Based Complem. Altern. Med.*, vol. 1, pp. 187-191, July 2004.
2. S. Xu, H. Okano, N. Tomita and Y. Ikada, "Recovery effects of a 180 mT static magnetic field on bone mineral density of osteoporotic lumbar vertebrae in ovariectomized rats", *Evid. Based Complem. Altern. Med.*, vol. 2011, Article ID 620984, 8 pages, 2011.
3. H. N. Mayrovitz and E. E. Groseclose, "Effects of a static magnetic field of either polarity on skin microcirculation", *Microvasc. Res.*, vol. 69, pp. 24-27, January 2005.
4. A. Ž. Ilić et al., "Analytical description of two-dimensional magnetic arrays suitable for biomedical applications", *IEEE Trans. Magnetics*, vol. 49, pp. 5656-5663, December 2013.
5. J. László et al., "Optimization of static magnetic field parameters improves analgesic effect in mice", *Bioelectromagnetics*, vol. 28, pp. 615-627, December 2007.
6. T. R. Ní Mhíocháin and J. M. D. Coey, "Permanent magnets", in *Physical Methods, Instruments and Measurements*, vol. III, Y. M. Tsipenyuk, Ed. Oxford, U.K.: Eolss Publishers, 2009 [Online]: <http://www.eolss.net>, Encyclopedia of Life Support Systems, under the auspices of the UNESCO.
7. I. R. Harris and A. J. Williams, "Magnetic materials", in *Materials Science and Engineering*, vol. II, R. D. Rawlings, Ed. Oxford, U.K.: Eolss Publishers, 2009 [Online]. Available: <http://www.eolss.net>, Encyclopedia of Life Support Systems, under the auspices of the UNESCO.
8. W. T. Benecki, "The permanent magnet market – 2015", *Proc. Magnetics 2013 Conf.*, Orlando, FL, USA, 2013.

A Comparison of Modal Electromagnetic Field Distributions in Analytical and Numerical Solutions

Miloš Davidović, Anđelija Ilić¹, Miodrag Tasić², Branislav Notaroš³, Milan Ilić⁴

Abstract – In this paper, a detailed comparison of modal electromagnetic field distribution in two canonical microwave cavities, obtained via analytical and recently introduced numerical approaches, is presented and discussed. While the analyzed problems, namely, those of a spherical cavity and a ridged cavity are relatively simple, they still provide valuable benchmarks for novel numerical methods, allowing for early estimates of accuracy, efficiency, and convergence properties of the method. Furthermore, study of field distributions may provide useful insights about strengths and weaknesses of the approximating vector spaces which are otherwise not possible.

Keywords – Microwave cavities, Higher order finite element method, B-spline solid modeling, Eigenfrequency, Eigenfield.

I. INTRODUCTION

Error estimates are a very important part of any kind of analysis performed in a modern electromagnetic (EM) engineering practice, especially for widely accepted methods such as finite element method (FEM) [1]. These kinds of estimates are also needed for all novel methods, whose properties are not yet studied in detail. Modern computational EM is largely oriented toward higher order methods, excellent survey of which can be found in [2]. Unfortunately, higher order methods require much more involvement from practicing engineers. Therefore, success (or failure) of EM engineering projects will still often be strongly determined by proficiency of practicing engineers in adequate formulation of the problem, i.e., use of sufficient number of details during geometrical modeling and meshing, setting reasonable prescribed accuracy, and interpretation of obtained numerical results. These skills are best honed by performing FEM

known problems, which present reasonable amount of difficulties encountered in practice (such as curved geometry, singular fields) but are not overwhelming. It is therefore desirable for any novel method, to be tested on well understood, but not trivial problems. With this in mind, the B-spline method for efficient analysis of three dimensional (3-D) microwave cavities, recently introduced in [3], was tested in terms of accuracy and efficiency. Testing of accuracy was taken beyond the usually performed eigenvalue test, and also includes testing of eigenfield solution. The analyzed method enables completely independent higher order modeling of both geometry and electromagnetic fields; the geometry modeling is done using trivariate B-splines (by exploiting their excellent approximation capabilities), while the field modeling is done using hierarchical higher order polynomial vector basis functions [4] (thus enabling very accurate and efficient approximation of fields). It is worth noting that while some other methods for geometry modeling may represent some forms of geometry more accurately (for example rational Bézier curves and non-uniform rational B-splines or NURBS [5], [6] can model conic sections exactly), they may also require specialized quadrature rules when used in numerical EM.

In this paper, we revisit the B-spline FEM modeling introduced in [3] and give additional insight in the convergence of the modal field solutions. Section II of the paper presents the B-spline modeling of solids in general as well as details of solid modeling of spherical and ridged cavity in particular. In Section III, the FEM field-expansion basis functions are described. In Section IV, numerical results are discussed including analysis of modal field distributions.

II. B-SPLINE SOLID MODELING

Presentation in this Section mainly follows [3] regarding general B-spline solid modeling, with additional details on analyzed examples of the spherical and the ridged cavity.

A. Univariate B-splines

Since solid modeling requires utilization of trivariate splines, and they are defined using univariate splines, some basic univariate splines definitions are in place. Note however, that while univariate spline definitions that will be given below are constructive in nature, i.e., they describe one possible algorithm for construction of splines, it is more advisable to implement more stable and efficient algorithms [7]. We use the following recurrent formula to define the B-spline functions:

Miloš Davidović is with the School of Electrical Engineering, University of Belgrade, 11120 Belgrade, Serbia (PhD student) and also with Laboratory for radiation measurements 100, Vinča Institute, University of Belgrade, 11001 Belgrade, Serbia, E-mail: davidovic@vinca.rs

¹Anđelija Ilić is with the Innovation Center, School of Electrical Engineering, University of Belgrade 11120 Belgrade, Serbia E-mail: andjelijailic@ieee.org

²Miodrag Tasić is with the School of Electrical Engineering, University of Belgrade, 11120 Belgrade, Serbia E-mail: tasic@etf.rs

³Branislav Notaroš is with the Department of Electrical and Computer Engineering, Colorado State University, Fort Collins, CO 80523-1373 USA E-mail: notaros@colostate.edu

⁴Milan Ilić is with the School of Electrical Engineering, University of Belgrade, 11120 Belgrade, Serbia, and also with the Department of Electrical and Computer Engineering, Colorado State University, Fort Collins, CO 80523-1373 USA E-mail: milanilic@etf.rs

$$B_{i,1}(u) = 1, u_i \leq u \leq u_{i+1} \text{ and } B_{i,1}(u) = 0, \text{ elsewhere,}$$

$$B_{i,m}(u) = \frac{u-u_i}{u_{i+m-1}-u_i} B_{i,m-1}(u) + \frac{u_{i+m}-u}{u_{i+m}-u_{i+1}} B_{i+1,m-1}(u), \quad m > 1 \quad (1)$$

where $0 \leq i \leq n$, $n > 0$, and $U = (u_0, u_1, \dots, u_{n+m})$ is a non-decreasing sequence of real numbers. U is called the knot vector of the corresponding spline family, and can be used to flexibly increase or decrease the number of splines and continuity of splines over knot vectors with multiplicities. Multiplicities, i.e., repetition of knots in knot vector, can lead to non-defined terms in Eq. (1), and if division by zero should occur when algorithm from Eq. (1) is followed, that term is replaced by zero. The function $B_{i,m}(u)$ is called the i -th B-spline of order m and degree $m-1$ with respect to the knot vector U . The following equations hold for a standard clamped uniform knot vector:

$$u_i = 0, 0 \leq i \leq m-1, \quad u_i = i-m+1, m \leq i \leq n, \quad \text{and} \quad (2)$$

$$u_i = n-m+2, n+1 \leq i \leq n+m,$$

where the term ‘‘uniform’’ refers to uniform spacing between internal knots, and the term ‘‘clamped’’ is due to end knot multiplicities.

B. Trivariate Splines and Hexahedron Parametrization

Using previously defined univariate B-splines, we can define a parametric hexahedron introducing a mapping $\mathbf{r} : (u, v, w) \rightarrow (x, y, z)$, $(u, v, w) \in [-1, 1] \times [-1, 1] \times [-1, 1]$ (cubical parent domain), such that it is interpolatory at the specified points of the global Cartesian space. To simplify the parameterization (without loss of generality) we employ the same order of B-splines ($m_u = m_v = m_w = m$) and the same knot vectors in all directions. A point within a hexahedron is thus defined by

$$\mathbf{r}(u, v, w) = \sum_{i,j,k=0}^n B_{i,m}(u) B_{j,m}(v) B_{k,m}(w) \mathbf{C}_{i,j,k}. \quad (3)$$

where $B_{i,m}, B_{j,m}, B_{k,m}$ are the splines over the same knot vector and $\mathbf{C}_{i,j,k}$ are the position vectors of the control points, found by solving the following system of equations:

$$\mathbf{r}_l = \sum_{i,j,k=0}^n B_{i,m}(u^l) B_{j,m}(v^l) B_{k,m}(w^l) \mathbf{C}_{i,j,k}, \quad l = 1, \dots, K, \quad (4)$$

where $K = (n+1)^3$, and with \mathbf{r}_l and (u^l, v^l, w^l) being the (global) position-vectors of the interpolation points of the solid and their (local) parametric coordinates, respectively. Note that other parameterization formulations are also possible (but slightly less simple). For example, Eq. (4) can be modified to include various additional conditions, such as prescribed tangent at certain points, etc. The choice of interpolation points and a knot vector depends on the particular solid that needs to be parameterized, and will be presented next.

C. Solid Modeling of the Spherical and Ridged cavity

Spherical cavity can be modeled as a solid in a number of ways (even when restriction to B-spline solid modeling is made). Note however, that utilization of polynomial models (or piece-wise polynomial) models are preferred, since rational functions would require specialized quadrature algorithms. We opted for the method described in previous section, with the choice of parametric and Cartesian points given by a simple analytical mapping [3]. This way, it is possible to have tunable geometrical accuracy, which is very important, especially when doing pointwise comparisons of the field quantities. Two solid spline models were used for the cavity, a more ‘‘crude’’ model, having only 125 interpolation points ($n = 4$), and geometrically refined model, having 1,000 interpolation points ($n = 9$).

Fig. 1 shows the spline functions used in the first model of the spherical cavity and parametric coordinate lines in the $w=0$ cut.

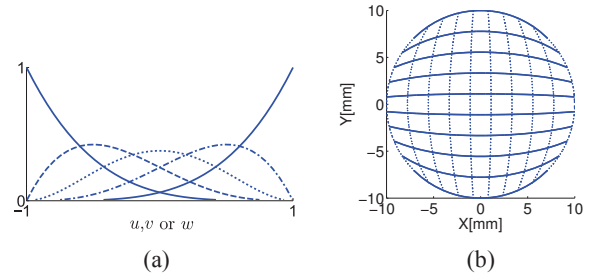


Fig. 1. (a) B-spline functions of order $m = 5$ used for the entire-domain modeling of a spherical cavity with the flat knot vector $(-1, 1)$ and (b) u - v coordinate lines in the $w=0$ cut

Note that both models are very precise and that visual inspection would not reveal any difference between the two. However, as we will show, eigenfield calculations are very sensitive and will reveal considerable differences between the two models.

Geometrical modeling of the ridged cavity is significantly simpler, partly because the cavity is swept geometry. Since, for simplicity, we use the same spline family in all three parametric directions, and 4 points are needed to describe the ridge, we will need a total of $4^3=64$ interpolation points. Fig. 2 shows the interpolation points in one w -cut and the spline family used in all three parametric directions.

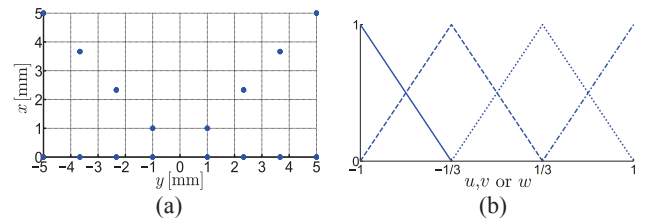


Fig. 2. (a) Interpolation points in one w -cut and (b) B-spline family adopted for parameterization of the ridged cavity

These two examples clearly show flexibility of B-spline modeling, as both arbitrary order and arbitrary number of functions can be used along a parametric direction.

III. FIELD EXPANSION

Approximation of electric field is given (within each hexahedral element) as:

$$\mathbf{E}^e = \sum_{l=1}^{N^e} \gamma_l^e \mathbf{f}_l^e \quad (5)$$

where \mathbf{f}_l^e are higher order vector basis functions with a total of N^e unknown field-distribution coefficients γ_l^e in the element. The basis functions are curl-conforming hierarchical polynomials of arbitrary field-approximation orders N_u^e , N_v^e , and N_w^e ($N_u^e, N_v^e, N_w^e \geq 1$) in the e -th element, which, for the reciprocal u -directed field vector, are given by:

$$\mathbf{f}_{uqst}^e = u^q P_s(v) P_t(w) \frac{\mathbf{a}_v^e \times \mathbf{a}_w^e}{\mathfrak{J}^e},$$

$$P_s(v) = \begin{cases} 1-v, & s=0 \\ v+1, & s=1 \\ v^s-1, & s \geq 2, \text{ even} \\ v^s-v, & s \geq 3, \text{ odd} \end{cases} \quad (6)$$

$$\mathfrak{J}^e = (\mathbf{a}_u^e \times \mathbf{a}_v^e) \cdot \mathbf{a}_w^e, \mathbf{a}_u^e = \frac{\partial \mathbf{r}^e}{\partial u}, \mathbf{a}_v^e = \frac{\partial \mathbf{r}^e}{\partial v}, \mathbf{a}_w^e = \frac{\partial \mathbf{r}^e}{\partial w},$$

where \mathfrak{J}^e is the Jacobian of the covariant transformation, and \mathbf{a}_u^e , \mathbf{a}_v^e , and \mathbf{a}_w^e are the unitary vectors along the parametric coordinates of the element and analogously for the v - and w -directed basis functions.

Field-expansion orders N_u^e, N_v^e, N_w^e in Eq. (6) are entirely independent from each other, and can be combined independently for the best overall performance of the method. Furthermore, because the basis functions are hierarchical (each lower-order set of functions is a subset of all higher-order sets), all of the parameters can be adopted anisotropically in different directions within an element, and nonuniformly from element to element in a model. Note that indices from Eq. (6) are “collapsed” into one index in Eq. (5). This scheme is commonly used when members of a set must be accessed in linear fashion. One well known example is from computer science when multidimensional arrays must be arranged in a linear sequence in memory.

It is interesting to note that basis functions defined by Eq.(6) can be classified into several different groups which play different role in FEM formulation. The first group consists of functions which have tangential component that vanishes on the element boundaries. In electric field approximation they do not directly participate in enforcement of boundary conditions. The *hp*-FEM literature commonly refers to these functions as the *bubble* functions. The second group consists of functions which have non vanishing tangential component on element boundaries, and are known as the *face* functions. These functions participate in

approximation of boundary conditions. Note that with functions defined in Eq. (6) it is sufficient to enforce continuity of face functions, and no special algorithms need to be devised for edge, face, and vertex functions.

After Galerkin testing procedure, details of which can be found in [3], a generalized eigenvalue problem is obtained. Eigenvalues and eigenvectors (which come in form of coefficients in Eq. (5)) are obtained as a solutions. Modal eigenfield is than easily obtained from Eq. (5).

IV. NUMERICAL RESULTS

For cavity problems, it is usually most important to obtain eigenfrequencies as accurately as possible. However, modal fields are also of interest. In the FEM algorithms the convergence is usually evaluated by comparison of S-parameters (for driven solutions), changes in overall scattering energy (for incident wave problems) or resonant frequencies (for eigenmode solutions) from pass to pass [8]. These quantities represent the results of the model as a whole, and usually converge more rapidly, i.e., with fewer unknowns, than the approximation of fields at individual points. However, it is interesting to study convergence of field solutions along with the convergence of eigenvalues, in order to gain better insight into needed number of unknowns, i.e., order of approximation, for specified accuracy. It is not uncommon for inexperienced engineers to set the prescribed accuracy too high, therefore considerably lengthening simulation times without any real benefit.

The electric field distribution for the dominant spherical mode obtained by the analytical solution [9] and by the entire domain B-spline solution, is given in Figs. 3 and 4, respectively. The field solutions are plotted directly from the computed corresponding eigenvectors, thus they are practically identical except for the difference in the eigenvector normalization (which is understandable) and except near the sphere “edges” (Fig. 4) where the entire-domain B-spline model has a discontinuous tangent (which is also easily appreciated and can be improved by adopting higher order geometrical model or *h*-refinement).

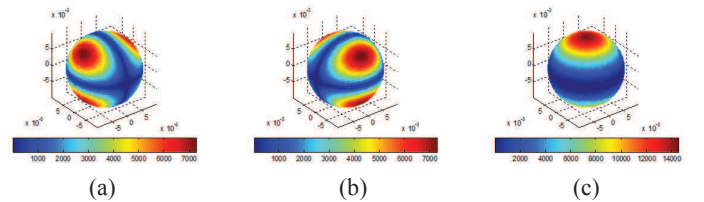


Fig. 3. Analytical solution: magnitudes of (a) x -, (b) y - and (c) z -components of the electric field for the first mode

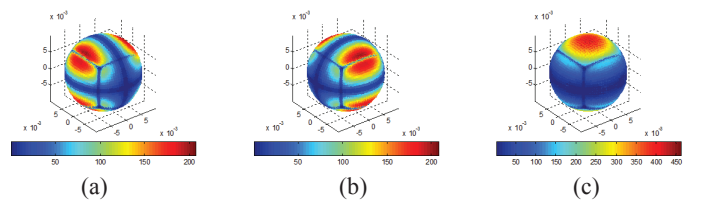


Fig. 4. B-spline solution (108 unknowns, “crude” geometry model): magnitudes of (a) x -, (b) y - and (c) z -components of the electric field for the first mode

Note that, in this case, any attempt to quantify the error of the field distribution throughout the element volume would be strongly biased by the significantly higher errors near these “edges”.

However, to establish an estimate of the accuracy and convergence of the solution of the electric field, when the number of unknowns is increased (by p -refinement), we compute the RMS error of the magnitude of the B-spline field solution relative to the analytical solution for the two models of spherical cavity in 1,016 and 1,736 surface points for the crude and refined models, respectively. Numerical results for the RMS error of the dominant mode eigenfield for the two solid models, along with the average eigenfrequency error for the first 11 modes, are given in Table I.

Results from Table I can be interpreted in the following way. Looking at the convergence of the eigenfrequencies, it is clear that both models have excellent convergence, i.e., error decreases monotonically and rapidly with the increase of the number of unknowns. Situation is less clear regarding modal field convergence.

TABLE I
ERROR IN CALCULATING EIGENFREQUENCY AND MODAL FIELD
IN A SPHERICAL CAVITY

	Error [%]			
	Average eigenfrequency error (11 modes)			
Crude model	2.8666	0.2011	0.1098	0.0501
Refined model	2.8179	0.1470	0.0661	0.0097
	RMS error in modal field (1st mode)			
Crude model	20.79	20.60	40.63	17.30
Refined model	10.29	9.70	5.11	5.08
Unknowns	108	240	450	756

It is evident that the error in modal field is several orders of magnitude larger than the error in eigenfrequencies. Also, with the refined model, the convergence is monotonic. On the other hand, the crude model shows high error despite excellent eigenvalue convergence. This can be attributed to the offset between the ideal spherical cavity used for exact analytical solution, and crude spline model of the sphere. Hence, there is effectively a significant mismatch of points when point-by-point comparison of fields is applied in presence of the rapidly changing fields (as can be seen from Figs. 3 and 4).

The ridged cavity (see [3] for more detailed figure of the cavity), is less grateful for comparison of modal field solutions because there is no readily available analytical solution. Hence, for the ridged cavity example, the B-spline solution and the reference numerical HFSS solution, for the dominant mode electric field distribution, are presented in the large number of sampling points in Fig. 5, where very similar distributions of fields can be observed. This is also confirmed by Fig. 6, where magnitude of the field is again plotted, but without 3D positional data, in order to include internal points in the comparison. Table II shows the relative error of the computed resonant free space wave number k_0 for the first 9 resonant modes.

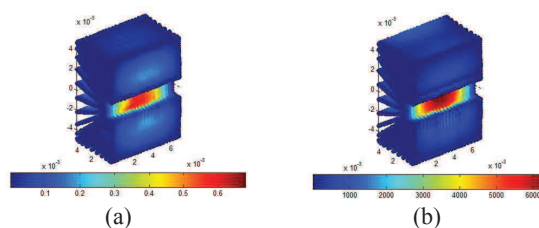


Fig. 5. Magnitude of the electric field of the first mode of the ridge taken in the large number (27,000 points) of sampling points: (a) HFSS and (b) B-spline solutions

As for the modal field solution, RMS “error” for the first mode is 28.88%, when calculated in 27,000 volume points. This is again several orders of magnitude larger than the error in computed eigenfrequencies. This can be attributed to the fact that p -refined basis functions used in B-spline model are too smooth to model the field near reentrant corners of the ridge, where the field is theoretically singular. Furthermore, since there is no available exact solution, quantification of the error strongly depends on the HFSS solution (and its convergence properties, number of adaptive passes, and initial mesh seeding).

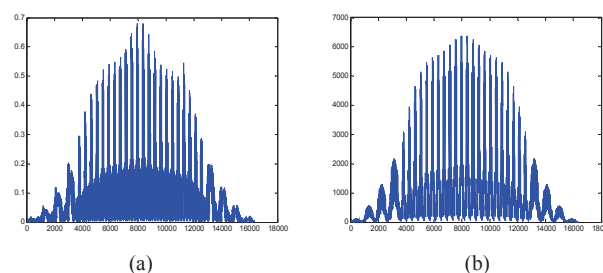


Fig. 6. Plot of magnitude of the electric field of the first mode of the ridge, without 3D positional data, a) HFSS, b) B-spline

TABLE II
ERROR IN CALCULATING k_0 IN THE RIDGED CAVITY

Mode	HFSS k_0 [cm ⁻¹]	B-spline Error [%]
Unknowns	3,017 t	276
1	5.091	0.0393
2	7.469	4.0969
3	7.853	0.4202
4	7.878	5.0774
5	8.019	3.8035
6	8.863	2.6853
7	8.9	4.3820
8	9.087	6.8119
9	10	3.9000

V. ACKNOWLEDGEMENTS

This work was supported by the Serbian Ministry of Education, Science, and Technological Development under grants ON171028 and TR-32005.

REFERENCES

- [15] J. M. Jin, *The Finite Element Method in Electromagnetics*, 2nd ed., John Wiley & Sons, New York, 2002.
- [16] B. M. Notaroš, "Higher order frequency-domain computational electromagnetics," *IEEE Trans. Antennas Propag.*, vol. 56, pp. 2251–2276, 2008.
- [17] M. D. Davidović, B. M. Notaroš and M. M. Ilić, "B-spline entire-domain higher order finite elements for 3-D electromagnetic modeling," *IEEE Microwave and Wireless Components Letters*, vol. 22, no. 10, pp.497–499, 2012.
- [18] M. M. Ilić, B. M. Notaroš, "Higher order hierarchical curved hexahedral vector finite elements for electromagnetic modeling," *IEEE Trans. Microw. Theory Techniques*, vol. 51, 1026–1033, 2003.
- [19] L. Valle, F. Rivas and M. F. Catedra, "Combining the moment method with geometrical modelling by NURBS surfaces and Bézier patches," *IEEE Trans. Antennas Propag.*, vol. 42, pp. 373–381, 1994.
- [20] R. Coccioli, G. Pelosi and S. Selleri, "Optimization of bends in rectangular waveguide by a finite-element genetic-algorithm procedure," *Microw. Opt. Techn. Let.*, vol. 16, pp. 287–290, 1997.
- [21] L. A. Piegl, W. Tiller, *The NURBS Book*, Springer-Verlag, 1997.
- [22] HFSS ver. 11, Ansoft Corporation, Pittsburgh, PA, 2007.
- [23] R. F. Harrington, *Time-Harmonic Electromagnetic Fields*, Wiley, 2001.

Hybrid Higher Order FEM-MoM Analysis of Continuously Inhomogeneous Electromagnetic Scatterers

Milan M. Ilić, *Member, IEEE*, Slobodan V. Savić, Andjelija Ž. Ilić, *Member, IEEE*, and Branislav M. Notaroš, *Senior Member, IEEE*

Abstract — A novel higher order entire-domain finite element technique is presented for accurate and efficient full-wave three-dimensional analysis of electromagnetic structures with continuously inhomogeneous material regions, using large (up to about two wavelengths on a side) generalized curved hierarchical curl-conforming hexahedral vector finite elements (of arbitrary geometrical and field-approximation orders) that allow continuous change of medium parameters throughout their volumes. The results demonstrate considerable reductions in both number of unknowns and computation time of the entire-domain FEM modeling of continuously inhomogeneous materials over piecewise homogeneous models.

Keywords — Computer-aided analysis, electromagnetic analysis, electromagnetic scattering, finite element method, higher order elements, inhomogeneous media, method of moments.

I. INTRODUCTION

IN electromagnetics (EM), the finite element method (FEM) in its various forms and implementations [1]-[4] has been effectively used for quite some time in full-wave three-dimensional (3D) computations based on discretizing partial differential equations. A tremendous amount of effort has been invested in the research of the FEM technique in the past 4 decades, making FEM methodologies and techniques extremely powerful and universal numerical tools for solving a broad range of both closed-region (e.g., waveguide and cavity) and open-region (e.g., antenna and scattering) problems. In the case of open-region problems, hybrid finite element-boundary integral (FE-BI) technique is used for the exact truncation of the unbounded spatial domain [5]-[6].

This work was supported by the Serbian Ministry of Science and Technological Development under grant TR-32005 and by the National Science Foundation under grants ECCS-0647380 and ECCS-0650719.

Milan M. Ilić is with the School of Electrical Engineering, University of Belgrade, Bulevar kralja Aleksandra 73, 11120 Belgrade, Serbia; (phone: 381-11-3370101; e-mail: milanilic@etf.rs).

Slobodan V. Savić is with the School of Electrical Engineering, University of Belgrade, Bulevar kralja Aleksandra 73, 11120 Belgrade, Serbia; (phone: 381-11-3218351; e-mail: ssavic@etf.rs).

Andjelija Ž. Ilić is with the Vinča Institute of Nuclear Sciences, Laboratory of Physics 010, P.O. Box 522, 11001 Belgrade, Serbia; (e-mail: andjelijailic@ieee.org).

Branislav M. Notaroš is with the ECE Department, Colorado State University, 1373 Campus Delivery, Fort Collins, CO 80523-1373, USA; (e-mail: notaros@colostate.edu).

For modeling and analyzing structures that contain inhomogeneous and complex electromagnetic materials, FEM technique is very efficient and well established as a method of choice. In almost every FEM technique, within a really abundant and impressive body of work in the field, the theory is developed and FEM equations are derived taking advantage of the inherent ability of FEM to directly treat continuously inhomogeneous materials (complex permittivity and permeability of the media can be arbitrary functions, or tensors, of spatial coordinates, e.g., $\epsilon(\mathbf{r})$ and $\mu(\mathbf{r})$, with \mathbf{r} standing for the position vector of a point in the adopted coordinate system). However, it appears that there are practically no papers on this subject, presenting a technique or computer code that actually implements $\epsilon(\mathbf{r})$ and $\mu(\mathbf{r})$ as continuous space function within a finite element (FE), thus enabling direct computation on finite elements that include an arbitrary (continuously) inhomogeneous material. Instead, FEM computations are carried out on a piecewise homogeneous approximate model of the inhomogeneous structure, with $\epsilon(\mathbf{r})$ and $\mu(\mathbf{r})$ replaced by the appropriate piecewise constant approximations. On the other hand, even from the geometrical modeling point of view, it is much simpler and faster to generate a model of the structure with a single, or few, large continuously inhomogeneous elements, than a mesh of a graded layered structure. In most of the practical situations, such an approach can dramatically reduce the time needed for an electromagnetic modeler to set up the problem and initially model the geometry, before any mesher [7] can be used to preprocess the data for analysis.

Numerical modeling employing continuously inhomogeneous finite elements is expected to find practical applications in analysis of a broad range of devices, systems, and phenomena in electromagnetics, including electromagnetic interaction with biological tissues and materials, absorbing coatings for reduction of radar cross sections of targets, scattering and diffraction from inhomogeneous dielectric lenses used for lens antennas and related structures.

For fully exploiting the modeling flexibility of continuously inhomogeneous finite elements, these elements should be electrically large, which implies use of the higher order field expansions within the elements, as

shown in our preliminary results in [8]. Since the fields in the low order FEM technique are approximated by the low-order basis functions, the elements must be electrically very small (on the order of a tenth of the wavelength in each dimension). Subdivision of the structure using such elements results in a discretization of the permittivity and permeability profiles as well, so that elements can be treated as homogeneous, i.e. their treatment as inhomogeneous would practically have no effect on the results. Within the higher order computational approach [9], on the other hand, higher order basis functions enable the use of electrically large geometrical elements (e.g., on the order of a wavelength in each dimension). We refer to the direct FEM computation on such elements as the entire-domain or large-domain analysis. Note that, in general, higher order FEM technique [10]-[14] can greatly reduce the number of unknowns for a given (homogeneous or inhomogeneous) problem and enhance the accuracy and efficiency of the analysis in comparison to the low-order solutions.

II. THEORY AND NUMERICAL IMPLEMENTATION

Consider an electromagnetic structure that contains some continuously inhomogeneous material regions, as shown in Fig. 1. In our analysis method, the computation domain is first tessellated using higher order geometrical elements in the form of Lagrange-type generalized curved parametric hexahedra of arbitrary geometrical orders $K_u, K_v,$ and K_w ($K_u, K_v, K_w \geq 1$), analytically described as [10]:

$$\mathbf{r}(u, v, w) = \sum_{i=0}^{K_u} \sum_{j=0}^{K_v} \sum_{k=0}^{K_w} \mathbf{r}_{ijk} L_i^{K_u}(u) L_j^{K_v}(v) L_k^{K_w}(w), \quad (1)$$

$$L_i^{K_u}(u) = \prod_{l=0, l \neq i}^{K_u} \frac{u - u_l}{u_i - u_l}, \quad -1 \leq u, v, w \leq 1,$$

where $\mathbf{r}_{ijk} = \mathbf{r}(u_i, v_j, w_k)$ are the position vectors of the interpolation nodes, $L_i^{K_u}(u)$ represent Lagrange interpolation polynomials, and similar for $L_j^{K_v}(v)$ and $L_k^{K_w}(w)$. Equation (1) defines a mapping from a cubical parent domain to the generalized hexahedron, as illustrated in Fig. 2.

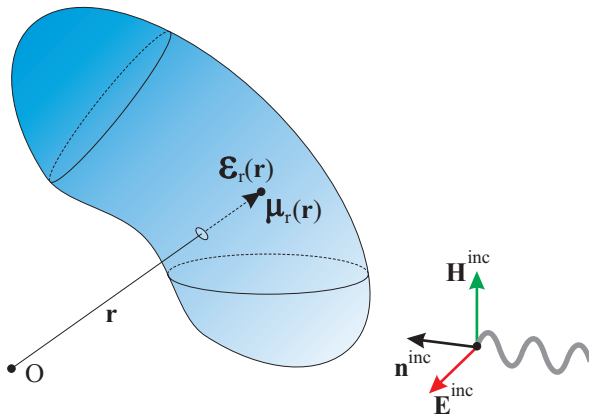


Fig. 1. Electromagnetic structure with continuously inhomogeneous material.

The electric field in the element, $\mathbf{E}(u, v, w)$, is approximated by means of curl-conforming hierarchical polynomial vector basis functions given in [10]; let us denote the functions by $\mathbf{f}(u, v, w)$, and the respective arbitrary field-approximation orders of the polynomial by $N_u, N_v,$ and N_w ($N_u, N_v, N_w \geq 1$). The higher order hierarchical basis functions with improved orthogonality and conditioning properties constructed from Legendre polynomials [12] may also be implemented.

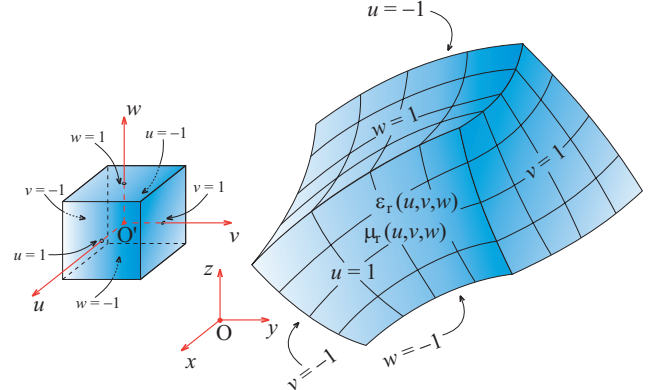


Fig. 2. Generalized curved parametric hexahedron defined by (1), with the continuous variation of medium parameters given by (2); cubical parent domain is also shown.

Continuous variation of medium parameters in the computation model can be implemented in different ways. We choose to take full advantage of the already developed Lagrange interpolating scheme for defining element spatial coordinates in (1), which can be conveniently reused to govern the change of both the complex relative permittivity and permeability, ϵ_r and μ_r , within the element shown in Fig. 2, as follows:

$$\epsilon_r(u, v, w) = \sum_{i=0}^{K_u} \sum_{j=0}^{K_v} \sum_{k=0}^{K_w} \epsilon_{r,ijk} L_i^{K_u}(u) L_j^{K_v}(v) L_k^{K_w}(w), \quad (2)$$

$$-1 \leq u, v, w \leq 1,$$

where $\epsilon_{r,ijk} = \epsilon_r(u_i, v_j, w_k)$ are the relative permittivity values at the point defined by position vectors of spatial interpolation nodes, \mathbf{r}_{ijk} , and similarly for μ_r . With such representation of material properties, we then solve for the unknown field coefficients by substituting the field expansion $\mathbf{E}(u, v, w)$ in the curl-curl electric-field vector wave equation [10], reading:

$$\nabla \times \mu_r^{-1}(u, v, w) \nabla \times \mathbf{E}(u, v, w) - k_0^2 \epsilon_r(u, v, w) \mathbf{E}(u, v, w) = 0, \quad (3)$$

where $k_0 = \omega \sqrt{\epsilon_0 \mu_0}$ stands for the free-space wave number. A standard Galerkin weak-form discretization of (3) yields:

$$\begin{aligned}
 & \int_V \mu_r^{-1}(u, v, w) [\nabla \times \mathbf{f}_t(u, v, w)] \cdot [\nabla \times \mathbf{E}(u, v, w)] dV \\
 & - k_0^2 \int_V \epsilon_r(u, v, w) \mathbf{f}_t(u, v, w) \cdot \mathbf{E}(u, v, w) dV \\
 & = - \oint_S \mu_r^{-1}(u, v, w) \mathbf{f}_t(u, v, w) \cdot \mathbf{n} \times [\nabla \times \mathbf{E}(u, v, w)] dS,
 \end{aligned} \quad (4)$$

where V is the volume of the element, bounded by the surface S , \mathbf{n} is the outward unit normal on S , and \mathbf{f}_t are the testing functions (the same as the basis functions). Once the field coefficients are found, all quantities of interest for the analysis are obtained in a straightforward manner.

III. RESULTS AND DISCUSSION

As an example of entire-domain FEM analysis of an open-region continuously inhomogeneous structure, consider a lossless cubical dielectric ($\mu_r = 1$) scatterer, of the side length $2a$, and a linear variation of ϵ_r from $\epsilon_r = 1$ at the surface to $\epsilon_r = 6$ at the center of the cube, as shown in Fig. 3. The scatterer is situated in free space and illuminated by a uniform plane wave incident normal to one face of the scatterer, as shown. The FEM domain is truncated at the cube faces by means of unknown electric and magnetic surface currents of densities \mathbf{J}_S and \mathbf{J}_{mS} , respectively, that are evaluated by the MoM/SIE, giving rise to a hybrid higher order FEM-MoM solution [6].

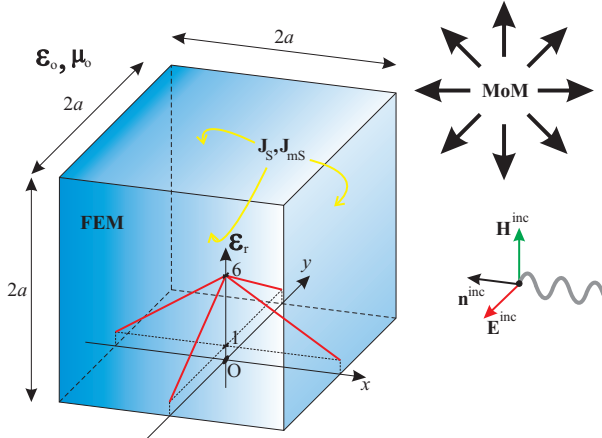


Fig. 3. FEM-MoM analysis of a lossless continuously inhomogeneous cubical dielectric scatterer. Single-element FEM domain with linear variation of permittivity.

To represent this permittivity variation using the expansions in (2), the cube is modeled by 7 trilinear hexahedral finite elements of the first geometrical order.

Namely, one small cube-like hexahedron, $\frac{a}{10}$ in length, is situated at the cube center and surrounded by 6 “cushion”-like hexahedra between the central cube and the scatterer surface, onto which 6 bilinear quadrilateral MoM patches are attached. The obtained model of the scatterer is shown in Fig. 4. The field/current approximation orders are 5 in all directions for all FE “cushions” and 4 in all directions for the central finite element and all MoM patches, resulting in 2560 FEM and 354 MoM unknowns, and a total of 339 s of simulation time for 35 frequencies.

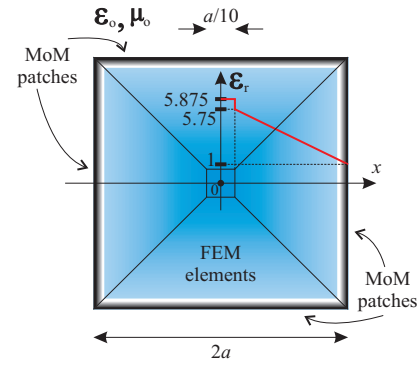


Fig. 4. Model of a lossless, continuously inhomogeneous cubical dielectric scatterer consisting of 7 finite elements and 6 quadrilateral MoM patches.

To both validate the continuously inhomogeneous FEM-MoM model of the scatterer and evaluate its efficiency against the piecewise homogeneous approximate model, the scattering results of the higher order FEM-MoM analysis using large finite elements with continuously changing ϵ_r are compared with the solution obtained by higher order FEM-MoM simulations of piecewise homogeneous approximate model of the structure in Fig. 4. Each of the 6 “cushions” of the continuous model are replaced, respectively by, $N_1 = 2, 3, 4,$ and 7 homogeneous thin “cushions” (plate-like layers), approximating the continuously inhomogeneous profile, which is illustrated in Fig. 5 for $N_1 = 4$. Each plate-like layer in layered models is represented by 6 finite elements of the first geometrical order. Field-approximation orders in these elements are 2 in the radial direction and 5 in transversal directions.

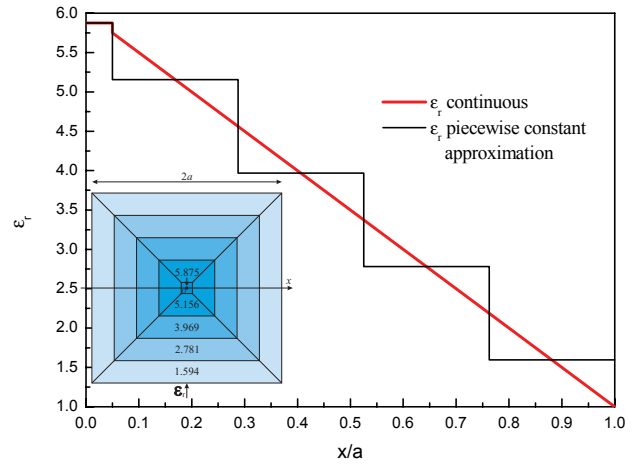


Fig. 5. Piecewise homogeneous approximate graded model ($N_1 = 4$) of the structure in Fig. 3, and piecewise constant approximation of relative permittivity profiles.

Shown in Fig. 6 is the normalized (to λ_0^2) monostatic radar cross section (RCS) of the cube (as a function of a/λ_0), λ_0 being the free space wavelength. We observe a very good convergence of the results obtained by the layered FEM-MoM technique to those for the continuous

FEM-MoM model, as N_1 increases, as well as an excellent agreement between the 7-layer and continuous FEM-MoM solution. Theoretically, only an infinite number of layers would give the exact solution to the problem in Fig. 3.

As an additional verification of the analysis, the higher order MoM technique based on the surface integral equation (SIE), i.e. MoM/SIE technique [14], is used to obtain a reference solution for the 7-layer model. An excellent agreement of the higher order MoM/SIE and the corresponding FEM-MoM results, for the 7-layer model, is observed.

The additional data shown in the legend of Fig. 6 gives a comparison of the number of unknowns used and the computation time for all 6 models. We conclude from the data shown that the continuous material model is substantially more efficient than the layered analysis. It is 34.16 times faster than the most accurate layered solution (for $N_1=7$), and the total number of unknowns is reduced 5.6 times.

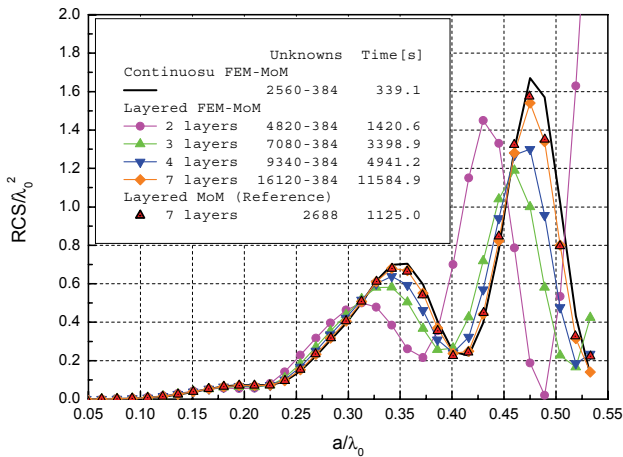


Fig. 6. Normalized monostatic radar cross section of the cubical scatterer in Fig. 3 (λ_0 is the free-space wavelength). Results using the continuous FEM-MoM, four different layered FEM-MoM models, and reference MoM/SIE model are compared.

All numerical results are obtained using HP EliteBook 8440p notebook computer with Intel i5-540 CPU running at 2.53 GHz and with 2 GB of RAM under Microsoft Windows 7 operating system.

IV. CONCLUSION

A novel higher order entire domain hybrid FEM-MoM technique for accurate and efficient full-wave 3D EM analysis using large (up to two wavelengths on a side) finite elements that allow continuous change of medium parameters throughout their volumes, has been presented. Lagrange-type generalized curved parametric hexahedra of arbitrary geometrical orders with the curl-conforming hierarchical polynomial vector basis functions of arbitrary

field-approximation orders and Lagrange interpolation scheme for variations of medium parameters have been used.

The validity, accuracy, and efficiency of the new technique have been demonstrated through an example of EM scatterer with linearly varying permittivity of the dielectric. The example has shown that effective higher order FEM hexahedral meshes, constructed from a very small number of large finite elements with p -refined field distributions of high approximation orders, is the method of choice for EM modeling of structures including material inhomogeneities. High efficiency, and considerable reductions in both number of unknowns and computation time of the entire-domain FEM modeling of continuously inhomogeneous material, in comparison with the piecewise homogeneous (layered) models, have been demonstrated.

REFERENCES

- [1] P. P. Silvester and R. L. Ferrari, *Finite Elements for Electrical Engineers*, 3rd ed., Cambridge University Press, 1996.
- [2] J.-M. Jin, *The Finite Element Method in Electromagnetics*, 2nd ed., John Wiley & Sons, New York, 2002.
- [3] J. L. Volakis, A. Chatterjee, and L. C. Kempel, *Finite Element Method for Electromagnetics*, 1st ed., IEEE Press, New York, 1998.
- [4] J. L. Volakis, K. Sertel, and B. C. Usner, *Frequency Domain Hybrid Finite Element Methods in Electromagnetics*, 1st ed., Morgan & Claypool Publishers, 2006.
- [5] J.-M. Jin, J. L. Volakis, and J. D. Collins, "A finite-element-boundary-integral method for scattering and radiation by two- and three-dimensional structures", *IEEE Antennas and Propagation Magazine*, Vol. 33, No 3, pp. 22-32, June 1991.
- [6] M. M. Ilić, M. Djordjević, A. Z. Ilić, and B. M. Notaroš, "Higher Order Hybrid FEM-MoM Technique for Analysis of Antennas and Scatterers", *IEEE Transactions on Antennas and Propagation*, Vol. 57, No. 5, pp. 1452-1460, May 2009.
- [7] S. V. Savić, M. M. Ilić, B. M. Kolundžija, and B. M. Notaroš, "Efficient Modeling of Complex Electromagnetic Structures Based on the Novel Algorithm for Spatial Segmentation Using Hexahedral Finite Elements", *Telfor Journal*, Vol. 2, No. 2, pp. 98-101, 2010.
- [8] M. M. Ilić, A. Z. Ilić, and B. M. Notaroš, "Continuously Inhomogeneous Higher Order Finite Elements for 3-D Electromagnetic Analysis", *IEEE Transactions on Antennas and Propagation*, Vol. 57, No. 9, pp. 2798-2803, September 2009.
- [9] B. M. Notaroš, "Higher Order Frequency-Domain Computational Electromagnetics", Special Issue on Large and Multiscale Computational Electromagnetics, *IEEE Transactions on Antennas and Propagation*, Vol. 56, No. 8, pp. 2251-2276, August 2008.
- [10] M. M. Ilić and B. M. Notaroš, "Higher order hierarchical curved hexahedral vector finite elements for electromagnetic modeling", *IEEE Transactions on Microwave Theory and Techniques*, Vol. 51, No. 3, pp. 1026-1033, March 2003.
- [11] M. M. Ilić, A. Ž. Ilić, and B. M. Notaroš, "Higher order large-domain FEM modeling of 3-D multiport waveguide structures with arbitrary discontinuities", *IEEE Transactions on Microwave Theory and Techniques*, Vol. 52, No. 6, pp. 1608-1614, June 2004.
- [12] M. M. Ilić and B. M. Notaroš, "Higher Order Large-Domain Hierarchical FEM Technique for Electromagnetic Modeling Using Legendre Basis Functions on Generalized Hexahedra", *Electromagnetics*, Vol. 26, No. 7, pp. 517-529, October 2006.
- [13] A. Ž. Ilić, S. V. Savić, M. M. Ilić, and B. M. Notaroš, "Analysis of Electromagnetic Scatterers Using Hybrid Higher Order FEM-MoM Technique", *Telfor Journal*, Vol. 1, No. 2, pp. 53-56, 2009.
- [14] B. M. Kolundžija, J. S. Ognjanović, and T. K. Sarkar, *WIPL-D Microwave: Circuits and 3D EM Simulation for RF & Microwave Applications*, WIPL-D & Artech House, February 2005.

Comparison of Approximate and Full-Wave Electromagnetic Numerical Modeling of Microstrip Matching Networks

B. Bukvić¹

A. Ilić²

M. M. Ilić^{1,3}

Abstract – We consider several planar microstrip circuit elements, often appearing as parts of microwave matching networks, as well as discrete chip components with associated pads. We analyze all considered elements and components using a circuit-based solver and full-wave electromagnetic solvers and compare the analysis results with measurements on manufactured prototypes, discussing the obtained differences and giving specific recipes for good modeling practices using different methods.

1 INTRODUCTION

The finite element method (FEM) and the method of moments (MoM) are widely recognized as the most flexible and versatile numerical methods for computational analysis of electromagnetic (EM) problems in the frequency domain. Both methods enable rigorous full-wave analysis of wide variety of radiating and scattering EM problems, including accurate analysis of microwave circuits, i.e., printed circuit boards (PCBs). On the other hand, in analysis and design of microwave circuits, approximate closed-form models of circuit elements (e.g., microstrip lines, discontinuities, bends, and interconnects) are widely used in the circuit-based simulators. This enables extremely rapid analysis of complex circuits because the closed-form models are represented in easily calculable form. The approximate planar microstrip-element models are generally based on the assumption of transversal electromagnetic (TEM) mode of propagation, or more precisely quasi-TEM mode, and they can rather accurately (with certain limitations) model many important quantities and effects, such as impedances, attenuation, dispersion, discontinuity, and even coupling effects [1]. Recently, in an effort to improve the closed-form models, novel models based on full-wave EM solutions of parameterized discontinuities have been developed [2].

However, the closed-form models of microstrip circuit elements have strict limitations because the underlying approximations are valid under certain assumptions (e.g., regarding the relative dimensions of the microstrip line width with respect to the substrate thickness, or conductor thickness, etc.) and they do not model all physical effects (e.g., radiation). In addition, circuit-based modeling is inherently approximate. Even with the full-wave EM simulation-based models, it essentially represents a domain decomposition method, where the elements are mutually connected at the ports (often not strictly defined) through which their circuit parameters (e.g.,

S-parameters) are coupled in a global matrix equation. Hence, many coupling and proximity effects are not accurately modeled.

On the other hand, modern full-wave numerical FEM and MoM solvers are nowadays capable of simulating linear parts of complete circuits within minutes, extremely accurately, taking into account all macroscopic physical EM phenomena, while running on cheap personal computers (PCs). In the analysis, ports are created for connection of lumped devices, i.e., transistors, diodes, and other discrete (chip) components, and the structure is solved for its multiport parameters in the desired frequency band. Lumped devices of the hybrid microwave circuit are then easily added within the circuit simulator.

However, although the described computational modeling procedures have been around for quite some time, researchers and designers still often wonder about the origins of discrepancies of solutions and what can be done to improve both circuit-based and full-wave modeling practices, which can additionally differ depending on the employed numerical method. Some works like [3] partially address this problem, but there appears to be no works that conduct a multitude of case studies with explanations and recipes for optimal circuit-based and full-wave modeling of both strictly planar microstrip elements and discrete chip components (including linear devices such as resistors, capacitors, and inductors) with associated pads. Instead, the discrepancies between circuit simulations and measurements are often contributed solely to inaccuracies of models of discrete (nonlinear) components (e.g., transistors), provided by manufacturers, which is not always the case.

In this work we consider several benchmark planar microstrip circuit elements often appearing as parts of microwave matching networks, or biasing networks attached to them. The examples include two versions of an open-ended stub L-tuner and a discrete surface mount device (SMD) component, i.e., a chip capacitor, soldered on associated pads and integrated with planar microstrip line, as an example of a typical hybrid microwave circuit. We analyze all considered benchmark examples using a circuit-based solver and a full-wave solver (FEM, MoM or both) and compare the analysis results with measurements on manufactured prototypes, discussing the obtained differences and giving specific recipes for good modeling practices using different methods.

¹ School of Electrical Engineering, University of Belgrade, Bulevar Kralja Aleksandra 73, 11120 Belgrade, Serbia, e-mail: bb115021p@student.etf.rs, milanilic@etf.rs, tel.: +381 11 3218329, fax: +381 11 3248681.

² Institute of Physics, University of Belgrade, Pregrevica 118, 11080 Zemun-Belgrade, Serbia, e-mail: angie@ipb.ac.rs.

³ Colorado State University, ECE Department, Fort Collins, CO, USA.

2 CIRCUIT MODELS, FULL-WAVE ELECTROMAGNETIC MODELS AND PROTOTYPES

We consider microwave circuits based on microstrip technology on a cheap FR-4 substrate of dielectric thickness $h = 0.8$ mm, relative permittivity $\epsilon_r = 4.5$, loss tangent $\tan\delta = 0.02$, and metallization thickness $t = 35$ μm .

For all examples we show, in Figs. 1–3, the circuit layout, the equivalent circuit model (where the width W and length L of microstrip lines are shown in mm), the geometry of the model prepared for the (FEM) full-wave simulation, and comparison of simulated and measured results.

The circuits are initially modeled using Microwave Office (MWO) circuit solver [4], from which all solutions marked as “Circuit” in Section 3 are generated. All microstrip lines used in the circuit models are based on the closed-form models except for the step transitions and open ended lines with end effect, which are modeled using EM-based models. The EM-based models facilitate better estimation of performance of discontinuities. Note, however, that employing closed-form models throughout the circuit (where possible), instead of the EM-based models, yields very similar results in the given examples. (Junctions can also be modeled using EM-based models with similar results.) We deliberately consider only the circuits without lines that are coupled due to the proximity effects (which are not taken into account in the circuit-based models).

Full-wave modeling is carried out using small-domain meshes and first-order basis functions, since this setup facilitates quick convergence in the given examples. Large-domain MoM modeling is also carried out applying general modeling rules laid out in [5] with appropriate edging and imaging techniques [6], [7], but these results are not shown here for brevity. In the FEM models, the main (in and out) ports are modeled as wave-ports [8], whereas in the MoM models, they are modeled as lumped ports (delta-function generators) [9]. All internal ports (e.g., where SMD components are connected) are modeled as lumped ports in both methods.

Standard PCB-mount SMA connectors are soldered onto manufactured prototypes, photographs of which are not shown for brevity, to facilitate measurements. The measurements are carried out using the Agilent N5227A vector network analyzer, calibrated employing the short-open-load-through (SOLT) standards. The measured results are then de-embedded in order to neutralize the influence of the SMA connectors.

We consider frequencies up to 5 GHz in all examples. Although the dielectric parameters of FR-4, ϵ_r and $\tan\delta$, vary considerably in the

considered frequency range [10], in this ongoing research we use constant dielectric parameters, given at the beginning of the section, in both circuit simulations and full-wave simulations. Of course, more precise parameters can be used if higher accuracy of the simulations is required.

3 RESULTS AND CONCLUSIONS

As the first two examples, consider two versions of the microstrip single-stub (symmetrized) L-tuner. Version 1 of the tuner, shown in Fig. 1(a)–(c), comprises narrow microstrip lines which comply with the restrictions (by a great margin) associated with the closed-form microstrip line model validity, i.e., $0.05 \leq W/h \leq 20$. On the other hand, version 2 of the tuner, shown in Fig. 2(a)–(c), comprises wide microstrip lines which do not comply with the defined restrictions (or the restrictions for the EM-based discontinuity models, which are stricter). Note from Fig. 2(b) that $W/h = 25$ for the widest line section in the model, which is above the given restriction.

From Fig. 1(d) we can conclude that all simulation results compare very well with measurements in this example, with full-wave simulations yielding marginally more accurate solutions than the circuit-based simulations. This was expected considering that the circuit in this example is very simple and the models of the circuit elements comply with the closed-form model restrictions.

On the other hand, when this is not the case, we see from Fig. 2(d) that the circuit-based model yields rather inaccurate predictions, whereas the full-wave simulations compare fairly well with measurements (especially at lower frequencies where the measured results are less dependent on the de-embedding parameters). In both examples, FEM and MoM full-wave simulation results are practically identical.

As the third example, consider an SMD 0805 (chip) capacitor mounted on associated pads in the middle of a 50Ω microstrip line, as shown in Fig. 3(a)–(c).

Fig. 3(d) shows comparison of the results obtained by simulations and measurements. Two circuit-based numerical models are considered: a simplest closed-form model, from Fig. 3(b), where the capacitor is modeled as an ideal lumped (zero-length) element, and a circuit where the capacitor from Fig. 3(b) (with associated $1 \text{ mm} \times 1.3 \text{ mm}$ pads) is modeled as a two-port network, with its S -parameters de-embedded from measurements (and parametrized). The FEM full-wave numerical model comprises the planar geometry from Fig. 3(c), simulated as a four port linear network, S -parameters of which are imported into the circuit simulator where the chip capacitor closed-form model (parallel R and C , in series with L) is attached between the two inner (lumped) ports.

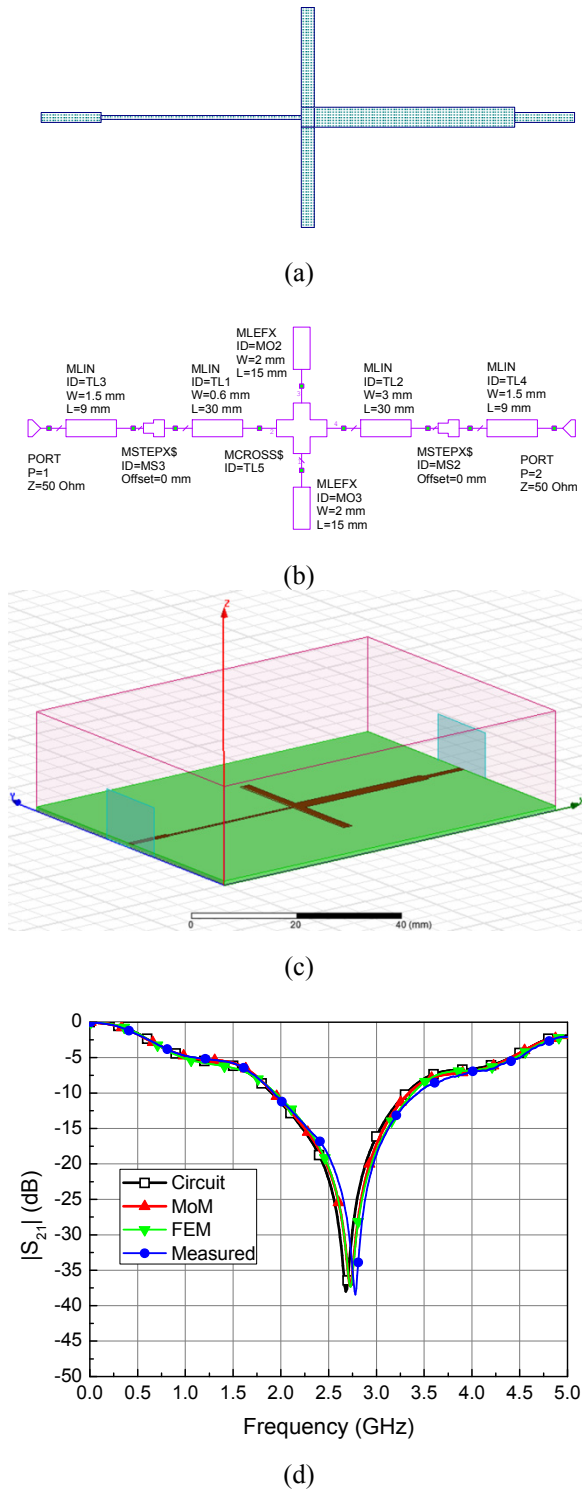


Figure 1: Microstrip single-stub L-tuner (version 1): (a) layout, (b) circuit model, (c) full-wave model, and (d) comparison of simulated and measured results.

The quality factor and the series resonant frequency of the chip capacitor were set to $Q = 80$ (at 100 MHz) and $f_r = 1800$ MHz, respectively. Noting that the greatest source of discrepancies in the results in

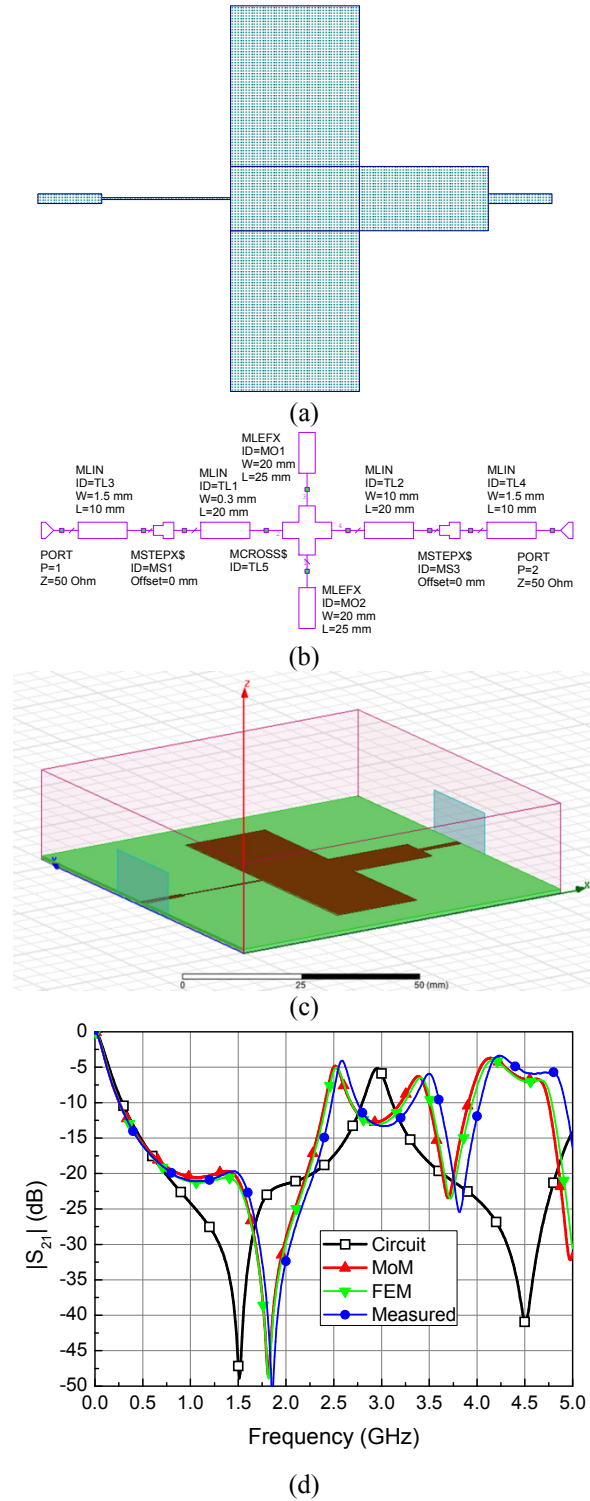


Figure 2: Microstrip single-stub L-tuner (version 2): (a) layout, (b) circuit model, (c) full-wave model, and (d) comparison of simulated and measured results.

this example emanates from the capacitor's series resonance (not modeled by the ideal capacitor, which makes the simple closed-form circuit model highly inaccurate), we can conclude from Fig. 3(d) that the

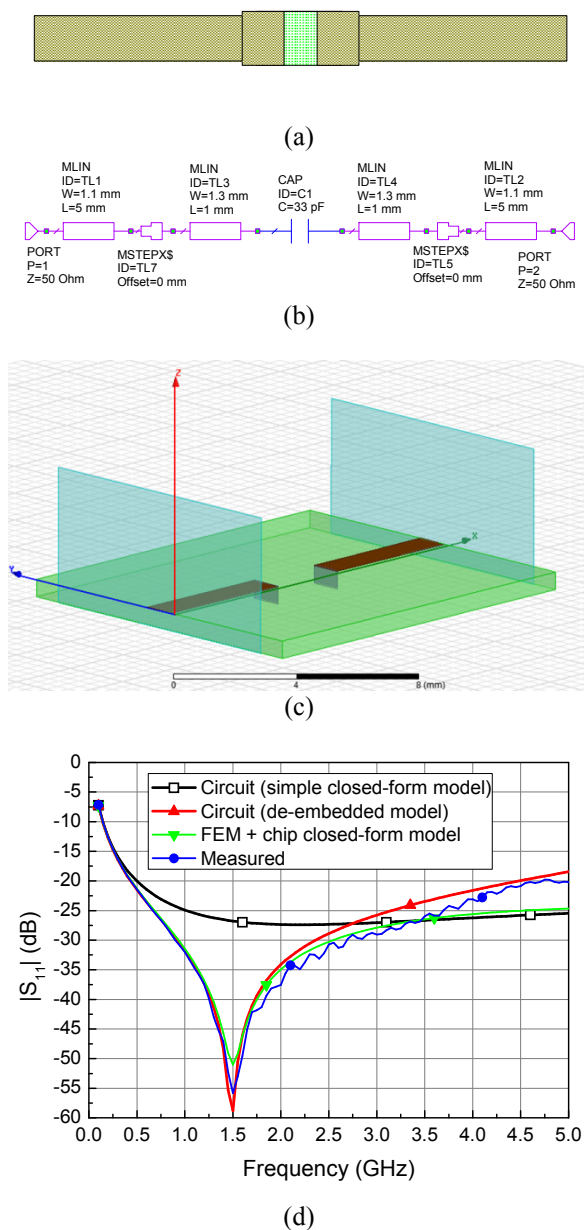


Figure 3: SMD capacitor ($C = 33$ pF): (a) layout, (b) circuit model, (c) full-wave model, and (d) comparison of simulated and measured results.

full-wave FEM planar circuit model, in conjunction with the chip capacitor closed-form model, yields the most accurate results (considering frequencies up to 3.5 GHz where the measurements are less dependent on the de-embedding parameters).

3 CONCLUSIONS

Comparisons of measurements with the results obtained by (i) combined full-wave and circuit-based analysis and (ii) fully circuit-based analysis, reveal discrepancies that range from almost nonexistent to

moderate, and sometimes extreme. Hence, the combined full-wave and circuit-based analysis is a must in the final stages of the microwave circuit design, although initial designs and optimizations are still faster and more comfortably done completely in the circuit-based environment. In addition, using adequate good quality models of discrete (chip) devices and components is of equal (high) importance.

Our future work will include more examples of planar circuits, discrete components, and complex hybrid circuits (involving nonlinear devices).

Acknowledgments

This work was supported by the Serbian Ministry of Education, Science, and Technological Development under Grant TR-32005.

References

- [1] E. Hammerstad and O. Jensen, "Accurate Models for Microstrip Computer-Aided Design," *IEEE MTT-S International Microwave Symposium*, Washington, DC, USA, 28–30 May, 1980, pp.407–409.
- [2] X-models from AWR Corporation; available: <http://www.awrcorp.com>.
- [3] R. Kipp et al., "Simulation of high-frequency integrated circuits incorporating full-wave analysis of microstrip discontinuities," *IEEE Transactions on Microwave Theory and Techniques*, vol. 41, no. 5, 1993, pp.848–854.
- [4] NI AWR Design Environment: Microwave Office; available: <http://www.awrcorp.com>.
- [5] E. M. Klopf et al., "Optimal modeling parameters for higher order MoM-SIE and FEM-MoM electromagnetic simulations," *IEEE Transactions on Antennas and Propagation*, vol. 60, no. 6, June 2012, pp.2790–2801.
- [6] B. Kolundzija et al., "Efficient method of moment analysis based on imaging and edging," *IEEE Antennas and Propagation Society International Symposium*, 2000, 16–21 July 2000, vol. 4, pp.2298–2301.
- [7] B. Kolundzija and B. Bajic, "Precise modeling of microstrip patch antennas (finite metallization, substrate and ground)," *IEEE Antennas and Propagation Society International Symposium*, 2002, 16–21 June 2002, vol.3, pp.434.
- [8] ANSYS HFSS; available: <http://www.ansys.com>.
- [9] WIPL-D; available: <http://www.wipl-d.com>.
- [10] A. R. Djordjević et al., "Wideband frequency-domain characterization of FR-4 and time-domain causality," *IEEE Transactions on Electromagnetic Compatibility*, vol. 43, no. 4, 2001, pp.662–667.

of freedom. Finally we numerically investigate the solution of the discrete system as well as its stability.

Eike Scholz, Thomas Eibert (*Technical University of Munich, Chair of High-Frequency Engineering, Arcisstraße 21, 80333 München*)

Sebastian Lange (*Wehrwissenschaftliches Institut für Schutztechnologien - ABC-Schutz, Humboldtstraße 100, 29633 Munster*)

A CAD Method Based on Hybrid FEM and Spherical Modes for Direct Domain Decomposition

Pedro Robustillo, Jesús Rubio, Juan Zapata, S. Juan R. Mosig*

Direct Domain Decomposition Methods (DDDM) are well known in waveguide problems since they provide design capabilities. One of the most efficient way of implementing a DDDM consists of expanding the field on the interfaces in terms of waveguide modes. For this purpose, the most usual analytical expansions in terms of coaxial, rectangular or circular waveguide modes have been used (J. Rubio, J. Arroyo, J. Zapata, Analysis of passive microwave circuits by using a hybrid 2-D and 3-D finite-element mode-matching method, *IEEE Trans. Microwave Theory and Tech.*, vol. 47, 1999, pp. 1746–1749). Although DDDM have been widely used for fast waveguide circuits analysis, they have been barely applied to radiation problems.

In this work, a DDDM based on spherical mode expansion for spherical or hemispherical interfaces is proposed. Convergence problems associated to these expansions on concave spherical ports will be discussed in order to choose the most adequate expansion in terms of incident/reflected waves or, alternately, standing waves. It will be also shown how the capabilities of the method can be strongly increased by using properties of rotation and translation of spherical modes.

Finally, the method will be applied to the analysis of on-board spacecraft antennas and lens based antenna systems.

Pedro Robustillo, S. Juan R. Mosig (*Ecole Polytechnique Fédérale de Lausanne, Lausanne, Switzerland, pedro.robustillo@epfl.ch, juan.mosig@epfl.ch*)

Jesús Rubio (*Escuela Politécnica, Universidad de Extremadura, Cceres, Spain, jesusrubio@unex.es*)

Juan Zapata (*ETSIT, Universidad Politécnica de Madrid, Madrid, Spain, jzapata@etc.upm.es*)

Finite Element 1-D Solutions in the Presence of Moving Media

Andjelija Ž. Ilić, Slobodan V. Savić, Milan M. Ilić*

The efficiency and versatility of the finite element method (FEM) in solving problems that involve complex, inhomogeneous and/or anisotropic variation of media parameters, advocates its utilization in both cutting-edge theoretical investigations and advanced real-world applications. Recently, we have proposed and developed a higher-order frequency-domain FEM technique for analysis of one-dimensional (1-D) electromagnetic (EM) problems involving moving media. The proposed method seems to be the first full-wave higher-order method of its kind. It has been validated against the analytical solutions, in two of the cases where these were available, namely, for the single-layer dielectric slab with the homogeneous permittivity and with the linearly varying permittivity (A.Ž. Ilić and M.M. Ilić, “Higher-order frequency-domain FEM analysis of EM scattering off a moving dielectric slab”, *IEEE Antennas and Wireless Propagation Letters*, vol. 12, pp. 890–893).

This paper investigates electromagnetic waves interaction with moving media consisting of multiple layers with continuously inhomogeneous media parameter profiles and nonuniform partial layer velocities. We perform detailed scattering analysis with respect to the layer velocities, plane wave polarization, angle of incidence, and media parameter profiles, considering both low and high velocities of the moving slabs. We discuss establishing of both natural and essential boundary conditions and the Lorentz transformations leading

to the appropriate FEM formulation. Convergence analysis is conducted with respect to the h -refinement and p -refinement. Reasons for the solution convergence breakdown are discussed, where applicable.

Applications of the novel FEM technique include the interaction of external EM fields with plasma jets for space propulsion and the applications to plasma wakefield acceleration (PWFA).

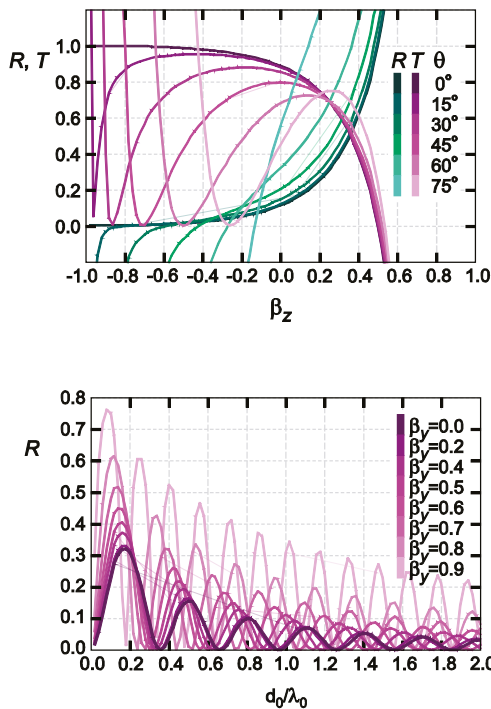


Fig. 1: top: Reflection and transmission coefficients for the homogeneous dielectric half-space ($\epsilon_r = 4$) moving in direction of plane wave propagation, for different angles of incidence θ . bottom: Reflection coefficients for the inhomogeneous slab with parabolic profile of relative permittivity, with maximum permittivity ($\epsilon_r = 4$) in the middle of the slab ($z = d_0/2$), and $\epsilon_r = 1$ at the slab–vacuum interfaces. Slab movement is transversal to direction of propagation of the normally incident plane wave.

Andjelija Ž. Ilić (*Institute of Physics, University of Belgrade, Pregrevica 118, 11080 Zemun-Belgrade, Serbia, andjelijailic@iee.org*)

Slobodan V. Savić (*School of Electrical Engineering, University of Belgrade, Bulevar Kralja Aleksandra 73, 11120 Belgrade, Serbia, milanilic@etf.rs*)

Milan M. Ilić (*Department of Electrical and Computer Engineering, Colorado State University, 1373 Campus Delivery, Fort Collins, CO 80523-1373, USA*)

Nonrigorous Symmetric Second-Order Absorbing Boundary Condition: Accuracy, Convergence and Possible Improvements

Slobodan V. Savić, Andjelija Ž. Ilić, Branislav M. Notaroš, Milan M. Ilić*

Approximate (local) absorbing boundary conditions (ABCs) are important and widely used means for truncation of computational domain in the finite element method (FEM) analysis of open electromagnetic (EM) problems in the frequency domain. Among ABCs, a symmetric second-order ABC appears to be a naturally preferred choice. On the other hand, this choice requires computation of the divergence term on the faces of elements belonging to the absorbing boundary surface (ABS) which is problematic because (i) the normal continuity of the fields is not enforced between adjacent elements in a standard weak-form discretization and (ii) analytical computation of divergence on div-nonconforming vector basis functions is not possible for the generalized curved finite elements. The influence of divergence term and its computation have been previously studied (V. N. Kanellopoulos and J. P. Webb, “The importance of the surface divergence term in the finite element-vector absorbing boundary condition method,” *IEEE Trans. Microw. Theory Techn.*, **43**, 1995, pp. 2168–2170) and an excellent rigorous symmetric FEM implementation has been proposed (M. M. Botha and D. B. Davidson, “Rigorous, auxiliary variable-based implementation of a second-order ABC for the vector FEM,” *IEEE Trans. Antennas Propag.*, **54**, 2006, pp. 3499–3504). However, all thus far reported conclusions pertain to analysis of the second-order ABC in small-domain FEM discretizations (where the sizes of finite element

edges are on the order of $\lambda/10$, λ being the wavelength at the operating frequency in the considered medium). In our recent work (S. V. Savić et al. "Accuracy analysis of the nonrigorous second-order absorbing boundary condition applied to large curved finite elements," *ICEAA 2015* Turin, Italy, 2015, pp. 58–61) we have reported our preliminary results on the analyses of performance of the nonrigorously implemented second-order ABC in coarse large-domain FEM meshes in the vicinity of ABS, which typically resides in free space, away from discontinuities. In this work we report the new results of our ongoing validation of accuracy of the proposed nonrigorous second-order ABC truncation method, with emphasis on the near field computations. Numerical models involve large-domain discretizations with curved finite elements and with truly higher order polynomial field expansions. The study includes both total-field and scattered-field FEM formulations, and possible improvements of truncation accuracy. Near field error comparison for a spherical PEC scatterer, of radius $a = 1$ m with ABS radius $b = 1.5$ m, for the first-order ABC and the proposed second-order ABC in $y = 0$ plane at $f = 300$ MHz are shown in Fig. 1.

Slobodan V. Savić (*School of Electrical Engineering, University of Belgrade, Bulevar Kralja Aleksandra 73, 11120 Belgrade, Serbia, milanilic@etf.rs*)

Andjelija Ž. Ilić (*Institute of Physics, University of Belgrade, Pregrevica 118, 11080 Zemun-Belgrade, Serbia, andjelijailic@iee.org*)

Branislav M. Notaroš, Milan M. Ilić (*Department of Electrical and Computer Engineering, Colorado State University, 1373 Campus Delivery, Fort Collins, CO 80523-1373, USA, notaros@colostate.edu*)

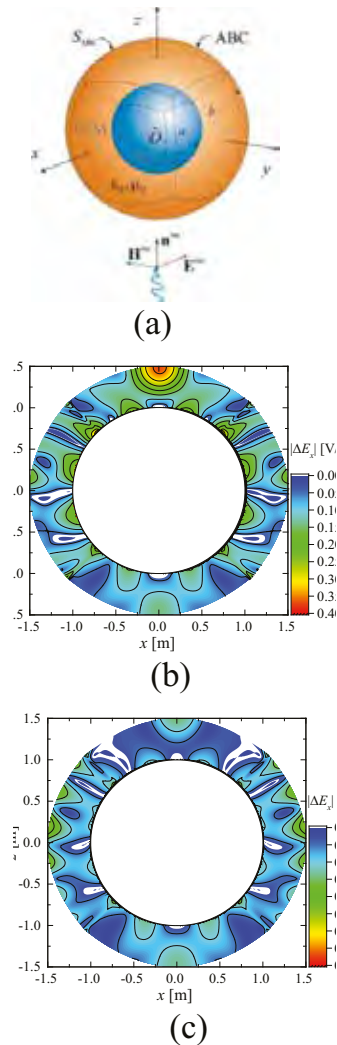


Fig. 1: (a) PEC spherical scatterer and absolute errors of computed electric field obtained by (b) the first-order ABC and (c) the proposed nonrigorous second-order ABC.

EVALUATION OF SMF EXPOSURE FIELD LEVELS AND GRADIENTS OBTAINABLE USING THE 2D MAGNETIC ARRAYS

Andjelija Ž. Ilić¹, Saša Ćirković¹, Jasna L. Ristić-Djurović¹

¹ Institute of Physics, University of Belgrade, Pregrevica 118, 11070 Zemun-Belgrade, Serbia

Abstract. Two-dimensional magnetic arrays have been proven useful as exposure setups for biomedical experiments with static magnetic fields. Different static magnetic field levels as well as vertical field gradients can be attained from these exposure setups by means of varying the geometrical parameters of an array and the type of magnetic material employed. Evaluation of obtainable field and gradient values has been conducted by varying one by one parameter. Several relevant parameters were chosen to represent the effects of input parameter changes on the magnetic flux density above the array. Calculations were conducted using the exact analytical expression.

Key words: non-ionizing radiation exposures, exposure setups, static magnetic field (SMF), two-dimensional magnetic arrays, parameter adjustment

1. INTRODUCTION

Effects of electromagnetic (EM) fields on biological systems can be either beneficial or adversarial. Static magnetic fields (SMF) of low and moderate intensity are shown to have mainly beneficial effects, based on empirical and collected experimental data. Observed therapeutic effects include those related to treating arthritis [1], healing bone fractures [2], and improving microcirculation [3]. Mechanisms of action of SMFs are not yet fully understood.

Experimental magnetic fields are generated using various arrangements of current coils or permanent magnets. Certain types of two-dimensional (2D) magnetic arrays have been successfully employed as exposure setups for SMF generation as well [4], [5]. The type of the array described in [4], with the magnetic axes of individual magnets equally oriented and perpendicular to the array's surface, produces the slowly decreasing magnetic field. In the considered case, individual magnets were distributed across a flat surface periodically at equal distances x_d and y_d in two orthogonal directions. The dominant field component is perpendicular to the surface of the array and an order of magnitude larger than other magnetic field components, provided that individual magnets are not too sparsely placed across the surface. Magnetic flux density variation in planes parallel to the array's surface is significantly smaller than the field decrease with distance from the surface. This allows for the definition of the field gradient perpendicular to the array's surface. This exposure setup therefore produces inhomogeneous magnetic field whose magnetic flux density as well as gradient vary predominantly in the direction perpendicular to the array's surface, with very slight variations in planes parallel to the surface.

This configuration enables studying the effects of both magnetic flux density and its gradient.

Different SMF field levels as well as field gradients can be attained by means of varying the geometrical parameters of an array and the type of magnetic material employed. We investigate the effects to the magnetic flux density and its gradient of varying several parameters, with the aim to define the range of SMF exposure field levels and gradients available for conducting experiments.

2. TWO-DIMENSIONAL MAGNETIC ARRAYS WITH EQUALLY ORIENTED MAGNETIC MOMENTS OF ARRAY ELEMENTS

In the investigation of obtainable exposure field levels and gradients we assume an array of N -by- N identical square cross-section magnets, equally spaced on a flat horizontal surface and kept in place by a non-magnetic substrate. We assume equal and vertical orientation of magnetic moments of all magnets. Were the magnets mounted on a ferromagnetic plate instead, similar analysis would apply, with the height of the magnets doubled due to the image theorem. Vertical

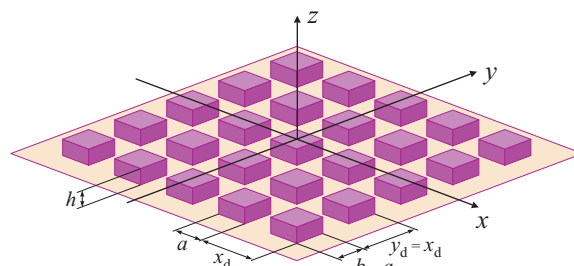


Fig. 1 Two-dimensional magnetic array

axis is denoted as the z -axis and the whole array is assumed to be symmetrical with respect to the x - and y -direction, as shown in Fig. 1. Rows of magnets are parallel to the x -axis, with the magnet centers spaced by x_d . Distance between the adjacent rows is $y_d = x_d$. Magnetic flux density distribution at the array's surface varies periodically from negative to positive B_z , since the magnetic flux lines partially close between the adjacent elements. With the increase in height, z , above the array's surface the majority of the magnetic flux lines add up together to form a resultant magnetic flux density B_z . Above a low-limit height for conducting experiments, $z = z_0$, magnetic flux density is positive everywhere except for the stray field above the array edges. With the further increase in height, magnetic flux density variation in horizontal planes decreases.

We define parameter $z_{1\%}$, as the height above the array above which field variation in the horizontal planes is less than 1%, and $\bar{B}_{z,1\%}$ as the corresponding mean magnetic flux density. Magnetic field vertical gradient decreases with height as well, with magnetic field decrease almost linear at larger heights.

Basic properties of several magnetic materials most commonly used for permanent magnets [6], [7] are listed in Table 1. Material remanent magnetization, B_r , and Curie temperature, T_c , as well as the maximum energy product, $(BH)_m$, must all be accounted for when choosing the right magnets for a particular application. Improved energy product is accompanied by the increased cost of permanent magnets, ranging from about 5 USD per kg for ferrites ($\text{BaFe}_{12}\text{O}_{19}$), to about 50 USD/kg for Alnico, and to about 120 USD/kg for samarium-cobalt and neodymium magnets [8]. High quality neodymium magnets are more expensive, up to about 200 USD/kg. Remanent magnetic flux density corresponds to bulk material, i.e., to a piece of material very long in the direction of magnetization. It is related to the magnetization per unit density, M_r , by the equation $B_r = \mu_0 \cdot \rho \cdot M_r$, where ρ represents the material density. Considering equivalent surface currents resulting from magnetization and real magnet dimensions, actual magnetic flux density is obtained analytically. For the magnetization in the z -direction, four vertical sides of each magnet can be replaced by the current sheets carrying the surface current density $J_{ms} = \rho \cdot M_r$.

Vertical component of the magnetic flux density, $B_z(x, y, z)$, is calculated as the sum of the contributions of all the magnets comprising the array. For a single square cross-section magnet of side length a and height h magnetic flux density is given by:

$$B_{z1}(x_1, y_1, z) = \frac{\mu_0 J_{ms}}{4\pi} \sum_{k=1}^4 \sum_{tp=0}^1 \sum_{tq=0}^1 (-1)^{(tp+tq+1)} \arcsin(p_k^{tp} \cdot q_k^{tq}),$$

$$p_k^{tp} = \frac{((-1)^{\lfloor \frac{k}{2} \rfloor} \lfloor \frac{tp}{2} \rfloor \frac{a-x_1}{2})^{m_2} \cdot ((-1)^{\lfloor \frac{k-1}{2} \rfloor} \lfloor \frac{tp}{2} \rfloor \frac{a-y_1}{2})^{m_1}}{\sqrt{((-1)^{\lfloor \frac{k}{2} \rfloor} \lfloor \frac{tp}{2} \rfloor \frac{a-x_1}{2})^{2m_2} + ((-1)^{\lfloor \frac{k-1}{2} \rfloor} \lfloor \frac{tp}{2} \rfloor \frac{a-y_1}{2})^{2m_1}}},$$

$$q_k^{tq} = \frac{\frac{\text{sgn}((-1)^{m_s} \frac{a-x_1}{2})^{m_1}}{(-\text{sgn}((-1)^{m_s} \frac{a-y_1}{2}))^{m_2}} \cdot (z+(1-tq) \cdot h)}{\sqrt{((-1)^{m_s} \frac{a-x_1}{2})^{2m_1} + ((-1)^{m_s} \frac{a-y_1}{2})^{2m_2} + (z+(1-tq) \cdot h)^2}},$$

$$m_1 = (1+(-1)^{k-1})/2, \quad m_2 = (1+(-1)^k)/2, \quad m_s = (1-\text{sgn}(k-\frac{5}{2}))/2.$$

In the above, x_1 and y_1 are the distances, measured in the direction of x -axis and y -axis, from the magnet center to the field point. Magnet side is denoted by k , numbers 1, 2, 3 and 4 corresponding to the negative x -axis, negative y -axis, positive x -axis and positive y -axis with respect to the magnet center. Square brackets stand for the integer division. Point of current entrance into the current sheet corresponds to $tp = 0$, and the point of current exit to $tp = 1$. Indices $tq = 0$ and $tq = 1$ denote the bottom surface or the top surface of the magnet. Derivation of the above equation, as well as the expressions for x -component and y -component of the magnetic flux density, are given in [4]. It has been shown in [4] that the B_z field component is dominant. Therefore, this evaluation considers only the dominant field component.

Table 1 Basic properties of typical commercial magnetic materials

Material	B_r (T)	$(BH)_m$ (kJ/m ³)	T_c (°C)	M_r (Am ² /kg)	J_{ms} (A/m)
BaFe ₁₂ O ₁₉	0.40	34	450	65.0	318.3
Alnico	1.25	43	860	142.1	994.7
SmCo ₅	0.88	150	720	85.4	700.3
Sm ₂ Co ₁₇	1.08	220	820	102.3	859.4
Nd ₂ Fe ₁₄ B	1.28	300	400	135.8	1018.6

3. RESULTS AND DISCUSSION

The surface current density, J_{ms} , enters the magnetic flux density equation as the multiplicative factor to scale the expression depending exclusively on the geometrical parameters of an array. Therefore, for a fixed given geometry of an array, difference in the achieved field levels for different magnetic materials corresponds to the ratio of remanent magnetization of materials. This is illustrated by the example shown in Fig. 2, where moderately sized magnets ($a = 8$ mm, $h = 5$ mm) were arranged with the gap between every two magnets equal to the magnet length a ($k_d = 1$). Please note that the parameter k_d is introduced as the ratio of the gap size to the magnet size. Corresponding center-to-center magnet spacing equals $x_d = (k_d+1) \cdot a$. Number of individual magnets in a row is taken equal to $N = 15$ in this as well as in the all other examples.

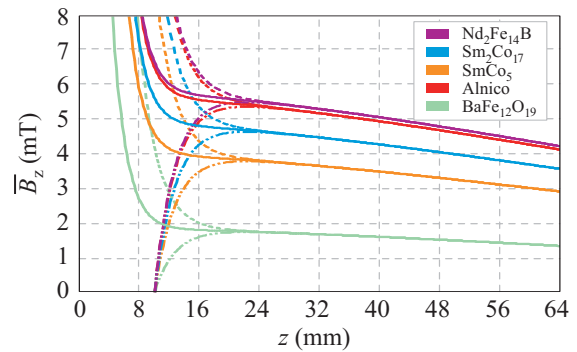


Fig. 2 Magnetic flux density along the magnet axis, along the magnet gap axis, and mean magnetic flux density in horizontal planes above the array, for magnetic materials listed in Table 1 ($a = 8$ mm, $h = 5$ mm, $x_d = 16$ mm)

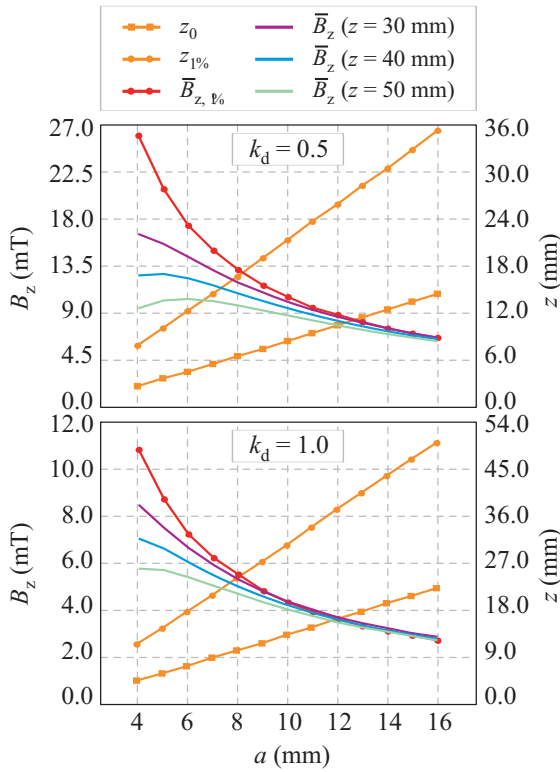


Fig. 3 Influence of the magnet side length, a , on several parameters describing the magnetic field above the array, with the relative spacing between the magnets kept fixed at half the side length (upper plot) and whole side length (lower plot)

In Fig. 2, magnetic flux density at the vertical axes through the magnet centers is represented by the dashed lines, and the one between every four magnets (axes where the x -spacings and y -spacings cross) is shown by the dash-dot-dot lines. Mean magnetic flux density in horizontal planes above the array is well approximated as the average of the two (depicted by the solid lines). Up to some low-limit height magnetic flux density along the magnet gap axis is negative as the flux lines close between the magnets. At the same height, right above the magnets the field is strong, so that all in all next to the surface the field intensity is strong, direction of magnetic flux lines alternates, and field gradients are very pronounced. After the limiting height, z_0 , magnetic flux densities above the magnets and between the magnets start converging to fast reach the height where the field variation everywhere in the horizontal planes lies below 1% of the mean field level in that plane. For the considered example, magnetic flux density is positive everywhere above the plane $z_0 = 10.2$ mm. The 1% threshold is $z_{1\%} = 24.0$ mm, and the B_z value for the strongest neodymium magnets at that height equals $\bar{B}_{z,1\%} = 5.5$ mT. In this particular example, field further decreases almost linearly.

Having in mind average mice height of about 30 mm, experimental volume for *in vivo* experiments can be taken from the height of about 25 mm to 55 mm. For *in vitro* experiments, a range of different field intensities is available by appropriate placement of specimens at different heights above the array. Mean magnetic flux density and its mean gradient in the experimental volume are determined by field averaging between the two limiting horizontal planes.

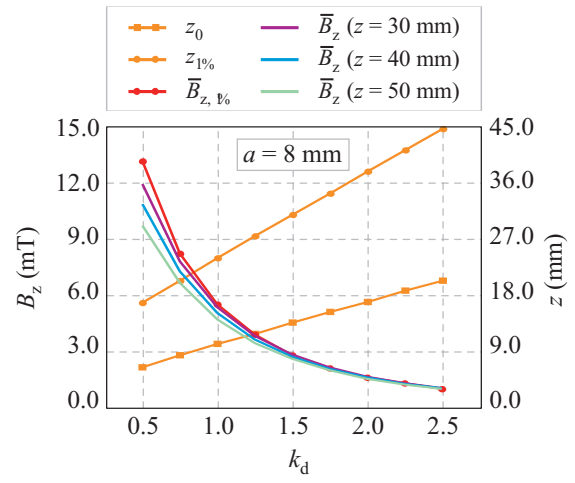


Fig. 4 Influence of the gap size, $k_d \cdot a$, between the two neighboring magnets on the parameters describing the magnetic field above the array

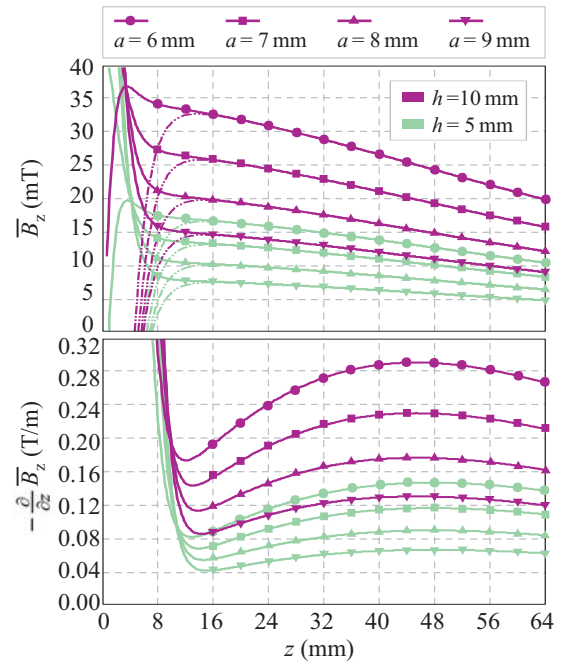


Fig. 5 Mean magnetic flux density and its mean gradient for the fixed center-to-center magnet spacing of $x_d = 12$ mm, for different ratios a versus $k_d \cdot a$, for two magnet heights h

Since the amount of data that could be depicted in Fig. 3 and Fig. 4 is limited, three heights, $z = 30$ mm, $z = 40$ mm, and $z = 50$ mm, were chosen to represent field variations resulting from the changes of input parameters.

Provided that the height of the magnets is relatively small with respect to the size of an array in lateral directions, doubling the magnet height results in twice the magnetic flux density. Height of the magnets can therefore be used to adjust the field levels. If the more homogeneous magnetic flux density is desired for the experiment, one magnetic array is placed below the experimental volume, and the other one on top. Resultant magnetic flux density is fairly homogeneous. Height of the magnets in Fig. 3 and Fig. 4 is fixed at $h = 5$ mm and in Fig. 5 it is compared with $h = 10$ mm.

Data presented in Fig. 3 analyze what are the effects to the field of the changes in magnet side length, a . The ratio gap size versus magnet size is kept fixed at $k_d = 0.5$ (upper plot) and $k_d = 1$ (lower plot). Both the low-limit height z_0 and the 1% threshold $z_{1\%}$ show linear dependence on the lateral size of the magnets. Magnetic field is higher and the two limiting heights, z_0 and $z_{1\%}$, are lower for the smaller magnets. Data shown in Fig. 3, Fig. 4 and Fig. 5 correspond to $\text{Nd}_2\text{Fe}_{14}\text{B}$ magnets. For other types of magnetic materials, data need to be scaled by the relative ratio of remanent magnetizations.

Parameters of interest are presented in Fig. 4 as a function of k_d , with the fixed values of other input data. Size of the magnets is kept at moderate $a = 8$ mm. Similar conclusions are drawn as in the previous example – smaller magnet spacing results in the stronger and higher quality magnetic field (in terms of field homogeneity in horizontal planes).

Figure 5 shows mean magnetic flux density and its mean gradient for the fixed center-to-center magnet spacing of $x_d = 12$ mm, value of x_d resulting in almost constant gradient about 40 to 48 mm height. Magnetic flux density decrease in that case shows the least variation from the linear one inside the experimental volume recommended for *in vivo* experiments (25 to 55 mm height above the array). It is demonstrated that the increase in height of the magnets results in almost the same relative increase in field intensity.

4. CONCLUSIONS

Generic example of the symmetrical two-dimensional magnetic array has been studied using the analytical expressions describing the magnetic flux density above the array. Evaluation of obtainable static magnetic field levels as well as vertical field gradients has been conducted by varying one by one parameter. Input parameters comprised magnet size and spacing (the geometrical parameters) and the type of magnetic material used. The collection of data and results presented can be used for preliminary design of 2D magnetic arrays.

Acknowledgement: This work was supported by the Ministry of Education, Science and Technological Development of Serbia through the project III-45003.

REFERENCES

1. N. Taniguchi, S. Kanai, M. Kawamoto, H. Endo and H. Higashino, "Study on application of static magnetic field for adjuvant arthritis rats", *Evid. Based Complem. Altern. Med.*, vol. 1, pp. 187-191, July 2004.
2. S. Xu, H. Okano, N. Tomita and Y. Ikada, "Recovery effects of a 180 mT static magnetic field on bone mineral density of osteoporotic lumbar vertebrae in ovariectomized rats", *Evid. Based Complem. Altern. Med.*, vol. 2011, Article ID 620984, 8 pages, 2011. doi:10.1155/2011/620984
3. H. N. Mayrovitz and E. E. Groseclose, "Effects of a static magnetic field of either polarity on skin microcirculation", *Microvasc. Res.*, vol. 69, pp. 24-27, January 2005.
4. A. Ž. Ilić, S. Ćirković, D. M. Djordjevic, S. R. De Luka, I. D. Milovanovich, A. M. Trbovich and J. L. Ristić-Djurović, "Analytical description of two-dimensional magnetic arrays suitable for biomedical applications", *IEEE Trans. Magnetics*, vol. 49, pp. 5656-5663, December 2013.
5. J. László, J. Reiczigel, L. Székely, A. Gasparics, I. Bogár, L. Bors, B. Rácz and K. Gyires, "Optimization of static magnetic field parameters improves analgesic effect in mice", *Bioelectromagnetics*, vol. 28, pp. 615-627, December 2007.
6. T. R. Ní Mhíocháin and J. M. D. Coey, "Permanent magnets", in *Physical Methods, Instruments and Measurements*, vol. III, Y. M. Tsipenyuk, Ed. Oxford, U.K.: Eolss Publishers, 2009 [Online]: <http://www.eolss.net>, Encyclopedia of Life Support Systems, under the auspices of the UNESCO.
7. I. R. Harris and A. J. Williams, "Magnetic materials", in *Materials Science and Engineering*, vol. II, R. D. Rawlings, Ed. Oxford, U.K.: Eolss Publishers, 2009 [Online]. Available: <http://www.eolss.net>, Encyclopedia of Life Support Systems, under the auspices of the UNESCO.
8. W. T. Benecki, "The permanent magnet market – 2015", in *Proc. Magnetics 2013 Conf.*, Orlando, FL, USA, 2013.

EXPERIMENTAL ELECTROMAGNET FOR *IN VIVO* EXPOSURE OF SMALL ANIMALS TO ELF ELECTROMAGNETIC FIELDS

Andjelija Ž. Ilić¹, Jasna L. Ristić-Djurović¹, Saša Ćirković¹, Milan M. Ilić²,
Alexander M. Trbovič³

¹ Innovation Center, School of Electrical Engineering, University of Belgrade, 11120 Belgrade, Serbia

² School of Electrical Engineering, University of Belgrade, 11120 Belgrade, Serbia

³ Department of Pathological Physiology, School of Medicine, University of Belgrade, 11000 Belgrade, Serbia

Abstract. *The ubiquitous presence of electromagnetic (EM) fields in living environment motivates investigation of their influence on biological systems. Existing research data shows a high degree of inconsistency, covers very limited regions of electromagnetic spectrum and in many cases lacks detailed and accurate description of the electromagnetic fields necessary for the replication of experiments. Exposure systems, designed specifically for biomedical research, offer the solution to the above problems. We present experimental electromagnet for in vivo small animal research. It covers both static magnetic field and extra-low frequency (ELF) electromagnetic field range, offering higher EM field intensities than those produced by most other systems.*

Key words: *electromagnetic (EM) fields, static magnetic field (SMF), biological effects, exposure system, in vivo, small animal research*

1. INTRODUCTION

Exposure systems, such as the ones described in [1]–[6], are specialized devices aimed at producing, controlling and monitoring electromagnetic fields for biomedical research. It is a prerequisite for an experiment to be well-designed and for the consistent interpretation of results that the desired fields are accurately adjusted and precisely known. Systems for the *in vitro* research, mostly due to the smaller volume involved, but also because of the relatively static experimental conditions, can be realized with greater precision. Also, most of the systems are intended for a narrow range of EM fields, often for a single frequency and lower field levels. With the notable increase of the variety of small commercial devices being produced and rapid extension of the utilized frequency ranges to the previously unused parts of the electromagnetic spectrum, it becomes increasingly important to systematically investigate the biomedical effects of various EM fields.

We have so far investigated the effects on mice of the two types of static magnetic fields (SMF): inhomogeneous, vertically declining SMF, whose mean magnetic flux density equals 1 mT and its mean gradient equals 0.02 T/m [7], and homogeneous SMF whose magnetic flux density is 128 mT [8]. Results show influence of both considered field types to the circulatory system in mice [9]–[11]. In continuation of our previous work we are interested in further analysis of SMFs of intensity 100 mT and more. Additionally, we plan to extend our research to other EM fields, starting with the extra-low frequency (ELF) range already shown to produce certain biological effects.

In order to employ it in our experiments as well as evaluate the prototype of a product that could be made commercially available, we are currently constructing the exposure system to cover both SMFs and the ELF field range. The most straightforward solution to obtain the required relatively strong field intensities is to use the solenoidal fields, either by placement of experimental animals within a solenoid or by usage of combined solenoidal fields with or without the ferromagnetic core. For the device functioning in the direct-current (DC) regime, DC current generator is to be used. Alternating-current (AC) current source will enable the production of sinusoidal electromagnetic fields. The device will be tested for as wide part of the ELF range, as possible to achieve. Frequency range of 0 Hz to 100 Hz is chosen as an initial requirement.

2. EXPERIMENTAL ELECTROMAGNET REQUIREMENTS AND INITIAL COIL DESIGN

Design requirements for an experimental EM field exposure system can be divided in several subgroups. Among the most important factors are the ones dictated by the user community, including compliance with the usual conditions and practices of a biomedical experiment as well as the ease of utilization. Therefore, experimental electromagnet is devised as a flexible device providing EM fields of different magnitudes, gradients, directions and frequencies. The constituent parts of this device belong to one of the five subgroups: copper wire coils, ferromagnetic (iron) cores, direct and alternating current generators, calibration and measurement equipment and accessory equipment. Accessory equipment has to be specific and very

carefully designed in order to enable flexible and modular use of the device. For example, biomedical experiment regulations and the recommendations for the result interpretation allow comparisons of different parameter influences only if all the data is acquired simultaneously as a result of a single experiment. Two copper wire coils are required if the effects of different static magnetic field directions, such as the same or opposite orientation with respect to the Earth's geomagnetic field, are to be compared. Otherwise, the accessory equipment has to ensure position and power supply adjustment for the two coils, in order to combine their EM fields for increased strength and homogeneity. For the higher EM field magnitudes, ferromagnetic cores have to be used as well. Calibration and measurement equipment includes the ambient EM field measurement panel as well as the equipment for monitoring other physical quantities, such as ambient temperature and temperature inside the experimental volume.

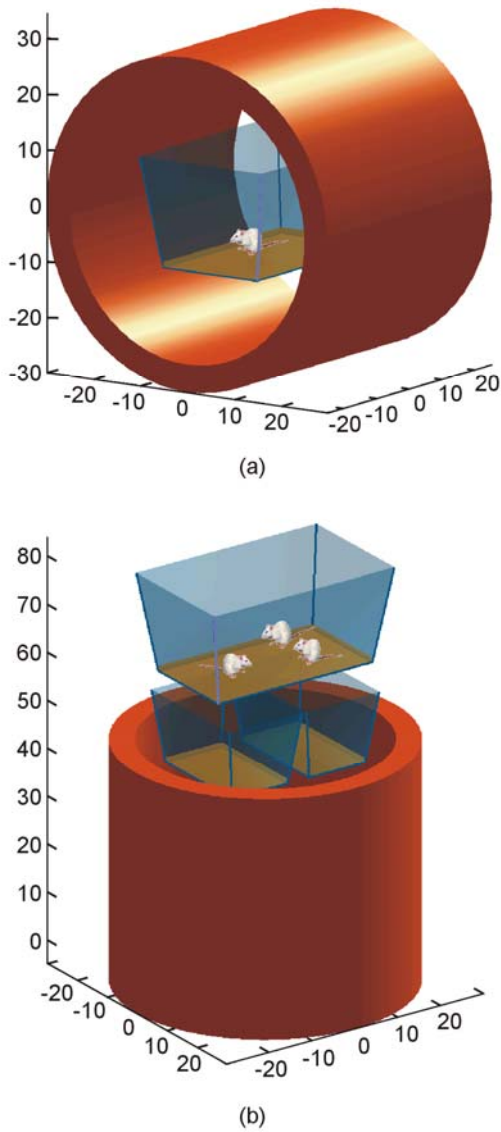


Fig. 1 Copper coils of the experimental electromagnet for *in vivo* exposure to ELF EM fields. To obtain the required relatively strong field intensities above 100 mT, coil size must enable placement of one or several cages inside the solenoid.

2.1. Minimal Size Requirements

For the *in vivo* experiments involving small animals such as mice, care has to be taken of usual routines and rules for their accommodation and treatment. A layer of sawdust is used for padding the cages for mice as this would resemble their natural habitat; animals are fed and watered in the cages. It is most convenient to enable placement of the whole cages occupied by animals within the experimental volume, without disturbing the animals. Not only that it facilitates organization of chronic and sub-chronic experiments; such practice is equally important for the short-term acute exposures to avoid stress as a factor interfering with the actual investigations.

Standard small cages or standard large cages are typically used. Width and length of the small standard cage are 165 mm and 260 mm, respectively, and its height equals 150 mm. Large standard cage is 260 mm wide, 420 mm long, and its height equals 185 mm. This imposes the inner copper coil diameter larger than 500 mm in order to enable its vertical placement as shown in part (b) of Fig. 1. Therefore, the coil stand will support its placement as in Fig. 1 (a), in order to study the influence of horizontally directed fields that penetrate animal's body in all different directions as an animal moves inside the cage, or as shown in Fig. 1 (b) to provide vertical field direction. The cage centered inside the coil results in the higher uniformity of the applied field distribution, whereas to study gradient fields the cage positioning toward the edges or just outside the coil would be appropriate. For the vertical placement of the coil, it can accommodate more than one cage including the combination of large and small cages.

For the preliminary analysis of power requirements and EM field levels that could be produced, we investigate the case where the coil length equals its inner diameter, $l = 2R = 500$ mm. To keep coil price and weight reasonable, its thickness is initially chosen equal to $R'' - R' = 150$ mm. Coil cross-section is shown in part (a) of Fig. 2.

2.2. Limiting Magnetomotive Force

From the user point of view, the need for any specialized power installations can be complicated, expensive and time consuming. Therefore, one of the main requirements for the designed device is to utilize the regular power network. Having in mind maximal wire current density not requiring water-cooling of $J_m = 3$ A/mm², as well as total maximum current of $I_m = 25$ A, we determine the optimal wire diameter of $d = 3$ mm. This choice is illustrated by the data presented in Table 1. Wire diameter d corresponds to the wire cross-section S_w and the number of coils in the given coil cross-section N .

$$N = \frac{S_{\text{coil}}}{S_w} = \frac{l(R'' - R')}{S_w}. \quad (1)$$

The total length of the wire used, l_w , and its resistivity, R , with the copper conductivity $\sigma_{\text{Cu}} = 58$ MS/m, can be assessed as

$$l_w \approx 2\pi \frac{R' + R''}{2} N, \quad R = \frac{1}{\sigma_{\text{Cu}}} \frac{l_w}{S_w}. \quad (2)$$

Table 1 Magnetomotive force NI and coil resistivity R

d (mm)	S_w (mm ²)	J ($\frac{A}{mm^2}$)	I (A)	N	R (Ω)
1	0.785	3.00	2.36	95493	4280.7
2	3.141	3.00	9.42	23873	267.5
3	7.068	3.00	21.21	10610	52.8
4	12.566	1.99	25.00	5968	16.7
5	19.635	1.27	25.00	3820	6.8

Critical parameter here is the active power that should not exceed 5.5 kW in the monophasic regime, under the condition of inductivity compensation for an AC current operation. If the regular power network is to be used, it will be necessary to decrease the current density, resulting in the maximal produced magnetic flux density of 150 mT. This is in agreement with the desired initial design requirements. The following analysis is given for several values of the current density and illustrates field levels that could be produced by the considered coil.

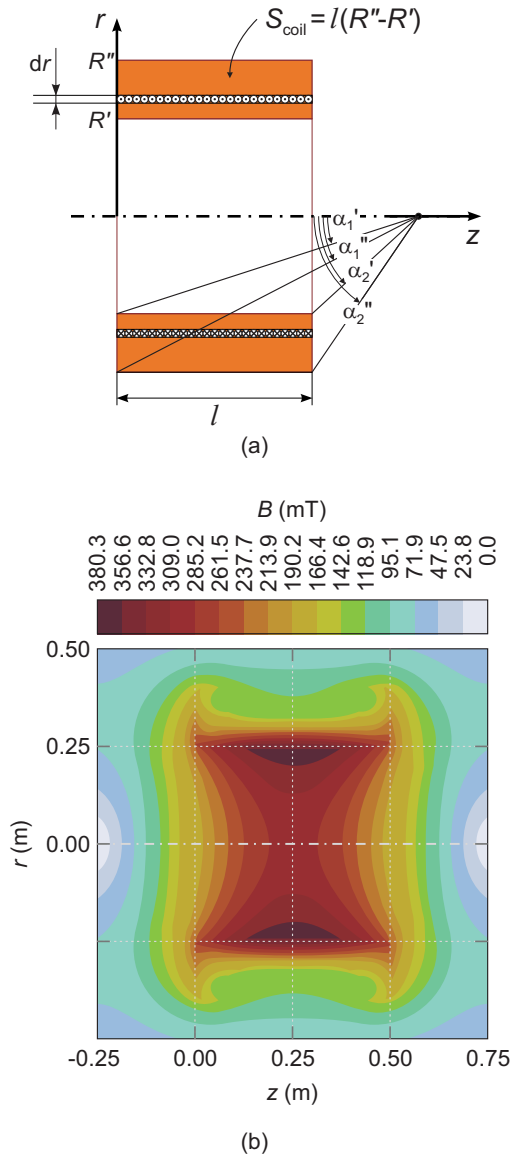


Fig. 2 Copper coil and the produced magnetic flux density. (a) Coil cross-section and the coordinate system used. (b) Calculated three-dimensional magnetic flux density inside and surrounding the coil.

3. MEAN ELECTROMAGNETIC FIELD PARAMETERS

The described copper coil is modeled using the commercially available Mermaid finite element suite for magnetostatics. Calculated magnetic flux density distribution inside and surrounding the coil, whose cross-section is shown in Fig. 2 (a), is presented in part (b) of Fig. 2. As seen from the figure, nonuniformity of the magnetic flux density distribution is less than 8% in the central part of a solenoid, for $r < 125$ mm and $z \in [18, 32]$ mm. Further modeling and optimization of this initial model is due, to additionally improve the field homogeneity in the central part of the device. For the experimenter, it is the mean magnetic flux density over the experimental volume (or the mean maximal magnetic flux density in the experimental volume for the time-varying ELF EM fields) that is of interest. Where applicable, mean z -axis gradient of the field, defined as $G_z(z) = -\text{grad}_z B_z(z)$, is another necessary parameter for the field description. Height of the experimental volume most often coincides with the average size of the animal, whereas exposed horizontal range coincides with the size of the cage bottom.

In the case of unavailability of CAE modeling tools such as Mermaid, magnetic flux density and its z -axis gradient can be approximately assessed using the analytical expressions for the magnetic flux density along the axis of a thick solenoid, $B_z(z)$.

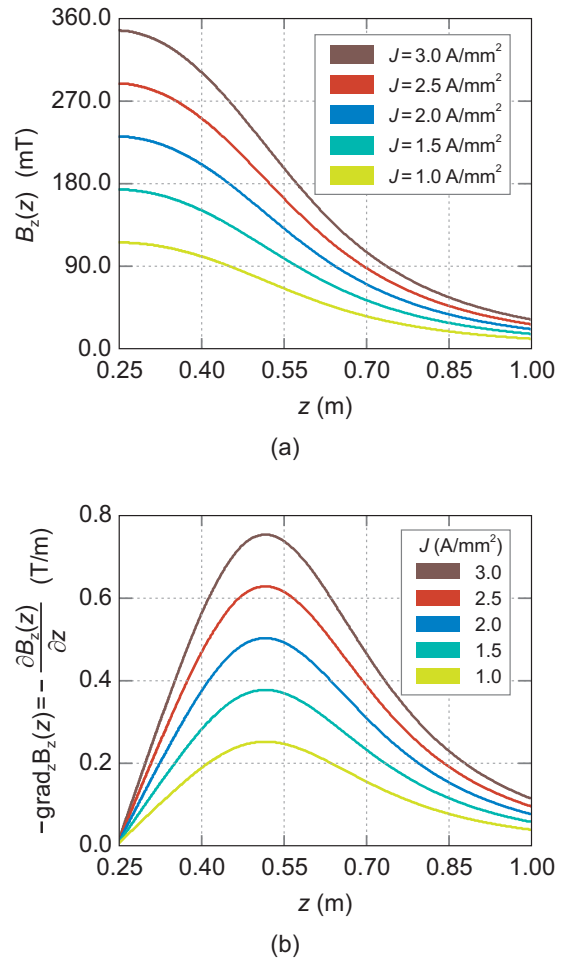


Fig. 3 Magnetic field produced with different coil currents. (a) Magnetic flux density at the solenoid axis. (b) The z -axis gradient of the magnetic flux density along the axis.

Integration, from $z = 0$ to $z = l$, of the magnetic flux density on the axis of many constituent circular loops yields an expression for the magnetic flux density along the axis of a thin solenoid:

$$B_z(z) = \frac{\mu_0 NI}{2l} (\cos \alpha_1 - \cos \alpha_2). \quad (3)$$

Angles α_1 and α_2 are denoted in Fig. 2 (a) for the inner layer of copper wire (primed) as well as the outermost layer (double primed). Free space permeability equals $\mu_0 = 4\pi \cdot 10^{-7}$. Further integration, from $r = R'$ to $r = R''$, of the z -axis field components due to layers of wire of thickness dr , magnetomotive force in each layer being equal to $Nldr/(R'' - R')$, results in magnetic flux density of a thick solenoid,

$$B_z(z) = \frac{\mu_0 NI}{2l(R'' - R')} \left(z \ln \frac{\tan(\frac{\pi + \alpha_1''}{4})}{\tan(\frac{\pi + \alpha_1'}{4})} - (z-l) \ln \frac{\tan(\frac{\pi + \alpha_2''}{4})}{\tan(\frac{\pi + \alpha_2'}{4})} \right). \quad (4)$$

Equation (4) has been used to calculate magnetic fields and their gradients for different coil current densities, given in Fig. 3 as an illustration of the electromagnet capabilities. For the vertical coil placement and usual experimental volume height of 35 mm, nonuniformity of the magnetic flux density with height is less than 0.1% and its gradient nonuniformity less than 0.2%. Using the curves such as ones given in Fig. 3, an appropriate combination of field strength and field gradient for exposure of animals can be chosen. Coils will be further optimized for higher field homogeneity in their central regions as well as stronger field gradients toward ends and outside the coils.

4. CONCLUSIONS

Novel exposure system for biomedical research, experimental electromagnet for both static magnetic field research and extra-low frequency EM field range, is described. Design guidelines and requirements for such system are defined and explained. These requirements mostly stem from the usual experimental routines and recommendations. Special care has to be taken to ensure flexibility and modularity of the device utilization. Initial electromagnet coil design has been carried on, showing that the desired field strength of 150 mT could be easily achieved using the regular power network available everywhere. Further design to improve field homogeneity and provide stronger field gradients is under way.

Acknowledgement: This work was supported by the Ministry of Education, Science and Technological Development of Serbia through the project III-45003, and in part by the Public Enterprise "Electric Power Industry of Serbia".

REFERENCES

1. M. A. Stuchly, D. W. Lecuyer and J. McLean, "Cancer promotion in a mouse-skin model by a 60-Hz magnetic field: I. Experimental design and exposure system", *Bioelectromagnetics*, vol. 12, pp. 261-271, October 1991.
2. T. Shigemitsu, K. Takeshita, Y. Shiga and M. Kato, "50-Hz magnetic field exposure system for small animals", *Bioelectromagnetics*, vol. 14, pp. 107-116, April 1993.
3. A. Paffi, F. Apollonio, G. A. Lovisolo, C. Marino, R. Pinto, M. Repacholi and M. Liberti, "Considerations for developing an RF exposure system: A review for *in vitro* biological experiments", *IEEE Trans. Microw. Theory Tech*, vol. 58, pp. 2702-2714, October 2010.
4. P. Koester, J. Sakowski, W. Baumann, H.-W. Glock, J. Gimsa, "A new exposure system for the *in vitro* detection of GHz field effects on neuronal networks", *Bioelectrochemistry*, vol. 70, pp. 104-114, January 2007.
5. L. Visek, P. Togni, J. Vrba and L. Oppl, "Design and comparison of exposure chambers for verification of microwave influence on biological systems", *PIERS Online*, vol. 3, pp. 1346-1350, August 2007.
6. T. Okuno, "A 100 mT-class ELF magnetic field exposure system for cultured cells", *Ind. Health*, vol. 34, pp. 113-123, February 1996.
7. A. Ž. Ilić, S. Čirković, D. M. Djordjević, S. R. De Luka, I. D. Milovanovich, A. M. Trbović and J. L. Ristić-Djurović, "Analytical description of two-dimensional magnetic arrays suitable for biomedical applications", *IEEE Trans. Magnetics*, vol. 49, pp. 5656-5663, December 2013.
8. S. Čirković, J. L. Ristić-Djurović, A. S. Vorozhtsov, A. Ž. Ilić and N. Nešković, "Method for fine magnet shaping in cyclotrons", *IEEE Trans. Nucl. Sci.*, vol. 56, pp. 2821-2827, October 2009.
9. D. M. Djordjević, S. R. De Luka, I. D. Milovanovich, S. Janković, S. Stefanović, S. Vesković-Moračanin, S. Čirković, A. Ž. Ilić, J. L. Ristić-Djurović and A. M. Trbović, "Hematological parameters' changes in mice subchronically exposed to static magnetic fields of different orientations", *Ecotoxic. Environm. Safety*, vol. 81, pp. 98-105, July 2012.
10. S. R. De Luka, D. M. Djordjević, I. D. Milovanovich, S. Janković, S. Stefanović, S. Vesković-Moračanin, S. Čirković, A. Ž. Ilić, J. L. Ristić-Djurović and A. M. Trbović, "Subchronic exposure to static magnetic field affects zinc and copper content in mice brain and liver", submitted to *Cell Biochem. Biophys*.
11. I. D. Milovanovich, D. M. Djordjević, S. R. De Luka, S. Čirković, A. Ž. Ilić, J. L. Ristić-Djurović and A. M. Trbović, "Static magnetic field of different orientations induces various biological changes in exposed mice", unpublished.

Convergence of the Higher Order Frequency-Domain FEM Solution to Scattering from a Moving Dielectric Slab

Milan M. Ilić, *Member, IEEE* and Andjelija Ž. Ilić, *Member, IEEE*

Abstract — We investigate the convergence of the higher order frequency-domain finite element method (FEM) solution to electromagnetic scattering from a relativistically moving inhomogeneous dielectric slab. Full wave numerical solutions are evaluated and validated by comparison with the analytical solutions.

Index terms — Electromagnetic analysis, finite element methods, higher order methods, Lorentz transformation, moving media, scattering.

I. INTRODUCTION

THE finite element method (FEM) is often referred to as the method of choice in treating inhomogeneous closed region problems in electromagnetics (EM) [1]. Through hybridization with the method of moments (MoM), as demonstrated in [2], [3], it becomes equally versatile and effective in the analysis of open structures.

All commercially available high frequency FEM EM codes, however, treat only stationary (non-moving) media. Recently, we have developed a novel higher order FEM for EM analysis of scattering from a moving dielectric slab [4], which appears to be the first demonstration of accurate and efficient higher order FEM modeling of macroscopic EM problems in the presence of relativistically moving media. Examples on the subject found in the literature include mostly analytical solutions, as in [5]–[7], and a few numerical solutions often limited to PEC mirrors [8]. Analytical solution and a low-order FEM solution for a stationary slab can be found in [1], whereas a higher order FEM solution (at normal incidence) can be found in [9], along with the convergence analysis for the stationary slab.

In this work we briefly revisit some details of the novel higher order FEM technique for one dimensional (1-D)

This work was supported by the Serbian Ministry of Education, Science, and Technological Development under grants TR-32005 and III-45003.

M. M. Ilić is with the University of Belgrade, School of Electrical Engineering, 11120 Belgrade, Serbia and also with the Colorado State University, Department of Electrical and Computer Engineering, Fort Collins, CO 80523-1373, USA (phone: +381-11-3370101, fax: +381-11-3248681, e-mail: milanilic@etf.rs).

A. Ž. Ilić is with the Innovation Center, School of Electrical Engineering, University of Belgrade, 11120 Belgrade, Serbia (e-mail: andjelijailic@ieee.org).

EM analysis in the presence of moving media and analyze in more detail accuracy and convergence of the method under h - and p -refinements, when relativistic effects are highly pronounced.

II. THEORY AND IMPLEMENTATION

Flat dielectric slab, stationary in its rest frame S' and infinite in the $x'O'y'$ plane, is moving at a constant velocity with respect to laboratory frame S (vacuum), as shown in Fig. 1. The proper thickness of the slab (in its rest frame) is d , and it can generally be inhomogeneous with relative permittivity ϵ_r and relative permeability μ_r , varying only as functions of z' . As viewed from the laboratory frame of reference, a uniform linearly polarized plane EM wave impinges obliquely onto the slab. Only the case for which the incident wave polarization remains unchanged under Lorentz transformations is considered here. Therefore, the movement of the slab is limited to the plane of incidence (yOz plane).

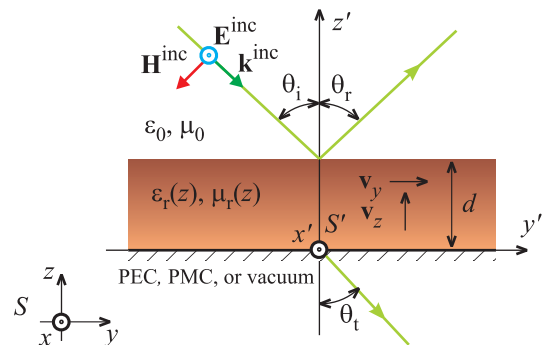


Fig. 1. Uniform plane wave scattering from a moving dielectric slab backed by a perfect electric conductor (PEC), perfect magnetic conductor (PMC), or vacuum.

Complete expressions for the plane wave scattering from the moving slab, along with accompanying Lorentz transformations [10], can be found in [4]. We repeat here only the parts relevant for understanding of the results in Section III. The incident wave

$$\mathbf{E}^{\text{inc}} = E_0 e^{-j\mathbf{k}^{\text{inc}} \cdot \mathbf{r}} \mathbf{i}_x, \quad (1)$$

is represented by its complex field intensity at the origin, E_0 , the incident-wave wave vector, $\mathbf{k}^{\text{inc}} = k_y \mathbf{i}_y + k_z \mathbf{i}_z$, and the position vector, $\mathbf{r} = x \mathbf{i}_x + y \mathbf{i}_y + z \mathbf{i}_z$. The angular frequency, ω , of the implied time-harmonic excitation,

normalized by the speed of light $c = 1/\sqrt{\epsilon_0\mu_0}$, corresponds to the wavenumber $|\mathbf{k}^{\text{inc}}| = \omega/c$. The angles of the incident, reflected and transmitted waves, θ_i , θ_r , and θ_t (which can be computed from respective wave vector components) are also shown in Fig. 1. The nonzero velocity vector components, \mathbf{v}_y and \mathbf{v}_z , correspond to the normalized slab velocity components

$$\beta_y = v_y/c, \quad \beta_z = v_z/c \quad (2)$$

and the Lorentz-transformation factors

$$\beta = \sqrt{\beta_y^2 + \beta_z^2}, \quad \gamma = 1/\sqrt{1-\beta^2}. \quad (3)$$

The electric field vector wave equation of the scattering problem reduces to

$$\frac{\partial}{\partial z'} \left(\alpha_F \frac{\partial E'_x}{\partial z'} \right) + \alpha_F \beta_F E'_x = 0, \quad (7)$$

$$\alpha_F = \frac{1}{\mu_r}, \quad \beta_F = \left(\frac{\omega'}{c} \right) \epsilon_r \mu_r - k_y'^2, \quad (8)$$

with associated boundary conditions and it is solved by the 1-D FEM in the S' rest frame employing the higher order field expansion, formally presented as

$$E'_x = \sum_{e=1}^M \sum_{j=1}^{n^e+1} a_j^e f_j^e, \quad (9)$$

with M being the number of uniformly sized 1-D elements, n^e the polynomial field-expansion order of the e -th element (here we use $n^e = n$ for all elements), f^e the polynomial basis functions locally defined on each element, and a^e the unknown complex coefficients. Standard discretization of (7), employing (9), yields

$$\sum_{j=1}^{n^e} a_j \left[- \int_{z_l^e}^{z_r^e} \alpha_F \frac{df_i}{dz'} \frac{df_j}{dz'} dz' + \int_{z_l^e}^{z_r^e} \alpha_F \beta_F f_i f_j dz' \right] = \int_{z_l^e}^{z_r^e} f_i g dz' - f_i \alpha_F \frac{dE'_x}{dz'} \Big|_{z_l^e}^{z_r^e} \quad (10)$$

in each element, where z_l^e and z_r^e are the left and right boundaries of the e -th element.

III. NUMERICAL RESULTS AND DISCUSSION

To facilitate comparison of our numerical results with the analytical solutions, we consider an example given in [5], [6]. Normal incidence ($\theta_i = 0$) of a uniform plane wave onto a homogeneous lossless dielectric slab with parameters $\epsilon_r = 2$ and $\mu_r = 1$ is analyzed. The (proper) thickness of the slab, d , corresponds to one-fourth of the wavelength at rest, λ_d , i.e., $d = \lambda_d/4$. Note that the power reflection and transmission coefficients defined in [5], [6] correspond to $|R|^2$ and $|T|^2$ defined in [4] and adopted here (at normal incidence).

The considered scattering problem is solved using higher order FEM, modeling the slab with a single 1-D element ($M = 1$) and employing the polynomial field expansion of the eight-order ($n = 8$). Fig. 2 shows the power reflection coefficients computed for the slab moving

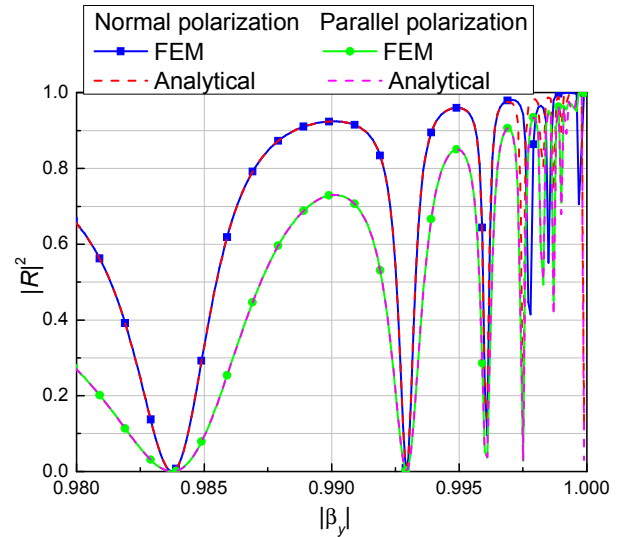


Fig. 2. Reflection coefficient $|R|^2$ for the slab moving transversally to direction of propagation of the plane wave vs. normalized slab velocity: comparison of the FEM solution and analytical solutions from [5], [6] for high velocities only.

transversally to direction of propagation of the plane wave, in case of normal and parallel polarizations, vs. normalized slab velocity $|\beta_y|$, at high velocities. (Note that the polarization is normal and parallel with respect to the moving direction.) We find an excellent agreement of the FEM and analytical solutions for velocities up to $|\beta_y| = 0.997$ with this literally entire domain FEM model.

More detailed convergence of solutions for the reflection coefficient under h - and p -refinements is presented in [4], hence we next investigate the convergence of the FEM solutions for the transmission coefficient, $|T|$, for the slab moving at high longitudinal velocities β_z . Employing, again, a constant polynomial field expansion of the eight-order ($n = 8$), the results of h -refinement of solutions are presented in Fig. 3.

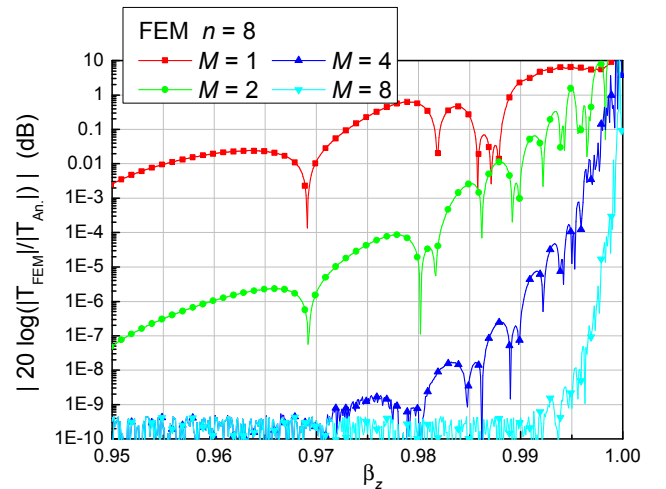


Fig. 3. Error of $|T|$ computed by FEM with respect to analytical solution vs. normalized slab longitudinal velocity at velocities close to the speed of light: convergence of the FEM solutions with h -refinement.

We can conclude from the figure that excellent convergence is achieved under h -refinement, with the appropriate choice of the (high) polynomial field expansion order. However, the errors in Fig. 3, obtained for the slab moving in the direction of the incident wave propagation, are different in magnitude (higher) than errors obtained for the slab moving transversally to the direction of the incident wave propagation. At first surprising, this fact can be partially attributed to the different nature of numerical problems arising in the two cases. Namely, as explained in [4], in case when $\beta_y \neq 0$, $\beta_z = 0$, the FEM computation is affected as if the frequency of the excitation is increased γ times, i.e., the slab becomes electrically larger as velocity increases, eventually becoming infinitely large as $|\beta_y| \rightarrow 1$. (Note that the length contraction in z -direction does not appear since $\beta_z = 0$.) On the other hand, when $\beta_y = 0$, $\beta_z \neq 0$, the FEM encounters a low frequency breakdown. Note that, at the same time, apparent slab thickness, wave number, k'_z , and angular frequency, ω' , all become very small in this case. Hence, overall numerical problems when the slab is moving along the direction of the wave propagation are different in nature from those appearing when this movement is transversal to the wave propagation direction.

IV. CONCLUSION

The numerical results demonstrate that convergence of FEM solutions for both reflection and transmission coefficients and for both high transversal and longitudinal velocities can be easily sustained with combined h - and p -refinements of the model, and accurate solutions can be obtained for velocities as high as $0.999c$.

Although the results presented here are of a limited scope, the method itself is not, as it enables scattering analysis for arbitrary lossy and continuously inhomogeneous slabs, as well as scattering from slabs comprised of layers moving with different transversal velocities. These cases will be studied in our future work.

REFERENCES

- [1] J. M. Jin, *The Finite Element Method in Electromagnetics*, 2nd ed. New York, NY, USA: Wiley, 2002.
- [2] M. M. Ilić, A. Ž. Ilić, and B. M. Notaroš, "Continuously inhomogeneous higher order finite elements for 3-D electromagnetic analysis," *IEEE Trans. Ant. Prop.*, vol. 57, no. 9, pp. 2798–2803, Sept. 2009.
- [3] M. M. Ilić, M. Djordjević, A. Ž. Ilić, and B. M. Notaroš, "Higher order hybrid FEM-MoM technique for analysis of antennas and scatterers," *IEEE Trans. Antennas and Propagation*, vol. 57, pp. 1452–1460, May 2009.
- [4] A. Ž. Ilić and M. M. Ilić, "Higher-Order Frequency-Domain FEM Analysis of EM Scattering Off a Moving Dielectric Slab", *IEEE Ant. Wireless Prop. Lett.*, Vol. 12, December 2013, pp. 890–893.
- [5] C. Yeh and K. F. Casey, "Reflection and transmission of electromagnetic waves by a moving dielectric slab," *Phys. Rev.*, vol. 144, no. 2, April 1966, pp. 665–669.
- [6] C. Yeh, "Reflection and transmission of electromagnetic waves by a moving dielectric slab. II. Parallel polarization," *Phys. Rev.*, vol. 167, no. 3, March 1968, pp. 875–877.
- [7] K. Tanaka and K. Hazama, "Reflection and transmission of electromagnetic waves by a moving inhomogeneous medium," *Radio Sci.*, vol. 7, no. 10, pp. 973-978, Oct. 1972.
- [8] F. Harfoush, A. Taflove, and G. A. Kriegsmann, "A numerical technique for analyzing electromagnetic wave scattering from moving surfaces in one and two dimensions," *IEEE Trans. Antennas Prop.*, vol. 37, no. 1, Jan. 1989.
- [9] V. V. Petrović and B. D. Popović, "Optimal FEM solutions of one-dimensional EM problems," *Inte. J. Numer. Model.: Electron. Networ., Devices and Fields*, vol. 14, 2001, pp. 49–68.
- [10] J. D. Jackson, *Classical electrodynamics*, 3rd ed. New York, NY, USA: Wiley, 1998.

Accurate and Efficient Curvilinear Geometrical Modeling Using Interpolation Parametric Elements in Higher Order CEM Techniques

Branislav M. Notaroš¹, Milan M. Ilić^{1,2}, Slobodan V. Savić², Nada J. Šekeljić¹, and Anđelija Ž. Ilić³

¹ Colorado State University, Department of Electrical and Computer Engineering, Fort Collins, CO 80523-1373 USA, notaros@colostate.edu, inadasek@engr.colostate.edu

² University of Belgrade, School of Electrical Engineering, 11120 Belgrade, Serbia, milanilic@etf.rs, ssavic@etf.rs

³ Vinča Institute of Nuclear Sciences, Laboratory of Physics 010, 11001 Belgrade, Serbia, andjelijailic@ieee.org

Abstract: Accurate and efficient curvilinear geometrical modeling using Lagrange-type generalized interpolation parametric elements in higher order computational electromagnetic techniques is presented. Examples demonstrate enhanced accuracy and efficiency of the analysis when uniformly distributed Lagrange geometrical interpolation nodes on curved and large elements are combined with high-order (p -refined) basis functions for current modeling.

Key words: electromagnetic analysis, numerical techniques, higher order modeling, curved parametric elements, geometrical mapping, integral-equation techniques, scattering.

1. Introduction

Higher order (also known as large-domain or entire-domain) approach in computational electromagnetics (CEM) utilizes higher order basis functions for the approximation of currents and/or fields defined on large surface and/or volume geometrical elements (e.g., on the order of a wavelength in each dimension) [1]-[4]. This enables considerable reductions in the number of unknowns for a given problem, enhances the accuracy and efficiency of the CEM analysis, and results in faster (higher order) convergence of the solution, when compared to traditional low-order (also referred to small-domain or subdomain) CEM tools. In hand with higher order basis functions, novel CEM tools often employ curvilinear elements for geometrical modeling of general electromagnetic structures [5]-[11].

This paper presents accurate and efficient curvilinear geometrical modeling in higher order CEM using Lagrange-type generalized interpolation parametric quadrilaterals as basic boundary elements in the method of moments (MoM) analysis in conjunction with the surface integral equation (SIE) formulation for radiation and scattering [9] and associated parametric hexahedra for volumetric modeling based on the finite element method (FEM) [10]. In particular, the paper discusses optimal placement of interpolation nodes on high-order geometrical elements and other related issues of curvilinear geometrical modeling. It demonstrates accurate and efficient models using uniformly distributed Lagrange geometrical

This work was supported by the National Science Foundation under grants ECCS-0650719 and ECCS-1002385 and by the Serbian Ministry of Science and Technological Development under grant TR-32005.

interpolation nodes on curved and large elements combined with high-order (p -refined) basis functions.

2. Curvilinear Geometrical Modeling Using Higher Order Interpolation Parametric Elements

As basic building blocks for surface geometrical modeling in MoM and hybrid techniques, we use Lagrange-type generalized curved parametric quadrilaterals of arbitrary geometrical orders K_u and K_v ($K_u, K_v \geq 1$), shown in Fig. 1 and analytically described as [9]

$$\mathbf{r}(u, v) = \sum_{k=0}^{K_u} \sum_{l=0}^{K_v} \mathbf{r}_{kl} L_k^{K_u}(u) L_l^{K_v}(v), \quad -1 \leq u, v \leq 1, \quad L_k^{K_u}(u) = \prod_{\substack{i=0 \\ i \neq k}}^{K_u} \frac{u - u_i}{u_k - u_i}, \quad (1)$$

where $\mathbf{r}_{kl} = \mathbf{r}(u_k, v_l)$ are position vectors of interpolation nodes, $L_k^{K_u}$ represent Lagrange interpolation polynomials, and u_i are the interpolation nodes along an interval $-1 \leq u \leq 1$, and similarly for $L_l^{K_v}(v)$. Electric and magnetic surface current density vectors, \mathbf{J}_s and \mathbf{M}_s , over every generalized quadrilateral in the model are approximated by means of divergence-conforming hierarchical-type polynomial vector basis functions in parametric coordinates u and v , with arbitrary current-expansion orders N_u and N_v ($N_u, N_v \geq 1$) [9], which are entirely independent from the element geometrical orders (K_u and K_v).

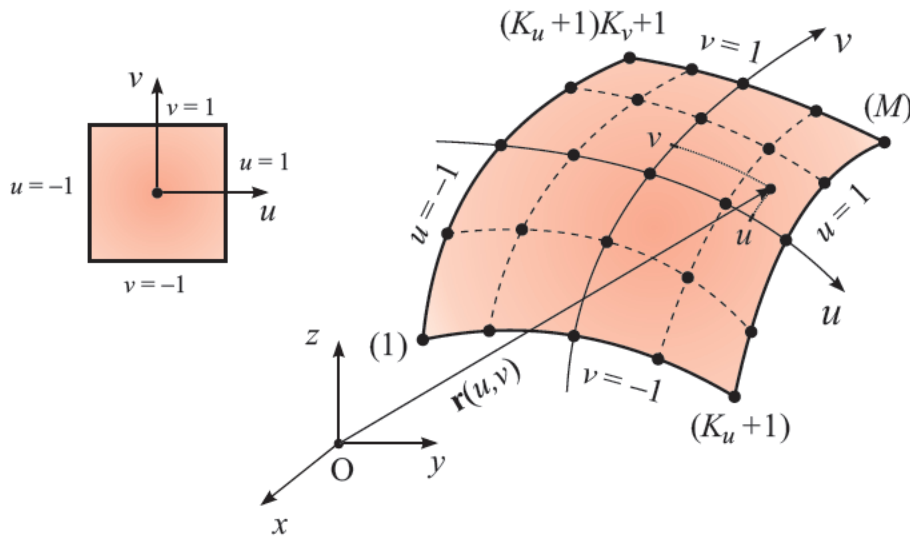


Fig. 1. Generalized curved parametric quadrilateral defined by (1); square parent domain is also shown.

In FEM and hybrid techniques, volumetric geometrical modeling of inhomogeneous materials is carried out using Lagrange-type interpolation generalized hexahedra, which are a volume (3-D) generalization of the quadrilateral patch in Fig. 1 [10], [11]. The electric field vector inside the FEM hexahedra is approximated by curl-conforming hierarchical vector expansions [10].

3. Numerical Results and Discussion

As the first example, consider a dielectric spherical scatterer of relative permittivity $\epsilon_r = 4$ and relative permeability $\mu_r = 1$ in free space. Its surface is modeled by means of six Lagrange quadrilateral patches (Fig. 1) of the fourth geometrical order ($K_u = K_v = 4$), and with basis functions of orders $N_u = N_v = 6$ for vectors \mathbf{J}_s and \mathbf{M}_s on all patches. Shown in Fig. 2 is the analytically obtained (Mie's

series) normalized monostatic radar cross section (RCS) of the scatterer, vs. a/λ , where a is the sphere radius and λ stands for the wavelength in the dielectric, and the computed results obtained using two models with different placements of interpolation nodes on Lagrange patches. In the first model, the interpolation nodes are obtained by mapping the uniformly distributed points of a square parent domain to one-sixth of a sphere within the cube-to-sphere mapping, that is, by projecting the square onto the spherical patch, with the common center (center of the sphere) as the projection center. Such a direct mapping actually results in a nonuniform distribution of interpolation nodes on the spherical patch, namely, it introduces significant distortion in the projected parametric space in a sense that the distances between the mapped points are quite different, whereas these distances are the same in the parent domain. The second model is created by mapping the unit parent square to one-sixth of the sphere in such a way to keep the points, that are uniformly distributed on the square, also uniformly distributed on the spherical patch, i.e., by positioning the Lagrange interpolation nodes in a uniform fashion. From the figure, we observe that the model with uniform nodes performs much better than the other model; namely, it gives accurate results in the whole range of frequencies considered, while the model with direct mapping results in noticeable errors even starting from relatively low frequencies and performs poorly at higher frequencies.

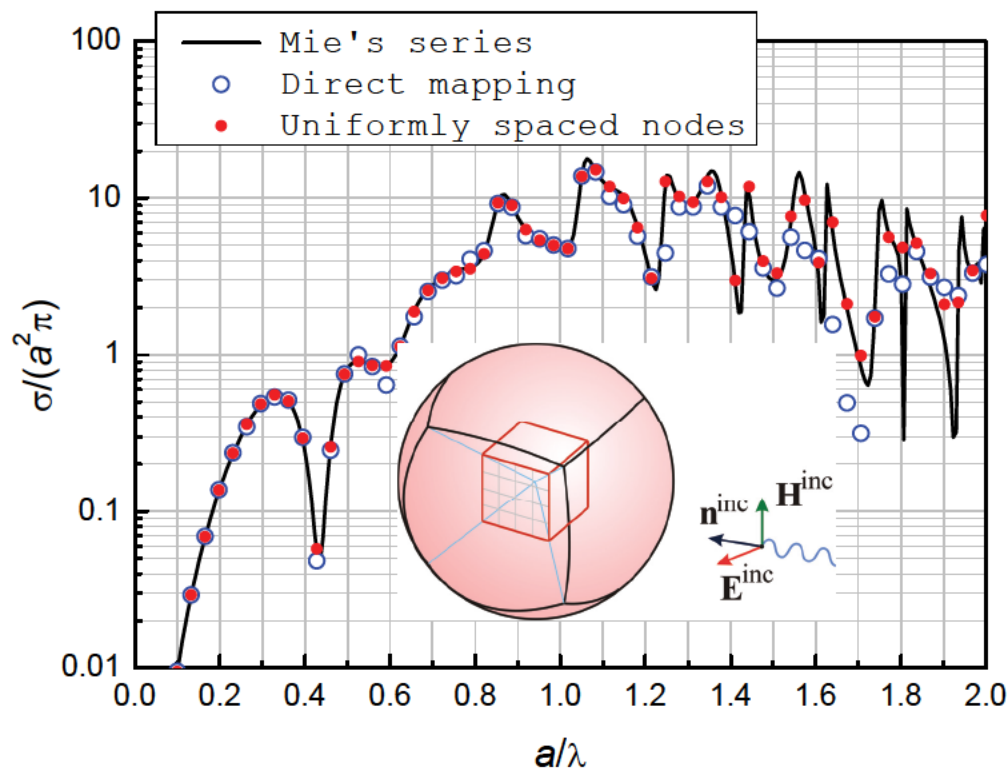


Fig. 2. Normalized monostatic RCS of a spherical dielectric ($\epsilon_r = 4$) scatterer (λ is the wavelength in the dielectric) computed by the higher order MoM-SIE technique using two geometrical models with different placements of interpolation nodes on Lagrange patches and by Mie's series (exact solution); mesh obtained by the cube-to-sphere mapping with uniformly spaced nodes is shown in the figure inset.

Accuracy improvement in the model with uniform nodes in the previous example is partially due to (i) more accurate geometrical representation of the spherical surface and (ii) better parametrization. The sole influence of the parametrization on the solution accuracy will generally vary with offset of the control points, frequency, adopted polynomial current approximation orders, integration accuracy, and on the

particular model being analyzed (e.g., if the edge effects are more or less pronounced), and hence it requires a thorough investigation. However, as an initial attempt to identify the sole influence of the parametrization on the solution accuracy, we consider here, as the second example, a simple metallic square plate scatterer of side length $a=1$ m illuminated by a plane wave with $E=1$ V/m parallel to a square edge (v -axis in the parent domain and x -axis in the child domain). In Fig. 3, we compare the RCS solutions and the surface current distributions (dominant, v -components) for the model with uniform nodes (simple bilinear quadrilateral, with $K_u = K_v = 1$) and a model with a fourth-order quadrilateral ($K_u = K_v = 4$) for which we offset the interpolation nodes in planes $v = \pm 0.5$ by ± 0.1 m, as shown in the bottom inset in Fig. 3. A significant difference in the current distributions can be observed, as well as a significantly more accurate RCS solution of the model with uniform nodes (when compared to a highly accurate hp -refined reference solution obtained by WIPL-D). (Note also the difference in the scales in the current distribution plots, which is by an order of magnitude, arising primarily due to pronounced edge effects in this example.)

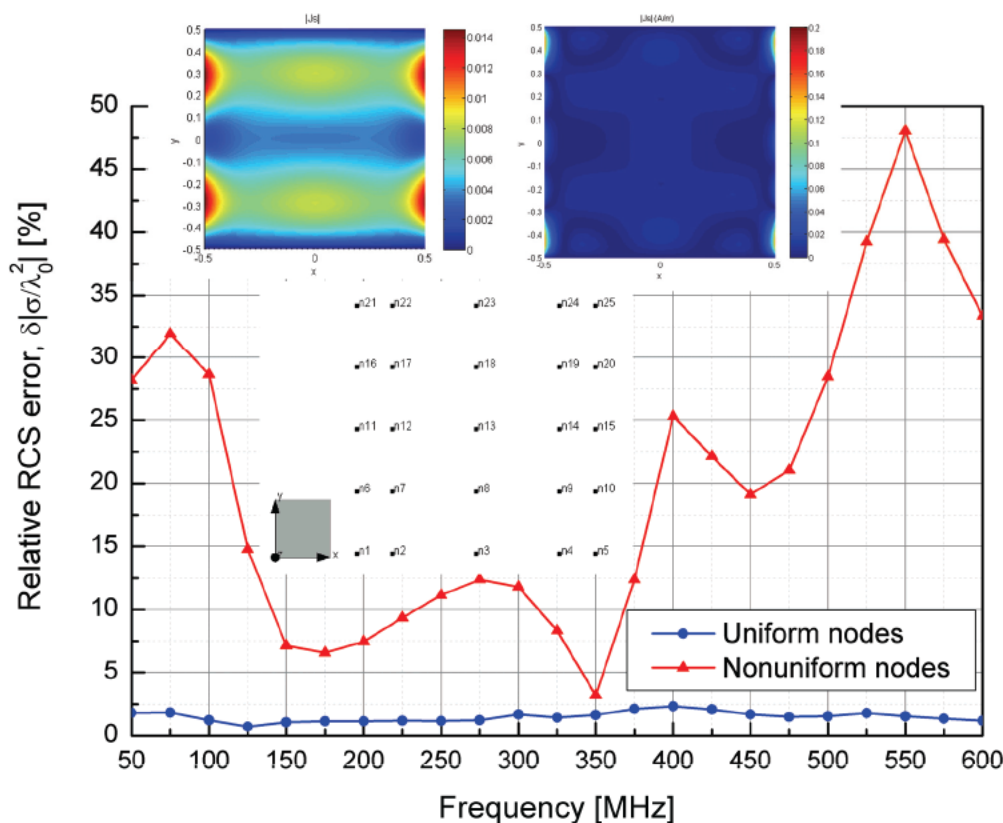


Fig. 3. Comparisons of the relative RCS errors and surface current distributions for a metallic square plate scatterer obtained by higher order MoM-SIE models with uniform and nonuniform distributions of geometrical interpolation nodes.

As the last example, we perform a higher order MoM-SIE RCS analysis of the NASA almond, a benchmark target established by the Electromagnetic Code Consortium (EMCC), at a frequency of $f=7$ GHz [12]. The model of the almond, shown in Fig. 4, is built (based on geometrical equations from [12]) using 56 quadrilateral curved elements with $K_u = K_v = 2$ and ensuring a nearly uniform distribution of interpolation nodes (there are a total of 226 nodes). We observe in Fig. 5 an excellent convergence of higher order MoM-SIE results with p -refinement, namely, with increasing the orders of basis functions from $N_u = N_v = 2$ to $N_u = N_v = 7$, while keeping the orders of Gauss-Legendre integration formulas in

computations of generalized Galerkin impedances and potential and field integrals to be $NGL_u = NGL_v = N_u + 2 = N_v + 2$ in all cases, as well as an excellent agreement of results for $N_u, N_v \geq 4$ with measurements.

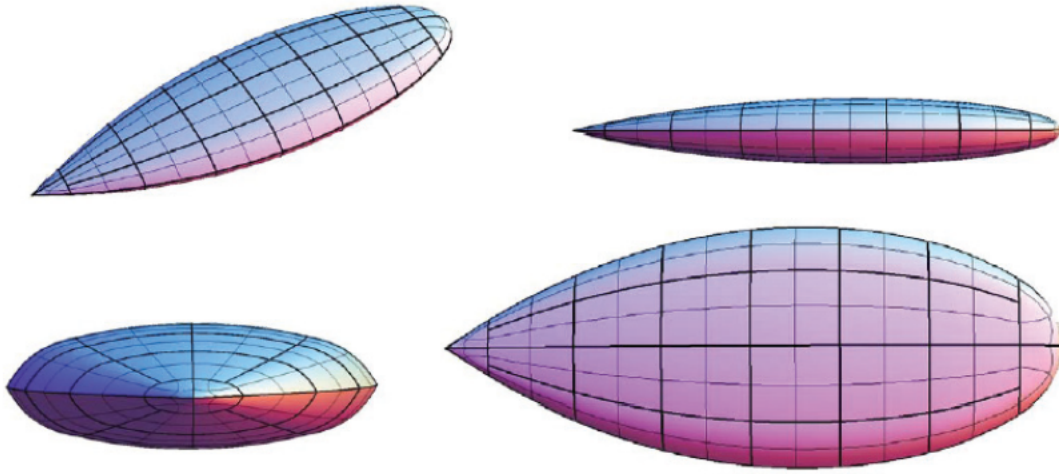


Fig. 4. Higher order geometrical model of the NASA metallic almond [12] using 56 curved quadrilateral elements with a nearly uniform distribution of interpolation nodes.

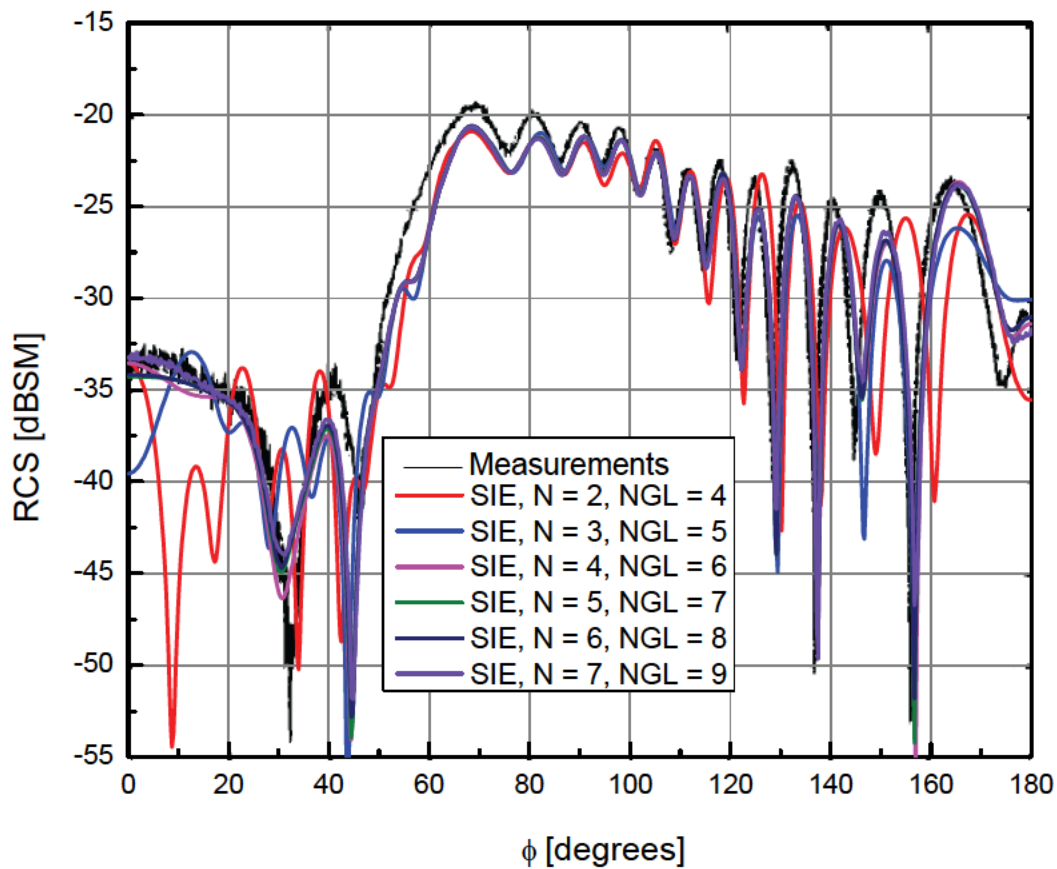


Fig. 5. Higher order MoM-SIE RCS analysis of the NASA almond at $f = 7$ GHz for the HH polarization using the geometrical model in Fig. 4: p -refinement and comparison with experimental results [12].

5. Conclusions

This paper has presented accurate and efficient geometrical models for higher order MoM-SIE analysis using uniformly distributed Lagrange geometrical interpolation nodes on curved and large elements combined with high-order (p -refined) basis functions for the approximation of electric and magnetic surface currents. Examples have included RCS analysis of a spherical dielectric scatterer using two geometrical models with different placements of interpolation nodes on Lagrange patches, evaluation of the RCS and current distributions for a metallic square plate scatterer obtained by higher order models with uniform and nonuniform distributions of geometrical interpolation nodes, and RCS analysis of a higher order model of the NASA metallic almond using curved quadrilateral elements with a nearly uniform distribution of geometrical interpolation nodes. Examples at the conference will also include higher order FEM and hybrid models.

References

- [1] B. M. Notaroš, "Higher order frequency-domain computational electromagnetics," Special Issue on Large and Multiscale Computational Electromagnetics, *IEEE Transactions on Antennas and Propagation*, Vol. 56, No. 8, pp. 2251-2276, August 2008.
- [2] B. M. Kolundzija and A. R. Djordjević "Electromagnetic Modeling of Composite Metallic and Dielectric Structures", Norwood, MA: *Artech House*, 2002.
- [3] J. M. Jin, K. C. Donepudi, J. Liu, G. Kang, J. M. Song, and W. C. Chew, "High-Order Methods in Computational Electromagnetics," in *Fast and Efficient Algorithms in Computational Electromagnetics*, W. C. Chew *et al*, Ed. Norwood, MA: *Artech House*, 2001.
- [4] R. D. Graglia, D. R. Wilton, and A. F. Peterson, "Higher order interpolatory vector bases for computational electromagnetics", *IEEE Trans. on Antennas and Propagation*, Vol. 45, No. 3, pp. 329-342, March 1997.
- [5] J. P. Swartz and D. B. Davidson, "Curvilinear vector finite elements using a set of hierarchical basis functions," *IEEE Transactions on Antennas and Propagation*, vol. 55, no. 2, pp. 440-446, February 2007.
- [6] W. Ding and G. Wang, "Treatment of singular integrals on generalized curvilinear parametric quadrilaterals in higher order method of moments," *IEEE Antennas and Wireless Propagation Letters*, vol. 8, pp. 1310-1313, 2009.
- [7] E. Martini, G. Pelosi, and S. Selleri, "A hybrid finite-element-modal-expansion method with a new type of curvilinear mapping for the analysis of microwave passive devices," *IEEE Transactions on Microwave Theory and Techniques*, vol. 51, pp. 1712-1717, June 2003.
- [8] L. Valle, F. Rivas, and M. F. Cátedra, "Combining the moment method with geometrical modelling by NURBS surfaces and Bézier patches," *IEEE Transactions on Antennas and Propagation*, vol.42, no.3, pp. 373- 381, March 1994.
- [9] M. Djordjevic and B. M. Notaros, "Double higher order method of moments for surface integral equation modeling of metallic and dielectric antennas and scatterers," *IEEE Transactions on Antennas and Propagation*, Vol. 52, No. 8, pp. 2118-2129, August 2004.
- [10] M. M. Ilic and B. M. Notaros, "Higher order hierarchical curved hexahedral vector finite elements for electromagnetic modeling," *IEEE Transactions on Microwave Theory and Techniques*, vol. 51, no. 3, pp. 1026-1033, March 2003.
- [11] M. M. Ilić, M. Djordjević, A. Ž. Ilić, and B. M. Notaroš, "Higher order hybrid FEM-MoM technique for analysis of antennas and scatterers," *IEEE Transactions on Antennas and Propagation*, vol. 57, pp. 1452-1460, May 2009.
- [12] A. C. Woo, H. T. G. Wang, M. J. Schuh, and M. L. Sanders, "Benchmark radar targets for the validation of computational electromagnetics programs," *IEEE Antennas and Propagation Magazine*, vol. 35, no. 1, pp. 84-89, February 1993.

Acceleration of Higher Order FEM Matrix Filling by OpenMP Parallelization of Volume Integrations

Slobodan V. Savić, Anđelija Ž. Ilić, *Member, IEEE*, Branislav M. Notaroš, *Senior Member, IEEE*, and Milan M. Ilić, *Member, IEEE*

Abstract — Parallelization of time-consuming volume integrations in the matrix filling is performed using OpenMP to provide a smooth transition of a higher order finite element method (FEM) code for electromagnetic analysis to the multi-core hardware architecture. In the process, the carefully constructed original computational scheme suited to maximally avoid the redundant computations in the higher order FEM is not affected. The results, in analysis of an electrically large dielectric scatterer, demonstrate acceleration of up to 2.28 times in a four-thread architecture.

Keywords — finite element methods, higher order methods, OpenMP, parallelization

I. INTRODUCTION

COMPUTER aided engineering is the mainstream of the scientific research in the various fields, and particularly in electromagnetics (EM), where the finite element method (FEM) has been well established as one of the most powerful, versatile, robust, and flexible numerical methods. The scale of the simulated models and the demands for computer resources, however, constantly increase, whereas the hardware improves not by operating at higher clock frequency, but by increasing the number of cores, when transitioning from one generation to the next. Hence, the existing computational algorithms have to be changed in order to take advantages of the new hardware architectures.

When developing a new (or adapting an existing) algorithm, decisions have to be made regarding both the selection of hardware (many-core architectures sacrifice the sequential performance of a single core within the processor in order to increase the parallel throughput for streaming workflow, and multi-core architectures sacrifice the parallel computational throughput of the entire processor in order to increase the performance of single

cores for low-latency computation [1]) and algorithms. Although the traditional first-order (or low-order) FEM algorithms are inherently parallelizable, because most of the time-consuming operations are local in character and can be done in parallel for several elements at a time (at the global level), this is not necessarily true for the higher order FEM algorithms (with orders significantly higher than two), where the adjacent elements share many identical unknowns. In speeding up such higher order FEM algorithms in the sequential (single-core) fashion, a lot of attention has been paid to avoiding redundant computations, thus enhancing the connections between the elements and reducing the possibility of straightforward parallelization. Although the higher order FEM algorithms have recently become very popular (they significantly reduce the required number of unknowns for a given problem, offer p - and hp -refinements, and reduce the dispersion error), the parallelization problem of such algorithms has not been sufficiently well addressed even though it is known that the algorithms being optimal for low-order (polynomial) expansion could be very inefficient for high-order expansions when computations are more closely coupled at the individual element, and the parallelization is performed at the element level rather than the global level [2].

In this paper we address the adaptation of the existing higher order FEM algorithm for a multi-core architecture by implementing parallelization of only the higher order volume integrations using OpenMP, and without influencing the nonredundant computation of the matrix elements. Since numerical integration takes up most of the matrix filling time [3], this part of our higher order FEM code is parallelized first as a prelude to a full parallelization of all phases in the future.

II. THEORY AND NUMERICAL RESULTS

In our higher order FEM [4], the FEM domain is truncated by means of unknown electric and magnetic surface currents of densities \mathbf{J}_S and \mathbf{J}_{mS} , respectively, that are evaluated by the MoM/SIE [5], giving rise to a hybrid higher order FEM-MoM technique [6].

To illustrate the effects of parallelization of the FEM volume integrations, we consider a lossless homogeneous cubical dielectric ($\epsilon_r = 2.25$) scatterer of side length a , as shown in the inset of Fig. 1. The scatterer is situated in free space and illuminated by plane wave incident

This work was supported by the Serbian Ministry of Education, Science and Technological Development under grant TR-32005 and by the National Science Foundation under grants ECCS-1002385.

Slobodan V. Savić is with the School of Electrical Engineering, University of Belgrade, Belgrade, Serbia (e-mail: ssavic@etf.rs).

Anđelija Ž. Ilić is with the Laboratory of Physics 010, Vinča Institute of Nuclear Sciences, Belgrade, Serbia (e-mail: andjelija.ili@ieee.org).

Branislav M. Notaroš is with the ECE Department, Colorado State University, Fort Collins, USA (e-mail: notaros@colostate.edu).

Milan M. Ilić is with the School of Electrical Engineering, University of Belgrade, Belgrade, Serbia and also with the ECE Department, Colorado State University, Fort Collins, USA (e-mail: milanilic@etf.rs).

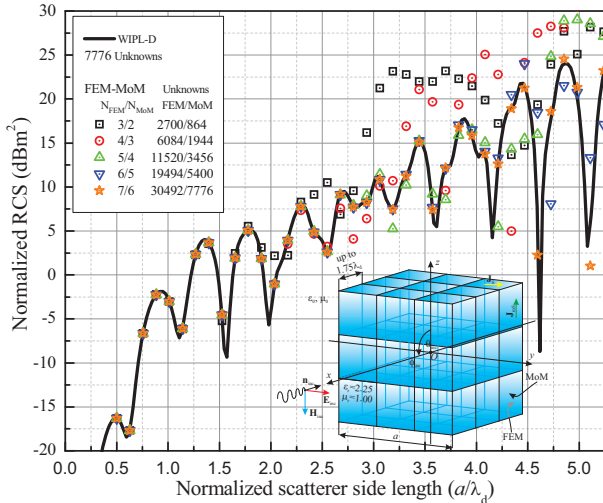


Fig. 1. Normalized monostatic radar cross section of the cubical scatterer from the inset.

normal to one of the scatterer faces ($\theta_{\text{inc}} = 90^\circ$ and $\phi_{\text{inc}} = 0^\circ$). In accordance with the conclusions from [7], the dielectric scatterer is geometrically modeled by 27 identical hexahedral finite elements (bricks) [4] closed by 54 identical MoM quadrilateral patches [5].

Shown in Fig. 1 is the normalized (to λ_0^2) monostatic radar cross section (RCS), as a function of a/λ_d , λ_0 and λ_d being the wavelength in free space and (scatterer) dielectric, respectively. The results are obtained for various orders of the field approximation polynomials (from $N_{\text{FEM}} = 3$ to 7) in the higher order FEM model, and for various polynomial orders of the electric and magnetic current expansions (from $N_{\text{MoM}} = 2$ to 6) in the higher order MoM model (p -refinement). Numbers of integration points in Gauss-Legendre integration formulas are $N_{\text{GL}_{\text{FEM}/\text{MoM}}} = N_{\text{FEM}/\text{MoM}} + 4$, in FEM and MoM technique respectively, as shown in [7]. The results are compared with the pure MoM solution obtained by the commercial software tool WIPL-D (reference). We observe a very good convergence of the results obtained by the hybrid higher order FEM-MoM technique with p -refinement (number of FEM/MoM unknowns is shown in the figure legend). We also observe that FEM-MoM results for $N_{\text{FEM}} = 7$, $N_{\text{MoM}} = 6$ match the reference results almost perfectly in the entire analyzed frequency range (side lengths of the FEM/MoM elements are up to $1.75 \lambda_d$), and this model will be used to estimate the FEM code matrix filling acceleration.

FEM matrix filling times obtained on a Windows 7 PC with Intel® Core™ i5-760 CPU (supporting 4 threads) @ 2.8 GHz and with 8 GB of RAM, as a function of number of used CPU threads, are shown in Fig. 2. Thread control was performed in two manners; (a) by the operating system (OS) through process affinity in the Task Manager, and (b) directly by the OpenMP in the Fortran code.

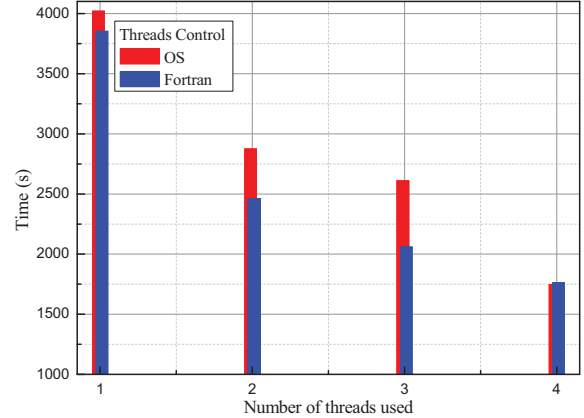


Fig. 2. FEM matrix filling times for different number of used CPU threads code.

We can conclude from the figure that significant acceleration (up to 2.28 times with four threads) can be achieved by parallelizing the FEM volume integrations alone in this example. In addition, it appears that it is generally more efficient to perform the thread control directly by the code, rather than by the OS.

III. CONCLUSIONS

To provide the smooth transition of the higher order FEM codes in EM to multi-core architectures, we have parallelized the volume integrations in the matrix filling using OpenMP. The original computational scheme, suited to maximally avoid the redundant computations in the higher order FEM, is hence not affected. The results, in analyzing an electrically large dielectric scatterer, have shown up to 2.28 times acceleration in a four-thread architecture. This ongoing effort will in the future include more sophisticated parallelization recipes, specially designed for the higher order FEM algorithms.

REFERENCES

- [1] G. R. Markall, A. Slemmer, D. A. Ham, P. H. J. Kelly, C. D. Cantwell, and S. J. Sherwin, "Finite element assembly strategies on multi- and many-core architectures," *Int. J. Numer. Meth. Fluids*, pp. 1-18, January 19 2012.
- [2] P. E. J. Vos, S. J. Sherwin, and R. M. Kirby, "From h to p efficiently: implementing finite and spectral/hp element methods to achieve optimal performance for low- and high-order discretisations," *J. Comput. Phys.*, vol. 229, pp. 5161-5181, July 1 2010.
- [3] A. Dziekonski, P. Sypek, A. Lamecki, and M. Mrozowski, "Finite element matrix generation on a gpu," *Progress In Electromagnetics Research*, vol. 128, pp. 249-265, May 31 2012.
- [4] M. M. Ilić and B. M. Notaroš, "Higher order hierarchical curved hexahedral vector finite elements for electromagnetic modeling," *IEEE Transactions on Microwave Theory and Techniques*, vol. 51, pp. 1026-1033, March 2003.
- [5] M. Djordjević and B. M. Notaroš, "Double higher order method of moments for surface integral equation modeling of metallic and dielectric antennas and scatterers," *IEEE Transactions on Antennas and Propagation*, vol. 52, pp. 2118-2129, August 2004.
- [6] M. M. Ilić, M. Djordjević, A. Ž. Ilić, and B. M. Notaroš, "Higher order hybrid FEM-MoM technique for analysis of antennas and scatterers," *IEEE Transactions on Antennas and Propagation*, vol. 57, pp. 1452-1460, May 2009.
- [7] E. M. Klopff, N. J. Šekeljčić, M. M. Ilić, and B. M. Notaroš, "Optimal modeling parameters for higher order MoM-SIE and FEM-MoM electromagnetic simulations," *IEEE Transactions on Antennas and Propagation*, vol. 60, pp. 2790-2801, June 2012.

Hybrid Higher Order FEM-MoM Analysis of Continuously Inhomogeneous Electromagnetic Scatterers

Milan M. Ilić, *Member, IEEE*, Slobodan V. Savić, Andjelija Ž Ilić, *Member, IEEE*, and Branislav M. Notaroš, *Senior Member, IEEE*

Abstract — A novel higher order entire-domain finite element technique is presented for accurate and efficient full-wave three-dimensional analysis of electromagnetic structures with continuously inhomogeneous material regions, using large (up to about two wavelengths on a side) generalized curved hierarchical curl-conforming hexahedral vector finite elements (of arbitrary geometrical and field-approximation orders) that allow continuous change of medium parameters throughout their volumes. The results demonstrate considerable reductions in both number of unknowns and computation time of the entire-domain FEM modeling of continuously inhomogeneous materials over piecewise homogeneous models.

Keywords — Computer-aided analysis, electromagnetic analysis, electromagnetic scattering, finite element method, higher order elements, inhomogeneous media, method of moments.

I. INTRODUCTION

IN electromagnetics (EM), the finite element method (FEM) in its various forms and implementations [1]-[4] has been effectively used in full-wave three-dimensional (3D) computations based on discretizing partial differential equations for quite some time. A tremendous amount of effort has been invested in the research of the FEM technique in the past 4 decades, making FEM methodologies and techniques extremely powerful and universally general numerical tools for solving a broad range of both closed-region (e.g., waveguide and cavity) and open-region (e.g., antenna and scattering) problems. In the case of open-region problems, hybrid finite element-boundary integral (FE-BI) technique is used for the exact truncation of the unbounded spatial domain [5]-[6].

This work was supported by the Serbian Ministry of Science and Technological Development under grant ET-11021 and by the National Science Foundation under grants ECCS-0647380 and ECCS-0650719.

Milan M. Ilić is with the School of Electrical Engineering, University of Belgrade, Bulevar kralja Aleksandra 73, 11120 Belgrade, Serbia; (phone: 381-11-3370101; e-mail: milanilic@etf.rs).

Slobodan V. Savić is with the School of Electrical Engineering, University of Belgrade, Bulevar kralja Aleksandra 73, 11120 Belgrade, Serbia; (e-mail: milanilic@etf.rs).

Andjelija Ž. Ilić is with the Vinča Institute of Nuclear Sciences, Laboratory of Physics 010, P.O. Box 522, 11001 Belgrade, Serbia; (e-mail: andjelijailic@ieee.org).

Branislav M. Notaroš is with the ECE Department, Colorado State University, 1373 Campus Delivery, Fort Collins, CO 80523-1373, USA; (e-mail: notaros@colostate.edu).

For modeling and analyzing structures that contain inhomogeneous and complex electromagnetic materials, FEM technique is very efficient and well established as a method of choice. In practically every FEM technique, within a really abundant and impressive body of work in the field, the theory is developed and FEM equations are derived taking advantage of the inherent ability of FEM to directly treat continuously inhomogeneous materials (complex permittivity and permeability of the media can be arbitrary functions, or tensors, of spatial coordinates, e.g., $\epsilon(\mathbf{r})$ and $\mu(\mathbf{r})$, with \mathbf{r} standing for the position vector of a point in the adopted coordinate system). However, it appears that there are practically no papers on this subject, in which technique or code, that actually implements $\epsilon(\mathbf{r})$ and $\mu(\mathbf{r})$ as continuous space function within one finite element, and enables direct computation on finite elements that include arbitrary (continuously) inhomogeneous material, is presented. Instead, FEM computations are carried out on piecewise homogeneous approximate model of the inhomogeneous structure, with $\epsilon(\mathbf{r})$ and $\mu(\mathbf{r})$ replaced by appropriate piecewise constant approximations. On the other hand, even from the geometrical modeling point of view, it is much simpler and faster to generate a model of the structure with a single (or a few) large continuously inhomogeneous elements than a mesh of a graded layered structure, which in many practical situations can dramatically reduce the time needed for the electromagnetic modeler to set up the problem and initially model the geometry, before any mesher [7] can be used to preprocess the data for the analysis.

Numerical modeling employing continuously inhomogeneous finite elements may find practical applications in analysis of a broad range of devices, systems, and phenomena in electromagnetics, including electromagnetic interaction with biological tissues and materials, absorbing coatings for reduction of radar cross sections of targets, scattering and diffraction from inhomogeneous dielectric lenses used for lens antennas and related structures.

For fully exploiting modeling flexibility of continuously inhomogeneous finite elements, these elements should be electrically large, which implies the use of higher order field expansions within the elements, as shown in our

preliminary results in [8]. Because the fields are approximated by low-order basis functions, when low-order FEM technique is used, the elements must be electrically very small (on the order of a tenth of the wavelength in each dimension). Subdivision of the structure using such elements results in a discretization of the permittivity and permeability profiles as well, so elements can be treated as homogeneous (i.e., their treatment as inhomogeneous would practically have no effect on the results). Within the higher order computational approach [9], on the other hand, higher order basis functions enable the use of electrically large geometrical elements (e.g., on the order of a wavelength in each dimension). We refer to the direct FEM computation on such elements as the entire-domain or large-domain analysis. Note that, in general, higher order FEM techniques [10]-[14] can greatly reduce the number of unknowns for a given (homogeneous or inhomogeneous) problem and enhance the accuracy and efficiency of the analysis when compared with low-order solutions.

II. THEORY AND NUMERICAL IMPLEMENTATION

Consider an electromagnetic structure that contains some continuously inhomogeneous material regions, as shown in Fig. 1. In our analysis method, the computation domain is first tessellated using higher order geometrical elements in the form of Lagrange-type generalized curved parametric hexahedra of arbitrary geometrical orders $K_u, K_v,$ and K_w ($K_u, K_v, K_w \geq 1$), analytically described as [10]

$$\mathbf{r}(u, v, w) = \sum_{i=0}^{K_u} \sum_{j=0}^{K_v} \sum_{k=0}^{K_w} \mathbf{r}_{ijk} L_i^{K_u}(u) L_j^{K_v}(v) L_k^{K_w}(w), \quad (1)$$

$$L_i^{K_u}(u) = \prod_{l=0, l \neq i}^{K_u} \frac{u - u_l}{u_i - u_l}, \quad -1 \leq u, v, w \leq 1,$$

where $\mathbf{r}_{ijk} = \mathbf{r}(u_i, v_j, w_k)$ are position vectors of interpolation nodes, $L_i^{K_u}$ represent Lagrange interpolation polynomials, and similar for $L_j^{K_v}(v)$ and $L_k^{K_w}$. Equation (1) defines a mapping from a cubical parent domain to the generalized hexahedron, as illustrated in Fig. 2.

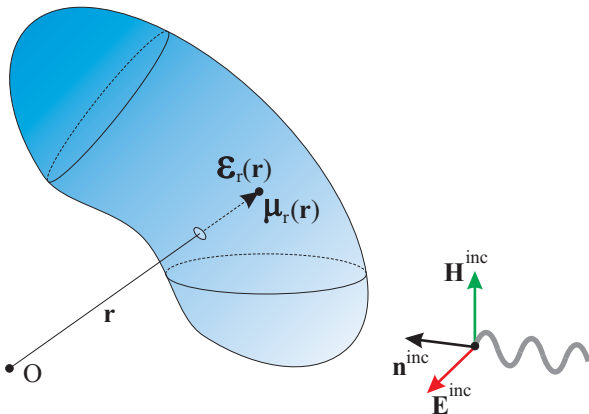


Fig. 1. Electromagnetic structure with continuously inhomogeneous material.

The electric field in the element, $\mathbf{E}(u, v, w)$, is approximated by means of curl-conforming hierarchical polynomial vector basis functions given in [10]; let us denote the functions by $\mathbf{f}(u, v, w)$, and the respective arbitrary field-approximation orders of the polynomial by $N_u, N_v,$ and N_w ($N_u, N_v, N_w \geq 1$). Higher order hierarchical basis functions with improved orthogonality and conditioning properties constructed from Legendre polynomials [12] may also be implemented.

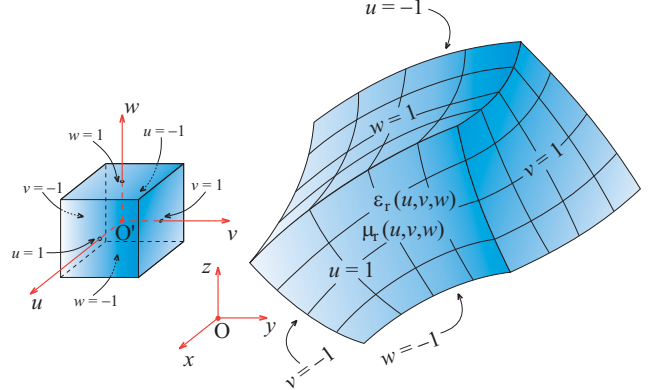


Fig. 2. Generalized curved parametric hexahedron defined by (1), with continuous variation of medium parameters given by (2); Cubical parent domain is also shown.

Continuous variation of medium parameters in the computation model can be implemented in different ways. In our technique, however, we choose to take full advantage of the already developed Lagrange interpolating scheme for defining element spatial coordinates in (1), which can be conveniently reused to govern the change of both the complex relative permittivity and permeability, ϵ_r and μ_r , within the element shown in Fig. 2, as follows:

$$\epsilon_r(u, v, w) = \sum_{i=0}^{K_u} \sum_{j=0}^{K_v} \sum_{k=0}^{K_w} \epsilon_{r,ijk} L_i^{K_u}(u) L_j^{K_v}(v) L_k^{K_w}(w), \quad (2)$$

$$-1 \leq u, v, w \leq 1,$$

where $\epsilon_{r,ijk} = \epsilon_r(u_i, v_j, w_k)$ are the relative permittivity values at the point defined by position vectors of spatial interpolation nodes, \mathbf{r}_{ijk} , and similarly for μ_r . With such representation of material, we then solve for the unknown field coefficients by substituting the field expansion $\mathbf{E}(u, v, w)$ in the curl-curl electric-field vector wave equation [10], which reads:

$$\nabla \times \mu_r^{-1}(u, v, w) \nabla \times \mathbf{E}(u, v, w) - k_0^2 \epsilon_r(u, v, w) \mathbf{E}(u, v, w) = 0, \quad (3)$$

where $k_0 = \omega \sqrt{\epsilon_0 \mu_0}$ stands for the free-space wave number. A standard Galerkin weak-form discretization of (3) yields:

$$\begin{aligned}
& \int_V \mu_r^{-1}(u, v, w) [\nabla \times \mathbf{f}_t(u, v, w)] \cdot [\nabla \times \mathbf{E}(u, v, w)] dV \\
& - k_0^2 \int_V \epsilon_r(u, v, w) \mathbf{f}_t(u, v, w) \cdot \mathbf{E}(u, v, w) dV \\
& = - \oint_S \mu_r^{-1}(u, v, w) \mathbf{f}_t(u, v, w) \cdot \mathbf{n} \times [\nabla \times \mathbf{E}(u, v, w)] dS,
\end{aligned} \tag{4}$$

where V is the volume of the element, bounded by the surface S , \mathbf{n} is the outward unit normal on S , and \mathbf{f}_t are testing functions (the same as basis functions). Once the field coefficients are found, all quantities of interest for the analysis are obtained in a straightforward manner.

III. RESULTS AND DISCUSSION

As an example of entire-domain FEM analysis of an open-region continuously inhomogeneous structure, consider a lossless cubical dielectric ($\mu_r = 1$) scatterer, of side length $2a$, and a linear variation of ϵ_r from $\epsilon_r = 1$ at the surface to $\epsilon_r = 6$ at the center of the cube, as shown in Fig. 3. The scatterer is situated in free space and illuminated by a uniform plane wave incident normal to one face of the scatterer, as shown in Fig. 3. The FEM domain is truncated at the cube faces by means of unknown electric and magnetic surface currents of densities \mathbf{J}_S and \mathbf{J}_{mS} , respectively, that are evaluated by the MoM/SIE, giving rise to a hybrid higher order FEM-MoM solution [6].

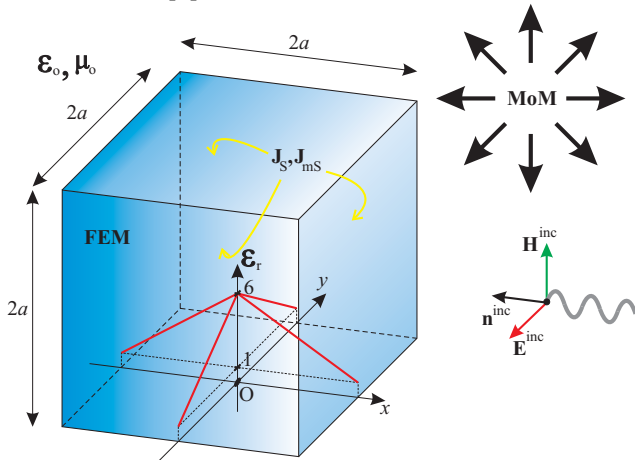


Fig. 3. FEM-MoM analysis of a lossless continuously inhomogeneous cubical dielectric scatterer. Single-element FEM domain with linear variation of permittivity.

To represent this permittivity variation using expansions in (2), the cube is modeled by 7 trilinear hexahedral FEM elements of the first geometrical order, namely, by one small cube-like hexahedral, $\frac{a}{10}$ in length, at the center and 6 “cushion”-like hexahedra between the central cube and the scatterer surface, onto which 6 bilinear quadrilateral MoM patches are attached, as shown in Fig. 4. The field/current approximation orders are 5 for all FEM “cushions” and 4 for the central FEM element and all MoM patches, in all directions, resulting in 2560 FEM and 354 MoM unknowns, and a total of 339 s of simulation time for 35 frequencies.

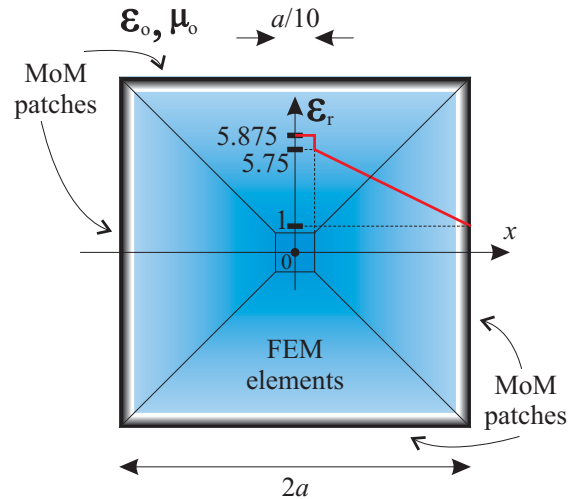


Fig. 4. Model of a lossless, continuously inhomogeneous cubical dielectric scatterer made of 7 FEM elements and 6 quadrilateral MoM patches.

To both validate the continuously inhomogeneous FEM-MoM model of the scatterer and evaluate its efficiency against piecewise homogeneous approximate model, the scattering results of the higher order FEM-MoM analysis using large FEM elements with continuously changing ϵ_r are compared with solution obtained by higher order FEM-MoM simulations of piecewise homogeneous approximate model of the structure in Fig. 4. Each of the 6 “cushions” of the continuous model are replaced, respectively by, $N_1 = 2, 3, 4,$ and 7 homogeneous thin “cushions” (plate-like layers), approximating the continuously inhomogeneous profile, which is illustrate in Fig. 5 for $N_1 = 4$. So, each plate-like layer in layered models is represented by 6 FEM elements of the first geometrical order. Field-approximation orders in these elements are 2 in the radial direction and 5 in transversal directions.

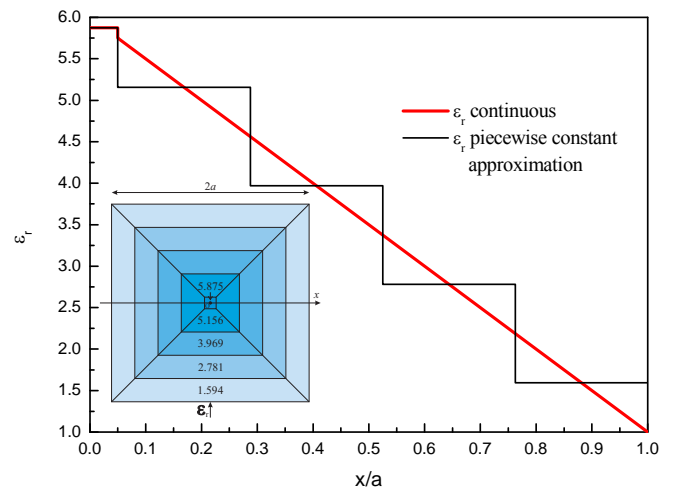


Fig. 5. Piecewise homogeneous approximate graded model ($N_1 = 4$) of the structure in Fig. 4, and piecewise constant approximation of relative permittivity profiles.

Shown in Fig. 6 is the normalized (to λ_0^2) monostatic radar cross section (RCS) of the cube (as a function of $\frac{a}{\lambda_0}$), λ_0 being the free space wavelength. We observe a monotonic convergence of the results obtained by the layered-FEM-MoM technique to those for the continuous-FEM-MoM model, as N_1 increases, as well as an excellent agreement between the 7-layer and continuous FEM-MoM solution (theoretically, only an infinite number of layers would give the exact solution to the problem in Fig. 3).

As an additional verification of the analysis, the 7-layer model is simulated using a higher order MoM technique based on the surface integral equation (SIE) approach (MoM/SIE technique) [14], as a reference solution, and an excellent agreement of these and the corresponding FEM-MoM results is observed for the 7-layer model.

We conclude from the data in the figure legend that the continuous material model is substantially more efficient than the layered analysis, namely, it is 34.16 times faster than the most accurate layered solution (for $N_1 = 7$), and 5.6 times reduction in the total number of unknowns is achieved.

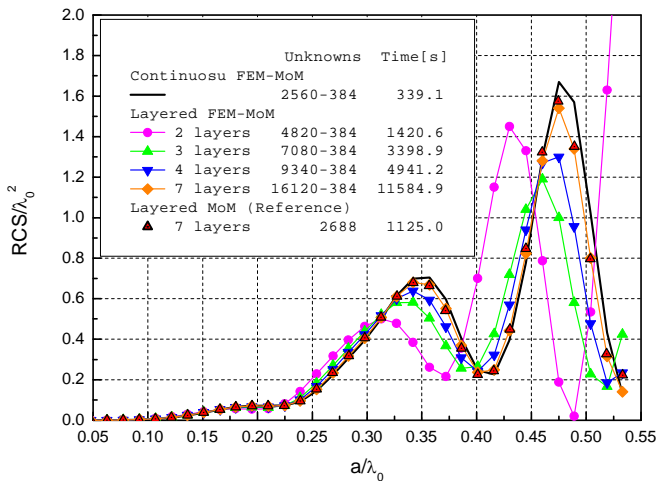


Fig. 6. Normalized monostatic radar cross section of the cubical scatterer in Fig. 3 (λ_0 is the free-space wavelength): results using the continuous-FEM-MoM, four different layered-FEM-MoM models, and reference MoM/SIE model.

All numerical results are obtained using Hewlett Packard EliteBook 8440p notebook computer with Intel i5-540 CPU running at 2.53 GHz and with 2 GB of RAM under Microsoft Windows 7 operating system.

IV. CONCLUSION

A novel higher order entire domain FEM technique for accurate and efficient full-wave 3D EM analysis using large (up to two wavelengths on a side) finite elements that allow continuous change of medium parameters throughout their volumes, has been presented. Lagrange-

type generalized curved parametric hexahedra of arbitrary geometrical orders with curl-conforming hierarchical polynomial vector basis functions of arbitrary field-approximation orders and Lagrange interpolation scheme for variations of medium parameters have been used.

The validity, accuracy, and efficiency of the new technique have been demonstrated through an example of EM scatterer with linearly varying permittivity of the dielectric. The example has shown that effective higher order FEM hexahedral meshes, constructed from a very small number of large finite elements with p -refined field distributions of high approximation orders, which is one of the strongest points of the higher order modeling paradigm, can be applied even in the presence of material inhomogeneities. High efficiency, and considerable reductions in both number of unknowns and computation time, of the entire-domain FEM modeling of continuously inhomogeneous material over piecewise homogeneous (layered) model, have been demonstrated.

REFERENCES

- [1] P. P. Silvester and R. L. Ferrari, *Finite Elements for Electrical Engineers*, 3rd ed., Cambridge University Press, 1996.
- [2] J. M. Jin, *The Finite Element Method in Electromagnetics*, 2nd ed., John Wiley & Sons, New York, 2002.
- [3] J. L. Volakis, A. Chatterjee, and L. C. Kempel, "Finite Element Method for Electromagnetics", *IEEE Press*, New York, 1998.
- [4] J. L. Volakis, K. Sertel, and B. C. Usner, *Frequency Domain Hybrid Finite Element Methods in Electromagnetics*, Morgan & Claypool Publishers, 2006.
- [5] J.-M. Jin, J. L. Volakis, and J. D. Collins, "A finite-element-boundary-integral method for scattering and radiation by two- and three-dimensional structures", *IEEE Antennas and Propagation Magazine*, Vol. 33, pp. 22-32, March 1991.
- [6] M. M. Ilić, M. Djordjević, A. Ž. Ilić, and B. M. Notaroš, "Higher Order Hybrid FEM-MoM Technique for Analysis of Antennas and Scatterers", submitted for *IEEE Transactions on Antennas and Propagation*, August 2008.
- [7] S. V. Savić, M. M. Ilić, B. M. Kolundžija, and B. M. Notaroš, "Efficient Modeling of Complex Electromagnetic Structures Based on the Novel Algorithm for Spatial Segmentation Using Hexahedral Finite Elements", submitted for *Telfor Journal*, 2010.
- [8] M. M. Ilić, A. Ž. Ilić, and B. M. Notaroš, "Continuously Inhomogeneous Higher Order Finite Elements for 3-D Electromagnetic Analysis", *IEEE Transaction on Antennas and Propagation*, Vol. 57, No. 9, pp. 2798-2802, September 2009.
- [9] B. M. Notaroš, "Higher Order Frequency-Domain Computational Electromagnetics", Special Issue on Large and Multiscale Computational Electromagnetics, *IEEE Transactions on Antennas and Propagation*, Vol. 56, No. 8, pp. 2251-2276, August 2008.
- [10] M. M. Ilić and B. M. Notaroš, "Higher order hierarchical curved hexahedral vector finite elements for electromagnetic modeling", *IEEE Transactions on Microwave Theory and Techniques*, Vol. 51, No. 3, pp. 1026-1033, March 2003.
- [11] M. M. Ilić, A. Ž. Ilić, and B. M. Notaroš, "Higher order large-domain FEM modeling of 3-D multipoint waveguide structures with arbitrary discontinuities", *IEEE Transactions on Microwave Theory and Techniques*, Vol. 52, No. 6, pp. 1608-1614, June 2004.
- [12] M. M. Ilić and B. M. Notaroš, "Higher order large-domain hierarchical FEM technique for electromagnetic modeling using Legendre basis functions on generalized hexahedra", *Electromagnetics*, Vol. 26, pp. 517-529, October 2006.
- [13] A. Ž. Ilić, S. V. Savić, M. M. Ilić, and B. M. Notaroš, "Analysis of Electromagnetic Scatterers Using Hybrid Higher Order FEM-MoM Technique", *Telfor Journal*, Vol. 1, No. 2, pp. 53-56, 2009.
- [14] B. M. Kolundžija, J. S. Ognjanović, T. K. Sarkar, D. S. Šumić, M. M. Paramentić, B. B. Janić, D. I. Olčan, D. V. Tošić, M. S. Tasić, *WIPL-D Microwave: Circuits and 3D EM Simulation of RF & Microwave Applications*, WIPL-D & Artech House, 2005.



STATIC MAGNETIC FIELD EFFECTS ON BIOCHEMICAL REACTIONS INVOLVING REACTIVE OXYGEN SPECIES

**Silvio R. De Luka¹, Andjelija Ž. Ilić², Saša Ćirković²,
Drago M. Djordjević¹, Jasna L. Ristić-Djurović²,
Alexander M. Trbovich¹**

1 School of Medicine, University of Belgrade, Belgrade, Serbia

2 Institute of Physics, University of Belgrade, Belgrade, Serbia

Reactive oxygen species (ROS) are toxic, short-lived, highly reactive by-products of normal physiological and metabolic cellular processes. The excessive production of ROS results in the damage of proteins, lipids, DNA and RNA. Aerobic cells possess antioxidant scavenging mechanisms that are protective against the ROS damage. These rely on the superoxide dismutase (SOD), catalase, glutathione peroxidase (GSHPx), vitamin E and vitamin C. The superoxide anion is converted to the hydrogen peroxide by the action of SOD: cytosolic (Cu/Zn-SOD), mitochondrial (Mn-SOD) or extracellular (Cu-SOD). Alterations in the expression of Cu/Zn-SOD have been implicated as a possible factor in several neurodegenerative disorders (Dröge 2002).

A static magnetic field (SMF) can, among other magnetobiological effects, induce changes in enzyme activity (Amara et al. 2006; Ghodbane et al. 2013). The metabolism of ROS becomes affected, with the reported effects to the lipid peroxidation, tissue damage, etc. whereas the strong and moderately strong SMF can act through the combination of several biophysical mechanisms, it is now accepted that the radical pair mechanism induces changes in the rates and yields of certain biochemical reactions under the influence of weak to moderate SMF (Rodgers 2009). These effects are strongly dependent on the SMF intensity, which could be a reason for the variability of the experimental results obtained by different research groups using various exposure setups.

Free radicals, including the reactive oxygen species, are ubiquitous in biology. Transition metal ions, the compounds of many proteins and enzymes, can act as radical species in biochemical reactions, enabling the modulation by the SMF of the redox cycles of metal-ion containing enzymes. This motivates the investigation not only into the exposure end effects such as the tissue damage, but also into the effects on the molecular level such as the distribution of various metals after exposure to the SMF. The current status of the observed effects to the organism is reviewed by putting into perspective the available data on the SMF induced effects as well as possible health implications.

References

- Dröge W. 2002. Free radicals in the physiological control of cell function. *Physiol Rev* 82: 47-95.
- Amara S. et al. 2006. Effects of subchronic exposure to static magnetic field on testicular function in rats. *Arch Med Res* 37(8):947-952.
- Ghodbane S. et al. 2013. Bioeffects of static magnetic fields: oxidative stress, genotoxic effects, and cancer studies. *BioMed Research International* 2013: 602987.
- Rodgers CT. 2009. Magnetic field effects in chemical systems. *Pure Appl Chem* 81(1): 19-43.



FOURTH INTERNATIONAL CONFERENCE ON RADIATION
AND APPLICATIONS IN VARIOUS FIELDS OF RESEARCH

May 23 - 27, 2016 | Niš | Serbia | rad-conference.org

BOOK OF ABSTRACTS



PUBLISHER: University of Niš, Faculty of Electronic Engineering
P.O.Box 73, 18000 Niš, Serbia
www.elfak.ni.ac.rs

FOR THE PUBLISHER: Prof. Dr. Dragan Mančić

EDITOR: Prof. Dr. Goran Ristić

COVER DESIGN: Vladan Nikolić, PhD

TECHNICAL EDITING: Vladan Nikolić, PhD and Sasa Trenčić, MA

PROOF-READING: Saša Trenčić, MA and Mila Aleksov, MA

PRINTED BY: Sven, Niš

PRINT RUN: 50 copies

The Fourth International Conference on Radiation and Applications in Various Fields of Research (RAD 2016) was financially supported by:

- Central European Initiative (CEI)
- Ministry of Education, Science and Technological Development of the Republic of Serbia

ISBN: 978-86-6125-160-3



EXPOSURE SYSTEM WITH HOMOGENEOUS STATIC AND ELF MAGNETIC FIELDS IN EXPERIMENTAL VOLUME

**Slavica Gajić¹, Saša Ćirković², Jasna Ristić-Djurović²,
Andjelija Ilić², Drago Djordjević³, Vesna Spasić-Jokić⁴**

1 School of Electrical Engineering, University of Banja Luka, Banja Luka, Bosnia and Herzegovina

2 Institute of Physics, University of Belgrade, Belgrade, Serbia

3 School of Medicine, University of Belgrade, Belgrade, Serbia

4 Faculty of Technical Sciences, University of Novi Sad, Novi Sad, Serbia

The omnipresence of electromagnetic fields not only in human environment but all over the Earth raises questions about the positive or negative nature, extent, and threshold levels of influence of this non-ionizing radiation on living organisms. In particular, it has been shown that static, magnetic and extremely low frequency (ELF) electromagnetic fields have significant effects on the skeletal, immune, cardio-vascular, reproductive, as well as the central nervous system. The complexity of electromagnetic fields, i.e., their magnitude, direction, orientation, spatial as well as temporal dependence and gradients, along with requirements related to the specifics of biomedical experiments, e.g., uncertainty of sample positions in *in vivo* experiments, requirements related to experimental volume size and orientation, temperature, light, etc., impose a challenging task to biomedical researchers when describing and specifying their experimental conditions. An exposure system which provides a homogeneous field throughout the experimental volume significantly reduces ambiguities. With the aim to provide the field that will also be scalable and relatively strong within the experimental volume that is large enough for *in vivo* as well as *in vitro* experiments, we considered a solenoid. High homogeneity of the field was achieved with inner modifications of solenoid cross-section. The designed exposure system provides the field with the maximum magnitude of 165 mT and homogeneity of 2 % in the experimental volume with the size of 30 cm x 30 cm x 40 cm.

Convergence of Modal Electromagnetic Fields in a B-spline Finite Element Method

Miloš Davidović, Andjelija Ilić, Miodrag Tasić, Branislav Notaroš, and Milan Ilić

Abstract— Convergence of finite-element-method solutions for electric field distributions of resonant modes is discussed and analyzed in two canonical microwave cavity problems when B-splines are utilized for geometrical modeling of elements. While the analyzed problems, namely, those of a spherical cavity and a ridged cavity, respectively, are relatively simple, they still provide valuable benchmarks for novel numerical methods, allowing for early estimates of accuracy, efficiency, and convergence properties of the method. Furthermore, curved geometry (in the case of a spherical cavity) and geometry with reentrant corners (in the case of a ridged cavity) illustrate versatile and flexible uses of B-splines for geometrical modeling of solids.

Index Terms— microwave cavities; higher order finite element method; B-spline solid modeling; eigenfrequency; eigenfield.

I. INTRODUCTION

THE finite element method (FEM) is one of the most important numerical tools in modern electromagnetic (EM) engineering practice [1]. Recently, higher order methods have become the mainstream in computational electromagnetics due to their increased versatility, convergence, and efficiency [2]. However, success (or failure) of EM engineering projects will still often be strongly determined by proficiency of practicing engineers in adequate formulation of the problem, i.e., use of sufficient number of details during geometrical modeling and meshing, setting reasonable prescribed accuracy, and interpretation of obtained numerical results. It is worth underlining that geometry and field models need to satisfy very different set of constraints, i.e., geometry models must conform to currently available computer aided design (CAD) industry solutions and limitation of fabrication processes, whereas electromagnetic fields must satisfy Maxwell's equations and adequate boundary conditions. With this in mind, the B-spline method for efficient analysis

This work was supported by the Serbian Ministry of Education, Science, and Technological Development under grants ON171028 and TR-32005.

Miloš Davidović is with the Laboratory for radiation measurements 100, Vinča Institute, University of Belgrade, 11001 Belgrade, Serbia, (e-mail: davidovic@vinca.rs).

Andjelija Ilić is with the Innovation Center, School of Electrical Engineering, University of Belgrade 11120 Belgrade, Serbia (e-mail: andjelijailic@iee.org).

Miodrag Tasić is with the School of Electrical Engineering, University of Belgrade, 11120 Belgrade, Serbia (e-mail: tasic@etf.rs).

Branislav Notaroš is with the Department of Electrical and Computer Engineering, Colorado State University, Fort Collins, CO 80523-1373 USA (e-mail: notaros@colostate.edu).

Milan Ilić is with the School of Electrical Engineering, University of Belgrade, 11120 Belgrade, Serbia, and also with the Department of Electrical and Computer Engineering, Colorado State University, Fort Collins, CO 80523-1373 USA (e-mail: milanilic@etf.rs).

of three dimensional (3-D) microwave cavities, introduced in [3], enables completely independent higher order modeling of both geometry and electromagnetic fields; the geometry modeling is done using trivariate B-splines (thus being very compatible with current CAD industry practices), while the field modeling is done using hierarchical higher order polynomial vector basis functions [4] (thus enabling very accurate and efficient approximation of fields). The most often alternatives to B-spline geometrical modeling and parameterization of curvilinear higher order elements (adopted here) are polynomial parameterizations (e.g., Lagrange polynomials, Bézier curves) and rational polynomial functions (e.g., rational Bézier curves and non-uniform rational B-splines or NURBS) [5], [6], although the latter may require utilization of specialized quadrature rules and may be less stable.

In this paper, we revisit the B-spline FEM modeling introduced in [3] and give additional insight in the convergence of the modal field solutions. Section II of the paper presents the B-spline modeling of solids in general as well as details of solid modeling of spherical and ridged cavity in particular. In Section III, the FEM field-expansion basis functions are described. In Section IV, numerical results are discussed and practical conclusions about the modal field convergence are given.

II. B-SPLINE SOLID MODELING

Presentation in this Section mainly follows [3] regarding general B-spline solid modeling, with additional details on analyzed examples of the spherical and the ridged cavity.

A. Univariate B-splines

Since solid modeling requires utilization of trivariate splines, and they are defined using univariate splines, some basic univariate splines definitions are in place. Note however, that while univariate spline definitions that will be given below are constructive in nature, i.e., they describe one possible algorithm for construction of splines, it is more advisable to implement more stable and efficient algorithms [7]. We use the following recurrent formula to define the B-spline functions:

$$B_{i,1}(u) = 1, u_i \leq u \leq u_{i+1} \text{ and } B_{i,1}(u) = 0, \text{ elsewhere,}$$
$$B_{i,m}(u) = \frac{u - u_i}{u_{i+m-1} - u_i} B_{i,m-1}(u) + \frac{u_{i+m} - u}{u_{i+m} - u_{i+1}} B_{i+1,m-1}(u), m > 1 \quad (1)$$

where $0 \leq i \leq n$, $n > 0$, and $U = (u_0, u_1, \dots, u_{n+m})$ is a non-decreasing sequence of real numbers. U is called the knot vector of the corresponding spline family, and can be used to flexibly increase or decrease the number of splines and continuity of splines over knot vectors with multiplicities. Multiplicities, i.e., repetition of knots in knot vector, can

lead to non-defined terms in (1), and if division by zero should occur when algorithm in (1) is followed, that term is replaced by zero. The function $B_{i,m}(u)$ is called the i -th B-spline of order m and degree $m-1$ with respect to the knot vector U . The following equations hold for a standard clamped uniform knot vector:

$$\begin{aligned} u_i &= 0, 0 \leq i \leq m-1, & u_i &= i-m+1, m \leq i \leq n, & \text{and} \\ u_i &= n-m+2, n+1 \leq i \leq n+m, \end{aligned} \quad (2)$$

where the term ‘‘uniform’’ refers to uniform spacing between internal knots, and the term ‘‘clamped’’ is due to end knot multiplicities.

B. Trivariate Splines and Hexahedron Parameterization

Using previously defined univariate B-splines, we can define a parametric hexahedron introducing a mapping $\mathbf{r} : (u, v, w) \rightarrow (x, y, z)$, $(u, v, w) \in [-1, 1] \times [-1, 1] \times [-1, 1]$ (cubical parent domain), such that it is interpolatory at the specified points of the global Cartesian space. To simplify the parameterization (without loss of generality) we employ the same order of B-splines ($m_u = m_v = m_w = m$) and the same knot vectors in all directions. A point within a hexahedron is thus defined by

$$\mathbf{r}(u, v, w) = \sum_{i,j,k=0}^n B_{i,m}(u)B_{j,m}(v)B_{k,m}(w) \mathbf{C}_{i,j,k}. \quad (3)$$

where $B_{i,m}, B_{j,m}, B_{k,m}$ are the splines over the same knot vector and $\mathbf{C}_{i,j,k}$ are the position vectors of the control points, found by solving the following system of equations:

$$\mathbf{r}_l = \sum_{i,j,k=0}^n B_{i,m}(u^l)B_{j,m}(v^l)B_{k,m}(w^l) \mathbf{C}_{i,j,k}, l = 1, \dots, K, \quad (4)$$

where $K = (n+1)^3$, and with \mathbf{r}_l and (u^l, v^l, w^l) being the (global) position-vectors of the interpolation points of the solid and their (local) parametric coordinates, respectively. Note that other parameterization formulations are also possible (but slightly less simple). For example, (4) can be modified to include various additional conditions, such as prescribed tangent at certain points, etc. The choice of interpolation points and a knot vector depends on the particular solid that needs to be parameterized, and will be presented next.

C. Solid Modeling of the Spherical and Ridged cavity

Spherical cavity can be modeled as a solid in a number of ways (even when restriction to B-spline solid modeling is made). Note however, that utilization of polynomial models (or piece-wise polynomial) models is preferred, since rational functions would require specialized quadrature algorithms. We opted for the method described in previous section, with the choice of parametric and Cartesian points given by a simple analytical mapping [3]. This way, it is possible to have tunable geometrical accuracy, which is very important, especially when doing pointwise comparisons of the field quantities. Two solid spline models were used for the cavity, a more ‘‘crude’’ model, having only 125 interpolation points ($n=4$), and geometrically refined model, having 1,000 interpolation points ($n=9$).

Fig. 1 shows the spline functions used in the first model

of the spherical cavity and parametric coordinate lines in the $w=0$ cut.

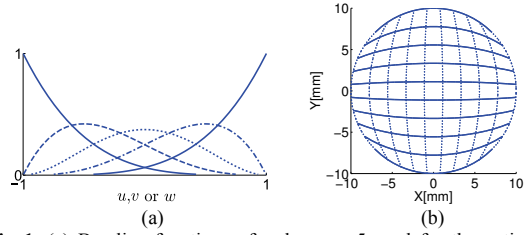


Fig. 1. (a) B-spline functions of order $m = 5$ used for the entire-domain modeling of a spherical cavity with the flat knot vector $(-1,1)$ and (b) u - v coordinate lines in the $w = 0$ cut.

Note that both models are very precise and that visual inspection would not reveal any difference between the two. However, as we will show, eigenfield calculations are very sensitive and will reveal great differences between the two models.

Geometrical modeling of the ridged cavity is significantly simpler, partly because the cavity is swept geometry. Since, for simplicity, we use the same spline family in all three parametric directions, and 4 points are needed to describe the ridge, we will need a total of $4^3 = 64$ interpolation points. Fig. 2 shows the interpolation points in one w -cut and spline the family used in all three parametric directions.

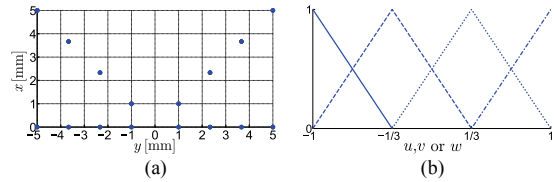


Fig. 2. (a) Interpolation points in one w -cut and (b) B-spline family adopted for parameterization of the ridged cavity.

These two examples clearly show flexibility of B-spline modeling, as both arbitrary order and arbitrary number of functions can be used along a parametric direction.

III. FIELD EXPANSION

Approximation of electric field is given (within each hexahedral element) as:

$$\mathbf{E}^e = \sum_{l=1}^{N^e} \gamma_l^e \mathbf{f}_l^e, \quad (5)$$

where \mathbf{f}_l are higher order vector basis functions with a total of N^e unknown field-distribution coefficients γ_l in the element. The basis functions are curl-conforming hierarchical polynomials of arbitrary field-approximation orders N_u^e, N_v^e , and N_w^e ($N_u^e, N_v^e, N_w^e \geq 1$) in the e -th element, which, for the reciprocal u -directed field vector, are given by:

$$\mathbf{f}_{uqst}^e = u^q P_s(v) P_t(w) \frac{\mathbf{a}_v^e \times \mathbf{a}_w^e}{\mathfrak{I}^e},$$

$$P_s(v) = \begin{cases} 1-v, & s=0 \\ v+1, & s=1 \\ v^s-1, & s \geq 2, \text{ even} \\ v^s-v, & s \geq 3, \text{ odd} \end{cases} \quad (6)$$

$$\mathfrak{J}^e = (\mathbf{a}_u^e \times \mathbf{a}_v^e) \cdot \mathbf{a}_w^e, \mathbf{a}_u^e = \frac{\partial \mathbf{r}^e}{\partial u}, \mathbf{a}_v^e = \frac{\partial \mathbf{r}^e}{\partial v}, \mathbf{a}_w^e = \frac{\partial \mathbf{r}^e}{\partial w},$$

where \mathfrak{J}^e is the Jacobian of the covariant transformation, and \mathbf{a}_u^e , \mathbf{a}_v^e , and \mathbf{a}_w^e are the unitary vectors along the parametric coordinates of the element and analogously for the v - and w -directed basis functions.

Field-expansion orders N_u^e, N_v^e, N_w^e in (6) are entirely independent from each other, and can be combined independently for the best overall performance of the method. Furthermore, because the basis functions are hierarchical (each lower-order set of functions is a subset of all higher-order sets), all of the parameters can be adopted anisotropically in different directions within an element, and nonuniformly from element to element in a model. Note that indices in (6) are “collapsed” into one index in (5). This scheme is commonly used when members of a set must be accessed in linear fashion. One well known example is from computer science when multidimensional arrays must be arranged in a linear sequence in memory.

After Galerkin testing procedure, details of which can be found in [3], a generalized eigenvalue problem is obtained. Eigenvalues and eigenvectors (which come in form of coefficients in (5)) are obtained as solutions. Modal eigenfield is then easily obtained from (5).

IV. NUMERICAL RESULTS

For cavity problems, it is usually most important to obtain eigenfrequencies as accurately as possible. However, modal fields are also of interest. In the FEM algorithms the convergence is usually evaluated by comparison of S-parameters (for driven solutions), changes in overall scattering energy (for incident wave problems) or resonant frequencies (for eigenmode solutions) from pass to pass [8]. These quantities represent the results of the model as a whole, and usually converge more rapidly, i.e., with fewer unknowns, than the approximation of fields at individual points. However, it is interesting to study convergence of field solutions along with convergence of eigenvalues, in order to gain better insight into the needed number of unknowns, i.e., order of approximation, for specified accuracy. It is not uncommon for inexperienced engineers to set the prescribed accuracy too high, therefore considerably lengthening simulation times without any real benefit.

The electric field distributions for the dominant spherical mode, obtained by the analytical solution [9] and by the entire domain B-spline solution, are given in Figs. 3 and 4, respectively. The field solutions are plotted directly from the computed corresponding eigenvectors, thus they are practically identical except for the difference in the eigenvector normalization and except near the sphere “edges” (Fig. 4) where the entire-domain B-spline model has a discontinuous tangent (which is easily appreciated and can be improved by adopting higher order geometrical model or h -refinement). Note that, in this case, any attempt to quantify the error of the field distribution throughout the

element volume would be strongly biased by the significantly higher errors near these “edges”.

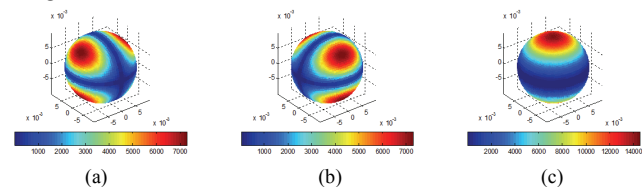


Fig. 3. Analytical solution: magnitudes of (a) x -, (b) y - and (c) z -components of the electric field for the first mode.

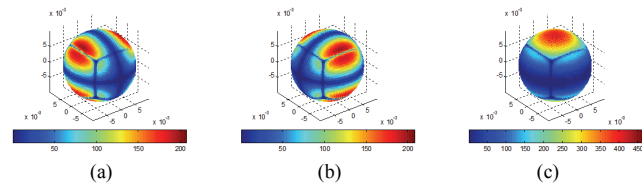


Fig. 4. B-spline solution (108 unknowns, “crude” geometry model): magnitudes of (a) x -, (b) y - and (c) z -components of the electric field for the first mode.

However, to establish an estimate of the accuracy and convergence of the solution of the electric field, when the number of unknowns is increased (by p -refinement), we compute the RMS error of the magnitude of the B-spline field solution relative to the analytical solution for the two models of spherical cavity in 1,016 and 1,736 surface points for the crude and refined models, respectively. Numerical results for the RMS error of the dominant mode eigenfield for the two solid models, along with the average eigenfrequency error for the first 11 modes, are given in Table I.

TABLE I
ERROR IN CALCULATING EIGENFREQUENCY AND MODAL FIELD IN A SPHERICAL CAVITY.

	Error [%]			
	Average eigenfrequency error (11 modes)			
Crude model	2.8666	0.2011	0.1098	0.0501
Refined model	2.8179	0.1470	0.0661	0.0097
	RMS error in modal field (1st mode)			
Crude model	20.79	20.60	40.63	17.30
Refined model	10.29	9.70	5.11	5.08
Unknowns	108	240	450	756

Results from Table I can be interpreted in the following way. Looking at the convergence of the eigenfrequencies, it is clear that both models have excellent convergence, i.e., error decreases monotonically and rapidly with the increase of the number of unknowns. Situation is less clear regarding modal field convergence. It is evident that the error in modal field is several orders of magnitude larger than the error in eigenfrequencies. Also, with the refined model, the convergence is monotonic. On the other hand, the crude model shows high error despite excellent eigenvalue convergence. This can be attributed to the offset between the ideal spherical cavity used for exact analytical solution, and crude spline model of the sphere. Hence, there is effectively a significant mismatch of points when point-by-point comparison of fields is applied in presence of the rapidly changing fields (as can be seen from Figs. 3 and 4).

The ridged cavity, shown in Fig. 5, is less grateful for comparison of modal field solutions because there is no readily available analytical solution. Hence, for the ridged cavity example, the B-spline solution and the reference

numerical HFSS solution, for the dominant mode electric field distribution, are presented in the large number of sampling points in Fig. 6, where very similar distributions of fields can be observed. Table II shows the relative error of the computed resonant free space wave number k_0 for the first 9 resonant modes.

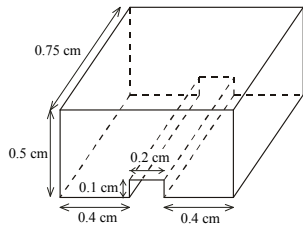


Fig. 5. Geometry of a ridged cavity.

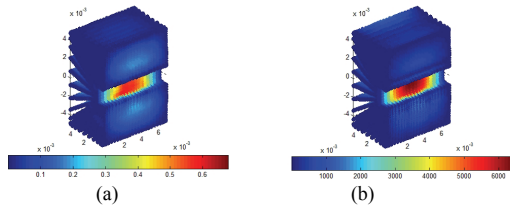


Fig. 6. Magnitude of the electric field of the first mode of the ridge taken in the large number (27,000 points) of sampling points: (a) HFSS and (b) B-spline solutions.

As for the modal field solution, RMS “error” for the first mode is 28.88%, when calculated in 27,000 volume points. This is again several orders of magnitude larger than the error in computed eigenfrequencies. This can be attributed to the fact that p -refined basis functions used in B-spline model are too smooth to model the field near reentrant corners of the ridge, where the field is theoretically singular. Furthermore, since there is no available exact solution, quantification of the error strongly depends on the HFSS

solution (and its convergence properties, number of adaptive passes, and initial mesh seeding).

TABLE II
ERROR IN CALCULATING k_0 IN THE RIDGED CAVITY.

Mode	HFSS k_0 [cm^{-1}]	B-spline Error [%]
Unknowns	3,017 t	276
1	5.091	0.0393
2	7.469	4.0969
3	7.853	0.4202
4	7.878	5.0774
5	8.019	3.8035
6	8.863	2.6853
7	8.9	4.3820
8	9.087	6.8119
9	10	3.9000

REFERENCES

- [1] J. M. Jin, *The Finite Element Method in Electromagnetics*, 2nd ed., John Wiley & Sons, New York, 2002.
- [2] B. M. Notaroš, “Higher order frequency-domain computational electromagnetics,” *IEEE Trans. Antennas Propag.*, vol. 56, pp. 2251–2276, 2008.
- [3] M. D. Davidović, B. M. Notaroš, and M. M. Ilić, “B-spline entire-domain higher order finite elements for 3-D electromagnetic modeling,” *IEEE Microwave and Wireless Components Letters*, vol. 22, no. 10, pp.497–499, 2012.
- [4] M. M. Ilić and B. M. Notaroš, “Higher order hierarchical curved hexahedral vector finite elements for electromagnetic modeling,” *IEEE Trans. Microw. Theory Techniques*, vol. 51, 1026–1033, 2003.
- [5] L. Valle, F. Rivas, and M. F. Cátedra, “Combining the moment method with geometrical modelling by NURBS surfaces and Bézier patches,” *IEEE Trans. Antennas Propag.*, vol. 42, pp. 373–381, 1994.
- [6] R. Coccioli, G. Pelosi, and S. Selleri, “Optimization of bends in rectangular waveguide by a finite-element genetic-algorithm procedure,” *Microw. Opt. Techn. Let.*, vol. 16, pp. 287–290, 1997.
- [7] L. A. Piegl and W. Tiller, *The NURBs Book*, Springer-Verlag, 1997.
- [8] HFSS ver. 11., Ansoft Corporation, Pittsburgh, PA, 2007.
- [9] R. F. Harrington, *Time-Harmonic Electromagnetic Fields*, Wiley, 2001.

ОЦЕНА ТЕХНИЧКОГ РЕШЕЊА

На основу сагласности Наставно-научног већа Електротехничког факултета у Београду датој на својој 758. седници одржаној 22.01.2013. године Комисија за студије трећег степена донела је одлуку да се прихвати техничко решење:

Назив техничког решења: Употреба МАДУ трака у биомедицинским експериментима

Аутори техничког решења: Анђелија Илић, Саша Ћирковић, Јасна Ристић – Ђуровић, Драго Ђорђевић, Александар Трбовић

Врста техничког решења: Битно побољшано решење на националном нивоу

М фактор техничког решења (М81-М86 фактор): М84

Београд, 15.01.2014.

Б.а. Председник Комисије за студије трећег степена

Бранко Колунџија
Проф. др Бранко Колунџија



Рецензија техничког решења

Битно побољшано техничко решење на националном нивоу (M84):

Употреба МАДУ трака у биомедицинским експериментима

Руководилац пројекта: Небојша Ромчевић

Одговорно лице: Анђелија Илић

Аутори: Анђелија Илић, Саша Ћирковић, Јасна Ристић-Ђуровић, Драго Ђорђевић, Александар Трбовић

Развијено: у оквиру пројекта Интегралних и интердисциплинарних истраживања (ИИИ), број ИИИ-45003

Година: 2013.

Примена: 01.03.2013.

Сматрам да су резултати истраживања описани у приложеној техничкој документацији техничко решење и да имају одговарајући стручни и научни допринос. О оригиналности резултата сведочи чињеница да су резултати детаљно описани у раду објављеном у међународном научном часопису *IEEE Transactions on Magnetics*, категорије M₂₂. На основу пружених података може се реализовати произвољан магнетски низ за употребу у биомедицини и прорачунати његови релевантни параметри. Такође, дати изрази су потпуно применљиви за генерички случај дводимензионог магнетског низа произвољне намене и могу послужити приликом пројектовања таквог низа.

Техничко решење припада широј области Примењена електромагнетика, са основном применом у области Биомедицинских наука, што је веома актуелно у светским оквирима. Састоји се од потпуних, егзактних, аналитичких изрази којима се описује магнетски низ; приближних изрази за брзу процену средњих параметара поља у експерименталној запремини; програма за прорачун електромагнетског поља у разматраној запремини; програма за одређивање жељених средњих параметара и упутства за употребу за кориснике решења. Провера је извршена нумерички и експериментално (мерењем поља).

Решење се засада употребљава од стране студената и сарадника Медицинског факултета у Београду за прецизну контролу и опис примењеног статичког магнетског поља у биомедицинским огледима. У доступној литератури није било примера коришћења дводимензионог магнетског низа у огледне сврхе, иако се сличне конфигурације магнета некада користе у клиничкој пракси али нажалост без прецизног познавања примењеног магнетског поља. У том смислу, решење може бити од користи и у клиничким применама.

У Београду, 20. новембра 2013.

Рецензент



Др Душко Борка, виши научни сарадник (ВНС)
Лабораторија за атомску физику (040),
Институт „Винча“, Београд

Рецензија техничког решења

Битно побољшано техничко решење на националном нивоу (M84):

Употреба МАДУ трака у биомедицинским експериментима

Руководилац пројекта: Небојша Ромчевић

Одговорно лице: Анђелија Илић

Аутори: Анђелија Илић, Саша Ћирковић, Јасна Ристић-Ђуровић, Драго Ђорђевић, Александар Трбовић

Развијено: у оквиру пројекта Интегралних и интердисциплинарних истраживања (ИИИ), број ИИИ-45003

Година: 2013.

Примена: 01.03.2013.

По увиду у техничку документацију горе наведеног решења, закључујем да оно испуњава услове да буде прихваћено као техничко решење. По мом мишљењу предложено решење има како стручни, тако и научни допринос. Потврду о научном доприносу представља и публикација категорије M₂₂ у међународном часопису *IEEE Transactions on Magnetics*, у потпуности посвећена опису техничког решења. У раду је дато довољно смерница за анализу и помоћ у пројектовању произвољног магнетског низа, чиме је омогућена директна примена решења од стране других заинтересованих корисника.

Техничко решење се односи на ширу научну област Примењене електромагнетике, а примена решења је интердисциплинарна и везана за област Биомедицинских наука, која се у свету тренутно веома брзо развија. Решење се заснива на комплетном скупу егзактних аналитичких израза за опис поља изнад дводимензионог магнетског низа, из њега изведених веома једноставних апроксимативних израза за процену средњих параметара магнетског поља и софтверској имплементацији ових теоријских резултата за потребе крајњег корисника.

Суштина техничког решења је да се веома прецизно одреде сви параметри од интереса статичког магнетског поља примењеног у огледној запремини и да се примењено поље веома детаљно опише, што је императив у научно-истраживачком раду. Теоријски резултати могу наћи и ширу примену, будући да су магнетски низови значајни и за микроактуаторске системе и микросензоре, планарне моторе и слично. Сви резултати су потврђени како нумеричком симулацијом тако и директно, мерењем магнетског поља.

Развијено решење се употребљава на Медицинском факултету у Београду.

У Београду, 20. новембра 2013.

Рецензент

Катарина Радуловић

Др Катарина Радуловић, научни саветник (НСВ)
Института за хемију, технологију и металургију,
Београд

Универзитет у Београду
Иновациони центар Електротехничког факултета

А. Илић, С. Ђирковић, Ј. Ристић-Ђуровић, Д. Ђорђевић и А. Трбовић

УПОТРЕБА МАДУ ТРАКА
У БИОМЕДИЦИНСКИМ ЕКСПЕРИМЕНТИМА
– Техничка документација –



Београд, 2013.

M84: Битно побољшано техничко решење на националном нивоу УПОТРЕБА МАДУ ТРАКА У БИОМЕДИЦИНСКИМ ЕКСПЕРИМЕНТИМА

Руководилац пројекта: Небојша Ромчевић
Одговорно лице: Анђелија Илић
Аутори: Анђелија Илић, Саша Ђирковић, Јасна Ристић-Ђуровић, Драго Ђорђевић, Александар Трбовић
Развијено: у оквиру пројекта Интегралних и интердисциплинарних истраживања (ИИИ), број ИИИ-45003
Година: 2013.
Примена: 01.03.2013.

Кратак опис

У склопу овог техничког решења, изведене су и дате егзактне формуле за рачунање магнетске индукције произвољног дводимензионог магнетског низа, на основу њих је предложен једноставан начин одређивања средњих параметара магнетског поља који су од интереса за кориснике оваквих низова, написана је процедура за MATLAB која рачуна расподелу поља и средње параметре за произвољан случај. За конфигурације које се уобичајено користе подаци су дати и табеларно, у оквиру “Упутства за употребу МАДУ трака у биомедицинским огледима“, припремљеног за студенте и сараднике Медицинског факултета у Београду.

Реализатори:

Иновациони центар Електротехничког факултета, Универзитет у Београду

Корисници:

Медицински факултет, Универзитет у Београду

Подтип решења:

Битно побољшано техничко решење на националном нивоу (M84)

Стање у свету

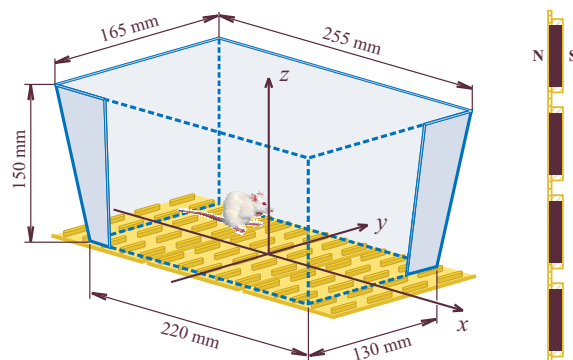
Стални магнети, као и њихове комбинације у виду површинских низова, користе се већ дуго времена у области физикалне терапије и рехабилитације. Иако сви механизми деловања нису у потпуности разјашњени, емпиријски је утврђен благотворан, односно позитиван, утицај на ублажавање тегоба проузрокованих артритисом, ублажавање запаљења и залечивање рана, ублажавање бола и стреса и побољшање микроциркулације [1]-[6]. Такође, различите комбинације сталних магнета су погодне као извор статичког магнетског поља у биомедицинским огледима *in vitro* или огледима на малим животињама, као у [7]. Овде је потребно нагласити, да током прегледа постојеће литературе нисмо наишли на пример коришћења дводимензионог магнетског

низа као што су МАДУ траке, медицинско средство патентирано за примену у физикалној терапији и рехабилитацији [8]. По три МАДУ траке су употребљене за формирање већих низова који покривају површину испод дна стандардног малог кавеза у нашим експериментима описаним у радовима [9], [10]. Генерички случај дводимензионог магнетског низа је анализиран у раду [1].

Упркос успешној употреби МАДУ трака у медицинској пракси, детаљан опис њихових карактеристика који је неопходан за опис изведених огледа и даље извођење закључака је био недоступан, укључујући и тачну вредност реманентне магнетске индукције материјала. Истраживање спроведено 2007. године је указало на то да непотпун или недовољно прецизан опис употребљених поља представља главни недостатак у великом броју публикација које се баве утицајем електромагнетских поља на живе организме [11]. Дводимензиони магнетски низови имају и велики број немедицинских примена, укључујући микроактуаторске системе, микросензоре, синхроне планарне моторе и магнетску левитацију. Међутим, велики низови се уобичајено анализирају применом Фуријеових низова, док се за конкретан случај низа мањег броја елемената најчешће користи моделовање коначним елементима. Изведени комплетни аналитички изрази за општи случај оваквог низа се могу једноставно применити, а погодни су и за оптимизацију параметара низа. Провера је извршена методом коначних елемената и мерењем.

Опис

На слици 1 је приказан начин употребе МАДУ трака у биомедицинским огледима. Коришћене су МАДУ траке типа L (large), које представљају низ од 5-пута-4 сталних магнета распоређених еквиливантно, у оба правца. За стандардни мали кавез (22,0 mm x 13,5 mm x 15,0mm) потребно је коришћењем три траке формирати низ од 15-пута-4 магнета, док се за стандардни велики кавез (38,0 mm x 21,0 mm x 18,5mm) формира низ од 12-пута-10 магнета коришћењем шест трака. За разлику од магнетских низова са супротно усмереним магнетским моментима суседних елемената, у једној или у обе димензије, или низова са ротираним магнетским моментима као што је то предложио К. Халбах [12], код којих је циљ остваривање што јаче магнетске индукције уз површину низа, скоро паралелне површи, променљивог смера између суседних редова, МАДУ траке спадају у низове код којих сви елементи имају идентичну оријентацију магнетских момената управну на површину низа. Као резултат, добија се магнетска индукција претежно управна на површину низа, изнад неке граничне висине увек истог знака, која споро опада са растојањем од површине низа. Варијације поља у појединачним водоравним равнима су знатно мање од варијација са променом висине, те се и магнетска индукција и градијент вертикалне компоненте магнетске индукције, који се показује довољним за опис промена поља, могу у првој апроксимацији сматрати функцијама само z -координате.



Слика 1. Дводимензиони магнетски низ погодан за коришћење у биомедицинским огледима. Приказан је усвојени референтни координатни систем. Произведено магнетско поље споро опада са растојањем од површине низа и прожима, односно покрива, целу огледну запремину.

Аналитички опис магнетског поља низа

Услед своје примарне намене да лако приањају на делове људског тела, попут магнетског завоја, МАДУ траке су реализоване уграђивањем појединачних магнета у супстрат од еластичног, гумастог дијамагнетика чији се утицај може у потпуности занемарити. Претпостављајући униформну магнетизацију по запремини сваког појединачног магнетића, сваки од њих се може заменити површинским Амперовим струјама, односно еквивалентним кратким соленоидом правоугаоног попречног пресека. На тај начин се проблем своди на одређивање магнетске индукције коначног броја правоугаоних површинских струјних расподела. Магнетска индукција једне правоугаоне траке се може добити коришћењем добро познатог израза за праву струјну нит коначне дужине који следи директно из Био-Саваровог закона:

$$B = \frac{\mu_0 dI}{4\pi d} (\sin \theta_2 - \sin \theta_1). \quad (1)$$

Јачина струје $dI = J_{ms} dz$ у нити инфинитезималне висине dz ствара у тачки поља F компоненту магнетске индукције, B , нормалну на раван дефинисану правцем жице и тачком F , смера усклађеног са правилом десне завојнице. Вектор површинске густине струје, \mathbf{J}_{ms} , је повезан са магнетизацијом, \mathbf{M} , преко $\mathbf{J}_{ms} = \mathbf{M} \times \mathbf{n}$, где је \mathbf{n} површинска нормала. Удаљеност тачке F од праве која садржи посматрану нит је означена са d и одговарајућа нормала на нит уједно служи као референтна оса за углове θ_1 и θ_2 , при чему индекси 1 и 2 одговарају тачкама уласка струје у нит и изласка из нити, респективно. Најповољнији интегрални за решавање се добијају уколико се угао између потега d и хоризонталне равни која садржи нит означи као ξ , и све остале величине израза преко овог угла. Након интеграције и сређивања изрази за хоризонталне компоненте магнетске индукције постају

$$\begin{aligned} B_x(x,y,z) &= \frac{\mu_0 J_{ms}}{4\pi} \sum_{i=-M}^M \sum_{j=-N}^{N-1} \sum_{k=1,3} \sum_{tp=0}^1 \sum_{tq=0}^1 \frac{(-1)^{(tp+tq+1)}}{\operatorname{sgn}((j+\frac{1}{2}) \cdot y_d + (-1)^{m_s + tp + 1} \frac{a}{2} - y)} \\ &\quad \cdot \ln \left(-|u_{i,j,k}^{a,tq}| + \sqrt{(u_{i,j,k}^{a,tq})^2 + (r_{i,j,k}^{a,tp})^2} \right), \\ B_y(x,y,z) &= \frac{\mu_0 J_{ms}}{4\pi} \sum_{i=-M}^M \sum_{j=-N}^{N-1} \sum_{k=2,4} \sum_{tp=0}^1 \sum_{tq=0}^1 \frac{(-1)^{(tp+tq)}}{\operatorname{sgn}(i \cdot x_d + (-1)^{m_s + tp} \frac{b}{2} - x)} \\ &\quad \cdot \ln \left(-|u_{i,j,k}^{b,tq}| + \sqrt{(u_{i,j,k}^{b,tq})^2 + (r_{i,j,k}^{b,tp})^2} \right), \\ r_{i,j,k}^{a,tp} &= \frac{(i x_d + (-1)^{m_s} \frac{b}{2} - x)}{((j+\frac{1}{2}) \cdot y_d + (-1)^{m_s + tp + 1} \frac{a}{2} - y)}, \quad r_{i,j,k}^{b,tp} = \frac{((j+\frac{1}{2}) \cdot y_d + (-1)^{m_s} \frac{a}{2} - y)}{(i x_d + (-1)^{m_s + tp} \frac{b}{2} - x)}, \\ u_{i,j,k}^{a,tq} &= \frac{(i x_d + (-1)^{m_s} \frac{b}{2} - x)}{\sqrt{(i x_d + (-1)^{m_s} \frac{b}{2} - x)^2 + (z + t + (1-tq) \cdot h)^2}}, \\ u_{i,j,k}^{b,tq} &= \frac{((j+\frac{1}{2}) \cdot y_d + (-1)^{m_s} \frac{a}{2} - y)}{\sqrt{((j+\frac{1}{2}) \cdot y_d + (-1)^{m_s} \frac{a}{2} - y)^2 + (z + t + (1-tq) \cdot h)^2}}, \quad m_s = \frac{1 - \operatorname{sgn}(k - \frac{5}{2})}{2}. \end{aligned} \quad (2)$$

Дужина, ширина и висина појединачног магнета, елемента низа, су означене као a , b и h , а међусобна одстојања у правцу x - и y -осе као x_d и y_d . Индекси i и j одговарају елементу i у реду j магнетског низа, док индекс k означава једну од четири струјне траке које одговарају посматраном елементу низа. За k једнако 1, 2, 3, или 4, струјна трака је померена за $\Delta x = -b/2$, $\Delta y = -a/2$, $\Delta x = b/2$, односно $\Delta y = a/2$, у односу на средиште посматраног елемента. Претпостављено је да се низ састоји од $(2M+1)$ -пута- $(2N)$ елемената, без губитка на општости. Горњи индекс $tp = 0$ односно $tp = 1$

одговара референтном смеру струје у струјној траци који је увек од 0 ка 1. Горњи индекс $tq = 0$ или $tq = 1$ означава доњу површину, $z = -t \cdot h$, или горњу површину, $z = -t$, магнета, где је t дебелина гуменог омотача МАДУ, траке у коју су уграђени магнети. Вертикална координата $z = 0$ према томе одговара ситуацији када узорак лежи на самој површини траке или трака приања уз узорак.

Вертикална компонента вектора магнетске индукције, која је у случају низа са истоветно оријентисаним појединачним магнетским моментима елемената управним на низ много већа од B_x , B_y , односно доминантна, износи

$$B_z(x, y, z) = \frac{\mu_0 J_{ms}}{4\pi} \sum_{i=-M}^M \sum_{j=-N}^{N-1} \sum_{k=1}^4 \sum_{tp=0}^1 \sum_{tq=0}^1 (-1)^{(tp+tq+1)} \arcsin(p_{i,j,k}^{tp} \cdot q_{i,j,k}^{tq}),$$

$$p_{i,j,k}^{tp} = \frac{(ix_d + (-1)^{\lfloor \frac{k}{2} \rfloor})^{tp} \frac{b}{2} - x)^{m_2} \cdot ((j + \frac{1}{2}) \cdot y_d + (-1)^{\lfloor \frac{k-1}{2} \rfloor})^{tp} \frac{a}{2} - y)^{m_1}}{\sqrt{(ix_d + (-1)^{\lfloor \frac{k}{2} \rfloor})^{1+(tp-1)m_2} \frac{b}{2} - x)^2 + ((j + \frac{1}{2}) \cdot y_d + (-1)^{\lfloor \frac{k-1}{2} \rfloor})^{1+(tp-1)m_1} \frac{a}{2} - y)^2}},$$

$$q_{i,j,k}^{tq} = \frac{\operatorname{sgn}(ix_d + (-1)^{m_s} \frac{b}{2} - x)^{m_1}}{(-\operatorname{sgn}((j + \frac{1}{2}) \cdot y_d + (-1)^{m_s} \frac{a}{2} - y))^{m_2}} \cdot (z + t + (1 - tq) \cdot h)}$$

$$\sqrt{(ix_d + (-1)^{m_s} \frac{b}{2} - x)^{2m_1} ((j + \frac{1}{2}) \cdot y_d + (-1)^{m_s} \frac{a}{2} - y)^{2m_2} + (z + t + (1 - tq) \cdot h)^2}},$$

$$m_1 = (1 + (-1)^{k-1})/2, \quad m_2 = (1 + (-1)^k)/2, \quad m_s = (1 - \operatorname{sgn}(k - \frac{5}{2}))/2.$$

Овде параметри p и q одговарају синусима углова θ_0 и ξ , где смо са θ_0 означили пројекцију угла θ на xOy раван. Оператор $[\cdot]$ означава целобројно дељење.

Са повећањем броја појединачних магнета у оба правца у хоризонталној равни, z -компонента вектора магнетске индукције тежи граничном случају бесконачног низа, када је она периодична са периодом x_d односно y_d , у правцу x - и y -осе, респективно. У случају коначног низа описана расподела вектора магнетске индукције одговара централном делу запремине изнад низа. Сматрајући хоризонталне компоненте вектора магнетске индукције довољно малим да се искључе из разматрања, максимум и минимум магнетске индукције у појединачној посматраној хоризонталној равни се могу изједначити са z -компонентом у одговарајућим тачкама, израчунатом на основу израза (3). Притом максимуму одговара магнетска индукција на вертикалној оси која пролази тачно кроз центар појединачног магнета у централном делу траке, $B_H(z)$. Минимум, $B_V(z)$, се налази као вредност на вертикалној оси која пролази кроз тачку пресека линија које тачно одговарају средини између суседних редова магнета у правцу x - и y -осе. Дефинишимо вертикални градијент магнетске индукције као:

$$G_z(x, y, z) = -\operatorname{grad}_z B_z(x, y, z) = -\frac{\partial B_z(x, y, z)}{\partial z}. \quad (4)$$

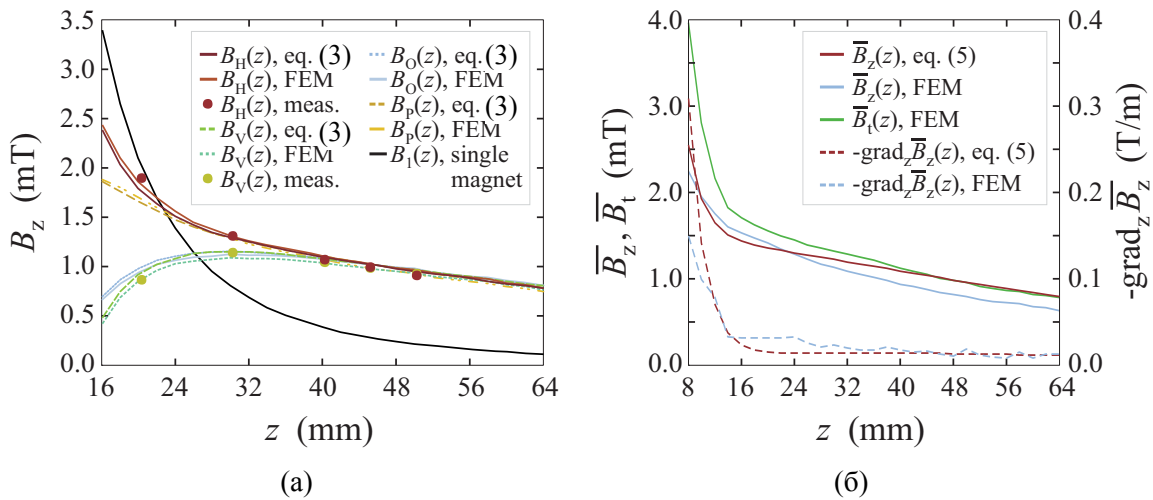
Тада се средња вредност магнетске индукције и усредњени вертикални градијент магнетске индукције у посматраним хоризонталним равнима могу проценити коришћењем аритметичке средине $B_H(z)$ и $B_V(z)$.

$$\overline{B_z(z)} = \frac{B_H(z) + B_V(z)}{2}, \quad \Delta B_z(z) = \frac{B_H(z) - B_V(z)}{2},$$

$$\overline{G_z(z)} = -\operatorname{grad}_z \overline{B_z} = -\frac{1}{2} \left(\frac{\partial B_H(z)}{\partial z} + \frac{\partial B_V(z)}{\partial z} \right) = \frac{G_H(z) + G_V(z)}{2}, \quad (5)$$

$$\Delta G_z(z) = \frac{G_H(z) - G_V(z)}{2}, \quad G_H = -\frac{\partial B_H(z)}{\partial z}, \quad G_V = -\frac{\partial B_V(z)}{\partial z}.$$

Код овде описаних трака број елемената низа је релативно мали (15 пута 4), док су величине појединачних магнета ($a \times b \times h = 24.4 \text{ mm} \times 4.8 \text{ mm} \times 4.8 \text{ mm}$), однос њихове дужине и ширине (aspect ratio) и растојања између редова ($x_d = 19.5 \text{ mm}$, $y_d = 36.0 \text{ mm}$) значајни. На неки начин, то је најнеповољнији случај за проверу предложеног приступа. Као што се види из дела (б) Сlike 2, и у овом неповољном случају се добија резултат задовољавајуће тачности, који се може искористити за брзу процену средњих параметара магнетског поља у огледној запремини. Такође, израз (5) може да послужи за процену магнетске индукције и њеног вертикалног градијента током прелиминарног дизајна низова са захтеваним средњим параметрима поља.



Слика 2. Поређење аналитички изведених израза са измереним подацима (“meas.”) и подацима израчунатим методом коначних елемената (“FEM”). (а) На већим висинама, z , разлике $B_H(z)$ и $B_V(z)$ постају скоро занемарљиве, а магнетска индукција опада линеарно. (б) Изрази (5) за средњу магнетску индукцију и средњи вертикални градијент индукције показују задовољавајуће слагање са резултатима нумеричког прорачуна (“FEM”), где је приказана и средња вредност укупне магнетске индукције $B_t = \sqrt{B_x^2 + B_y^2 + B_z^2}$. Изрази (5) су погодни за брзу процену параметара поља у огледној запремини, као и приликом прелиминарног дизајна дводимензионих магнетских низова.

Контролна мерења магнетског поља низа

Мерења магнетског поља МАДУ трака имала су двојаку намену. Најпре, подаци о тракама су били веома непотпуни и мерењем је утврђена реманентна магнетизација употребљених магнета. Као друго, мерења су послужила да се потврде изведени аналитички изрази као и да се провере резултати добијени нумеричком симулацијом.

Мерна мрежа се састојала од по двадесет и једне тачке у сваком од три реда, два изнад магнета и трећег између ова два реда, у равнима паралелним xOy равни. Мерни корак у правцу x - и y -осе је износио $x_d/2 = 9.75 \text{ mm}$, односно $y_d/2 = 18.0 \text{ mm}$, што одговара максимумима и минимумима магнетске индукције. Мерења су извршена коришћењем дигиталног тесламетра DTM 151 (Group 3, New Zealand), са резолуцијом мерења од 0.005 mT и прецизношћу читавања од 0.01% , у коришћеном опсегу до 0.3 T [13].

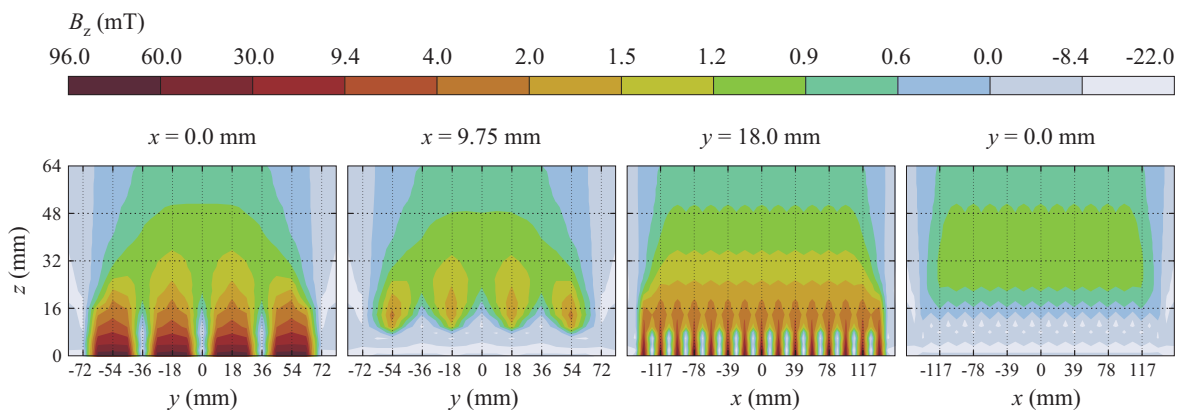
Познато је да су магнети израђени од хексагоналног баријум хексаферита ($\text{BaFe}_{12}\text{O}_{19}$), једног од најчешће коришћених тврдих магнетских материјала, услед ниске производне цене и веома добрих феромагнетских својстава. Киријева температура је висока и износи $T_C = 450^\circ\text{C}$. Магнетска индукција када је материјал у zasiћењу износи $B_s = 480 \text{ mT}$, што када се узме у обзир густина материјала $\rho = 4.9 \cdot 10^3 \text{ kg/m}^3$ одговара магнетизацији у zasiћењу $M_s = 78.0 \text{ A} \cdot \text{m}^2/\text{kg}$. За разлику од ових својстава која не зависе од микроструктуре материјала, реманентна магнетизација може доста

да варира у зависности од производног процеса, посебно времена синтеровања и примењене температуре. Уз коришћење израза (3), довољно је прецизно измерити магнетску индукцију за неколико вредности z -координате (висине), на посматраној вертикалној оси кроз магнет у центру низа. Како смо због провере резултата вршили мерења у већем броју тачака, за карактеризацију материјала мерењем коришћени су усредњени подаци о максимумима и минимумима магнетске индукције за пет хоризонталних равни, $z \in \{19.4, 29.4, 39.4, 44.4, 49.4\}$ mm. За посматрани низ, за пробну вредност реманентне магнетизације M_r , одређене су на основу (3) функције $B_H(z)$ и $B_V(z)$, а затим мултипликативна константа која даје најмање средњеквадратно одступање у односу на усредњене мерене податке. Након корекције, добија се $M_r = 60.0 \text{ A}\cdot\text{m}^2/\text{kg}$.

Укупно, изведене су три групе мерења. Најпре, мерењем са једне и друге стране траке на самој површини трака установљена је магнетска индукција (55.70 ± 7.22) mT и (54.34 ± 7.22) mT, дата као (средња вредност \pm стандардна девијација). Грешка ручно изведеног мерења, услед јачег или слабијег приањања сонде на мек гумени омотач или благог нагиба у односу на хоризонталну раван, је највећа на површини траке, те су добијене вредности нешто ниже од теоријски предвиђених 59.62 mT. Друга група мерења је изведена са једним слојем, а трећа са по два и три слоја МАДУ трака, за вредности z -координате: $z \in \{4.4, 6.5, 9.4, 19.4, 29.4, 39.4, 44.4, 49.4\}$ mm. Релативна варијабилност резултата, процењена као однос стандардне девијације и средње вредности, је два пута мања за други и трећи скуп мерења у односу на прву групу.

Поређење са нумерички израчунатим подацима

Магнетска индукција МАДУ трака је такође израчуната коришћењем софтверског пакета Metmaid за магнетостатику [14], [15]. Дати програмски пакет, који служи за дизајн делова уређаја од перманентних или електромагнета, користи скаларне коначне елементе првог реда за рачунање магнетостатичког потенцијала. Добијени резултати су показали одлично слагање са аналитичким изразима, што је приказано на Слици 2. Илустрације ради, на Слици 3 је приказана расподела магнетске индукције изнад трака за четири вертикална пресека, укључујући и расипно поље. Доминантна, B_z , компонента чини више од 96% укупне магнетске индукције у делу изнад магнета у центру и више од 80% укупне магнетске индукције свуда у централном делу траке.



Слика 3. Варијација магнетске индукције у огледној запремини добијена нумеричким прорачуном. Овде је приказана доминантна, B_z , компонента за два пресека паралелна yOz равни и два пресека паралелна xOz равни, од којих по један полови магнете а други одговара тачно средини између два суседна реда магнета. За пресеке паралелне xOz равни расипно магнетско поље се налази изван огледне запремине и претпоставке о периодичности магнетске индукције су потпуно оправдане. У овом конкретном случају, број магнета у правцу y -осе је мали а њихово међусобно растојање значајно, што чини аналитичку процену (5) само апроксимативном.

Модификација поља у огледној запремини

Некада је потребно остварити жељене, захтеване средње параметре статичког магнетског поља у експерименталној запремини. Једноставан начин повећања магнетске индукције за фактор који не зависи од висине изнад низа је употреба више слојева трака, као што је то приказано на Слици 4 (а). За различите комбинације пораста магнетске индукције и њеног вертикалног градијента, изрази (5) се могу употребити као почетан алат у пројектовању новог низа жељених карактеристика. Ово је илустровано у делу (б) Слике 4. За потребе корисника МАДУ трака, на основу горе изложеног, састављено је “Упутство за употребу МАДУ трака у биомедицинским огледима“. Такође, написана је процедура за рачунар која за задати низ и огледну запремину ограничену двома хоризонталним равнима $z = h_1$ и $z = h_2$, одређује средње параметре магнетског поља у огледној запремини, као што је за неколико уобичајених случајева приказано у Табели I и Табели II. Тренутно се упутство и поменута процедура у MATLAB-у користе од стране студената и сарадника Медицинског факултета у Београду.

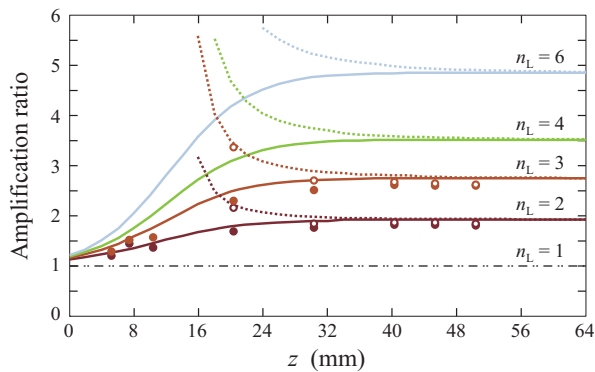
ТАБЕЛА I
СРЕДЊИ ПАРАМЕТРИ МАГНЕТСКОГ ПОЉА
У ОГЛЕДНОЈ ЗАПРЕМИНИ

h_1 (mm)	h_2 (mm)	$\overline{B_z}$ (mT)	$\overline{B_t}$ (mT)	$\overline{G_z}$ (T/m)
0.0 *	10.0	15.4394	16.1613	1.8549
0.0 *	20.0	9.1341	9.6192	1.0302
0.0 *	30.0	6.6632	7.0497	0.7165
16.0	46.0	1.1371	1.3127	0.0223
24.0	54.0	0.9719	1.1476	0.0176
32.0	62.0	0.8442	1.0122	0.0141

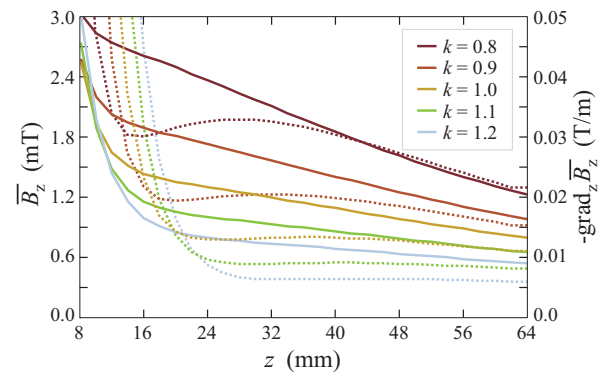
* за прва три реда коришћено је $|B_z|$

ТАБЕЛА II
СРЕДЊИ ПАРАМЕТРИ МАГНЕТСКОГ ПОЉА
ЗА ВИШЕ СЛОЈЕВА МАДУ ТРАКА

h_1 (mm)	h_2 (mm)	$\overline{B_z}$ (mT)	$\overline{B_t}$ (mT)	$\overline{G_z}$ (T/m)
Два слоја				
16.0	46.0	2.1932	2.5316	0.0431
24.0	54.0	1.8715	2.2096	0.0350
32.0	62.0	1.6214	1.9442	0.0276
Три слоја				
16.0	46.0	3.4402	3.9597	0.0636
24.0	54.0	2.7465	3.2406	0.0518
32.0	62.0	2.3294	2.7931	0.0402



(a)



(б)

Слика 4. (а) Повећање магнетске индукције коришћењем више слојева МАДУ трака. Како средња магнетска индукција опада линеарно са висином, значајан фактор увећања поља, скоро једнак броју трака n_L , се добија постављањем једне траке на другу. Пуне линије одговарају максималној индукцији, $B_H(z)$, испрекидане минималној, $B_V(z)$, док су одговарајући измерени подаци приказани пуним и празним кружићима, респективно. (б) Илустрација коришћења приближних израза (5) у прелиминарном дизајну магнетског низа жељених средњих параметара поља. Приказане су промене средње магнетске индукције (пуне линије) и њеног вертикалног градијента (испрекидане линије) са модификацијом растојања између редова магнета за фактор k , овде узет једнак у правцу x - и y -осе.

Закључак

Изведени су комплетни изрази за магнетску индукцију произвољног дводимензионог магнетског низа, који осим осталих примена може да буде погодан извор магнетског поља у биомедицинским експериментима. Мерењем је извршено одређивање реманентне магнетизације материјала, а такође и потврђени аналитички изрази и нумерички прорачуни методом коначних елемената. Припремљена је процедура у MATLAB-у која за потребе корисника рачуна средње параметре поља у огледној запремини, а подаци за најчешће случајеве приказани и табеларно.

Литература

- [1] A. Ž. Ilić, S. Ćirković, D. M. Djordjevic, S. R. De Luka, I. D. Milovanovich, A. M. Trbovich, J. L. Ristić-Djurović, "Analytical description of two-dimensional magnetic arrays suitable for biomedical applications," *IEEE Transactions on Magnetics*, vol. 49, No. 12, Dec. 2013.
- [2] M. I. Weintraub, G. I. Wolfe, R. A. Barohn *et al.*, "Static magnetic field therapy for symptomatic diabetic neuropathy: a randomized, double-blind, placebo-controlled trial," *Archives of Physical Medicine and Rehabilitation*, vol. 84, no. 5, pp. 736–746, May 2003.
- [3] N. A. Segal, Y. Toda, J. Huston *et al.*, "Two configurations of static magnetic fields for treating rheumatoid arthritis of the knee: a double-blind clinical trial," *Archives of Phys. Med. and Rehab.*, vol. 82, no. 10, pp. 1453–1460, Oct. 2001.
- [4] C. Vallbona, C. F. Hazlewood, and G. Jurida, "Response of pain to static magnetic fields in postpolio patients: a double-blind pilot study," *Arch. of Phys. Med. and Rehab.*, vol. 78, no. 11, pp. 1200–1203, Nov. 1997.
- [5] H. N. Mayrovitz and E. E. Groseclose, "Effects of a static magnetic field of either polarity on skin microcirculation," *Microvascular Research*, vol. 69, no. 1–2, pp. 24–27, Jan. 2005.
- [6] Y. Yan, G. Shen, K. Xie *et al.*, "Wavelet analysis of acute effects of static magnetic field on resting skin blood flow at the nail wall in young men," *Microvascular Research*, vol. 82, no. 3, pp. 277–283, Nov. 2011.
- [7] A. H. Hashish, M. A. El-Missiry, H. I. Abdelkader, R. H. Abou-Saleh, "Assessment of biological changes of continuous whole body exposure to static magnetic field and extremely low frequency electromagnetic fields in mice," *Ecotoxicology and Environm. Safety*, vol. 71, pp. 895–902, Nov. 2008.
- [8] D. Mandić, "Surface magnetised elastic magnetic stripe and application," Patent No. (WO1999060581), available online at: <http://patentscope.wipo.int/search/en/WO1999060581>.
- [9] D. M. Djordjević, S. R. De Luka, I. D. Milovanovich, S. Janković, S. Stefanović, S. Vesković-Moračanin, S. Ćirković, A. Ž. Ilić, J. L. Ristić-Djurović, A. M. Trbovich, "Hematological parameters' changes in mice subchronically exposed to static magnetic fields of different orientations," *Ecotoxicology and Environm. Safety*, vol. 81, pp. 98–105, July 2012.
- [10] S. R. De Luka, D. M. Djordjević, I. D. Milovanovich *et al.*, "Subchronic exposure to static magnetic field affects zinc and copper content in mice brain and liver," submitted for publication.
- [11] A. P. Colbert, H. Wahbeh, N. Harling *et al.*, "Static magnetic field therapy: a critical review of treatment parameters," *Evidence Based Complem. and Alternative Med.*, vol. 6, no. 2, pp. 133–139, June 2009.
- [12] K. Halbach, "Design of permanent multipole magnets with oriented rare earth cobalt material," *Nucl. Instruments and Methods*, vol. 169, no. 1, pp. 1–10, Feb. 1980.
- [13] Group3, *DTM-151 Digital Teslameter with serial communications*, User's Manual.
- [14] MERMAID 2D and 3D User's Guide, SIM, Novosibirsk, Russia, 1994.
- [15] N. A. Dubrovin, E. A. Simonov, S. B. Vorozhtsov, "MERMAID 3D code in ATLAS applications," ATLAS Note ATL-TECH-2001-003, CERN, Geneva 2001.

**Техничко решење је развијено у Иновационом центру Електротехничког факултета у Београду, у оквиру пројекта број ИИИ-45003 Министарства просвете, науке и технолошког развоја Србије
Штампано децембра 2013.**